Université de Strasbourg

Institut Terre & Environnement de Strasbourg | ITES | UMR 7063 de l'Université de Strasbourg & CNRS & ENGEES

École doctorale Sciences de la terre et de l'environnement | ED 413 Université de Strasbourg

École doctorale sciences de la terre et de l'environnement

Institut Terre et Environnement de Strasbourg

THÈSE

présentée par

Mélanie BALLAY

soutenue le : **10 octobre 2024**

pour obtenir le grade de : **Docteur de l'université de Strasbourg**

Discipline/ Spécialité : Sciences de la Terre et de l'Environnement

Étude pétrologique et géochimique d'une marge passive pauvre en magma : le cas de la transition océan-continent Australie-Antarctique

THÈSE dirigée par :

M. ULRICH Marc	Maitre de conférences, Université de Strasbourg – ITES
M. MANATSCHAL Gianreto	Professeur des Universités, Université de Strasbourg – ITES

RAPPORTEURS :

M. CEULENEER Georges	Directeur de recherches, Université de Toulouse – GET
Mme GODARD Marguerite	Directrice de recherches, Géosciences Montpellier

AUTRES MEMBRES DU JURY :

M. CHAZOT Gilles	Professeur des Universités, Université de Bretagne Occidentale – IUEM
Mme KACZMAREK Mary-Alix	Maîtresse de conférences, Université de Toulouse – GET
M. MÜNTENER Othmar	Professeur des Universités, Université de Lausanne (Suisse)
M. SAUTER Daniel	Directeur de recherches, Université de Strasbourg – ITES

Résumé étendu

Les marges passives, c'est-à-dire des transitions océans-continent sismiquement inactives, marquent géographiquement, topographiquement, tectoniquement, mais également temporellement la transition entre une zone de lithosphère continentale et une zone de lithosphère océanique. En effet, ces zones enregistrent temporellement la transition géodynamique entre un rifting continental et une expansion océanique. Les marges passives sont classées en plusieurs types : transformantes, riches en magma ou pauvres en magma ; on comprend donc d'ores et déjà la place que peut avoir le magma dans ces systèmes. Et pourtant, il s'agit sans doute du paramètre le moins bien contraint dans les nombreux modèles de formation des marge passives dont on dispose. Longtemps apparentées à de simples extensions géographiques de dorsales, l'étude des marges passives pauvres en magma a montré qu'elles constituent un type magmatique à part entière et dont l'impact sur la formation de la zone de transition ne peut être négligé, indépendamment du type de marge étudiée. Les marges passives pauvres en magma représentent ~50% de ces marges passives, et constituent une zone clé pour l'étude spatio-temporelle de la mise en place des rides médio-océaniques. En effet, les marges enregistrent latéralement cette évolution temporelle du passage d'une lithosphère continentale à une lithosphère océanique en accrétion au niveau de la ride médio-océanique avec notamment la présence des premiers magmas produits. Le dogme actuel, largement débattu, propose que marges passives riches en magma sont formées dû à un budget magmatique très important lors de l'ouverture, ce qui les lie très généralement à la présence d'un point chaud, on parle dans ce cas de rifting actif. A contrario, les marges passives pauvres en magma seraient contrôlées par la tectonique, entrainant une exhumation mantellique importante au plancher océanique et un déficit d'extrusion magmatique. Ce faible budget magmatique est alors attribué à une ouverture lente ne permettant pas d'atteindre la fusion partielle du manteau sous-jacent, ou en de rares endroits. Mais, les discussions scientifiques actuelles proposent également que cela soit lié à de faibles gradients thermiques ou à l'hérédité mantellique sous-continentale. Cette question du budget magmatique ainsi que du lien entre magmatisme et manteau sous-jacent est au cœur des discussions actuelles et constitue la prochaine étape dans les modélisations numériques de formation d'une zone de marge passive pauvre en magma.

Les études des marges riftées peu magmatiques se sont portées sur quelques rares endroits géographiques dont les marges actuelles conjuguées d'Ibérie-Terre-Neuve et les paléo-marges téthysiennes présentent dans les Alpes. Leurs études ont permis de développer, notamment grâce à des approches pétrologiques et géochimiques sur les roches mantelliques, un modèle simple mais communément accepté, où le manteau sous-continental exhumé est subdivisé en plusieurs domaines en fonction de son héritage, des processus de fusion et/ou des interactions qu'il a subi avec le magma ascendant. Ce modèle, ainsi que les études préalables ont démontré l'importance de l'héritage mantellique dans la formation de ces marges, posant la question principale de sa validité dès lors que l'on s'éloigne de la zone européenne.

La marge australienne, draguée lors de deux campagnes océanographiques du Marion Dufresne (MD80 en 1994 et MD110 en 1998), est un lieu de choix pour confronter ce modèle a un autre héritage, plus ancien. En effet, situées le long de la zone Diamantine (sud-ouest de l'Australie), entre le domaine continental du Yilgarn Craton (zone bordière Méso-Protérozoïque) et la dorsale sud-est indienne, ces deux missions ont permis de collecter près de 600 échantillons, parmi lesquels des péridotites à spinelle et plagioclase exceptionnellement bien préservées de l'altération hydrothermale ainsi que des basaltes, gabbros et pyroxénites. Le premier objectif de cette étude est de montrer le rôle de l'héritage mantellique et de la refertilisation dans le mécanisme de rifting et la rupture sur les marges riftées pauvres en magma, afin de comprendre la géodynamique de leur mise en place. Le second objectif est de caractériser thermodynamiquement cette transition entre un domaine mantellique continental (où les processus tectoniques sont majoritaires) et une zone océanique où la thermicité joue un rôle prédominant, modifiée drastiquement sous l'effet de l'ascension des magmas et de la remontée de l'asthénosphère sous-jacente. Enfin, le troisième objectif est de déterminer les caractéristiques géochimiques des produits magmatiques afin notamment d'identifier leur source, au regard de la complexité de l'océan Indien, entre zone de dorsale lente et non loin du point chaud de Kerguelen. L'ensemble du travail de cette thèse se base sur une approche pétrologique et géochimique menée sur les échantillons dragués le long de la zone Diamantine, cette dernière agissant comme un réel enregistreur des processus magmatiques associés à l'ouverture océanique. Enfin, mon travail

constituait également à contribuer au développement d'une nouvelle méthode d'analyse quantitative par micro-fluorescence X (μ-XRF).

La première partie, constituant l'introduction générale de la thèse, permettra de présenter l'étude et de revenir sur les grandes questions scientifiques actuelles qui en émanent, en faisant dans un premier temps un état de l'art de la formation des marges pauvres en magma, d'un point de vue tectonique dans une moindre mesure mais surtout pétrologique, avec l'étude des péridotites et des produits magmatiques associés au processus de rifting. Dans un second temps, il est important de comprendre les motivations concernant la localisation des deux campagnes océanographiques MD80 et MD110, au niveau de la zone Diamantine, où le lien entre la zone de transition et la croute océanique issue de la dorsale sud-est-indienne est complexe.

Le premier chapitre concerne la méthode d'analyse développée lors de cette thèse, qu'est l'analyse quantitative in situ par μ-fluorescence X, sous la forme d'un article dont l'objectif est qu'il soit soumis ultérieurement par M. Ulrich, directeur de cette thèse et initiateur de la méthode. L'analyse in situ par μ-XRF présente de nombreux avantages : économique, le prix de cette machine représentant 1/5ème du prix d'une microsonde électronique ; compacte, la machine est dite de « paillasse » tout en pouvant analyser des échantillons de grande taille (jusqu'à 330 cm^2) ; à spectre large, elle permet de détecter tous les éléments majeurs et mineurs dans les silicates, oxydes ou minéraux hydratés sans ajout de temps d'acquisition ; non-destructive, les échantillons gardant leur intégrité au cours de l'analyse ; et enfin simple d'utilisation, puisqu'il est possible de laisser facilement quelqu'un en autonomie effectuer ses analyses… ce qui ne fut par contre pas le cas pour la mise en place de cette méthode.

Le second chapitre, correspond à un article soumis à Earth and Planetary Sciences Letters, dont le titre est « The role of mantle inheritance and refertilisation during breakup at magma-poor rifted margins: what can we learn from the SW-Australia margin? ». En effet l'étude des interactions entre les roches mantelliques et les liquides magmatiques sur les marges riftées pauvres en magma, qui représentent pourtant près de la moitié des marges mondiales, est jusqu'à présent limitée par l'accès aux échantillons. Les concepts actuels sont donc principalement basés sur des études de la Téthys occidentale et du domaine de

l'Atlantique Nord méridional, et il n'est pas certain qu'ils soient applicables à d'autres marges de rift pauvres en magma. Nous présentons ainsi dans cet article une étude sur les péridotites de la zone Diamantine le long de la marge australienne sud-ouest, échantillonnées lors des campagnes océanographiques MD80 et MD110. Les données pétrologiques montrent l'existence de deux types de péridotites : la lherzolite à spinelle, qui représente le manteau sous-continental hérité (SCLM) avant la séparation de l'Australie et de l'Antarctique, et la péridotite à plagioclase formée par l'interaction avec des liquides magmatiques syn-rift à basse pression dans le champ de stabilité du plagioclase lors de l'exhumation du SCLM. Les types de manteau observés ainsi que les processus magmatiques et mantelliques (fusion et refertilisation) identifiés dans les péridotites de la zone Diamantine sont très similaires à ceux documentés dans les marges fossiles alpines-apennines et actuelles ibériques, démontrant ainsi que ces processus sont indépendants de l'héritage du SCLM. Des vestiges de cet héritage mantellique peuvent être préservés dans le manteau refertilisé, ce qui suggère une transition progressive d'un manteau hérité à un manteau refertilisé au cours de la rupture. Enfin, cette étude met en évidence le rôle de l'héritage et de la refertilisation en tant que principales caractéristiques de contrôle du rifting final et de la rupture sur les marges riftées pauvres en magma.

Dans un troisième chapitre, il s'agira de donner des arguments thermodynamiques aux processus de refertilisation mis en évidence dans le troisième chapitre en caractérisant les conditions thermiques et barométriques auxquelles se sont formées et ont évoluées les péridotites à spinelle et plagioclase de la zone Diamantine. En effet, les minéraux de ces roches ont montré des variations importantes dans leur chimie, proposant qu'il y ait une paragenèse primaire et une paragenèse secondaire, qui peuvent cohabiter dans certaines péridotites à plagioclases, refertilisées. Les thermomètres et baromètres utilisés sont basés sur la répartition des éléments chimiques au sein des minéraux préservés caractéristiques des péridotites. Les coefficients de partagent attribuent la capacité à chaque minéral de conserver ou non un élément au sein de sa structure minéralogique. Ainsi, étudier ces deux types de péridotites avec cet angle de vue permet de les différencier d'un point de vue physico-chimique : il y a d'une part des roches à l'équilibre (les lherzolites à spinelles,) et d'autre part des roches ayant subi une perturbation ou déséquilibre lié au passage d'un liquide magmatique avec lequel elles ont interagi (les péridotites refertilisées – les

lherzolites à plagioclases). Cette partie permet également de caractériser les processus et vitesses de refroidissement au sein des marges passives, postérieurement au passage des liquides magmatiques refertilisant. Dans un dernier temps, cette étude montre l'impact de la refertilisation sur l'effacement de l'héritage du SCLM et le passage rapide à une lithosphère typique des zones d'accrétion. Ce chapitre est sous la forme d'un manuscrit en construction dans l'optique d'une soumission au journal Geology.

Le quatrième chapitre se concentre sur l'étude des produits magmatiques dragués le long de la zone Diamantine, afin d'identifier notamment la source des basaltes produits le long des marges passives pauvres en magma. Des analyses en éléments majeurs, traces et isotopiques, ont pu être faites sur quasiment tous les points de dragage des campagnes MD80 et MD110, permettant ainsi de quadriller la zone de transition océan-continent. La localisation très particulière de la zone Diamantine, liée à l'ouverture de l'Océan Sud-est Indien séparant l'Australie de l'Antarctique, mais très proche de plateaux océaniques (Kerguelen, Broken Ridge, 90°E Ridge, Plateau Naturaliste) propose une certaine complexité. Deux groupes de produits magmatiques ont pu être identifiés, l'un à l'ouest possédant des caractéristiques proches de celles des plateaux océaniques, l'autre à l'est possédant des caractéristiques géochimiques plus proches de celles des dorsales océaniques. Cette dualité, bien que pouvant être attribuée à une complexité locale, a également été identifiée dans des études préalables sur les produits magmatiques dans les marges passives pauvres en magma de la zone téthysienne, proposant ainsi également qu'il puisse s'agir d'un processus commun des zones de transition océan-continent, ce qui a de grandes implications sur les questions de budget magmatique dans les marges riftées. Ce chapitre est rédigé sous la forme d'un manuscrit qui sera soumis dans les prochains mois au journal « Geochemistry, Geophysics, Geosystems ».

Dans un cinquième chapitre, il était important de remettre en lien l'ensemble des travaux effectués sur les péridotites et les produits magmatiques présents. Ce chapitre constitue donc une synthèse de ce travail sur les marges passives pauvres en magma, permettant ainsi de discuter les résultats de ce manuscrit dans leur ensemble en les mettant en perspective avec les travaux antérieurs sur les autres marges peu magmatiques. L'étude des différentes roches évoquées permet ainsi de proposer un modèle global des processus

magmatiques affectant les marges peu magmatiques mais également de donner des éléments de discussion relatifs aux questions que nous avons pu poser en introduction tel que l'effet d'un héritage mantellique plus ancien ou son importance sur le budget magmatique et donc la nature de la marge passive.

Enfin, une dernière partie, conclusive, permettra également de recenser les perspectives qui émanent de ce travail, notamment les implications sur les modélisations numériques ou encore l'importance des pyroxénites, roches présentes exclusivement dans le manteau hérité et dont le rôle sur la nature des magmas dans les OCT restent mal contraints.

« *La recherche n'est pas seulement une question de répondre à des questions, mais de découvrir les questions auxquelles personne n'a encore pensé.* »

Claude Lévi-Strauss

"A PhD is not just a degree; it's an attitude of never giving up"

Michio Kaku

Remerciements

Et voilà le temps d'écrire cette page de remerciements, celle que j'ai toujours lu dans les autres thèses, en pensant au jour où je devrais écrire les miens… ils clôturent 3 ans de vie, c'est sans doute pour cela qu'il est si difficile d'écrire cette dernière page.

A tous ceux qui ont été là, de près ou de loin, pour un passage ou depuis tant d'années, merci.

Avant toute chose, je souhaiterai exprimer toute ma gratitude aux membres du jury, Daniel Sauter, président du jury, Georges Ceuleneer, Marguerite Godard, Mary-Alix Kaczmarek, et également à Othmar Müntener et Gilles Chazot, merci pour vos précieux conseils et vos encouragements tout au long de ma thèse.

Un grand merci à tous ceux que je n'aurai pas encore cité mais qui auront contribué à la mise en place de cette thèse par la recherche des échantillons, Dan, Marie-Odile Beslier, Jacques Girardeau, Bernard Mercier de Lépinay, sans oublier notre défunt Marc Munschy et Jean-Marc Brendle (c'est définitivement une histoire de famille !) qui ont participé aux campagnes en mer… pour m'avoir permis de travailler sur des échantillons d'une si grande valeur. Ce travail n'est clairement pas à la hauteur de tout ce qu'il est possible de faire avec vos échantillons mais j'espère qu'il aura contribué à ouvrir de nouvelles perspectives.

Tout a commencé là où tout se finira à nouveau, dans le Massif central. Qui aurait cru que j'en rentrerai avec un autre avenir que celui de prof d'SVT dans le 93… certainement pas moi ! Mais, toi Marc, tu y as cru, sans doute bien plus que moi, et durant toute la thèse. Je te suis sincèrement reconnaissante de m'avoir poussée dans mes retranchements et de m'avoir fait confiance. Un grand merci également pour toute ton aide durant ces 3 années, j'ai vraiment aimé travailler avec toi.

Un grand merci également à mon deuxième directeur, Gianreto. Je sais que pour toi mon cursus un peu particulier représentait aussi un défi, merci pour ta patience, ta bienveillance, tes encouragements, tes conseils… on ne se connaissait pas beaucoup, mais j'ai été ravie et je me sens très chanceuse d'avoir pu travailler avec toi. Ta capacité à dormir si peu et ta facilité à parler avec des métaphores me fascineront toujours !

Pour finir, je dirai simplement que vous formez sans doute le meilleur duo que j'aurai pu espérer en direction de thèse, un peu comme le ying et le yang, toujours complémentaires. Merci pour votre disponibilité sans faille et pour les nombreuses discussions scientifiques que l'on a pu avoir au cours de cette thèse.

Mais ne l'oublions pas, vous n'êtes pas seuls dans cette équipe ! Merci Francis (promis je finirai les polariseurs avant de repartir), Benoit (d'apparence si innocent mais…par pitié, arrête d'essayer de m'enfermer dans mon bureau), Julia (tu as été une bouffée d'oxygène dans cette équipe 100% masculine), et tous les autres ! N'oublions pas notre doyenne, Anne-Marie,

j'admire ta carrière scientifique en tant que femme à une époque où comme nous le savons tous, il était encore bien plus difficile de s'imposer.

Enfin, les doctorants du 4ème et du 5ème (on ne citera pas les rongeurs), Mérédith, sans doute une des plus petites par la taille mais un pilier du labo, Roxane, tes jeux de mots toujours aussi mal associés, Estelle, ton rire et ta joie de vivre, Bastien, Joachim, Camille, Charlotte, Emile, Charles, Joao, Harmony… Même si j'étais sans doute un peu moins présente en fin de thèse, j'ai vraiment beaucoup apprécié la faire à vos côtés. Gabriella, you are the sun of our office, thank you so much to be here and for so many discussions with you! Boa sorte com sua tese, você é o melhor !

Merci également à Dilek Karaygit et Ghenima Begriche, nos gestionnaires, sans oublier Didier, que l'on peut appeler à la rescousse dès qu'il y a un problème au bâtiment, j'ai énormément de respect pour le travail que vous faites.

Merci aux étudiants pour leur aide (Alexandra, Clément, Guillaume, Sophie) et surtout à Grégory avec qui j'ai passé de nombreuses heures à scier les échantillons, j'espère que vous vous épanouirez dans un de ces beau métier que compte la géol !

Enfin, j'ai eu la chance de traverser un peu le Rhin pour aller dans ce magnifique labo, niché dans la forêt de Karlsruhe. C'est là-bas que j'ai connu Alex, merci pour tout ton soutien durant toute la thèse (et ton canapé aussi), tu as été un vrai pilier ! Et qu'auraient été les semaines là-bas sans Clifford, Simon, Aratz, Rémi parfois ! J'adore l'ambiance de ce labo, tout comme l'apéro du patron le vendredi soir !

Merci à Bastien, Yannick, Antonin, Philippe pour votre accueil dans les grisons, je n'oublierais pas ce magnifique terrain.

Je tiens à remercier enfin ceux qui m'ont formée juste avant la thèse, Armelle, François, Jérémy et Quentin, vous représentez un tournant dans ma vie : la prépa ne s'est pas faite sans douleur mais je ne travaillerai plus jamais de la même manière, tout est plus simple aujourd'hui.

Pour terminer, je voudrais remercier ceux qui me suivent depuis toujours… mes parents. Vous m'avez appris à me surpasser même si le stress reste toujours mon paramètre le plus limitant… mais surtout que thèse ou non, le diplôme et le métier ne change pas les gens, il sert juste à être heureux de ce que l'on fait tous les matins en allant travailler. Mention spéciale pour toi Rom's, mon coloc de toujours, celui qui sait interpréter correctement et bien mieux que moi mon ressenti sur les examens… (oups). Promis, cette fois c'est la dernière !
Hélène, Delphine, Oriane, Alexis, Mimoune, Joseph, Lucas, Joël, Damien, Romain, Thibaut, vous avez été mes bouffées d'oxygène pendant ces trois années !

Et enfin, last but not least, Robin, que dire sinon merci… le reste tu le sais déjà. Cette page marque aussi la fin de notre relation à distance et le début d'une nouvelle vie…

Sommaire

Résumé ... *3*

Remerciements ... *10*

INTRODUCTION ... *17*

1. Observations et évolution des concepts et modèles ... *20*

1.1. Structure et répartition mondiale des marges passives ... 20

1.2. Passage d'une lithosphère continentale stable à une zone d'accrétion océanique : l'importance de l'étude de la transition océan-continent ... 22

1.3. Les marges passives pauvres en magma : conditions de mise en place ... 24

1.3.1. Aspects pétro-géochimiques ... 24

1.3.2. Évolution des conditions de pression et température des roches mantelliques ... 34

1.3.3. Premiers produits éruptifs formés lors de l'ouverture ... 36

2. Le cas de la marge passive sud-ouest australienne ... ***38***

2.1. L'histoire géologique et géodynamique de l'océan Indien ... 38

2.2. Les missions océanographiques MD80 et MD110 ... 41

3. Méthodes d'analyse ... ***45***

3.1. Analyses géochimiques en roche totale ... 45

3.2. Analyses *in situ* ... 47

3.3. Analyses isotopiques et séparations minéralogiques ... 48

4. Questions scientifiques et approche choisie ... ***49***

CHAPITRE I – Acquisition de données in situ en éléments majeurs par µ-XRF ... *53*

1. Méthodologie générale et matériel disponible au laboratoire ITES ... ***55***

2. Paramétrisation ... ***59***

2.1. Intensité électrique de mesure ... 59

2.2. Sensibilité ... 60

2.3. Effet d'épaisseur non-infinie ... 61

2.4. Préparation de standards sur lame : une approche originale ... 62

2.5. Temps d'acquisition ... 63

3. Quantification par µ-XRF ... ***64***

3.1. Processus physique sous-jacent : accéder à une donnée (semi)-quantitative ... 64

3.2. Mesures initiales sur standards internationaux ... 66

3.3. Calibrations du signal ... 68

3.4. Détermination des valeurs de LOD et LOQ ... 69

*4. Résultats et discussion **70***

4.1. Résultats sur standards internationaux 70

4.2. Limites liées à la méthode XRF et solutions proposées 72

4.3. Effets de matrice 72

5. Application sur échantillons naturels : le test sur les échantillons de la zone Diamantine 74

5.1. Analyses *in situ* 74

5.2. Calibration de cartographies chimiques 76

Conclusion et perspectives 77

CHAPITRE II – Le rôle de l'héritage et de la refertilisation du manteau au cours de la rupture dans les marges passives pauvres en magma : que pouvons-nous apprendre de la marge sud-ouest de l'Australie ? 79

1. Introduction 81

2. Mantle-melt interactions recorded in OCTs: state of the art 82

2.1. The OCT: a tape-recorder of break-up processes 82

2.2. Inheritance vs. mantle-melt interactions during breakup: a petrological approach 84

3. Geological settings 84

3.1. The Australia-Antarctica conjugate margins 84

3.2. The Diamantina Zone 84

3.3. Debates and remaining questions 84

4. Samples and analytical methods 85

4.1. Origin of samples 85

4.2. Analytical methods 85

5. Results 85

5.1 Sample petrography 85

5.2. Mineral chemistry 85

5.2.1. Clinopyroxene 85

5.2.2. Orthopyroxene 87

5.2.3. Spinel 87

5.2.4. Olivine 87

5.2.5. Plagioclase 87

5.3. Geothermobarometry 87

6. Discussion 87

6.1. Exhumed mantle peridotites along the Diamantina zone: what do they record? 87

6.1.1. Two mantle-types 87

6.1.2. Sp-lherzolite: a subcontinental lithospheric mantle inheritance 87

6.1.3. Pl-lherzolites: a tape recorder of mantle-melt reactions during exhumation 90

6.2. The Diamantina mantle rocks: how do they fit the Alpine-Iberia model? 92
6.2.1. Depend mantle-melt interactions on type of inherited mantle? 92
6.2.2. Can a direct genetic link between inherited and refertilized mantle type be proven? 93
6.3. The Iberia-Alpine mantle-melt interaction model: what did we learn from the SW-Australia margin? 93
7. Conclusion 93
Bibliographie 94

CHAPITRE III – Étude des conditions thermo-barométriques des péridotites de la zone Diamantine 97
Introduction 99
1. The Diamantina zone peridotites 100
2. Two-pyroxenes thermo-barometry and speedometry 101
2.1. In-situ chemistry 101
2.2. Thermometry and barometry 103
3. Discussion 105
3.1. Zonation – chemical mapping of the refertilisation 105
3.2. Temperature evolution during refertilisation 105
3.3. Mantle types 1 and 2 follow different P-T paths 106
3.4. Comparison with the other margins: the refertilisation erase mantle inheritance thermicity 107
Conclusion 108

CHAPITRE IV – Étude des produits magmatiques de la zone Diamantine 109
Introduction 112
1. Geological setting 114
2. Sample and analytical methods 118
2.1. Origin of samples and localization along the diamantina zone 118
2.2. Whole rock composition 118
2.2.1. Major element concentrations 118
2.2.2. Trace element concentration 119
2.2.3. Isotopes measurement 119
2.3. In situ analysis 120
2.3.1. Mineral major element concentrations 120
2.3.2. Mineral trace element concentrations 121
3. Results 121
3.1. Petrology of basalts from the Diamantina zone 121

3.2. Bulk rock major and trace elements geochemistry 122

3.3. Minerals major and trace elements geochemistry 126

3.4.1. Clinopyroxene 126

3.4.2. Plagioclase 126

3.4.3. Olivine 127

4. Discussion 127

4.1. Basalt heterogeneity along of the Diamantina zone 127

4.2. A multiple origin of basalts: imaging the heterogeneity of mantle source/inherited mantle in magma-poor rifted margin 129

4.3. Sources and timing of basalts emplacement: implication for Gondwana-break-up .. 130

4.4. Comparison with others magma-poor rifted margins and implication for magmatic budget in magma-poor rifted margins 131

Conclusion 132

CHAPITRE V – Synthèse et Discussion 134

1. L'étude de la zone Diamantine confirme le modèle de formation des marges passives pauvres en magma développée en zone européenne 135

2. Héritage mantellique et refertilisation sont à l'origine du budget magmatique des marges passives pauvres en magma 135

3. Les basaltes de marge passive reflètent une hétérogénéité de source 136

CONCLUSION 138

Bibliographie 142

Annexes 161

INTRODUCTION

Les marges passives constituent un sujet d'étude essentiel non seulement pour leur importance dans la compréhension de la dynamique lithosphérique mais aussi pour les implications économiques qui en découlent. Ces zones de transition entre une zone continentale déjà très étudiée et une zone océanique dont le fonctionnement est déjà bien contraint, concentrent une grande partie des richesses mondiales en termes d'hydrocarbures. Cela pourrait donc paraitre caduc pour les décennies à venir, mais c'est sans compter le potentiel économique lié aux ressources naturelles renouvelables dont elles disposent.

Dans le cadre de cette thèse, je me suis particulièrement intéressée aux marges passives dites pauvres en magma dont les conditions de mise en place sont encore largement débattues.

Les marges passives se différencient des zones de subduction et des zones transformantes par le fait qu'elles sont localisées au sein même des plaques lithosphériques et ne comptent que très peu d'activité sismique, bien que des mouvements verticaux importants peuvent y être observés. Elles marquent la transition spatiale entre une lithosphère continentale, composée d'un domaine mantellique et d'une croûte felsique épaisse (35 km), contrastant avec le domaine océanique formé d'une lithosphère composée également d'un domaine mantellique mais sur lequel est situé une croute océanique mafique beaucoup plus fine (6 - 10 km). La courbe de Trabert (Fig. i-1) qui montre la répartition bimodale des altitudes sur la Terre montre très bien cette dualité. Elle est connue depuis les temps de Wegener qui s'en servira dans sa théorie de la dérive des continents. Pour autant, les mécanismes à l'origine de ces zones charnières sont encore très mal compris, tout comme la localisation précise de la délimitation des domaines continentaux et océaniques.

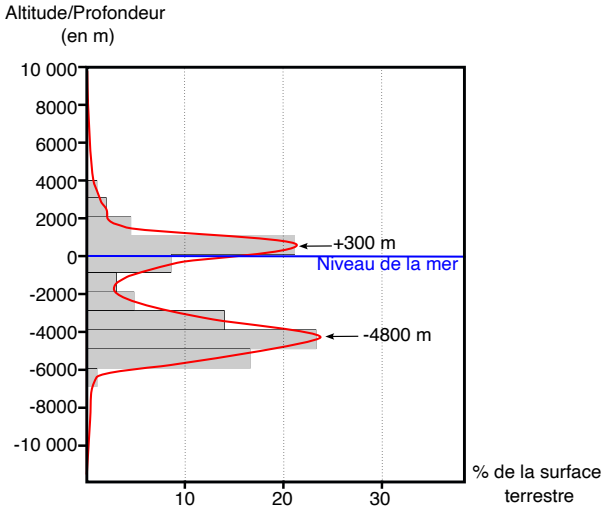


Fig.i-1 – *Courbe bimodale des altitudes (d'après Wegener, 1929)*

Cette courbe montre un aspect très important de cette zone de transition : elle marque le passage entre une zone immergée et une zone émergée, ce qui découle de deux zones dont l'équilibre isostasique est atteint à des altitudes différentes. Cela est lié aux lithologies de densité différentes entre la lithosphère continentale et la lithosphère océanique. Pourtant, il est encore difficile de distinguer les deux au sein de la transition océan-continent (OCT) à partir des données géophysiques, sans données géologiques directes (échantillons collectés par forage ou dragage).

La compréhension des processus liés à la formation des limites de plaques est l'un des plus grands défis qui restent à relever dans le domaine de la tectonique des plaques. Si les processus aux frontières de plaques divergentes au niveau des dorsales médio-océaniques sont relativement bien connus, ceux aux transitions océan-continent (OCT), le sont beaucoup moins. Elles sont le siège des premiers magmas produits lors de la rupture lithosphérique. Comment s'opère la transition d'une lithosphère continentale stable à une zone dominée par le magmatisme à l'origine de l'accrétion d'une nouvelle lithosphère océanique ? Cela est essentiel car c'est bel et bien au niveau des OCTs que l'on va avoir accès à l'histoire de la mise en place de ces zones d'accrétion océanique. En effet, les zones de transition océan - continent enregistrent latéralement les phases temporelles successives du rifting, permettant ainsi d'interpréter en termes temporels les variations spatiales des processus caractérisés au sein de l'OCT et donc les conditions de leur mise en place.

La juxtaposition d'un domaine océanique clairement magmatique et d'un domaine continental implique nécessairement une rupture lithosphérique. Si la rupture de la croute continentale apparait comme un évènement tectonique simple à identifier, son équivalent mantellique l'est beaucoup moins. La pétrologie semble être la clé pour répondre à ce problème puisque le manteau sous-continental et le manteau océanique présentent des différences géochimiques importantes.

Ainsi, la zone de transition océan-continent constitue le lieu spatio-temporel de transition entre le domaine continental et le domaine océanique et ainsi le lieu de prédilection pour étudier la mise en place des zones d'accrétion océanique. Enfin, pour comprendre les conditions, l'évolution et les processus dans lesquels de nouvelles frontières de plaques

divergentes se forment, il est nécessaire d'étudier des roches mantelliques et magmatiques dérivées de ces OCT. Cependant, il n'existe qu'une poignée de sites dans le monde où les OCT sont accessibles à l'échantillonnage. Concernant les marges passives pauvres en magma, la plupart de ces sites appartiennent au système alpin/ibérique issu de la rupture de la Pangée, avec un manteau lithosphérique sous-continental (SCLM) porteur d'un fort héritage varisque.

1. Observations et évolution des concepts et modèles

1.1. Structure et répartition mondiale des marges passives

Les marges passives montrent un grand point commun : le passage d'une zone d'affinité continentale à une zone d'affinité océanique au sein d'une même plaque lithosphérique.

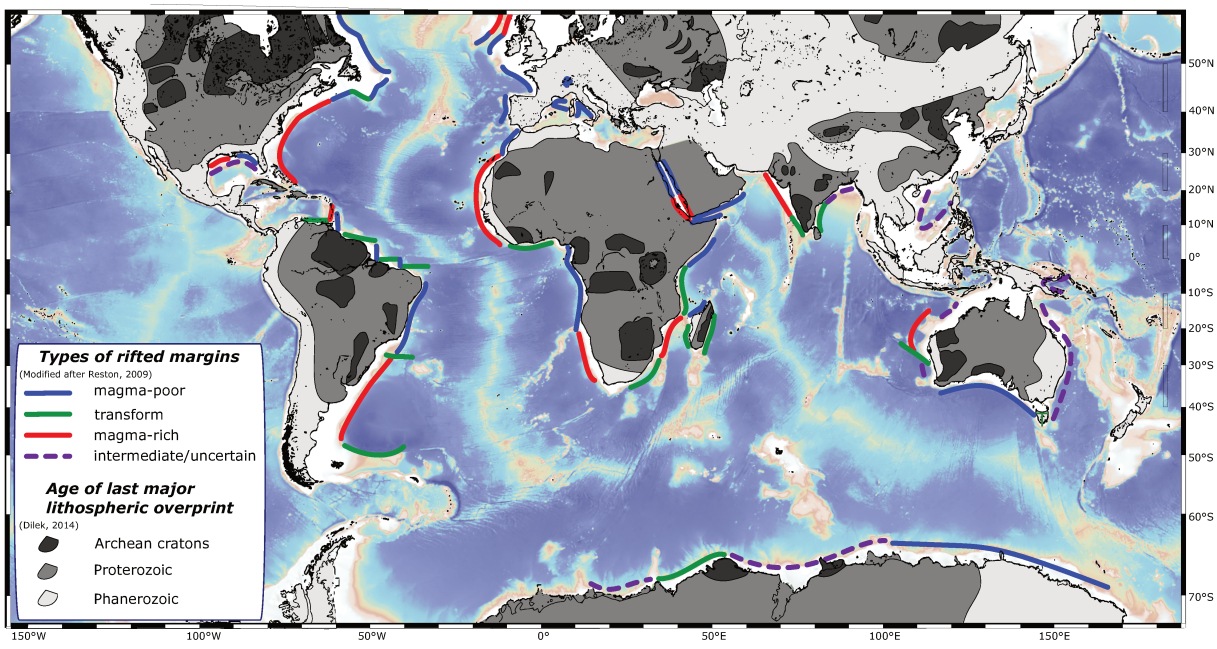


Fig. i-2 – *Carte de la répartition des marges riftées (type de marge d'après Reston, 2009 ; carte réalisée sur Géomapapp d'après données GMRT)*

Elles sont habituellement différenciées en deux groupes, selon leur budget magmatique (Reston, 2009 ; Fig. i-2) :

- les **marges passives riches en magma** (anciennement dites volcaniques), en rouge sur la carte mondiale (Fig. i-2) où le matériel effusif est clairement visible en surface ;

- les **marges passives pauvres en magma** (anciennement dites non volcaniques, en bleu sur la carte mondiale (Fig. i-2) où la présence de roches d'origine magmatique est parcellaire en surface.

Qu'il s'agisse de marges passives pauvres ou riches en magma, la transition entre le domaine continental et le domaine océanique, définit comme la transition océan-continent peut être divisée en trois grands domaines (fig. i-3) :

- Un **domaine proximal :** il s'agit d'un domaine clairement continental, peu aminci, comportant quelques failles listriques. La zone est généralement définie par un parallélisme entre le toit du socle et le Moho.

- La « **necking zone** » également appelée zone d'étranglement : la croûte continentale est étirée et amincie de manière brutale. L'épaisseur crustale passe de 30 km à 10 km (Sutra et al., 2013) avec une remontée rapide du Moho qui apparait convergent avec le toit du socle.

- Un **domaine distal** : cette zone correspond à la transition océan-continent (OCT) *sensu stricto* et concentre les plus grandes différences entre marges passives pauvres et riches en magma. C'est dans cette zone que les premiers produits éruptifs sont localisés ainsi que du manteau exhumé dans le cadre d'une marge passive pauvre en magma. La zone de rupture lithosphérique se situe dans le domaine de manteau exhumé par des failles de détachement (Peron-Pinvidic & Manatschal, 2010 ; Whitmarsh et al., 2001) mais y est encore très difficile à identifier.

  Dans le cas de marges passives riches en magma, des domaines magmatiques importants ont pu être mis en évidence tel que les « Seaward Dipping Reflectors » correspondant à des épanchements volcaniques ou un corps à haute vélocité en profondeur, sous-plaquant la croute continentale hyper-étirée (Franke, 2013).

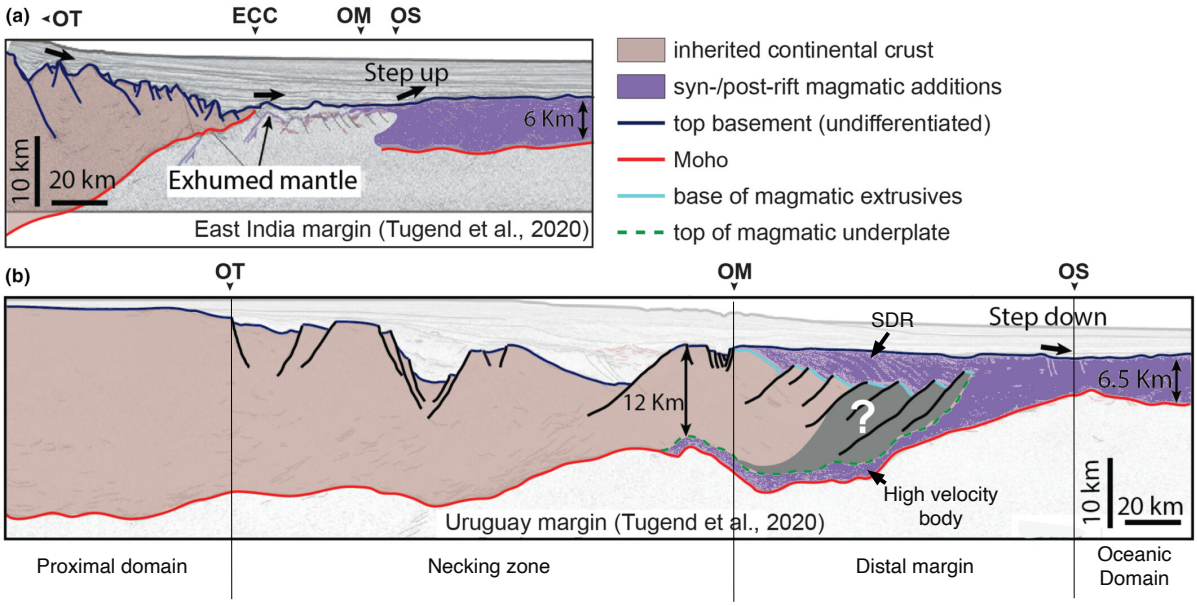


Fig. i-3 : *Schéma de marge passive pauvre en magma (haut) et riche en magma (bas) (modifié d'après Chenin et al., 2024). Les delimitations OT, onset of crustal thinning; OM, onset of extrusive magmatism; OS, onset of steady-state seafloor spreading; ECC, edge of the continental crust ont été définis par Chenin et al. (2024).*

1.2. Passage d'une lithosphère continentale stable à une zone d'accrétion océanique : l'importance de l'étude de la transition océan-continent

Le fait de classer les marges passives selon la quantité de magma réside dans une volonté de distinguer ces deux types de marge selon leur mode de formation. Pendant des décennies, les marges passives riches et pauvres en magma étaient attribuées à la conséquence de processus de rifting différents : les marges passives « volcaniques » résultent d'un rifting actif avec implication d'un point chaud tandis que les marges passives « non volcaniques » résultent d'un rifting passif où les processus tectoniques sont majoritaires et le magmatisme inhibé. Il est désormais assez bien contraint que ce modèle ne peut être accepté de manière aussi univoque (Tugend et al., 2018). Le point commun réside dans le fait que la formation d'un marge passive résulte d'un processus de rifting dont le stade ultime est l'accrétion océanique. La figure i-4 montre un modèle de rifting proposé pouvant être à l'origine d'une marge passive pauvre en magma.

Quatre grandes phases sont visibles sur ce schéma (Fig. i-4 ; Péron-Pinvidic & Manatschal, 2009) :

- **La phase d'étirement** (a) : la déformation est distribuée à grande échelle avec la formation de bassins sédimentaires de type hémi-grabens
- **La phase d'amincissement** (b) : elle constitue en une phase progressive de localisation de la déformation. La croute continentale est amincie et déformée avec le début de la mise en place de blocs basculés. De grandes zones de cisaillement permettent progressivement l'exhumation de niveau crustaux et/ou mantelliques.
- **La phase d'exhumation** (c) : le manteau sous-continental est exhumé par des failles de détachement qui traversent la croûte fragilisée et exhument des roches mantelliques serpentinisées sur le plancher océanique.
- **La phase d'accrétion océanique** (d) : lors de cette phase, la localisation irrévocable des processus thermiques et mécaniques dans une zone étroite permet de définir une (proto-)ride océanique où commence l'activité magmatique.

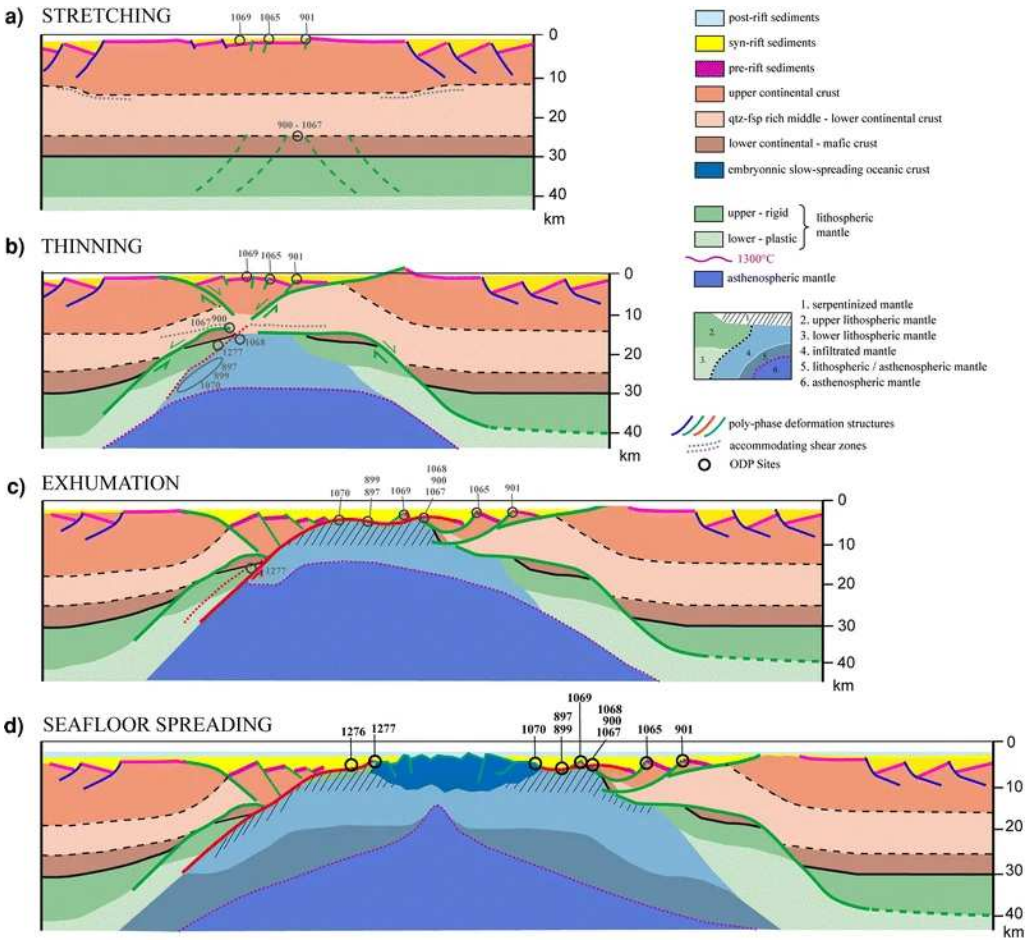


Fig. i-4 : *Modèle conceptuel montrant l'évolution du rifting à partir des observations du système de rift Ibérie/Terre-Neuve (d'après Péron-Pinvidic & Manatschal, 2009).*

Cela met également en évidence le fait que dans les environnements de marge passive pauvre en magma, la rupture continentale et le début de l'accrétion océanique sont étroitement liés à l'exhumation mantellique (manteau sous-continental et/ou océanique) par des processus tectoniques asymétriques (Cannat et al., 2006 ; Manatschal & Müntener, 2009). Il est donc difficile de déterminer la limite précise entre domaine continental et domaine océanique. Des études sur la marge passive ibérique ont montré qu'il n'y a pas de limite nette entre l'OCT et la première croute océanique mais plutôt une zone transitionnelle où l'exhumation mantellique par détachement s'est produite avant la rupture de la croute continentale (Péron-Pinvidic et al., 2007 ; Manatschal & Müntener, 2009).

1.3. Les marges passives pauvres en magma : conditions de mise en place

1.3.1. Aspects pétro-géochimiques

L'étude sur des échantillons des marges passives pauvres en magmas est limité à quelques rares zones parmi lesquelles les marges conjuguées Ibérie et Terre-Neuve ou les paléomarges passives de la Western Téthys (Fig. i-5).

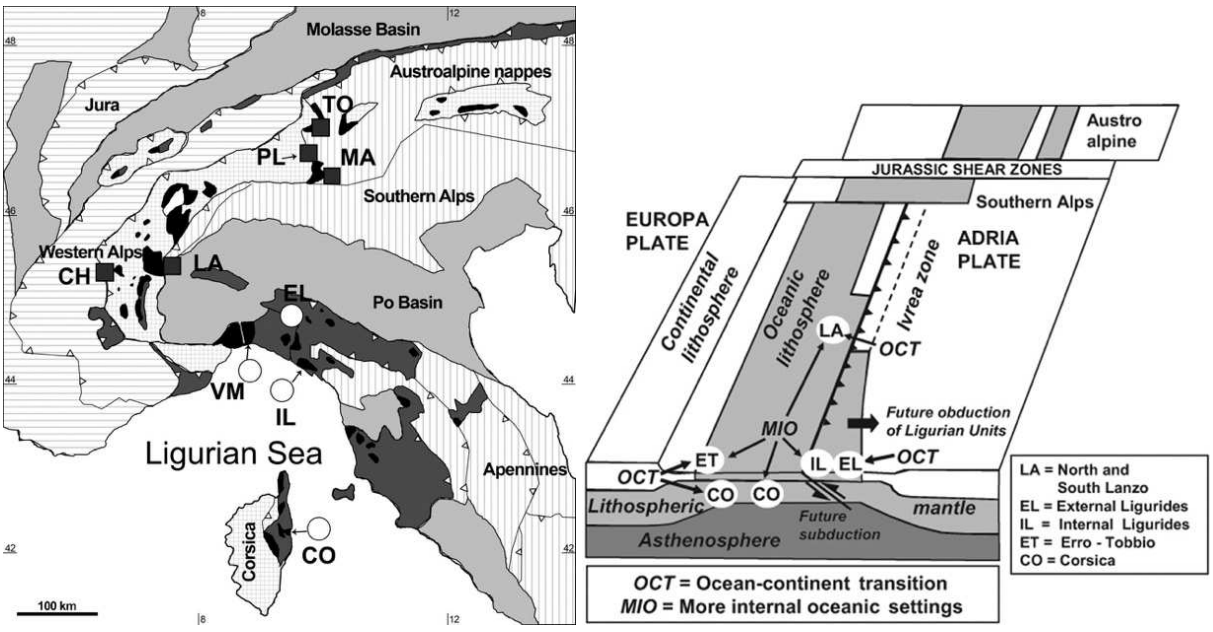


Fig. i-5 : *Carte de la répartition des zones d'études des paléo-marges passives de la Western Téthys à l'heure actuelle (gauche) et sa reconstruction paléogéographique (droite). Alpes Centrales : TO—Totalp, MA—Malenco, PL—Platta; Alpes de l'ouest : LA—Lanzo, CH—Chenaillet; Ligurides: VM—Voltri Massif, EL—External Ligurides, IL—Internal Ligurides; Corse :—CO (Monte Maggiore). D'après Piccardo et al. (2009)*

A partir des études proposées sur les échantillons de ces zones (Fig. i-5), la suite de l'introduction tente de donner un état des lieux de la recherche sur les marges passives peu magmatiques.

La mise en place des marges peu magmatiques comprend 2 processus majeurs : l'exhumation du domaine mantellique sous-continental hérité d'une part ; et l'implication de processus magmatiques d'autre part parmi lesquels la fusion partielle et l'interaction de ces domaines exhumés avec des liquides magmatiques infiltrés. Les nombreuses études pétro-géochimiques sur le manteau des marges fossiles téthysiennes et les marges actuelles Ibérie-Terre Neuve ont permis d'établir un modèle de coupe de marge passive pauvre en magma (Picazo et al., 2016 ; Fig. i-6). Plusieurs domaines mantelliques y sont décrits, se succédant au sein de la marge :

- Une **zone sous-continentale** héritée **:** le manteau de type 1
- Une **zone infiltrée** par des liquides magmatiques : le manteau de type 2
- Une **zone océanique** : le manteau de type 3

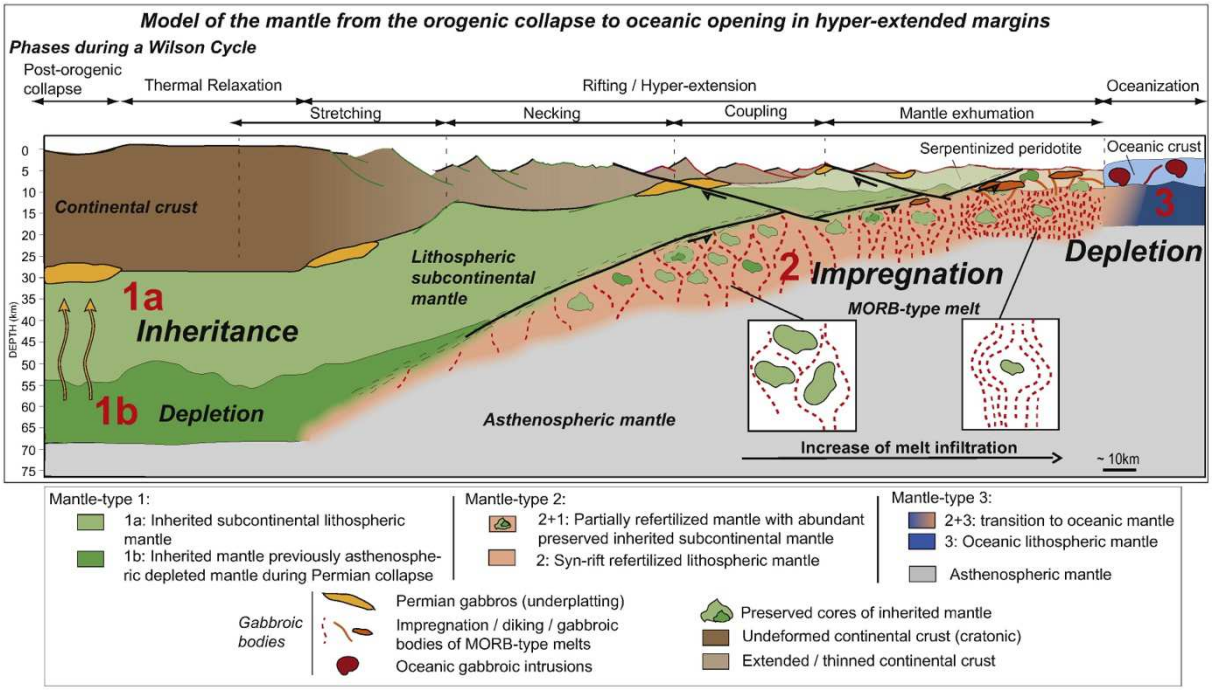


Fig i-6 : *Section interprétative des observations pétrologiques et des interprétations en termes de types de manteau à partir de la compilation des données sur les éléments majeurs du clinopyroxène et du spinelle le long d'une marge hyper-étirée (Picazo et al., 2016).*

Cette section interprétative fait état de trois grands domaines mantelliques très différents. Ces domaines constituent le premier degré d'hétérogénéité mantellique au sein de la marge passive pauvre en magma. Le manteau de type 2 est d'autant plus hétérogène du fait des nombreux processus magmatiques qui s'y déroulent. Sur cette coupe schématique, on y trouve également du manteau sous-continental hérité (dit de « type 1a ») qui est localement appauvri lors de la remontée de l'asthénosphère (dit de « type 1b ») ici à l'époque permienne (puisqu'il s'agit d'un modèle sur lithosphère européenne) pendant l'effondrement post-orogénique, où sont associés des gabbros sous-plaqués (en jaune - Hansmann et al., 2001 ; Schaltegger & Brack, 2007). Le manteau sous-continental hérité de type 1 est refertilisé par des liquides magmatiques de type MORB qui percolent (lignes rouges en pointillés) formant ainsi le manteau sous-continental refertilisé de type 2. La quantité de liquides magmatiques percolant augmente vers l'océan tandis que les reliques préservées du manteau hérité (noyaux vert clair) diminuent. La nouvelle lithosphère océanique est créée par refroidissement de l'asthénosphère à l'origine de la croute océanique (manteau dit de « type 3 ») et a donc une origine totalement différente. La conséquence la plus importante de ces travaux est le fait que le manteau sous-continental hérité a une grande importance dans la mise en place de la marge passive pauvre en magma.

1.3.1.1. L'héritage mantellique sous-continental

Dans les marges passives pauvres en magma, le manteau exhumé par les processus tectoniques liés au rifting est d'origine sous-continentale (Manatschal, 2004 ; Manatschal & Müntener, 2009). Ces travaux ont permis de comprendre que, lors de la formation des marges passives, le manteau lithosphérique sous-continental peut être étiré et exhumé par des détachements sans être recouvert par une croûte océanique. Cette exhumation peut conduire à l'exposition directe du manteau aux eaux océaniques (Manatschal, 2004 ; présence de brèches d'ophicalcites à Lanzo, Pelletier & Müntener, 2006) qui peuvent influencer la composition chimique du manteau (notamment par des processus de serpentinisation) et son comportement rhéologique (Tucholke et al., 2007).

De nombreuses études font maintenant état de manteau sous-continental exhumé au sein des paléo-marges passives pauvres en magma téthysiennes : Totalp (Froitzheim et al.,

1996, Müntener et al., 2004), Malenco (Hermann & Müntener, 1996 ; Müntener & Hermann, 1996), Upper Platta et Tasna (Manatschal et al., 2006 ; Müntener et al., 2004), Erro-Tobbio (Piccardo et al., 2007b), Lanzo nord (Bodinier et al., 1991 ; Piccardo et al., 2004; Kaczmarek & Müntener, 2008, 2010) sont décrits comme composés de manteau de type 1 dans le modèle de Picazo et al. (Fig.i-6 Picazo et al., 2016). De même, du manteau sous-continental exhumé a été mis en évidence au niveau de la marge ibérique actuelle (Manatschal & Bernoulli, 1999 ; Chazot et al., 2005).

Ce manteau sous-continental est dit « hérité ». Cela fait référence au fait qu'il est particulièrement hétérogène car influencé par l'histoire tectonique et thermique de ces régions potentiellement polyphasées. Quels sont alors les points communs qui permettent d'identifier un manteau sous-continental ?

Pour qu'un manteau puisse être qualifié de sous-continental hérité, il doit présenter (Picazo et al., 2016) :

- Des traces d'appauvrissement ou de fusion partielle liés à une phase tectonique antérieure au rifting et peut donc devenir très hétérogène selon son histoire complexe (Puziewicz et al., 2020)

- Une hétérogénéité lithologique : son histoire complexe engendre la présence de lithologies variées (Bodinier & Godard, 2014) dont des péridotites plus ou moins résiduelles avec possiblement des phlogopites ainsi que des pyroxénites (Müntener et al., 2004). Cette hétérogénéité est visible à l'échelle du km à celle du centimètre (Fabriès et al., 1998 ; Borghini et al.,2013).

- Être bordé de croute continentale inférieure. Dans le cas d'une marge passive actuelle, il n'est pas difficile d'établir cette proximité mais cela peut devenir plus problématique pour des zones fossiles.

Le manteau sous-continental associé aux marges passives pauvres en magma étudié dans les paléo-marges téthysiennes a permis l'identification de deux types de manteau hérité : le

manteau de type 1a (Fig. i-6 – Picazo et al., 2016) qui est fertile, enrichi, situé directement sous la croute continentale et le manteau de type 1b, situé à des profondeurs plus importantes et généralement plus appauvri.

Le manteau de type 1a, isolé du manteau sous-jacent et des processus convectifs, n'est que peu confronté à des processus de fusion partielle lors d'évènements tectoniques passés. Il s'agit donc d'un manteau fertile, avec de nombreuses veines de pyroxénites (Müntener et al., 2010 ; Bodinier et al., 1991) dont les températures d'équilibre calculées sont de l'ordre de 850 - 950°C (Müntener et al., 2000 ; 2004), dans le champ de stabilité du spinelle, en accord avec un équilibre thermique et un refroidissement lent lié à sa position superficielle dans la lithosphère. Ce type de manteau est typiquement observé à Malenco, Totalp ou Tasna (Müntener et al., 2010). Les âges enregistrés par ces roches dans la zone des Alpes-Apennins sont très variables, relatifs au dernier cycle de Wilson enregistré avant le rifting, allant d' $\cong$ 400 Ma dans les ligures externes (Rampone et al., 1995) à ~ 2.5 Ga dans les Pyrénées et des âges protérozoïque dans les Alpes orientales (Meisel et al., 1996 ; 1997).
Sur un aspect plus géochimique, les éléments majeurs et traces ainsi que les données isotopiques des péridotites du manteau de type 1a témoignent d'événements multiples et montrent que les hétérogénéités ont été acquises au cours d'un (ou plusieurs) cycles orogéniques (Picazo et al., 2016 ; McCarthy & Müntener, 2015). Les clinopyroxène sont nombreux et ont une chimie typique des péridotites fertiles, avec une teneur élevée en Na_2O (> 1 wt%) et Al_2O_3 (5-9 wt%) et faible en Cr_2O_3 (0.5 - 1 wt%), (Müntener et al., 2010). Les spinelles sont également marqueurs de ce type mantellique avec de faibles Cr# (Cr/Cr + Al $\cong$ 0.1 - 0.2), une faible teneur en TiO_2 (< 0.2 wt%) et un Mg# élevé (0.6 - 0.8) (Müntener et al., 2010), caractéristiques de taux de fusion partielle faibles (Hellebrand et al., 2001). Pour autant, bien que globalement fertiles, l'étude des péridotites sous-continentales héritées de marges passives pauvres en magma ont montré des chimies complexes des péridotites fertiles aux péridotites appauvries (Müntener et al., 2004 ; Piccardo et al., 2007a, 2007b).

Le **manteau de type 1b**, est situé en dessous du manteau de type 1a dans la coupe interprétative de Picazo et al. (2016). Ce manteau est dit post-orogénique et appauvri. Son appauvrissement est directement lié à la localisation plus en profondeur dans la lithosphère

et aux processus auxquels il a été soumis durant plusieurs cycles orogéniques. Les processus magmatiques tel que la fusion partielle touchent plus facilement cette zone qui est donc régulièrement « nettoyée » au cours des cycles de Wilson successifs. Il est typiquement retrouvé dans des zones comme Civrari (McCarthy & Müntener, 2015) où Lanzo sud (Bodinier et al., 1991 ; Kaczmarek & Müntener, 2008) où il est interprété comme issu d'un diapir asthénosphérique provenant d'un domaine à grenat. Les lithologies fréquemment retrouvées sont des harzburgites (McCarthy & Müntener, 2015), où les clinopyroxènes résiduels montrent des teneurs en Na_2O et TiO_2 faibles (< 0.1 wt% ; Picazo et al., 2016), caractéristiques de taux de fusion partielle élevés. Des datations ont pu être effectuées dans les Alpes et proposent un âge Permien pour les zones de Civrari, Platta et les Ligurides Internes (McCarthy & Müntener, 2015). Associés à cet épisode de collapse post-orogénique, des gabbros sont formés et sous-plaqués au niveau de la croute continentale (Petri et al., 2017).

Le manteau de type 1, largement exhumé le long de la marge passive pauvre en magma est donc sous-continental et peut avoir subi de nombreux processus différents aux cours de cycles de Wilson antérieurs, modifiant localement la géochimie et la lithologie des roches qui le composent. Le manteau sous-continental est ainsi fondamentalement hétérogène du fait de son héritage.

1.3.1.2. Le domaine refertilisé : siège d'interactions roche – liquide magmatique

Le schéma général de Picazo et al. (2016 – Fig.i-6) montre la présence d'un domaine très important, qui marque réellement la transition entre le domaine continental et le domaine océanique : le domaine refertilisé ou « manteau de type 2 ». La caractéristique principale de ce domaine mantellique néo-formé est qu'il est soumis à la percolation de liquides magmatiques formés en profondeur par l'ascension de l'asthénosphère. Lorsque les liquides magmatiques percolent à travers les péridotites mantelliques, des interactions entre la matière fondue et la roche peuvent avoir lieu. Ce domaine refertilisé correspond ainsi à un domaine hybride, où le domaine hérité et une nouvelle composition chimique se superposent. Le résultat dépend majoritairement de la composition de chaque membre de l'interaction et

des paramètres physiques auxquelles elles ont lieu (température, pression). Deux grands processus ont ainsi pu être identifiés, associés à l'exhumation mantellique (Fig.i-7 et Fig.i-8 ; Rampone et al., 2020 ; Van der Wal & Bodinier, 1996 ; Godard et al., 2000 ; Dijkstra et al., 2003 ; Müntener & Piccardo, 2003 ; Piccardo et al. 2004b) :

- Le « **reactive porous flow** » en domaine à spinelle, qui s'opère à système ouvert (Fig.i-7-1)

Ce processus à lieu dans le domaine à spinelle, au cours de l'ascension des péridotites liée aux processus d'exhumation auxquelles elles sont soumises lors du rifting. Le comportement réactif des liquides magmatiques est attribué à leur progressive sursaturation en olivine et sous-saturation en pyroxènes (Kelemen, 1990 ; Kelemen et al., 1990, 1995a, b, 1997, 2000 ; Grove et al.,1992). Ces caractéristiques expliquent la réaction chimique qui a lieu au sein des péridotites du manteau sous-continental à des profondeurs et températures importantes (Rampone et al., 2020) : Pyroxene + melt → olivine + melt. A cette réaction sont associées des textures très particulières où les pyroxènes apparaissent « corrodés ». La réaction de dissolution-précipitation contribue à modifier la composition chimique du liquide magmatique percolant et de la péridotite. Des modèles géochimiques ont pu être faits sur les terres rares et ont montré un enrichissement en REE moyennes à lourdes (Rampone & Borghini 2008). Les liquides néoformés vont ensuite percoler à des profondeurs plus faibles.

- L'**imprégnation mantellique**, en domaine à plagioclase, qui s'opère en système fermé (Fig.i-7-2)

Les liquides magmatiques ascendant interagissent avec les roches mantelliques appauvries (généralement du manteau de type 1b) où recristallisent des minéraux secondaires tels que le plagioclase et le clinopyroxène avec des textures lobées (Kaczmarek & Müntener, 2008). Ce processus engendre la **refertilisation** des péridotites (Rampone & Borghini, 2008 ; Rampone et al., 2020). Des changements drastiques ont également pu être identifiés dans les minéraux primaires de ces roches avec notamment une baisse des concentrations en Al_2O_3 dans les clinopyroxènes et une augmentation de la teneur en Nd (Hellebrand et al., 2003 ; Müntener et al., 2010 ; Kaczmarek & Müntener, 2008). Le manteau de type 2 a pu être identifié dans plusieurs zones des paléomarges téthysiennes tel que Lower Platta (Müntener et al., 2010),

Lanzo sud (Kaczmarek & Müntener, 2010), Monte Maggiore en Corse (Basch et al. 2018), Erro Tobbio (Rampone & Borghini, 2008) ou les Ligurides Internes.

Ainsi, plusieurs différences entre ces deux processus sont notables : d'un côté le système est ouvert lorsqu'il s'agit de « reactive porous flow » et fermé lorsqu'il s'agit d'imprégnation. Ils n'ont pas lieu dans le même domaine, le « reactive porous flow » ayant lieu dans le domaine à spinelle, la refertilisation en domaine à plagioclase, ce qui implique une temporalité différente lors de l'exhumation mais également une différence dans les phases impliquées au cours des réactions (dissolution ou précipitation de pyroxènes, implication de l'olivine ou du plagioclase).

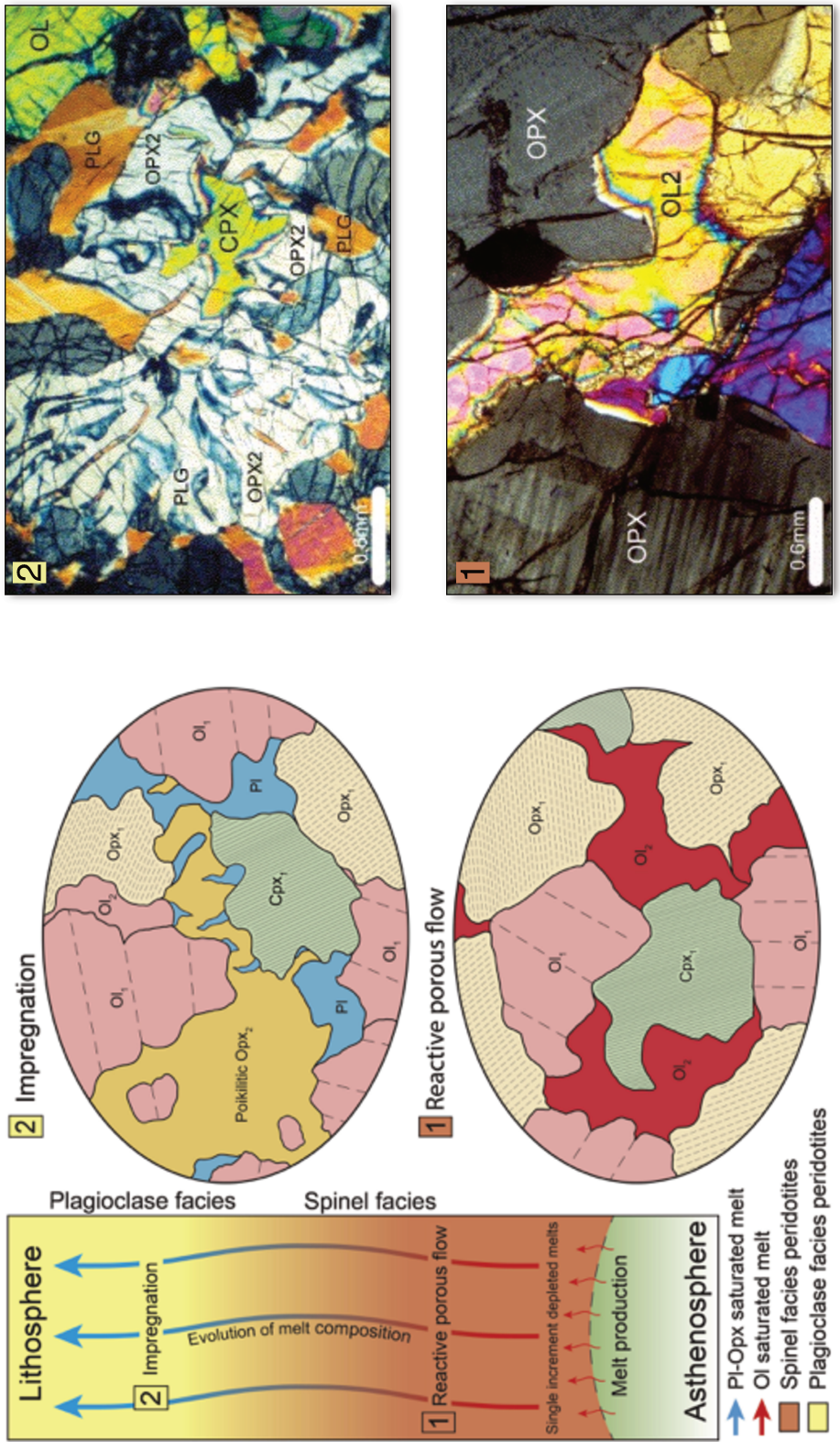


Fig.i-7 : *Évolution progressive des microstructures dans les péridotites du manteau au cours de leur remontée liée à l'extension et de l'histoire de l'interaction fonte-roche associée, du faciès spinelle à des profondeurs plus faibles du faciès plagioclase (d'après Rampone et al., 2020)*

Les processus présents auxquels sont soumis les péridotites au sein de la marge passive pauvre en magma sont localisés et s'opèrent sur les roches du manteau sous-continental hérité. En plus de l'hétérogénéité déjà présente, le « reactive porous flow » et l'imprégnation participent à créer un manteau lithosphérique hautement hétérogène, très différent d'un manteau océanique (Fig.i-8, Rampone et al., 2020). L'ensemble de ces processus contribuent à l'érosion thermochimique de la lithosphère par percolation de liquides magmatiques qui entrainent une modification de la composition et de la rhéologie de la lithosphère, permettant le passage d'une zone de transition océan-continent à un système d'accrétion lent (Piccardo et al., 2009).

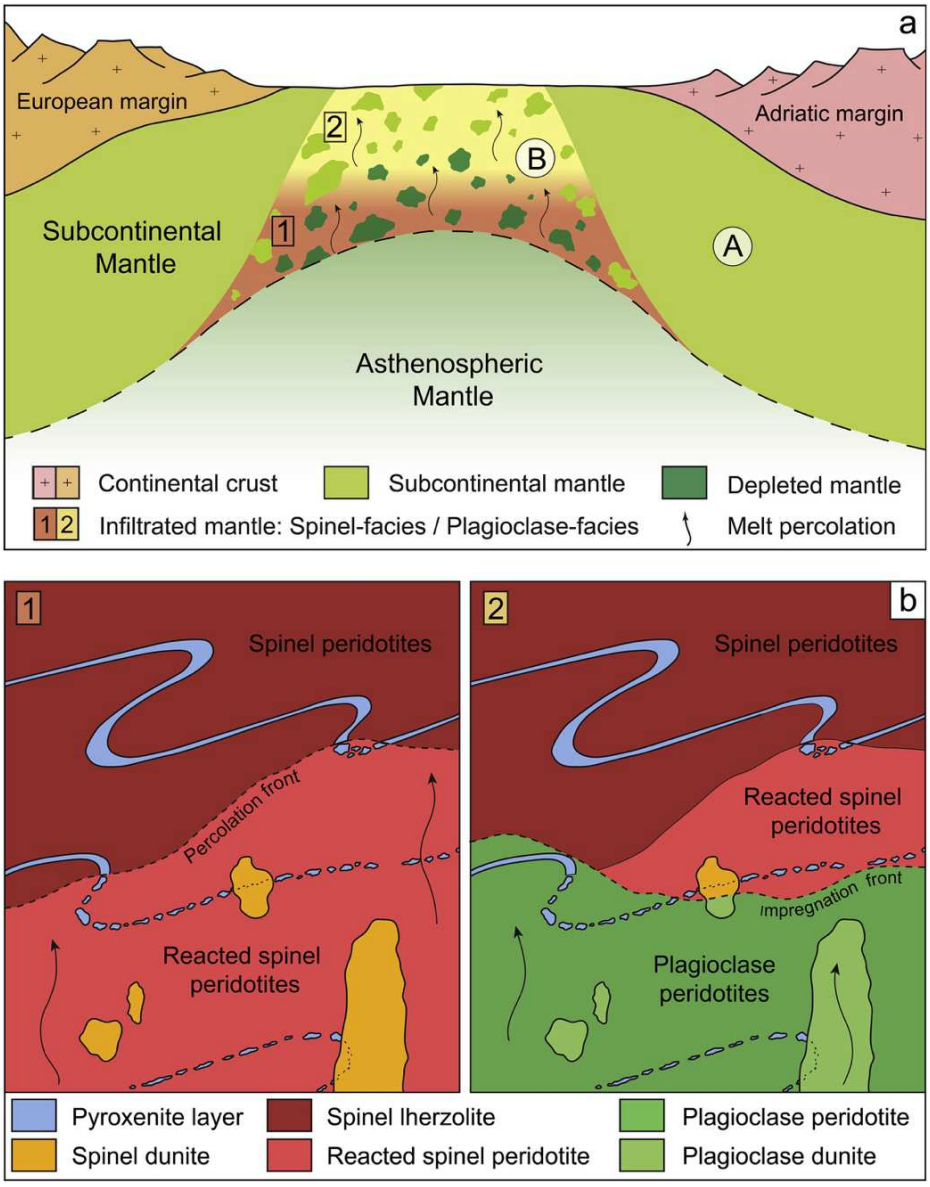


Fig.i-8 : *Description schématique simplifiée et répartition spatiale des différents processus rencontrés dans la formation d'une marge passive pauvre en magma (cas du paléo-domaine téthysien - redessiné d'après Manatschal et Müntener, 2009 ; d'après Rampone et al., 2020).*

Ces processus sont néanmoins très dépendants de conditions thermodynamiques dans lesquels ils ont lieu (pression – température). Ils ont lieu au cours de l'exhumation, constituant ainsi de réels indices pour l'étude des chemins d'exhumation suivis par les roches.

1.3.2. Évolution des conditions de pression et température des roches mantelliques

Le processus d'océanisation, dont les premiers stades sont enregistrés dans la marge passive, engendre le passage d'un domaine lithosphérique stable à un domaine dominé par les processus magmatiques.

Au cours de l'extension, le manteau asthénosphérique, moins dense que la lithosphère sus-jacente, est entraîné vers le haut afin de maintenir l'équilibre isostatique (McKenzie, 1978). Si l'extension de la lithosphère se produit à une vitesse suffisante pour empêcher une perte significative de chaleur par conduction à partir du manteau remontant, l'asthénosphère recoupera le solidus de péridotite et entrera en fusion partielle (Fig. i-9). Si l'ascension est plus lente et permet une perte de chaleur suffisante par conduction, l'asthénosphère maintiendra des températures sous le solidus, supprimant la fusion partielle.

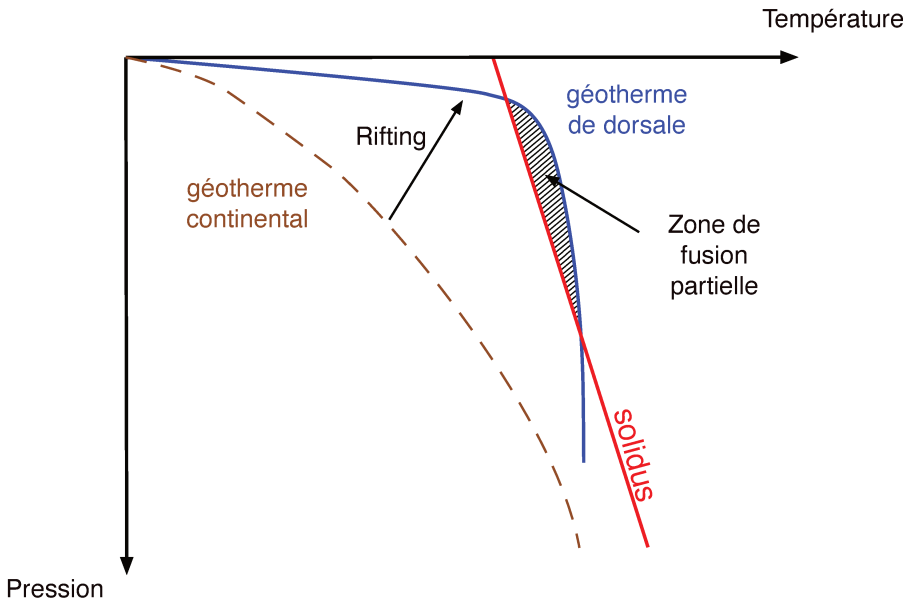


Fig. i-9 : Évolution schématique du géotherme et fusion partielle lors du rifting

Du fait des processus différents auxquels sont soumis les roches au cours du processus de rifting, les conditions de pression et température auxquels ils sont soumis sont variables. Deux types de chemins P-T sont mis en évidence (Fig. i-10) :

- Les chemins P-T dits « **froids** », tel que cela a pu être montré pour Malenco, Totalp ou Upper Platta (Müntener et Piccardo, 2003 ; Müntener et al., 2010 ; Borghini et al, 2011). Il est proposé que les péridotites sont exhumées passivement au cours de l'extension (Erro Tobbio - Strating et al., 1993 ; Iberia margin - Chazot et al., 2005). Dans ce cas, lorsque du plagioclase est formé, il est issu d'une rééquilibration subsolidus du plagioclase lors du passage à un domaine à pression plus faible (Rampone et al.,1993 ; Borghini et al., 2010).

- Les chemins P-T dits « **chauds** », tel que cela a pu être montré pour Lower Platta (Müntener et al., 2010) ou dans les ligurides externes (Montanini et al., 2006 ; Piccardo et al., 2009).

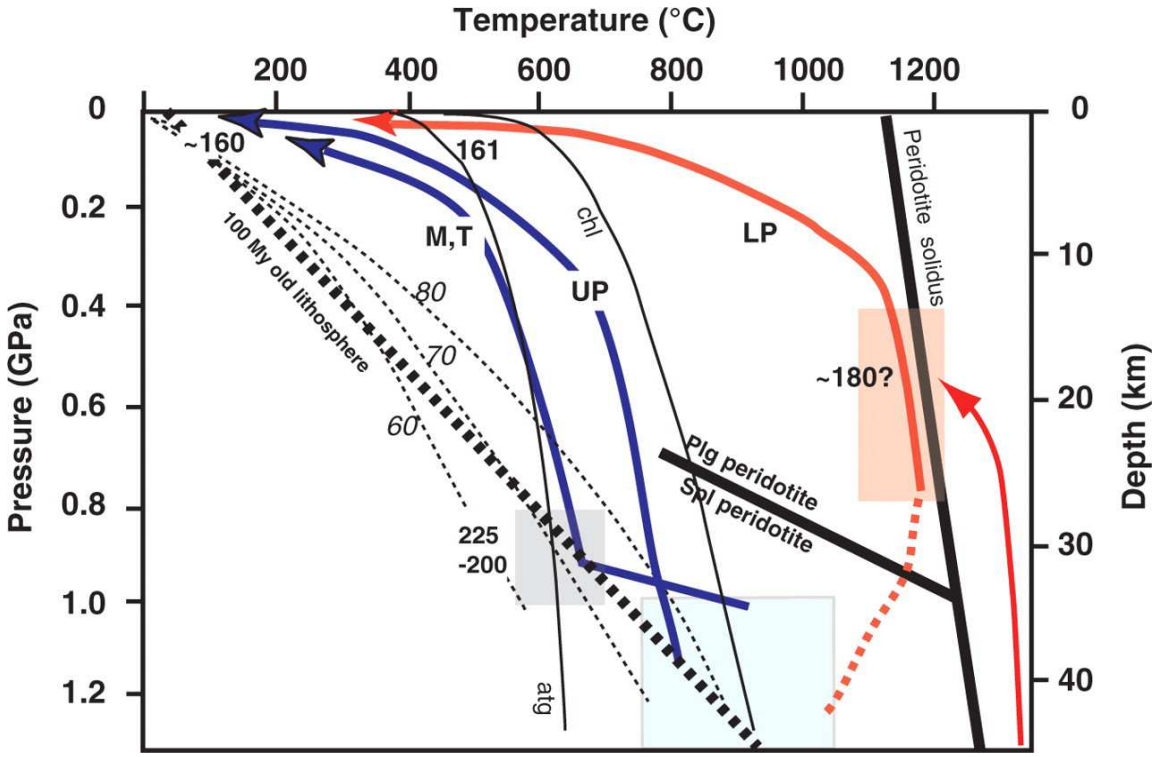


Fig. i-10 : *Illustration schématique des trajectoires pression-température des péridotites des différents domaines d'étude lors de la mise en place de la marge passive pauvre en magma. M: Malenco, T : Totalp, UP : Upper Platta, LP : Lower Platta. D'après Müntener et al., 2010.*

La présence de ces deux chemins de pression-température dans une zone parfois géographiquement très restreinte s'explique par le fait qu'il s'agit de roches ayant subi une perturbation ou déséquilibre, lié au passage d'un liquide magmatique avec lequel elles ont interagi. L'étude des conditions thermodynamiques qu'ont subi ces roches peut ainsi être un indicateur des conditions d'exhumation suivis par les péridotites au cours des processus de rifting.

1.3.3. Premiers produits éruptifs formés lors de l'ouverture

Une des questions principales qui se pose lorsque l'on étudie les marges passives pauvres en magmas c'est d'expliquer l'origine de la faible activité magmatique visible en surface. Le premier paramètre que les chercheurs tentent de quantifier, c'est le budget magmatique lors de la rupture. Est-ce que du magma s'est formé lors du rifting ?

Plusieurs études tendent à proposer que seule une très faible proportion de magma soit formée, expliquée par une température potentielle du manteau trop faible (Rooney et al., 2023) ou encore par une exhumation du manteau lithosphérique trop lente (Bown & White, 1994 ; Lavier & Manatschal, 2006), empêchant la remontée de l'asthénosphère suffisamment vite pour qu'elle atteigne la fusion partielle par décompression adiabatique (Smye et al., 2017). Mais, en prenant en compte les processus d'imprégnation mantelliques développés précédemment, d'autres explications ont été proposées. Les travaux sur la zone de Lanzo (Kaczmarek & Müntener, 2008) ou sur d'autres zones refertilisées alpines tel que Lower Platta (Müntener et al., 2010) ont mis en évidence que jusqu'à 12% de liquides basaltiques peuvent être stockés dans les péridotites, qui est ainsi vue pour certains auteurs comme une « éponge lithosphérique ». Ils proposent que la distinction entre marge passive pauvre en magma et riche en magma est liée à la stagnation des liquides magmatiques en profondeur.

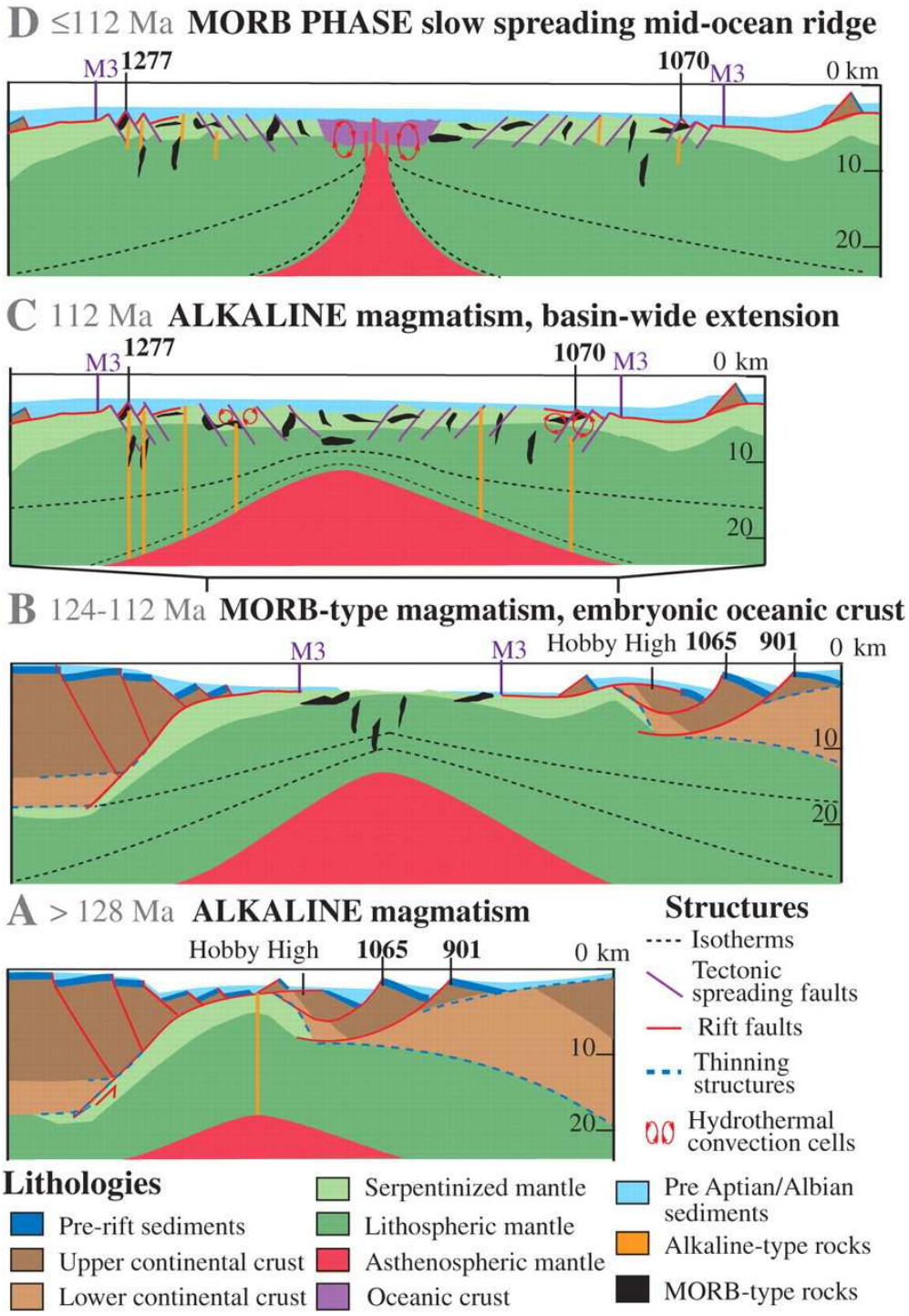


Fig. i-11 – *Modèle tectono-magmatique de l'initiation de l'accrétion océanique dans le sud de l'Atlantique Nord montrant les différentes phases alcalines et tholéiitiques (Jagoutz et al. 2007, modifié d'après Péron-Pinvidic et al. 2007 et Tucholke et al. 2007).*

L'étude pétro-géochimique des produits magmatiques arrivés en surface est essentielle pour répondre à ces questions. Les études sur les marges passives Ibérie – Terre-Neuve et alpines montrent que le magmatisme a une géochimie transitoire entre des liquides de type N- à E-MORB et des liquides magmatiques plus alcalins (Fig. i-11 ; Jagoutz et al., 2007 ; Amann et al., 2019). Les roches formées sont des basaltes, des Mg-gabbros, des Fe-Ti-P gabbros et des diorites (Desmurs et al., 2002). La (les) source(s) mantellique(s) de ces basaltes et gabbros sont très mal définies. De manière générale dans une zone d'accrétion océanique, les liquides basaltiques proviennent d'un réservoir appauvri nommé Depleted MORB Mantle (DMM). Ils sont formés par décompression adiabatique de l'asthénosphère au cours de sa remontée à des profondeurs plus basses. L'hétérogénéité des produits magmatiques des marges passives montrent que ce seul réservoir ne peut expliquer l'ensemble des roches produites et une interaction avec le manteau sous-continental, avec une source mixte péridotite-pyroxénite, a pu être proposée (Amann et al., 2019).

Enfin, l'ensemble de ces études sur les marges passives pauvre en magmas reposent un héritage sous-continental commun. Étudier d'autres types de marges, en dehors de l'espace européen est donc essentiel afin de tester ce modèle, donnant une importance considérable aux échantillons dragués le long de la marge sud-ouest australienne.

2. Le cas de la marge passive sud-ouest australienne

2.1. L'histoire géologique et géodynamique de l'océan Indien

Dans cette thèse, je me suis concentrée sur des échantillons provenant de l'Océan Indien, et plus particulièrement de la marge sud-ouest australienne, au niveau de la zone appelée « zone Diamantine » (Heezen & Tharp, 1965). Cette zone, considérée comme une marge peu magmatique (Direen et al., 2007) fait plus de 1600 km de long et 150 km de large. Elle s'inscrit dans l'histoire géodynamique de l'Océan Indien, résultant de la fragmentation du dernier supercontinent Gondwana ou Pangée (Fig. i-12).

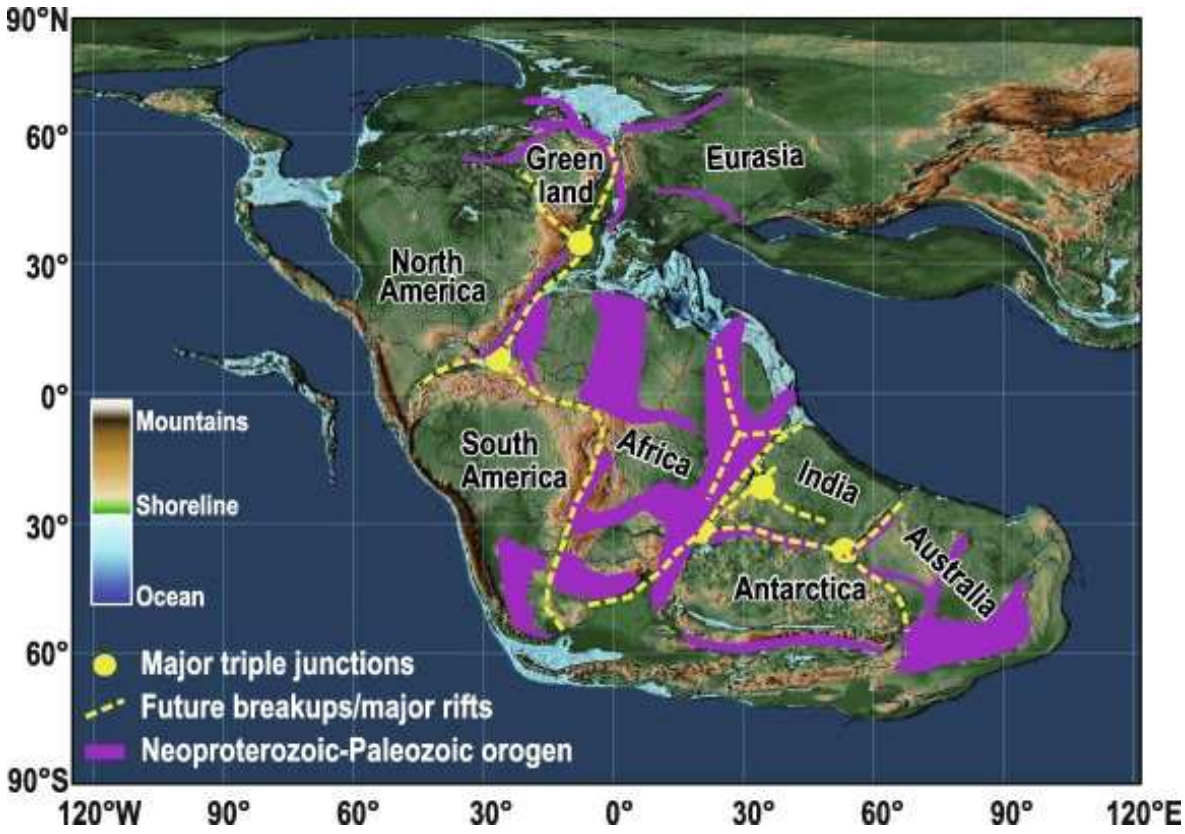


Fig. i-12 : *Reconstruction de la Pangée à 205 Ma d'après la reconstruction paléogéographiques compilées PALOMAP Paleo Atlas pour Gplates (Scotese, 2016). D'après Guan et al., 2021.*

La zone Diamantine se situe sur la marge sud-ouest de l'Australie (Fig. i-13), qui résulte de la séparation entre l'Australie et l'Antarctique (Munschy, 1998) ayant abouti à l'actuelle zone d'accrétion de la dorsale sud-est indienne (SEIR). Plusieurs structures majeures sont présentes autour de la zone d'intérêt :

- La dorsale sud-est indienne au sud : zone d'accrétion océanique lente

- Le plateau de Kerguelen à l'ouest : ce plateau océanique résulte de l'épanchement du point chaud de Kerguelen lors de plusieurs phases successives à partir de 130 Ma (Coffin et al., 2002 ; Duncan, 2002). Il forme initialement avec Broken Ridge un seul et même plateau océanique qui subira un rifting vers 43 Ma.

- La discordance Australie-Antarctique au sud-est : il s'agit d'une zone anormalement froide dont l'origine reste débattue. Certains auteurs proposent que cette zone marque le passage entre la zone mantellique indienne et pacifique (Kempton et al., 2002), tandis que d'autres auteurs proposent la présence d'un ancien slab de subduction (Gurnis & Müller, 2003).

- Le continent australien au nord : la zone sud-ouest australienne, est constituée d'un craton (Yilgarn Craton) bordé au sud par un orogène Mésoprotérozoïque (Albany-Fraser ; Maier et al., 2016 ; Spaggiari et al., 2015) proposant un héritage mantellique très ancien.

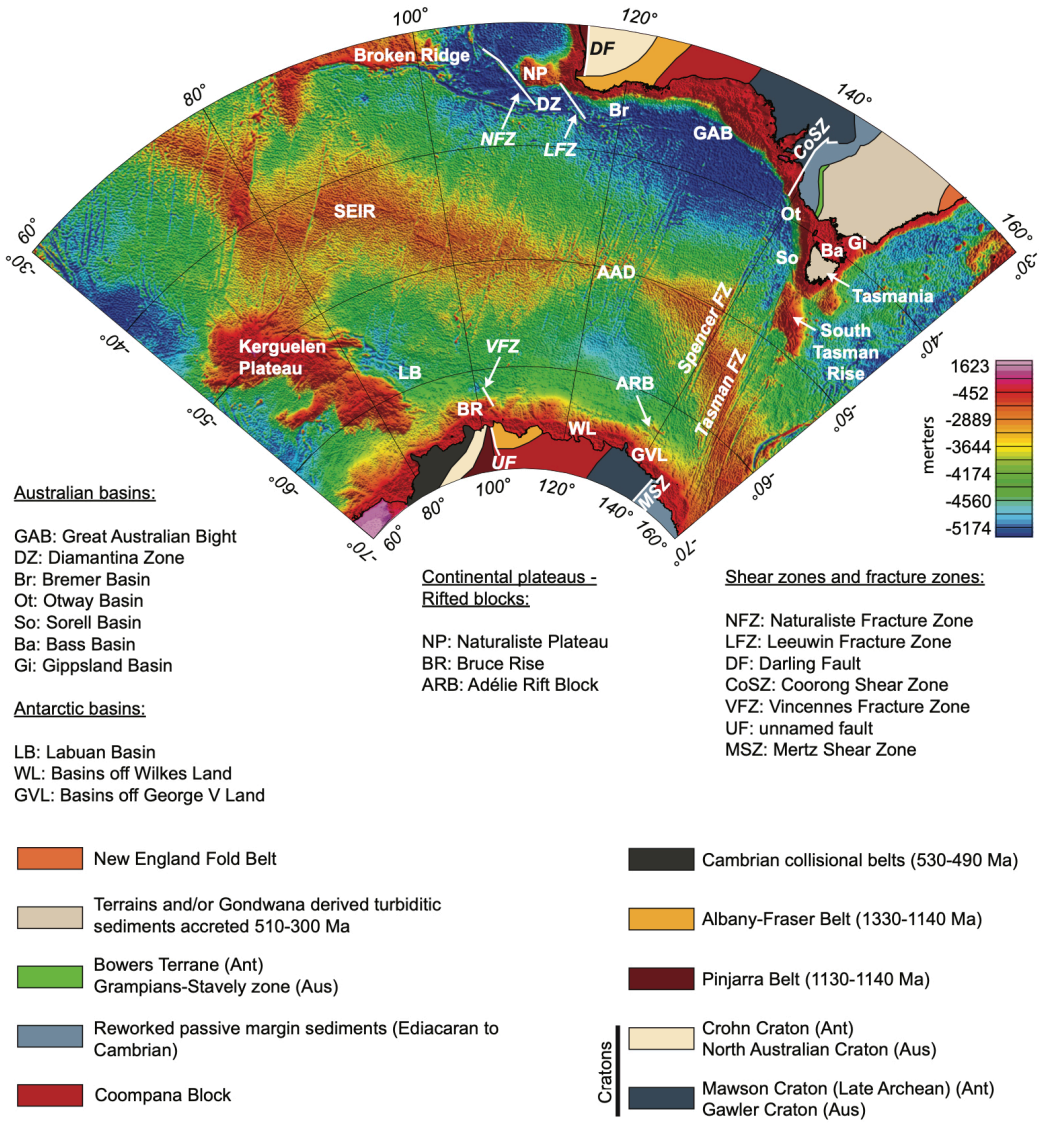


Fig. i-13 : *Carte structurale de l'Océan Indien du sud-est (d'après Gillard, 2014)*

Les études bathymétriques de la zone diamantine mettent en évidence une zone très accidentée, recoupée par des zones de fracture d'orientation NO-SE : la zone de fracture Naturaliste au centre (Chatin et al., 1998) et la zone de fracture de Leeuwin à l'est (Fig. i-13 ; Fig. i-14). Plusieurs études proposent que le bassin conjugué de Diamantine est le bassin de Labuan (Munschy, 1998 ; Magri et al., 2024) bien qu'il n'y ait pas de consensus quant aux correspondances des zones de fractures.

L'étude de Nicholls et al. (1987), antérieure aux campagnes océanographiques MD80 et MD110, se focalisait sur quelques échantillons de lherzolites à spinelles et clinopyroxénites draguées le long de la zone Diamantine. L'étude, très parcellaire, ne fait état que des éléments majeurs de quelques clinopyroxènes qui montrent des valeurs élevées en Na_2O (> 1.5 wt%), moyens en Al_2O_3 (4.6 - 5.4 wt%), et des spinelles dont les Mg# (Mg/(Mg+Fe)) sont homogènes (0.722 < Mg# < 0.733) pour des Cr#(Cr/(Cr+Al)) plus variables (0.198 < Cr# < 0.334).
Plus à l'est, une étude s'est focalisée sur la marge passive située au niveau de Tasmanie (McCarthy et al., 2020). Cette étude a montré la présence de péridotites exhumées sur le plancher océanique. Ces péridotites sont des lherzolites à spinelles et à plagioclases, ainsi que des pyroxénites. Les résultats proposent qu'il s'agissent de péridotites d'affinité sous-continentale, bien que des interactions avec un liquide magmatique ne sont pas exclus par les auteurs.

2.2. Les missions océanographiques MD80 et MD110

Deux campagnes océanographiques, MD80 et MD110, ont dragué le fond marin au niveau de la zone Diamantine dans les années 1990. La campagne MD80 a eu lieu en 1994 sous la direction de Marc Munschy et la campagne MD110 en 1998 sous la direction de Jean-Yves Royer et Marie-Odile Beslier (Royer and Beslier, 1998), toutes deux sur l'hauturier Marion Dufresnes de la flotte océanographique française.
L'objectif de ces missions était d'étudier la structure de la marge continentale sud-ouest australienne, afin de déterminer dans un premier temps l'origine de la formation de ce bassin, zone clé pour comprendre l'ouverture initiale de l'Océan Indien Oriental. Plusieurs origines potentielles étaient déjà proposées : une zone d'expansion océanique (dorsale), une zone

d'étirement du plateau des Kerguelen (Munschy, 1994) ou encore issue de la fragmentation du Gondwana (Royer & Beslier, 1998). Des données de bathymétrie (ayant permis d'obtenir les cartes utilisées tout au long de cette thèse), sismique, gravimétrie, magnétisme ont été récoltées ainsi que des échantillons par dragage. Une coupe a ainsi pu être obtenu et traitée.

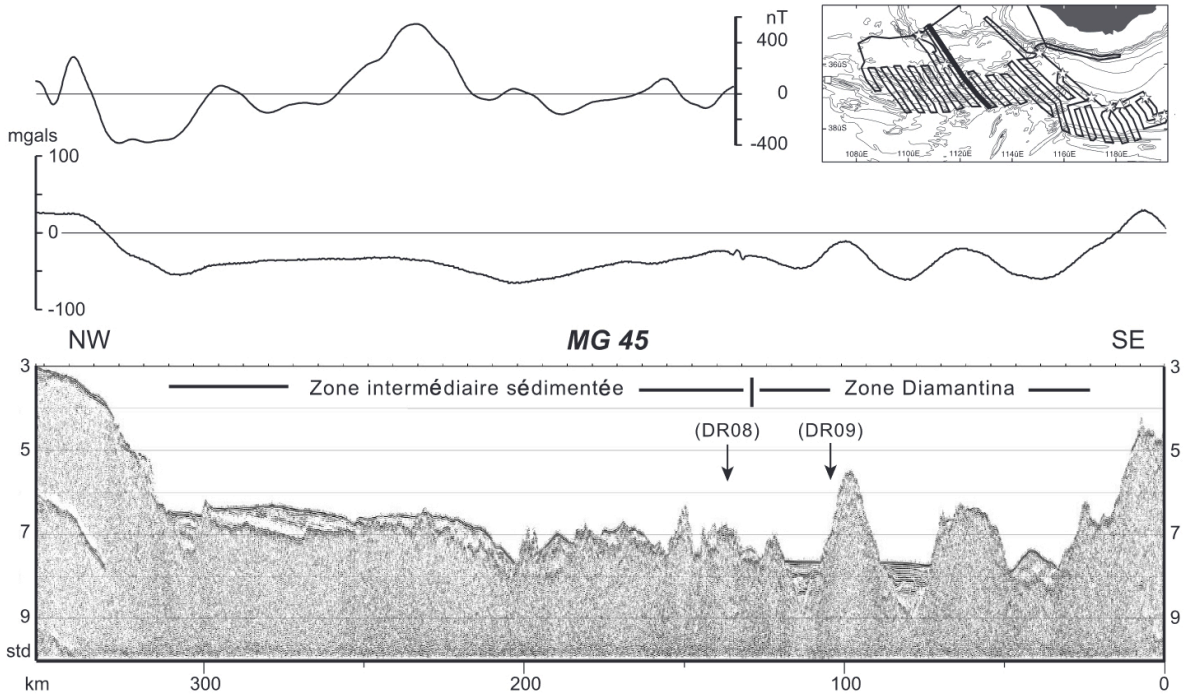
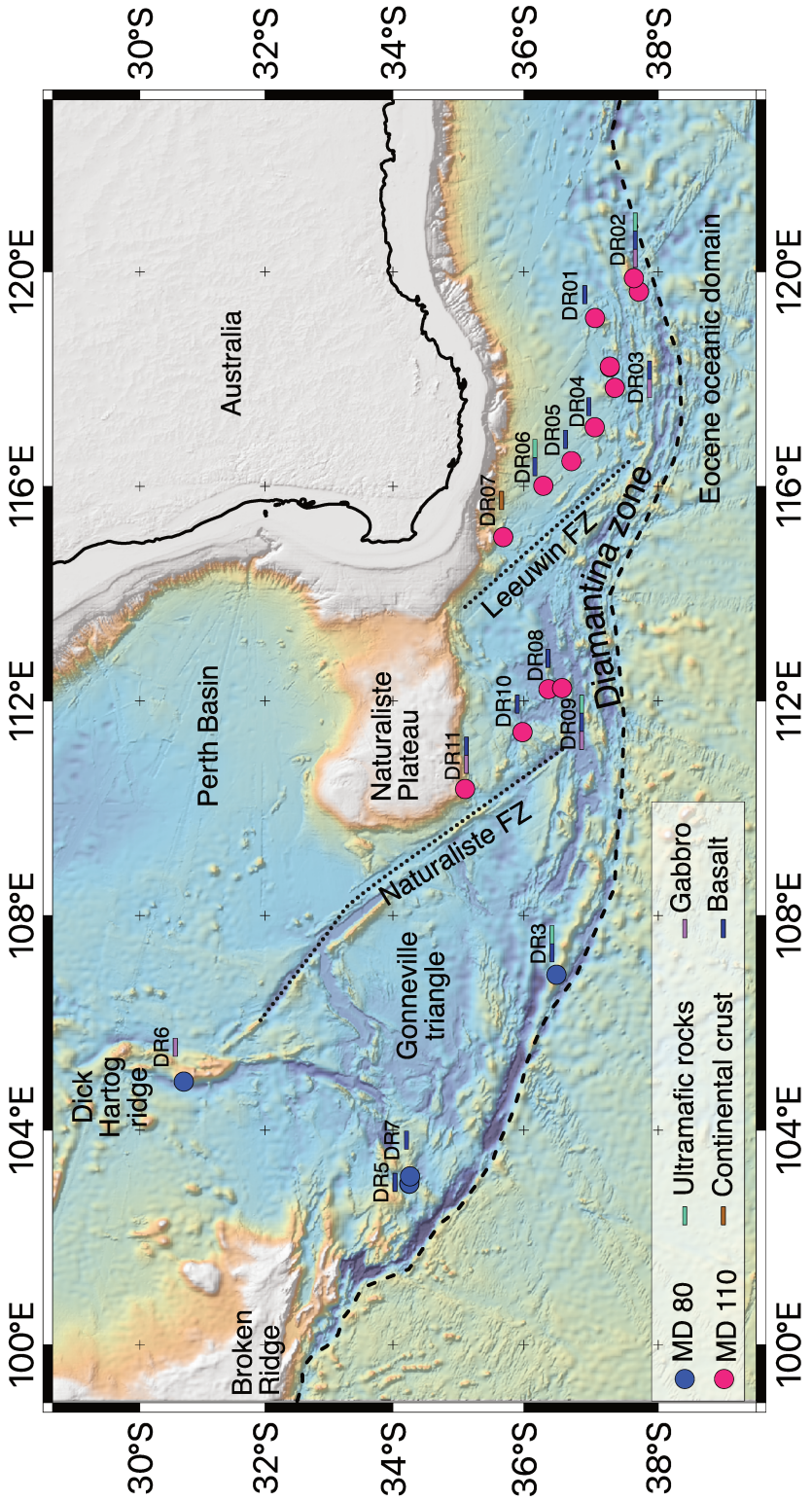


Fig. i-14 : *Profil sismique, gravimétrique et magnétique MG45 (d'après Beslier et al., 2004).*

Bien qu'ayant eu lieu dans les années 90, les deux campagnes océanographiques ayant échantillonné des roches sur le plancher océanique de la zone Diamantine n'ont été que très peu étudiées. La majorité des études concernent les données géophysiques (Munschy, 1998 ; Rotstein et al., 2001 ; Belviso et al., 2004 ; Direen et al., 2007 ; Halpin et al., 2008 ; Magri et al., 2024). Seul un papier préliminaire fait état d'une étude pétrographique des échantillons dragués lors de la campagne MD110 (Beslier et al., 2004), bien qu'une thèse ait déjà permis l'étude de quelques échantillons de la campagne MD80 et ayant donné lieu à une publication (Chatin et al., 1998). Les points de dragage sont visibles sur la figure i-15.


30°S
32°S
34°S
36°S
38°S
100°E
104°E
108°E
112°E
116°E
120°E
Australia
Perth Basin
Naturaliste Plateau
Leeuwin FZ
Naturaliste FZ
Diamantina zone
Eocene oceanic domain
Gonneville triangle
Dick Hartog ridge
Broken Ridge
DR01
DR02
DR03
DR04
DR05
DR06
DR07
DR08
DR09
DR10
DR11
DR3
DR5
DR6
DR7
MD 80
MD 110
Ultramafic rocks
Continental crust
Gabbro
Basalt

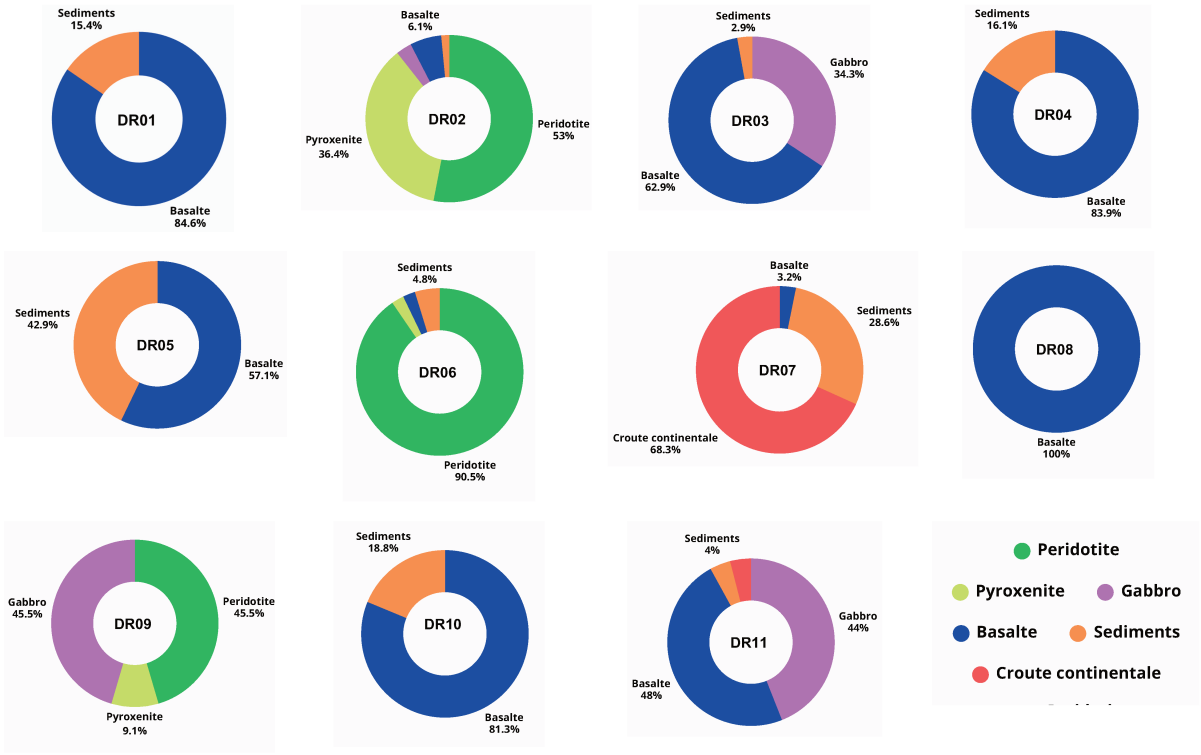


Fig.i-15 : a. *Carte bathymétrique de la zone de Diamantina, sud-Est de l'océan Indien. Les points de couleur indiquent l'emplacement des dragues MD80 et MD110 et les lithologies des échantillons dragués (Chatin et al., 1998 ; Beslier et al., 2004). b. Proportions lithologiques pour chaque point de dragage.*

Au total, 199 échantillons ont été collectés à partir de 5 dragues lors de la campagne MD80 (7 dragues initiales mais dont 2 ont échoué), et 342 échantillons à partir de 11 dragues lors de la campagne MD110 (11 dragues réussies sur 14 tentées), couvrant une large zone le long de la zone de Diamantina (Fig.i-15). Les échantillons dragués comprennent des roches ultramafiques (péridotites, pyroxénites), des roches magmatiques (gabbros, basaltes, diorites, granites), des roches métamorphiques (métasédiments, gneiss, amphibolite), des sédiments, des brèches et des nodules polymétalliques selon la répartition ci-dessous.

Dans les rapports de campagne, les scientifiques font déjà état de péridotites exceptionnellement préservées sur la campagne MD110, mais à l'état de brèches dans la campagne MD80.

Les travaux de Chatin et al. (1998) sur les échantillons de MD80 ont montré une affinité mantellique sous-continentale pour les péridotites et des compositions alcalines à transitionnelles pour les basaltes, lié à l'activité du point chaud de Kerguelen.

Les travaux préliminaires de Beslier et al. (2004) sur les échantillons de MD110 ont confirmé la succession de deux phases tectoniques majeures de rifting où peu de produits magmatiques sont formés. La zone Diamantine correspond à la formation d'une large zone de transition océan-continent où des péridotites et pyroxénites affleurent directement sous les sédiments et ne sont que rarement associées à des roches mafiques. Ces travaux préliminaires ont permis d'aboutir à une coupe schématique à travers la zone Diamantine qui permet de déterminer différentes zones au sein de la marge passive (Fig. i-16).

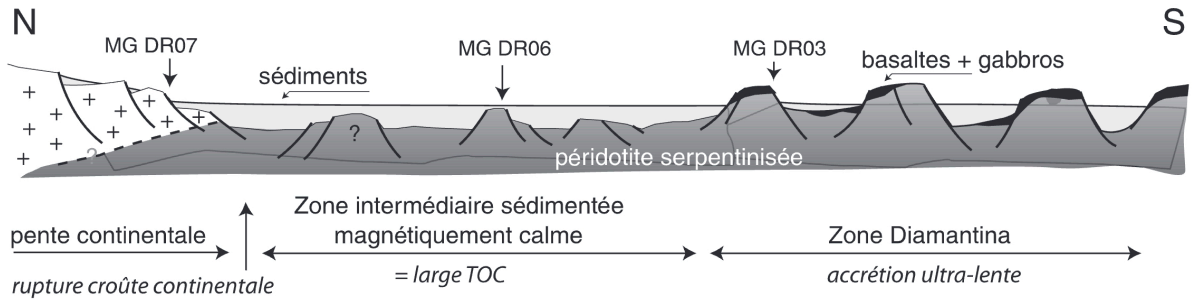


Fig. i-16 *: Coupe schématique de la marge au sud-ouest de l'Australie, déduite des données de la campagne MD110 (d'après Beslier et al., 2004)*

3. Méthodes d'analyse

Les rapports des campagnes MD80 et MD110 (Munschy, 1994 ; Royer & Beslier, 1998) disposent d'inventaires des échantillons collectés réalisés directement sur le navire au cours de la campagne. A partir de cet inventaire et d'une étude macroscopique des roches, les échantillons ont été triés selon leur lithologie. Les plus préservés de l'altération hydrothermale et dont les blocs sont assez grands ont été sélectionnés afin d'effectuer des analyses en roche totale et sur minéraux en *in situ* sur lame mince.

3.1. Analyses géochimiques en roche totale

Les analyses en roches totales ont été effectués sur des poudres ayant subi plusieurs étapes : sciage, broyage sur broyeur à disques en WC ou dans des broyeurs en agate selon

l'échantillon (fraction finale < 100 µm) puis sur une pulvérisette dans des broyeurs planétaires à billes d'agate (fraction finale de l'ordre du µm).
Deux fractions ont été séparées : l'une pour les analyses en éléments majeurs sur µ-XRF au sein du laboratoire ITES de Strasbourg, l'autre pour les analyses en éléments traces par LA-ICP MS au sein du laboratoire KIT de Karlsruhe.
L'analyse en éléments majeurs se fait sur des échantillons anhydres, c'est-à-dire dont on a effectué la perte au feu préalablement permettant d'évaluer la quantité d'eau.

La concentration en éléments majeurs (et certains éléments mineurs) des roches totales ont été déterminées par µ-XRF sur une Bruker M4 Tornado. Équipée d'une anode en rhodium collimatée, elle fonctionne à une tension de 50 kV et une intensité de 700 µA, produisant ainsi une taille de spot de 1 mm de diamètre. Le temps de comptage par point est fixé à 300 secondes. Les rayons X réémis par l'échantillon sont détectés par deux spectromètres XFlash® silicon drift detector de 60 mm^2 avec une résolution énergétique inférieure à 135 eV à 250 000 cps (mesurée sur MnK_α). Pour chaque échantillon, 10 répliques ont été effectuées à la surface de la pastille afin d'assurer une bonne reproductibilité des mesures. Les spectres µ-XRF ont été déconvolués à l'aide du logiciel Bruker Esprit, permettant de calculer les concentrations en utilisant la méthode de quantification par les paramètres fondamentaux (FP). La précision de la quantification est améliorée par l'application de facteurs de correction déterminés après des analyses répétées sur poudres de standards internationaux comprenant le microgabbro PM-S, la dolérite WS-E, la péridotite DTS-2b et le granite AC-E (Jochüm et al., 2016).

Les concentrations en éléments traces des roches totales ont été mesurées sur des pastilles de poudre pressée (préparées selon la méthode décrite par Patten et al., 2023) à l'Institut de Technologie de Karlsruhe. L'analyse a été effectuée sur un laser Excimer Teledyne de 193 nm couplé à un ICP-MS (Element XR ThermoFisher) par ablation laser-spectrométrie de masse à plasma inductif avec les paramètres suivants : diamètre du cratère d'ablation de 85 µm ; fréquence d'impulsion de 10 Hz, 5 $J.cm^{-2}$; et flux de He, Ar et N de 0.3 $L.min^{-1}$, 0.85 $L.min^{-1}$, et 10 $mL.min^{-1}$, respectivement. Un total de 5 points a été analysé pour chaque échantillon et un total de 10 points pour chaque standard. L'étalonnage et la qualité des données ont été effectués à l'aide des standards internationaux BCR-2, BHVO-1, BHVO-2 et

USGS-BIR-1. La réduction des données a été effectuée à l'aide du logiciel Iolite 4 (Paton et al., 2011), en suivant la méthode de limite de détection de Pettke et al. (2012).

3.2. Analyses in *situ*

Les analyses des minéraux sur lame mince ont été effectuées via différentes méthodes : les éléments majeurs ont été mesurés par une technique novatrice de µ-XRF couplée à des données microsonde acquises au laboratoire Géoressources de Nancy. Les détails de la mise en place de cette méthode sont détaillés dans le chapitre 1.

Pour les minéraux trop petits pour être analysés par µ-XRF (< 40 µm, typiquement pour les inclusions minérales ou des pyroxènes avec des exsolutions), des analyses supplémentaires ont été effectuées avec une microsonde électronique CAMECA SX100 (EPMA) au Service Commun de Microscopie Électronique et de Microanalyses (SCMEM, Géoressources Nancy). Toutes les analyses des éléments majeurs, Na, Mg, Al, Si, K, Ca, Ti, Cr, Mn, Fe, Ni, ont été effectuées par rapport à des étalons minéraux naturels et synthétiques : albite (Si, Na), corindon (Al), andradite (Ca), olivine (Mg), hématite (Fe), $MnTiO_3$ (Mn,Ti), NiO (Ni), orthoclase (K). La tension d'accélération et le courant du faisceau étaient respectivement de 15 kV et 12 nA, le temps de comptage était de 10 s. Le faisceau était focalisé à ~2 µm.

Concernant les analyses en éléments traces, ils ont été effectués dans deux laboratoires différents selon s'il s'agit de roches ultramafiques ou mafiques.

Les concentrations en éléments traces dans les minéraux des péridotites et pyroxénites ont été déterminées par LA-ICP-MS à Georessources Nancy. Cette méthode implique un laser nanoseconde excimer 193nm de ESI New Wave Research combiné à un ICP-MS triple quadrupole Agilent 8900. Les ablations laser ont été réalisées avec un taux d'impulsion constant de 5 Hz, un diamètre d'ablation de 60-100 µm de diamètre sauf pour l'olivine où le diamètre d'ablation a été fixé à 120 µm pour améliorer le rapport signal/bruit. Le nombre d'impulsions était de 200, ce qui est suffisant pour former un signal long et stable pour l'intégration. Le matériau ablaté est transporté à l'aide d'un flux constant d'He et mélangé à de l'Ar dans un mélangeur coaxial cyclonique avant d'entrer dans la torche ICP et d'être ionisé. Les ions sont ensuite échantillonnés, accélérés et focalisés avant d'être séparés et analysés dans le spectromètre de masse. Les concentrations de ^{29}Si (préalablement connues par µ-XRF

ou microsonde électronique) ont été utilisées comme standard interne, et le verre rhyolitique synthétique SRM 610 du NIST (Pearce et al., 1997) a été utilisé comme standard externe. La réduction des données a été effectuée à l'aide du logiciel Iolite 4 (Paton et al., 2011) où la limite de détection a été déterminée selon la méthode de Pettke et al. (2012). Les standards NIST SRM 612 et BHVO-2 ont été analysés en tant qu'inconnus pour garantir la précision et l'exactitude des mesures.

Les concentrations en éléments traces des minéraux contenus dans les basaltes et gabbros ont été déterminés par LA-ICP-MS au laboratoire Karlsruhe Institut für Technologie (KIT) de Karlsruhe, sur le même équipement et dans les mêmes conditions que pour les analyses LA-ICP-MS de la roche totale, avec un diamètre d'ablation de 40 µm. Les données précédemment déterminées pour le silicium et le fer ont été utilisées en tant que standard interne. L'étalonnage et la qualité des données ont été vérifiés à l'aide des standards BCR-2, BHVO-1, BHVO-2 et USGS-BIR-1. La réduction des données a été effectuée avec le logiciel Iolite 4 (Hellstrom et al., 2008 ; Paton et al., 2011) et en suivant la méthode de calcul pour la limite de détection de Pettke et al. (2012).

3.3. Analyses isotopiques et séparations minéralogiques

Afin d'effectuer des analyses isotopiques, des basaltes nano-broyés ont été envoyés au laboratoire SARM de Nancy qui a déterminé les rapports en $^{143}Nd/^{144}Nd$. Les rapports en $^{176}Hf/^{177}Hf$ ont été mesurés par Harmony Suire et Dr. Marion Garçon au laboratoire Magmas et Volcans de Clermont-Ferrand.

Concernant les péridotites, les analyses ont été effectuées sur des clinopyroxènes séparés et broyés. Les échantillons ont d'abord été sélectionnés, broyés dans un broyeur à disques, tamisés selon différentes fractions (< 50 µm, $50 < X < 100$ µm, $100 < X < 250$ µm, $250 < X < 500$ µm), lavés au bac à ultrasons afin d'éliminé les poussières collées sur les grains (échantillon placé dans un bac à ultrasons pendant 1h dans de l'eau ultrapure milliQ®) puis séchés en étuve. Enfin, un tri manuel à l'aide d'un aimant a été effectué afin d'éliminer les fractions les plus magnétiques (ex : ilménite) avant d'effectuer des passages successifs au séparateur magnétique (Franz) à intensités de plus en plus élevés (20 mA, 80 mA, 0.2 A, 0.4 A,

0.6 A, 1 A). Les clinopyroxènes se situent à des ampérages de l'ordre de 0.6 - 0.7 A. Le dernier passage à 1 A permet d'éliminer les calcites résiduelles.

La pureté des clinopyroxènes séparés a été vérifiée à l'aide de cartographies sur µ-XRF tel que décrit par Ulrich et al. (2014). Ils ont ensuite été broyés manuellement en broyeur à agate avant de subir le protocole d'attaque décrit par Chauvel et al. (2010). Environ 100 mg de poudre de roche ont été dissous dans un mélange HF-HNO_3-$HClO_4$ (proportions 5:1:1) dans des béchers Savillex, pendant 7 jours à 140°C sur une plaque chauffante. La solution a ensuite été évaporée et le résidu dissous dans du HNO3 concentré et évaporé avant d'être dilué dans environ 40 ml de HNO_3 7N.

La mesure précise des isotopes du Nd et du Hf nécessite une séparation chimique de ces deux éléments afin de limiter les interférences isobariques et les effets de matrice lors de la mesure des rapports isotopiques sur MC-ICP-MS (Multi-Collector-Inductively Coupled Plasma-Mass Spectrometer). La séparation chimique des éléments à analyser se fait grâce à des colonnes à résines échangeuses d'ions. Pour les échantillons sélectionnés, et pour séparer les isotopes Hf et Nd, 3 passages sur colonnes ont été nécessaires. Le protocole de séparation de l'Hf utilisé est celui de Blichert-Toft (1997).

4. Questions scientifiques et approche choisie

Cette introduction montre à quel point la compréhension des OCT qui enregistrent les processus liés à la formation des limites de plaques, constitue l'un des plus grands défis qui reste à relever dans le domaine de la tectonique des plaques. Si les processus aux frontières de plaques divergentes au niveau des dorsales médio-océaniques sont relativement bien connus, ceux aux transitions océan-continent, siège des premiers magmas produits lors de la rupture lithosphérique, le sont beaucoup moins.

Comment s'opère la transition d'une lithosphère continentale stable à une zone dominée par le magmatisme à l'origine de l'accrétion d'une nouvelle lithosphère océanique ? Comme cela a été décrit au cours de l'introduction, la zone de transition océan-continent constitue le lieu spatio-temporel de transition entre le domaine continental et le domaine océanique et ainsi le lieu de prédilection pour étudier la mise en place des zones d'accrétion océanique. Quelles sont les conditions de mise en place d'une marge passive pauvre en

magma ? Quels paramètres contrôlent le budget magmatique plus bas et doivent ainsi être étudiés lorsque l'on s'intéresse aux marges passives pauvres en magma ?

Répondre à ces grands questionnements réside dans l'étude plus précise des différents paramètres de mise en place des marges passives pauvres en magma, en prenant en compte les études précédemment développées :

- Quelle est l'importance de l'héritage dans la formation des marges peu magmatiques et en ce sens, est-ce que le modèle communément accepté (Picazo et al., 2016) est valable pour l'ensemble des marges passives peu magmatiques ?
- Quels sont les conditions thermodynamiques d'exhumation des marges riftées peu magmatiques ? Est-ce qu'il existe des paramètres communs à ce type de marges ? Avec les zones de rides médio-océaniques ?
- Quel est la place du magmatisme dans la formation des marges ? Quelle est l'origine des liquides magmatiques ? Sont-ils comparables à ceux formés dans une zone d'accrétion océanique ? Est-ce que la proximité à un point chaud tel que la zone Diamantine modifie les conditions de mise en place des produits magmatiques ?

Après un premier chapitre développant la méthode d'analyse *in situ* par µ-XRF mise en place lors de la thèse, le manuscrit a été découpé en plusieurs chapitres permettant de répondre à ces grandes questions scientifiques, en étudiant les différentes roches draguées par les deux campagnes océanographiques.

Le chapitre 2 correspond à un article intitulé « The role of mantle inheritance and refertilisation during breakup at magma-poor rifted margins: what can we learn from the SW-Australia margin? » soumis dans la revue Earth and Planetary Science Letters. Dans cet article, nous discutons d'abord des caractéristiques du manteau hérité. Puis nous abordons les processus de fusion du manteau liés à la rupture et enregistrés dans les roches du manteau exhumées le long de l'OCT de Diamantine. Ensuite, nous évaluons l'applicabilité du modèle alpin/ibérique en comparant les processus de fusion du manteau associés à la rupture d'un SCLM protérozoïque avec ceux du SCLM paléozoïque de l'Ibérie et du Téthys occidental.

Le chapitre 3 se focalise sur l'évolution des conditions thermiques du manteau au cours de l'exhumation, liée aux processus de rifting. Ce chapitre se présente sous la forme d'un

article en préparation, intitulé « Probing the thermal regime of the mantle during lithospheric break-up » dans l'optique d'une soumission dans la revue « Geology ». Il tente d'éclairer les conditions de la transition entre une lithosphère stable, épaissie et ancienne contrôlée par des aspects mécaniques et des processus tectoniques, et une zone d'accrétion océanique produisant une lithosphère fine, chaude, contrôlée par des aspects thermiques et des processus magmatiques.

Enfin, le chapitre 4 concerne l'étude des produits magmatiques draguées le long de la zone Diamantine. La finalisation des processus d'océanisation se caractérise par l'apparition de la première proto-croûte océanique et pose ainsi la question de l'origine des premiers basaltes océaniques au cours du processus de rifting. Cette question est d'autant plus complexe dans la zone Australie - Antarctique puisque la première croûte océanique se met en place non loin du plateau de Kerguelen posant la question d'une implication d'un point chaud. L'objectif de ce chapitre, présenté sous la forme d'un article en préparation qui sera soumis à la revue « Geochemistry, geophysics, geosystems », est d'effectuer une première caractérisation de ces basaltes et d'en identifier la source, dans le cadre de l'ouverture océanique.

Ces trois chapitres, présentés sous la forme d'articles soumis ou en préparation, sont suivis d'un chapitre de discussion synthétisant l'ensemble des résultats. Dans cette dernière partie nous procédons également à un comparatif synthétique des conclusions ayant pu être établies sur la zone Diamantine aux conclusions formulées préalablement sur les autres marges passives pauvres en magma (Western Téthys et zones adjacentes et les marges conjuguées Ibérie – Terre-Neuve), permettant de répondre aux questions soulevées lors de cette introduction.

CHAPITRE 1

Acquisition de données in situ en éléments majeurs par µ-XRF

Ce premier chapitre concerne la mise en place de la méthode d'analyse que j'ai développée lors de cette thèse, c'est-à-dire l'analyse quantitative *in situ* par μ-fluorescence X (μ-XRF). L'analyse par μ-XRF permet d'analyser les compositions en éléments majeurs et quelques éléments mineurs présents au sein d'un minéral, directement sur lame mince. Ces analyses peuvent ainsi constituer une donnée quantitative ponctuelle, aussi fiable que celle produite par une microsonde, mais également permettre une cartographie de la composition chimique d'une zone restreinte (un minéral) ou même de l'ensemble de la lame mince.

Dans ce chapitre, le principe général ainsi que la mise en place de la méthode de quantification *in situ* sera présentée tout en y intégrant les limites actuelles.

Outre le fait que cette machine était présente dans le laboratoire, la volonté de la mise en place de cette méthode durant la thèse s'explique par le fait qu'elle présente de nombreux avantages : économique, le prix de cette machine représentant 1/5ème du prix d'une microsonde électronique ; compacte, la machine est dite de « paillasse » tout en pouvant analyser des échantillons de grande taille (jusqu'à 550 cm^2) ; à spectre large, elle permet de détecter tous les éléments majeurs et mineurs dans les silicates, oxydes ou minéraux hydratés sans ajout de temps d'acquisition ; non-destructive, les échantillons gardant leur intégrité au cours de l'analyse ; et enfin simple d'utilisation, puisqu'il est possible de laisser facilement quelqu'un en autonomie effectuer ses analyses.

Enfin, étant un outil utilisant des rayons X, la certification RECIPROCS radioprotection du CNRS a été validée dès le début de la thèse.

1. Méthodologie générale et matériel disponible au laboratoire ITES

Les analyses en µ-fluorescence X ont été effectuées sur une M4 Tornado de l'entreprise Bruker© acquise au sein du laboratoire de l'ITES (Fig. I-1) en 2018.

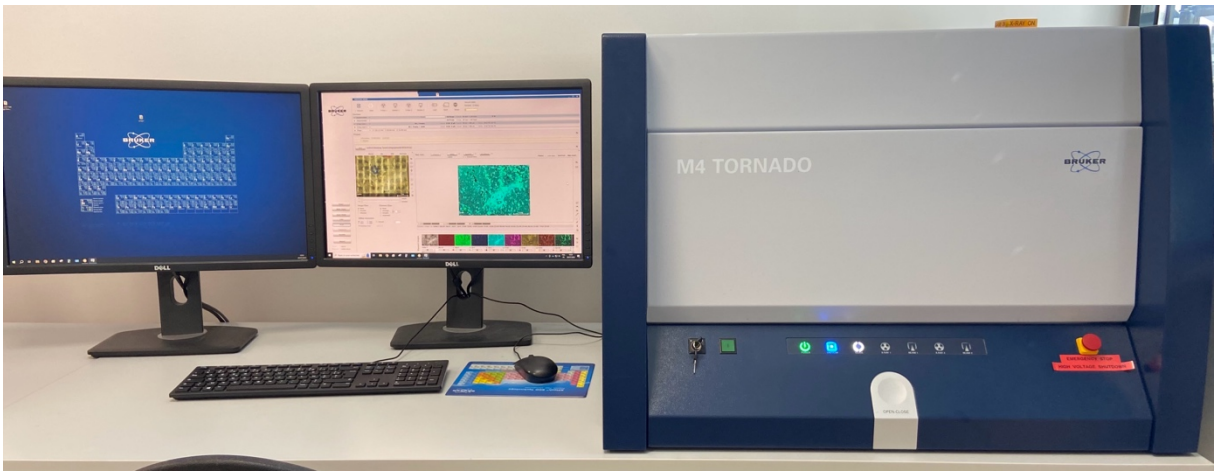


Fig. I-1 – *Installation M4 Tornado© Bruker au laboratoire ITES de Strasbourg*

Le principe de l'analyse *in situ* en µ-XRF est simple, il se base sur l'émission d'une onde électromagnétique dirigée vers l'échantillon et l'analyse de sa réponse par des récepteurs (Fig.I-2).

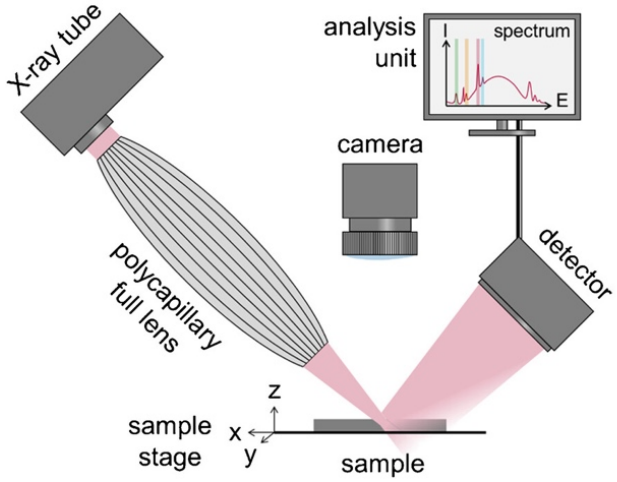


Fig. I-2 – *Principe d'analyse de la µ-XRF (d'après Heimler et al., 2023)*

Le M4 Tornado© est munie de deux sources en rhodium :

- une anode en rhodium polycapillarisée qui émet un faisceau de rayons X d'un diamètre de 20 µm,
- une anode en rhodium collimatée dont le faisceau incident a un diamètre d'1 mm.

Les détecteurs sont deux spectromètres de type Silicon Drift Detectors (SDD) – avec une surface de 60 mm^2 – pouvant être utilisés simultanément. L'ensemble des paramètres de la Bruker M4 Tornado© sont répertoriés en Table I-1.

Taille de la chambre d'acquisition	L x l x h : 600 mm x 350 mm x 260 mm	
Taille des échantillons	L x l : 330mm x 170mm Poids maximal : 5kg	
Sources	Anodes en rhodium	
	Polycapillarisée (∅ = 20 µm)	Analyses *in situ*, cartographie chimique
	Collimatée (∅ = 1 mm)	Analyses roche totale
Paramètres d'excitation	50kV, 30W	
Détecteurs	Deux spectromètres XFlash® silicon drift detector Utilisation en simultané des deux détecteurs	
Paramètres de détection	Diamètre de détection	60 mm^2
	Résolution	<135 eV à 250 000 cps (mesuré sur $^{Mn}K_{\alpha}$).
Évaluation du spectre	Identification des pics, correction des artefacts et du bruit de fond, calcul de la surface des pics, quantification à l'aide de modèles basés sur des normes et sans normes	

Table I.1 – *Données techniques µ-XRF Bruker M4 Tornado*

Lors d'une analyse *in situ*, la source en rhodium polycapillarisée émet un rayonnement d'une intensité de 400 µA pour les silicates et 150 µA pour les minéraux de type oxydes avec une

tension de 50 kV. Les électrons présents au sein des éléments chimiques de l'échantillon sont alors excités par ce rayonnement, ce qui peut conduire à l'éjection d'un ou plusieurs électrons d'une orbitale interne. En réaction à cette structure atomique instable, les électrons des orbitales supérieures passent dans l'orbitale inférieure comblant le vide laissé par l'électron éjecté (Fig. I-3). Au cours de ce processus, une fluorescence est émise sous la forme de photons qui sont émis avec une énergie égale à la différence d'énergie entre les deux orbitales, ce qui est donc propre à chaque échantillon. La longueur d'onde de l'onde émise peut être calculée à l'aide de la loi de Planck :

$$\lambda = \frac{h * c}{\Delta E}$$

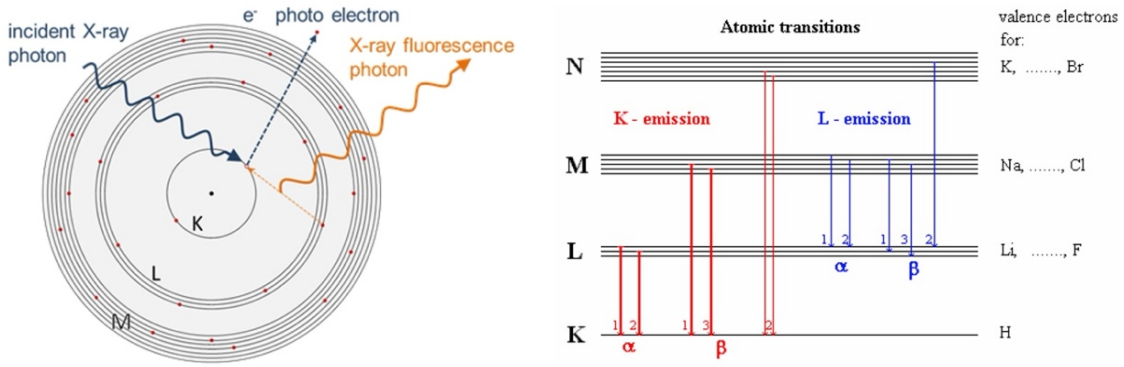


Fig. I-3 – *Principe de la fluorescence induite par rayonnement X sur le modèle atomique de Bohr (gauche) et changements de couches électroniques induits (droite) (https://www.bruker.com/fr/products-and-solutions/elemental-analyzers/xrf-spectrometers/how-does-xrf-work.html)*

L'intensité et la fréquence de cette fluorescence émise par chaque atome sous la forme de photons (Fig. I-3-gauche), sont directement captés par les deux spectromètres SDD. Enfin, les émissions dues aux transitions vers l'orbitale K, à partir de sont appelées émissions K-α. Les émissions dues aux transitions vers l'orbitale K à partir de l'orbitale M (troisième orbitale) sont appelées émissions K-β. Ces K-α et K-β sont connues et propres à chaque élément chimique, permettant ainsi d'identifier l'origine de n'importe quel ray (Fig. I-3-droite). La réponse spectrale de l'échantillon, enregistrée par les spectromètres SDD subit alors une analyse

mathématique, permettant par itérations d'interpréter le spectre en données semi-quantitatives d'éléments chimiques, du sodium au rhodium (Fig. I-4).

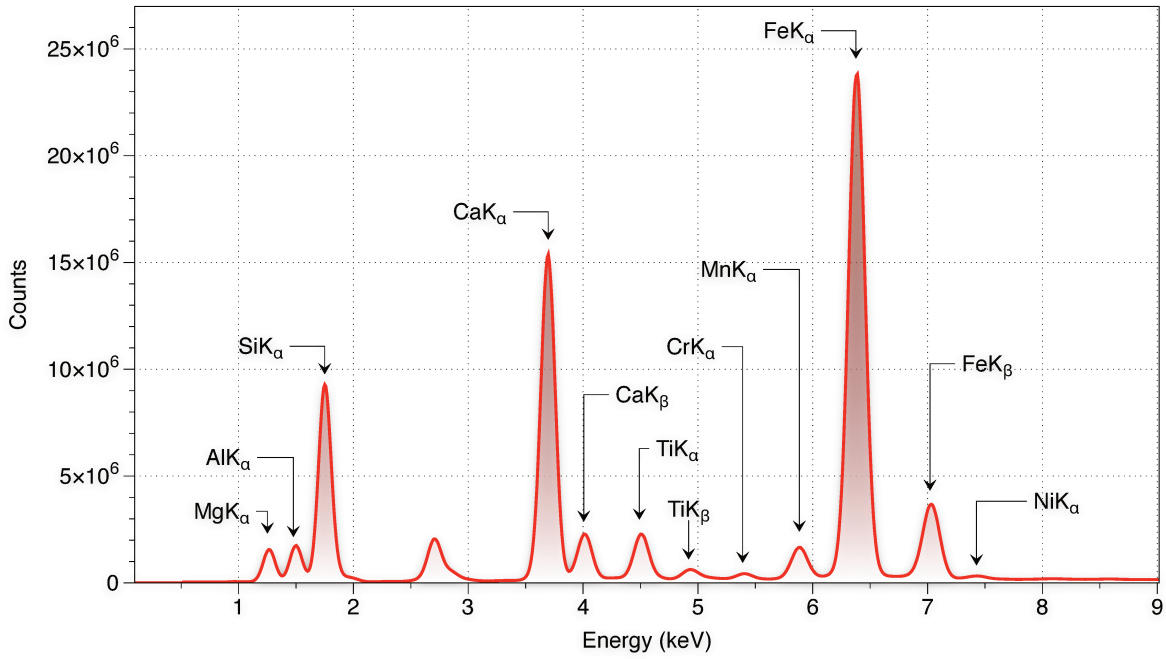


Fig. I-4 – *Spectre de fluorescence et analyse élémentaire d'un clinopyroxène*

A chaque pic du spectre (Fig. I-4) est associé une intensité de fluorescence. Cette intensité est proportionnelle à la concentration dans l'échantillon (Fig. I-5), permettant ainsi d'accéder à la composition chimique réelle de l'échantillon.

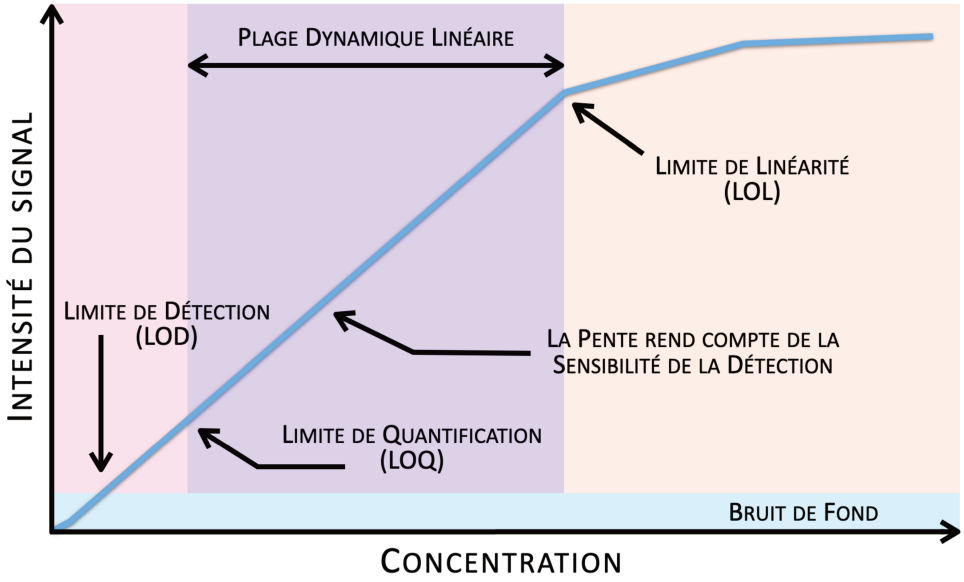


Fig. I-5 – *Intensité de la fluorescence en fonction de la concentration en un élément chimique au cours d'une analyse (Pugniere, 2012)*

Plusieurs limites sont identifiées sur ce diagramme :

- une limite basse au-dessous de laquelle la concentration dans l'échantillon est trop basse pour être mesurée quantitativement,
- une limite haute au-delà de laquelle la relation intensité du signal/concentration n'est plus linéaire.

Le signal doit donc se situer entre ces deux bornes, nommée plage dynamique linéaire, pour que la concentration réelle puisse être mesurée. Cela dépend de plusieurs paramètres de mesure détaillés ci-dessous.

2. Paramétrisation

2.1. Intensité électrique de mesure

Après plusieurs mesures, la plage linéaire dynamique (Fig. I-5) et donc la proportionnalité entre intensité du signal et concentration réelle a pu être définie pour une valeur de « dead time » inférieure à 20%. Le « dead time » (calculé automatiquement par le logiciel) correspond au pourcentage de perte de signal, par perte de photons ou saturation des détecteurs.

En effet, deux paramètres peuvent faire augmenter ce « dead time » :

- Le rayonnement met un certain temps à arriver jusqu'au détecteur et ce détecteur met également du temps à répondre à l'arrivée d'un photon : ce temps est considéré comme un temps mort durant lequel aucun photon n'est capté. Pour le spectromètre de la μ-XRF, le nombre de coups enregistrés est alors inférieur au nombre de coups réels.
- Lorsque la puissance est trop importante, les photons sont trop nombreux pour être captés par les spectromètres qui atteignent la saturation. Cela constitue même le principal paramètre à l'origine de l'augmentation du « dead time ».

Par conséquent, pour corriger l'intensité des rayonnements émis par des échantillons dont la teneur en éléments peut être très différente, il est nécessaire de déterminer la puissance (P = U x I) adéquate de la source qui répond à l'équilibre entre puissance assez élevée pour engendrer un signal mesurable et assez faible pour que le temps mort ne soit pas trop important. Pour une tension U de 50 kV, l'intensité I sera différente en fonction du type d'échantillon considéré modifiant ainsi la puissance finale P. Elle est imposée ici à I = 400 µA pour les silicates et I = 150 µA pour les minéraux de type oxyde métalliques dont la concentration en éléments à forte fluorescence (e.g. les métaux de transitions) est généralement élevée (> 1 wt%).

2.2. Sensibilité

Lorsque l'on effectue des mesures sur des standards internationaux avec ces nouveaux paramètres de puissance bien définis, il devrait donc y avoir une seule relation de proportionnalité entre l'intensité mesurée par les spectromètres et la concentration réelle dans le minéral. Sur le MgO (Fig. I-6a) on observe effectivement cette proportionnalité, pour de larges gammes de variations de concentration. Par contre, l'Al_2O_3 (Fig. I-6b) ne répond pas à cette proportionnalité. Pour cet élément chimique, on voit très clairement que la concentration en FeO influe sur l'intensité de mesure en Al_2O_3. Plus la concentration en FeO est élevé dans l'échantillon, plus l'Al_2O_3 est sous-évalué.

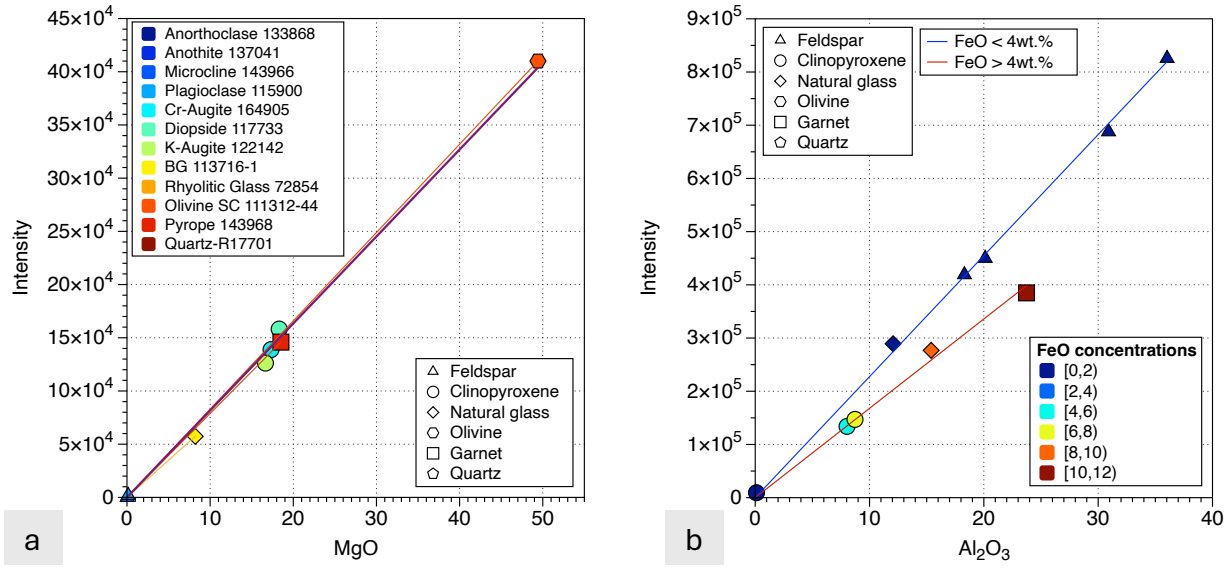


Fig. I-6 – *Intensités de mesure sur le MgO (a) et l'Al_2O_3 (b)*

Cet effet est connu et lié à un processus physique : le fer agit comme source d'excitation secondaire de l'aluminium (Perret et al., 2014 ; Flude et al., 2017). Bien que visible sur les intensités, ce processus physique est corrigé par les paramètres fondamentaux de la µ-XRF, ce qui n'a donc pas d'influence sur les concentrations mesurées (voir section 3.1).

2.3. Effet d'épaisseur non-infinie

Selon l'élément chimique considéré, le rayonnement induit K_α pénètre plus ou moins en profondeur. Cette pénétration est dépendant du numéro atomique et de la matrice de l'échantillon : Dans le cas de silicates, pour des éléments légers (Na, Mg, Si, Al), la profondeur de pénétration du rayonnement induit est négligeable (<10 µm). En revanche, pour les éléments plus lourds (Ni, Cu, Zn), la profondeur de pénétration peut dépasser la centaine de µm, ce qui s'avère problématique dans le cas d'une analyse in situ effectuée sur un matériel de profondeur « non-infinie », i.e. pour des éléments dont la profondeur d'excitation théorique est supérieure à l'épaisseur de l'échantillon. La figure I-6 montre que dans le cas d'une analyse de silicate sur lame mince de 30 µm, l'échantillon sera considéré comme d'épaisseur non-infinie à partir du Cr.

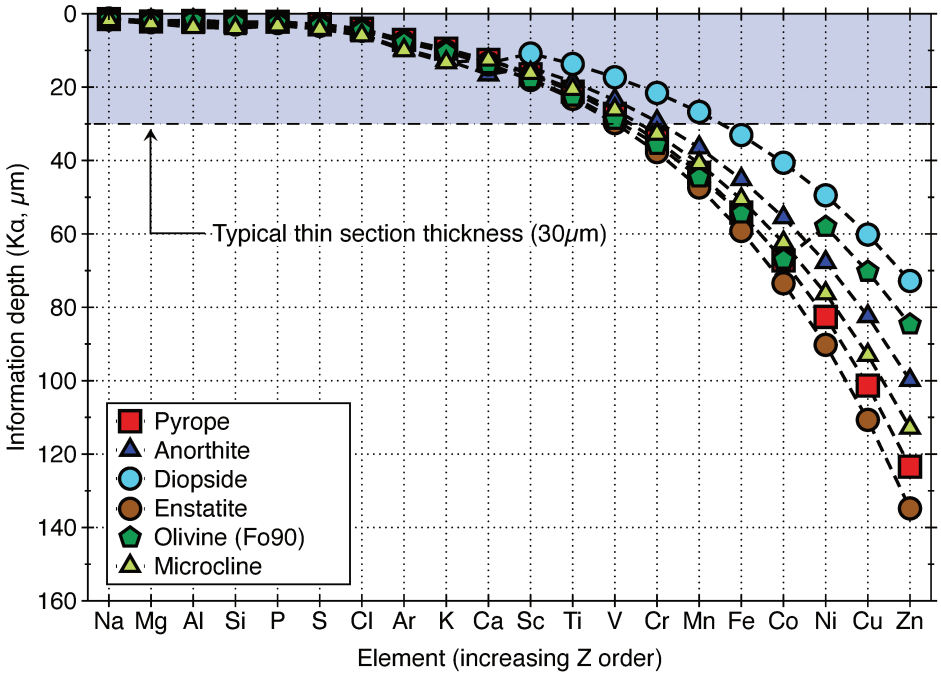


Fig. I-6 - *Rayonnement induit K_α en fonction du numéro atomique (Z), calculée pour différentes matrices à une intensité de 400 µA et une tension de 50 kV (https://xrfcheck.bruker.com/InfoDepth).*

Ainsi, à compter du Cr, l'intensité mesurée sera inférieure à l'intensité théorique, affectant ainsi la mesure des concentrations sur ces éléments. L'analyse quantitative demeure possible dans le cas d'échantillon d'épaisseur non-infinie, mais elle nécessite d'appliquer des méthodes de correction de matrice adéquates tenant compte de la dépendance complexe de l'intensité du rayonnement fluorescent de l'analyse par rapport à la composition de la matrice complète et à l'épaisseur de l'échantillon (Sitko, 2009).

2.4. Préparation de standards sur lame : une approche originale

Pour s'affranchir du problème d'épaisseur, plusieurs standards internationaux sur lesquels la méthode a été développée (Table I.2) ont dû être préparé dans les mêmes conditions, c'est-à-dire en lame mince avec une épaisseur de 30 µm (Fig.I-7).

Nom	**Référence NMNH#**	**Origine (localité)**
Anorthite	NMNH 137041	Great Sitkin Island, Alaska, USA
Anorthoclase	NMNH 133868	Kakanui, New Zealand
Chromium augite	NMNH 164905	Nye County, Nevada, USA
Kakanui augite	NMNH 122142	Kakanui, New Zealand
Diopside	NMNH 117733	Natural Bridge, New York, USA
Basaltic glass	NMNH 113716-1	Indian Ocean
Rhyolitic glass	NMNH 72854	Yellowstone National Park, Wyoming, USA
Microcline	NMNH 143966	Unknown
San Carlos olivine	NMNH 111312-44	San Carlos, Arizona, USA
Plagioclase	NMNH 115900	Lake County, Oregon, United States
Pyrope	NMNH 143968	Kakanui, New Zealand
Quartz	NMNH R17701	Hot Springs, Arkansas, USA

Table I-2 – *Standards internationaux provenant du Smithonian National Museum of Natural History et utilisés pour la calibration sur silicates*



Fig. I-7 – *Standard international d'olivine NMNH 111312-44 préparé sur lame mince (LPA)*

2.5. Temps d'acquisition

Le temps d'acquisition doit également être déterminé pour effectuer des analyses précises et reproductibles. Le temps après lequel la fluorescence est stabilisée peut varier en fonction du numéro atomique de l'élément chimique (Fig. I-8).

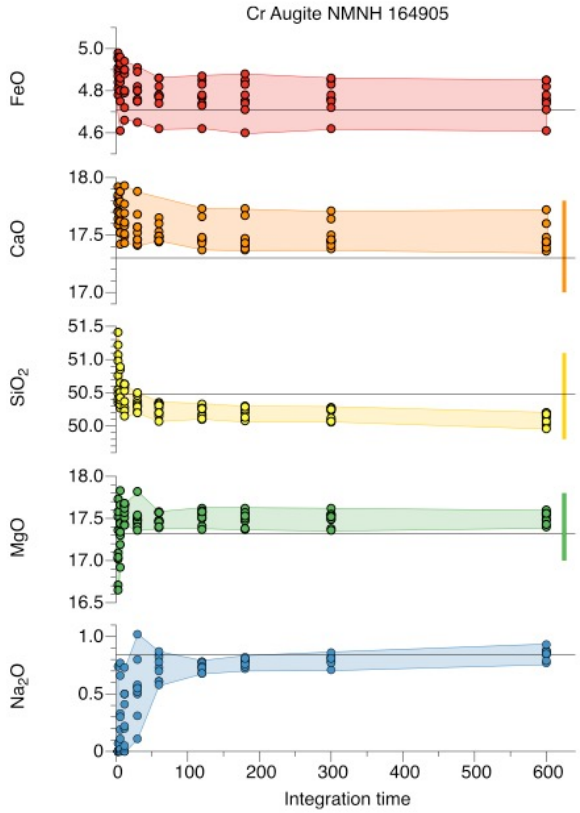


Fig. I-8 – *Effet du temps d'acquisition (s) sur l'évolution de la concentration mesurée (wt%) sur le standard NMNH 164905 (Cr-augite). Les barres de couleur à droite du diagramme correspondent aux gammes de variation des concentrations dans la littérature. La droite noire horizontale correspond à la valeur de référence NMNH (Jarosewich et al., 1980).*

Dix points ont été effectués sur un standard (répartis sur l'ensemble des fragments disponibles) et ont été analysés selon des temps d'acquisition de 10, 20, 30, 60, 120, 180, 300 et 60 secondes (sans calibration). Seul le temps d'acquisition est modifié, la localisation des 10 points entre les différentes analyses restant la même. On observe une dispersion importante des concentrations mesurées pour des temps d'intégration faibles qui varient en fonction de l'élément chimique considéré. Mais, à partir de 100 s d'acquisition, on observe que la dispersion des points ne varie plus (elle reflète simplement les variations intrinsèques de chimie des minéraux). Néanmoins, 100 s de temps d'acquisition apparait trop faible pour le sodium, l'élément considéré le plus léger. Pour autant, la différence de mesure entre 180 s et 600 s est extrêmement faible et ne permet finalement que de faire baisser légèrement la limite de détection (voir sous-partie 3.4).

Ainsi, le temps d'analyse a été défini à la suite de ces tests à 180 s en analyse de routine. Ce temps peut néanmoins être allongé ou raccourci selon la précision recherchée et nécessite un avis éclairé entre temps d'analyse acceptable, limite de détection, quantité de sodium présent dans l'échantillon et précision requise.

3. Quantification par µ-XRF

3.1. Processus physique sous-jacent : accéder à une donnée (semi)-quantitative

Lors de l'acquisition, le spectre mesuré par les spectromètres est déconvolué par le logiciel associé à la M4 Tornado©. Sur la base d'une relation linéaire entre la concentration et l'intensité de la fluorescence, le logiciel présent sur la µ-XRF calcule ensuite par itérations à partir du spectre, la composition chimique qui produirait le même spectre que celui détecté (Fig. I-4). Ce calcul se base sur l'équation de Sherman (1956) :

$$I_{\mathrm{fl}} = C_i * K_i * \int_{E_{abs,i}}^{E_{max}} I_0(E) * \tau_{i,E} * Q_i\left(E, E_{fl}\right) * \frac{1}{\mu^*} dE$$

Où

I_{fl}	Intensité de fluorescence
C_i	Concentration de l'élément
K_i	Paramètre instrumental
$I_0(E)$	Spectre d'excitation
$\tau_{i,E}$	Coefficient de photo-absorption
μ^*	Coefficient d'atténuation
$Q_i(E, E_{fl})$	Facteur de production des photons

} Paramètres fondamentaux

En effet, cette équation n'est pas réversible. C'est pourquoi à partir d'une concentration potentielle, le logiciel recalcule le spectre qui y correspond et le compare ensuite au spectre mesuré (Fig. I-8), de manière itérative. Selon l'allure du spectre et les écarts au spectre calculé, le logiciel recalcule un spectre en modifiant les concentrations, jusqu'à arriver à une correspondance. A chaque pic du spectre (Fig. I-4) est associé une intensité de fluorescence. Cette intensité est proportionnelle à la concentration dans l'échantillon (Fig. I-5), permettant ainsi d'accéder à la composition chimique réelle de l'échantillon.

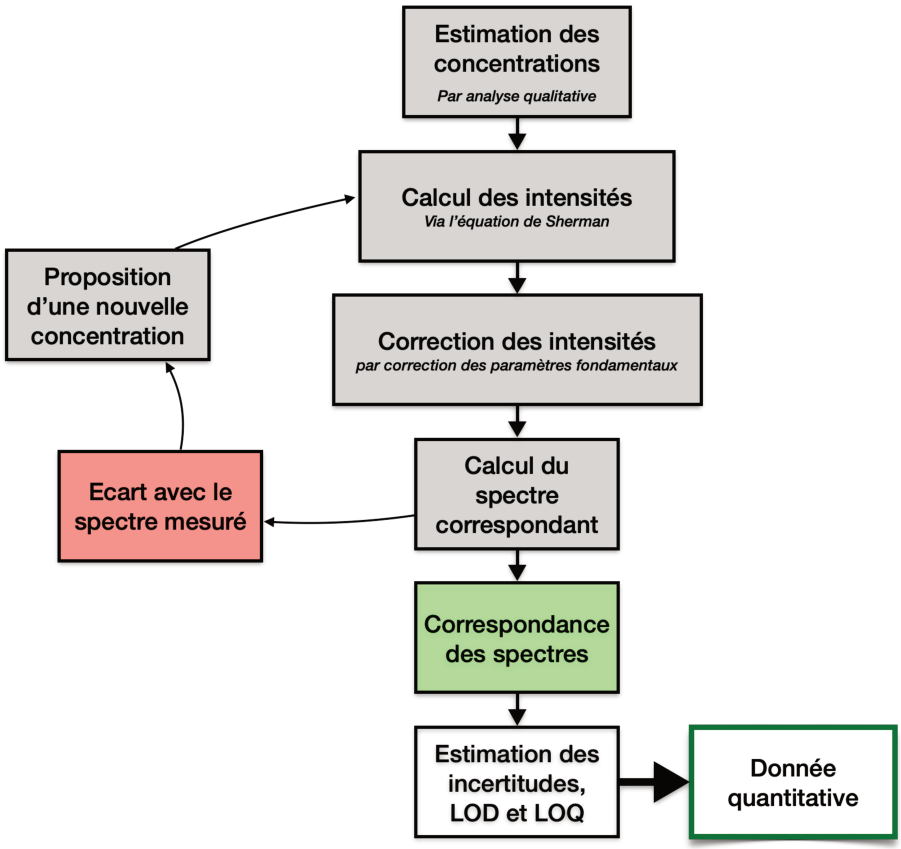


Fig. I-8 – *Le processus de quantification (modifié d'après Webinar – Bruker « Back to the roots »)*

3.2. Mesures initiales sur standards internationaux

Dans un premier temps, des analyses sur standards internationaux (NMNH – liste disponible en tableau I-2) ont été effectuées. Les résultats sont répertoriés en Figure I-9. Ces résultats montrent deux choses principales :

- On observe dans la très grande majorité des cas une répartition de type gaussienne,
- Le pic d'amplitude de la gaussienne est décalé par rapport à la valeur de concentration communément acceptée dans l'échantillon (pointillés rouges – Jarosewich et al., 1980).

Bien que cela puisse paraître contre-intuitif, le paramètre le plus important n'est pas que la valeur mesurée par la μ-XRF à ce stade soit le plus proche de la valeur de référence mais plutôt que la répartition des valeurs se fasse selon une gaussienne la plus fine possible (Fig. I-8). En effet, la largeur du pic de gaussienne définit la précision de la mesure. La valeur mesurée par rapport à la valeur de référence peut quant à elle être corrigée sur le logiciel de la μ-XRF afin d'accéder à une donnée réellement quantitative et juste (calibration).

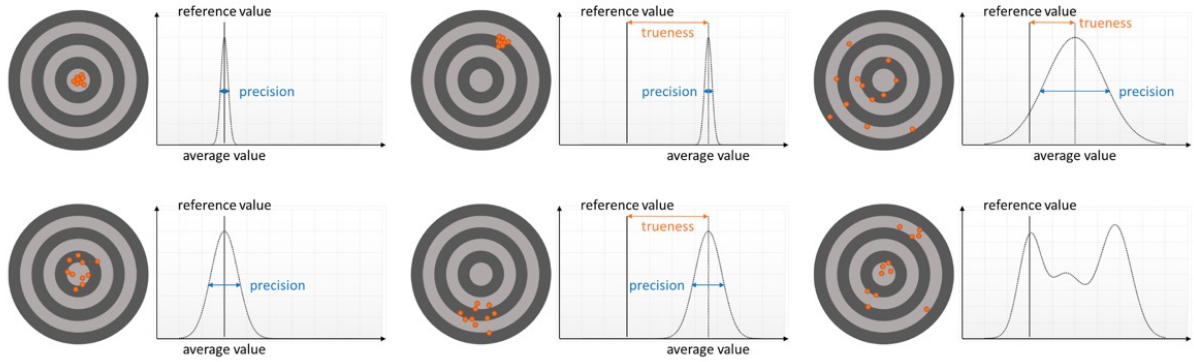
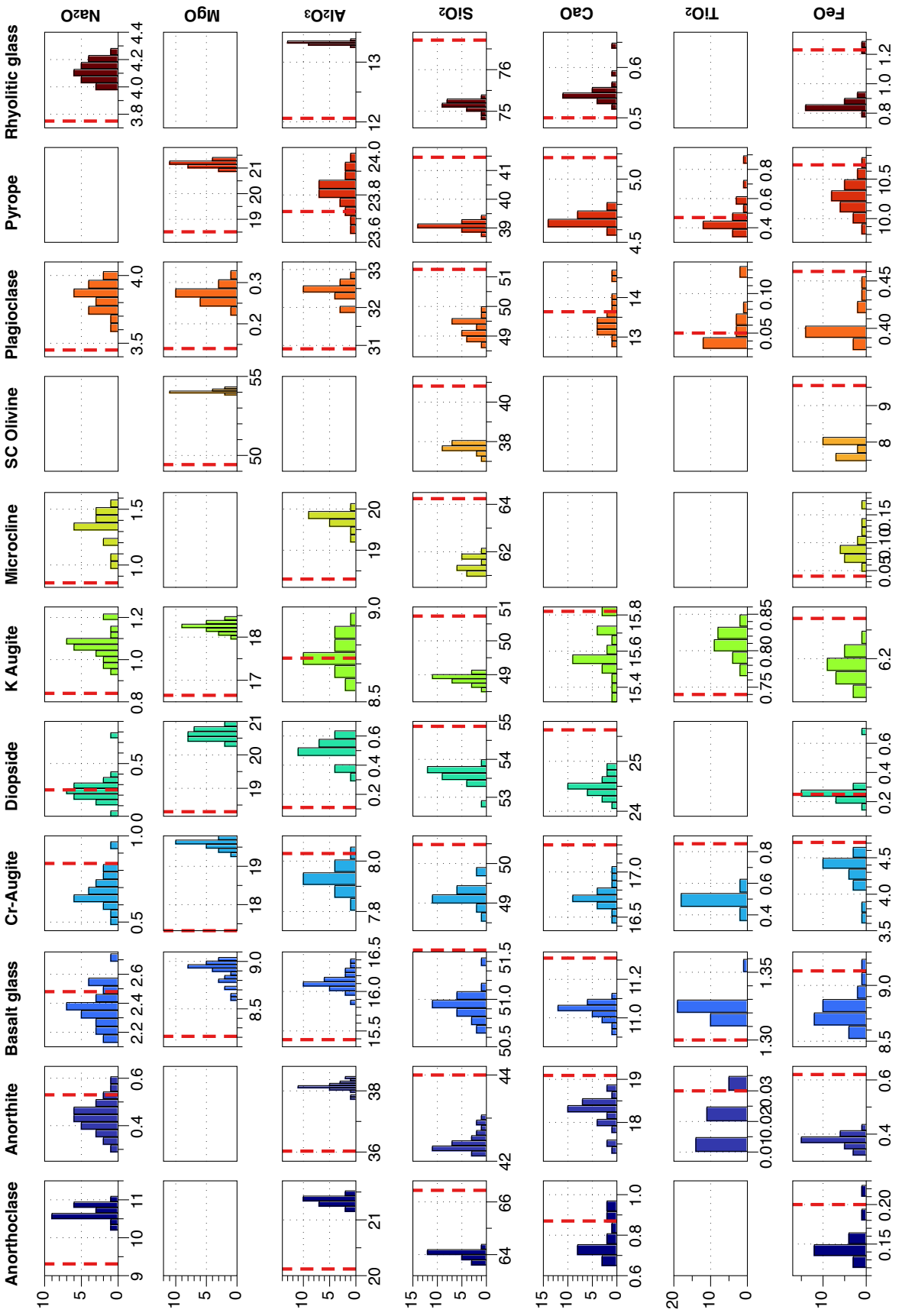


Fig. I-10 – *Effet de la répartition des analyses pour 10 mesures réalisées sur le même échantillon sur la précision de mesure (Webinar Bruker – « Back to the Roots »)*

En utilisant une calibration à l'aide de standards internationaux préparés dans les mêmes conditions que les échantillons naturels à analyser, il est possible de passer à des données (semi-)quantitatives pour n'importe quel échantillon, en tenant compte des effets de matrice détaillés plus haut. Nous avons donc effectué une calibration par type de matrice (silicates, olivines, oxydes, matrice hydratée).

Fig. I-9 – *Concentrations mesurées par 10 points d'analyse en μ-XRF sur standards NMNH.*



3.3. Calibrations du signal

Afin de définir la valeur des facteurs de correction, > 30 analyses ont été effectuées sur les 12 standards internationaux (Table I-2) sans correction (« XRF standardless ») et comparés à la valeur de référence (« standards » ; Jarosewich et al., 1980) pour chaque élément chimique.

Si l'on observe les résultats pour l'Al_2O_3 par exemple (Fig. I-11), on observe une relation linéaire entre la concentration mesurée et la valeur de référence (R^2 = 0.9996). La valeur du coefficient directeur de cette fonction affine reliant concentration mesurée et valeur de référence (a_{Al2O3} = 0.9472) correspond à la valeur du facteur de correction à appliquer sur la μ-XRF pour l'Al_2O_3. Cette opération a ensuite été répétée pour l'ensemble des éléments chimiques mesurés.

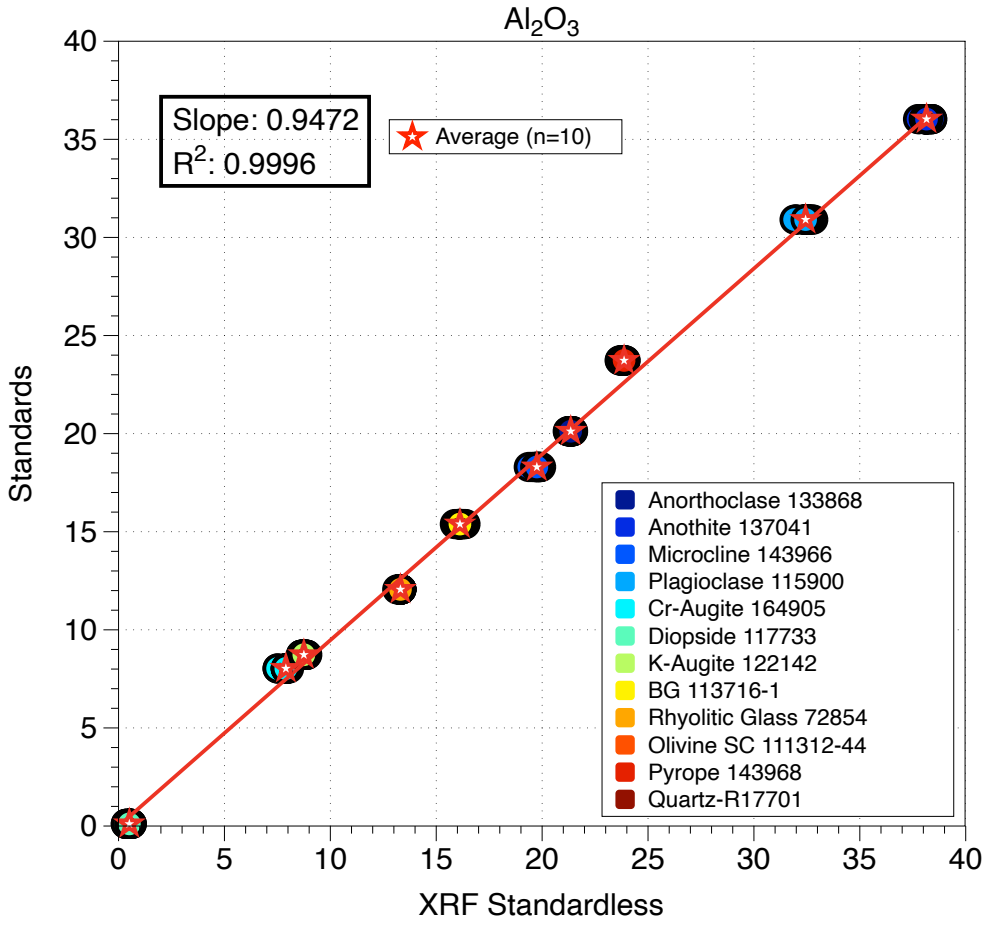


Fig. I-11 – *Résultats des analyses sans correction (« XRF standardless ») comparés à la valeur de référence standards pour les standards NMNH*

3.4. Détermination des valeurs de LOD et LOQ

Mettre en place une nouvelle technique analytique nécessite de déterminer les limites de détection (LOD) et limites de quantification (LOQ). Pour cela, les formules suivantes d'Inczédy et al. (2000) ont été utilisées :

$$LOD = \frac{3}{S}\sqrt{BG} \qquad \text{et} \qquad LOD = \frac{10}{S}\sqrt{BG}$$

Avec S la sensibilité et BG l'intensité du bruit mesuré par la µ-XRF.

La limite de quantification d'une méthode analytique est la plus petite quantité ou concentration d'un composé pouvant être déterminée quantitativement avec un niveau acceptable de précision et d'exactitude au niveau d'un échantillon (Figure 1.5). Les valeurs de LOD et LOQ ont été déterminées sur l'ensemble des mesures de chaque standard international analysé. Les résultats sont répertoriés en Table I-3.

	Na2O	**Mg**	**Al**	**Si**	**P**	**K**
	n = 216	n = 163	n = 242	n = 284	n = 29	n = 118
Moyenne LOD (wt%)	0.117	0.029	0.012	0.007	0.011	0.002
Moyenne LOD (ppm)	868	177	63	31	48	13
Moyenne LOQ (wt%)	0.421	0.098	0.039	0.022	0.037	0.005
Moyenne LOQ (ppm)	3124	726	292	164	272	39
σ	0.033	0.006	0.004	0.001	0.001	0.001

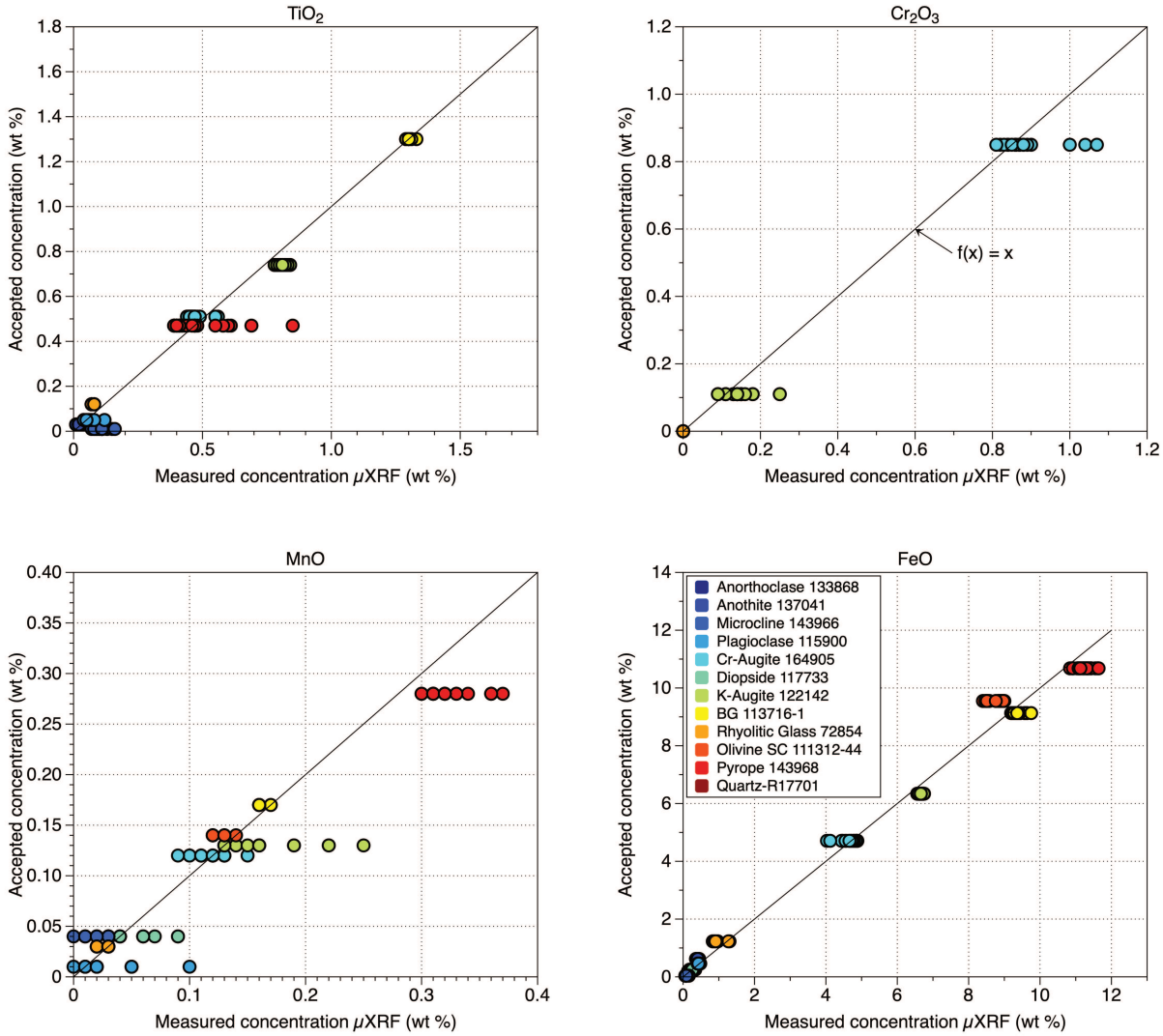
	Ca	**Ti**	**Cr**	**Mn**	**Fe**	**Ni**
	n = 226	n = 196	n = 45	n = 212	n = 260	n = 18
Moyenne LOD (wt%)	0.001	0.002	0.001	0.000	0.000	0.000
Moyenne LOD (ppm)	5.5	11.9	8.7	2.7	2.4	2.6
Moyenne LOQ (wt%)	0.003	0.007	0.004	0.001	0.001	0.001
Moyenne LOQ (ppm)	19	49	31	9	8	8
σ	0.000	0.004	0.001	0.000	0.000	0.000

Table I-3 – *Limites de détection (LOD) et limites de quantification (LOQ) sur l'ensemble des standards internationaux mesurés.*

4. Résultats et discussion

4.1. Résultats sur standards internationaux

L'ensemble des données de standards internationaux ont été calibrées avec la méthode décrite précédemment. Afin de définir la précision et l'exactitude des mesures, la valeur de chaque point d'analyse est comparée à la valeur de référence (Jarosewich, 1980). Ces résultats sont visibles en figure I-12. La courbe noire permet de visualiser le point de correspondance parfaite entre concentration mesurée et concentration de référence.



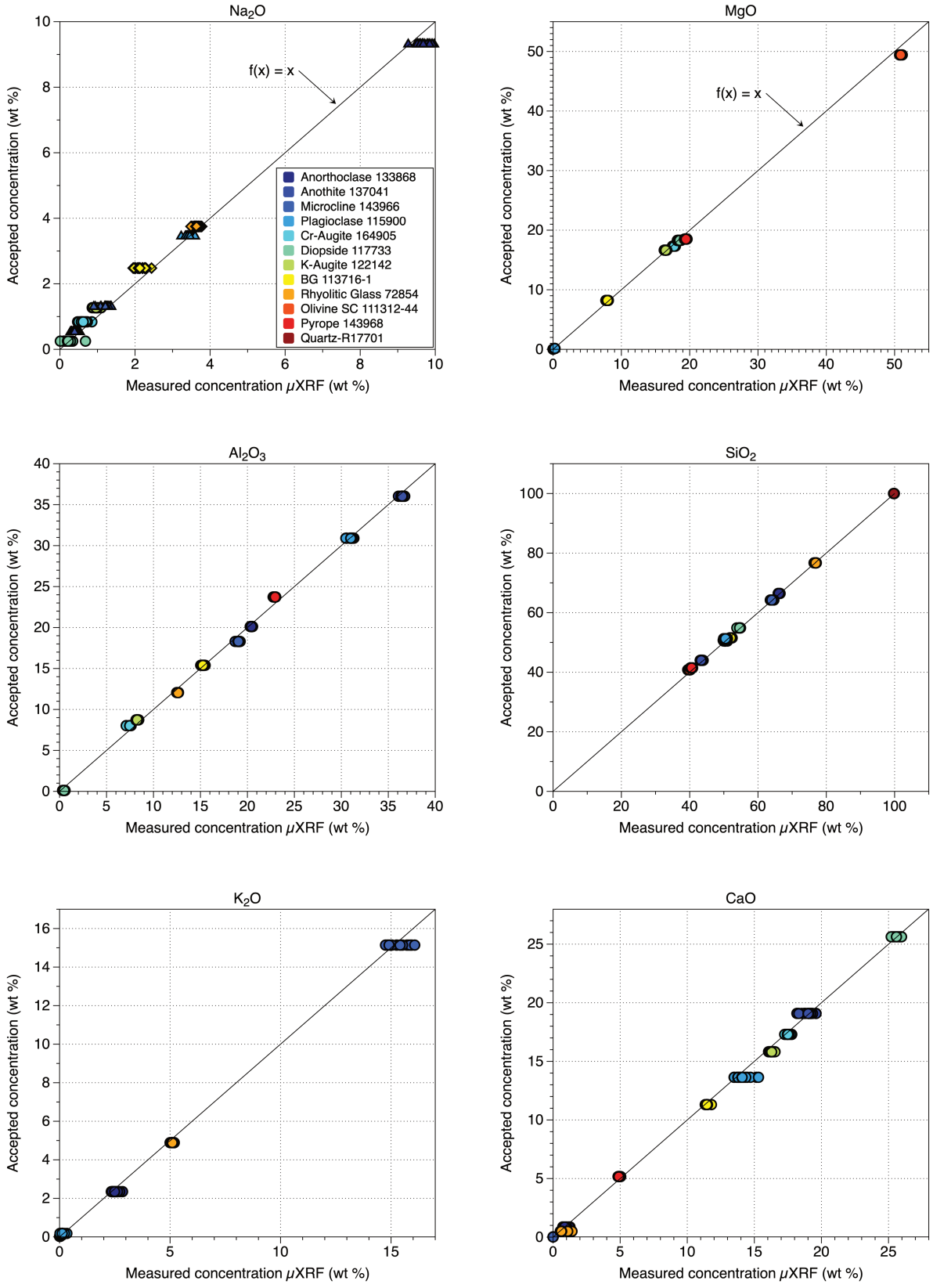


Fig. I-12 – *Données standards calibrées en fonction de la concentration de référence*

4.2. Limites liées à la méthode XRF et solutions proposées

La méthode d'analyse par µ-XRF a, comme toutes les autres méthodes d'analyse, des avantages et des limites qu'il convient de prendre en compte lorsque l'on veut l'utiliser.

Le diamètre des points d'analyse est de 20 µm en *in situ* par µ-XRF. Dans un premier temps, par rapport à une microsonde classique (diamètre minimal d'1 µm), cela peut paraitre être un inconvénient. Mais, ces données en éléments majeurs sont ensuite utilisées comme standard interne pour calibrer les données d'éléments traces acquises par LA-ICP MS. Or, ces données d'éléments traces sont obtenues avec des diamètres d'ablation entre 60 et 100 µm, rendant les analyses µ-XRF plus appropriées.

Néanmoins, l'utilisation répétée de la µ-XRF a montré qu'il n'est pas possible d'analyser des minéraux de seulement 20 µm de diamètre. Les rayons X ont tendance en effet à exciter les éléments présents aux abords du cercle d'analyse.

Les limites de détection, par rapport à une microsonde classique où elles sont généralement comprises entre 10 et 200 ppm, sont légèrement plus élevées pour certains éléments légers (Na, Mg) mais bien plus faibles pour des éléments tel que le fer ou le calcium (Table I-3).

Enfin, du fait d'un interférence avec le fer, les teneurs en cobalt ne peuvent que très difficilement être déterminées. La K_α du cobalt ($^{Co}K\alpha$ = 6,930.32) se situe dans le pied de la K_β du fer ($^{Fe}K_\beta$ = 7,057), ce qui nuit à la visibilité du pic du cobalt.

4.3. Effets de matrice

L'analyse chimique par µ-XRF est influencée de manière significative par le type de minéral du fait de la matrice du minéral analysé. Par exemple, la concentration en fer dans l'olivine de San Carlos (NMNH 111312-44) est clairement sous-évaluée (Figure I-13) par rapport à la valeur de référence (Jarosewich et al. 1980), ce qui s'explique par le fait qu'elle ne suit pas la même relation linéaire que les autres standards internationaux mesurés. Cette différence s'explique par un effet de matrice, qui est défini comme l'effet de l'influence de l'environnement chimique d'un atome sur l'intensité de son signal (Morrison et al., 1979). La matrice fait référence à l'ensemble des éléments et composés chimiques présents dans l'échantillon, qui peuvent interagir avec les rayons X incidents et émis, modifiant ainsi les

intensités des signaux détectés. Une matrice dense ou contenant des éléments à numéro atomique élevé peut absorber ou atténuer les rayons X plus efficacement, réduisant la sensibilité de détection pour certains éléments.

Par conséquent, pour obtenir des résultats précis, il est essentiel de corriger les effets de matrice ou d'utiliser des standards de composition similaire pour effectuer une autre calibration spécifique de ce type de matrice (Chebakova et al., 2021).

De nombreuses olivines d'échantillons très différents ont donc été analysés (olivines de basaltes et olivines de péridotites - Massif central et marge passive australienne) par microsonde électronique afin d'affiner la calibration. Une seconde calibration, spécifique aux olivines a ainsi été obtenue.

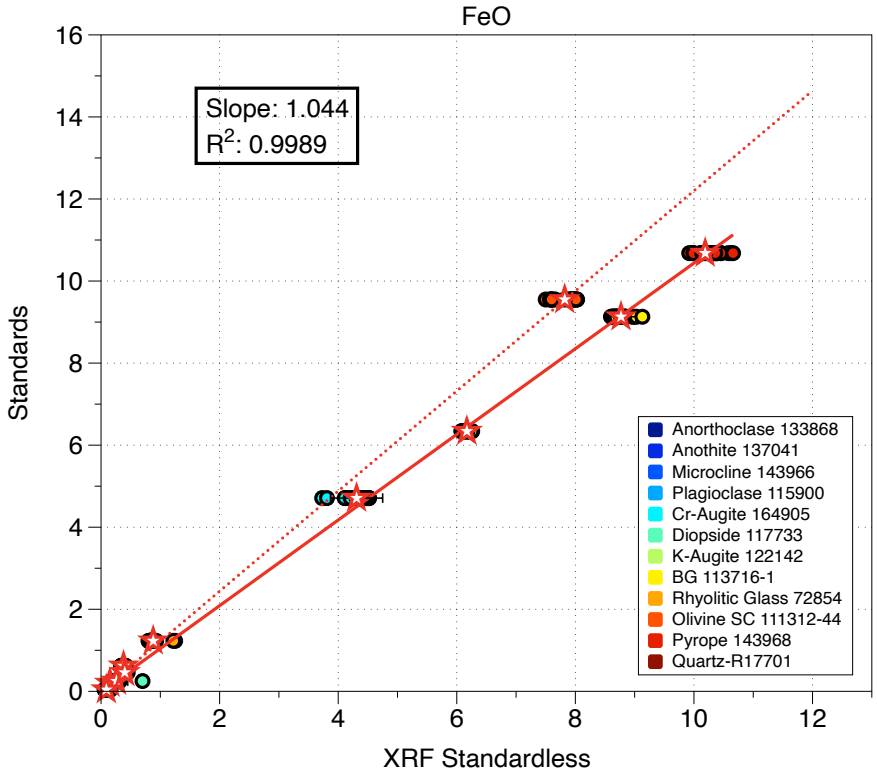
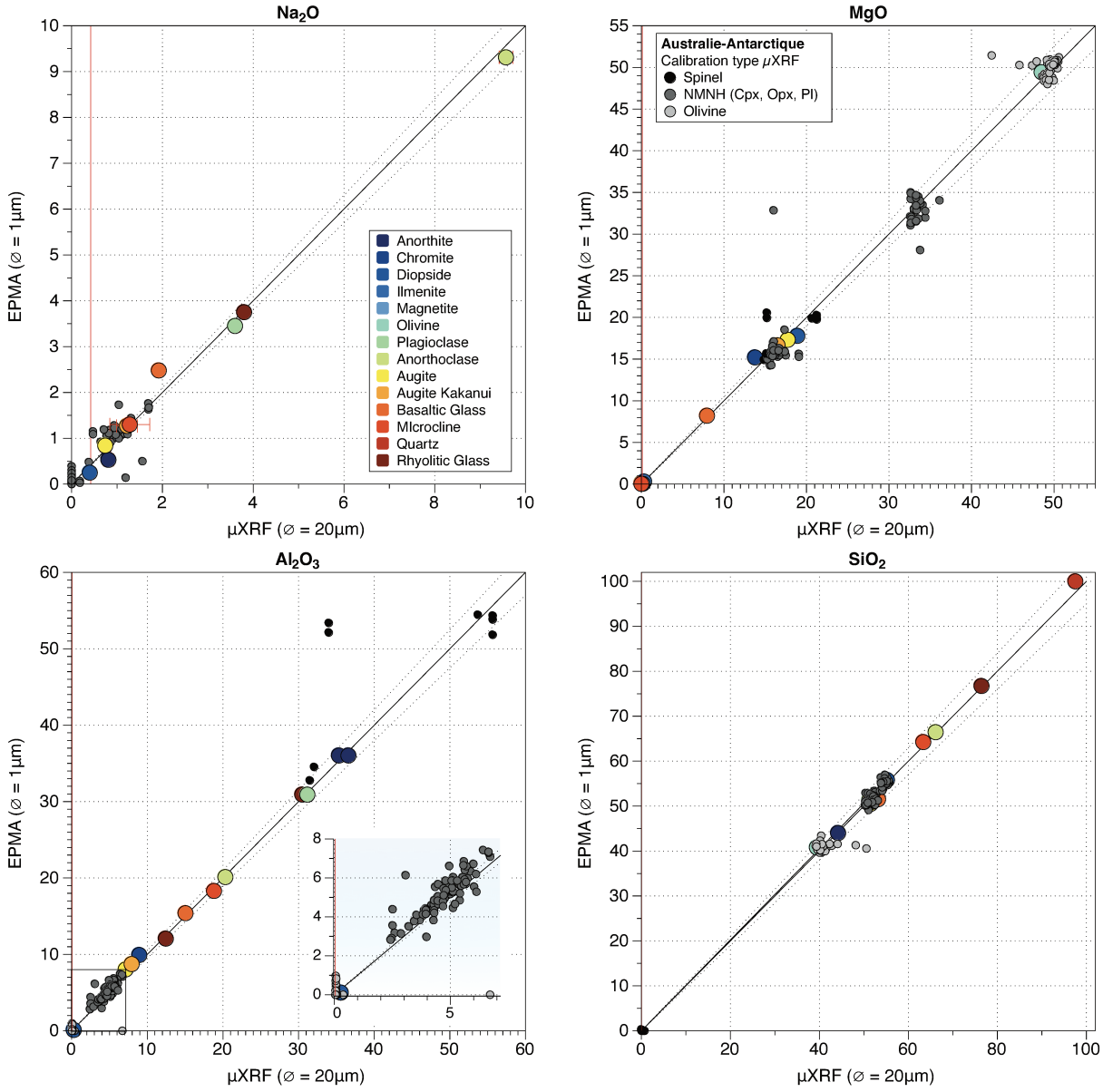


Fig I-13 – *Mesure de FeO sur standards internationaux NMNH par μ-XRF, comparativement aux valeurs de standards (Jarosewich et al., 1980).*

5. Application sur échantillons naturels : le test sur les échantillons de la zone Diamantine

5.1. Analyses *in situ*

Plusieurs minéraux ont été analysés en microsonde électronique et μ-XRF dans les échantillons de basaltes, péridotites et pyroxénites de la zone Diamantine (Fig.I-14). En utilisant les différentes calibrations (silicates, olivines, oxydes), le comparatif des données μ-XRF / microsonde montre que les analyses sont dans un intervalle de confiance de 5% d'écart à la valeur, confirmant qu'elles puissent être utilisées comme données quantitatives.



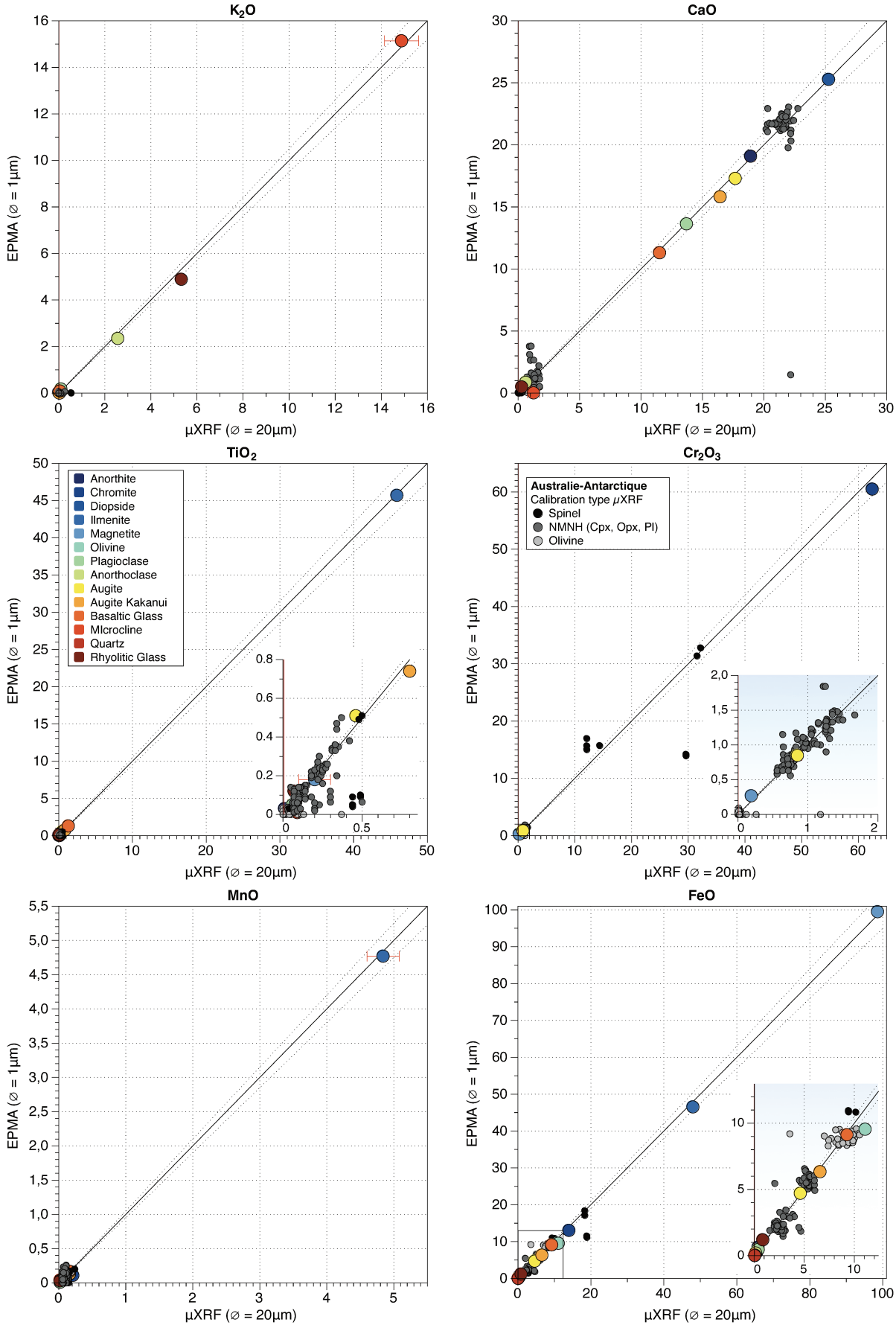


Fig. I-14 – *Données in situ calibrées par μ-XRF en fonction de la concentration mesurée par microsonde électronique sur échantillons naturels*

5.2. Calibration de cartographies chimiques

A partir de ces données *in situ,* plusieurs points répartis dans la lame mince ont été utilisés pour calibrer des cartes chimiques (Fig.I-15) effectuées sur l'ensemble de la lame selon la procédure développée par Ulrich et al. (2014). Il est ainsi possible d'effectuer une reconnaissance et quantification minéralogique sur l'ensemble de la lame ou encore d'observer les variations chimiques élémentaires ou encore de ratios tel que le Cr# ou le Mg# très utilisés en pétrologie. Dans la mesure où le temps de comptage par point ne peut être aussi élevé que lors d'une analyse *in situ (voir section 2.3)*, ces cartographies chimiques sont dites semi-quantitatives.

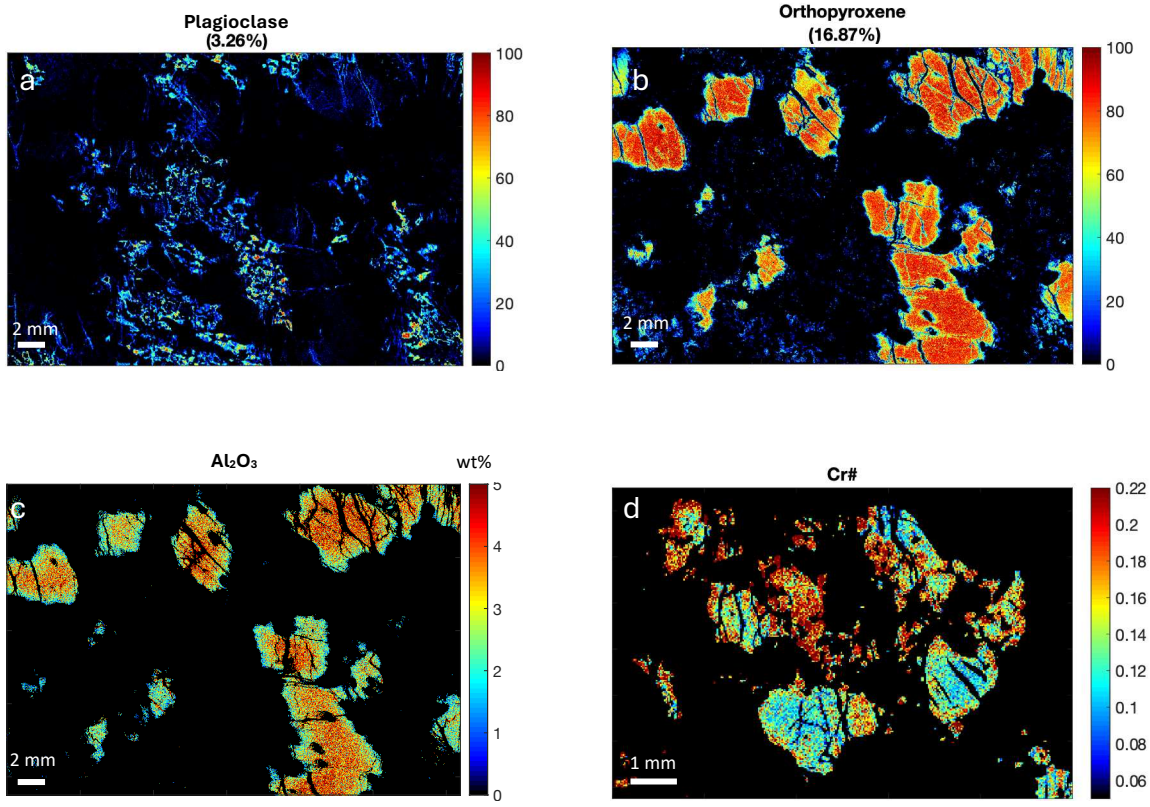


Fig. I-15 – *Cartographie chimique de la lame mince de péridotite DR06-161C. a : identification de plagioclases ; b : identification d'orthopyroxènes ; c : cartographie chimique de l'Al2O3 dans les orthopyroxènes ; d : calcul du Cr# (Cr/(Cr+Al)) dans un clinopyroxène de la lame mince.*

CONCLUSION ET PERSPECTIVES

En conclusion, la méthode d'analyse *in situ* par μ-XRF se distingue par sa capacité à analyser des éléments légers (dès le sodium) à lourds avec une préparation d'échantillon minimale et une grande rapidité d'acquisition. Cela la rend particulièrement utile pour des analyses à grande échelle et pour la calibration de cartographies chimiques des échantillons, effectuées également sur cette machine. Après une longue période de calibration, la μ-XRF présente au laboratoire ITES de Strasbourg montre désormais de bons résultats comparativement à la méthode classique de la microsonde électronique avec une précision de mesure qui permet d'obtenir des données quantitatives. Toutefois, chaque méthode présente aussi des limites. La μ-XRF peut être moins précise pour quantifier certains éléments légers et a un diamètre d'analyse supérieur à celui de la microsonde électronique. Bien que cela peut paraitre être une contrainte, cette taille de spot plus grande est plus appropriée pour la réduction de données en ablation laser puisque similaire. En somme, une utilisation généraliste de la μ-XRF combinée à de la microsonde électronique pour les analyses nécessitant une taille de spot plus petite, peut offrir une vision plus complète et compétitive de la composition chimique des échantillons géologiques.

CHAPITRE 2

Le rôle de l'héritage et de la refertilisation du manteau au cours de la rupture dans les marges passives pauvres en magma : que pouvons-nous apprendre de la marge sud-ouest de l'Australie ?

Ce second chapitre, s'intéresse aux roches ultramafiques exhumées le long de la transition océan-continent de la marge sud-ouest australienne.

L'étude des interactions entre les roches mantelliques et les liquides magmatiques sur les marges riftées pauvres en magma, qui représentent pourtant près de la moitié des marges mondiales, est limitée par l'accès aux échantillons. Les concepts actuels sont principalement basés sur des études des paléo-marges téthysiennes et du domaine de l'Atlantique Nord méridional, posant la question de leur applicabilité à d'autres marges pauvres en magma où l'héritage serait différent. Cet article montre une étude sur les péridotites de la zone Diamantine le long de la marge sud-ouest australienne, échantillonnées lors des campagnes océanographiques MD80 et MD110. Il permet de discuter d'abord des caractéristiques du manteau hérité, puis des processus de fusion et d'interactions du manteau liés à la rupture, pour finir par évaluer l'applicabilité du modèle alpin/ibérique au domaine sud-ouest australien.

Cet article a été publié dans la revue *Earth and Planetary Sciences Letters*, sous le titre « The role of mantle inheritance and refertilisation during breakup at magma-poor rifted margins: what can we learn from the SW-Australia margin? ».

Les « Supplementary materials » de l'article dans sa version publiée par le journal EPSL sont disponibles à la fin du manuscrit de thèse. D'autres documents sont également disponibles donnant un aperçu global des lithologies des roches sur lesquelles se basent ces travaux.

Les modèles de fusion partielle et de refertilisation sont également le fruit d'une longue réflexion et de nombreux tests, tant sur les conditions initiales (manteau primitif, manteau appauvri, minéraux présents et proportions modales) que sur les modalités (taux de fusion, domaines impliqués et changement de domaines d'équilibre de la phase alumineuse, proportions modales lors de la fusion et de la recristallisation) ou sur les agents impliqués lors de la refertilisation (liquides magmatiques enrichis, appauvris…). Les modèles présentés dans cette publication ne sont ainsi qu'un maigre extrait de l'ensemble des versions travaillées.

Earth Planet. Sci. Lett. 653 (2025) 119212



Contents lists available at ScienceDirect

Earth and Planetary Science Letters

journal homepage: www.elsevier.com/locate/epsl





The role of mantle inheritance and refertilization during breakup at magma-poor rifted margins: What can we learn from the SW-Australia margin?

Mélanie Ballay *, Marc Ulrich, Gianreto Manatschal

Institut Terre et Environnement de Strasbourg-EOST, CNRS-UMR 7063, Université de Strasbourg, 5 Rue René Descartes, 67084 Strasbourg, France

ARTICLE INFO

Keywords:
Magma-poor rifted margin
Refertilization
Mantle-melt interaction
Magmatic processes modeling

ABSTRACT

The study of mantle-melt interactions at magma-poor rifted margins, accounting for about half of the world margins, is so far limited by the access to samples. Present concepts are therefore mainly based on studies of the Western Tethys and southern North Atlantic domain, and it remains unclear if they are applicable to other magma-poor rifted margins. Here, we present a study of well-preserved peridotites dredged along the south-western Australian margin (Diamantina Zone). Our petrological data show that two types of peridotites occur: spinel lherzolite, which represents the inherited subcontinental mantle (SCLM) before the separation of Australia and Antarctica, and plagioclase peridotite formed by syn-rift melt entrapment at low pressure in the plagioclase stability field during mantle exhumation. The observed mantle types as well as the mantle-melt processes identified in the Diamantina peridotites are very similar to those documented in the Alpine-Apennine and Iberia margins. Hence, the Alpine/Iberia model of magma-poor rifted margins may be globally applicable and does not depend on the SCLM inheritance. Remnants of mantle inheritance may be preserved in the refertilized mantle, suggesting a progressive transition from an inherited to a refertilized mantle during breakup. Finally, this study highlights the role of inheritance and refertilization as the main features controlling final rifting and breakup at magma-poor rifted margins.

1. Introduction

Understanding plate boundaries and the processes linked to their formation are among the major remaining challenges in plate tectonics. While processes at divergent plate boundaries at Mid Ocean Ridges (MOR) are relatively well constrained, those at Ocean Continent Transitions (OCTs), where lithospheric breakup occurs, are much less understood. Since the thermodynamic conditions and processes responsible for the formation of a new plate boundary likely differ from those acting at steady-state MORs, the latter cannot be considered as analogues to the former. Thus, characterizing the tectonic, magmatic, and hydrothermal processes and their feedback, and constraining the P-T-t conditions at which new divergent plate boundaries form are of primary importance in the understanding of lithospheric breakup processes. In the last two decades, several studies have demonstrated that mantle and magmatic rocks derived from OCTs record a complex history (Chazot et al., 2005; Ferrari et al., 2022; Manatschal and Müntener, 2009; Montanini et al., 2006; Müntener et al., 2010; Müntener and Manatschal, 2006; Picazo et al., 2016; Rampone et al., 2020). However, there are only a handful of sites worldwide where OCTs are accessible to sampling. Most of these sites belong to the Alpine/Iberian system that resulted from the breakup of Pangea, with a subcontinental lithospheric mantle (SCLM) carrying a strong Variscan inheritance. The study of the Alpine/Iberian mantle rocks led to the development of an influential generic model that was applied to all magma-poor rifted margins (Fig. 1), which account for half of the world present-day rifted margins (Fig. 2A). A main highlight of the Alpine/Iberian model is that mantle inheritance plays a key role (Ferrari et al., 2022; Picazo et al., 2016). Therefore, a legitimate question is whether the Alpine/Iberia model can also be extrapolated to magma-poor margins that experienced different pre-rift histories? However, answering this question and testing the role of mantle inheritance require access to mantle rocks from OCTs with different pre-rift histories is required.

In this paper, we focus on mantle inheritance and mantle-melt reactions recorded in poorly investigated samples dredged along the Diamantina zone, located at the magma-poor southwest Australian

* Corresponding author.
E-mail address: mballay@unistra.fr (M. Ballay).

https://doi.org/10.1016/j.epsl.2025.119212
Received 1 June 2024; Received in revised form 1 January 2025; Accepted 10 January 2025
Available online 21 January 2025
0012-821X/© 2025 The Authors. Published by Elsevier B.V. This is an open access article under the CC BY license (http://creativecommons.org/licenses/by/4.0/).

margin. We present new results from well-preserved mantle rocks that result from rifting and breakup along the Australia-Antarctica margins, overprinting a Proterozoic lithosphere. The aim of our study is twofold: we first discuss the inherited mantle characteristics and breakup-related mantle-melt processes recorded in mantle rocks exhumed along the Diamantina OCT; then, we evaluate the applicability of the Alpine/Iberian model by comparing mantle-melt processes associated with breakup of a Proterozoic SCLM with those from the Iberia-Western Tethys Paleozoic SCLM. Our results are finally used to test whether the depletion/refertilization hypothesis controlling the magma-budget and magma-retardation required to form magma-poor rifted margins can be globally extrapolated.

2. Mantle-melt interactions recorded in OCTs: state of the art

2.1. The OCT: a recording area for breakup processes

OCTs at magma-poor rifted margins form, by definition, the spatial and temporal transition between crustal and lithospheric breakup. They also form the limit between continental and oceanic lithospheres on either side and document the transition from tectonic extension to magmatic dominated accretion. While crustal breakup (i.e., the

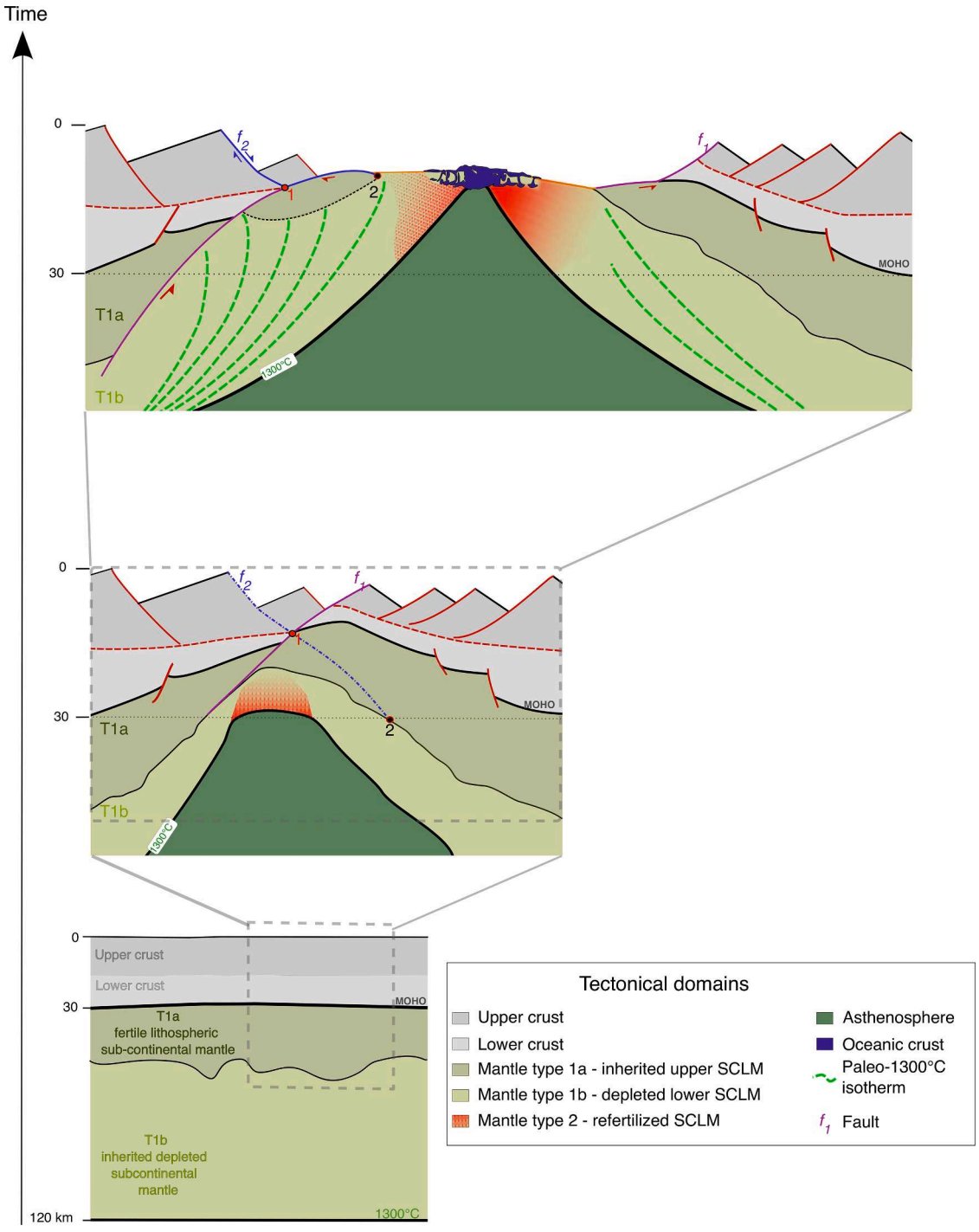
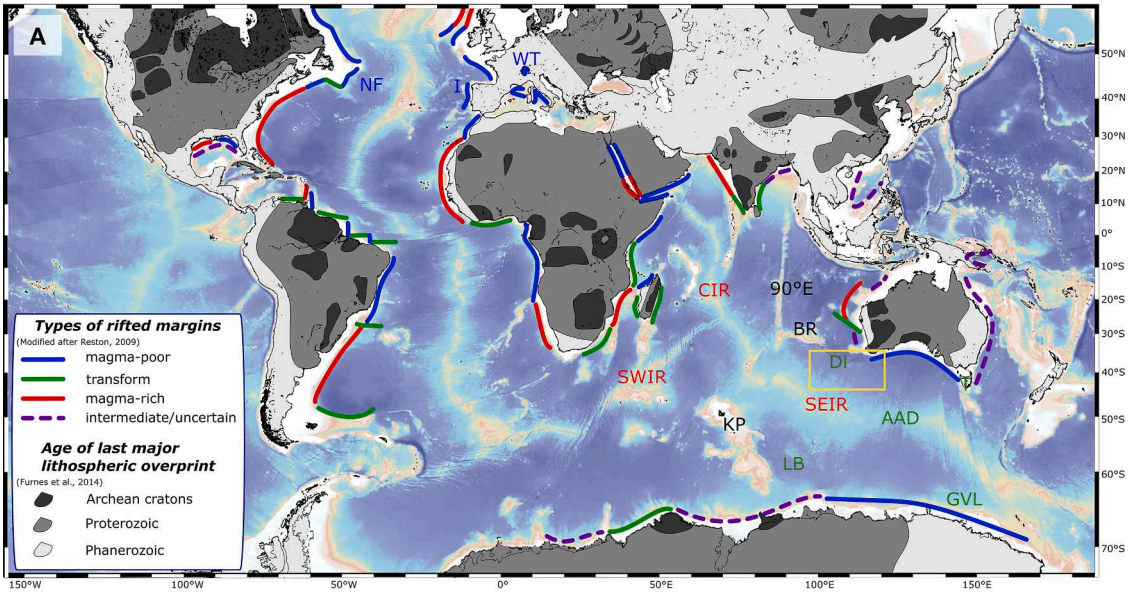


Fig. 1. Spatial and temporal evolution of the SCLM from rifting to seafloor spreading showing a direct link between the different temporal stages and the evolution of the SCLM along cross-sections of the evolving rifted margin.

separation of continental crust followed by exhumation of SCLM) is relatively easy to locate in space and time using seismic data (Chenin et al., 2024), lithospheric breakup, which corresponds to the onset of seafloor spreading, is more difficult to locate and requires a direct access to mantle and magmatic rocks. So far only few OCTs have been studied from a petrological point of view, among which the Iberia and its conjugate Newfoundland margins in the southern North Atlantic and the fossil remnants of the Western Tethys margins in the Alps are the best documented ones (Basch et al., 2019; Boillot et al., 1987; Borghini and Rampone, 2007; Chazot et al., 2005; Chenin et al., 2017; Ferrari et al., 2022; Manatschal and Müntener, 2009; McCarthy and Müntener, 2015; Müntener et al., 2010; Müntener and Manatschal, 2006; Piccardo et al., 2014, 2007; Rampone et al., 2020; Rampone and Borghini, 2008; Tribuzio et al., 2004, 2016; Tucholke et al., 2004). Using a statistical approach on mantle rock data from the Western Tethys system, Picazo et al. (2016) defined three major mantle types. A mantle type 1 located close to the continent and corresponding to the SCLM sensu stricto, which may (1a) or may not (1b) have undergone depletion events pre-dating rift onset. A mantle type 2 that underwent melt percolation and trapping, forming a large domain of refertilized mantle. And finally, a mantle type 3, corresponding to a typical, depleted abyssal peridotite, formed at a steady-state MOR. Although this subdivision is of first order,



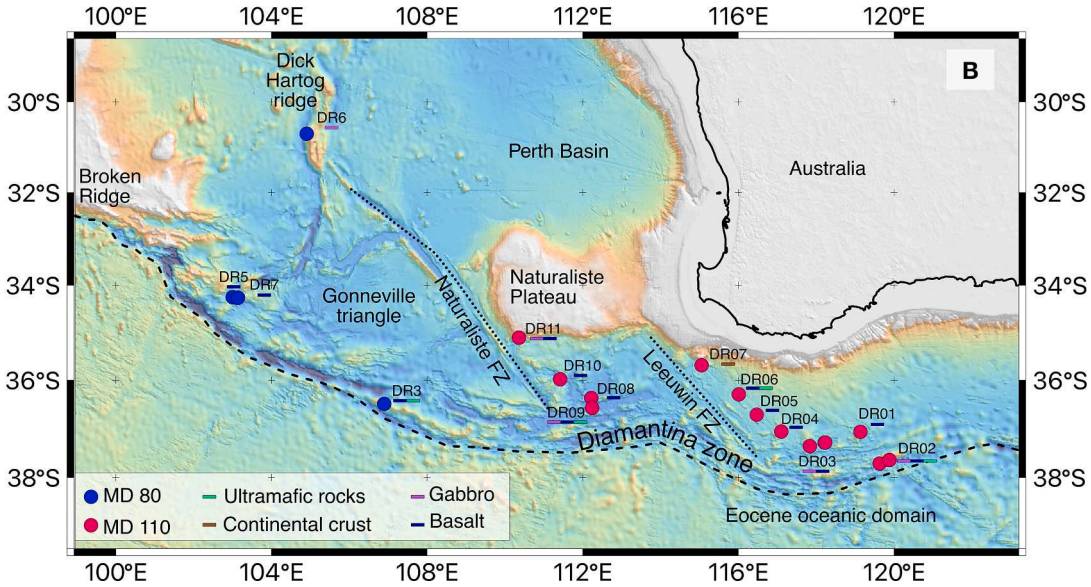


Fig. 2. A) Overview of the world's rifted margins (modified from Reston, 2009) and continental terranes with the age of the last major lithospheric overprint (data from Furnes et al., 2014). The yellow rectangle indicates the location of the Diamantina Zone. 90°E: Ninety-East Ridge; AAD: Australia-Antarctica Discordance; BR: Broken Ridge; CIR: Central Indian Ridge; Di: Diamantina Zone; GVL: Basins off George V Land; I: Iberia margin; KP: Kerguelen Plateau; LB: Labuan Basin; NF: Newfoundland margin; SEIR: South East Indian Ridge; SWIR: South West Indian Ridge; T: Tasmania; WT: Western Tethys. **B)** Bathymetric map of the Diamantina zone, South East Indian Ocean. Colored dots indicate the location of MD80 and MD110 dredges and the lithologies of dredged samples (Chatin et al., 1998; Beslier et al., 2004).(For interpretation of the references to color in this figure legend, the reader is referred to the web version of this article.)

it nevertheless illustrates that two aspects need to be considered when describing mantle rocks from OCTs: (i) inheritance, i.e., the mantle state and its composition prior to onset of rifting, and (ii) mantle-melt reactions occurring during the breakup.

2.2. Inheritance vs. mantle-melt interactions during breakup: a petrological approach

Our knowledge about the processes and conditions operating during magma-poor breakup are mainly based on petrological studies that focused on three aspects: i) defining the nature and state (P/T) of mantle rocks recording the pre-rift state, i.e., the SCLM inheritance (Müntener and Manatschal, 2006); ii) characterizing the reactions between the mantle and melts percolating through the SCLM (Montanini et al., 2006; Müntener et al., 2010; Piccardo et al., 2007; Rampone et al., 1997, 2020; Rampone and Borghini, 2008), and iii) quantifying the P-T-t conditions related to exhumation during rifting (Dygert and Liang, 2015; Smye et al., 2017). These studies highlighted how partial melting, exhumation and/or refertilization processes during breakup are recorded by mantle rocks. Since the chemical composition of major and trace elements in mantle minerals is sensitive to P-T conditions, mineral chemistry is a major tool that can be used to characterize the evolution of mantle-melt reactions. For instance, Cr# in spinel is correlated to heavy rare earth elements (HREE) in co-existing clinopyroxene. Hence, it can be used directly as a proxy to quantify partial melting degree in absence of late metasomatic events (Hellebrand et al., 2001). Spinel with elevated titanium contents ($TiO_2 > 0.2$ wt%) is indicative of melt percolation or mafic intrusions within the peridotite, and therefore can be used to track mantle-melt reactions (Müntener and Manatschal, 2006; Picazo et al., 2016). These studies showed that mineral textures and chemical compositions of clinopyroxene and plagioclase also show contrasted variations whether peridotites are subjected to partial melting, sub-solidus re-equilibration and/or refertilization.

Although inherited SCLM is mainly formed of porphyroclastic, fertile sp-lherzolite (5–15 % clinopyroxene), harzburgites or significant proportions of spinel and garnet pyroxenites can be observed as well (up to 10 %; Bodinier et al., 2008; Müntener et al., 2010). Clinopyroxene has high sodium ($Na_2O \sim 1.5$ wt%) and aluminum ($Al_2O_3 = 5$–9 wt%) contents. Plagioclase may occasionally be present in inherited SCLM at the rim of spinel grains, indicating a sub-solidus reaction of cpx + opx + sp = 2ol + pl (e.g., Borghini et al., 2010; Herzberg, 1978; Rampone et al., 1993). However, the presence of Pl-peridotite can also result from mantle refertilization by percolating melts (Kaczmarek and Müntener, 2008; Rampone et al., 1997; Seyler and Bonatti, 1997). In the latter scenario, plagioclase crystallizes together with pyroxenes and/or olivine due to porous flow migration of melts, leading to the partial replacement of the initial porphyroclastic assemblage (Kaczmarek and Müntener, 2008). A direct consequence of the plagioclase-clinopyroxene co-crystallization is the depletion of Na_2O and Al_2O_3 in pyroxenes. The trace element content of the latter is also deeply modified compared to clinopyroxene of inherited SCLM, showing light rare-earth elements (LREE) and Zr enrichments and Eu and Sr depletion (e.g., Piccardo et al., 2007; Rampone et al., 1993). Previous studies from the Western Tethys showed that up to 12% of melt can be trapped in the refertilized mantle (Müntener et al., 2010). In addition, inherited SCLM can show contrasting P-T paths. It can either equilibrate at relatively low temperature (850–950 °C; Borghini et al., 2011; Montanini et al., 2006; Müntener et al., 2010) in the spinel stability field and reach the seafloor following a cold exhumation path. Alternatively, in the infiltrated mantle domain it follows a hot exhumation path, recording a temperature increase (~1100 °C) due to melt percolation at shallow depths in the plagioclase stability field (Basch et al., 2019; Piccardo et al., 2009; Müntener et al., 2010; Rampone and Borghini, 2008).

3. Geological setting

3.1. The Australia–Antarctica conjugate margins

Fragmentation of southeastern Gondwana resulted in the separation of Australia and Antarctica and the formation of the SE Indian Ocean. This process was also responsible for the formation of a wide OCT of exhumed mantle along the SW Australian margin, referred to as the Diamantina zone (Beslier et al., 2004). This zone is assumed to represent the conjugate of the Labuan basin, located at the Antarctica margin (Fig. 2B; Munschy, 1998). Both margins show an architecture typical of a magma-poor rifted margin (Sutra et al., 2013), including segmented necking and hyperextended domains, bounded oceanward by an exhumed mantle domain. The abundant mantle rocks and sparse MORB-type magmatic rocks dredged from the Diamantina zone (Beslier et al., 2004; Munschy et al., 1994; Royer et al., 1998), as well as the basement architecture (Fig. 1) share many similarities with the Iberia-Newfoundland and fossil Alpine Tethyan margins (Alps). A major difference, however, is that Australia-Antarctica margins resulted from the rifting of a much older SCLM, including the Mesoproterozoic Fraser-Albany orogeny (Maier et al., 2016; Spaggiari et al., 2015) and the Archean 3.10 to 2.60 Ga old Yilgarn craton (Champion and Cassidy, 2007). Another important difference is the complex formation, rifting and breakup of the Broken Ridge and Kerguelen magmatic plateau, whose implication in the evolution of the study area remains debated (Magri et al., 2024).

3.2. The Diamantina Zone

The Diamantina Zone has been the focus site of the two oceanic cruises MD80 and MD110 that dredged the samples investigated in this study. The zone is located at the SW Australia margin, limited by the Naturaliste Plateau to the north, the Broken Ridge Plateau to the west and the Tasmania-George V Land to the east (Fig. 2A). The Diamantina zone shows E-W trending ridges ranging between 3000 and 6000 m water depth. The topography (Fig. 2B) is highly heterogeneous, undulating in a N090° to N130° direction (Munschy, 1998). To the north, seismic reflection lines show north dipping tilted blocks separated by south-dipping normal faults (Direen et al., 2007, 2013; Munschy, 1998). The Diamantina Zone is interpreted as a wide, segmented, hyperextended domain, bounded southward by a wide domain of exhumed subcontinental mantle and proto-oceanic crust (Beslier et al., 2004, Gillard et al., 2015; Sayers et al., 2001). The zone is divided into three segments separated by NW-SE trending fracture zones. The first segment, located in the western part, is limited along the Naturaliste fracture zone, interpreted as a Mesozoic transform fault (Chatin et al., 1998), from a central segment located between 111°E and 115°E. The latter is separated along the Leeuwin fracture zone from an eastern segment located between 115°E and 120°E, directly south of the Australian continent (Fig. 2B).

3.3. Debates and remaining questions

The rift evolution along the Diamantina zone is still debated. Recent studies suggest that the zone formed during Late Jurassic/Early Cretaceous rifting followed by mantle exhumation and early seafloor spreading that eventually failed (Gillard et al., 2015). A later event resulted in the breakup and separation of the Broken Ridge-Kerguelen magmatic plateau at about 45 Ma (Magri et al., 2024), and the formation of the present spreading system between Australia and Antarctica. While this post-45 Ma history is well described, little is known about the much older mantle exhumation stage. This is mainly due to the absence of clear magnetic anomalies, due to the Cretaceous quiet period. Out of all samples dredged during the two campaigns, only one age has been measured on a basalt from the dredge 7 of MD80 cruise (Chatin et al., 1998). It yielded an age of 93±4 Ma using the $^{40}Ar/^{39}Ar$ method on

plagioclase and bulk rock. Although the age of mantle exhumation in the Diamantine zone remains unclear, the fact that it took place during the magnetic quiet zone seems undeniable. Also the conditions at which mantle exhumation occurred are still largely unknown. Chatin et al. (1998) discussed the nature of mantle inheritance and suggested refertilization. However, no clear petrological and geochemical constraints have been presented. Nicholls et al. (1981) published limited petrological results from only three lherzolite samples that already showed marked variations in their mineral chemistry with notably high Mg#. Here, we focus on a set of mantle samples that were exhumed to the seafloor during the Early Cretaceous predating breakup. Based on new petrological and mineral chemistry data, we document for the first time the conditions and processes of magma-poor mantle exhumation of a Proterozoic mantle lithosphere.

4. Samples and analytical methods

4.1. Origin of samples

The samples presented in this study were collected during the two successive MD80 and MD110 oceanic cruises in the 1990s, both operated by the Marion Dufresne research vessel. These oceanic cruises were designed to constrain the mechanisms of crustal thinning and lithospheric breakup and to explore when and how this breakup occurred. Numerous publications used the geophysical data collected during the two cruises (e.g., Bernard et al., 2005; Direen et al., 2007; Halpin et al., 2008; Magri et al., 2024; Rotstein et al., 2001), but only a few studies dealt with the dredged samples (Beslier et al., 2004; Chatin et al., 1998).

A total of 199 samples were recovered from 5 dredges during MD80 cruise, and 342 samples from 11 dredges during MD110 cruise, covering a wide area along the Diamantina zone (Fig. 2B). The dredged samples include ultramafic (peridotites, pyroxenites), magmatic (gabbros, basalts, diorites, granites) and metamorphic rocks (metasediments, gneiss, amphibolite), in addition to sediments, breccias and polymetallic nodules. Here, we focus on dredge sites where ultramafic rocks were collected, i.e., DR02, DR06 and DR09 sites from MD110 and DR03 from MD80. MD80-DR3 was dredged on a northward tilted block, west of the Naturaliste fracture zone. MD110-DR06 was located along the Leeuwin fracture zone, MD110-DR02 and DR09 were dredged further south on both sides of the Leeuwin fracture zone (Fig. 2B). All samples underwent hydrothermal alteration, with a degree of serpentinization varying from 25 to almost 100 %. However, relics of primary minerals (mainly pyroxene and spinel, less commonly olivine) were found in most of the samples presented in this study. A total of 47 samples were analyzed, including 10 samples from the MD110-DR02, 20 samples from the MD110-DR06, 10 samples from the MD110-DR09 and 7 samples from the MD80-DR3.

4.2. Analytical methods

Major element concentrations of minerals were measured by micro-X-ray fluorescence (μ-XRF) at the Institut Terre et Environnement de Strasbourg (ITES, France) and by electron microprobe at Service Commun de Microscopie Électronique et de Microanalyses (Nancy, France). Chemical maps were also obtained using μ-XRF at ITES. Trace element concentrations were analyzed using a laser ablation inductively coupled plasma mass spectrometer (LA-ICP-MS) at Georessources Nancy (France). Additional details about the analytical methods, including analytical conditions, standardization and the whole dataset are given in supplementary materials.

5. Results

5.1. Sample petrography

The nature of the dredged peridotites is largely dominated by lherzolites of which two different types can be distinguished. A first type, widely observed (MD80-DR03 and MD110-DR02 and DR09), corresponds to Sp-lherzolites. Interestingly, numerous pyroxenites were dredged together with the Sp-lherzolites. Despite some samples showing proto-mylonitic textures (particularly for samples recovered from DR09 site), most Sp-lherzolites are unstrained, showing coarse-grained to porphyroclastic textures. Serpentinization is generally extensive (up to 95 %), but most samples keep their primary mineral fabric and contain relics of pyroxene and spinel (Fig. 3A and B). Olivine, however, was completely serpentinized. Orthopyroxene occurs as porphyroclasts, while clinopyroxene is generally smaller, both exhibiting cleavages filled with exsolution lamellae of the complementary pyroxene. Spinels are relatively large (up to 2 mm), show sub-euhedral shapes and are of a light brown color (Fig. 3B). Some spinels in MD80-DR3 show reaction coronas of chloritized plagioclase. It should be noted that only small grains of clinopyroxene and spinel were found in serpentinite clasts embedded in carbonates in MD80-DR3.

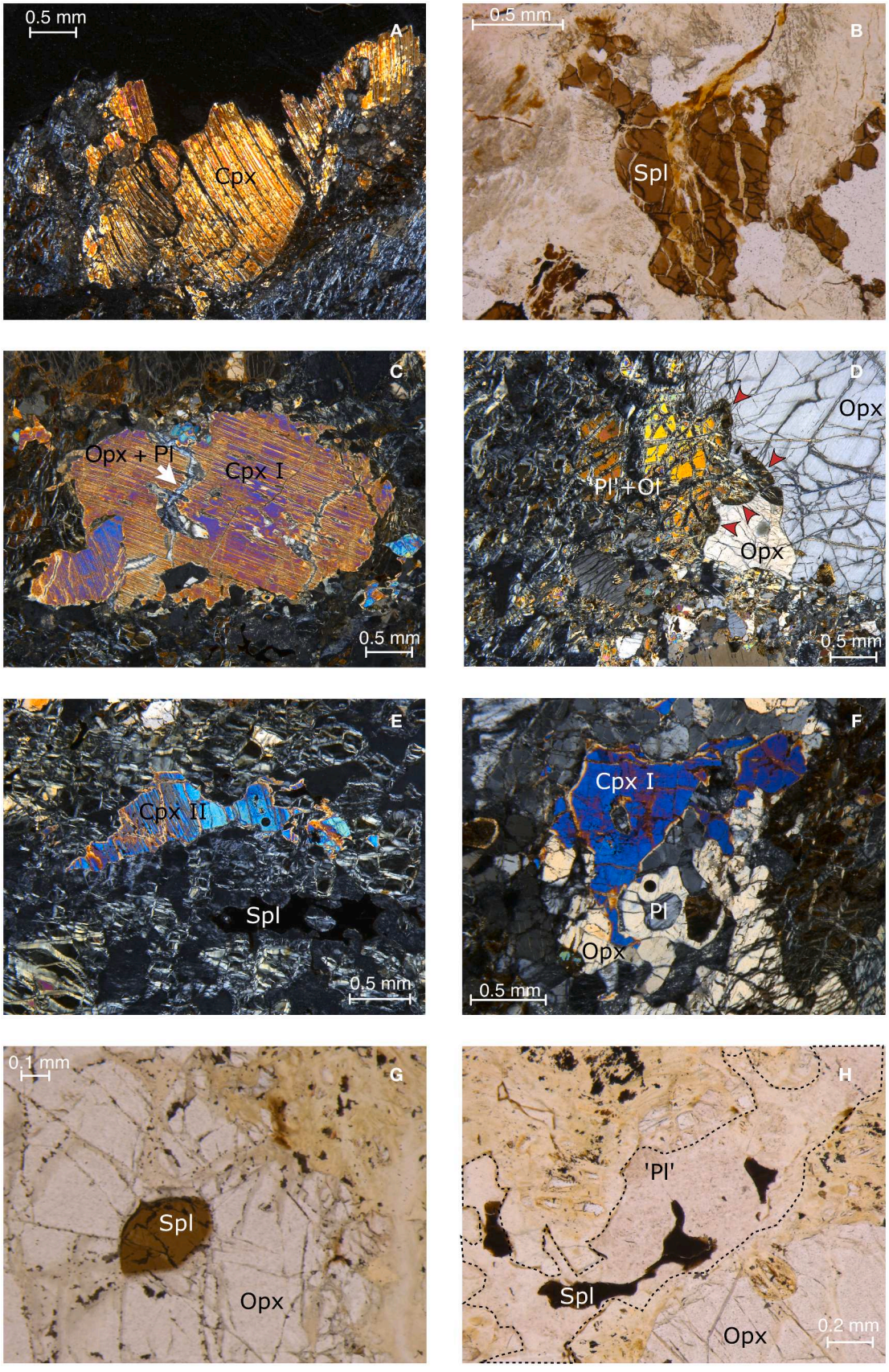
A second type, corresponding to Pl-lherzolites, was only found in MD110-DR06 (Fig. 3C to H). Compared to Sp-lherzolite, they are better preserved from serpentinization (30–50 % of serpentine), and thus contain more relics of primary minerals, including olivine grains preserved in the core of serpentine mesh textures (Fig. 3D). Orthopyroxene shows porphyroclastic textures, with irregular, concave grain boundaries filled with olivine (Fig. 3D). Clinopyroxene is small, with a rounded and lobate texture and occur interstitially in the primary porphyroclastic mineral assemblage (Fig. 3E and F). Interestingly, clinopyroxene is systemically associated with plagioclase (Fig. 4). The latter is largely replaced by chlorite (Fig. 3C-D-E-H) but preserved grains can be found (Fig. 3F), rarely surrounding spinel (Fig. 3H) but rather interstitial. Spinel displays heterogeneous shapes: most grains have irregular, holly-leaf shapes with a dark-brown color (Fig. 3H), whereas others, occurring as inclusions within orthopyroxene porphyroclast (Fig. 3G), share similarities in color and shape with spinel from Sp-lherzolites (Fig. 3B).

5.2. Mineral chemistry

5.2.1. Clinopyroxene

All clinopyroxenes have a composition corresponding to diopside, with chemical compositions that vary depending on the host rock. In Sp-lherzolite, clinopyroxene shows high Na_2O concentrations (0.8–1.8 wt %; Fig. 5A, C) with high Mg# (Mg/(Mg+Fe); 0.91 to 0.95; Fig. 5A). It also shows high Cr_2O_3 contents (0.7–2 wt%, Fig. 5B) with higher values in MD110-DR02 and lower values in MD80-DR3, and Al_2O_3 ranging from 4 to 8 wt% with homogenous values at the sample scale. No significant core-to-rim zonation is observed. Trace element patterns of clinopyroxene from Sp-lherzolite show distinct shapes depending on their respective dredge sites (Fig. 6). At MD110-DR02 and DR09, clinopyroxene is depleted in incompatible elements with Pb, Sr and Zr-Hf negative anomalies. It is characterized by LREE depletion ($(La/Sm)_N \sim 0.1$) and show flat HREE patterns. Clinopyroxenes from site MD80 are less depleted in LREE without any fractionation between MREE and HREE.

Clinopyroxene from Pl-lherzolites is characterized by lower Na_2O (<0.7 wt%; Fig. 5A, C) and Mg# (mean at 0.909±0.02) relative to Sp-lherzolites. Al_2O_3 compositions show a similar range (3 - 8 wt%; Fig. 5B, D) to that of clinopyroxene of Sp-lherzolites. A significant difference exists, however, between porphyroclasts and neoblasts. The chemical maps show that porphyroclasts exhibit core-to-rim zonation (Fig. 4) with high Al_2O_3 concentrations at the core (up to 8 wt%, Fig. 5D) and lower at the rim (3 wt%). The opposite is observed for Cr_2O_3 concentrations, leading to higher Cr# at the clinopyroxene rims than in the cores (0.2 vs. 0.1, respectively; Fig. 4H). Trace element patterns are also depleted in incompatible elements and show deeper Sr and Pb negative anomalies compared to clinopyroxene in Sp-lherzolites. REE patterns are slightly less depleted in LREE with humped M- to HREE patterns ($(Gd/Yb)_N > 1$) and a negative Eu anomaly ($Eu/Eu^* \sim 0.89$).



(caption on next page)

Fig. 3. Microphotographs of **A)** a preserved clinopyroxene (Cpx) porphyroclast (cross-polarized) (MD110-DR02-A27) and **B)** typical brown colored spinel (plan polarized) in highly serpentinized Sp-lherzolite (MD110-DR02-A66). **C)** Peritectic plagioclase (Pl) – orthopyroxene (Opx) assemblage replacing a primary clinopyroxene pophyroclast (Cpx I) in Pl-lherzolite (MD110-DR06-171). **D)** Orthopyroxene porphyroclast with corroded rims (holly-leaf texture, red arrows) with corrosion embayments filled by olivine (Ol) and plagioclase (here altered into chlorite, 'Pl'; MD110-DR06-161A). **E)** Secondary clinopyroxene neoblast (Cpx II) in assemblage with plagioclase ('Pl') near an amoeboid spinel (MD110-DR06-161A). **F)** Original, former clinopyroxene porphyroclast (Cpx I) consumed during mantle-melt reaction, forming typical othopyroxene-plagioclase assemblage (MD110-DR06-162B). **G)** Spinel in inclusion within orthopyroxene in Pl-lherzolite, similar in shape to spinel found in Sp-lherzolite (MD110-DR06-161A). **H)** Typical dark-colored Cr-rich spinel in Pl-lherzolite, with plagioclase coronae (dashed line) suggesting sub-solidus spinel-to plagioclase transition (MD110-DR06-161A).(For interpretation of the references to color in this figure legend, the reader is referred to the web version of this article.)

5.2.2. Orthopyroxene

Orthopyroxene in Sp-lherzolite has high Mg# (ranging from 0.90 to 0.95 – mean at 0.92). Al_2O_3 and CaO contents vary from 3 to 6 wt% and 0.4 to 3 wt% respectively, and major element profiles do not show any core-to-rim zonation. Chondrite-normalized REE patterns show strong fractionation between L- and HREE with a strong depletion in LREE (usually below the limit of detection).

Orthopyroxene from Pl-lherzolites has lower Mg# (0.89 to 0.92) and strong core-to-rim zonations in Al_2O_3 and Cr_2O_3. Clinopyroxene porphyroclasts show similar trends (Fig. 5). Cores contain ~5 wt% Al_2O_3 while rims have Al_2O_3 concentrations <2.5 wt%. Cr_2O_3 concentrations show core-to-rim enrichment from ~0.6 to 0.8 wt%, leading to the same Cr# range than that reported in clinopyroxene porphyroclasts. SiO_2 and MgO also show increasing concentrations from core to rim. The REE concentrations are slightly higher in Pl-lherzolite orthopyroxene relative to those in Sp-lherzolite, with a similar strong L- to HREE fractionation. REE concentrations also show zonation, with a typical LREE depletion at the crystal rim relative to the core (see supplementary materials).

5.2.3. Spinel

Spinels show contrasting compositions between Sp- and Pl-lherzolites. Spinels from Sp-lherzolite have high Mg# (0.74–0.85) and low Cr# (0.0.9–0.26) (Fig. 7A and B). They also show low TiO_2 contents (<0.15 wt%). The degree of partial melting (F) calculated based on spinel Cr# (Hellebrand et al., 2001) shows that peridotites at MD110-DR02, DR09 and MD80-DR03 underwent relatively low degrees of melting (F<10 %; Fig. 7C). In contrast, spinels from Pl-lherzolite have lower Mg# (0.52 to 0.79), higher Cr# (0.19 to 0.56) and high TiO_2 concentrations (>0.2 wt%, up to 0.79 wt%). Interestingly, some spinels found in inclusions within orthopyroxenes show compositions like those of spinels from Sp-lherzolite (Cr# 0.128 to 0.175; Mg# 0.77 to 0.85; TiO_2<0.15 wt%) and similar calculated F of 3–7 % (Fig. 7C).

5.2.4. Olivine

Relics of olivine were only found in Pl-lherzolite (Figs. 3 and 4), while in Sp-lherzolite, olivine was completely altered into serpentine. Olivine shows high MgO (48.0–51.4 wt%) and low FeO (6.2–9.6 wt%), resulting in a relatively high Mg# in the range of 0.90–0.93. NiO abundances varies from 0.23 to 0.46 wt%. Trace element concentrations were almost systematically below the limit of detection.

5.2.5. Plagioclase

Fresh plagioclase only occurs in 2 samples (MD110-DR06-162B and MD110DR06-168). In other samples, plagioclase is replaced by chlorite (Fig. 3). Plagioclase has compositions corresponding to labradorite to bytownite (An71 ± 8). REE patterns show LREE enrichment (up to 2 times chondrite concentrations) and a strong depletion in HREE (< 0.1 times chondrite, heaviest REE being systematically < LOD; see supplementary figure). They also show a prominent positive Eu anomaly (Eu/Eu* ~ 7.8).

5.3. Geothermobarometry

To estimate the equilibrium temperature and pressure for the various peridotites from the Diamantina zone, mineral compositions were used to calculate several geothermobarometric estimates (e.g., Ca-in-orthopyroxene ($T_{Ca\text{-}in\text{-}opx}$) and 2 pyroxenes ($T_{BKN}$; Brey and Köhler, 1990)). The only barometer available so far for spinel peridotite uses calcium concentration in olivine (D'Souza et al., 2019). However, no olivine was preserved in Sp-lherzolites, so a pressure of 15 kbars was assumed for temperature calculation. Temperatures (T_{BKN}) were obtained for MD110-DR02 (944 ± 53 °C), MD110-DR09 (943 ± 85 °C) and MD80-DR3 (944±28 °C) respectively. Significantly higher temperatures were calculated using $T_{Ca\text{-}in\text{-}opx}$ (1230 ± 87 °C and 1139 ± 127 °C, 1238 ± 124 °C respectively). This may reflect the presence of clinopyroxene exsolution lamellae under the spot analysis of EPMA and μ-XRF. These higher temperatures may correspond to those reached prior to clinopyroxene exsolution (Cherniak and Liang, 2022; Jollands and Müntener, 2019;). For Pl-lherzolite, we combined thermometers with the FACE (Fumagalli et al., 2017) and the anorthite-based barometers (Borghini et al., 2010, 2011). We found a pressure of 7 kbar and a slightly higher T_{BKN} of 1013 ± 46 °C compared to Sp-lherzolites. $T_{Ca\text{-}in\text{-}opx}$ for Pl-lherzolite are also more elevated (1178 ± 54 °C).

6. Discussion

6.1. Exhumed mantle peridotites along the Diamantina Zone: what do they record?

6.1.1. Two mantle types

Dredged mantle samples from the Diamantina Zone can be subdivided into two groups: Sp-lherzolite and Pl-lherzolite (Fig. 3). While Sp-lherzolites are widespread and occur at sites MD110-DR02, DR09 and MD80-DR3, Pl-lherzolites have only been found at MD110-DR06, located along the Leeuwin fracture zone (Fig. 2B). Considering the stability domains of spinel and plagioclase, the occurrence of two types of peridotites indicates that these rocks were formed at two distinct depths. Many pyroxenites were dredged with Sp-lherzolites at sites MD110-DR02 and DR09 but were very scarce at site MD110-DR06. At this site peridotites were almost exclusively Pl-lherzolite. This suggests that we are not only dealing with two different types of peridotite, but that we are also dealing with two different domains of the mantle.

6.1.2. Sp-lherzolite: a subcontinental lithospheric mantle inheritance

Sp-lherzolites found at the various dredging sites in the Diamantina Zone contain Na_2O-rich clinopyroxene (between 0.8 and 1.8 wt%) with high Mg# (> 0.90; Fig. 5) and spinel with low Cr# and high Mg# (Fig. 7). All these features suggests a sub-continental mantle origin. This result is consistent with geophysical modelling (Laat et al., 2023) and a geochemical composition assumed for SCLM of Mesoproterozoic age (Maier et al., 2016). The high Mg# (Mg# > 0.74) and low Cr# in spinel are indicative of a fertile composition of Sp-lherzolite. It also implies that the latter underwent relatively low degrees of partial melting (<10 %) of unknown age (Fig. 7). Additional information about the melting conditions recorded by Sp-lherzolites can be obtained from the chemical composition of clinopyroxene. Fig. 8 shows the concentrations of Nd_N vs. Na_2O in clinopyroxene. These two elements are of particular interest since both are sensitive to the degree of partial melting and have approximately the same incompatibility at low pressure ($D_{Na}^{Cpx/l} \approx D_{Nd}^{Cpx/l} \sim 0.2$; Blundy et al., 1995). However, at high pressure in the garnet stability field, Na becomes less incompatible than Nd

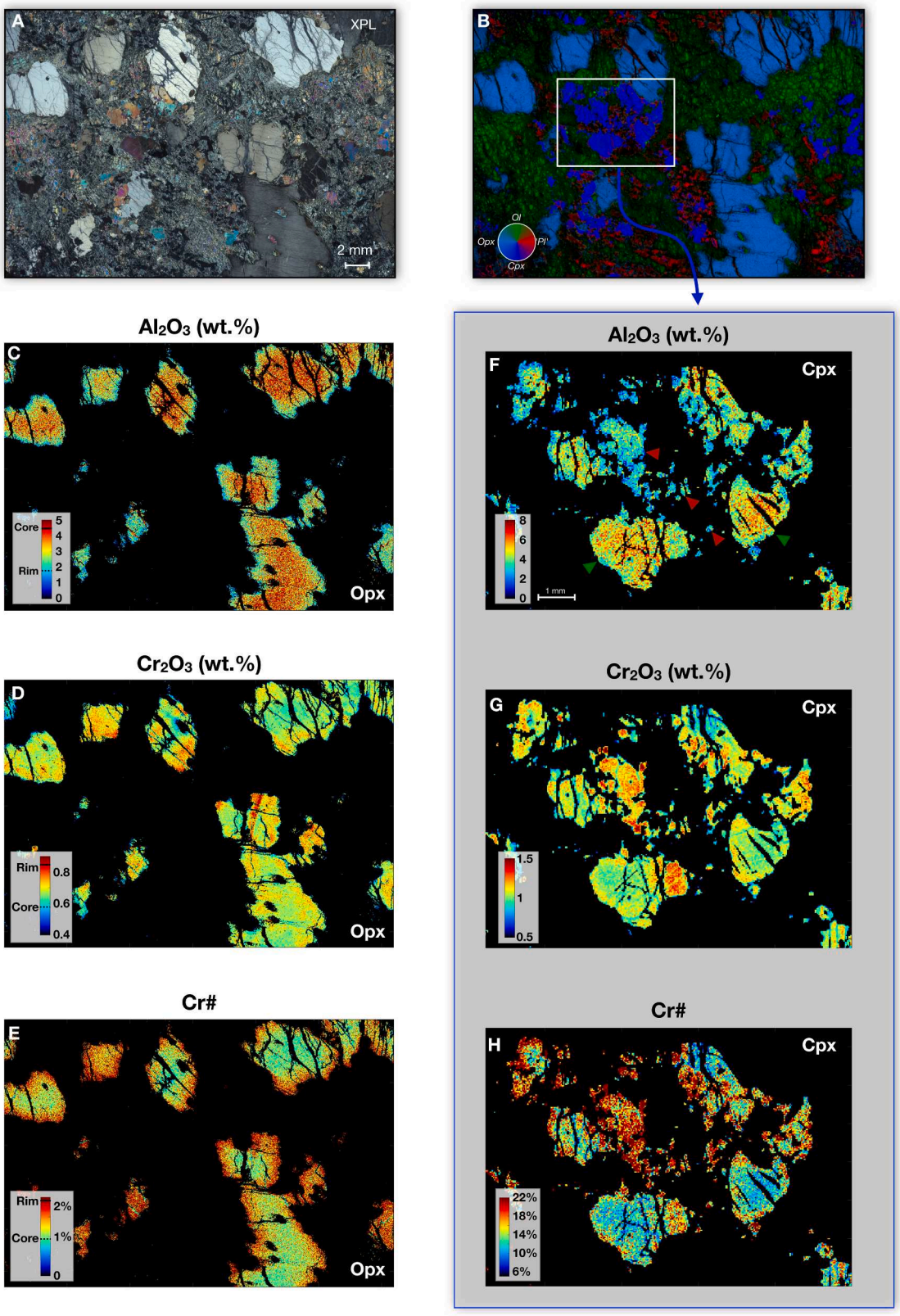


Fig. 4. A) Cross-polarized microphotographs of a Pl-lherzolite sample (MD110-DR06-161c). **B)** Phase map showing mineralogical distribution of A). **C)** Al_2O_3, **D)** Cr_2O_3 and **E)** Cr# compositions of orthopyroxene in Pl-lherzolite showing core-to-rim zonations. **F), G), H)** Same as C), D), E), respectively, for clinopyroxene. Red arrows in F) show unzoned Cpx neoblasts, while green arrows locate zoned, primary Cpx porphyroclasts. The phase and concentrations maps were calculated based on μ-XRF chemical maps applying the approach of Ulrich et al. (2014).(For interpretation of the references to color in this figure legend, the reader is referred to the web version of this article.)

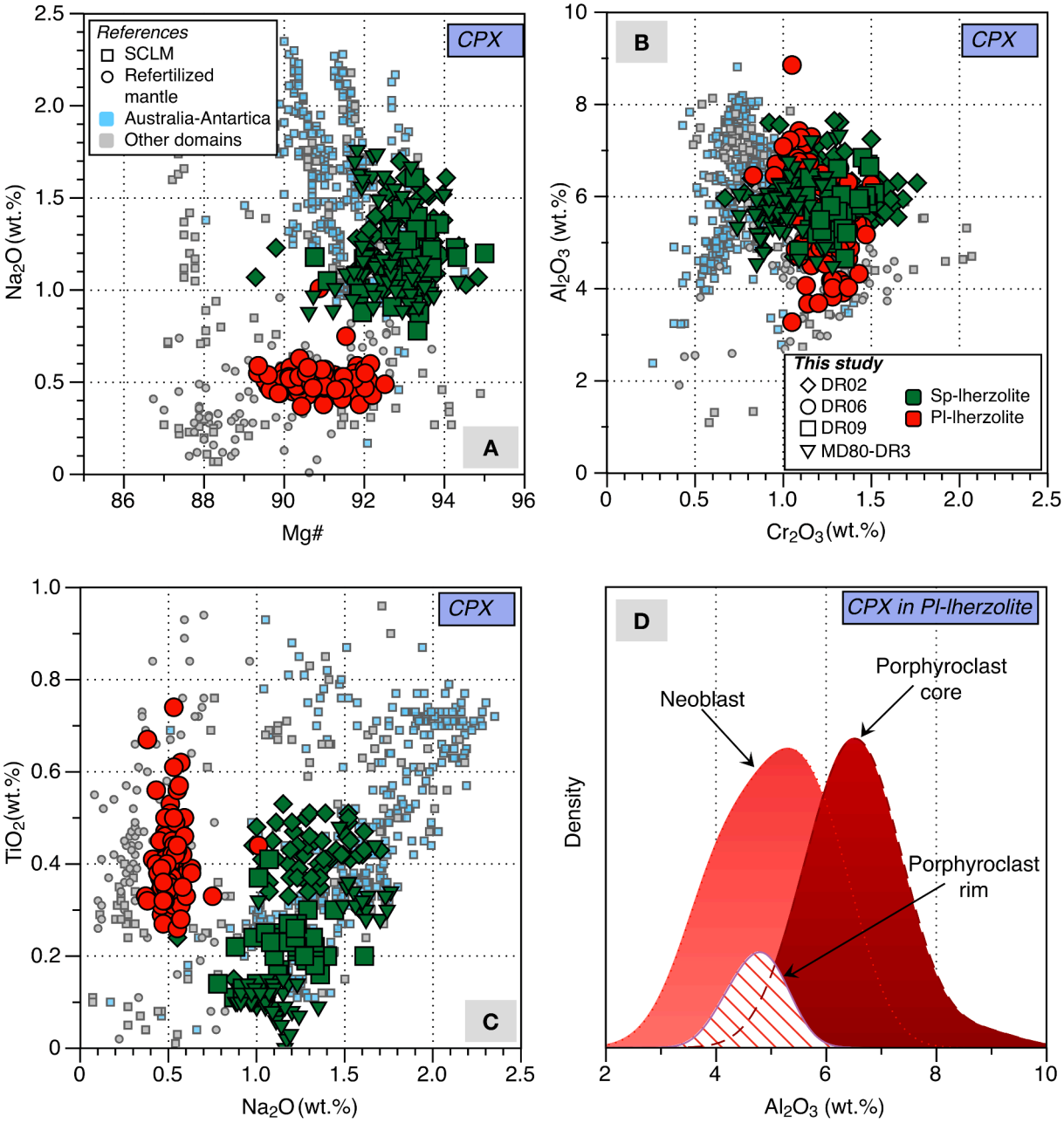


Fig. 5. Major element compositions of clinopyroxene in Sp- and Pl-peridotites from the Diamantina zone. **A)** Na_2O (wt%) vs. Mg# **B)** Al_2O_3 (wt%) vs. Cr_2O_3 (wt%) **C)** TiO_2 (wt%) vs. Na_2O (wt%) **D)** Kernel density distribution of Al_2O_3 concentrations in clinopyroxene from Pl-lherzolites, showing that neoblasts are depleted in Al_2O_3 relative to primary porphyroclasts. Data from Australia-Antarctica (blue - Beyer, 2002; McCarthy et al., 2020; Delpech et al., 2021) and other domains (grey - passive margins compilation from Picazo et al., 2016; Müntener et al. 2004; 2010; Müntener and Manatschal, 2006; Rampone et al., 1996; and Lena Through peridotites from Hellebrand and Snow, 2003) are shown for comparison.

($D_{Na}^{Cpx/l}$ ~0.5; Blundy et al., 1995). Applying the modeling approach of Hellebrand et al. (2002) and Müntener et al. (2010), we calculated the theoretical evolution of the Na_2O and Nd composition of clinopyroxene during the partial melting of a lherzolite. Na_2O concentrations of clinopyroxene in most Sp-lherzolites are higher than the depleted mantle (DM) clinopyroxene (0.89 wt%; Workman and Hart, 2005). Therefore, a primitive mantle-like composition was assumed for the starting material (McDonough and Sun, 1995). Two melting models were calculated assuming melting in the spinel or garnet stability field (curves A and B respectively, Fig. 8A). A third "polybaric" model was developed with 2, 4 and 6% of melting of a garnet peridotite followed by conversion of modal assemblages into spinel peridotite (Johnson et al., 1990) and additional melting in the spinel mantle field (curves C_2, C_4, C_6, Fig. 8A). This latter model fits most of the data and highlights that Sp-peridotites along the Diamantina zone underwent partial melting degree that rarely exceeded 10 %. This result is in good agreement with estimates based on Cr# in spinel (Fig. 7). More specifically, our model shows that MD110-DR02 and some MD80DR3 Sp-lherzolites are residual after 2–4 % melting in the garnet stability field, followed by melting in the spinel stability field. These estimates are very similar to those previously made for the peridotites of the Central Alps (Müntener et al., 2010).

Interestingly, other samples from MD80-DR3 and MD110-DR09 are better explained by melting occurring almost exclusively in the garnet stability field (up to 8–9 %), with only low melting (<2 %) in the spinel mantle domain, making them more comparable to the Lena Trough peridotites described by Hellebrand and Snow (2003). However, this

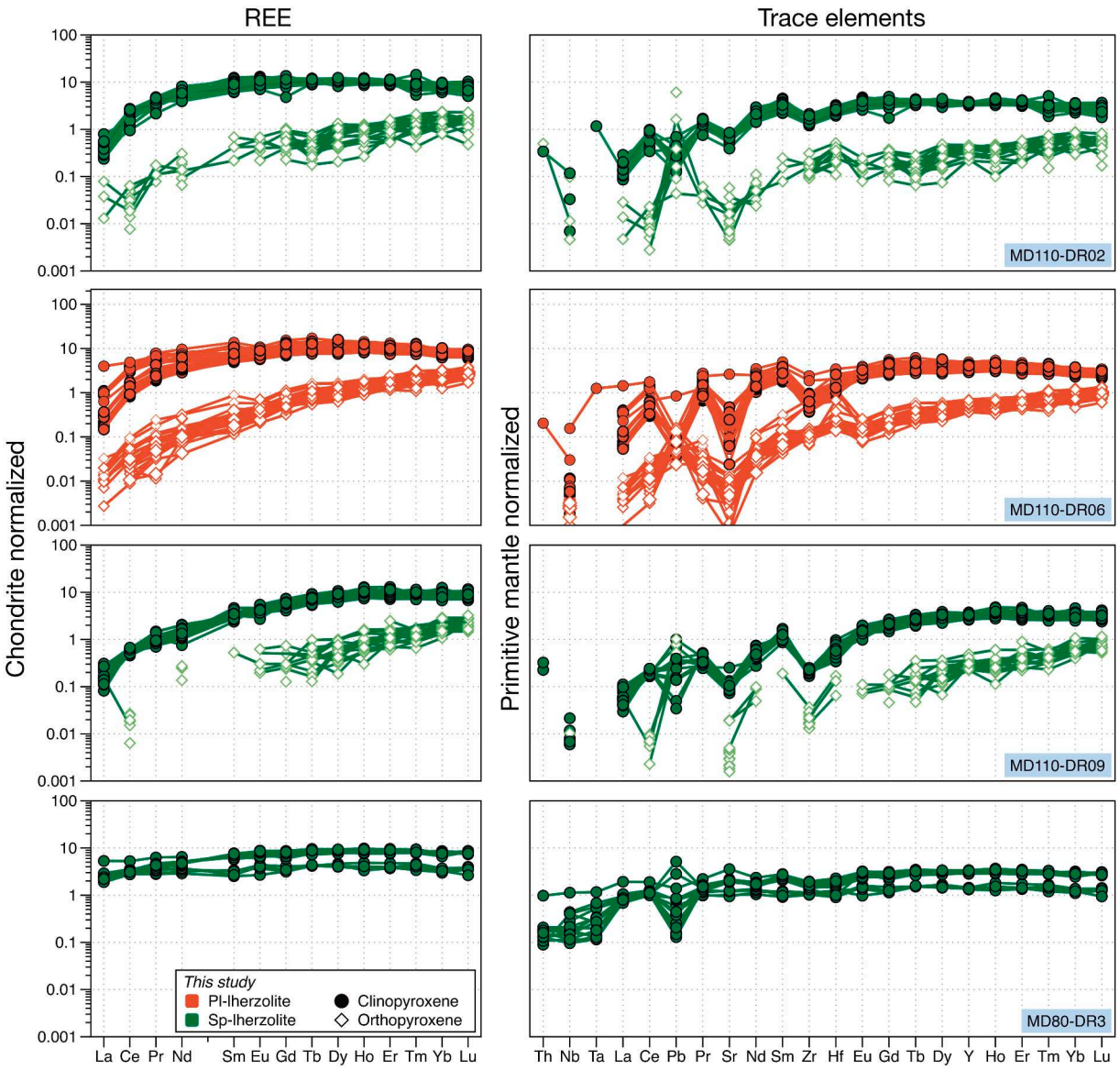


Fig. 6. Rare earth and trace element patterns of pyroxenes in Sp- and Pl-lherzolites from the Diamantina zone. REE are normalized to C1 chondrites (Anders and Grevesse, 1989) and trace elements are normalized to the Primitive Mantle (McDonough and Sun, 1995).

model failed at reproducing the low Na_2O/high Nd_N concentrations of MD110-DR06 Pl-lherzolites, which suggests that they derive from another magmatic process.

6.1.3. Pl-lherzolite: a tape recorder of mantle-melt reactions during exhumation

The Pl-lherzolites show very different textures from those observed in the Sp-lherzolites. These include corroded orthopyroxene with corrosion embayment filled by olivine (Fig. 3D), pre-existing clinopyroxene porphyroclasts partially replaced by orthopyroxene and plagioclase assemblage (Fig. 3C), and interstitial clinopyroxene neoblasts in close association with interstitial plagioclase (Fig. 3E). All these textures evidence the occurrence of melt impregnation rather than sub-solidus reactions (e.g., Kaczmarek and Müntener, 2008; Müntener et al., 2010; Rampone and Borghini, 2008). Olivine embayment on pyroxenes (Fig. 3D) are characteristic of reactive porous flow, occurring at spinel facies and known to crystallize olivine at the expense of pyroxene (Basch et al., 2020; Piccardo et al., 2007; Rampone et al., 2020). This process is distinct from the refertilization process, which consists of impregnation by percolating melts at the plagioclase facies (Fig. 3E, F).

Mantle-melt reactions are also indicated by mineral chemistry such as high TiO_2 concentrations in spinel and slight LREE enrichment and "humped shaped" middle to heavy REE patterns of clinopyroxene. The difference between Cr# of clinopyroxene and Cr# of spinel (Fig. 9) is also in favor of melt-rock interaction rather than subsolidus reequilibration (Müntener and Manatschal, 2006). Na_2O and Al_2O_3 depletion and Sr and Eu negative anomalies in clinopyroxene are indicative of co-crystallization with plagioclase, consistently to that was reported in Pl-lherzolites from the Alpine-Apennine ophiolites (Basch et al., 2019; Borghini and Rampone, 2007; Kaczmarek and Müntener, 2010; Müntener et al., 2004; Rampone et al., 1995). The refertilization assumption was tested in Fig. 8B by simple mass balance modelling the addition of N-MORB-type melts (1 % increment) in a depleted peridotite at shallow depth in the plagioclase stability field. The Na_2O and Nd compositions of residual peridotite were calculated after 4 % of melting in the garnet stability field, followed by 4% additional melting under spinel facies conditions. The elemental zonation reported in orthopyroxene from Pl-lherzolites, characterized by core-to-rim Al_2O_3 and CaO depletion and MgO enrichment (Fig. 4), indicates that this mineral experienced a transition from spinel-to-plagioclase facies (Borghini et al., 2010; Smye

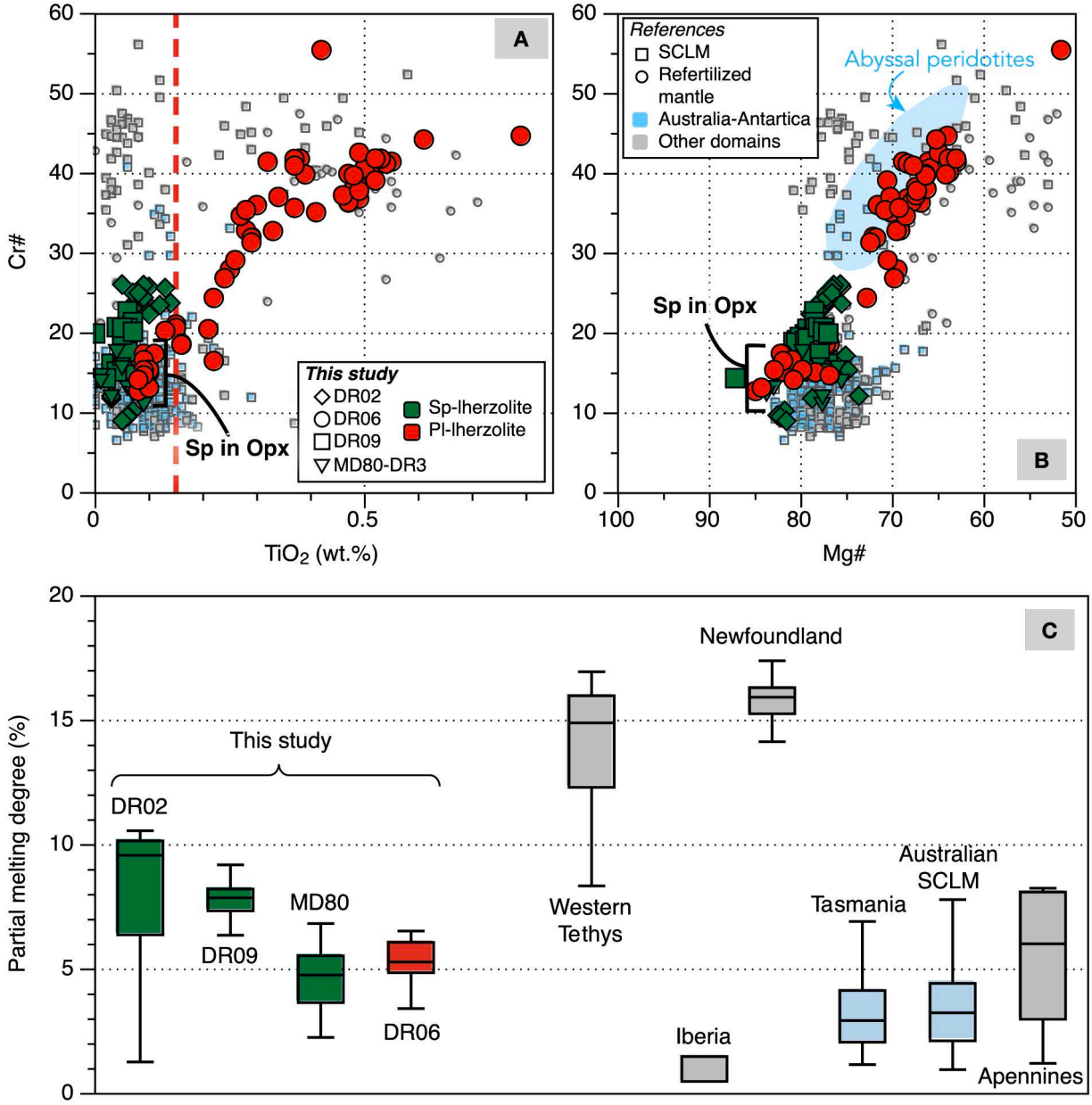


Fig. 7. Major element compositions of spinels from the Diamantina zone. **A)** Cr# vs. TiO_2 (wt%); **B)** Cr# vs. Mg#; **C)** Comparison between partial melting degrees recorded by peridotites exhumed along the Diamantina zone with data from other margins worldwide. The partial melting degrees were calculated as a function of Cr# of spinels, applying the following equation: F (%) = 10 ln(Cr#) + 24, valid for Cr# values ranging from 0.1 to 0.6 (Hellebrand et al., 2001). Only spinels with TiO_2 <0.15 wt% were considered, preventing effects of melt percolation on the chemical composition of spinel. Data from literature are the same as for Fig. 5.

et al., 2017; Witt-Eickschen and Seck, 1991). This transition was considered in our model by the conversion of spinel into plagioclase (completely converted - light red star; 50 % - dark red star) according to the following equation: Sp + Cpx + Opx = 2 Ol + Pl (Rampone et al., 1993). The crystallization modes during refertilization were assumed to be Z_{cpx}/Z_{plg} = 0.09/0.04 (Müntener et al., 2010). Our results show that small fractions of melt entrapment and crystallization lead to a steeper evolution of the Na_2O/Nd_N ratio in clinopyroxene compared to melting trends.

This evolution matches well with the composition of clinopyroxene in Pl-lherzolites. The amount of melt (up to 5%) stored in Pl-lherzolites of the Diamantina zone is also consistent with previous estimates calculated for impregnated peridotites from the Alpine-Apennine system or the Iberia margin (Abe, 2001; Müntener et al., 2010; Rampone et al., 2020). It should be noted that Müntener et al. (2010) performed additional tests about the nature of the refertilized agent (from depleted to enriched melts). Their conclusions were that the nature of melts does not significantly affect the refertilization trends but only controls the amount of refertilization.

The refertilized domain could thus be considered as a hybrid domain where inherited SCLM is modified by a later melt percolation. Our calculations show that the chemistry of Pl-lherzolites is not controlled by the nature of the refertilizing agent but rather depends on the mantle chemical composition prior to refertilization. This result demonstrates that SCLM inheritance has a considerable incidence on the final chemistry of the refertilized mantle (especially the type of SCLM – that means T1a or T1b, which defines the fertility of the inherited mantle) but does not control the processes involved in the formation of magma-poor rifted margins.

Finally, the partial melting models developed in this study demonstrate that, when the starting point is aligned with the regional geological history (DMM source or primitive mantle), the same

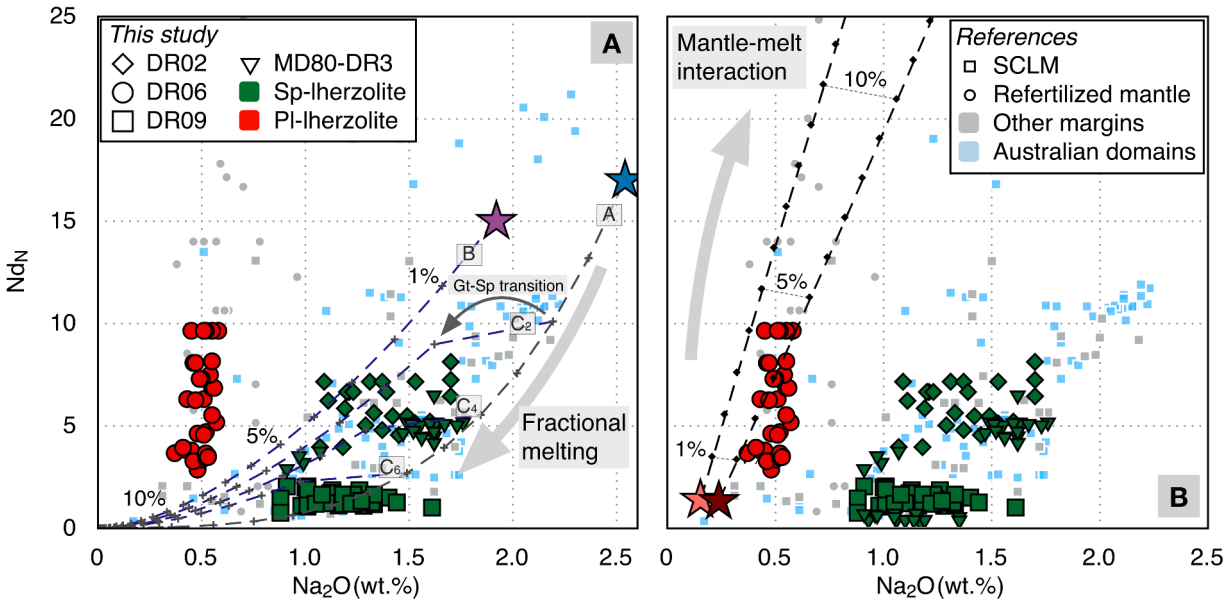


Fig. 8. Na_2O vs. Nd_N concentrations in clinopyroxene of Diamantina zone peridotites. **A)** Melting modeling of clinopyroxene of a primitive-like mantle source starting at garnet [A] and spinel [B] stability fields. [C_2], [C_4] and [C_6] dashed blue curves simulate a "polybaric" melting with 2 %, 4 % and 6 % of melting in the garnet stability field followed by additional melting in the Sp-peridotite field. **B)** refertilization modeling of a depleted source after 4 % of melting in the garnet stability field, followed by 4 % melt extraction under spinel facies conditions and sub-solidus re-equilibration in the plagioclase stability field (the light red star indicates full Sp-to-Pl replacement while the dark red star considers only 50 % of Sp is converted into Pl, using the univariant reaction of Rampone et al., 1993). The refertilization agent is a N-MORB-type melt, black dots along the refertilization curves indicate 1 % melt increment. Melting and refertilization models are modified from Hellebrand and Snow (2003) and Müntener et al. (2010). Additional parameters are given in the text.(For interpretation of the references to color in this figure legend, the reader is referred to the web version of this article.)

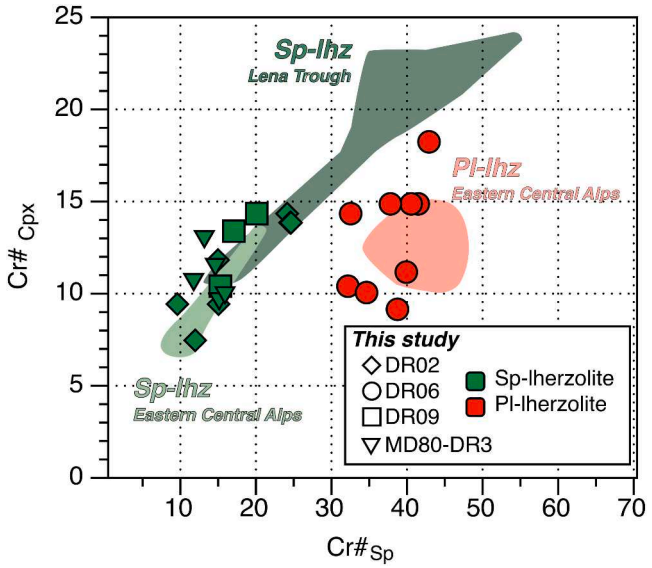


Fig. 9. $Cr\#_{Cpx}$ vs. $Cr\#_{Sp}$ of the peridotites from the Diamantina Zone. Sp-peridotites from Lena Trough are from Hellebrand and Snow (2003); Sp- and Pl-lherzolites from Eastern Central Alps are from Müntener et al. (2004; 2010).

processes are involved, i.e., an initial partial melting phase in a garnet-facies domain, then a transition to the spinel-facies domain and finally partial melting in the spinel-facies domain. In the same way, regardless of the chemistry of the refertilizing liquid or the crystallization modes, the chemistry of pyroxenes will be modified (in terms of REE, Na_2O, Al_2O_3 and Cr_2O_3 in particular) but not the process itself, which always takes place under similar PT conditions.

6.2. *The Diamantina mantle rocks: how do they fit the alpine-iberia model?*

The research in mantle rocks from OCTs is almost entirely based on studies from samples from the Iberia-Newfoundland and Western Tethys systems. These studies highlighted the heterogeneous composition of the SCLM (Picazo et al., 2016; Vauchez et al., 2000) and the importance of refertilization during lithospheric breakup (Müntener et al., 2004), which we refer to as the so-called Alpine-Iberia model. This model proposed that the inherited SCLM corresponding to mantle T1, was progressively refertilized and modified, giving rise to mantle T2. However, a direct genetic link between T1 and T2 is not so common in petrographic observations. It is also important to note, that the Alpine-Iberia model is based on a relatively regional data set and has not been constrained elsewhere in domains exhibiting a different and much older pre-rift inheritance. In this context, the mantle rocks derived from the Diamantina zone are of a particular importance, since they derive from the Mesoproterozoic Fraser orogenic domain, which separates the margin from the Archean Yilgarn craton. Thus, the subcontinental mantle exhumed along the SW Australia margin is necessarily older than the one from the Iberia-Newfoundland and Alpine domains and consequently their inheritance is likely different. Hence, a major question is whether the mantle rocks from the Diamantina zone provide new observations that either reject, support, or complete the Alpine-Iberia model.

6.2.1. *Do mantle-melt interactions depend on the type of inherited mantle?*

Picazo et al. (2016) compiled a large amount of petrological and geochemical data from the Iberia and Western Tethys systems, which allowed to map the distribution of mantle T1 and T2. Along the Diamantina Zone, the same mantle subdivision occurs. In both the Alps and the Diamantina examples, pyroxenites are commonly observed within the inherited SCLM (Müntener et al., 2004) but are rarely observed in the refertilized domains (Pl-lherzolite). Na_2O concentrations of clinopyroxene from the inherited mantle in the Diamantina Zone are in line

with those reported from the Alps. In contrast, CaO content is particularly high compared to the Alpine equivalents. Partial melting estimates, based on Cr# of spinel, show degrees < 11 %, which is much lower than those reported from the Alps (8–16 %) or Newfoundland (up to 17 %), but still higher than those from Iberia (< 3 %). In the refertilized domain, clinopyroxene has lower Na_2O and Al_2O_3, and higher Cr_2O_3 contents compared to those from the Alps and Iberia. When comparing the chemistry of these clinopyroxenes as a function of their domain in the OCT notable differences can be seen in terms of Al_2O_3 and Cr_2O_3, which are interpreted as variations of degrees of refertilization. This may be the result of a continuous process that converts the inherited mantle, with its intrinsic variability, into increasingly homogeneous clinopyroxene in the refertilized mantle (Picazo et al., 2016). Thus, variations in major elements in clinopyroxene from MD110-DR06 peridotite remains preserved only in some porphyroclasts. This is particularly true for some elements (i.e., Al_2O_3). This may be attributed to various degrees of melt infiltration and the related thermal evolution (Borghini et al., 2023). However, the lack of variation in Na_2O concentration, which remains constant at low values, could be the sign of a previous high partial melting rate. This observation may be characteristic of the mantle type 1b, i.e., an inherited depleted subcontinental mantle.

6.2.2. *Can a direct genetic link between inherited and refertilized mantle type be proven?*

In the Alpine-Iberia model, the link between the inherited subcontinental mantle (T1) and the refertilized mantle (T2) has been assumed (Muntener et al., 2010; Picazo et al., 2016), but it has never been clearly demonstrated. Interestingly, some spinels are found embedded in orthopyroxene porphyroclasts with contrasting color and texture relative to darker spinels with holly-leaf textures that dominantly occur in Pl-lherzolites (Fig. 3). Their high Mg# (up to 0.86), low Cr# (<0.2) and TiO_2 (<0.2 wt%) differ from those affected by melt percolations (Mg# <0.73; Cr# >0.28; TiO_2 >0.2 wt%). However, they share similarities in texture and chemistry with spinel of Sp-lherzolites (Fig. 7). Moreover, similar estimates of partial melting degree were obtained from these spinels (5–7 %) like those from the Sp-lherzolites. These embedded spinels could have been preserved from melting and refertilization events and could thus represent the missing link between Sp-lherzolite (mantle T1a) and Pl-lherzolite (mantle T2). Thus, the Diamantina peridotites do not only follow the predictions of the Alps-Iberia model, but they also complete the model by showing that these spinels might be the missing link between the inherited SCLM and its refertilization during exhumation.

6.3. *The Iberia-Alpine mantle-melt interaction model: what did we learn from the SW-Australia margin?*

About half of the world rifted margins show seismic characteristics of magma-poor rifted margins (Fig. 2A; Reston, 2009). However, at present only samples from a very small portion of these margins have been sampled. This limits our understanding of the processes controlling the formation of magma-poor systems and leaves questions such as how, and to what extent inheritance of the SCLM can control the magmatic budget during breakup difficult to answer. It remains also questionable if the mantle-melt interaction processes described in the Alpine-Iberian model can be considered as globally applicable to explain magma starvation or delay of melt extrusion at all magma-poor rifted margins? Our results show that mantle-melt processes at the Diamantina Zone, despite very different age and inheritance of the SCLM, show similar processes during breakup and the same mantle subdivision (T1 and T2) along the OCT. These processes include the refertilization of the inherited SCLM, a process that leads to the delay of melt extrusion at the seafloor. In this context, the nature of the inherited mantle, particularly the lower SCLM, may be of importance. Studies in the Iberia-Newfoundland and Western Tethys systems show that mantle type 1 can be divided into two subtypes. A fertile SCLM, referred to as mantle type 1a that is distinct from a depleted mantle referred to as type 1b that has undergone partial melting events occurring before the onset of rifting, probably during a previous post-orogenic or subduction event (Picazo et al., 2016). The presence of mantle T1b is fundamental since it may explain why these margins evolved as so-called magma-poor margins. Indeed, the presence of a depleted lower lithospheric mantle may explain why melts were not directly extracted at the seafloor but were first stored within the deeper and depleted SCLM. Thus, the occurrence of mantle T1b at other magma-poor margins could provide further support for the idea that the depleted nature of the lower SCLM could be a fundamental feature in the formation of magma-poor margins. In this frame, our study shows that the primary minerals found in Pl-lherzolites show evidence of an older partial melting event, similar to the T1b-type mantle described by Picazo et al. (2016). Our study further supports the idea that the presence of a depleted lower SCLM may be at the origin of retardation of magma-emplacement at the seafloor, favoring mantle exhumation (Chenin et al., 2024). Thus, we propose that the occurrence of a depleted lower SCLM may constitute a major control on the formation of magma-poor rifted margins.

7. Conclusion

The petrology of the peridotites exhumed along the Australia-Antarctica ocean continent transition zone demonstrates the occurrence of two mantle domains along the SW Australia OCT. Similarly to what has been described earlier from the Iberia and Western Tethys margins, Sp-lherzolites correspond to an inherited sub-continental mantle while Pl-lherzolites are formed during melt infiltration at low pressure in the plagioclase stability field during exhumation of the SCLM. Based on an older heritage, the samples of the Diamantina zone enable us to show that the Alpine-Iberia model of magma-poor rifted margins is more broadly applicable. Traces of this inheritance are preserved in the refertilized mantle with relicts characterized by distinctive textures and chemistry, demonstrating the link between mantle type 1b (lower part of the SCLM that experienced an older depleted mantle) and 2. In addition, we show that the inherited nature of the SCLM could control the formation of magma-poor margins. Indeed, melt storage in the depleted lower SCLM during mantle exhumation may delay magma extraction at the seafloor and may explain the formation of magma-poor rifted margins.

CRediT authorship contribution statement

Mélanie Ballay: Writing – review & editing, Writing – original draft, Methodology, Investigation, Formal analysis, Data curation, Conceptualization. **Marc Ulrich:** Writing – review & editing, Writing – original draft, Visualization, Validation, Supervision, Software, Resources, Project administration, Methodology, Investigation, Funding acquisition, Formal analysis, Data curation, Conceptualization. **Gianreto Manatschal:** Writing – review & editing, Writing – original draft, Visualization, Validation, Supervision, Software, Resources, Project administration, Methodology, Investigation, Funding acquisition, Formal analysis, Data curation, Conceptualization.

Declaration of competing interest

The authors declare that they have no known competing financial interests or personal relationships that could have appeared to influence the work reported in this paper.

Acknowledgments

Marie Odile Beslier and Jacques Girardeau are gratefully acknowledged for giving us full access to the samples from the MD110 oceanographic campaign. The authors warmly thank John Moine for his help

during sample preparations and Meredith Morin for her preliminary work on MD110 samples during her Master internship. Thin section production and μ-XRF analyses were performed at the CoRTecS PeMCI plateform of ITES, University of Strasbourg. Chantal Pfeiffert is warmly thanks for her help during LA-ICP-MS measurements and Olivier Rouer for his help during EPMA measurements at Georessources Nancy. This study benefited of the financial support of the French Ministry of Higher Education and Research, and the M6 consortium (GM).

Supplementary materials

Supplementary material associated with this article can be found, in the online version, at doi:10.1016/j.epsl.2025.119212.

Data availability

Is in supplementary.

References

Abe, N., 2001. Petrochemistry of serpentinized peridotite from the Iberia Abyssal Plain (ODP Leg 173): its character intermediate between suboceanic and subcontinental upper mantle. Geol. Soc., Lond., Spec. Publ 187, 143–159. https://doi.org/10.1144/gsl.sp.2001.187.01.08.

Anders, E., Grevesse, N., 1989. Abundances of the elements: meteoritic and solar. Geochim. Cosmochim. Acta 53, 197–214. https://doi.org/10.1016/0016-7037(89)90286-x.

Basch, V., Rampone, E., Borghini, G., Ferrando, C., Zanetti, A., 2019. Origin of pyroxenites in the oceanic mantle and their implications on the reactive percolation of depleted melts. Contrib. Min. Petr. 174, 97. https://doi.org/10.1007/s00410-019-1640-0.

Basch, Borghini, G., Fumagalli, P., Rampone, E., Gandolfo, A., Ferrando, C., 2020. Plagioclase-facies thermobarometric evolution of the External Liguride pyroxenite-bearing mantle. Ofioliti 45 (1), 1–12. https://doi.org/10.4454/ofioliti.v45i1.529.

Bernard, A., Munschy, M., Rotstein, Y., Sauter, D., 2005. Refined spreading history at the Southwest Indian Ridge for the last 96 Ma, with the aid of satellite gravity data. Geophys. J. Int. 162, 765–778. https://doi.org/10.1111/j.1365-246x.2005.02672.x.

Beslier, M.-O., Royer, J.-Y., Girardeau, J., Hill, P.J., Boeuf, E., Buchanan, C., Chatin, F., Jacovetti, G., Moreau, A., Munschy, M., Partouche, C., Robert, U., Thomas, S., 2004. A wide ocean-continent transition along the south-west Australian margin: first results of the MARGAU/MD110 cruise. Bull. Soc. Géol. France 175, 629–641. https://doi.org/10.2113/175.6.629.

Beyer, E.E., 2002. Evolution of the Lithosphere beneath Tasmania and Western Norway. PhD Thesis. Macquarie University. https://doi.org/10.25949/19432517.v1.

Blundy, J.D., Falloon, T.J., Wood, B.J., Dalton, J.A., 1995. Sodium partitioning between clinopyroxene and silicate melts. J. Geophys. Res.: Solid Earth 100, 15501–15515. https://doi.org/10.1029/95jb00954.

Bodinier, J.-L., Garrido, C.J., Chanefo, I., Bruguier, O., Gervilla, F., 2008. Origin of pyroxenite–peridotite veined mantle by refertilization reactions: evidence from the ronda peridotite (Southern Spain). J. Pet. 49, 999–1025. https://doi.org/10.1093/petrology/egn014.

Boillot, G., Winterer, E.L., Meyer, A.W., et al., 1987. In: Proceedings of the Ocean Drilling Program, Initial Reports, 103: College Station, TX (Ocean Drilling Program). https://doi.org/10.2973/odp.proc.ir.103.1987.

Borghini, G., Fumagalli, P., Arrigoni, F., Rampone, E., Berndt, J., Klemme, S., Tiepolo, M., 2023. Fast REE re-distribution in mantle clinopyroxene via reactive melt infiltration. Geochem. Perspect. Lett. 26, 40–44. https://doi.org/10.7185/geochemlet.2323.

Borghini, G., Fumagalli, P., Rampone, E., 2011. The geobarometric significance of plagioclase in mantle peridotites: a link between nature and experiments. Lithos 126, 42–53. https://doi.org/10.1016/j.lithos.2011.05.012.

Borghini, G., Fumagalli, P., Rampone, E., 2010. The stability of plagioclase in the upper mantle: subsolidus experiments on fertile and depleted lherzolite. J. Petrol. 51, 229–254. https://doi.org/10.1093/petrology/egp079.

Borghini, G., Rampone, E., 2007. Postcumulus processes in oceanic-type olivine-rich cumulates: the role of trapped melt crystallization versus melt/rock interaction. Contrib. Miner. Pet. 154, 619–633. https://doi.org/10.1007/s00410-007-0217-5.

Brey, G.P., Köhler, T., 1990. Geothermobarometry in four-phase Lherzolites II. New Thermobarometers, and practical assessment of existing thermobarometers. J. Petrol. 31, 1353–1378. https://doi.org/10.1093/petrology/31.6.1353.

Champion, D.C., Cassidy, K.F., 2007. An overview of the Yilgarn Craton and its crustal evolution. Geosci. Austr. Record. 14, 8–13.

Chatin, F., Robert, U., Montigny, R., Whitechurch, H., 1998. La zone Diamantine (océan Indien oriental), témoin de la séparation entre l'Australie et l'Antarctique : arguments pétrologiques et géochimiques. Compt. Acad. Sci. Earth Planet Sci. 326, 839–845. https://doi.org/10.1016/s1251-8050(98)80022-0.

Chazot, G., Charpentier, S., Kornprobst, J., Vannucci, R., Luais, B., 2005. Lithospheric mantle evolution during continental break-up: the West Iberia non-volcanic passive margin. J. Petrol. 46, 2527–2568. https://doi.org/10.1093/petrology/egi064.

Chenin, P., Manatschal, G., Picazo, S., Müntener, O., Karner, G., Johnson, C., Ulrich, M., 2017. Influence of the architecture of magma-poor hyperextended rifted margins on orogens produced by the closure of narrow versus wide oceans. Geosphere 13, 559–576. https://doi.org/10.1130/ges01363.1.

Chenin, P., Tomasi, S., Kusznir, N., Manatschal, G., 2024. Linking rifted margin crustal shape with the timing and volume of magmatism. Terra Nova 36, 53–61. https://doi.org/10.1111/ter.12690.

Cherniak, D.J., Liang, Y., 2022. Calcium diffusion in enstatite, with application to closure temperature of the Ca-in-opx thermometer. Geochim. Cosmochim. Acta 332, 124–137. https://doi.org/10.1016/j.gca.2022.06.018.

Delpech, G., Scott, J.M., Grégoire, M., Moine, B.N., Li, D., Liu, J., Pearson, D.G., Meer, Q. H.A.van der, Waight, T.E., Michon, G., Guillaume, D., O'Reilly, S.Y., Cottin, J.-Y., Giret, A., 2021. The subantarctic lithospheric mantle. Geol. Soc. Lond. Memoirs M56. https://doi.org/10.1144/m56-2020-13. -2020–13.

Direen, N.G., Borissova, I., Stagg, H.M.J., Colwell, J.B., Symonds, P.A., 2007. Nature of the continent-ocean transition zone along the southern Australian continental margin: a comparison of the Naturaliste Plateau, SW Australia, and the central Great Australian Bight sectors. Geol. Soc. Lond. Special Publ. 282, 239–263. https://doi.org/10.1144/sp282.12.

Direen, N.G., Stagg, H.M.J., Symonds, P.A., Norton, I.O., 2013. Variations in rift symmetry: cautionary examples from the Southern Rift System (Australia-Antarctica). Geol. Soc. Lond. Special Publ. 369, 453–475. https://doi.org/10.1144/sp369.4.

D'Souza, R.J., Canil, D., Coogan, L.A., 2019. Geobarometry for spinel peridotites using Ca and Al in olivine. Contrib. Min. Petr. 175, 5. https://doi.org/10.1007/s00410-019-1647-6.

Dygert, N., Liang, Y., 2015. Temperatures and cooling rates recorded in REE in coexisting pyroxenes in ophiolitic and abyssal peridotites. Earth Planet. Sci. Lett. 420, 151–161. https://doi.org/10.1016/j.epsl.2015.02.042.

Ferrari, E., Montanini, A., Tribuzio, R., 2022. Rifting evolution of the lithospheric subcontinental mantle: New insights from the External Ligurian ophiolites (Northern Apennine, Italy). Lithos 410, 106571. https://doi.org/10.1016/j.lithos.2021.106571.

Fumagalli, P., Borghini, G., Rampone, E., Poli, S., 2017. Experimental calibration of Forsterite–Anorthite–Ca-Tschermak–Enstatite (FACE) geobarometer for mantle peridotites. Contrib. Min. Petr. 172, 38. https://doi.org/10.1007/s00410-017-1352-2.

Furnes, H., de Wit, M., Dilek, Y., 2014. Precambrian Greenstone Belts Host Different Ophiolite Types. In: Dilek, Y., Furnes, H. (Eds.), Evolution of Archean Crust and Early Life. Modern Approaches in Solid Earth Sciences, 7. Springer, Dordrecht, pp. 1–22.

Gillard, M., Autin, J., Manatschal, G., Sauter, D., Munschy, M., Schaming, M., 2015. Tectonomagmatic evolution of the final stages of rifting along the deep conjugate Australian-Antarctic magma-poor rifted margins: constraints from seismic observations. Tectonics 34, 753–783. https://doi.org/10.1002/2015tc003850.

Halpin, J.A., Crawford, A.J., Direen, N.G., Coffin, M.F., Forbes, C.J., Borissova, I., 2008. Naturaliste Plateau, offshore Western Australia: a submarine window into Gondwana assembly and breakup. Geology 36, 807–810. https://doi.org/10.1130/g25059a.1.

Hellebrand, E., Snow, J.E., 2003. Deep melting and sodic metasomatism underneath the highly oblique-spreading Lena Trough (Arctic Ocean). Earth Planet Sci. Lett. 216, 283–299. https://doi.org/10.1016/s0012-821x(03)00508-9.

Hellebrand, E., Snow, J.E., Dick, H.J.B., Hofmann, A.W., 2001. Coupled major and trace elements as indicators of the extent of melting in mid-ocean-ridge peridotites. Nature 410, 677–681. https://doi.org/10.1038/35070546.

Hellebrand, E., Snow, J.E., Hoppe, P., Hofmann, A.W., 2002. Garnet-field melting and late-stage refertilization in 'residual' abyssal peridotites from the Central Indian Ridge. J. Petrol. 43, 2305–2338. https://doi.org/10.1093/petrology/43.12.2305.

Herzberg, C.T., 1978. Pyroxene geothermometry and geobarometry: experimental and thermodynamic evaluation of some subsolidus phase relations involving pyroxenes in the system CaO-MgO-Al2O3-SiO2. Geochim. Cosmochim. Acta 42, 945–957. https://doi.org/10.1016/0016-7037(78)90284-3.

Johnson, K.T.M., Dick, H.J.B., Shimizu, N., 1990. Melting in the oceanic upper mantle: an ion microprobe study of diopsides in abyssal peridotites. J. Geophys. Res. Solid Earth 95, 2661–2678. https://doi.org/10.1029/jb095ib03p02661.

Jollands, M.C., Müntener, O., 2019. Testing orthopyroxene diffusion chronometry on rocks from the Lanzo Massif (Italian Alps). J. Geophys. Res.: Solid Earth 124, 7822–7841. https://doi.org/10.1029/2018jb016963.

Kaczmarek, M.-A., Müntener, O., 2008. Juxtaposition of melt impregnation and hightemperature shear zones in the upper mantle; field and petrological constraints from the lanzo peridotite (Northern Italy). J. Pet. 49, 2187–2220. https://doi.org/10.1093/petrology/egn065.

Kaczmarek, M.-A., Müntener, O., 2010. The variability of peridotite composition across a mantle shear zone (Lanzo massif, Italy): interplay of melt focusing and deformation. Contrib. Miner. Pet. 160, 663–679. https://doi.org/10.1007/s00410-010-0500-8.

Laat, J.I.de, Lebedev, S., Celli, N.L., Bonadio, R., Melo, B.C.de, Rawlinson, N., 2023. Structure and evolution of the Australian plate and underlying upper mantle from waveform tomography with massive data sets. Geophys. J. Int. 234, 153–189. https://doi.org/10.1093/gji/ggad062.

Magri, L., Whittaker, J.M., Coffin, M.F., Hochmuth, K., Gürer, D., Williams, S., Bernardel, G., Uenzelmann-Neben, G., 2024. Tectono-stratigraphic evolution of the kerguelen large igneous province: the conjugate William's ridge-broken ridge rifted margins. J. Geophys. Res.: Solid Earth 129 (3), e2023JB027493. https://doi.org/10.1029/2023jb027493.

Maier, S., Spaggiari, B., Kirkland, K., Roberts, M., 2016. The Evolution of Mafic and Ultramafic Rocks of the Mesoproterozoic FraserZone, Albany-Fraser Orogen, and Implications For the Ni-Cu sulphide Potential of the Region.

Manatschal, G., Müntener, O., 2009. A type sequence across an ancient magma-poor ocean–continent transition: the example of the western Alpine Tethys ophiolites. Tectonophysics 473, 4–19. https://doi.org/10.1016/j.tecto.2008.07.021.
McCarthy, A., Müntener, O., 2015. Ancient depletion and mantle heterogeneity: revisiting the Permian-Jurassic paradox of Alpine peridotites. Geology 43, 255–258. https://doi.org/10.1130/g36340.1.
McCarthy, A., Falloon, T.J., Sauermilch, I., Whittaker, J.M., Niida, K., Green, D.H., 2020. Revisiting the Australian-Antarctic ocean-continent transition zone using petrological and geophysical characterization of exhumed subcontinental mantle. Geochem., Geophys., Geosystems 21. https://doi.org/10.1029/2020gc009040.
McDonough, W.F., Sun, S.-s., 1995. The composition of the Earth. Chem. Geol. 120, 223–253. https://doi.org/10.1016/0009-2541(94)00140-4.
Montanini, A., Tribuzio, R., Anczkiewicz, R., 2006. Exhumation history of a garnet pyroxenite-bearing mantle section from a continent–ocean transition (Northern Apennine Ophiolites, Italy). J. Pet. 47, 1943–1971. https://doi.org/10.1093/petrology/egl032.
Munschy, M., 1998. La zone de Diamantine, témoin de la séparation de l'Australie et de l'Antarctique: arguments géophysiques. C. R. l'Acad. Sci. - Ser. IIA - Earth Planet. Sci. 327, 533–540. https://doi.org/10.1016/s1251-8050(99)80035-4.
Müntener, O., Manatschal, G., 2006. High degrees of melt extraction recorded by spinel harzburgite of the Newfoundland margin: the role of inheritance and consequences for the evolution of the southern North Atlantic. Earth Planet Sci. Lett 252, 437–452. https://doi.org/10.1016/j.epsl.2006.10.009.
Müntener, O., Manatschal, G., Desmurs, L., Pettke, T., 2010. Plagioclase peridotites in ocean–continent transitions: refertilized mantle domains generated by melt stagnation in the shallow mantle lithosphere. J. Petrol. 51, 255–294. https://doi.org/10.1093/petrology/egp087.
Müntener, O., Pettke, T., Desmurs, L., Meier, M., Schaltegger, U., 2004. Refertilization of mantle peridotite in embryonic ocean basins: trace element and Nd isotopic evidence and implications for crust–mantle relationships. Earth Planet Sci. Lett. 221, 293–308. https://doi.org/10.1016/s0012-821x(04)00073-1.
Nicholls, I.A., Ferguson, J., Jones, H., Marks, G.P., Mutter, J.C., 1981. Ultramafic blocks from the ocean floor southwest of Australia. Earth Planet Sci. Lett. 56, 362–374. https://doi.org/10.1016/0012-821x(81)90140-0.
Picazo, S., Müntener, O., Manatschal, G., Bauville, A., Karner, G., Johnson, C., 2016. Mapping the nature of mantle domains in Western and Central Europe based on clinopyroxene and spinel chemistry: evidence for mantle modification during an extensional cycle. Lithos 266, 233–263. https://doi.org/10.1016/j.lithos.2016.08.029.
Piccardo, G.B., Padovano, M., Guarnieri, L., 2014. The Ligurian Tethys: mantle processes and geodynamics. Earth-Sci. Rev. 138, 409–434. https://doi.org/10.1016/j.earscirev.2014.07.002.
Piccardo, G.B., Vannucci, R., Guarnieri, L., 2009. Evolution of the lithospheric mantle in an extensional setting: Insights from ophiolitic peridotites. Lithosphere 1, 81–87. https://doi.org/10.1130/l30.1.
Piccardo, G.B., Zanetti, A., Müntener, O., 2007. Melt/peridotite interaction in the Southern Lanzo peridotite: field, textural and geochemical evidence. Lithos 94, 181–209. https://doi.org/10.1016/j.lithos.2006.07.002.
Rampone, E., Borghini, G., 2008. Melt migration and intrusion in the Erro-Tobbio peridotites (Ligurian Alps, Italy): insights on magmatic processes in extending lithospheric mantle. Eur. J. Mineral 20, 573–585. https://doi.org/10.1127/0935-1221/2008/0020-1807.
Rampone, E., Borghini, G., Basch, V., 2020. Melt migration and melt-rock reaction in the Alpine-Apennine peridotites: insights on mantle dynamics in extending lithosphere. Geosci. Front. 11, 151–166. https://doi.org/10.1016/j.gsf.2018.11.001.
Rampone, E., Hofmann, A.W., Piccardo, G.B., Vannucci, R., Bottazzi, P., Ottolini, L., 1995. Petrology, mineral and isotope geochemistry of the external liguride peridotites (Northern Apennines, Italy). J. Petrol. 36, 81–105. https://doi.org/10.1093/petrology/36.1.81.
Rampone, E., Hofmann, A.W., Piccardo, G.B., Vannucci, R., Bottazzi, P., Ottolini, L., 1996. Trace element and isotope geochemistry of depleted peridotites from an N-MORB type ophiolite (Internal Liguride, N. Italy). Contrib. Miner. Pet. 123, 61–76. https://doi.org/10.1007/s004100050143.
Rampone, E., Piccardo, G.B., Vannucci, R., Bottazzi, P., 1997. Chemistry and origin of trapped melts in ophioilitic peridotites. Geochim. Cosmochim. Acta 61, 4557–4569. https://doi.org/10.1016/s0016-7037(97)00260-3.
Rampone, E., Piccardo, G.B., Vannucci, R., Bottazzi, P., Ottolini, L., 1993. Subsolidus reactions monitored by trace element partitioning: the spinel- to plagioclase-facies transition in mantle peridotites. Contrib. Miner. Pet. 115, 1–17. https://doi.org/10.1007/bf00712974.
Reston, T.J., 2009. The structure, evolution and symmetry of the magma-poor rifted margins of the North and Central Atlantic: a synthesis. Tectonophysics 468, 6–27. https://doi.org/10.1016/j.tecto.2008.09.002.
Rotstein, Y., Munschy, M., Bernard, A., 2001. The Kerguelen Province revisited: additional constraints on the early development of the Southeast Indian Ocean. Mar. Geophys. Res. 22, 81–100. https://doi.org/10.1023/a:1010345608833.
Royer, J.-Y, Beslier, M.-O., Hill, P.J., 1998. Rapport De Campagne MD110/MARGAU. Géosciences Azur, p. 113. https://doi.org/10.17600/98200020. Villefranche-sur-Mer.
Sayers, J., Symonds, P.A., Direen, N.G., Bernardel, G., 2001. Nature of the continent-ocean transition on the non-volcanic rifted margin of the central Great Australian Bight. Geol. Soc., Lond., Spéc. Publ 187, 51–76. https://doi.org/10.1144/gsl.sp.2001.187.01.04.
Seyler, M., Bonatti, E., 1997. Regional-scale melt-rock interaction in lherzolitic mantle in the Romanche Fracture Zone (Atlantic Ocean). Earth Planet. Sci. Lett. 146, 273–287. https://doi.org/10.1016/s0012-821x(96)00220-8.
Smye, A., Seman, S., Hudak, M., Crispin, K., 2017. Rates of mantle cooling and exhumation during rifting constrained by REE-in-pyroxene speedometry. Geochem. Geophys. Geosyst. 18, 2510–2525. https://doi.org/10.1002/2017gc006957.
Spaggiari, C.V., Kirkland, C.L., Smithies, R.H., Wingate, M.T.D., Belousova, E.A., 2015. Transformation of an Archean craton margin during Proterozoic basin formation and magmatism: the Albany–Fraser Orogen, Western Australia. Precambrian Res. 266, 440–466. https://doi.org/10.1016/j.precamres.2015.05.036.
Sutra, E., Manatschal, G., Mohn, G., Unternehr, P., 2013. Quantification and restoration of extensional deformation along the Western Iberia and Newfoundland rifted margins. Geochem., Geophys., Geosyst. 14, 2575–2597. https://doi.org/10.1002/ggge.20135.
Tribuzio, R., Garzetti, F., Corfu, F., Tiepolo, M., Renna, M.R., 2016. U–Pb zircon geochronology of the Ligurian ophiolites (Northern Apennine, Italy): implications for continental breakup to slow seafloor spreading. Tectonophysics 666, 220–243. https://doi.org/10.1016/j.tecto.2015.10.024.
Tribuzio, R., Thirlwall, M.F., Vannucci, R., 2004. Origin of the Gabbro–Peridotite association from the Northern Apennine Ophiolites (Italy). J. Pet. 45, 1109–1124. https://doi.org/10.1093/petrology/egh006.
Munschy, M., 1994. Diamantine – MD80 cruise, RV Marion Dufresne, 10.17600/94200040.
Tucholke, B.E., Sibuet, J.-C., Klaus, A., et al., 2004. Proceedings of the ODP, Initial Reports, 210: College Station, TX (Ocean Drilling Program). 10.2973/odp.proc.ir.210.2004.
Ulrich, M., Muñoz, M., Guillot, S., Cathelineau, M., Picard, C., Quesnel, B., Boulvais, P., Couteau, C., 2014. Dissolution–precipitation processes governing the carbonation and silicification of the serpentinite sole of the New Caledonia ophiolite. Contrib. Miner. Pet. 167, 952. https://doi.org/10.1007/s00410-013-0952-8.
Vauchez, A., Tommasi, A., Barruol, G., Maumus, J., 2000. Upper mantle deformation and seismic anisotropy in continental rifts. Phys. Chem. Earth, Part A: Solid Earth Geodesy 25, 111–117. https://doi.org/10.1016/s1464-1895(00)00019-3.
Witt-Eickschen, G., Seck, H.A., 1991. Solubility of Ca and Al in orthopyroxene from spinel peridotite: an improved version of an empirical geothermometer. Contrib. Min. Petr. 106, 431–439. https://doi.org/10.1007/bf00321986.
Workman, R.K., Hart, S.R., 2005. Major and trace element composition of the depleted MORB mantle (DMM). Earth Planet. Sci. Lett. 231, 53–72. https://doi.org/10.1016/j.epsl.2004.12.005.

CHAPITRE 3

Étude des conditions thermo-barométriques des péridotites de la zone Diamantine

Ce troisième chapitre s'intéresse aux conditions de pression et températures auxquelles les péridotites de la zone Diamantine ont été soumises.

La formation d'une marge passive traduit le passage d'une zone continentale froide dominée par les processus tectoniques à un système d'accrétion océanique, dominé par les processus magmatiques et caractérisé par une anomalie thermique importante. Le but de cette étude est notamment d'identifier les conditions thermo-barométriques des deux types mantelliques mis en évidence dans le chapitre 2 (sous-continental et refertilisés), afin d'identifier les conséquences de la refertilisation et de préciser le rôle de l'héritage mantellique.

Ce chapitre est présenté sous la forme d'un article en préparation pour une soumission à la revue *Geology*.

PROBING THE THERMAL REGIME OF THE MANTLE DURING LITHOSPHERIC BREAK-UP

INTRODUCTION

Lithospheric break-up constitutes a transition from rifting to a steady state seafloor spreading regime, and such a transition from inherited subcontinental to oceanic mantle domains is intimately linked to mantle-melt interactions and evolution of the mantle thermal state along the margin. While this transition seems fast and focused on the case of volcanic rifted margins, it is more complex and transitional in the case of magma-poor rifted margins, which are characterized by the lack of magmatism and exhumation of mantle rocks along the seafloor. Direct access to samples from the Western Tethys and Iberia margins allowed to propose a general model with 3 mantle domains:

- The mantle type 1, inherited, equilibrated sub-continental mantle.
- The mantle type 3, asthenospheric mantle which produce the oceanic crust.
- The mantle type 2, between the two aforementioned domains, which undergoes mantle melt interaction.

However, relatively little is known about the thermal regime recorded in these rocks during breakup, its impact on its magma budget, and what PT paths these mantle rocks follow during exhumation? While some data exist from the Western Tethys/Iberia domain, virtually no data exist yet from other magma-poor rifted margins. Here we present new data from the southwestern Australian margin and compare this data with existing data with the aim to establish the thermal regime of the lithospheric mantle during breakup.

1. The Diamantina zone peridotites

Our case study, the south-west Australian passive margin, is a magma-poor rifted margin composed mainly of two mantle domains which do not operate in the same way along the margin. The more proximal domain is characterized by an inherited Mesoproterozoic subcontinental mantle, revealed by the presence of spl-lherzolite. The second, refertilized domain is characterized by the presence of pl-lherzolite and marks the transition to the future oceanic accretionary regime controlled by magma production. This study focuses on spinel lherzolites (spl-lherzolites) and plagioclase lherzolites (pl-lherzolites), which were selected according to their serpentinization rate in order to build up a consistent and representative database from the 4 dredging points of the MD80 (dredging point MD80-DR3) and MD110 (dredging point MD110-DR02, MD110-DR06 and MD110-DR09) oceanographic campaigns (Fig. 1). All the analytical methods details and chemical compositions results can be found in the supplementary files.

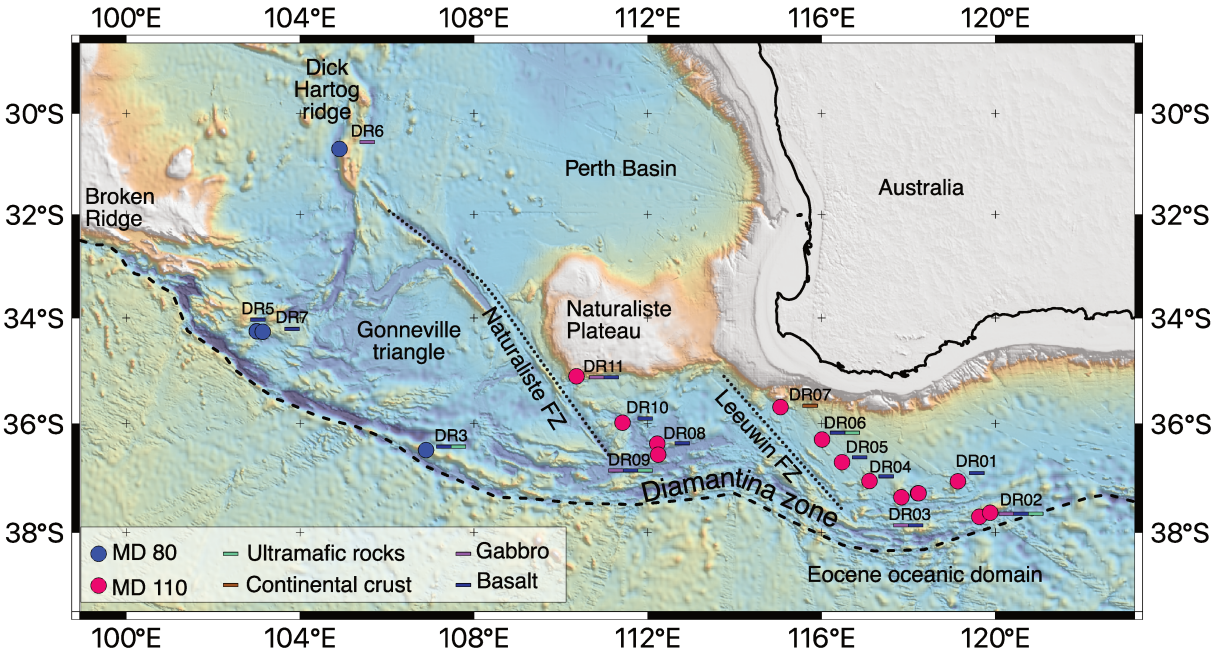


Fig.III-1 *- Bathymetric map of the Diamantina zone, South-East Indian Ocean. Colored dots indicate the location of MD80 and MD110 dredges and the lithologies of dredged samples (Chatin et al, 1998; Beslier et al, 2004) whose DR02, DR06, DR09 and DR3 correspond to the dredged points of the samples used in this study.*

2. Two-pyroxenes thermo-barometry and speedometry

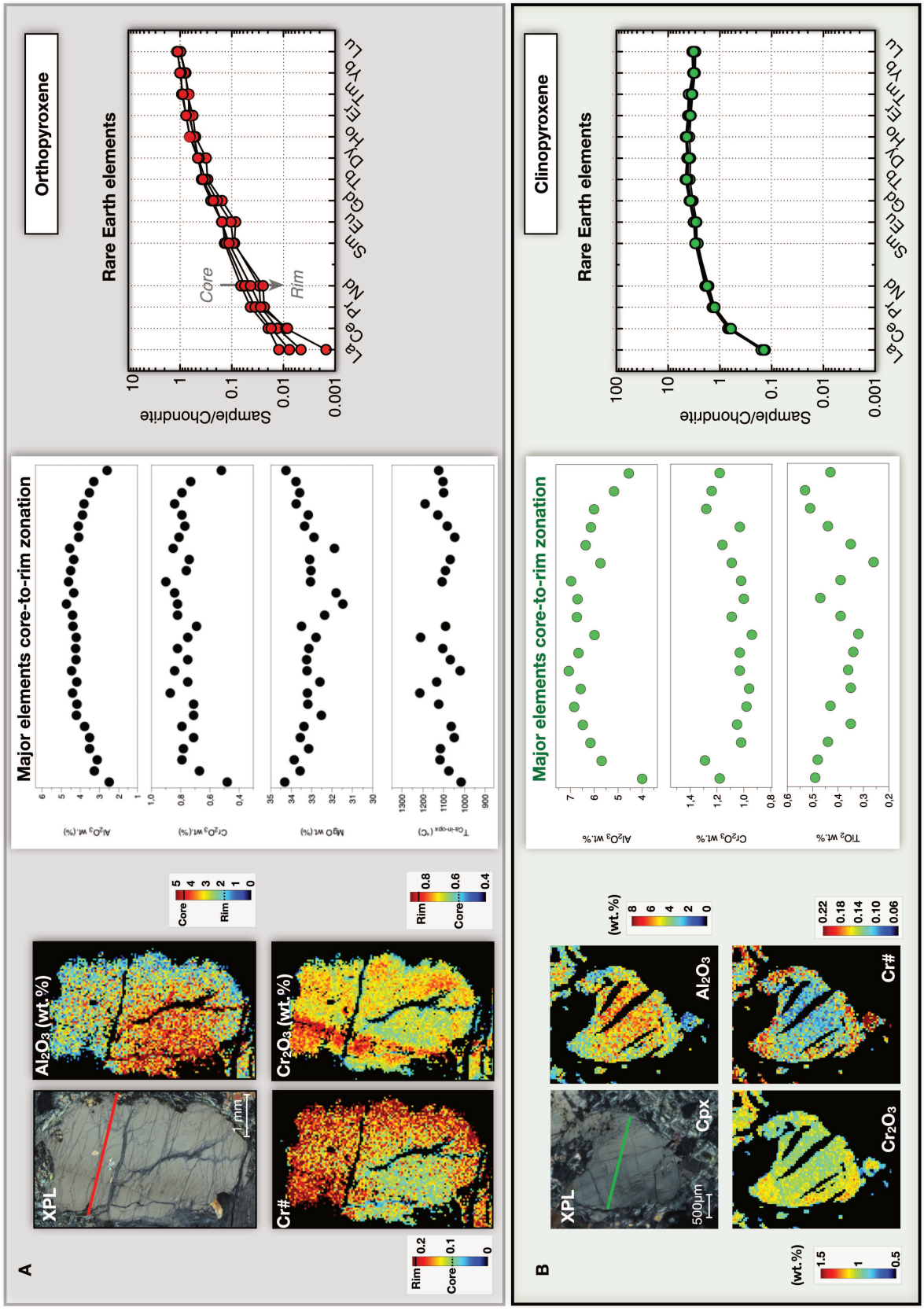
2.1. In-situ chemistry

In this study we focus on Sp-lherzolite for the dredged points DR02, DR09 and MD80-DR3 and Pl-lherzolite from the dredged point DR06 (Fig. 1). In Sp-lherzolite, only spinel, orthopyroxene, and relicts of clinopyroxene were found while olivine and plagioclase could be found preserved in pl-lherzolite. All the clinopyroxenes and orthopyroxenes presented in this study have a composition corresponding to diopside and enstatite respectively, but their composition varies depending on the host rock (See supplementary materials for further information).

While no significant zonation in major or trace elements in clinopyroxene's or orthopyroxene's Sp-lherzolites are apparent, the porphyroclast in Pl-lherzolite exhibits pronounced core-to-rim zonation (Fig. 2). In orthopyroxene porphyroclast from pl-lherzolite we observe significant differences between the rims and cores, reflecting the diffusion of elements. Zonation is particularly high in Al_2O_3, Cr_2O_3 and CaO, with higher contents in the core. On the other hand, MgO is higher at the rim and lower in the core. In the orthopyroxenes from pl-lherzolites, we observe slight but remarkable differences between the LREE content of the core and the rim, so a zonation with high values at the core decreasing to the rim.

These differences are also observed within the clinopyroxene porphyroclast with higher Al_2O_3 at the core (up to 8 wt.%) and lower at the rim (3 wt.%) and reversed zoning in Cr_2O_3 (high values at the rim, up to 1.9 wt.%). Neoblast (interstitial clinopyroxene linked to the percolating melt) show similar chemistry to the rim of porphyroclast, according that the zonation is linked to interaction with the percolating melt. Concerning trace elements, the clinopyroxenes of pl-lherzolites with an interstitial texture (neoblasts) show higher enrichment in REE contents than porphyroclastic clinopyroxenes.

Fig. III-2 – *Core-to-rim zonation in orthopyroxene (a) and clinopyroxene (b) in pl-lherzolites (MD110-DR06-161C).*



2.2. Thermometry and barometry

In order to estimate the equilibrium temperature and pressure for Sp- and Pl-lherzolite, mineral compositions were used to calculate several geothermo-barometers. Considering thermometry, we use the classical Ca-in-orthopyroxene ($T_{Ca\text{-}in\text{-}opx}$) and 2 pyroxenes ($T_{BKN}$; Brey & Köhler, 1990) thermometers, additionally to the REE-Y 2 pyroxenes thermometer (T_{REE}; (Liang et al.,2013)) in all the samples.

So far, the only barometer available for spinel peridotite uses calcium concentration in olivine (D'Souza et al., 2019). However, no olivine was preserved in Sp-lherzolite, so a pressure of 15 kbars was assumed for temperature calculation, in accordance with the pressure equilibrium of spinel phases in peridotites. Thus, a temperature of T_{BKN}~940°C was obtained in Sp-lherzolite from DR02, DR09 and MD80-DR3 (944±53°C, 943±85°C and 944±28°C respectively) (Fig. 3). Slightly higher temperatures were calculated using $T_{Ca\text{-}in\text{-}opx}$ (1230±87°C and 1139±127°C, 1238±124°C respectively). Considering the T_{REE} thermometer, based on the trace elements partitioning between clinopyroxene and orthopyroxene, a temperature of 959±90°C for Sp-lherzolite from the DR02 dredge points were calculate, 1007±72°C for those of DR09 and 917±20°C for the Sp-lherzolite from MD80-DR3 (Fig. 3).

Considering Pl-lherzolite, we combined thermometers with the four phases FACE barometer (Fumagalli et al., 2017) and the anorthite-based barometer {Borghini.2010, Borghini et al., 2011}. For the anorthite barometer, only two samples could be carried out because of the lack of preserved plagioclase in the others pl-lherzolites. The results of these barometer show a pressure of 6.64±0.7 kbars, consistent with an equilibration in the plagioclase stability field. The FACE barometer (Fumagalli et al., 2017) was applied in a single sample (MD110-DR06-162B) since it was the only one containing the 4 minerals required for its application and give a pressure of 6.85 kbars, consistent with the anorthite barometer. We also use a pressure of 7 kbars to compute the following thermometers.

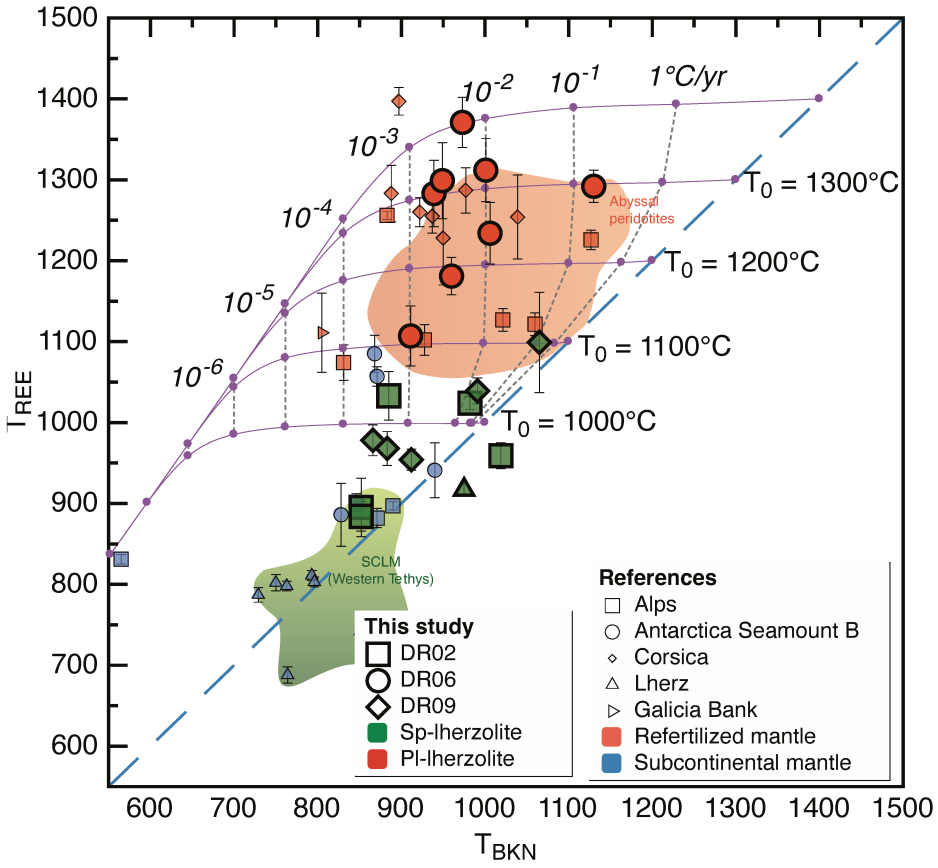


Fig.III-3 – *Thermal evolution and speedometry of SCLM and refertilized peridotites. T_{BKN} is the Cpx-Opx thermometer of Brey and Köhler, 1990; T_{REE} is the Cpx-Opx thermometer of Liang et al., 2013. Models are calculated for a sphere with a 5 mm effective radius at a range of cooling rates (10^{-9} < dT/dt < 1°C/yr, Dodson, 1973; Ganguly and Tirone, 1999, Dygert and Liang, 2015). Data from the Alps (Platta, Müntener et al., 2010; Lanzo, Smye et al., 2017), Antarctica (McCarthy et al., 2020), Corsica (Rampone et al., 2008), Lherz (Riches and Rogers, 2011), Galicia Bank (Chazot et al., 2005).*

The mantle type 2, characterized by the samples of the MD110-DR06 dredge point, show similar temperature compared to sp-lherzolite for thermometers based on major elements (T_{BKN} of 1013±46°C and $T_{Ca\text{-}in\text{-}opx}$=1178±54°C) but higher temperature for the thermometers based on trace elements composition (T_{REE} = 1268°C±83°) (Fig. 3). The Sp-Ol thermometer and Al-Ca in olivine thermometer cannot be used in these samples because they are based on Sp-Ol partitioning which aren't in equilibrium in pl-lherzolite.

3. DISCUSSION

3.1. Zonation – chemical mapping of the refertilisation

Orthopyroxene and clinopyroxene exhibits chemical zonation in pl-lherzolites (Fig. 2). Although core-rim zonation may be the consequence during exhumation of the transition from the spinel stability field to the plagioclase stability field (Kaczmarek & Müntener, 2008; Witt-Eickschen & Seck, 1991), several parameters show that they could be here interpreted as an evidence of mantle refertilization by percolating melts (Rampone et al., 1997; Seyler & Bonatti, 1997; Kaczmarek & Müntener, 2008; Jollands & Müntener, 2019). In a first order, the difference between Cr# of clinopyroxene and Cr# of spinels (Ballay et al, in review) or the presence of cpx neoblast and associated pl-cpx neoblast also claim to a melt-rock interaction, instead plagioclase formed by subsolidus reequilibration (Müntener & Manatschal, 2006). More precisely, we can see on the chemical maps, that the zonation in porphyroclast is linked with the proximity to neoblast (Fig. 2). Moreover, this zonation is particularly marked in aluminum, a chemical element trapped by neoformed plagioclase. They are also visible in trace elements. Since the neoblast record the melt flow area, it suggests that these core-to-rim zonation are a direct consequence of melt-rock interaction.

3.2. Temperature evolution during refertilisation

The thermometers calculations were performed on pl- and sp-lherzolite. T_{BKN} show a similar temperature in sp-lherzolite and pl-lherzolite, in good accordance with the proposition that they are from a common origin in the continental lithosphere. While the sp-lherzolite show similar results with thermometers based on major and trace elements, T_{BKN} and T_{REE} on pl-lherzolites are significantly different (T_{BKN} = 1013°C±46°; T_{REE} = 1268°C±83°) with ΔT = 255°C, referring a chemical disequilibrium consequently of the refertilisation. Indeed, the refertilisation implies melt-rock interactions with chemical exchanges between the melts and the country peridotite. These exchanges are particularly high in trace elements, which explains that we have different T_{REE} temperatures but similar T_{BKN} temperatures. This thermal difference also shows a reopening of the system from its sub-continental origins, during which trace and major elements do not behave in the same way towards the mineral, due to

different partition coefficients and different concentrations between the mineral and the percolating melt.

3.3. Mantle types 1 and 2 follow different P-T paths

The opening of the system, imaged by the zonation showing a disequilibrium in the refertilized samples, clearly demonstrate that the refertilized and non-refertilized domains do not follow the same pressure-temperature paths. Sp-lherzolite, characteristics of a T1a inherited mantle type, follow a fast exhumation path through the spinel and plagioclase stability field, without ever reaching temperatures allowing partial melting or even the transition from spinel to plagioclase during the final rifting (Fig. 4). On the other hand, pl-lherzolite are characterized by similar T_{BKN} temperature, inherited from subcontinental mantle, while T_{REE} is significantly higher, recording melt-percolation. This suggests that the P-T path followed by these rocks underwent a significant temperature rise during the retrograde path, i.e. during exhumation. The cooling rates followed by these peridotites (10^{-2}°C/year to 10^{-3}°C/year; Fig. 4) show that post-refertilization cooling is intermediate between typical oceanic lower crustal lithosphere dominated by conductive cooling and lithospheric hydrothermal-assisted cooling (Coogan et al., 2002; Dygert et al., 2015, 2017; VanTongeren et al., 2008). During ocean opening, there is a balance between cooling on the one hand, brought about by exhumation processes, and heating on the other, linked to the presence of magma. Thus, type T1a mantle, characterized by sp-lherzolite, suggests essentially tectonic cooling, while type 2 mantle traces a hot magmatic event, i.e. magma-induced cooling.

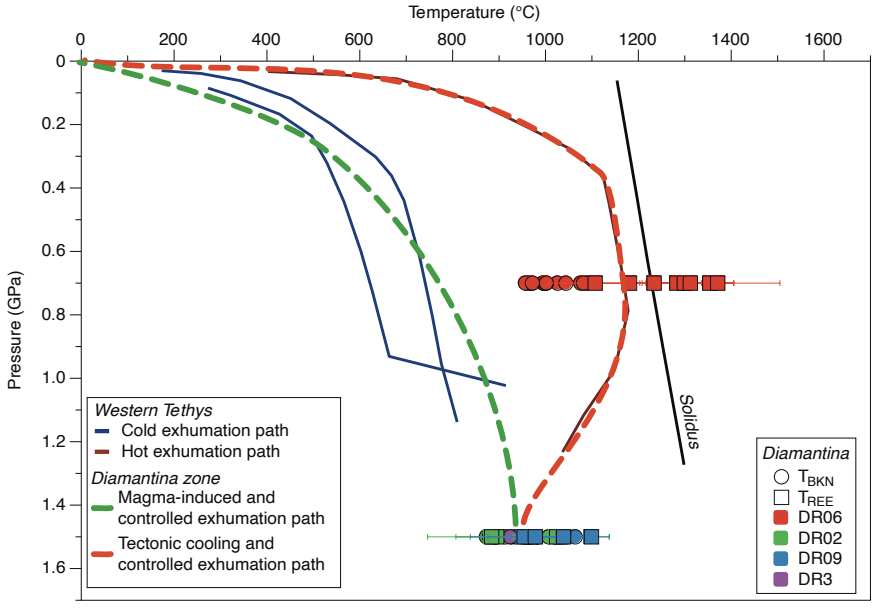


Fig.III-4 – *P-T paths followed by Sp- and Pl-lherzolites. Hot exhumation path from the Northern External Ligurides Units (Montanini et al., 2006), cold and hot exhumation paths from the Western Tethys (Müntener et al, 2010).*

3.4. Comparison with the other margins: the refertilisation erase mantle inheritance thermicity

Samples of the T1a mantle type in the Diamantina zone show higher temperature than inherited peridotites from the European domains while refertilized samples show exactly the same range of temperatures. The initial stage, i.e. the inherited subcontinental mantle, is of a Proterozoic age in the Diamantina zone, according to several arguments which may explain the high equilibrium temperatures. Indeed, the adjacent sub-continental mantle is thick and of a Meso-Proterozoic age (Maier et al, 2016; Laat et al., 2023) and the modal composition of the pl-lherzolites dredge in the Diamantine zone combined to Mg# in olivine suggest a Proterozoic origin too (see supplementary materials). Although the inheritance in the Iberia margin or in the Western Tethys zone is more recent, the temperatures recorded by the refertilized lherzolites are similar (Fig. 3). This indicates that the initial difference in terms of thermicity due to the inheritance is completely erased by the refertilisation which is common in all magma-poor rifted margins. Although this may seem anecdotal, it has huge implications for understanding the development of the oceanic accretionary zone in the sense that if one wants to understand inheritance, it is necessary and important to focus on the non-refertilized zones, where type 1 mantle is exhumed and preserved. Moreover, the temperatures recorded by the minerals in pl-lherzolites are similar, as are the cooling rates followed by the rocks after refertilization, although the initial stage, in terms of age, temperature or lithospheric thickness, was not the same. Thus, this is proposing major implications for the involvement of magma in the development of exhumation structures during the formation of an oceanic accretionary zone. Indeed, the fact that the inherited depleted peridotites follow the same cooling rates and skim the solidus without ever crossing it, could be the reason for a limited magmatic budget (Smye et al., 2017).

CONCLUSION

The study of peridotites from the Diamantina zone show 2 mantle domains with 2 thermal regimes: T1a, inherited, show similar T_{REE} and T_{BKN}; T2, with high T_{REE} values showing a disequilibrium due to the mantle-melt interaction. The different thermal regime in T1a (spl-lherzolites) and T2 (pl-lherzolites) is linked to the passage or not of a magmatic liquid percolating through the rocks and could be interpreted in terms of different exhumation paths where cooling is not due to the same processes (tectonic cooling versus magma induced and controlled paths). The refertilized samples registers similar system closure temperatures, regardless of inheritance while the inherited samples of the Diamantina zone show high temperature, due to older inheritance. Also, refertilization processes erase the thermal mantle's heritage. The implications of this work are multiple, but above all opens new doors concerning the dynamic modeling of the final phases of breakup, where questions of magmatic budget and the effect of magmatism on margin tectonics are issues of prime importance at present.

CHAPITRE 4

Étude des produits magmatiques de la zone Diamantine

Ce quatrième chapitre concerne l'étude des produits magmatiques dragués le long de la zone Diamantine.

La finalisation des processus d'océanisation se caractérise par l'apparition de la première proto-croûte océanique et pose ainsi la question de l'origine des premiers basaltes océaniques au cours du processus de rifting. La localisation très particulière de la marge passive pauvre en magma sud-ouest australienne, liée à l'ouverture de l'Océan Sud-est Indien séparant l'Australie de l'Antarctique, mais également très proche de plateaux océaniques (Kerguelen, Broken Ridge, 90°E Ridge, Plateau Naturaliste) propose une certaine complexité et une incertitude sur la source des basaltes produits.

Des analyses en éléments majeurs, traces et isotopiques, ont pu être faites sur de nombreux points de dragage des campagnes MD80 et MD110, permettant ainsi de quadriller la zone de transition océan-continent.

L'ensemble de ce chapitre, présenté sous la forme d'un article en préparation qui sera soumis à la revue « Geochemistry, Geophysics, Geosystems », est d'effectuer une première caractérisation de ces basaltes et d'en identifier la source, dans le cadre de l'ouverture océanique.

Multicomponent magmatic activity recorded in the basalts of the Diamantina zone

Ballay Mélanie[1], Ulrich Marc[1], Manatschal Gianreto[1], Patten Clifford[2], Peillod Alexandre[3], Aratz Beranoaguirre[4], Garçon Marion[5], Suire Harmony[1], Kuznir Nick[6]

[1] Institut Terre et Environnement de Strasbourg-EOST, CNRS-UMR 7063, Université de Strasbourg, 5 Rue René Descartes, 67084 Strasbourg, France

[2] Institute of Mineralogy and Petrography, University of Innsbruck, Innrain 52, A-6020 Innsbruck, Austria

[3] Chair of Geochemistry and Economic Geology, Karlsruher Institut für Technologie, KIT, Campus Süd, Adenauerring 20b, Gebäude 50.40, 76131 Karlsruhe, Germany

[4] FIERCE (Frankfurt Isotope & Element Research Center), Goethe University Frankfurt am Main, Altenhöferallee 1, 60438 Frankfurt am Main, Germany

[5]Laboratoire Magma et volcans, Campus Universitaire des Cézeaux, 6 Avenue Blaise Pascal, 63170 Aubière, France

[6] Earth, Ocean and Ecological Sciences, School of Environmental Sciences, University of Liverpool, Jane Herdman Building, Liverpool, L69 3GP, United Kingdom

Keywords: basalt, lithospheric break up, magma-poor rifted margin, Kerguelen mantle plume, Indian ocean.

INTRODUCTION

The onset of magma production due to rifting and decompression and/or hot spot activity is undeniably a key process in the formation of an oceanic accretionary system. It marks the transition from a cold and thick continental lithosphere to a hot and thin oceanic lithosphere. While the mantle-melt processes involving magma-production and their link to advection, convection and spreading rates are relatively well-understood at MORs, they are yet little constrained at systems linked to break-up recorded in Ocean-Continent Transitions (OCT), discussed in this study. In addition to the understanding of the processes and their interaction during breakup, the nature of the involved subcontinental mantle has to be considered. It is inevitably inherited from its previous dynamic history, which results in an additional complexity. Thus, while the basalt chemistry at MORs reflects the parameters of emplacement mainly controlled by spreading rates, the basalt chemistry at OCTs is more difficult to interpret, even more if break-up occurred in the presence of a hot spot. Here we investigate, samples dredged from the southwestern Australia Diamantina Zone, which is among a handful of sites where such rare samples have been sampled.

The origin of the southwestern Australian margin is complex, and its geodynamic evolution remains debated. Several sources (Kerguelen plume, inherited subcontinental or depleted asthenosphere mantle) and processes (decompression, plume) can be at the origin of the basalts dredged along the magma-poor southwestern Australia OCT. Previous studies describe magmatic products attributed to the Kerguelen plume to occur over a wide area including the Kerguelen Plateau, Broken Ridge, Ninety-East Ridge, Bunbury basalts, Naturaliste Plateau (Fig. 1) and emplaced from 130 Ma onwards (Weis et al. 1993; Coffin et al., 2002; Duncan, 2002; Ingle et al., 2002; Neal et al., 2002; Direen et al., 2017; Magri et al., 2024). The magmatic products of the Diamantine Zone, located east of Broken Ridge/Kerguelen Plateau and documenting a long-lasting rift evolution giving rise to the formation of the South-East Indian Ridge (Fig. 2), have been yet little studied. At present, their origin as either hotspot and/or as break-up related decompression magmatism is not identified yet. Moreover, the temporal and spatial relationships between rifting and mantle plume remains yet little constrained as well as their control on the development of the OCT between Australia and Antarctica documented in our samples from the Diamantina Zone. Previous studies (Coffin et al., 2002) suggested alternating phases of plume-activity and rifting

events, i.e., polyphase rifting and magmatic events, which add additional complexity to the study of the magmatic processes.

The aim of this study is to determine the origin of the basalts extruded along the Diamantina zone. The formation of an OCT often shows an alternation in the nature of the magmas, which has been described from both Iberia (Jagoutz et al., 2007) and the fossil margins of the Alpine Tethys exposed in the Alps of Western Europe (Amann et al., 2019). However, the presence of the nearby Kerguelen hotspot may also be at the origin of magmatic products. Thus, the main question addressed in this study is to unravel how hot spot and mid-oceanic ridge can interact in the context of an OCT, resulting here in a magma-starved break-up. In this study we present new data on basalts dredged from the Diamantina Zone, located between the magma-poor southwestern Australian passive margin and the Kerguelen/Broken Ridge hot spot.

1. GEOLOGICAL SETTING

The evolution of the southeast Indian oceanic realm is complex, including, since 130 Ma, periods of intense hot-spot activity (Coffin et al., 2002; Duncan, 2002) that alternate with ridge accretion and mantle exhumation responsible for the formation of new oceanic lithosphere (Pyle et al., 1995; Direen et al., 2011). This study focuses on samples dredged from the southeast Indian Ocean (Fig. 1a; Munschy, 1994; Royer and Beslier, 1998). They are located between longitude 103°E and 120°E, i.e. from the easter part of the Broken Ridge to the Diamantina zone and between latitude 30°S and 38°S, i.e. from the Dick Hartdog Ridge to the Eocene oceanic domain formed by the Southeast Indian Ridge. The vicinity of the Kerguelen plume with its long-lasting magmatic activity (Coffin et al., 2002; Olierook et al., 2016; Magri et al., 2024) raise the question about its role during rifting and breakup along the Diamantina zone.

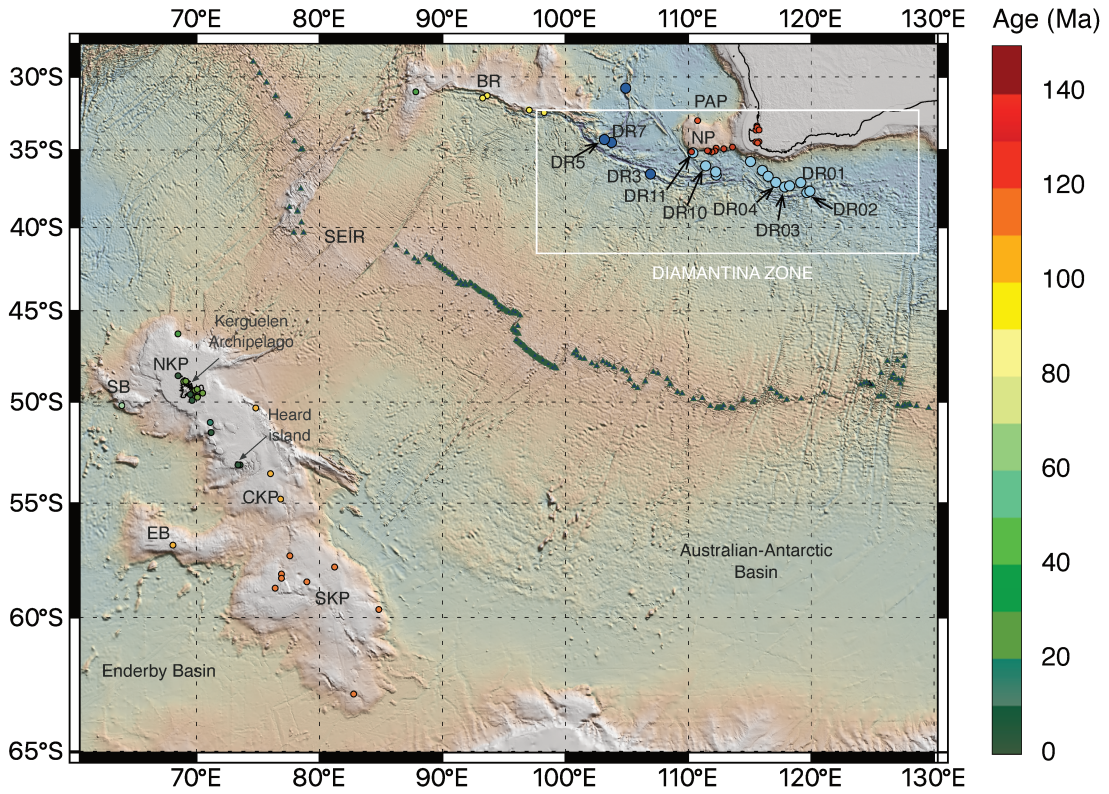


Fig. IV-1a - *Global map of the Southeast Indian Ocean. BR: Broken Ridge; EB: Elan Bank; CKP: Central Kerguelen Plateau; NP: Naturalist Plateau; NKP: Northern Kerguelen Plateau; PAP: Perth Abyssal Plain; SEIR: Southeast Indian Ridge; SKP: Southern Kerguelen Plateau. Age of references are as the color scale bar (Olierook et al., 2017 and references therein). This study: MD80 in large blue circles, MD110 in large light blue circles; no ages determination.*

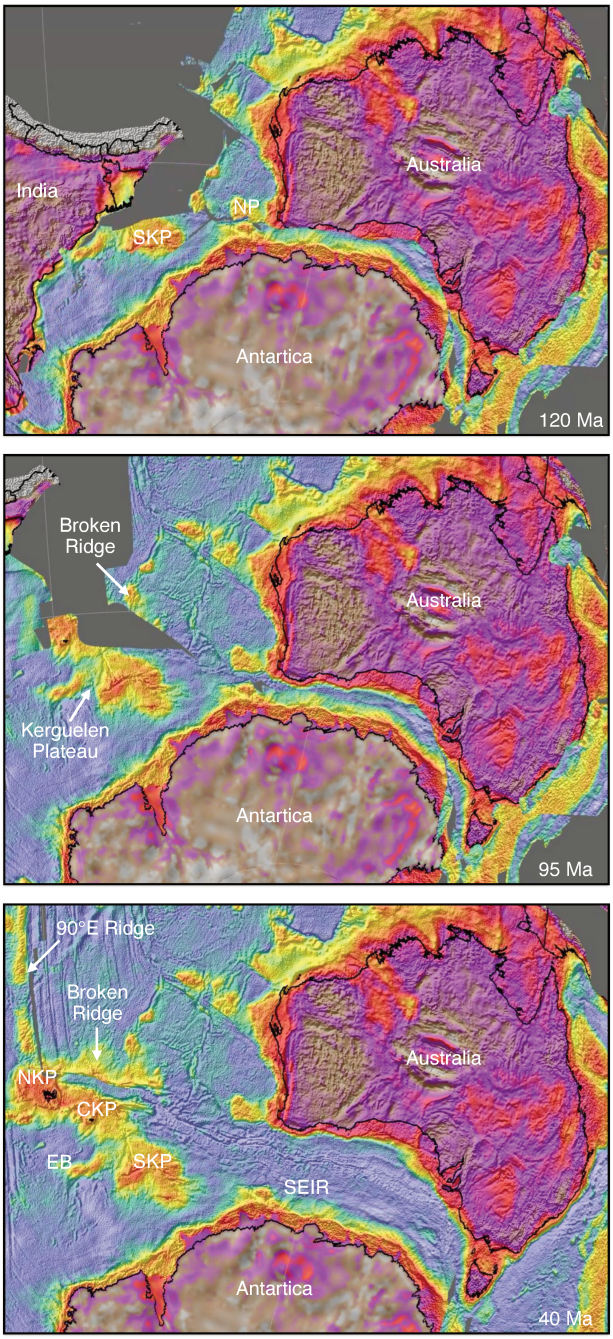


Fig. IV-1b - *Cinematic reconstruction at 120 Ma, 95 Ma and 40 Ma (Crustal thickness - GPlate2, Müller et al., 2019).*

The rift evolution along the Diamantina zone is complex and still debated as well as the link between the Kerguelen mantle plume and continental break up. Rifting between Australia and Antarctica is assumed to begin during the Callovian (Totterdell et al., 2000; Maritati et al., 2021) with the formation of distributed half grabens. Although the occurrence of exhumed mantle is well constrained, its age is much less. It is generally assumed that it occurred from 95 to 83 Ma (Sayer et al., 2001) and even up to 45 Ma (White et al., 2013). Onset of the

Kerguelen mantle plume is also ill defined, however, the emplacement of the first magmas related to the plume are generally assumed to occur around 130 Ma (Frey et al., 2000; Wallace et al., 2002; Coffin et al., 2002). Thus, the Kerguelen hotspot may have formed after onset of rifting between Australia and Antarctica and has been divided into several periods interspersed with periods of inactivity (Coffin et al., 2002). Most of these magmatic products are located above a zone of oceanic lithosphere, which is consistent with an independent rifting period that precedes the first activity of the Kerguelen hotspot. The isotopic source of the Kerguelen hotspot appears to be homogeneous but composed of two major phases: a pre-Miocene phase and a post-Miocene phase, undoubtably linked to its current intra-plate character or to interactions with depleted reservoirs in its early stages (Mattieli et al., 2002). A second rifting period affected the Kerguelen plateau itself, which was initially associated with Broken Ridge, resulting in the actual magma-poor rifted William's Ridge-Broken Ridge conjugate margins (Magri et al., 2024). The South-East Indian Ocean thus shows several alternating phases of rifting and intense hotspot activity. The formation of the first oceanic crust on the Diamantina zone is known to take place during the Cretaceous (Fig. 1b), so-called the magnetic quiet zone, and thus the age of the first oceanic crust between Australia and Antarctica is still unclear, although several studies suggest an age of ~95 Ma (Veevers et al., 1986; Chatin et al., 1998; Tikku and Cande, 1999). Some recent studies even suggest an earlier age for the first basalts leading to the Gondwana break-up (Magri et al., 2024; Olierook et al., 2019), up to 147Ma (Olierook et al., 2019).

This first order reconstruction of Gondwana break-up to the setting up of the Southeast Indian Ridge (SEIR) includes a lot of unknowns, especially the timing and the position of the first basalts leading to the break-up. About the first rifting period, it is well known that it took place, but the timing, the velocity, which types of magmatic rocks were produced, or the origin of this movement remains debated. The MD110 rocks are located in this area, but no age has been determined in the literature yet. Some recent studies on basalts of the Bunbury area (Fig. 1a; on continental Australia near the Naturaliste Plateau), shown that magmatism associated to Gondwana break-up was setting up between 147 and 124 Ma without excess of oceanic magmatism (Olierook et al., 2019). Other recent studies suggest that this zone formed during Late Jurassic/Early Cretaceous rifting resulted in mantle exhumation and early seafloor spreading that eventually failed (Gillard et al., 2015). Some spreading is already recorded at

the west of the Naturaliste Plateau, between 126 and 124 Ma (Harry et al., 2020). Overall, the main consequence is an advancement of the previous mentioned 95 Ma of formation of the first basalts associated with the Gondwana break-up to an older age. Finally, an age of 112 to 119 Ma was measured on basalts from the Southern Kerguelen Plateau (Coffin et al. 2002) near the Labuan Basin estimated to be setting up before 118 Ma (Rotstein et al., 2001) which is known to be the conjugate of the Diamantina zone (Munschy, 1998; Beslier et al., 2004; Magri et al., 2024). If we focus a little more on the western part of the Diamantina zone where MD80 samples were dredged, wedged between the end of Broken Ridge and the Kerguelen Plateau, again the post 45 Ma history is well described but little is known about the much older first stages. However, an $^{40}Ar/^{39}Ar$ age on plagioclase and bulk rock of 93 ± 4 Ma on a basalt from the MD80-DR7 dredge point was measured (Chatin et al., 1998). This age is consistent with other ages of c. 95 Ma on the east of Broken Ridge (Neal et al., 2002). The emplacement of these basalts marks the end of a first phase of Kerguelen plume activity (c. 120-95 Ma, Coffin et al., 2002) that formed Broken Ridge and the South-Central part of the Kerguelen Plateau (Fig. 1a and 1b). Although the 120-95 Ma period is well established (Kerguelen/Broken Ridge), earlier magmatic activities (e.g. Bunburry basalts, Comei Province, Wallaby Plateau) could be associated with the Kerguelen hotspot (Harry et al., 2020), but alternative studies (Olierook et al., 2017; 2019) proposed that some of this volcanism could also be associated with the rifting between Australia and Antarctica, without any involvement of the Kerguelen hotspot. Discussions are ongoing as to the thermal involvement of the plume, which would have led to the partial melting of mantle rocks present beneath the concerned zone (Olierook et al. 2019).

Based on new petrological; major and trace elements; and isotopic chemistry, we document for the first time a set of mafic samples that were dredged at the seafloor of the Diamantina zone. The way here is to show that the basalts of MD80 and MD110 oceanic campaign are heterogeneous, as well as all the basalts from the passive margins of the Southeast Indian Ocean, due to several sources caused by inheritance and mantle activity, in the way of all the other studies on magma-poor passive margins (Desmurs et al., 2002; Saccani et al., 2015; Amann et al., 2020). We show here that a great part of the samples is linked to the magmatic provinces of circum-eastern Gondwana (Bunburry + Comei + Wallaby + Rajmahal-Bengal-sylhet; Olierook et al., 2017), whose source is not only the Kerguelen hot spot but a mixed source between a lithospheric mantle and an impoverished asthenospheric

mantle. Indeed, the study of passive margin basalts, although essentially on terranes of the present-day European zone (Western Tethys, Iberia/Newfoundland), have shown that they belong to a different category from oceanic rift basalts (MORBs) with quite distinct geochemical characteristics, linked to their formation and emplacement conditions (Amann et al., 2020). Several sources have been identified, demonstrating the mantle heterogeneity that can give rise to the formation of the first rifted margin basalts.

2. SAMPLE AND ANALYTICAL METHODS

2.1. Origin of samples and localization along the Diamantina zone

The samples presented in this study were collected during the two successive MD80 and MD110 oceanic cruises in the 90's, both operated by the Marion Dufresne research vessel (Munschy et al., 1994; Royer et al., 1998). The aims were to constrain the mechanisms of crustal thinning and lithospheric break-up and to explore when and how this break-up occurred. While numerous publications exist on the geophysical data sampled during the two cruises (e.g., Bernard et al., 2005; Direen et al., 2007; Halpin et al., 2008; Magri et al., 2024; Rotstein et al., 2001) only a few papers documented the dredged samples (Beslier et al., 2004; Chatin et al., 1998, Ballay et al., in review). A total of 199 samples were recovered from 5 dredges during the MD80 cruise, and 342 samples from 11 dredges during the MD110 cruise, covering a wide area along the Diamantina zone (Fig. 1). The dredged samples include ultramafic rocks (peridotites, pyroxenites), gabbros, basalts, diorites, granites, metamorphic rocks (metasediments, gneiss, amphibolite), sediments, breccias and polymetallic nodules. Here, we focus on dredged sites where mafic rocks were collected, i.e., DR03, DR05-DR07 from MD80 cruise and DR01, DR02, DR03, DR04, DR08, DR09, DR10 and DR11 sites from MD110 cruise.

2.2. Whole rock composition

2.2.1. Major element concentrations

Whole rock major element concentrations were measured on a micro-X-Ray Fluorescence (μ-XRF) Bruker M4 Tornado at Institut Terre et Environnement de Strasbourg (ITES, France). Before the analysis, the whole rock samples were milled with a disk mill and

nanomilled in an agate mill. Then, their loss on ignition (LOI) was determined by heating the sample to 1000 °C for 3h. Finally, pressed powder pellets were made using a 10-ton press. For each sample, 10 measurements were performed at random location on each pellet to ensure the reproducibility at the pellet surface. A collimated Rh source operating at 700 µA with an accelerating voltage of 50 kV was used, resulting in a 1-mm spot-size in diameter at the sample surface. Two energy-dispersive silicon drift detectors of 125 eV resolution, and with an active area of 60 mm^2 each were used to measure fluorescence spectra (300 s counting time per spectrum). Measurements were performed in a vacuum chamber at 2 mbar to minimize air absorption and ensure the best signal/noise ratio. µ-XRF spectra were deconvoluted using the Bruker Esprit software, which allowed to calculate the concentrations by using the standardless Fundamental Parameter (FP) quantification method.

2.2.2. Trace element concentration

Whole rock trace element concentrations were measured on pressed powder pellets (see Patten et al., 2023) at the Karlsruhe Institute of Technology (Germany). Analysis was performed on a Teledyne 193 nm Excimer Laser coupled to an ICP-MS (Element XR ThermoFisher) by laser ablation-inductively coupled plasma-mass spectrometry with the following parameters: diameter of ablation crater of 85 µm; pulse rate of 10 Hz, fluence of 5 $J \cdot cm^{-2}$; and He, Ar, and N flow of 0.3 $L \cdot min^{-1}$, 0.85 $L \cdot min^{-1}$, and 10 $mL \cdot min^{-1}$, respectively. A total of 5 points were analyzed on each sample and a total of 10 points on each standard. Calibration and data quality were performed using the standards BCR-2, BHVO-1, BHVO-2, and BIR-1. Data reduction was done using Iolite 4 software (Hellstrom et al., 2008; Paton et al., 2011), following the limit of detection method of Pettke et al. (2012).

2.2.3. Isotopes measurement

Whole rock isotopic compositions of Nd were measured at the SARM at Nancy (France) while Nd and Hf isotopic compositions were performed at the "Laboratoire Magmas et Volcans" of Clermont-Ferrand (France). $^{143}Sm/^{144}Nd$ and $^{176}Lu/^{177}Hf$ ratios were computed using the $^{143}Nd/^{144}Nd$ ratios, Sm and Nd elemental composition (Weis et al., 2023) and using $^{176}Hf/^{177}Hf$, Lu and Hf elemental compositions (Borghini et al., 2021) respectively. An age of

93 My (obtained for MD80-DR5 basalts; Chatin et al., 1998) was chosen for the MD80-DR5 and MD80-DR7 samples, to recalculate the $^{176}Hf/^{177}Hf_i$ and $^{143}Nd/^{144}Nd_i$ isotopic ratios in order to compute a corrected εNd and εHf. Taking into account the different average age of the rocks around the dredged area of the MD110 and MD80-DR3 samples (see geological setting section), an age of 120 My was assumed to calculate the $^{176}Hf/^{177}Hf_i$ and $^{143}Nd/^{144}Nd_i$ isotopic ratios of these samples.

2.3. In situ analysis

2.3.1. Mineral major element concentrations

The mineral major element concentrations were determined using a micro-X-Ray Fluorescence (μ-XRF) Bruker M4 Tornado at Institut Terre et Environnement de Strasbourg (ITES, France). Measurements were performed using a Rh anode operating at 400 μA, with an accelerating voltage of 50 kV. Polycapillary lenses were used to focus the X-ray beam down to 20 μm full-width-at-half-maximum at the sample surface. The counting time per point was set to 180 s. μ-XRF spectra were deconvoluted using the Bruker Esprit software, which allowed to calculate the concentrations by using the standardless Fundamental Parameter (FP) quantification method. The accuracy of quantification is improved by the application of correction factors determined after repeated analyses of Smithsonian National Museum of Natural History mineral standards (Jarosewich et al., 1980) of anorthite (137041), augite (164905 and 122142), diopside (117733), plagioclase (115900) and San Carlos olivine (111312-44). Total Fe content was calculated on a divalent basis, as FeO. For minerals that were too small to be analyzed by μ-XRF (< 2 times the spot size of μ-XRF, typically the olivine), additional analyses were carried out with a CAMECA SX100 electron micro-probe (EPMA) at Service Commun de Microscopie Électronique et de Microanalyses (SCMEM, Nancy, France). All analyses of major elements, Na, Mg, Al, Si, K, Ca, Ti, Cr, Mn, Fe, Ni, were made against natural and synthetic mineral standard: albite (Si, Na), corundum (Al), andradite (Ca), olivine (Mg), hematite (Fe), $MnTiO_3$ (Mn,Ti), NiO (Ni), orthoclase (K). Acceleration voltage and beam current were 15 kV and 12 nA, respectively, the counting time was 10 s. The beam was focused to ~2 μm. Structural formulae were calculated based on the following number of oxygens: olivine, 4; pyroxenes, 6; plagioclase, 12.

2.3.2. Mineral trace element concentrations

The mineral trace element concentrations were determined by LA-ICP-MS at the Karlsruhe Institute of Technology (Germany), on the same equipment and same conditions as for the whole rock LA-ICP-MS analyses, with spot size of 40 µm. Silicium and iron previously determined data were used for internal standard calibration. Calibration and data quality were checked using the standards BCR-2, BHVO-1, BHVO-2, and USGS-BIR-1. Data reduction was performed with the Iolite 4 software (Hellstrom et al., 2008; Paton et al., 2011) and following the limit of detection method of Pettke et al. (2012).

3. Results

3.1. Petrology of basalts from the Diamantina zone

Magmatic rocks exposed on the seafloor of the Diamantina zone occur as gabbros, dolerites, basalts and pillow lavas. Basalts exhibit intersertal to porphyric textures with a common mineralogy of clinopyroxene-plagioclase phenocrysts embedded in a fine-grained matrix made of glass and plagioclase ± minor cpx. Only one basalt from dredging point MD110-DR06 (129A) contains olivine. Some samples from dredge points MD110-DR10 and MD110-DR11, close to the Naturaliste Plateau, show a texture closer to dolerite with the presence of amphibole.

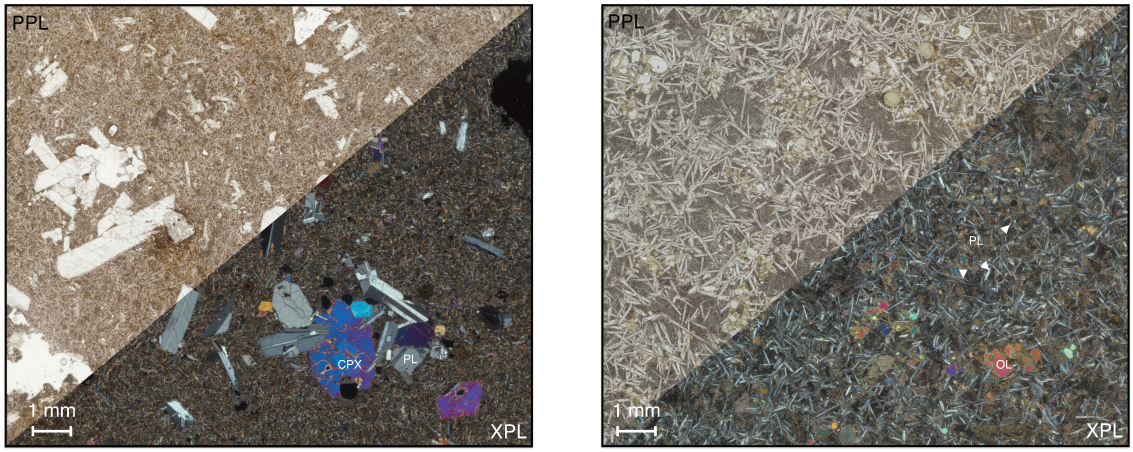


Fig. IV-2 - *Microscopic observation of basalt from the MD80-DR5 dredged point (a) and the MD110-DR04 dredged point (b). Cpx : clinopyroxène; Ol : olivine ; Pl : plagioclase.*

3.2. Bulk rock major and trace elements geochemistry

Considering their geochemical compositions, the volcanic rocks of the Diamantina zone range between sub-alkaline and alkaline basalt (Fig. 3) with a contrasting different geochemistry between samples from the MD80-DR5/MD80-DR7 dredged points (Group 1; SiO_2: 45-51 wt%; $Na_2O + K_2O$: 4-7 wt%) and the MD110/MD80-DR3 dredged samples (Group 2; SiO_2: 45-50 wt%; $Na_2O + K_2O < 5$ wt%). Mg# are low in general with only 4 samples with Mg# higher than 0.60, showing that they are made of differentiated liquids rather than primary melts.

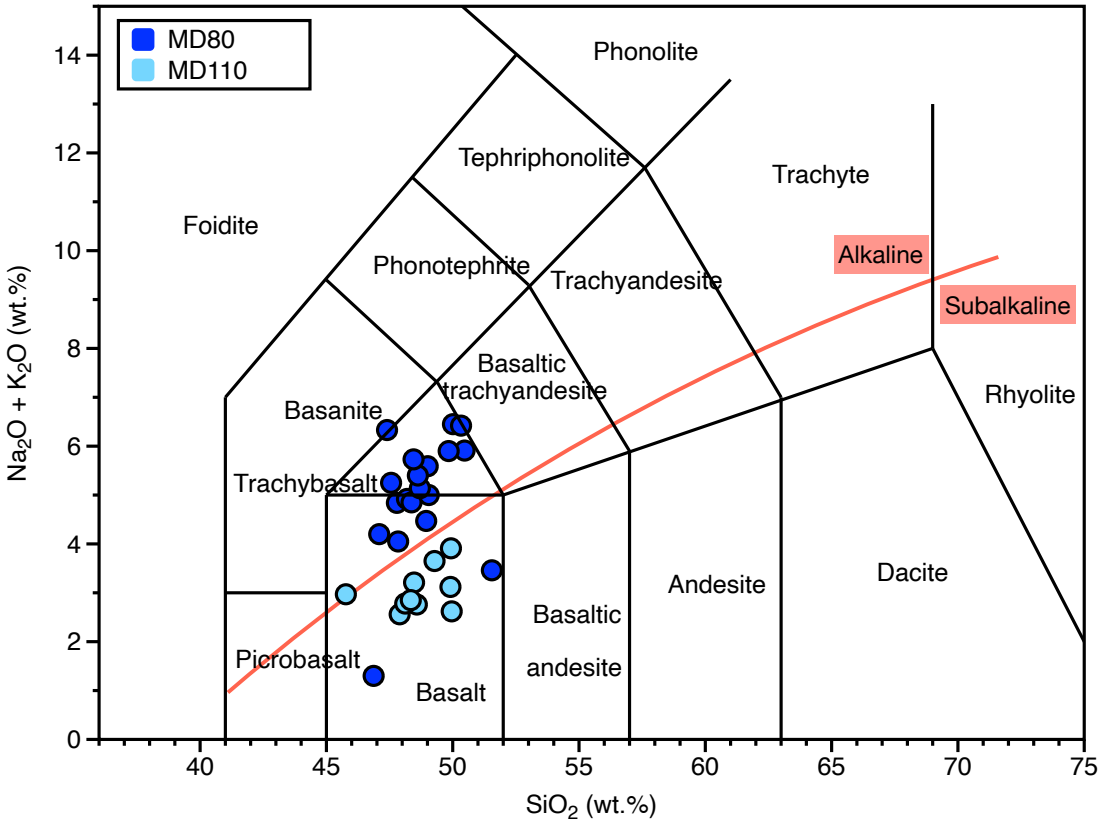


Fig. IV-3 – *Geochemical Total alkali-silica (TAS) classification diagram for the Diamantina basalts. The red line distinguishes alkaline from subalkaline basalts (after Irvine and Baragar, 1971).*

Group 1 shows also high TiO_2 content (>1.8 wt%), and high Al_2O_3 (ranging from 14.5 to 18 wt%) with the highest TiO_2 values corresponding to the highest Al_2O_3 values. This concordance is not visible in the samples from Group 2 with lower TiO_2 content (< 1.9 wt%), and Al_2O_3 ranging from 11 to 18.5 wt%. While Na_2O distribution seems to be normal for seafloor basalts ($2 < Na_2O < 3.5$ wt%), CaO concentrations is rather high and vary between 7 and 13 wt%. The

trace element concentrations of the basalts from the Group 1 (MD80-DR5 and DR7) show homogeneous PM-normalized patterns characterized by strong enrichments in incompatible elements, positive Nb-Ta and Zr-Hf anomaly (Fig. 4). The REE patterns show a very high fractionation in LREE with a significant enrichment (50-150 times chondrite concentrations) but lower HREE fractionation and concentrations (10-20 times chondrite concentrations). $(Sm/Yb)_N$ ratios are high and range between 2.5 and 3 with Yb = 2.42 ppm in average (± 0.24 2sd). The $(La/Sm)_N$ ratio of basalts from the Group 1 ranges between 4.5 - 5.8 while Nb/Yb > 10 and Y/Nb < 1.5 (Fig. 5a, b and c).

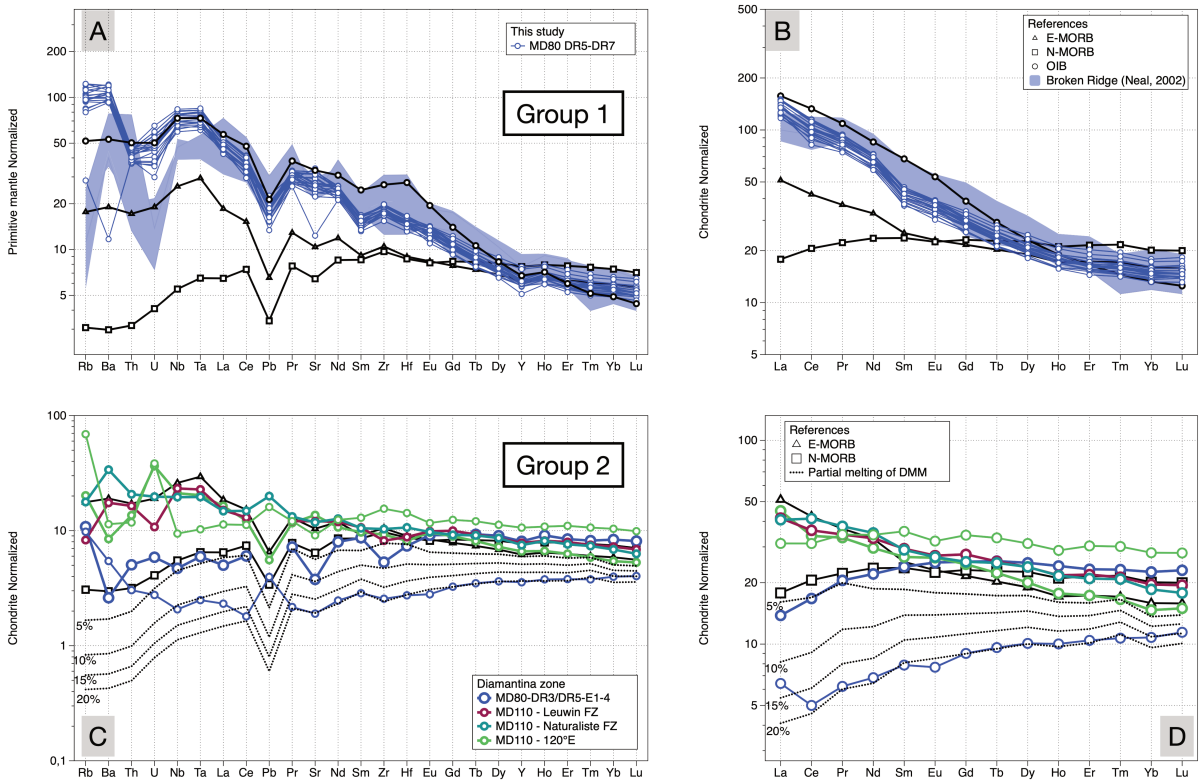


Fig. IV-4 – Trace elements pattern and REE patterns of basalts from the Diamantina zone. N- and E- MORB are from Gale et al., 2013. OIB from Sun and McDonough, 1989. DMM from Salters and Stracke, 2004. Dashed lines in fig. c and d are models of a fractional, non-modal melting (aggregate) in the spinel zone of a DMM source.

The basalts in Group 2 (MD110 and MD80-DR3) show heterogeneous but globally undepleted pattern without any Zr-Hf anomaly. Except for one sample (MD80-DR3), they show a light continuous fractionation between LREE and HREE: the $(La/Sm)_N$ ratio ranges between 0.5-1.8 (Fig. 5b) and $(Sm/Yb)_N$ ratio ranges between 0.8-1.1. The basalt dredged at

the MD80-DR3 point show a different pattern with a negative fractionation in LREE ($(La/Sm)_N$ = 0.58) and no HREE fractionation ($(Sm/Yb)_N$=1.06).

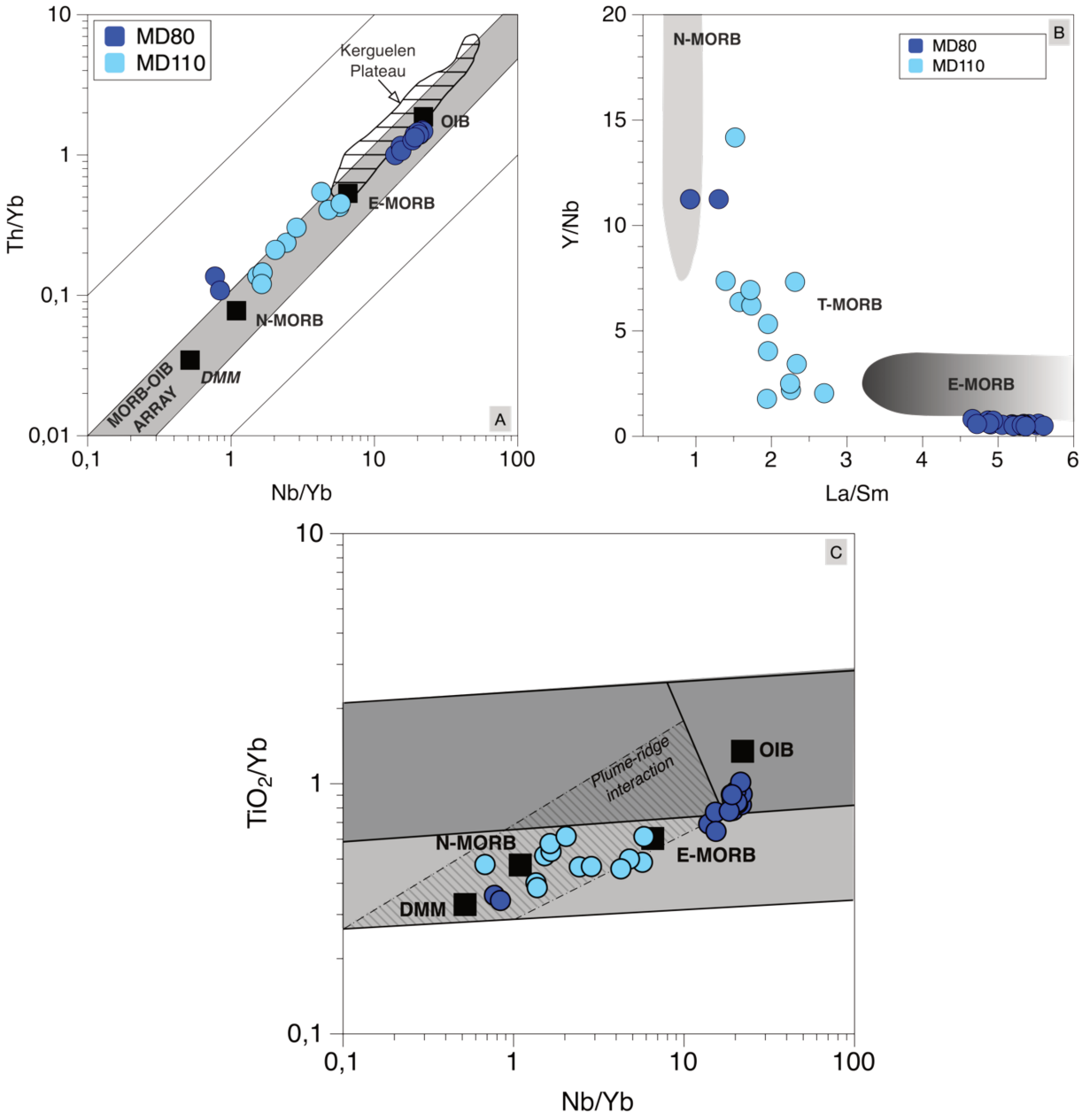


Fig. IV-5 – *Trace elements ratios-based classification diagram for the Diamantina basalts. A: MORB-OIB array after Pearce, 2008; DMM from Salters and Stracke, 2004; N- and E-MORB from Gale, 2013; OIB from Sun and McDonough. 1989. B: N-MORB and E-MORB fields are from Leroux et al., 2002 and Chazot et al, 2005 Nd and Hf isotopic compositions. C: TiO_2/Yb vs Nb/Yb. See a and b for magmatic poles references; ranges from Pearce et al., 2014*

Present-day Sm-Nd and Lu-Hf isotopic compositions of the basalts are shown in Fig. 6. Consistently with the trace elements patterns, basalts from the MD80 dredged points show two different groups. The Group 1, composed of MD80-DR5 and MD80-DR7 basalts dredged

near the Broken Ridge, show a narrow range of low $^{143}Nd/^{144}Nd$ and $^{176}Hf/^{177}Hf$ ratios ($^{143}Nd/^{144}Nd = 0.512663 \pm 10$; $^{176}Hf/^{177}Hf = 0.282976 \pm 33$) with high $(La/Sm)_N > 3$ (Fig. 6b and c). The MD80-DR3 basalt shows lower $(La/Sm)_N < 1$ with higher isotopic ratios ($^{143}Nd/^{144}Nd = 0.512929 \pm 14$; $^{176}Hf/^{177}Hf = 0.283334 \pm 4$) while MD110 basalts define a rather moderate range of $^{143}Nd/^{144}Nd$ and $^{176}Hf/^{177}Hf$ ratios ($^{143}Nd/^{144}Nd = 0.512887 \pm 108$; $^{176}Hf/^{177}Hf = 0.283162 \pm 93$) with one point considered to be an outlier. This point is a basalt of the MD110-DR11 dredged point, located near the Naturalist Plateau, which show very low isotopic ratios and negative ε_{Nd}.

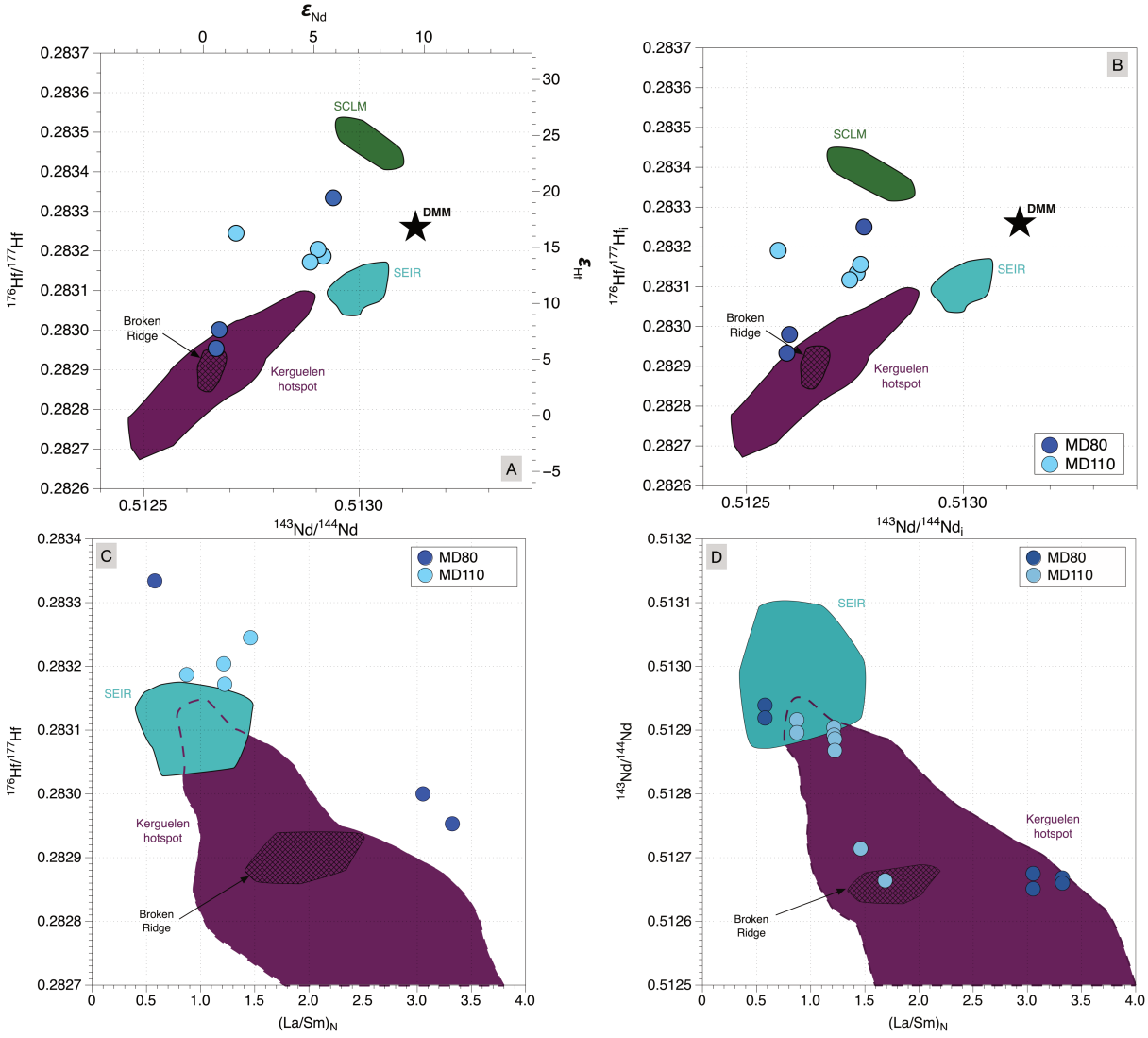


Fig. IV-6 – *Isotopic constrain of Diamantina zone basalts. A: $^{176}Hf/^{175}Hf$ vs $^{143}Nd/^{144}Nd$ and B: $^{176}Hf/^{175}Hf_i$ vs $^{143}Nd/^{144}Nd_i$ recalculated at 93 Ma for MD80-DR5 samples and 120 Ma for MD110 samples (as discussed in the text). c. $^{176}Hf/^{177}Hf$ vs $(La/Sm)_N$. SEIR from Mahoney et al., 2002 with Hf geochemistry from Hanan et al., 2013; Kerguelen Hotspot from Olierook et al., 2017 and references therein. Broken ridge from Neal et al., 2002 and Hf isotopy from Ingle et al., 2003. d. 143Nd/144Nd vs $(La/Sm)_N$.*

3.3. Minerals major and trace elements geochemistry

Major and trace elements analysis were performed in situ on clinopyroxene, plagioclase and olivine in 17 basalts from the Diamantina zone. Considering the MD80 samples, only MD80-DR5 basalts could be analyzed, due of the small grain size of the minerals in MD80-DR3 and MD80-DR7 dredged samples.

3.4.1. Clinopyroxene

Clinopyroxene in basalt from the Diamantina zone show diopside (basalts from MD110-DR01, DR08 and MD80-DR5 dredged points) to augite composition (basalts from MD110-DR10 and DR03b dredged points). Except the MD110-DR01 basalt, which show more ferrous compositions (Mg# = 0.71±0.01), they show homogeneous Mg# with an average at 0.87±0.03 in all dredged points. Concerning trace elements, they show a slightly negative Eu anomaly with Eu/Eu* ~0.90 in MD110 basalts and Eu/Eu*~0.92 in MD80 basalts. $(Sm/Yb)_N$ ratios are very heterogeneous in MD80 samples with values ranging from 2.14 to 3.81 for a narrow range of Yb (average of 1±0.41 ppm) while it's the opposite for clinopyroxene of the MD110 dredged points ($0.6 < (Sm/Yb)_N < 1.65$; Yb = 0.5-5.5 ppm).

3.4.2. Plagioclase

Plagioclase has compositions corresponding to labradorite to bytownite (An72 ± 7) in basalts while the samples showing more dolerite textures from the DR11 dredge point show heterogeneous composition with compositions from oligoclase to labradorite (An% ranging from 26.9 to 73.5). REE patterns from MD80 samples show high LREE fractionation with a variable enrichment (1-10 times chondrite concentrations) and a strong depletion in HREE (<0.5 times chondrite, heaviest REE being systematically <LOD; Fig. 6). MD110 plagioclase show lower fractionation in LREE and HREE with no significant enrichment in LREE but higher HREE concentrations (0.1-1 times chondrite concentrations) than MD80 plagioclase. They show all a positive Eu anomaly with Eu/Eu* ~11.8 in MD110 basalts and Eu/Eu* ~14.8 in MD80 basalts.

3.4.3. Olivine

Olivine was found as phenocryst and analyzed in only one sample of basalt from the MD110-DR04 dredged point. Olivine shows MgO ranging from 42.52 to 46.64 wt.% and FeO from 11.89 to 13.34 wt.%, given a relatively variable Mg# in the range of 0.858-0.875 and NiO concentration averaging at 0.21 wt% (σ = 0.02) and MnO at 0.21 wt% (σ = 0.04). Trace elements are mostly under the limit of detection but Y concentration ranges between 0.14 and 0.24 ppm and Cr between 261 and 440ppm.

4. DISCUSSION

4.1. Basalt heterogeneity along of the Diamantina zone

Although all basalts dredged along the Diamantina zone are in the MORB-OIB array (Fig. 5a), they can be divided in two major groups depending on their chemical compositions. While the basalts located to the west of the Diamantine zone, i.e. those dredged at points MD80-DR5 and MD80-DR7 (Fig. 1a), are highly enriched and thus constitute the group 1, those located further east (MD80-DR3, MD110) are more depleted and constitute the group 2 in a first order. Group 1 is enriched and close to the OIB pole and Group 2 is composed of MORB ranging from N- to E-MORB (Fig. 5b).

- Group 1 – enriched basalts linked to Broken Ridge-Kerguelen Plateau

Group 1 basalts fall within the alkaline basalt range, with compositions of basalt to trachybasalt type (Fig. 3), characterized by high alkali content ($Na_2O + K_2O > 4$ wt%). These basalts contain clinopyroxene and plagioclase phenocrysts with a typical microlithic texture. Some phenocrysts of olivine were described in the literature (Chatin, 2000) although there were never observed in our sample set. These enriched basalts yield low Mg#, showing that they are made of differentiated liquids rather than primary melts. They concordant high TiO_2 content (> 1.8 wt%), and high Al_2O_3 (ranging from 14.5 to 18 wt%) with high TiO_2/Yb ratios are in good evidence of OIB-like melts. Nb/Yb is known to be a good proxy of enrichment, as well as Ti/Yb consists of a mantle-plume source melting proxy (Pearce, 2014). Both are high in this samples with Nb/Yb>10 and TiO_2/Yb > 0.4 (Fig. 5c), showing they are following an enriched,

OIB-like magmatic series. The trace elements pattern and rare earth spectra (Fig. 4a) show significant enrichment, particularly in LREE. A comparison with reference spectra suggests an OIB (Ocean Island Basalts from Sun and McDonough, 1989) origin, consistent with the alkaline series identified previously. The patterns are particularly close to the spectra of the basalts dredged along Broken Ridge (Neal et al., 2002). A strong fractionation in HREE is present, suggesting that the source contained garnet.

- Group 2 – transitional basalts linked to Gondwana break-up?

The basalts of the MD110 and MD80-DR3 dredged points belong to the sub-alkaline basalt field, with basalt-like compositions. In line with the geodynamic context, an AFM diagram confirms that these basalts come from a tholeiitic series, typical of oceanic rift zones. Only 2 points are outside the trend, dolerite MD110-DR09-296 and basalt MD110-DR11-321 which are located close to the Naturaliste Plateau (Fig. 1a) related to crustal contamination as attested by negative εNd. Y/Nb vs. La/Sm ratios show a transitional MORB (T-MORB) nature of these basalts, i.e. intermediate between a normal and enriched MORBs. A similar classification is obtained in Nb/Yb vs. Th/Yb diagram (Fig. 5a and b). Trace element spectra are much less enriched compared to the Group 1 of basalt, with undepleted patterns and values close to those of MORBs (Fig. 4c and d). The most depleted samples show a small HREE fractionation proposing some involvement of garnet in the source. The heterogeneity of this basalt group is the most surprising feature compared with basalts of Group 1. Although this may be due to variations in partial melting degrees, followed by fractional crystallization events, such assumption does not explain all the trace elements patterns suggesting that several sources may be involved. More precisely, one sample of the MD80-DR5 dredged point is characterized by a lower alkali content and depleted trace element pattern, similar to MD80-DR3 basalts, which is characteristic of the Group 2. This could be anecdotic but, in this context, it shows another time that this area is at the quarter of several geodynamic processes and that multiple mantles sources may be involved in the Diamantina basalts.

4.2. A multiple origin of basalts: imaging the heterogeneity of mantle source/inherited mantle in magma-poor rifted margin

In order to constrain the mantle source that gave rise to the basalts sampled in the Diamantine zone by partial melting, it is necessary to focus on the isotope ratios determined on the bulk rocks. Because of the prolonged time spent in seawater, as evidenced by the Pb and Sr anomalies in trace element pattern, it is not possible to exploit the isotopes ratios associated to these two elements. On the other hand, since the Sm/Nd and Lu/Hf radiogenic pairs are much less sensitive to seawater interaction, it makes sense to use these isotopic pairs as source trackers.

$^{143}Nd/^{144}Nd$ and $^{176}Hf/^{177}Hf$ ratios of basalts from the Diamantina zone are heterogeneous regarding their localization. The Group 1 shows $^{143}Nd/^{144}Nd$ and $^{176}Hf/^{177}Hf$ ratios that are in the field of Broken Ridge data, further enhancing the possibility of a common source, i.e. the Kerguelen Mantle plume (Duncan, 2002; Neal et al., 2002).

The Group 2, however, is more radiogenic than the Kerguelen plume (Fig. 6). Nd isotope ratios (Fig. 6a,b and d) plot between a DMM-type source (such as the South-East Indian Ridge) and a hotspot-type source (Kerguelen plume head; Weis et al., 1993). The same observation could be made for $^{176}Hf/^{177}Hf$ ratios (Fig. 6a, b and c). But, the $^{176}Hf/^{177}Hf$ ratios are too radiogenic to be consistent with the $^{143}Nd/^{144}Nd$ isotope ratios if the source is a mixed source between a DMM and the Kerguelen plume head (Fig. 6a and b). First of all, the age of formation of these rocks being assumed to be, it's important to realize that this result is independent of the age recalculation based on the isotopic composition. The calculation of $^{143}Nd/^{144}Nd$ and $^{176}Hf/^{177}Hf$ isotope ratios according to sample age cannot be the source of this discrepancy, since this decoupling is only accentuated when recalculated at initial age of formation (Fig. 6a – today and b – recalculated at the age of formation). The high Lu/Hf relative to Sm/Nd ratios argue in favor of an old mantle source but several possibilities are presented in the bibliography to generate this decoupling between Hf and Nd isotopic ratios which result in the shift of the sample plots out of the mantle-OIB array (Pearce, 2008). First, an amount of recycled continental sediments could not be a possibility, since this would have shifted the isotope ratios down to negative epsilon values (Eisele et al., 2002). Two other possibilities could explain this discrepancy: a recycled pelagic sediment plus oceanic crust gives this same result

(Patchett et al., 1984; Chauvel and Blichert-Toft, 2001) as well as a source of subcontinental lithospheric mantle (Schmidberger et al., 2002). In fact, the first possibility cannot be considered since we are looking precisely at a process that gives rise to the formation of oceanic crust so this oceanic crust couldn't be the source of these basalts at the same time.
The second possibility, a source composed of subcontinental lithospheric mantle, was already proposed in other magma-poor rifted margin (Amann et al., 2020) but the main problem is that it is difficult to fully evaluate the composition of a typical SCLM, known to be inherited and to have recorded several prior magmatic events. Schmidberger et al. (2002) proposed that the Hf isotopic compositions of sub-continental mantle peridotites is characterized by a more radiogenic Hf isotopic signature than that estimated for a typical "depleted" mantle, potentially formed in the garnet stability field. This is in good accordance with our previous observation. To consider the possibility of a SCLM as an end-member sources of the basalts, we plot the Nd and Hf isotopic ratios of Sp-lherzolites of the Diamantina zone (MD110-DR02 dredged peridotites; Fig. 6) which are known to be exhumed subcontinental mantle (Ballay et al., 2024, in review). Attested by high $^{176}Hf/^{177}Hf$ isotopic ratios measured in these spinel lherzolites, the inherited SCLM seems to be a good candidate as a potential endmember of a mixed source.

4.3. Sources and timing of basalts emplacement: implication for Gondwana-break-up

Numerous basalts sampled in southeast Indian area, initially attributed to Kerguelen hotspot activity, are now suspected of being linked to the break-up of Gondwana (Olierook et al., 2019). Indeed, all early products of the "Greater Kerguelen LIP" (Comei Provinve – Bunbury Basalt – Naturaliste Plateau – Wallaby Plateau; Olierook et al., 2019 and references therein) are proposed to be related to the break-up of Gondwana, as they are associated with continental rifts (Chen et al., 2018; Direen et al., 2017; Olierook et al., 2015a, 2016 and 2017). They all attest the importance of continental and subcontinental magmatic production (Olierook et al., 2017). The basalts of the Diamantine zone, more specifically those belonging to the Group 2, fit into this framework since they show characteristics that are more depleted

than a single source of the Kerguelen mantle plume and close to the results of a sub-continental mantle source.

4.4. Comparison with others magma-poor rifted margins and implication for magmatic budget in magma-poor rifted margins

In the same way as on the Alpine Tethys margin (Amann et al., 2020; Jagoutz et al., 2007; Renna et al., 2018), several magmatic series are found in a restricted geographical area on the Diamantina zone. Some of these studies (Amann et al., 2020; Montanini et al., 2008) already proposed an implication of the inherited subcontinental mantle in the formation of MORB type basalts. Here, we showed that chemistry of basalts of the Diamantina zone can only be explained by an implication of a sub-continental mantle component. This, further emphasizing the importance of taking into account inherited mantle chemistry in the study of basalts in magma-poor passive margin.

The sub-continental mantle is exhumed in the Diamantina zone and was also dredged by the MD80 and MD110 oceanographic campaigns ((Munschy, 1994; Royer and Beslier, 1998; Ballay et al., in review). These samples show a petrology particularly depleted in clinopyroxenes with very high Mg#, suggesting an old age of this mantle, which corresponds to our previous conclusions. An interesting study of the slowest part of the Southwest Indian Ridge (Meyzen et al., 2005) suggest that the low magma budget is not the consequence of anomalously cold temperature of the mantle but rather to the presence of a very depleted zone (with little or no clinopyroxene). Here, we propose that the thermal anomaly at the margin of the hotspot may have triggered partial melting of the inherited sub-continental mantle, which is heterogeneous. Thus we suggest that the little magma budget is not due to a lower potential temperature of the mantle but to the non-fertile lithology of the inherited mantle. Moreover, the fact that there is still a mantle plume component shows that the presence of the hot-spot, although leading to the formation of basalts, does not necessarily result in magma-rich rifted margins.

CONCLUSION

To conclude, we presented here new data on magmatic rocks, located southwest of the magma-poor Australian passive margin and determined a heterogeneous geochemistry of the basalts in the Diamantina zone, with two different magmatic series. In the context of an OCT, we first show that magma-poor passive margin basalts can have very heterogeneous chemistry. Although a first group, located to the west, near Broken Ridge, clearly shows a hotspot affinity, a second group, located to the east, show more heterogeneous and depleted compositions. Secondly, we presented isotopic results that show that although the geochemical analysis of the Group 2 basalts may suggest oceanic ridge (depleted mantle) and hotspot interactions (mantle plume), isotopic evidence clearly shows that these two sources alone cannot explain the basalts of the southwestern Australian magma-poor passive margin suggesting the involvement of a sub-continental mantle. On a broader scale, the study of these magmatic products suggests an explication for the low magma budget of magma-poor rifted margins, linked to the mantle inheritance of the sub-continental mantle.

CHAPITRE 5

Synthèse et discussion

1. L'étude de la zone Diamantine confirme le modèle de formation des marges passives pauvres en magma développé en zone européenne

Initialement développé sur le domaine européen, le modèle de Picazo et al. (2016) communément accepté montrait déjà l'importance de l'héritage mantellique et des processus de refertilisation dans la mise en place d'une marge passive pauvre en magma. Il était néanmoins nécessaire de tester et confronter ce modèle lorsque l'héritage mantellique est différent.

L'observation et l'analyse d'échantillons sur l'ensemble de la zone Diamantine a montré que l'ensemble des processus décrits (« reactive porous flow », « refertilisation ») sont présents dans la formation de cette marge, indépendamment de l'héritage mantellique plus ancien. Ces processus agissent en faveur d'une érosion thermique et chimique de la lithosphère menant progressivement à l'accrétion océanique. La chimie des péridotites sous-continentales est initialement très hétérogène, à l'instar des roches mantelliques analysées dans d'autres domaines sous-continentaux (Puziewicz at al., 2020). Les caractéristiques chimiques du manteau sous-continental exhumé sont similaires avec l'implication d'un manteau sous-continental fertile (type 1a) et un autre manteau sous-continental appauvri (type 1b) qui subit la refertilisation.

Enfin, une grande diversité de péridotites et de basaltes, inhérents à la formation de la marge passive pauvre en magma ont été retrouvés, notamment en raison de cet héritage mantellique. Les processus de refertilisation, identifiés dans la zone Diamantine, comme dans d'autres zones de marges passive pauvre en magma (paléo-marges téthysiennes notamment) ne font qu'ajouter à cette hétérogénéité mantellique. L'héritage mantellique et la refertilisation apparaissent ainsi comme des clés de compréhension de la mise en place des marges passives pauvres en magma.

2. Héritage mantellique et refertilisation sont à l'origine du budget magmatique des marges passives pauvres en magma

Lorsque l'on observe des marges passives pauvres en magma, le déficit de magmatisme en surface est attribué généralement à l'absence de production de liquides magmatiques. Le budget magmatique faible de ces marges, est expliqué par 2 paramètres :

- un temps d'exhumation des roches mantelliques trop long, empêchant le passage du solidus par rééquilibrage thermique conductif

- une température potentielle du manteau trop faible, limitant la fusion partielle

Une des premières questions est de savoir si le budget magmatique est réellement plus faible ou si le liquide magmatique est bien produit mais non visible en surface ?

En effet, 2 grands points ont pu être confirmés dans cette thèse et remettent en question ce modèle :

- la refertilisation des roches montre que des liquides magmatiques sont produits mais peuvent être stockés dans la lithosphère sous-continentale (Müntener et al., 2010 ; Kaczmarek & Müntener, 2008) ;

- la présence du point chaud de Kerguelen à proximité propose que la faible production de liquides magmatiques ne soit pas attribuée à une température potentielle du manteau trop faible mais plutôt au caractère trop appauvri des péridotites sous-continentales héritées dont le point de fusion est plus haut.

Les péridotites exhumées sont appauvries et le liquide magmatique qui percole ne parvient pas à la surface puisqu'il cristallise en profondeur dans ces péridotites réactives. En complément, les profondeurs importantes de refertilisation confirment cela, puisque nous avons calculé des pressions de 7 kbars sur les péridotites refertilisées. Cette valeur est intermédiaire avec les pressions calculées sur la zone Australie-Antarctique est (> 8 kbars ; McCarthy et al., 2020) mais légèrement plus élevé par rapport aux pressions qui ont pu être calculées dans les péridotites de la Western Téthys (3 – 5 kbars ; Grove et al., 1992 ; Mccarthy and Müntener, 2019). Des pressions allant jusqu'à 6.6 kbars ont été mises en évidence pour des pyroxénites imprégnées de Monte Maggiore (Corse ; Basch et al., 2019). La refertilisation a donc lieu dans la zone de stabilité du plagioclase à des profondeurs variables et potentiellement sur l'ensemble de cette zone, proposant qu'une grande quantité de magma peut y être stockée puisque répartie sur un grand volume.

3. Les basaltes de marge passive reflètent une hétérogénéité de source

L'étude des basaltes de marges passives montrent une grande hétérogénéité (Amann et al., 2019 ; Jagoutz et al., 2007). Cela incite certains auteurs à aller jusqu'à définir les basaltes de marges passives pauvre en magma comme une catégorie à part entière, tout comme c'est déjà le cas dans les zones de subduction (type majoritaire IAB), les points chauds (type majoritaire OIB) ou les dorsales (type majoritaire MORB). Amann et al. (2019) proposera le nom d'OCT-Basalts.

Quelques travaux (Amann et al., 2019) ont proposé l'implication du manteau sous-continental dans la formation de ces basaltes, ce qui est clairement confirmé ici. Bien qu'ayant

un héritage mantellique différent, l'étude des basaltes de la zone Diamantine montre que cette hétérogénéité est valable en dehors de la zone européenne. Plus encore, bien que très proche d'un point chaud, on observe toujours le même type de basaltes.

A cela, s'ajoute l'activité du point chaud de Kerguelen qui ajoute à la complexité de la zone. De manière générale dans l'Océan Indien, l'activité de points chauds (au nombre de 3 : Kerguelen, Réunion, Marions) a souvent été mis en cause dans l'ouverture de nouvelles zones océaniques ou de sauts de dorsale. Pour autant, les dorsales sud-ouest indienne (SWIR) et sud-est indienne (SEIR) montrent des taux d'expansion océanique extrêmement bas. Dans ces zones également, l'héritage mantellique et sa composition minéralogique ont été mis en cause dans le taux d'accrétion très bas (Meyzen et al., 2005). Les produits magmatiques de la zone Diamantine, montrent eux aussi une très grande hétérogénéité, avec des zones où l'implication géochimique du manteau de Kerguelen est clairement identifiée (basaltes issus de points de dragages MD80).

Ainsi, le lien entre point chaud et ouverture – taux d'expansion océanique, déjà clairement remis en question par certaines études (Sauter et al., 2023), est mis à mal dans la zone Diamantine et de manière générale, dans l'Océan Indien.

Finalement, lorsque l'on parle de budget magmatique sur les marges passives dites pauvres en magma, il parait désormais essentiel d'inclure une étude sur l'héritage mantellique du manteau sous-continental exhumé, en plus des paramètres déjà connus.

CONCLUSION

ET

PERSPECTIVES

En conclusion, l'objectif de cette thèse était d'identifier les processus mis en jeu dans la formation de la marge passive pauvre en magma sud-ouest australienne et de mieux comprendre leur importance dans la mise en place d'une zone d'accrétion océanique. Les principaux résultats sont les suivants :

- Deux domaines mantelliques (sous-continental et refertilisé), aux lithologies distinctes (lherzolites à spinelles ou à plagioclases) sont identifiées dans la zone Diamantine. Ces deux domaines résultent des processus de fusion partielle et d'interactions magma-manteau, dont le « reactive porous flow » et la refertilisation sont contemporains du rifting.

- Les processus de fusion partielle, de « reactive porous flow » et d'imprégnation auxquels est soumis le manteau sous-continental, sont communs à l'ensemble des marges passives pauvres en magma. Cela corrobore le modèle communément accepté de Picazo et al. (2016), indépendamment de l'héritage mantellique.

- Le domaine sous-continental est largement refertilisé par des liquides magmatiques percolants effaçant progressivement l'héritage mantellique, d'un point de vue minéralogique, géochimique et thermique. Le rifting peut ainsi être vu comme un point de « réinitialisation » du cycle de Wilson.

- Les lherzolites à spinelles sont des roches à l'équilibre thermodynamique, tandis que les lherzolites à plagioclase ont subi une perturbation ou déséquilibre lié au passage d'un liquide magmatique avec lequel elles ont interagi. Les péridotites refertilisées suivent pour autant des taux de refroidissement similaires, indépendamment de l'héritage mantellique initial.

- La refertilisation peut être vue comme un processus de stockage de magma en profondeur, proposant une explication à l'aspect « pauvre en magma ». Le budget magmatique apparent des marges passives pauvres en magma serait donc plutôt à attribuer au caractère appauvri des péridotites issues de la partie inférieure du manteau sous-continental hérité (Manteau de type T1-b ; Picazo et al., 2016) où le magma est stocké d'une part et qui ne génèrent que peu de liquides magmatiques d'autres part.

- Le budget magmatique ne dépend pas que de la vitesse d'exhumation et de la température potentielle du manteau mais également de l'héritage sous-continental et l'implication d'une phase d'appauvrissement dans une phase antérieure du cycle de Wilson.

- Les basaltes de la zone Diamantine montrent une grande hétérogénéité compositionnelle, tel que cela a pu être montré dans d'autres marges passives pauvres en magma en zone européenne. Cette hétérogénéité peut être attribuée à une multitude de sources dont le manteau sous-continental fait partie.

Cette étude, concentrée initialement sur des échantillons dragués le long de la marge passive Australie-Antarctique a permis de tester la validité du modèle alpin mais également d'étendre les conclusions sur les marges passives pauvres en magma. Cela a permis de mettre en lumière des processus géodynamiques complexes et spécifiques, influencés par les conditions mantelliques et en particulier le rôle de la partie inférieure du manteau sous-continental sur le budget magmatique de ces marges.

Enfin, ce travail de thèse a permis de proposer quelques pistes de réponses aux grandes questions développées lors de l'introduction mais elles soulèvent de nouvelles interrogations :

- De nombreuses pyroxénites ont été échantillonnées notamment au point de dragage MD110-DR02. Elles sont extrêmement bien préservées de l'altération hydrothermale. Ces roches montrent une très grande diversité de lithologies et de textures : clinopyroxénites avec des textures mylonitiques, orthopyroxénites au textures porphyriques, websterites à spinelles et plagioclases sont retrouvées parmi le panel d'échantillons proposés. Les textures et les premières analyses en éléments majeurs et traces proposent des interactions avec des liquides magmatiques dans certains échantillons tandis que d'autres en sont totalement exempts. Quelle est la place de ces pyroxénites dans la mise en place de la marge passive pauvre en magma ? Interviennent-elles dans la formation des produits magmatiques ? Une étude pétrographique, géochimique et isotopique de ces échantillons pourrait permettre d'apporter une première réponse. L'étude de ces roches peut également permettre d'étudier l'évolution du manteau sous-continental relatif à l'ouverture océanique puisque les pyroxénites sont présentes dans le manteau sous-continental mais sont absentes du manteau refertilisé.

- Est-ce que les processus mis en évidence le long de la zone Diamantine sont visibles aux abords de cette zone ? Des travaux récents ont mis en évidence des lherzolites à plagioclase, mais potentiellement non refertilisés à l'est de la zone Diamantine (McCarthy et al., 2020) : comment cela s'organise le long de la marge passive ? Est-ce que l'on peut déterminer des zones préférentielles de refertilisation le long des marges ? Des travaux menés à l'est de Diamantine identifiaient déjà une ride de socle avec comme questionnement l'implication de processus magmatique dans leur formation. La campagne MD67 - KERSIMER a permis d'échantillonner pas moins d'1,5 tonnes de roches sur le bassin de Labuan, conjugué de la zone Diamantine. Quelques basaltes ont été

étudiés lors d'une thèse (Chatin, 1997) mais des péridotites auraient également été draguées et n'ont jamais fait l'objet de recherches, pouvant permettre de compléter l'étude sur la zone sud-est Indienne et de répondre à ces questionnements.

- La température potentielle du manteau à l'origine des produits magmatiques a été évoquée au cours de ce manuscrit. Le géothermomètre Al-in-olivine (Coogan et al., 2014), basé sur les compositions chimiques des olivines et spinelles des basaltes, permet de calculer la température potentielle de la péridotite source. Or, des spinelles et olivines ont été identifiées dans les basaltes de la MD80-DR7 (Chatin, 1997). Un accès à ces compositions permettrait donc d'évaluer la température potentielle du manteau et d'évaluer l'implication thermique du point chaud de Kerguelen.
- Quel est la temporalité des processus mis en évidence dans cette thèse ? La datation des lherzolites à spinelle et des lherzolites à plagioclase pourrait apporter une première réponse. Bien que des analyses isotopiques en néodyme et en hafnium ont été effectuées sur minéraux séparés, il y en a encore trop peu pour que cela soit significatif et qu'une réponse puisse y être apportée. La rareté des clinopyroxènes préservés dans les lherzolites à spinelle empêche cette caractérisation. Mais, avec l'essor des méthodes d'analyse, si la possibilité d'effectuer des analyses isotopiques directement sur lame mince se présente, cela pourrait constituer une première solution et ainsi permettre la détermination de l'âge de la refertilisation et du manteau sous-continental exhumé. Cela pourrait également ajouter des arguments pour déterminer l'âge de l'ouverture océanique avec les premiers stades d'exhumation mantellique. En effet, les reconstructions paléogéographiques sont encore très imprécises sur les premiers stades de l'ouverture dans cette zone.

Bibliographie

Abe, N. (2001). Petrochemistry of serpentinized peridotite from the Iberia Abyssal Plain (ODP Leg 173): its character intermediate between suboceanic and sub-continental upper mantle. *Geological Society, London, Special Publications* **187**, 143–159.

Amann, M., Ulrich, M., Manatschal, G., Pelt, E., Epin, M., Autin, J. & Sauter, D. (2019). Geochemical characteristics of basalts related to incipient oceanization: The example from the Alpine-Tethys OCTs. *Terra Nova* **32**, 75–88.

Anders, E., Grevesse, N. (1989). Abundances of the elements: meteoritic and solar. *Geochim. Cosmochim* **53**, 197–214.

Basch, V., Rampone, E., Crispini, L., Ferrando, C., Ildefonse, B. & Godard, M. (2018). From mantle peridotites to hybrid troctolites: Textural and chemical evolution during melt-rock interaction history (Mt. Maggiore, Corsica, France). *Lithos* **323**, 4–23.

Basch, V., Rampone, E., Borghini, G., Ferrando, C., Zanetti, A. (2019). Origin of pyroxenites in the oceanic mantle and their implications on the reactive percolation of depleted melts. Contrib. Min. Petr. **174**, 97.

Basch, Borghini, G., Fumagalli, P., Rampone, E., Gandolfo, A., Ferrando, C. (2020). Plagioclase-facies thermobarometric evolution of the External Liguride pyroxenite-bearing mantle. Ofioliti **45 (1),** 1–12.

Belviso, S., Moulin, C., Bopp, L. & Stefels, J. (2004). Assessment of a global climatology of oceanic dimethylsulfide (DMS) concentrations based on SeaWiFS imagery (1998-2001). *Canadian Journal of Fisheries and Aquatic Sciences* **61**, 804–816.

Bernard, A., Munschy, M., Rotstein, Y. & Sauter, D. (2005). Refined spreading history at the Southwest Indian Ridge for the last 96 Ma, with the aid of satellite gravity data. *Geophysical Journal International* **162**, 765–778.

Beslier, M.-O. *et al.* (2004). A wide ocean-continent transition along the south-west Australian margin: first results of the MARGAU/MD110 cruise. *Bulletin de la Société Géologique de France* **175**, 629–641.

Beyer, E.E. (2002). Evolution of the Lithosphere beneath Tasmania and Western Norway. PhD Thesis. Macquarie University.

Blichert-Toft, J., Chauvel, C. & Albarède, F. (1997). Separation of Hf and Lu for high-precision isotope analysis of rock samples by magnetic sector-multiple collector ICP-MS. *Contributions to Mineralogy and Petrology* **127**, 248–260.

Blundy, J. D., Falloon, T. J., Wood, B. J. & Dalton, J. A. (1995). Sodium partitioning between clinopyroxene and silicate melts. *Journal of Geophysical Research: Solid Earth* **100**, 15501–15515.

Bodinier, J.-L., Menzies, M. A. & Thirlwall, M. F. (1991). Continental to Oceanic Mantle Transition—REE and Sr-Nd Isotopic Geochemistry of the Lanzo Lherzolite Massif. *Journal of Petrology* **Special_Volume**, 191–210.

Bodinier, J.-L., Garrido, C. J., Chanefo, I., Bruguier, O. & Gervilla, F. (2008). Origin of Pyroxenite–Peridotite Veined Mantle by Refertilization Reactions: Evidence from the Ronda Peridotite (Southern Spain). *Journal of Petrology* **49**, 999–1025.

Bodinier, J.-L. & Godard, M. (2014). Orogenic, Ophiolitic, and Abyssal peridotites. *Treatise on Geochemistry (Second Edition)* 103–167.

Boillot, G., Winterer, E.L., Meyer, A.W. (1987). Proc. ODP, Init. Repts., 103: College Station, *TX (Ocean Drilling Program).*

Borghini, G. & Rampone, E. (2007). Postcumulus processes in oceanic-type olivine-rich cumulates: the role of trapped melt crystallization versus melt/rock interaction. *Contributions to Mineralogy and Petrology* **154**, 619–633.

Borghini, G., Fumagalli, P. & Rampone, E. (2010). The Stability of Plagioclase in the Upper Mantle: Subsolidus Experiments on Fertile and Depleted Lherzolite. *Journal of Petrology* **51**, 229–254.

Borghini, G., Fumagalli, P. & Rampone, E. (2011). The geobarometric significance of plagioclase in mantle peridotites: A link between nature and experiments. *Lithos* **126**, 42–53.

Borghini, G., Rampone, E., Zanetti, A., Class, C., Cipriani, A., Hofmann, A. W. & Goldstein, S. L. (2013). Meter-scale Nd isotopic heterogeneity in pyroxenite-bearing Ligurian peridotites encompasses global-scale upper mantle variability. *Geology* **41**, 1055–1058.

Borghini, G., Rampone, E., Zanetti, A., Class, C., Cipriani, A., Hofmann, A. W. & Goldstein, S. L. (2016). Pyroxenite Layers in the Northern Apennines' Upper Mantle (Italy)—Generation by Pyroxenite Melting and Melt Infiltration. *Journal of Petrology* **57**, 625–653.

Borghini, G., Rampone, E., Class, C., Goldstein, S., Cai, Y., Cipriani, A., Hofmann, A. W. & Bolge, L. (2021). Enriched HfNd isotopic signature of veined pyroxenite-infiltrated peridotite as a possible source for E-MORB. *Chemical Geology* **586**, 120591.

Borghini, G., Fumagalli, P., Arrigoni, F., Rampone, E., Berndt, J., Klemme, S. & Tiepolo, M. (2023). Fast REE re-distribution in mantle clinopyroxene via reactive melt infiltration. *Geochemical Perspectives Letters* **26**, 40–44.

Bown, J. W. & White, R. S. (1994). Variation with spreading rate of oceanic crustal thickness and geochemistry. *Earth and Planetary Science Letters* **121**, 435–449.

Brey, G. P. & Köhler, T. (1990). Geothermobarometry in Four-phase Lherzolites II. New Thermobarometers, and Practical Assessment of Existing Thermobarometers. *Journal of Petrology* **31**, 1353–1378.

Cannat, M., Sauter, D., Mendel, V., Ruellan, E., Okino, K., Escartin, J., Combier, V. & Baala, M. (2006). Modes of seafloor generation at a melt-poor ultraslow-spreading ridge. *Geology* **34**, 605–608.

Champion, D. C. & Cassidy, K. F. (2007). An overview of the Yilgarn Craton and its crustal evolution. *Geoscience Australia*.

Chatin F., Etude des mécanismes de mise en place et de formation des roches plutoniques océaniques dans deux contextes géodynamiques différents. Thèse de doctorat, Université de Strasbourg, 1997, 522.

Chatin, F., Robert, U., Montigny, R. & Whitechurch, H. (1998). La zone Diamantine (océan Indien oriental), témoin de la séparation entre l'Australie et l'Antarctique : arguments pétrologiques et géochimiques. *Comptes Rendus de l'Académie des Sciences - Series IIA - Earth and Planetary Science* **326**, 839–845.

Chauvel, C. & Blichert-Toft, J. (2001). A hafnium isotope and trace element perspective on melting of the depleted mantle. *Earth and Planetary Science Letters* **190**, 137–151.

Chazot, G., Charpentier, S., Kornprobst, J., Vannucci, R. & Luais, B. (2005). Lithospheric Mantle Evolution during Continental Break-Up: The West Iberia Non-Volcanic Passive Margin. *Journal of Petrology* **46**, 2527–2568.

Chebakova, K. A., Dzidziguri, E. L., Sidorova, E. N., Vasiliev, A. A., Ozherelkov, D. Yu., Pelevin, I. A., Gromov, A. A. & Nalivaiko, A. Yu. (2021). X-ray Fluorescence Spectroscopy Features of Micro- and Nanoscale Copper and Nickel Particle Compositions. *Nanomaterials* **11**, 2388.

Chen, T., Li, G., Frank, M. & Ling, H. (2013). Hafnium isotope fractionation during continental weathering: Implications for the generation of the seawater Nd-Hf isotope relationships. *Geophysical Research Letters* **40**, 916–920.

Chenin, P., Manatschal, G., Picazo, S., Müntener, O., Karner, G., Johnson, C. & Ulrich, M. (2017). Influence of the architecture of magma-poor hyperextended rifted margins on orogens produced by the closure of narrow versus wide oceans. *Geosphere* **13**, 559–576.

Chenin, P., Tomasi, S., Kusznir, N. & Manatschal, G. (2024). Linking rifted margin crustal shape with the timing and volume of magmatism. *Terra Nova* **36**, 53–61.

Cherniak, D.J., Liang, Y., 2022. Calcium diffusion in enstatite, with application to closure temperature of the Ca-in-opx thermometer. Geochim. Cosmochim. Acta **332**, 124–137.

Coffin, M. F., Pringle, M. S., Duncan, R. A., Gladczenko, T. P., Storey, M., Müller, R. D. & Gahagan, L. A. (2002). Kerguelen Hotspot Magma Output since 130 Ma. *Journal of Petrology* **43**, 1121–1137.

Coogan, L. A., Saunders, A. D. & Wilson, R. N. (2014). Aluminum-in-olivine thermometry of primitive basalts: Evidence of an anomalously hot mantle source for large igneous provinces. *Chemical Geology* **368**, 1–10.

Coogan, L. A., Jenkin, G. R. T. & Wilson, R. N. (2002). Constraining the cooling rate of the lower oceanic crust: a new approach applied to the Oman ophiolite. *Earth and Planetary Science Letters* **199**, 127–146.

D'Souza, R. J., Canil, D. & Coogan, L. A. (2019). Geobarometry for spinel peridotites using Ca and Al in olivine. *Contributions to Mineralogy and Petrology* **175**, 5.

Delpech, G., Scott, J.M., Gregoire, M., Moine, B.N., Li, D., Liu, J., Pearson, D.G., Meer, Q. H.A.van der, Waight, T.E., Michon, G., Guillaume, D., O'Reilly, S.Y., Cottin, J.-Y., Giret, A. (2021) The subantarctic lithospheric mantle. Geol. Soc. Lond. Memoirs **M56**.

Desmurs, L., Müntener, O. & Manatschal, G. (2002). Onset of magmatic accretion within a magma-poor rifted margin: a case study from the Platta ocean-continent transition, eastern Switzerland. *Contributions to Mineralogy and Petrology* **144**, 365–382.

Dijkstra, A. H., Barth, M. G., Drury, M. R., Mason, P. R. D. & Vissers, R. L. M. (2003). Diffuse porous melt flow and melt-rock reaction in the mantle lithosphere at a slow-spreading ridge: A structural petrology and LA-ICP-MS study of the Othris Peridotite Massif (Greece). *Geochemistry, Geophysics, Geosystems* **4**.

Dilek, Y., Furnes, H. & Wit, M. de (2013). Evolution of Archean Crust and Early Life. *Modern Approaches in Solid Earth Sciences* 1–22.

Direen, N. G., Borissova, I., Stagg, H. M. J., Colwell, J. B. & Symonds, P. A. (2007). Nature of the continent-ocean transition zone along the southern Australian continental margin: a comparison of the Naturaliste Plateau, SW Australia, and the central Great Australian Bight sectors. *Geological Society, London, Special Publications* **282**, 239–263.

Direen, N. G., Stagg, H. M. J., Symonds, P. A. & Colwell, J. B. (2011). Dominant symmetry of a conjugate southern Australian and East Antarctic magma-poor rifted margin segment. *Geochemistry, Geophysics, Geosystems* **12**, n/a-n/a.

Direen, N. G., Stagg, H. M. J., Symonds, P. A. & Norton, I. O. (2013). Variations in rift symmetry: cautionary examples from the Southern Rift System (AustraliaAntarctica). *Geological Society, London, Special Publications* **369**, 453–475.

Direen, N. G., Cohen, B. E., Maas, R., Frey, F. A., Whittaker, J. M., Coffin, M. F., Meffre, S., Halpin, J. A. & Crawford, A. J. (2017). Naturaliste Plateau: constraints on the timing and evolution of the Kerguelen Large Igneous Province and its role in Gondwana breakup. *Australian Journal of Earth Sciences* **64**, 1–19.

Duncan, R. A. (2002). A Time Frame for Construction of the Kerguelen Plateau and Broken Ridge. *Journal of Petrology* **43**, 1109–1119.

Dygert, N. & Liang, Y. (2015). Temperatures and cooling rates recorded in REE in coexisting pyroxenes in ophiolitic and abyssal peridotites. *Earth and Planetary Science Letters* **420**, 151–161.

Dygert, N., Kelemen, P. B. & Liang, Y. (2017). Spatial variations in cooling rate in the mantle section of the Samail ophiolite in Oman: Implications for formation of lithosphere at mid-ocean ridges. *Earth and Planetary Science Letters* **465**, 134–144.

Eisele, J., Sharma, M., Galer, S. J. G., Blichert-Toft, J., Devey, C. W. & Hofmann, A. W. (2002). The role of sediment recycling in EM-1 inferred from Os, Pb, Hf, Nd, Sr isotope and trace element systematics of the Pitcairn hotspot. *Earth and Planetary Science Letters* **196**, 197–212.

Fabriès, J., Lorand, J.-P. & Bodinier, J.-L. (1998). Petrogenetic evolution of orogenic lherzolite massifs in the central and western Pyrenees. *Tectonophysics* **292**, 145–167.

Ferrari, E., Montanini, A. & Tribuzio, R. (2022). Rifting evolution of the lithospheric subcontinental mantle: New insights from the External Ligurian ophiolites (Northern Apennine, Italy). *Lithos* **410**, 106571.

Flude, S., Haschke, M., Storey, M. & Harvey, J. (2017). Application of benchtop micro-XRF to geological materials. *Mineralogical Magazine* **81**, 923–948.

Franke, D. (2013). Rifting, lithosphere breakup and volcanism: Comparison of magma-poor and volcanic rifted margins. *Marine and Petroleum Geology* **43**, 63–87.

Frey, F. A., Weis, D., Borisova, A. YU. & Xu, G. (2002). Involvement of Continental Crust in the Formation of the Cretaceous Kerguelen Plateau: New Perspectives from ODP Leg 120 Sites. *Journal of Petrology* **43**, 1207–1239.

Froitzheim, N. & Manatschal, G. (1996). Kinematics of Jurassic rifting, mantle exhumation, and passive-margin formation in the Austroalpine and Penninic nappes (eastern Switzerland). *GSA Bulletin* **108**, 1120–1133.

Fumagalli, P., Borghini, G., Rampone, E. & Poli, S. (2017). Experimental calibration of Forsterite–Anorthite–Ca-Tschermak–Enstatite (FACE) geobarometer for mantle peridotites. *Contributions to Mineralogy and Petrology* **172**, 38.

Furnes, H., de Wit, M., Dilek, Y. (2014). Precambrian Greenstone Belts Host Different Ophiolite Types. In: Dilek, Y., Furnes, H. (Eds.), Evolution of Archean Crust and Early Life. *Modern Approaches in Solid Earth Sciences*, **7**. Springer, Dordrecht, 1–22.

Gale, A., Dalton, C. A., Langmuir, C. H., Su, Y. & Schilling, J. (2013). The mean composition of ocean ridge basalts. *Geochemistry, Geophysics, Geosystems* **14**, 489–518.

Gillard, M., *Évolution tectono-magmatique menant à l'océanisation sur les marges passives pauvres en magma : exemple des marges Australie-Antarctique.* Thèse de doctorat, Université de Strasbourg, 2014, 250.

Gillard, M., Autin, J., Manatschal, G., Sauter, D., Munschy, M. & Schaming, M. (2015). Tectonomagmatic evolution of the final stages of rifting along the deep conjugate Australian-Antarctic magma-poor rifted margins: Constraints from seismic observations. *Tectonics* **34**, 753–783.

Godard, M., Jousselin, D. & Bodinier, J.-L. (2000). Relationships between geochemistry and structure beneath a palaeo-spreading centre: a study of the mantle section in the Oman ophiolite. *Earth and Planetary Science Letters* **180**, 133–148.

Grove, T.L., Kinzler, R.J. and Bryan, W.B. (1992) Fractionation of mid-ocean ridge basalt

(MORB). Mantle Flow and Melt Generation at Mid-Ocean Ridges. *Washington, DC: AGU*, 281-310.

Guan, H., Geoffroy, L. & Xu, M. (2021). Magma-assisted fragmentation of Pangea: Continental breakup initiation and propagation. *Gondwana Research* **96**, 56–75.

Gurnis, M. & Müller, R. D. (2003). Evolution and Dynamics of the Australian Plate. *Geological Society of America Special Papers* 2003 **372**, 417-429.

Halpin, J. A., Crawford, A. J., Direen, N. G., Coffin, M. F., Forbes, C. J. & Borissova, I. (2008). Naturaliste Plateau, offshore Western Australia: A submarine window into Gondwana assembly and breakup. *Geology* **36**, 807–810.

Harry, D. L. *et al.* (2020). Evolution of the Southwest Australian Rifted Continental Margin During Breakup of East Gondwana: Results From International Ocean Discovery Program Expedition 369. *Geochemistry, Geophysics, Geosystems* **21**.

Hansmann, W., Müntener, O., Hermann, J.(2001). U-Pb zircon geochronology of a tholeiitic intrusion and associated migmatites at a continental crust-mantle transition, Val Malenco, Italy. *Schweizerische Mineralogische und Petrographische Mitteilungen*. **81**. 239-255.

Heezen, B.C., Tharp, M. (1965). A discuss to accompany the physiographic diagram of the indian ocean. *New York*, *Geol.Soc.Amer*., **Special paper 82**, 88-89.

Heimler, K., Gottschalk, C. & Vogt, C. (2023). Confocal micro X-ray fluorescence analysis for the non-destructive investigation of structured and inhomogeneous samples. *Analytical and Bioanalytical Chemistry* **415**, 5083–5100.

Hellebrand, E., Snow, J. E., Dick, H. J. B. & Hofmann, A. W. (2001). Coupled major and trace elements as indicators of the extent of melting in mid-ocean-ridge peridotites. *Nature* **410**, 677–681.

Hellebrand, E., Snow, J. E., Hoppe, P. & Hofmann, A. W. (2002). Garnet-field Melting and Late-stage Refertilization in 'Residual' Abyssal Peridotites from the Central Indian Ridge. *Journal of Petrology* **43**, 2305–2338.

Hellebrand, E. & Snow, J. E. (2003). Deep melting and sodic metasomatism underneath the highly oblique-spreading Lena Trough (Arctic Ocean). *Earth and Planetary Science Letters* **216**, 283–299.

Hellstrom, J., Paton, C., Woodhead, J. and Hergt, J. (2008). Iolite: software for spatially resolved LA-(quad and MC) ICPMS analysis. *Mineralogical Association of Canada short course series*, **40**, 343-348.

Hermann, J. and Müntener, O. (1996) Exhumation-related structures in the Malenco-Margna system: implications for paleogeography and its consequences for rifting and Alpine tectonics. *Schweizerische Mineralogische und Petrographische Mitteilungen*, **81**: 239-255.

Hermann, J., Müntener, O., Trommsdorff, V., Hansmann, W. & Piccardo, G. B. (1997). Fossil crust-to-mantle transition, Val Malenco (Italian Alps). *Journal of Geophysical Research: Solid Earth* **102**, 20123–20132.

Herzberg, C. T. (1978). Pyroxene geothermometry and geobarometry: experimental and thermodynamic evaluation of some subsolidus phase relations involving pyroxenes in the system CaO-MgO-Al2O3-SiO2. *Geochimica et Cosmochimica Acta* **42**, 945–957.

Inczédy J, Lengyel T, Ure AM (2000) Compendium on analytical nomenclature. *International Union of Pure and Applied Chemistry*. http://media.iupac.org/publications/analytical_compendium/. Accessed 20 Aug 2024

Ingle, S., Weis, D., Scoates, J. S. & Frey, F. A. (2002). Relationship between the early Kerguelen plume and continental flood basalts of the paleo-Eastern Gondwanan margins. *Earth and Planetary Science Letters* **197**, 35–50.

Ingle, S., Weis, D., Doucet, S. & Mattielli, N. (2003). Hf isotope constraints on mantle sources and shallow-level contaminants during Kerguelen hot spot activity since ~120 Ma. *Geochemistry, Geophysics, Geosystems* **4**.

Jagoutz, O., Müntener, O., Manatschal, G., Rubatto, D., Péron-Pinvidic, G., Turrin, B. D. & Villa, I. M. (2007). The rift-to-drift transition in the North Atlantic: A stuttering start of the MORB machine? *Geology* **35**, 1087–1090.

Jarosewich, E., Nelen, J. A. & Norberg, J. A. (1980). Reference Samples for Electron Microprobe Analysis. *Geostandards Newsletter* **4**, 43–47.

Jochum, K. P., Weis, U., Schwager, B., Stoll, B., Wilson, S. A., Haug, G. H., Andreae, M. O. & Enzweiler, J. (2016). Reference Values Following ISO Guidelines for Frequently Requested Rock Reference Materials. *Geostandards and Geoanalytical Research* **40**, 333–350.

Johnson, K. T. M., Dick, H. J. B. & Shimizu, N. (1990). Melting in the oceanic upper mantle: An ion microprobe study of diopsides in abyssal peridotites. *Journal of Geophysical Research: Solid Earth* **95**, 2661–2678.

Jollands, M. C. & Müntener, O. (2019). Testing Orthopyroxene Diffusion Chronometry on Rocks From the Lanzo Massif (Italian Alps). *Journal of Geophysical Research: Solid Earth* **124**, 7822–7841.

Kaczmarek, M.-A. & Müntener, O. (2008). Juxtaposition of Melt Impregnation and High-Temperature Shear Zones in the Upper Mantle; Field and Petrological Constraints from the Lanzo Peridotite (Northern Italy). *Journal of Petrology* **49**, 2187–2220.

Kaczmarek, M.-A. & Müntener, O. (2010). The variability of peridotite composition across a mantle shear zone (Lanzo massif, Italy): interplay of melt focusing and deformation. *Contributions to Mineralogy and Petrology* **160**, 663–679.

Kelemen, P.B. (1990) Reaction between ultramafic rock and fractionating basaltic magma. 1.Phase-relations, the origin of calc-alkaline magma series, and the formation of discordant dunite. *Journal of Petrology*, **31**: 51-98.

Kelemen, P.B., Joyce, D.B., Webster, J.D. and Holloway, J.R. (1990) Reaction between ultramafic rock and fractionating basaltic magma. 2. Experimental investigation of reaction between olivine tholeiite and harzburgite at 1150°C-1050°C and 5Kb. *Journal of Petrology*, **31**: 99-134.

Kelemen, P.B., Hitehead, J.A., Aharonov, E. and Jordahl, K.A. (1995a) Experiments on flow focussing in soluble porous media, with applications to melt extraction from the mantle. *Journal of Geophysical Res*earch, **100**: 475-496.

Kelemen, P.B., Shimizu, N. and Salters, V.J.M. (1995b) Extraction of mid-ocean-ridge basalt from the upwelling mantle by focused flow of melt in dunite channels. *Nature,* **375**: 747–753.

Kelemen, P.B., Hirth, G., Shimizu, N., Spiegelman, M. and Dick, H.J.B. (1997a) A review of melt migration processes in the adiabatically upwelling mantle beneath oceanic spreading ridges. *Philosophical Transcript of the Royal Society, London,* **355**: 283-318.

Kelemen, P.B., Braun, M. and Hirth, G. (2000) Spatial distribution of melt conduits in the mantle beneath oceanic spreading ridges: Observations from the Ingalls and Oman ophiolites. *Geochemistry, Geophysics, Geosystems,* **1**, 1999GC000012.

Kempton, P. D., Pearce, J. A., Barry, T. L., Fitton, J. G., Langmuir, C. & Christie, D. M. (2002). Sr-Nd-Pb-Hf Isotope Results from ODP Leg 187: Evidence for Mantle Dynamics of the Australian-Antarctic Discordance and Origin of the Indian MORB Source. *Geochemistry, Geophysics, Geosystems* **3**, 1–35.

Laat, J. I. de, Lebedev, S., Celli, N. L., Bonadio, R., Melo, B. C. de & Rawlinson, N. (2023). Structure and evolution of the Australian plate and underlying upper mantle from waveform tomography with massive data sets. *Geophysical Journal International* **234**, 153–189.

Lavier, L. L. & Manatschal, G. (2006). A mechanism to thin the continental lithosphere at magma-poor margins. *Nature* **440**, 324–328.

Liang, Y., Sun, C. & Yao, L. (2013). A REE-in-two-pyroxene thermometer for mafic and ultramafic rocks. *Geochimica et Cosmochimica Acta* **102**, 246–260.

Magri, L., Whittaker, J. M., Coffin, M. F., Hochmuth, K., Gürer, D., Williams, S., Bernardel, G. & Uenzelmann-Neben, G. (2024). Tectono-Stratigraphic Evolution of the Kerguelen Large Igneous Province: The Conjugate William's Ridge-Broken Ridge Rifted Margins. *Journal of Geophysical Research: Solid Earth* **129**.

Maier, Smithies, Spaggiari, Barnes, Kirkland, Kiddie & Roberts, M. (2016). The evolution of mafic and ultramafic rocks of the Mesoproterozoic Fraser Zone, Albany-Fraser Orogen, and implications for the Ni-Cu sulphide potential of the region. *Geological Survey of Western Australia*, Record **2016/8**, 49p.

Manatschal, G. (2004). New models for evolution of magma-poor rifted margins based on a review of data and concepts from West Iberia and the Alps. *International Journal of Earth Sciences* **93**, 432–466.

Manatschal, G. & Bernoulli, D. (1999). Architecture and tectonic evolution of nonvolcanic margins: Present-day Galicia and ancient Adria. *Tectonics* **18**, 1099–1119.

Manatschal, G., Engström, A., Desmurs, L., Schaltegger, U., Cosca, M., Müntener, O. & Bernoulli, D. (2006). What is the tectono-metamorphic evolution of continental break-up: The example of the Tasna Ocean–Continent Transition. *Journal of Structural Geology* **28**, 1849–1869.

Manatschal, G. & Müntener, O. (2009). A type sequence across an ancient magma-poor ocean–continent transition: the example of the western Alpine Tethys ophiolites. *Tectonophysics* **473**, 4–19.

Maritati, A., Halpin, J. A., Whittaker, J. M., Daczko, N. R. & Wainman, C. C. (2021). Provenance of Upper Jurassic–Lower Cretaceous strata in the Mentelle Basin, southwestern Australia, reveals a trans-Gondwanan fluvial pathway. *Gondwana Research* **93**, 128–141.

Mattielli, N., Weis, D., Blichert-Toft, J. & Albarède, F. (2002). Hf Isotope Evidence for a Miocene Change in the Kerguelen Mantle Plume Composition. *Journal of Petrology* **43**, 1327–1339.

McCarthy, A. & Müntener, O. (2015). Ancient depletion and mantle heterogeneity: Revisiting the Permian-Jurassic paradox of Alpine peridotites. *Geology* **43**, 255–258.

McCarthy, A. & Müntener, O. (2019). Evidence for ancient fractional melting, cryptic refertilization and rapid exhumation of Tethyan mantle (Civrari Ophiolite, NW Italy). *Contributions to Mineralogy and Petrology* **174**, 69.

McCarthy, A., Falloon, T. J., Sauermilch, I., Whittaker, J. M., Niida, K. & Green, D. H. (2020). Revisiting the Australian-Antarctic Ocean-Continent Transition Zone Using Petrological and Geophysical Characterization of Exhumed Subcontinental Mantle. *Geochemistry, Geophysics, Geosystems* **21**.

McDonough, W. F. & Sun, S. -s. (1995). The composition of the Earth. *Chemical Geology* **120**, 223–253.

McKenzie, D. (1978). Some remarks on the development of sedimentary basins. *Earth and Planetary Science Letters* **40**, 25–32.

Meisel, T., Biino, G. G. & Nägler, T. F. (1996). Re-Os, Sm-Nd, and rare earth element evidence for Proterozoic oceanic and possible subcontinental lithosphere in tectonized ultramafic lenses from the Swiss Alps. *Geochimica et Cosmochimica Acta* **60**, 2583–2593.

Meisel, T., Melcher, F., Tomascak, P., Dingeldey, C. & Koller, F. (1997). Re-Os isotopes in orogenic peridotite massifs in the Eastern Alps, Austria. *Chemical Geology* **143**, 217–229.

Meyzen, C. M., Ludden, J. N., Humler, E., Luais, B., Toplis, M. J., Mével, C. & Storey, M. (2005). New insights into the origin and distribution of the DUPAL isotope anomaly in the Indian Ocean mantle from MORB of the Southwest Indian Ridge. *Geochemistry, Geophysics, Geosystems* **6**.

Montanini, A., Tribuzio, R. & Anczkiewicz, R. (2006). Exhumation History of a Garnet Pyroxenite-bearing Mantle Section from a Continent–Ocean Transition (Northern Apennine Ophiolites, Italy). *Journal of Petrology* **47**, 1943–1971.

Montanini, A., Tribuzio, R. & Vernia, L. (2008). Petrogenesis of basalts and gabbros from an ancient continent–ocean transition (External Liguride ophiolites, Northern Italy). *Lithos* **101**, 453–479.

Morrison, G. H., Cheng, K. L. & Grasserbauer, M. (1979). General Aspects of Trace Analytical Methods—IV. Recommendations for Nomenclature, Standard Procedures and Reporting of Experimental Data for Surface Analysis Techniques. *Pure and Applied Chemistry* **51**, 2243–2250.

Munschy, M., (1994). Diamantine – MD80 cruise, RV Marion Dufresne.

Munschy, M. (1998). La zone de Diamantine, témoin de la séparation de l'Australie et de l'Antarctique : arguments géophysiques. *Comptes Rendus de l'Académie des Sciences - Series IIA - Earth and Planetary Science* **327**, 533–540.

Müntener, O. & Hermann, J. (1996). The Val Malenco lower crust - upper mantle complex and its field relations (Italian Alps). *Schweizerische mineralogische und petrographische Mitteilungen* **102**, 20123–20132.

Müntener, O., Hermann, J. & Trommsdorf, V. (2000). Cooling History and Exhumation of Lower-Crustal Granulite and Upper Mantle (Malenco, Eastern Central Alps). *Journal of Petrology* **41**, 175–200.

Müntener, O. & Piccardo, G. B. (2003). Melt migration in ophiolitic peridotites: the message from Alpine-Apennine peridotites and implications for embryonic ocean basins. *Geological Society, London, Special Publications* **218**, 69–89.

Müntener, O., Pettke, T., Desmurs, L., Meier, M. & Schaltegger, U. (2004). Refertilization of mantle peridotite in embryonic ocean basins: trace element and Nd isotopic evidence and implications for crust–mantle relationships. *Earth and Planetary Science Letters* **221**, 293–308.

Müntener, O. & Manatschal, G. (2006). High degrees of melt extraction recorded by spinel harzburgite of the Newfoundland margin: The role of inheritance and consequences for the evolution of the southern North Atlantic. *Earth and Planetary Science Letters* **252**, 437–452.

Müntener, O., Manatschal, G., Desmurs, L. & Pettke, T. (2010). Plagioclase Peridotites in Ocean–Continent Transitions: Refertilized Mantle Domains Generated by Melt Stagnation in the Shallow Mantle Lithosphere. *Journal of Petrology* **51**, 255–294.

Neal, C. R., Mahoney, J. J. & Chazey, W. J. (2002). Mantle Sources and the Highly Variable Role of Continental Lithosphere in Basalt Petrogenesis of the Kerguelen Plateau and Broken Ridge LIP: Results from ODP Leg 183. *Journal of Petrology* **43**, 1177–1205.

Nicholls, I. A., Ferguson, J., Jones, H., Marks, G. P. & Mutter, J. C. (1981). Ultramafic blocks from the ocean floor southwest of Australia. *Earth and Planetary Science Letters* **56**, 362–374.

Olierook, H. K. H. *et al.* (2015a). Age and geochemistry of magmatism on the oceanic Wallaby Plateau and implications for the opening of the Indian Ocean. *Geology* **43**, 971–974.

Olierook, H. K. H., Jourdan, F., Merle, R. E., Timms, N. E., Kusznir, N. & Muhling, J. R. (2016). Bunbury Basalt: Gondwana breakup products or earliest vestiges of the Kerguelen mantle plume? *Earth and Planetary Science Letters* **440**, 20–32.

Olierook, H. K. H., Merle, R. E. & Jourdan, F. (2017). Toward a Greater Kerguelen large igneous province: Evolving mantle source contributions in and around the Indian Ocean. *Lithos* **282**, 163–172.

Olierook, H. K. H., Jiang, Q., Jourdan, F. & Chiaradia, M. (2019). Greater Kerguelen large igneous province reveals no role for Kerguelen mantle plume in the continental breakup of eastern Gondwana. *Earth and Planetary Science Letters* **511**, 244–255.

Patchett, J. & Chauvel, C. (1984). The mean life of continents is currently not constrained by Nd and Hf isotopes. *Geophysical Research Letters* **11**, 151–153.

Paton, C., Hellstrom, J., Paul, B., Woodhead, J. & Hergt, J. (2011). Iolite: Freeware for the visualisation and processing of mass spectrometric data. *Journal of Analytical Atomic Spectrometry* **26**, 2508–2518.

Pearce, N. J. G., Perkins, W. T., Westgate, J. A., Gorton, M. P., Jackson, S. E., Neal, C. R. & Chenery, S. P. (1997). A Compilation of New and Published Major and Trace Element Data for NIST SRM 610 and NIST SRM 612 Glass Reference Materials. *Geostandards Newsletter* **21**, 115–144.

Pearce, J. A. (2008). Geochemical fingerprinting of oceanic basalts with applications to ophiolite classification and the search for Archean oceanic crust. *Lithos* **100**, 14–48.

Pearce, J. A. (2014). Immobile Element Fingerprinting of Ophiolites. *Elements* **10**, 101–108.

Pelletier, L. & Müntener, O. (2006). High-pressure metamorphism of the Lanzo peridotite and its oceanic cover, and some consequences for the Sesia–Lanzo zone (northwestern Italian Alps). *Lithos* **90**, 111–130.

Péron-Pinvidic, G., Manatschal, G., Minshull, T. A. & Sawyer, D. S. (2007). Tectonosedimentary evolution of the deep Iberia-Newfoundland margins: Evidence for a complex breakup history. *Tectonics* **26**.

Péron-Pinvidic, G. & Manatschal, G. (2009). The final rifting evolution at deep magma-poor passive margins from Iberia-Newfoundland: a new point of view. *International Journal of Earth Sciences* **98**, 1581–1597.

Perrett, G. M., Campbell, J. L., Glasauer, S. & Pardo, R. (2014). Quantitative determination of mineral phase effects observed in APXS analyses of geochemical reference materials. *X-Ray Spectrometry* **43**, 359–366.

Petri, B., Mohn, G., Skrzypek, E., Mateeva, T., Galster, F. & Manatschal, G. (2017). U–Pb geochronology of the Sondalo gabbroic complex (Central Alps) and its position within the Permian post-Variscan extension. *International Journal of Earth Sciences* **106**, 2873–2893.

Pettke, T., Oberli, F., Audétat, A., Guillong, M., Simon, A. C., Hanley, J. J. & Klemm, L. M. (2012). Recent developments in element concentration and isotope ratio analysis of individual fluid inclusions by laser ablation single and multiple collector ICP-MS. *Ore Geology Reviews* **44**, 10–38.

Picazo, S., Müntener, O., Manatschal, G., Bauville, A., Karner, G. & Johnson, C. (2016). Mapping the nature of mantle domains in Western and Central Europe based on clinopyroxene and spinel chemistry: Evidence for mantle modification during an extensional cycle. *Lithos* **266**, 233–263.

Piccardo G.B., Müntener O., Zanetti A., Romairone A., Bruzzone S., Poggi E. and Spagnolo

G. (2004a) The Lanzo South peridotite: melt-peridotite interaction in the mantle lithosphere of the Jurassic Ligurian Tethys. *Ofioliti* **29**: 37-62.

Piccardo, G. B., Muntener, O., Zanetti, A. & Pettke, T. (2004b) Ophiolite peridotites of the

Alpine-Apennine system: mantle processes and geodynamic relevance. *International Geological Review,* **40**, 1119-1159.

Piccardo, G. B., Zanetti, A. & Müntener, O. (2007). Melt/peridotite interaction in the Southern Lanzo peridotite: Field, textural and geochemical evidence. *Lithos* **94**, 181–209.

Piccardo, G.B., Zanetti, A., Pruzzo, A. and Padovano, M. (2007b) The North Lanzo peridotite body (NW Italy): Lithospheric mantle percolated by MORB and alkaline melts. *Periodico di Mineralogia*, **76**: 199–221.

Piccardo, G. B., Vannucci, R. & Guarnieri, L. (2009). Evolution of the lithospheric mantle in an extensional setting: Insights from ophiolitic peridotites. *Lithosphere* **1**, 81–87.

Piccardo, G. B., Padovano, M. & Guarnieri, L. (2014). The Ligurian Tethys: Mantle processes and geodynamics. *Earth-Science Reviews* **138**, 409–434.

Presnall, D. C. (1976). Alumina content of enstatite as a geobarometer for plagioclase and spinel lherzolite. *American Mineralogist*.

Pugnière, P. *Contribution à l'amélioration de la quantification des acides nucléiques par qPCR et RT-qPCR.* Thèse de doctorat. Médecine humaine et pathologie. Université de Grenoble, 2012.

Puziewicz, J., Matusiak-Małek, M., Ntaflos, T., Grégoire, M., Kaczmarek, M.-A., Aulbach, S., Ziobro, M. & Kukuła, A. (2020). Three major types of subcontinental lithospheric mantle beneath the Variscan orogen in Europe. *Lithos* **362**, 105467.

Pyle, D. G., Christie, D. M., Mahoney, J. J. & Duncan, R. A. (1995). Geochemistry and geochronology of ancient southeast Indian and southwest Pacific seafloor. *Journal of Geophysical Research: Solid Earth* **100**, 22261–22282.

Rampone, E., Piccardo, G. B., Vannucci, R., Bottazzi, P. & Ottolini, L. (1993). Subsolidus reactions monitored by trace element partitioning: the spinel- to plagioclase-facies transition in mantle peridotites. *Contributions to Mineralogy and Petrology* **115**, 1–17.

Rampone, E., Hofmann, A. W., Piccardo, G. B., Vannucci, R., Bottazzi, P. & Ottolini, L. (1995). Petrology, Mineral and Isotope Geochemistry of the External Liguride Peridotites (Northern Apennines, Italy). *Journal of Petrology* **36**, 81–105.

Rampone, E., Piccardo, G. B., Vannucci, R. & Bottazzi, P. (1997). Chemistry and origin of trapped melts in ophioiitic peridotites. *Geochimica et Cosmochimica Acta* **61**, 4557–4569.

Rampone, E. & Borghini, G. (2008). Melt migration and intrusion in the Erro-Tobbio peridotites (Ligurian Alps, Italy): Insights on magmatic processes in extending lithospheric mantle. *European Journal of Mineralogy* **20**, 573–585.

Rampone, E., Borghini, G. & Basch, V. (2020). Melt migration and melt-rock reaction in the Alpine-Apennine peridotites: Insights on mantle dynamics in extending lithosphere. *Geoscience Frontiers* **11**, 151–166.

Renna, M. R., Tribuzio, R., Sanfilippo, A. & Thirlwall, M. (2018). Role of melting process and melt–rock reaction in the formation of Jurassic MORB-type basalts (Alpine ophiolites). *Contributions to Mineralogy and Petrology* **173**, 31.

Reston, T. J. (2009). The structure, evolution and symmetry of the magma-poor rifted margins of the North and Central Atlantic: A synthesis. *Tectonophysics* **468**, 6–27.

Rooney, T. O., Brown, E. L., Bastow, I. D., Arrowsmith, J. R. & Campisano, C. J. (2023). Magmatism during the continent – ocean transition. *Earth and Planetary Science Letters* **614**, 118189.

Rotstein, Y., Munschy, M. & Bernard, A. (2001). The Kerguelen Province revisited: Additional constraints on the early development of the Southeast Indian Ocean. *Marine Geophysical Researches* **22**, 81–100.

Royer, J.-Y, Beslier, M.-O., Hill, P.J. (1998) Rapport De Campagne MD110/MARGAU. Géosciences Azur, p. 113. Villefranche-sur-Mer.

Saccani, E., Dilek, Y., Marroni, M. & Pandolfi, L. (2015). Continental margin ophiolites of Neotethys: Remnants of Ancient Ocean–Continent Transition Zone (OCTZ) lithosphere and their geochemistry, mantle sources and melt evolution patterns. *Episodes* **38**, 230–249.

Salters, V. J. M. & Stracke, A. (2004). Composition of the depleted mantle. *Geochemistry, Geophysics, Geosystems* **5**.

Sauter, D., Manatschal, G., Kusznir, N., Masquelet, C., Werner, P., Ulrich, M., Bellingham, P., Franke, D. & Autin, J. (2023). Ignition of the southern Atlantic seafloor spreading machine without hot-mantle booster. *Scientific Reports* **13**, 1195.

Sayers, J., Symonds, P. A., Direen, N. G. & Bernardel, G. (2001). Nature of the continent-ocean transition on the non-volcanic rifted margin of the central Great Australian Bight. *Geological Society, London, Special Publications* **187**, 51–76.

Schaltegger, U. & Brack, P. (2007). Crustal-scale magmatic systems during intracontinental strike-slip tectonics: U, Pb and Hf isotopic constraints from Permian magmatic rocks of the Southern Alps. *International Journal of Earth Sciences* **96**, 1131–1151.

Schmidberger, S. S., Simonetti, A., Francis, D. & Gariépy, C. (2002). Probing Archean lithosphere using the Lu–Hf isotope systematics of peridotite xenoliths from Somerset Island kimberlites, Canada. *Earth and Planetary Science Letters* **197**, 245–259.

Seyler, M. & Bonatti, E. (1997). Regional-scale melt-rock interaction in lherzolitic mantle in the Romanche Fracture Zone (Atlantic Ocean). *Earth and Planetary Science Letters* **146**, 273–287.

Sherman, J. (1956). The theoretical derivation of fluorescent X-ray intensities from mixtures. *Spectrochimica Acta* **7**, 283–306.

Sitko, R. (2009). Quantitative X-ray fluorescence analysis of samples of less than 'infinite thickness': Difficulties and possibilities. *Spectrochimica Acta Part B: Atomic Spectroscopy* **64**, 1161–1172.

Smye, A., Seman, S., Hudak, M. & Crispin, K. (2017). Rates of mantle cooling and exhumation during rifting constrained by REE-in-pyroxene speedometry. *Geochemistry, Geophysics, Geosystems* **18**, 2510–2525.

Spaggiari, C. V., Kirkland, C. L., Smithies, R. H., Wingate, M. T. D. & Belousova, E. A. (2015). Transformation of an Archean craton margin during Proterozoic basin formation and magmatism: The Albany–Fraser Orogen, Western Australia. *Precambrian Research* **266**, 440–466.

Strating, E. H. H., Rampone, E., Piccardo, G. B., Drury, M. R. & Vissers, R. L. M. (1993). Subsolidus Emplacement of Mantle Peridotites during Incipient Oceanic Rifting and Opening of the Mesozoic Tethys (Voltri Massif, NW Italy). *Journal of Petrology* **34**, 901–927.

Sun, S. -s & McDonough, W. F. (1989). Chemical and isotopic systematics of oceanic basalts: implications for mantle composition and processes. *Geological Society, London, Special Publications* **42**, 313–345.

Sutra, E., Manatschal, G., Mohn, G. & Unternehr, P. (2013). Quantification and restoration of extensional deformation along the Western Iberia and Newfoundland rifted margins. *Geochemistry, Geophysics, Geosystems* **14**, 2575–2597.

Tagle, R., Reinhardt F.. *Back to the Roots* [en ligne]. Berlin: Bruker, 2023. [Consulté le 25.07.2024]. Disponible sur https://www.bruker.com/en/news-and-events/webinars/2023/advantages-of-standard-supported-micro-xrf-quantification.html?scrollToFormContent=webinar-form

Totterdell, J. M., J. E. Blevin, H. I. M. Struckmeyer, B. E. Bradshaw, J. B. Colwell, and J. M. Kennard (2000), A new sequence framework for the Great Australian Bight: Starting with a clean slate, *APPEA* J., **40**, 95–117.

Tribuzio, R., Thirlwall, M. F. & Vannucci, R. (2004). Origin of the Gabbro–Peridotite Association from the Northern Apennine Ophiolites (Italy). *Journal of Petrology* **45**, 1109–1124.

Tribuzio, R., Garzetti, F., Corfu, F., Tiepolo, M. & Renna, M. R. (2016). U–Pb zircon geochronology of the Ligurian ophiolites (Northern Apennine, Italy): Implications for continental breakup to slow seafloor spreading. *Tectonophysics* **666**, 220–243.

Tikku, A. A. & Cande, S. C. (1999). The oldest magnetic anomalies in the Australian-Antarctic Basin: Are they isochrons? *Journal of Geophysical Research: Solid Earth* **104**, 661–677.

Tucholke, B.E., Sibuet, J.-C., Klaus, A., et al., 2004. Proc. ODP, Init. Repts., 210: College Station, *TX (Ocean Drilling Program).*

Tucholke, B. E., Sawyer, D. S. & Sibuet, J.-C. (2007). Breakup of the NewfoundlandIberia rift. *Geological Society, London, Special Publications* **282**, 9–46.

Ulrich, M., Muñoz, M., Guillot, S., Cathelineau, M., Picard, C., Quesnel, B., Boulvais, P. & Couteau, C. (2014). Dissolution–precipitation processes governing the carbonation and silicification of the serpentinite sole of the New Caledonia ophiolite. *Contributions to Mineralogy and Petrology* **167**, 952.

VanTongeren, J. A., Kelemen, P. B. & Hanghøj, K. (2008). Cooling rates in the lower crust of the Oman ophiolite: Ca in olivine, revisited. *Earth and Planetary Science Letters* **267**, 69–82.

Vauchez, A., Tommasi, A., Barruol, G. & Maumus, J. (2000). Upper mantle deformation and seismic anisotropy in continental rifts. *Physics and Chemistry of the Earth, Part A: Solid Earth and Geodesy* **25**, 111–117.

Veevers, J. J. (2012). Reconstructions before rifting and drifting reveal the geological connections between Antarctica and its conjugates in Gondwanaland. *Earth-Science Reviews* **111**, 249–318.

Wal, D. V. der & Bodinier, J.-L. (1996). Origin of the recrystallisation front in the Ronda peridotite by km-scale pervasive porous melt flow. *Contributions to Mineralogy and Petrology* **122**, 387–405.

Wallace, P. J., Frey, F. A., Weis, D. & Coffin, M. F. (2002). Origin and Evolution of the Kerguelen Plateau, Broken Ridge and Kerguelen Archipelago: Editorial. *Journal of Petrology* **43**, 1105–1108.

Wegener, A. L. (1929). *Die Entstehung der Kontinente und Ozeane*. Friedrich vieweg & sohn. 231.

Weis, D., Frey, F. A., Leyrit, H. & Gautier, I. (1993). Kerguelen Archipelago revisited: geochemical and isotopic study of the Southeast Province lavas. *Earth and Planetary Science Letters* **118**, 101–119.

Witt-Eickschen, G. & Seck, H. A. (1991). Solubility of Ca and Al in orthopyroxene from spinel peridotite: an improved version of an empirical geothermometer. *Contributions to Mineralogy and Petrology* **106**, 431–439.

White, L. T., Gibson, G. M. & Lister, G. S. (2013). A reassessment of paleogeographic reconstructions of eastern Gondwana: Bringing geology back into the equation. *Gondwana Research* **24**, 984–998.

Whitmarsh, R. B., Manatschal, G. & Minshull, T. A. (2001). Evolution of magma-poor continental margins from rifting to seafloor spreading. *Nature* **413**, 150–154.

Workman, R.K., Hart, S.R. (2005) Major and trace element composition of the depleted MORB mantle (DMM). *Earth Planet. Sci. Lett.* **231**, 53–72.

ANNEXES

Table des annexes

1 - Annexes du chapitre n°2

A. Lames minces de péridotites et pyroxénites en LPA et LPNA 163

B. Annexes publiées dans le journal EPSL

B.1. Zonations des orthopyroxènes et éléments traces des plagioclases 167

B.2. Localisation et descriptions pétrographiques des échantillons de dragage de la zone de Diamantina 170

B.3. Standards µ-XRF et LA-ICPMS 171

B.4. Éléments de quantification en µ-XRF et LA-ICPMS 172

B.5. Table de données – compositions chimiques des minéraux *179*

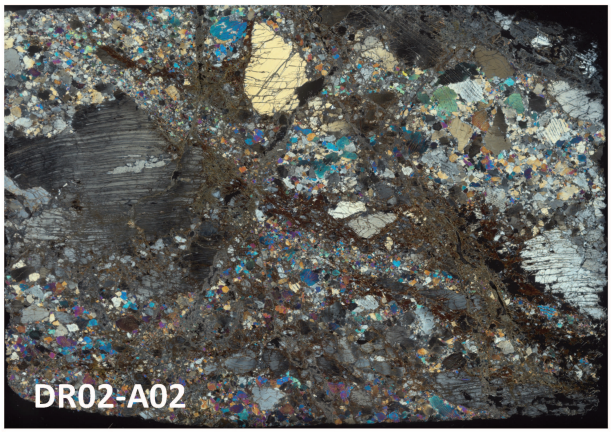
2 - Annexes du chapitre n°3

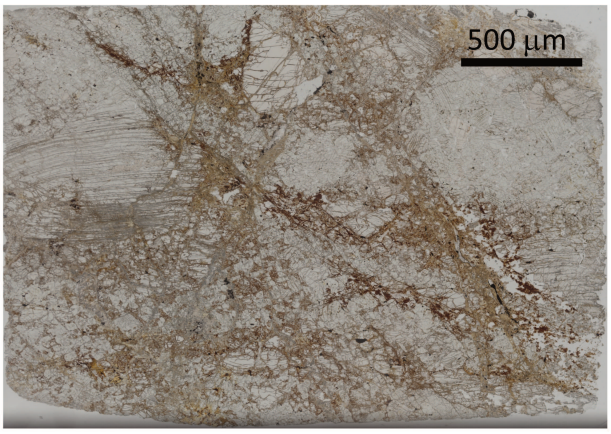
A. Classification des péridotites *208*

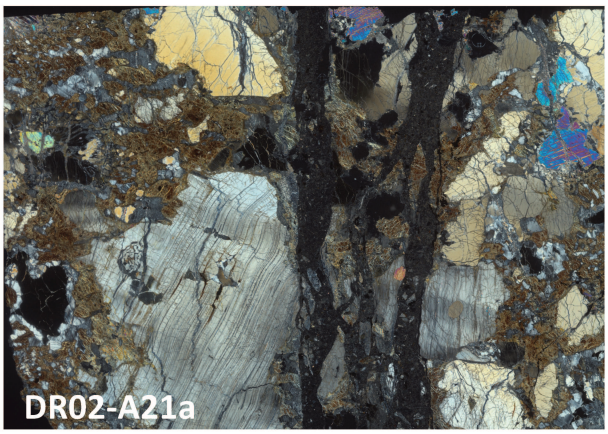
3 - Annexes du chapitre n°4

A. Table de données – compositions chimiques des minéraux *209*

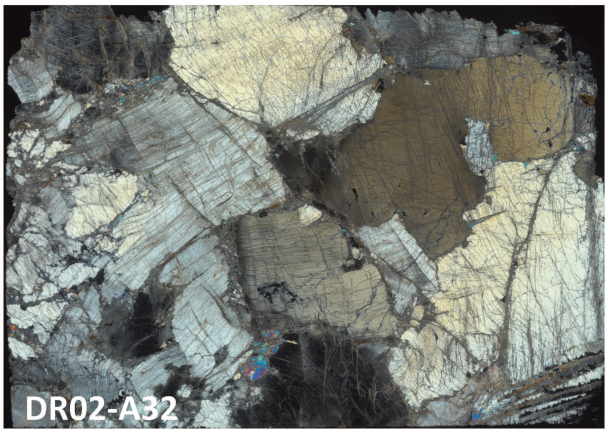
B. Table de données – compositions chimiques des roches totales *233*


DR02-A02

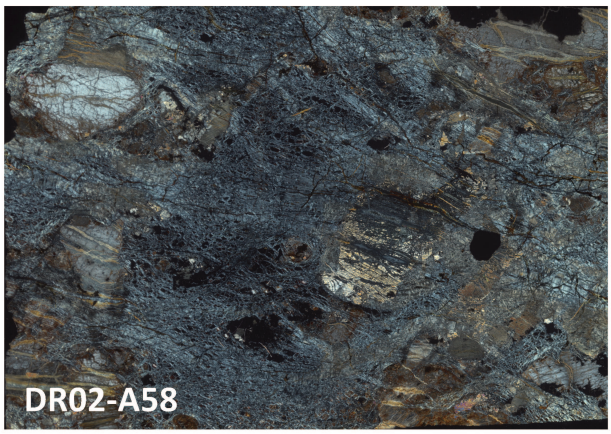

500 µm

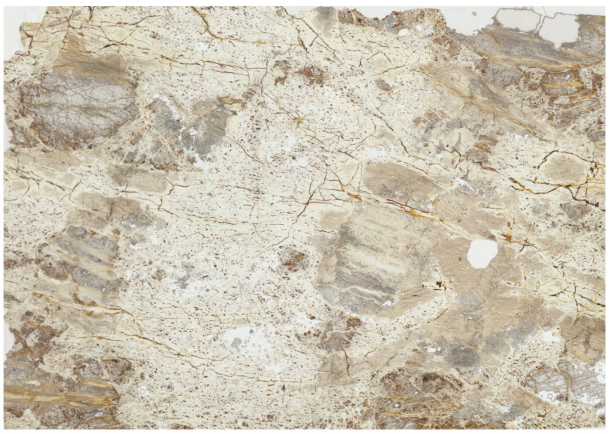

DR02-A21a

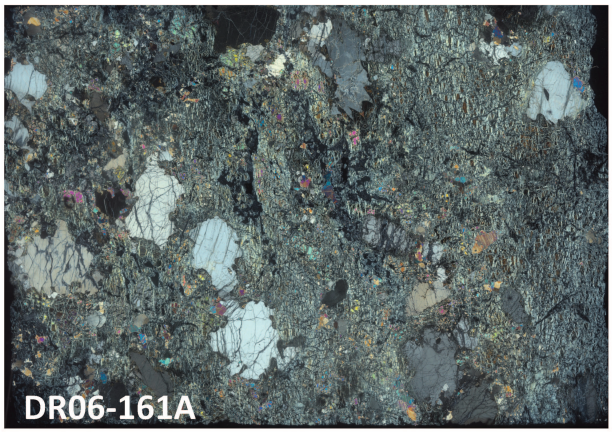


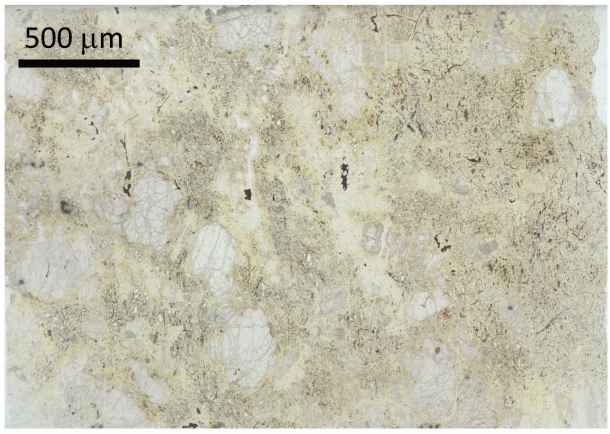

DR02-A32

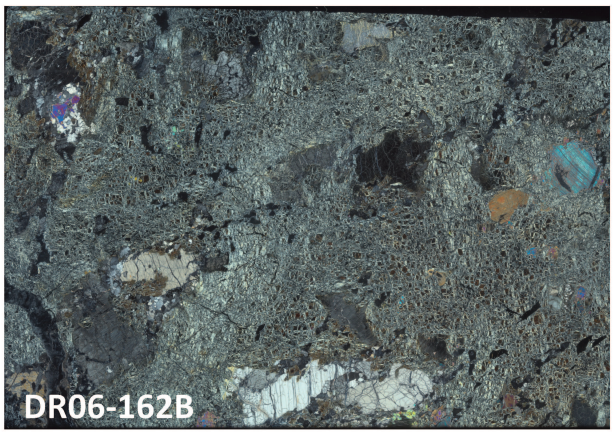



DR02-A58

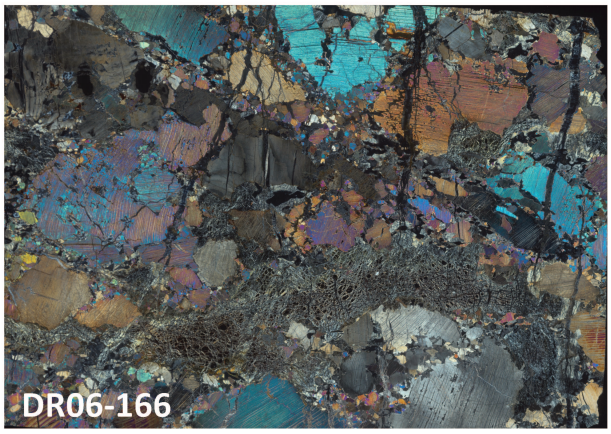



DR06-161A

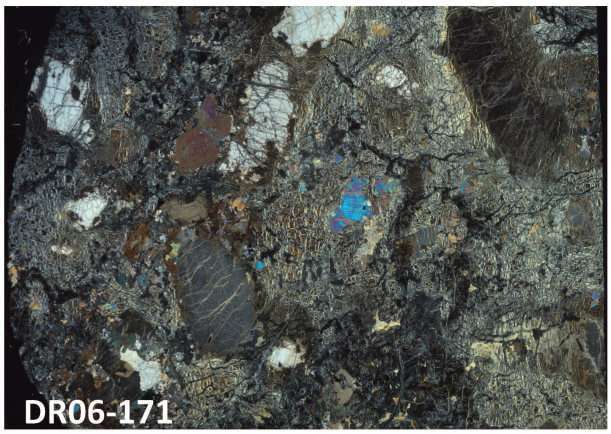

500 µm


DR06-162B



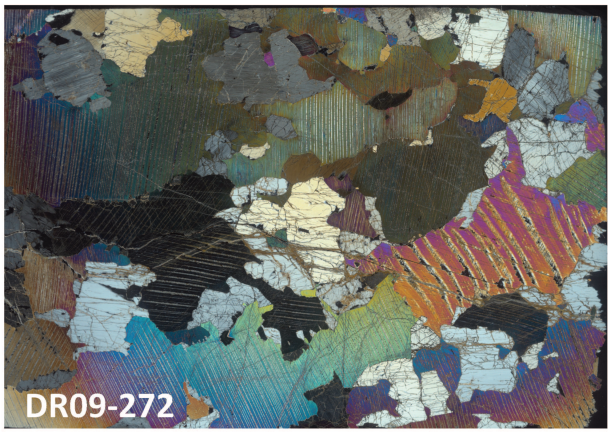

DR06-166

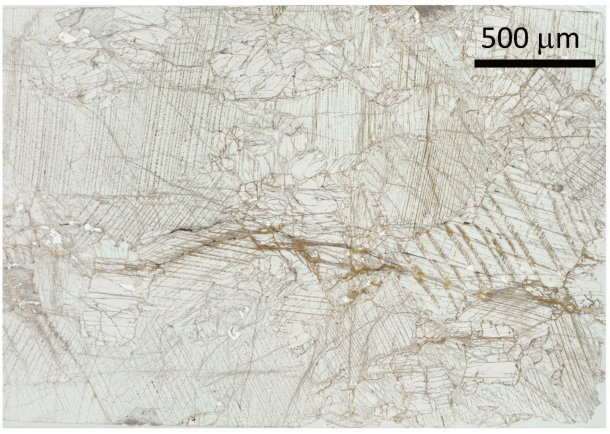


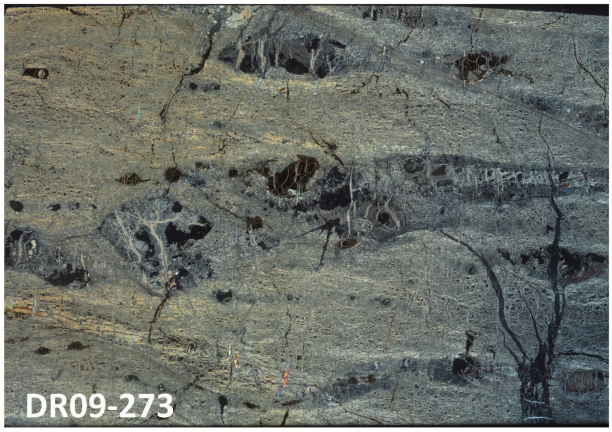

DR06-171

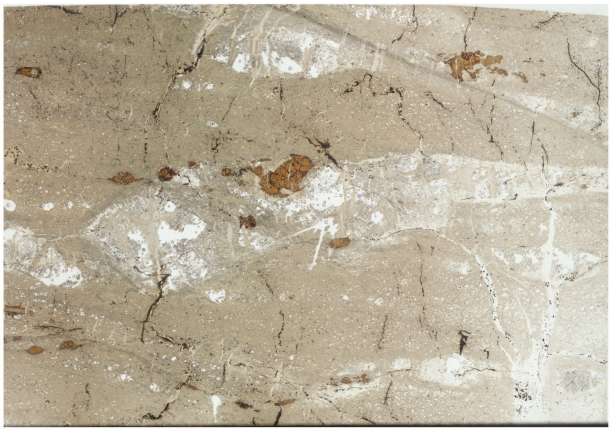


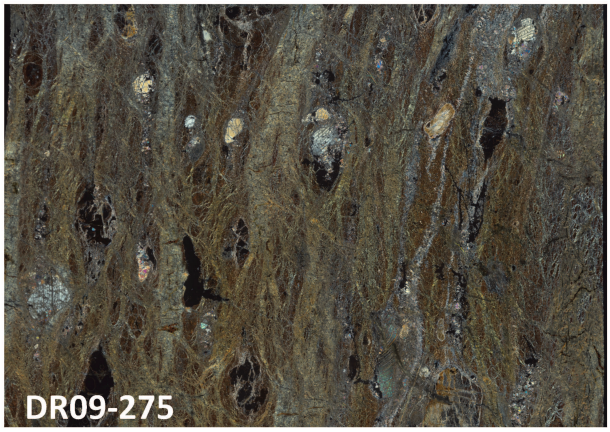
Lames minces de péridotites et pyroxénites en LPA et LPNA – MD110-DR09



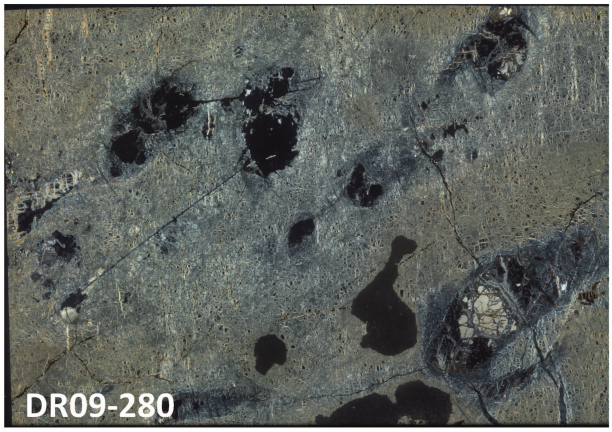






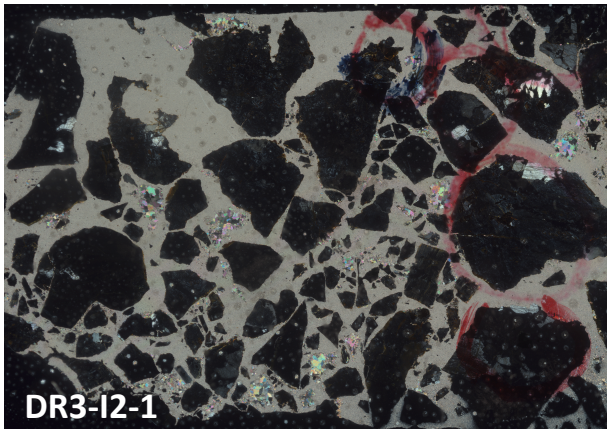


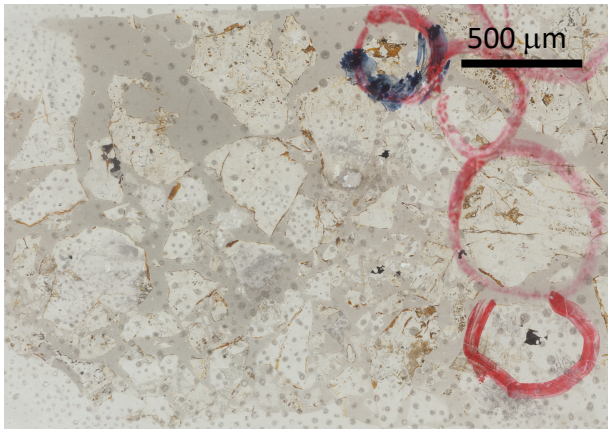


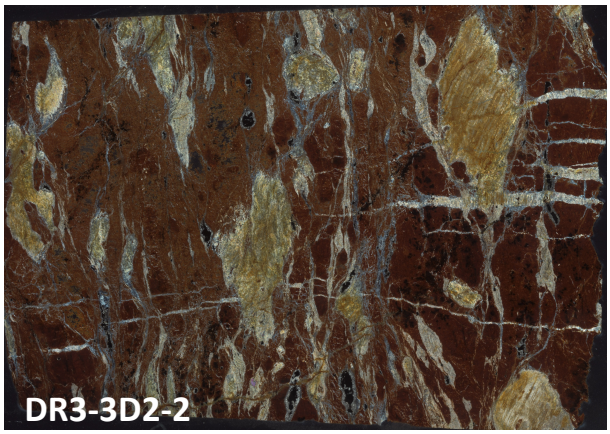


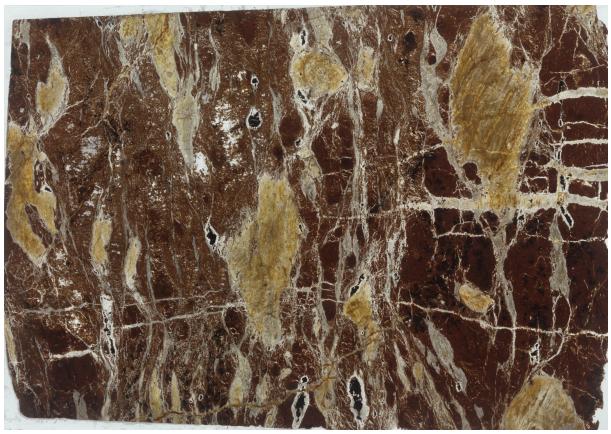


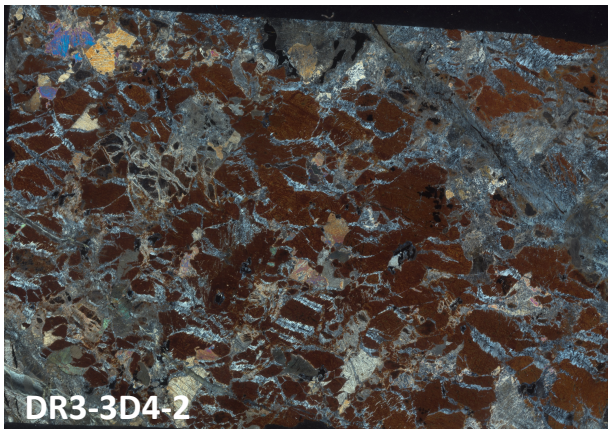
Lames minces de péridotites et pyroxénites en LPA et LPNA – MD80-DR3













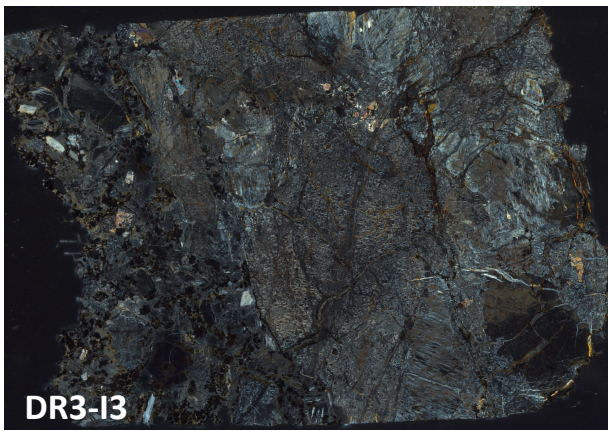




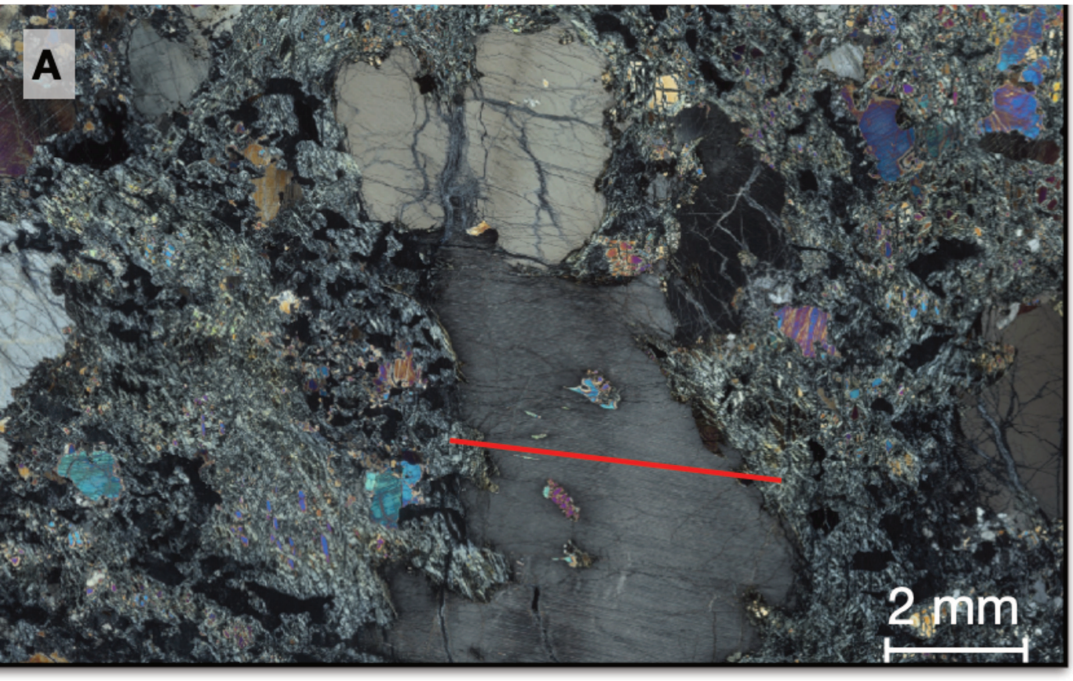
Fig. S1 – Core-to-rim zonation in an orthopyroxene from the pl-lherzolite DR06-161c.

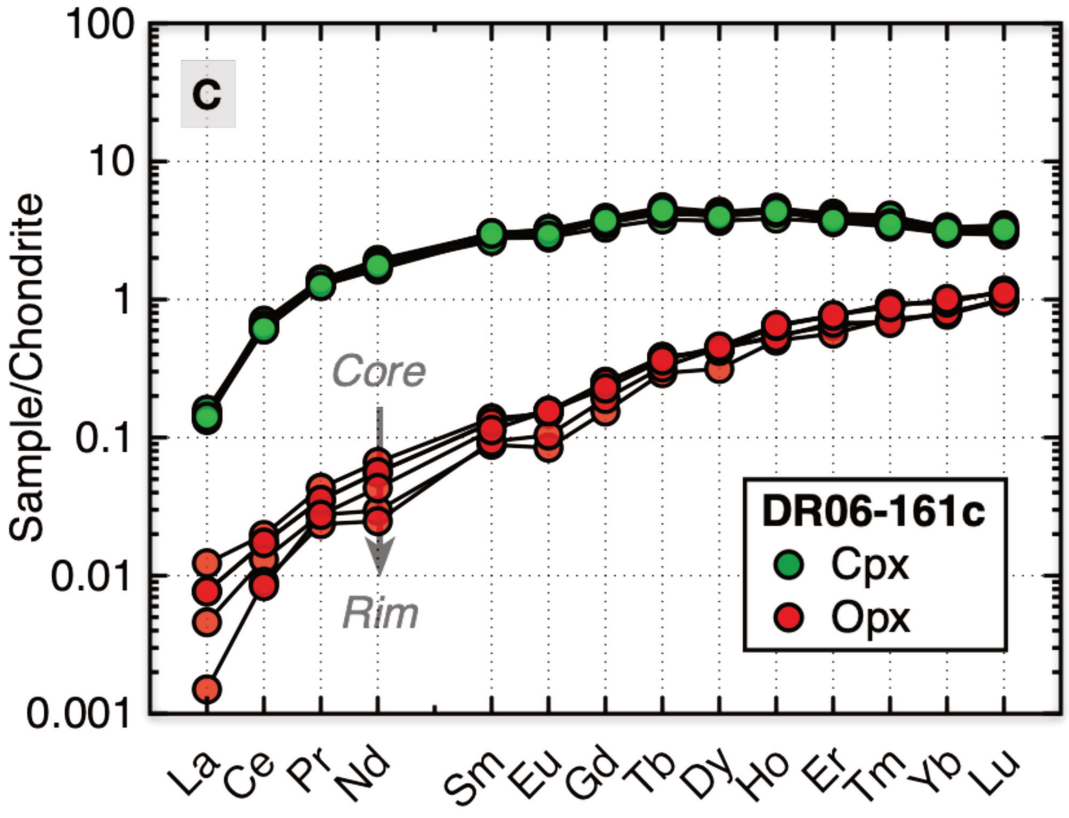
A: Orthopyroxene porphyroclast of sample MD110-DR06-161C analyzed by µ-XRF (XPL). The red line indicates the location of the rim-to-rim profile in panel B.

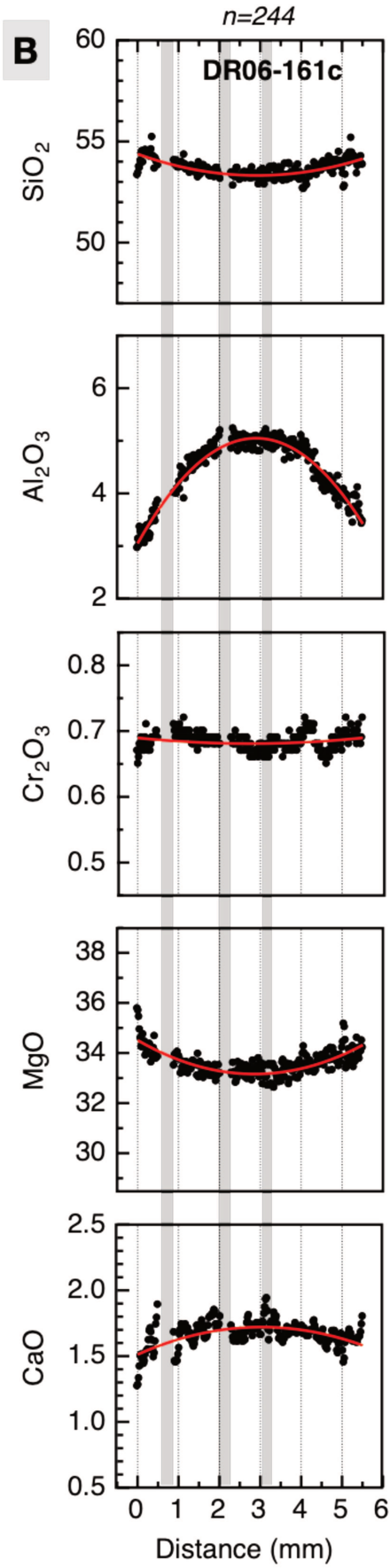
B: Rim-to-rim profile of major elements measured by µ-XRF (n = 244)

C: REE patterns showing a core-ro-rim zonation in orthopyroxene (normalized to C1 chondrites; Anders and Grevesse, 1989). No zonation is observed in clinopyroxene analyzed within the same sample.

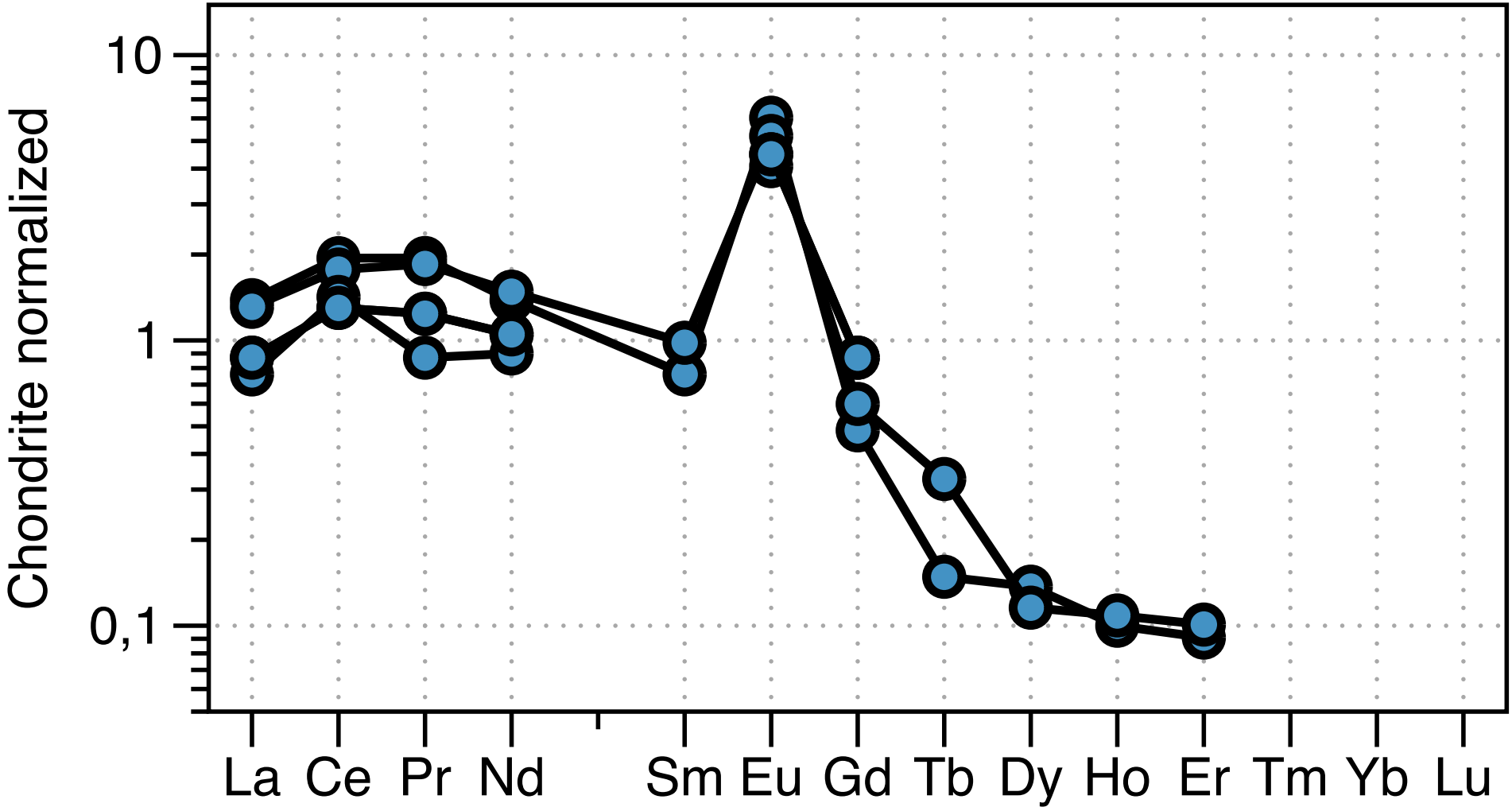
Fig. S2 - Rare earth element patterns of plagioclase in Pl-lherzolites from the Diamantina zone. REE are normalized to C1 chondrites (Anders and Grevesse, 1989).


A
2 mm


C
Sample/Chondrite
100
10
1
0.1
0.01
0.001
Core
Rim
DR06-161c
Cpx
Opx
La
Ce
Pr
Nd
Sm
Eu
Gd
Tb
Dy
Ho
Er
Tm
Yb
Lu


B
n=244
DR06-161c
SiO2
Al2O3
Cr2O3
MgO
CaO
Distance (mm)

Plagioclases



Annexes chapitre 2 - B2 - Localisation et descriptions pétrographiques des échantillons de dragage de la zone de Dia

Supplementary table: location and petrographic descriptions of the dredges samples from the Diamantina Zone

Dredge location	Sample no.	Rock type	Texture	Modal composition							Observat
				Ol	Cpx	Opx	Spl	Pl	Chlorite	Serp.	
MD110-DR02A 119°38,1'E 37°43,2'S	A03	Sp-lherzolite	Porphyroclastic	-	Trace	++	+	-	-	++++	
	A05	Sp-lherzolite	Protomylonitic	-	+	+	+	-	-	++++	
	A13	Sp-lherzolite	Protomylonitic	-	Trace	Trace	Trace	-	-	++++	crosscut
	A27	Sp-lherzolite	Porphyroclastic	-	+	+	+	-	-	++++	
	A40	Sp-harzburgite	Porphyroclastic	-	+	Trace	Trace	-	-	++++	<10% py
	A48	Sp-lherzolite	Porphyroclastic	-	+	+	Trace	-	-	+++	
	A50	Sp-lherzolite	Coarse-grained	-	+	++	Trace	-	-	+++	Large por
	A58	Sp-lherzolite	Coarse-grained	-	+	+	Trace	-	-	++++	
	A64	Sp-lherzolite	Porphyroclastic	-	+	+	+	-	-	++++	
	A66	Sp-lherzolite	Porphyroclastic	-	Trace	+	+	-	-	++++	
MD110-DR06 116°00,9'E 36°17,8'S	158A	Pl-lherzolite	Porphyroclastic	-	+	++	Trace	-	+	++++	Chlorite r
	158B	Pl-lherzolite	Porphyroclastic	-	+	+	Trace	-	+	++++	Chlorite r
	159B	Sp-Lherzolite	Porphyroclastic	+++	+	+	Trace	-	-	+++	
	160A	Pl-lherzolite	Porphyroclastic	-	+	+	Trace	-	+	+++	Chlorite r
	161A	Pl-lherzolite	Porphyroclastic	++	+	++	Trace	-	+	+++	Chlorite r
	161C	Pl-lherzolite	Coarse-grained	+	+	++	Trace	-	+	+++	Chlorite r
	162A	Pl-lherzolite	Porphyroclastic	-	+	++	Trace	-	+	+++	Chlorite r
	162B	Pl-lherzolite	Porphyroclastic	+	+	++	Trace	Trace	+	+++	Chlorite r
	162C	Peridotite	Porphyroclastic	-	+	+	Trace	-	-	+++	Undefined primary p
	164A	Pl-lherzolite	Coarse-grained	-	+	++	Trace	-	+	+++	Chlorite r
	167A	Pl-lherzolite	Porphyroclastic	-	+	+	Trace	-	Trace	+++	Chlorite r
	168	Pl-lherzolite	Protomylonitic	-	++	++	Trace	Trace	+	+++	Chlorite r
	172	Pl-lherzolite	Porphyroclastic	-	+	+	Trace	-	Trace	+++	Chlorite r
	173	Pl-lherzolite	Porphyroclastic	+	+	++	Trace	-	+	+++	Chlorite r
	B1	Pl-lherzolite	Coarse-grained	-	+	++	Trace	-	+	+++	Chlorite r
	B2	Pl-lherzolite	Coarse-grained	+	++	++	Trace	-	-	+++	
	B4	Pl-lherzolite	Coarse-grained	+++	++	++	Trace	-	+	+++	Chlorite r
	B5	Peridotite	Porphyroclastic	-	+	+	Trace	-	-	+++	Undefined primary p
	B7	Pl-lherzolite	Coarse-grained	-	+	++	Trace	-	+	+++	Chlorite r
	B8	Pl-lherzolite	Porphyroclastic	-	+	++	Trace	-	+	+++	Chlorite r
MD110-DR09 112° 14,5' E 36° 34,7' S	273	Sp-lherzolite	Protomylonitic	-	Trace	Trace	+	-	-	++++	
	273b	Sp-lherzolite	Protomylonitic	-	+	Trace	Trace	-	-	++++	
	275	Sp-lherzolite	Protomylonitic	-		Trace	+	-	-	++++	
	275b	Sp-lherzolite	Protomylonitic	-	-	++	+	-	-	++++	
	277	Sp-lherzolite	Protomylonitic	-	+	+	Trace	-	-	++++	
	279	Sp-lherzolite	Protomylonitic	-	+	+	Trace	-	-	++++	
	280	Sp-lherzolite	Protomylonitic	-	Trace	+	Trace	-	-	++++	
	280b	Sp-lherzolite	Protomylonitic	-	Trace	Trace	Trace	-	-	++++	
	281	Sp-lherzolite	Protomylonitic	-	Trace	Trace	Trace	-	-	++++	
	281b	Sp-lherzolite	Protomylonitic	-	+	Trace	Trace	-	-	++++	
MD80-DR3 106"54 E 36"30 S	3D2	Sp-lherzolite	Coarse-grained	-	+	-	Trace	-	Trace	++++	Highly we
	D4-1	Sp-lherzolite	Porphyroclastic	-	+	-	Trace	-	Trace	++++	Highly we
	D4-2	Sp-lherzolite	Porphyroclastic	-	+	-	Trace	-	Trace	++++	Highly we
	G2-2	Sp-lherzolite	Porphyroclastic	-	+	Trace	Trace	-	-	+++	Serpentin
	I2	Sp-lherzolite	Porphyroclastic	-	+	-	Trace	-	-	++++	Serpentin
	I3	Sp-lherzolite	Porphyroclastic	-	Trace	Trace	Trace	-	-	++++	Serpentin
	DR3	Sp-lherzolite	Porphyroclastic	-	Trace	-	Trace	-	-	+++	

Modal proportion : « - » not present; « Trace » < 1%; « + » 1-10%; « ++ » 10-30%; « +++ » 30-60%; «++++ » 60-100%.

Annexes chapitre 2 - B3 - Standards µ-XRF et LA-ICPMS

		Li7	B11	Na23	Mg24	Si29	K39	Ca43	Ca44	Sc45	Ti47	V51	Cr52	Co59	Ni60	Rb85	Sr88	Y89	Zr90	Nb93	Cs133	Ba137	La139	Ce140	Pr141	Nd146	Sm147	Eu153	Gd157	Tb159	Dy163	Ho165	Er166	Tm169	Yb172	Lu175	Hf178	Ta181	Pb208	Th232	U238
NG1_2904	610a-1	465	349	99777	432	327180	467	82175	81900	453	449	448	405	408	457	425	514	460	446	464	365	451	438	449	445	427	450	445	445	436	434	445	451	430	445	436	432	443	426	455	460
NG1_2904	610a-2	471	351	99213	432	327180	461	82157	82383	457	454	453	411	412	461	426	518	465	451	466	367	453	442	457	451	433	455	449	454	438	441	454	460	440	456	443	439	451	427	460	464
NG1_2904	610-3	466	349	98429	434	327180	466	82380	82441	455	450	448	409	410	459	427	516	459	446	467	368	453	441	455	448	432	456	448	450	440	441	449	457	436	452	441	435	445	425	456	460
NG1_2904	610-4	466	350	99575	429	327180	461	81653	81868	451	452	450	406	411	458	425	515	463	448	464	367	453	441	454	448	427	453	447	447	437	436	452	455	438	453	441	439	450	427	458	463
NG1_2904	610-5	470	348	100342	431	327180	464	82181	82302	457	453	453	408	410	457	428	516	463	449	465	365	452	439	456	452	433	452	445	449	435	435	447	454	433	447	435	430	445	425	457	460
NG1_2904	610-6	470	353	99080	435	327180	467	82356	81884	456	453	449	409	410	461	424	515	463	449	464	365	451	439	450	445	429	451	448	450	437	437	449	454	435	450	441	437	445	427	458	463
NG1_2904	612a-1	41	34.2	103606	57.9	336061	70	84111	84091	40.7	39.7	41.7	38.9	37.2	38.9	33.7	86.1	43.5	41.2	42.9	44.1	39.5	39.7	41.9	41.9	36.6	38.5	37.3	38.8	40.7	36.5	41.7	39.5	40.2	39.2	39.9	38	40.5	37	39.7	38.5
NG1_2904	612a-2	41.2	34.2	103396	57.9	336061	68	83958	83655	40.7	39.5	42.1	39.4	37.2	38.7	34	86.1	43.9	40.9	43	44.1	38.8	39.6	41.7	41.7	36	38.1	37.4	38.7	40.5	36.4	41.7	39.9	39.9	39.1	39.7	38.1	40.5	36.1	39.1	37.9
NG1_2904	612-3	39.3	33.3	114383	55.4	336061	66.6	80901	84213	39.4	38.5	40.2	37.3	35.4	37.6	32	82.3	42.2	39.4	40.9	42.3	38	37.8	39.6	39.5	34.2	36.5	35.2	36.7	38.6	35.1	39.2	37.7	38.5	37.2	37.6	36.4	38.2	35.6	37.7	36.9
NG1_2904	612-4	39.4	33.4	114083	55.3	336061	65.7	80667	83704	39.1	38.3	40.1	37.1	35.5	37.6	32.5	82.7	41.7	39.4	40.9	42.5	37.8	38.1	40.1	40.1	34.4	35.6	36	37.3	38.7	35.2	39.8	37.9	38.5	36.8	38	36.5	38.4	35.7	38	37
NG1_2904	612-5	40.1	33.7	110393	56.9	336061	68.2	82249	84850	40.4	38.1	41	37.8	35.9	38	32.7	83.1	42.4	40.2	41	42.4	37.6	38.4	40.3	40.3	34.5	37.1	35.5	36.7	39.1	35.8	39.6	38.2	38.6	38.3	38.4	36.5	38.6	35.7	38	37.1
NG1_2904	612-6	40.4	33.5	110347	56.9	336061	67.1	83327	84982	41	38.6	41.2	37.5	35.8	38.1	32.6	83.6	43	40.4	41.6	43.2	38.7	38.6	40.6	40.5	34.8	37.5	36.5	37.8	39.4	35.5	40.3	38.9	39.3	38.2	38.5	36.6	38.9	35.9	39	37.4
NG2_2904	610-7	468	348	100787	431	327180	466	81870	82072	453	450	450	408	409	455	422	510	459	444	462	364	448	437	448	445	427	447	442	445	432	432	445	452	432	445	436	430	441	421	452	457
NG2_2904	610-8	468	352	97659	433	327180	461	82407	82201	457	454	450	408	411	462	430	522	466	453	467	368	456	444	459	452	434	460	452	454	442	443	453	458	437	454	443	440	452	432	463	467
NG2_2904	610-9	470	351	99366	431	327180	465	82928	82363	455	452	451	409	412	457	426	514	463	447	464	367	453	439	452	448	430	454	447	450	437	438	450	456	436	450	439	436	447	426	459	461
NG2_2904	610-10	466	349	99525	434	327180	463	81474	81924	455	452	449	407	409	460	425	516	461	449	466	365	451	441	454	448	430	452	447	448	436	436	448	454	434	450	439	434	445	426	456	462
NG2_2904	612-7	40.6	33	110245	58.1	336061	68.9	82811	84658	40.1	38.3	40.9	38.7	36.7	38.6	33.6	85.9	42.9	40.1	42.5	44	38.6	39.1	41.7	41.5	35.2	37.3	36.4	37.8	39.9	35.6	40.5	38.5	39.2	37.5	38.5	36.5	39.4	37.6	38.7	39.2
NG2_2904	612-8	40.2	32.9	109471	57.4	336061	66	81943	84096	39.9	38.3	40.5	37.5	35.9	37.8	32.7	84.4	42	39.6	42.3	43.4	38.2	38.8	41.1	40.9	34.8	36.7	36.1	36.7	39.5	35.4	39.9	38.3	39	37.5	38.7	36.4	39.2	36.7	38.3	38.3
NG2_2904	612-9	41.1	34.8	98202	59.3	336061	69.8	85947	84213	41.4	40.7	41.9	38.5	37.2	39.6	34	87	43.2	40.9	43.5	44.5	40.7	39.9	41.9	41.6	35.3	38	37	38	39.9	35.8	40.8	38.8	40.1	38.7	39	37.7	39.9	38.1	38.9	38.4
NG2_2904	612-10	41.4	35.3	98013	59.8	336061	69.6	85624	83817	41.3	40.6	42.3	38.8	37.3	39.2	33.7	86.1	42.8	40.6	43.1	44.7	39.5	38.9	42.2	41.9	36	37.7	37.2	38.3	40.3	36.4	41.1	39.4	39.9	38.7	39.1	37.6	40.1	38.1	38.7	39.2
NG3_2904	610-11	471	352	98617	435	327180	467	82248	82226	456	452	452	409	411	461	427	519	463	451	466	367	454	442	453	447	429	452	447	449	435	435	447	455	434	448	437	433	446	424	456	460
NG3_2904	610-12	465	348	101218	428	327180	461	81941	82048	453	452	447	406	409	456	424	512	460	445	464	364	449	438	453	450	432	456	447	449	439	439	451	455	437	452	442	438	446	429	459	465
NG3_2904	610-13	467	349	98602	434	327180	465	82631	82195	456	450	449	407	410	458	427	518	462	449	467	367	453	441	455	448	433	454	447	449	437	438	449	457	435	452	440	435	446	424	457	461
NG3_2904	610-14	469	351	100191	430	327180	463	81716	82101	454	455	451	409	410	460	424	514	462	448	463	365	451	439	451	448	428	452	447	449	437	436	449	453	435	448	438	435	446	427	457	462
NG4_2904	612-11	40.9	34.6	103711	58.6	336061	77.8	85026	85465	41.2	39.9	41.8	39.1	37.3	39.4	34.1	86.6	43.6	40.8	43.1	44.9	39.7	39.3	42.3	42.1	35.8	38.5	37.4	38.4	39.9	36.6	41.1	40	40.1	38.9	39	37.8	39.9	39.3	39.4	39.3
NG4_2904	612-12	40.8	34.8	106799	58.3	336061	70.7	84295	85442	41.1	39.5	41.4	38.8	37	39.6	33.8	86.2	43.2	40.6	42.4	44.2	39.7	39	41.5	41.5	35.7	37.8	36.7	38.8	40.4	36.7	41.1	39.5	40	39.3	39.3	38.3	40	39.1	39.5	39
NG4_2904	612-13	41.2	35.6	98260	59.2	336061	71.8	85403	84946	41.2	39.6	42.6	39.6	37.8	40.3	34.2	87.1	43.6	41.3	43.6	44.6	39.5	39.2	41.6	41.5	36.1	37.9	36.8	38.7	39.9	36.6	41.3	40.1	40	39.1	38.9	37.8	39.7	38	38.8	38.9
NG4_2904	612-14	41	33.7	97619	58.1	336061	71	85403	84411	41.3	39.6	41.8	38.9	37.3	39.7	33.9	85.8	42.6	40.4	42.7	43.4	38.9	38.9	41.5	41.4	35.8	37.9	37	38.2	39.6	36.3	40.4	39.6	39.7	38.5	38.7	38.1	39.8	38.1	39	38.8
NG4_2904	610-15	468	351	101872	432	327180	465	82609	82978	459	454	455	412	413	464	430	518	466	450	467	367	453	441	454	448	430	455	447	451	440	441	452	458	438	454	441	433	448	423	457	461
NG4_2904	610-16	468	349	97532	432	327180	463	81711	81604	451	450	447	405	408	455	422	514	459	446	464	365	451	439	452	448	430	452	447	448	434	434	446	451	432	447	438	437	445	430	458	463
NG4_2904	610-17	470	350	101067	433	327180	464	82041	82194	452	451	453	409	411	459	427	515	459	446	466	367	453	440	454	448	430	453	449	448	435	434	446	453	432	449	434	430	443	426	452	460
NG4_2904	610-18	466	350	98269	431	327180	464	82271	82133	457	453	448	407	410	459	424	517	466	451	464	364	451	440	452	448	430	453	445	450	440	442	453	457	438	451	444	441	449	426	464	464
NG4_2904	612-15	42	34.4	100622	61.7	336061	70.9	85914	84963	43.5	40.1	45.8	41.4	39.3	39.6	35.3	93.1	45.9	41.8	47.2	46.2	40.2	42	44.5	44.6	35.7	38.4	38.6	37.8	41.1	36	41.9	39.7	40.4	38.6	39.5	37.7	41.5	37	39.7	39.6
NG4_2904	612-16	37.7	32.3	115171	57.6	336061	65.6	79759	84443	42.2	36.9	42.5	38.3	36.3	36.1	31.9	85.7	44.3	40.7	43.3	41.8	36.1	38.1	39.9	39.8	32.2	35	34.7	35.6	39	34.9	40.9	38.4	39.8	37.3	38.8	36.7	39.2	33.8	37.5	35.6
NG4_2904	612-17	41.2	33.8	102967	60.2	336061	76.8	83699	83914	43.1	39.4	44	39.6	37.8	39.4	34.2	88.3	44.8	41.1	44.5	44.4	39	39.5	42.3	42.1	35.4	37.6	37	37.3	39.7	35.5	40.2	38.6	39.4	38.2	38.5	37.5	39.9	36.8	38	37.9
NG4_2904	612-18	41.9	34.5	95355	61.2	336061	70.8	86055	84352	44.2	40.9	45	39.9	38.6	39.5	34.7	89.5	45.9	42.6	45.2	44.9	39.5	39.8	42.7	42.7	36.3	38.6	37.5	38.3	40.9	36.7	41.4	39.4	39.7	38.9	39.3	38.1	40.1	37.1	38.5	38
Session 1 - day1	G_NIST610	468	350	99507	432	327180	464	82153	82157	455	452	450	408	410	459	426	516	462	448	465	366	452	440	453	448	430	453	447	449	437	437	449	455	435	450	439	435	446	426	457	462
Session 1	2SD	3.94	2.69	2461	3.77	0	4.21	760	591	4.6	3.51	4.74	3.77	2.83	4.85	4.4	5.44	4.97	4.71	3.09	2.63	3.63	3.58	5.25	4.29	4.44	5.66	4.36	4.82	4.76	6.48	5.68	5.18	5.42	6.12	5.93	7	5.71	5.08	6.31	4.5
Session 1	RSD (%)	0.42	0.38	1.24	0.44	0	0.45	0.46	0.36	0.51	0.39	0.53	0.46	0.34	0.53	0.52	0.53	0.54	0.53	0.33	0.36	0.4	0.41	0.58	0.48	0.52	0.62	0.49	0.54	0.54	0.74	0.63	0.57	0.62	0.68	0.68	0.8	0.64	0.6	0.69	0.49
Session 1																																									
Session 1	G_NIST612	40.6	34	105147	58.3	336061	69.8	83727	84456	41.2	39.2	42.1	38.7	37	38.8	33.5	86.1	43.4	40.7	43	43.9	38.9	39.1	41.5	41.4	35.3	37.5	36.7	37.8	39.8	35.9	40.7	39	39.6	38.3	38.9	37.3	39.7	37	38.7	38.2
Session 1	2SD	2.04	1.73	12829	3.42	0	6.64	3941	1113	2.69	2.1	3.09	2.13	2.1	2.07	1.85	5.13	2.38	1.58	3.12	2.25	2.16	1.87	2.35	2.37	2.04	1.99	1.85	1.8	1.4	1.19	1.51	1.5	1.22	1.53	1.13	1.42	1.65	2.75	1.35	2.14
Session 1	RSD	2.51	2.55	6.1	2.93	0	4.76	2.35	0.66	3.26	2.68	3.68	2.75	2.84	2.67	2.77	2.98	2.75	1.95	3.62	2.57	2.78	2.39	2.83	2.86	2.89	2.65	2.52	2.38	1.76	1.65	1.86	1.92	1.54	1.99	1.46	1.9	2.08	3.72	1.74	2.8
Session 1	Trueness (%)	1.08	0.87	1.24	14.23	0.29	12	1.5	0.64	3.29	10.81	8.36	6.37	4.12	0.13	6.79	9.8	13.3	7.28	10.5	2.73	1.07	8.72	8.11	9.26	0.66	0.59	3.04	1.27	5.96	1.23	6.3	2.67	7.52	2.22	4.99	1.75	5.45	4.11	2.37	2.08
NG1_2804	610-1	468	350	94341	434	327180	468	82351	82005	454	451	451	410	416	468	429	522	464	453	469	369	458	447	458	456	438	460	451	450	439	440	450	461	438	455	439	440	448	425	456	460
NG1_2804	610-2	469	350	94056	436	327180	462	82477	82347	458	453	456	413	414	471	432	522	470	453	469	372	461	448	459	456	437	460	454	459	447	448	456	461	440	458	448	441	452	432	465	467
NG1_2804	610-3	470	353	104659	429	327180	462	81855	82546	456	452	446	406	400	447	418	503	459	444	460	362	446	432	448	442	421	445	443	449	433	432	447	450	431	445	437	432	444	424	454	459
NG1_2804	610-4	466	347	104603	430	327180	464	81892	81679	452	452	446	403	410	449	424	515	455	442	461	361	443	434	447	439	424	446	440	438	428	428	442	448	431	442	432	427	441	424	453	460
NG1_2804	612-1	40.1	36.2	99052	58.1	336061	66.9	84789	84861	42.6	40.6	43	40.2	38.8	40.2	34.9	91.3	46.1	42.6	45.5	47.4	40.3	43	44.4	45.2	37.2	39.4	39.2	40.4	43.8	37.7	44.5	40.8	43.2	40.4	42.9	39.3	43.5	39.8	42.6	41.7
NG1_2804	612-2	40.4	34.6	98664	58.6	336061	66.3	84772	85049	42	39.9	42.7	40	38.7	39.9	35.1	90.6	45.7	41.9	45.2	47.3	40.1	42.7	44.6	44.9	36.9	39.6	39.2	39.5	43.7	37.7	44.3	41.1	42.7	39.8	42.6	39.9	43.4	40.2	42.7	42.1
NG1_2804	612-3	40.7	35.4	109982	58.3	336061	66.6	83586	85145	41.5	38.6	41.5	39.1	36.8	38.1	33.6	88.2	43.9	40.5	43.7	45.5	39.4	41.2	43.3	43.4	35.9	37.8	38	38.3	41.8	36.2	42.7	39.4	41.4	38.7	41.3	38.4	41.5	39.3	41	40.4
NG1_2804	612-4	40.5	34.5	108951	58.1	336061	65	83493	84887	42.1	38.7	42.5	38.8	36.8	37.7	33.8	87.9	44.4	40.8	43.8	45	38.6	41.4	43.2	43.4	35.8	38.1	37.7	38.4	42.5	36.9	42.7	39.5	41.6	39	41.3	38.2	41.5	39.3	40.9	40.5
NG2_2804	610-5	461	345	94723	434	327180	465	82862	82372	456	449	449	405	409	463	423	505	454	443	463	369	451	440	451	446	428	453	448	448	437	433	445	451	430	448	437	433	443	425	455	461
NG2_2804	610-6	460	350	96061	430	327180	468	82722	81423	447	455	450	409	412	460	425	514	454	440	463	367	452	439	454	449	429	453	446	443	431	434	443	449	431	448	436	434	445	429	457	466
NG2_2804	610-7	471	354	102665	434	327180	463	81700	82258	456	451	452	413	410	460	431	525	469	451	466	365	451	439	455	449	429	453	444	448	438	438	450	456	436	451	439	435	448	422	455	462
NG2_2804	610-8	480	351	104211	430	327180	460	81292	82523	461	454	449	405	409	452	425	518	470	458	468	363	454	442	452	448	433	454	450	457	442	443	459	463	443	453	445	438	448	428	462	457
NG2_2804	612-5	41.1	33.6	101400	58.4	336061	68.2	84491	84781	42	38.8	41.9	39	37.2	39.5	34.3	88.5	45.1	42	44.8	47.1	40.3	41.6	43.0	43.6	35.6	38.3	37.9	39.3	42.7	37.4	43.2	40.4	41.8	39.6	41.5	38.9	42.1	40	41.2	40.9
NG2_2804	612-6	41.4	35.7	101364	58.9	336061	65.9	84333	85110	41.8	39.8	42.4	39.2	37.7	39.3	33.9	88.2	45.2	41.6	44.1	46.5	40	41.5	44.0	43.9	36.3	38.8	38.5	39.3	42.8	37.3	43.6	40.5	41.9	39.7	41.7	38.7	42.2	39.6	41.2	41
NG2_2804	612-7	42.2	35.9	109324	59.7	336061	66.5	84983	85102	40.9	39.7	42.2	39.7	37.7	39.2	34.4	88.8	44.4	41.1	44.7	46	39.5	40.6	43.3	43.5	35.5	37.5	37.9	37.8	41.5	35.9	41.8	39	40.6	37.9	40	36.9	40.7	39	39.3	40
NG2_2804	612-8	41.6	35.2	109207	59.2	336061	66.5	84044	85680	42	39	42.3	39.1	37.1	37.9	34	87	45.1	41.6	44.1	45.6	38.7	40.7	42.6	43.3	35.4	37.6	37.6	38.7	42.1	36.5	42.2	39.2	41.2	38.4	41.2	38.4	41.5	39.6	40.2	39.7
NG3_2804	610-9	483	368	98395	443	327180	468	82731	82152	458	460	454	416	416	469	429	516	461	447	466	365	453	438	451	445	428	450	444	447	436	435	445	453	433	447	434	431	443	426	454	459
NG3_2804	610-10	457	338	100283	422	327180	460	81465	82147	452	445	446	400	405	449	422	515	463	449	464	367	450	443	455	451	433	459	450	451	438	439	452	457	437	454	445	441	451	427	461	464
NG3_2804	610-11	468	349	99298	431	327180	466	82026	81981	452	453	450	412	412	457	425	516	461	449	464	366	450	440	454	447	427	451	447	445	436	434	447	453	431	448	437	431	442	423	453	461
NG3_2804	610-12	469	351	99485	434	327180	462	82288	82325	458	451	450	405	407	461	427	515	462	447	466	366	454	440	452	450	434	455	447	453	438	440	451	457	439	453	440	438	450	430	461	462
NG3_2804	612-9	39.6	31.4	105530	57.1	336061	66.8	81599	84292	41.8	38.1	42.1	38.6	37.6	37.8	34.2	88.5	45.5	41.4	44.4	45.2	38.8	41.9	43.8	44.5	35.7	38.6	38.3	38.8	43.3	37.1	44.1	40.5	42.7	39.9	41.9	38.9	43	39.3	41.5	41
NG3_2804	612-10	39.7	32.3	106592	56.4	336061	65.2	81041	84472	41	37.6	41.4	38.5	37.6	37.8	33.7	88.9	44.7	41	44.4	45.7	38.5	41.3	43.5	43.5	34.9	37.2	37.6	38	42.6	36.4	43.3	39.6	41.2	38.5	40.9	37.9	41.7	38.8	41.0	40.5
NG3_2804	612-11	40.7	34.3	111446	57	336061	67.5	83374	85206	41	39	42.3	39.8	37.8	39.4	34.6	87.5	43.9	40.6	43.5	45.2	39.4	40.4	43.0	43.5	35.9	37.6	38.1	38.8	41.5	35.8	41.9	39.00	40.5	38.5	40.1	37.6	40.8	37.9	39.7	39.3
NG3_2804	612-12	40.3	34.9	113962	56.8	336061	66.3	83523	85268	40.9	39.3	41.5	39	37.2	38	34.1	87.5	43.7	40.6	43.5	44.8	39.4	40.4	42.8	42.8	35.7	37.6	37.8	37.7	41.2	35.6	42	38.7	40.4	38.4	39.6	37.2	40.7	37.8	39.8	39.9
NG4_2804	610-13	470	351	99930	435	327180	471	82372	82107	456	454	453	412	410	460	424	516	461	447	466	365	452	440	453	448	431	451	444	448	436	435	448	454	435	450	439	435	447	424	456	461
NG4_2804	610-14	466	350	98634	429	327180	459	81932	82185	454	451	447	405	410	457	427	515	463	449	464	368	452	440	453	448	429	456	450	450	438	439	450	456	435	450	439	435	445	428	458	462
NG4_2804	610-15	470	350	100765	435	327180	467	82022	82125	457	454	455	411	411	462	426	515	462	446	468	366	453	441	453	450	433	453	448	450	439	440	453	456	437	451	440	436	448	429	461	466
NG4_2804	610-16	466	350	98082	430	327180	461	82291	82162	454	450	447	406	409	456	425	516	462	450	463	366	451	439	453	446	427	453	446	448	436	435	446	454	434	449	438	435	445	423	455	458
NG4_2804	612-13	39.5	29.1	111249	56.5	336061	64.8	81388	83992	40.5	38.2	41.5	36	37.1	38.7	33.4	86.2	43.4	40.3	42.9	43.7	37.8	39.9	42.3	42.2	35.4	37.3	37.3	37.9	41.2	35.9	42.1	39.6	40.3	38.5	40.1	37.8	40.6	34.7	39.9	39.4
NG4_2804	612-14	40	33.9	106284	57.7	336061	66.2	83671	84725	41.3	39	41.6	39	37.2	38.5	33.9	87.3	43.8	40.8	43.5	44.8	38.6	40.1	42.5	42.9	35.5	38.5	37.9	38

The role of mantle inheritance and refertilisation during breakup at magma-poor rifted margins: what can we learn from the SW-Australia margin?

Supplementary materials

1. In situ major element concentrations

Although it is an unconventional technique, benchtop micro-X-Ray Fluorescence (µ-XRF) has gained significant interest in the geosciences over the past decade. Its non-destructive nature and its ability to produce large-scale chemical maps and accurately determine the bulk rock concentrations of major and even some trace elements make it a valuable tool in this field (e.g. Flude et al., 2017; Vansteenberge et al., 2020, Kaskes et al., 2021). Semi-quantitative data can be acquired by Fundamental Parameter based "standardless" quantification of X-ray spectra. However, quantitative analyses on thin section (in a similar manner to electron microprobe analysis, EPMA) are more difficult to achieve, since: (i) accurate quantification requires appropriate standards and a type-calibration to correct the data; (ii) thin section of 30 µm corresponds to sample of a non-infinite thickness, which may cause underestimation of concentrations for some elements. Infinite thickness is defined as the minimum requisite thickness of a sample to absorb all the x-rays of the primary X-ray beam emitted from an XRF instrument. If the infinite thickness is not met, then some of the X-rays are lost from the sample, resulting in an underestimation of some elements. To ascertain which elements are affected by non-infinite thickness for a 30µm thin section, we plotted in Figure S1 below the information depth (i.e. depth of Kα penetration) for all elements in increasing Z order calculated for different silicate matrixes. The aforementioned calculations demonstrate that a 30 µm thin section cannot be considered of an infinite thickness for elements heavier than V. This effect may thus results in significant underestimations of some major element concentrations like Fe.

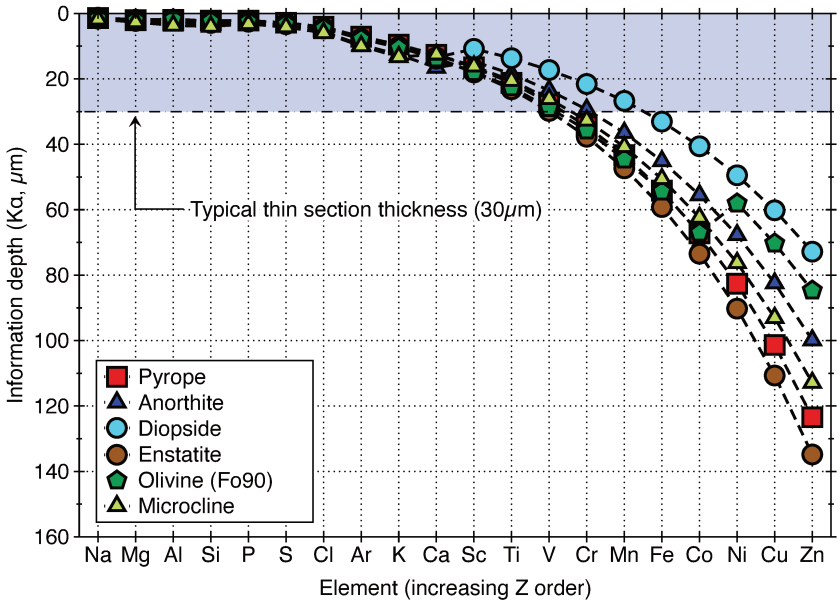


Figure S1: Information depth calculated for elements from Z=11 to Z=30 (assuming a Rh source at a voltage of 50kv and a pressure of 2 mbar). Among the major and minor elements analyzed by µ-XRF, Cr, Mn, Fe and Ni are excited at depth > 30 µm.

In this study, we present in situ major element concentrations of silicate minerals (olivine, pyroxenes, plagioclase) and oxides (spinel) determined by µ-XRF, using a Bruker M4 Tornado at Institut Terre et Environnement de Strasbourg (ITES, France). Our original approach was to prepare mineral standards as thin sections and deconvolute µ-XRF spectra by applying the Fundamental Parameter (FP) quantification method, which is commonly used for matrix correction in quantitative analysis of samples of less than infinite thickness (Sitko, 2009). A series of 12 microbeam standards of the Smithsonian National Museum of Natural History (NMNH, Jarosewich et al., 1980) were mounted into an epoxy resin section, fixed to a glass slide, lapped and polished down to 30 µm-thick. µ-XRF spectra were then acquired on these standards using a Rh anode operating at 400 µA for silicates and 150 µA for spinel, with an accelerating voltage of 50 kV. Polycapillary lenses were used to focus the X-ray beam down to 20 µm full-width-at-half-maximum at the sample surface. The counting time per point was set to 180 s. µ-XRF spectra were deconvoluted using the Bruker Esprit software, which allowed to calculate concentrations by using the standardless FP quantification method. The accuracy of quantification was improved by the application of correction factors determined after ~30 repeated analyses of each NMNH mineral standards. The results of quantification for NMNH mineral standards and Enstatite 131709 (McGuire et al., 1992) analyzed as unknown reproduced with a precision better than 5% (1σ) and an accuracy of 5% or better from accepted values for most analytes (Figure S2, see also supplementary table 1 for all results). This also illustrates that our approach provides precise and accurate data even for the heaviest elements that are concerned by the non-infinite thickness of the thin section.

In addition to reference materials, the concentrations of some crystals previously determined by µ-XRF were also measured by EPMA. In most cases, the analyses are aligned along the 1:1 line. Nevertheless, occasional small dispersions are observed for pyroxenes, particularly in MgO and CaO. These dispersions are likely the result of the simultaneous analysis of thin exsolution lamellae of the companion pyroxene due to the large spot size of the µ-XRF, which is approximately 10 times larger than that of the EPMA. Consequently, for minerals that were insufficiently sized to be analyzed by µ-XRF (less than two times the spot size of µ-XRF, typically for mineral inclusions or pyroxene with tightened exsolution lamellae), supplementary analyses were conducted with a CAMECA SX100 EPMA at Service Commun de Microscopie Électronique et de Microanalyses (SCMEM, Nancy, France). All analyses of major elements, Na, Mg, Al, Si, K, Ca, Ti, Cr, Mn, Fe, Ni, were made against natural and synthetic mineral standard: albite (Si, Na), corundum (Al), andradite (Ca), olivine (Mg), hematite (Fe), $MnTiO_3$ (Mn,Ti), NiO (Ni), orthoclase (K). Acceleration voltage and beam current were 15 kV and 12 nA, respectively, the counting time was 10 s. The beam was focused to ~2 µm. Structural formulae were calculated based on the following number of oxygens: olivine, 4; pyroxenes, 6; spinel, 8. The whole dataset is available as supplementary table 1.

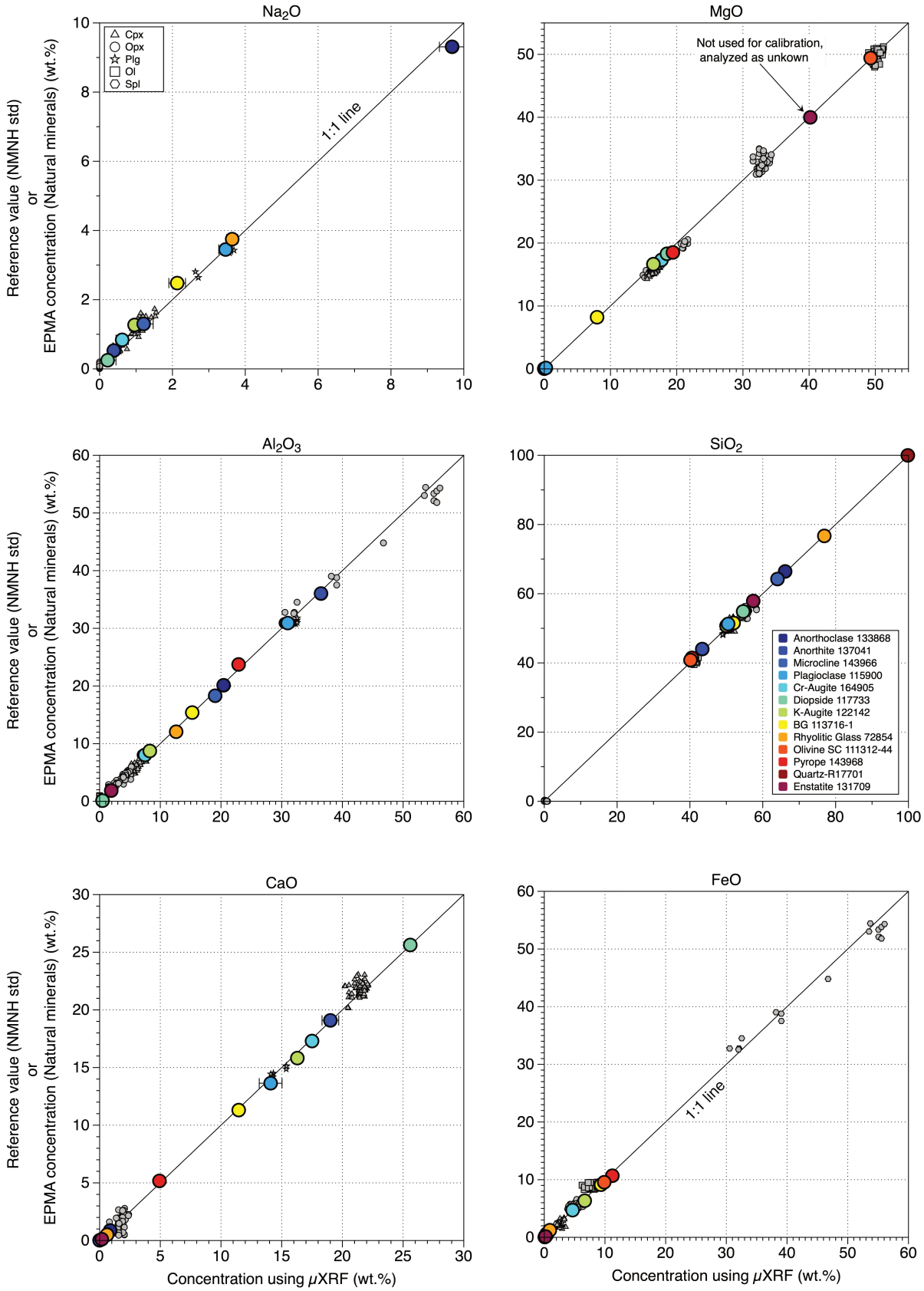


Figure 2: μ-XRF concentrations vs. NMNH microbeam standard values (large colored dots) and EPMA concentrations of crystals analyzed by the two methods (grey points)

2. µ-XRF chemical maps

µ-XRF chemical maps were recorded on-the-fly with an accelerating voltage of 50 kV and a beam current of 400 µA. The acquisition time was 3 ms per pixel, with a total of approximately 40 cycles (dwell time of ~120 ms per pixel) and a 20 µm step interval in both directions. The scale bar on each map corresponds to the intensity of the Kα lines of the elements (Mg, Al, Si, Ca, Cr, Fe, and Ni) calculated from the integration of a specified region of interest (ROI) within the energy range of the XRF spectra. Subsequently, ROI maps are employed to generate phase maps through the utilization of a Matlab-based code, previously developed by Muñoz et al. (2008) and Ulrich et al. (2014). The phase map calculation begins with the determination of pure mineral phases that are anticipated to be present in the sample, with the objective of creating standard spectra. Subsequently, a linear combination of the various standard spectra is performed for each pixel of the map, with the aim of fitting each individual spectrum. The resulting maps provide quantitative information regarding the distribution of minerals that have been previously identified in the sample, based on observations made under a microscope, X-ray diffraction (XRD) and/or Raman analyses. Quantified maps were calculated based on ROI maps, applying to each pixel the same type-calibration as for in situ measurements (Figure S3).

3. Mineral trace element concentrations

The mineral trace element concentrations were determined by LA-ICP-MS at Georessources Nancy. This method involves a laser nanosecond excimer 193nm from ESI New Wave Research combined to an Agilent 8900 QQQ ICP-MS. Laser ablations were performed with a constant 5 Hz pulse rate, with an ablation crater of 60–80 µm in diameter except for olivine where ablation crater was set to 120 µm to improve the signal/noise ratio. The number of pulses was 200, which is sufficient to form a long and stable signal for integration. The ablated material is transported using a constant He flow and mixed with Ar in a cyclone coaxial mixer before entering the ICP torch and being ionized. The ions are then sampled, accelerated, and focused before being separated and analyzed in the mass spectrometer. Gas blank was collected for 30 seconds after every ablation of standards and unknowns and subtracted to the raw counts. ^{29}Si concentrations (previously known from µ-XRF and EPMA measurements) were used as the internal standard, and the NIST SRM 610 synthetic rhyolitic glass (Pearce et al., 1997) was used for calibration. The NIST SRM 612 and BHVO-2 standards were run as unknown every 10 analyses (~1 hour) during and after calibration and interspersed between mineral analyses for drift regression calculation to ensure precision and accuracy of the measurements. Data reduction was performed using Iolite 4 software (Hellstrom et al., 2008; Paton et al., 2011), following the standard methods of Pettke et al. (2012). Drift regression was assumed to be linear and drift corrected analyses of NIST SRM 612 reproduced with a precision better than 5% (1σ) for all elements. Standard BHVO-2 was also analyzed every ~1 h and analyses after drift correction obtained from NIST SRM 612 also reproduced within 5% for all elements. Accuracies on NIST SRM 612 and BHVO-2 were 5% or better and between 5 and 10%, respectively from accepted values from the GeoReM database (Jochum et al., 2005) (Supplementary data).

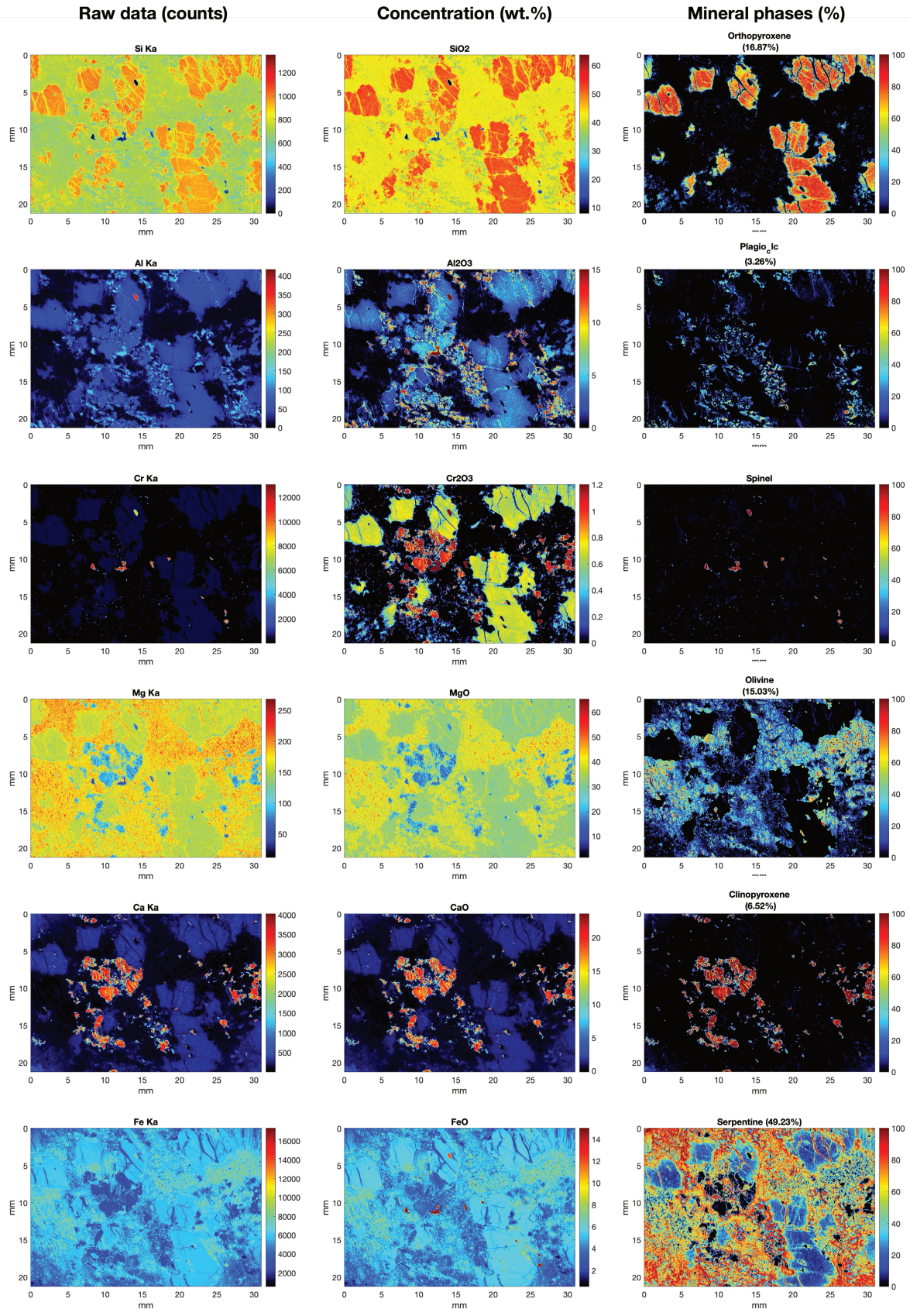


Figure S3: µ-XRF ROI (left), concentration (center) and mineral phase (right) maps of sample MD110-DR06-161c (see section 2. µ-XRF chemical maps for additional information about the acquisition of ROI maps and subsequent calculations of concentration and mineral phase maps).

References

Flude, S., Haschke, M., Storey, M., Harvey, J., 2017. Application of benchtop micro-XRF to geological materials. Miner. Mag. 81, 923–948. https://doi.org/10.1180/minmag.2016.080.150

Hellstrom, J., Paton, C., Woodhead, J. and Hergt, J., 2008. Iolite: software for spatially resolved LA-(quad and MC) ICPMS analysis. Mineralogical Association of Canada short course series, 40, 343-348.

Jarosewich, E., Nelen, J.A., Norberg, J.A., 1980. Reference Samples for Electron Microprobe Analysis. Geostandard Newsletters 4, 43–47. https://doi.org/10.1111/j.1751-908x.1980.tb00273.x

Jochum, K.P., Nohl, U., Herwig, K., Lammel, E., Stoll, B., Hofmann, A.W., 2005. GeoReM: A New Geochemical Database for Reference Materials and Isotopic Standards. Geostand. Geoanalytical Res. 29, 333–338. https://doi.org/10.1111/j.1751-908x.2005.tb00904.x

Kaskes, P., Déhais, T., de Graaff, S.J., Goderis, S., and Claeys, P., 2021. Micro–X-ray fluorescence (μXRF) analysis of proximal impactites: High-resolution element mapping, digital image analysis, and quantifications. Large Meteorite Impacts and Planetary Evolution VI: Geological Society of America Special, 550, 171–206, https://doi.org/10.1130/2021.2550(07)

McGuire, A.V., Francis, C.A., Dyar, M.D., 1992. Mineral standards for electron microprobe analysis of oxygen. American Mineralogist 77, 1087–1091.

Muñoz, M., Pascarelli, S., Aquilanti, G., Narygina, O., Kurnosov, A., Dubrovinsky, L., 2008. Hyperspectral μ-XANES mapping in the diamond-anvil cell: analytical procedure applied to the decomposition of (Mg,Fe)-ringwoodite at the upper/lower mantle boundary. High Press. Res. 28, 665–673. https://doi.org/10.1080/08957950802517625

Paton, C., Hellstrom, J., Paul, B., Woodhead, J., Hergt, J., 2011. Iolite: Freeware for the visualisation and processing of mass spectrometric data. J. Anal. At. Spectrom. 26, 2508–2518. https://doi.org/10.1039/c1ja10172b

Pearce, N.J.G., Perkins, W.T., Westgate, J.A., Gorton, M.P., Jackson, S.E., Neal, C.R., Chenery, S.P., 1997. A Compilation of New and Published Major and Trace Element Data for NIST SRM 610 and NIST SRM 612 Glass Reference Materials. Geostand. Newsl. 21, 115–144. https://doi.org/10.1111/j.1751-908x.1997.tb00538.x

Pettke, T., Oberli, F., Audétat, A., Guillong, M., Simon, A.C., Hanley, J.J., Klemm, L.M., 2012. Recent developments in element concentration and isotope ratio analysis of individual fluid inclusions by laser ablation single and multiple collector ICP-MS. Ore Geol. Rev. 44, 10–38. https://doi.org/10.1016/j.oregeorev.2011.11.001

Sitko, R., 2009. Quantitative X-ray fluorescence analysis of samples of less than 'infinite thickness': Difficulties and possibilities. Spectrochim. Acta Part B: At. Spectrosc. 64, 1161–1172. https://doi.org/10.1016/j.sab.2009.09.005

Ulrich, M., Muñoz, M., Guillot, S., Cathelineau, M., Picard, C., Quesnel, B., Boulvais, P., Couteau, C., 2014. Dissolution–precipitation processes governing the carbonation and silicification of the serpentinite sole of the New Caledonia ophiolite. Contrib. Miner. Pet. 167, 952. https://doi.org/10.1007/s00410-013-0952-8

Vansteenberge, S., Winter, N.J. de, Sinnesael, M., Xueqin, Z., Verheyden, S., Claeys, P., 2020. Benchtop μXRF as a tool for speleothem trace elemental analysis: Validation, limitations and application on an Eemian to early Weichselian (125–97 ka) stalagmite from Belgium. Palaeogeogr., Palaeoclim., Palaeoecol. 538, 109460. https://doi.org/10.1016/j.palaeo.2019.109460

B.5. Table de données – compositions chimiques en éléments majeurs des clinopyroxènes

Analysis	Mineral	Analytical method	Location	Sample	Rock type	Texture	Mineral	Na_2O	MgO	Al_2O_3	SiO_2	K_2O	CaO	TiO_2	Cr_2O_3	MnO	FeO	Total	Na	Mg	Al	AlIV	AlVI	Si	K	Ca	Ti	Cr	Mn	Fe_2	Total
MD110-DR02-A03 00	Cpx	µXRF	MD110-DR02	A03	Sp-lherzolite	Porph.	Core	1.07	15.57	7.61	52.69	0.01	20.15	0.36	0.92	0.04	1.51	99.93	0.08	0.84	0.32	0.10	0.23	1.90	0.00	0.78	0.01	0.03	0.00	0.05	4.00
MD110-DR02-A03 00	Cpx	µXRF	MD110-DR02	A03	Sp-lherzolite	Porph.	Core	1.00	15.48	6.08	51.37	0.02	22.40	0.48	0.78	0.07	2.24	99.92	0.07	0.84	0.26	0.14	0.12	1.86	0.00	0.87	0.01	0.02	0.00	0.07	4.00
MD110-DR02-A03 00	Cpx	µXRF	MD110-DR02	A03	Sp-lherzolite	Porph.	Core	0.98	16.16	7.56	50.65	0.02	20.29	0.44	0.98	0.07	2.52	99.67	0.07	0.87	0.32	0.17	0.15	1.83	0.00	0.79	0.01	0.03	0.00	0.08	4.00
MD110-DR02-A03 01	Cpx	µXRF	MD110-DR02	A03	Sp-lherzolite	Porph.	Core	1.11	15.36	6.40	50.85	0.03	22.33	0.49	0.82	0.07	2.45	99.91	0.08	0.83	0.27	0.16	0.11	1.84	0.00	0.87	0.01	0.02	0.00	0.07	4.00
MD110-DR02-A05 00	Cpx	µXRF	MD110-DR02	A05	Sp-lherzolite	Porph.	Core	0.87	16.19	5.97	51.16	0.05	22.52	0.15	0.67	0.08	2.08	99.74	0.06	0.87	0.25	0.15	0.10	1.85	0.00	0.87	0.00	0.02	0.00	0.06	4.00
MD110-DR02-A13 00	Cpx	µXRF	MD110-DR02	A13	Sp-lherzolite	Porph.	Core	0.55	16.62	6.18	51.27	0.01	21.38	0.24	0.96	0.07	2.63	99.91	0.04	0.90	0.26	0.14	0.12	1.86	0.00	0.83	0.01	0.03	0.00	0.08	4.00
MD110-DR02-A13 00	Cpx	µXRF	MD110-DR02	A13	Sp-lherzolite	Porph.	Core	0.52	16.38	5.89	51.14	0.01	21.83	0.37	0.89	0.08	2.59	99.70	0.04	0.89	0.25	0.14	0.11	1.86	0.00	0.85	0.01	0.03	0.00	0.08	4.00
MD110-DR02-A13-11	Cpx	EPMA	MD110-DR02	A13	Sp-lherzolite	Porph.	Core	0.48	15.71	4.85	50.87	0.02	23.04	0.35	0.89	0.09	3.26	99.55	0.03	0.86	0.21	0.14	0.07	1.86	0.00	0.90	0.01	0.03	0.00	0.10	4.00
MD110-DR02-A27 00	Cpx	µXRF	MD110-DR02	A27	Sp-lherzolite	Porph.	Core	1.18	15.91	6.87	50.57	0.00	21.35	0.40	1.20	0.07	2.36	99.91	0.08	0.86	0.29	0.17	0.12	1.83	0.00	0.83	0.01	0.03	0.00	0.07	4.00
MD110-DR02-A27 00	Cpx	µXRF	MD110-DR02	A27	Sp-lherzolite	Porph.	Core	1.26	15.47	7.31	51.28	0.00	21.09	0.37	1.11	0.06	1.84	99.79	0.09	0.83	0.31	0.15	0.16	1.85	0.00	0.82	0.01	0.03	0.00	0.06	4.00
MD110-DR02-A27 01	Cpx	µXRF	MD110-DR02	A27	Sp-lherzolite	Porph.	Core	1.11	16.00	6.92	51.45	0.00	20.27	0.41	1.15	0.08	2.48	99.87	0.08	0.86	0.29	0.14	0.15	1.86	0.00	0.78	0.01	0.03	0.00	0.07	4.00
MD110-DR02-A27 01	Cpx	µXRF	MD110-DR02	A27	Sp-lherzolite	Porph.	Core	1.21	15.46	6.70	50.94	0.01	21.50	0.47	1.20	0.06	2.35	99.90	0.09	0.83	0.29	0.16	0.13	1.84	0.00	0.83	0.01	0.03	0.00	0.07	4.00
MD110-DR02-A27-1	Cpx	EPMA	MD110-DR02	A27	Sp-lherzolite	Porph.	Core	1.31	15.15	6.76	50.78	0.00	21.48	0.37	1.27	0.01	2.20	99.33	0.09	0.82	0.29	0.15	0.14	1.85	0.00	0.84	0.01	0.04	0.00	0.07	4.00
MD110-DR02-A27-12	Cpx	EPMA	MD110-DR02	A27	Sp-lherzolite	Porph.	Core	1.20	15.09	6.38	51.35	0.00	21.31	0.49	1.23	0.00	2.03	99.08	0.08	0.82	0.27	0.13	0.15	1.87	0.00	0.83	0.01	0.04	0.00	0.06	4.00
MD110-DR02-A27-2	Cpx	EPMA	MD110-DR02	A27	Sp-lherzolite	Porph.	Core	1.19	15.16	5.86	51.79	0.01	22.15	0.37	1.03	0.09	1.94	99.59	0.08	0.82	0.25	0.12	0.13	1.88	0.00	0.86	0.01	0.03	0.00	0.06	4.00
MD110-DR02-A27-3	Cpx	EPMA	MD110-DR02	A27	Sp-lherzolite	Porph.	Core	1.36	15.32	6.56	51.19	0.01	21.23	0.35	1.16	0.00	2.18	99.36	0.10	0.83	0.28	0.14	0.14	1.86	0.00	0.83	0.01	0.03	0.00	0.07	4.00
MD110-DR02-A27-9	Cpx	EPMA	MD110-DR02	A27	Sp-lherzolite	Porph.	Core	1.25	14.63	7.25	49.97	0.01	21.87	0.42	1.50	0.03	1.88	98.80	0.09	0.80	0.31	0.17	0.14	1.83	0.00	0.86	0.01	0.04	0.00	0.06	4.00
MD110-DR02-A40 00	Cpx	µXRF	MD110-DR02	A40	Sp-lherzolite	Porph.	Core	1.24	16.34	5.53	51.78	0.01	21.62	0.39	1.21	0.05	1.74	99.91	0.09	0.88	0.23	0.13	0.10	1.87	0.00	0.83	0.01	0.03	0.00	0.05	4.00
MD110-DR02-A40 00	Cpx	µXRF	MD110-DR02	A40	Sp-lherzolite	Porph.	Core	1.27	15.72	5.99	51.43	0.02	21.32	0.42	1.50	0.06	2.19	99.92	0.09	0.85	0.26	0.14	0.11	1.86	0.00	0.83	0.01	0.04	0.00	0.07	4.00
MD110-DR02-A40-1	Cpx	EPMA	MD110-DR02	A40	Sp-lherzolite	Porph.	Core	1.03	15.92	4.70	51.36	0.00	22.74	0.41	1.06	0.00	1.64	98.85	0.07	0.87	0.20	0.12	0.08	1.88	0.00	0.89	0.01	0.03	0.00	0.05	4.00
MD110-DR02-A40-2	Cpx	EPMA	MD110-DR02	A40	Sp-lherzolite	Porph.	Core	1.35	15.42	5.51	51.23	0.00	21.86	0.40	1.52	0.00	2.00	99.30	0.10	0.84	0.24	0.14	0.10	1.86	0.00	0.85	0.01	0.04	0.00	0.06	4.00
MD110-DR02-A40-6	Cpx	EPMA	MD110-DR02	A40	Sp-lherzolite	Porph.	Core	1.52	15.31	6.01	49.90	0.00	21.37	0.49	1.60	0.12	2.17	98.49	0.11	0.84	0.26	0.17	0.09	1.83	0.00	0.84	0.01	0.05	0.00	0.07	4.00
MD110-DR02-A40-9	Cpx	EPMA	MD110-DR02	A40	Sp-lherzolite	Porph.	Core	1.61	15.45	5.80	51.68	0.01	21.30	0.47	1.62	0.07	2.07	100.09	0.11	0.83	0.25	0.14	0.11	1.86	0.00	0.82	0.01	0.05	0.00	0.06	4.00
MD110-DR02-A48 00	Cpx	µXRF	MD110-DR02	A48	Sp-lherzolite	Porph.	Core	1.42	15.80	6.35	51.55	0.00	20.51	0.41	1.55	0.07	2.25	99.91	0.10	0.85	0.27	0.14	0.13	1.86	0.00	0.79	0.01	0.04	0.00	0.07	4.00
MD110-DR02-A48 00	Cpx	µXRF	MD110-DR02	A48	Sp-lherzolite	Porph.	Core	1.53	15.93	6.26	51.40	0.00	20.51	0.41	1.53	0.07	2.28	99.92	0.11	0.86	0.27	0.15	0.12	1.85	0.00	0.79	0.01	0.04	0.00	0.07	4.00
MD110-DR02-A48 00	Cpx	µXRF	MD110-DR02	A48	Sp-lherzolite	Porph.	Core	1.07	16.55	4.92	51.43	0.01	20.72	0.34	1.24	0.07	3.54	99.89	0.08	0.89	0.21	0.14	0.07	1.86	0.00	0.80	0.01	0.04	0.00	0.11	4.00
MD110-DR02-A48-11	Cpx	EPMA	MD110-DR02	A48	Sp-lherzolite	Porph.	Core	1.51	14.56	5.50	50.99	0.00	20.94	0.46	1.37	0.00	1.77	97.10	0.11	0.81	0.24	0.10	0.14	1.90	0.00	0.84	0.01	0.04	0.00	0.06	4.00
MD110-DR02-A48-11	Cpx	EPMA	MD110-DR02	A48	Sp-lherzolite	Porph.	Core	1.60	14.74	5.39	51.34	0.02	21.05	0.42	1.34	0.02	1.86	97.79	0.11	0.81	0.23	0.10	0.13	1.90	0.00	0.83	0.01	0.04	0.00	0.06	4.00
MD110-DR02-A48-1b	Cpx	EPMA	MD110-DR02	A48	Sp-lherzolite	Porph.	Core	1.49	15.60	6.07	50.97	0.01	20.14	0.42	1.44	0.02	1.99	98.14	0.11	0.85	0.26	0.13	0.13	1.87	0.00	0.79	0.01	0.04	0.00	0.06	4.00
MD110-DR02-A48-2	Cpx	EPMA	MD110-DR02	A48	Sp-lherzolite	Porph.	Core	1.52	14.60	6.01	50.26	0.00	21.09	0.51	1.59	0.00	1.79	97.36	0.11	0.81	0.26	0.13	0.13	1.87	0.00	0.84	0.01	0.05	0.00	0.06	4.00
MD110-DR02-A48-23	Cpx	EPMA	MD110-DR02	A48	Sp-lherzolite	Porph.	Core	1.70	14.58	6.32	50.46	0.00	20.96	0.43	1.65	0.12	1.99	98.22	0.12	0.80	0.27	0.14	0.13	1.86	0.00	0.83	0.01	0.05	0.00	0.06	4.00
MD110-DR02-A48-23	Cpx	EPMA	MD110-DR02	A48	Sp-lherzolite	Porph.	Core	1.70	14.58	6.32	50.46	0.00	20.96	0.43	1.65	0.12	1.99	98.22	0.12	0.80	0.27	0.14	0.13	1.86	0.00	0.83	0.01	0.05	0.00	0.06	4.00
MD110-DR02-A48-23	Cpx	EPMA	MD110-DR02	A48	Sp-lherzolite	Porph.	Core	1.70	14.58	6.32	50.46	0.00	20.96	0.43	1.65	0.12	1.99	98.22	0.12	0.80	0.27	0.14	0.13	1.86	0.00	0.83	0.01	0.05	0.00	0.06	4.00
MD110-DR02-A48-8	Cpx	EPMA	MD110-DR02	A48	Sp-lherzolite	Porph.	Core	1.18	15.45	4.19	51.39	0.00	21.14	0.33	1.29	0.11	1.80	96.90	0.08	0.86	0.18	0.08	0.10	1.92	0.00	0.85	0.01	0.04	0.00	0.06	4.00
MD110-DR02-A50-12	Cpx	EPMA	MD110-DR02	A50	Sp-lherzolite	Porph.	Core	1.28	15.28	6.56	50.26	0.04	21.10	0.50	1.08	0.00	2.43	98.53	0.09	0.83	0.28	0.16	0.12	1.84	0.00	0.83	0.01	0.03	0.00	0.07	4.00
MD110-DR02-A50-13	Cpx	EPMA	MD110-DR02	A50	Sp-lherzolite	Porph.	Core	1.30	14.42	7.62	49.63	0.00	20.68	0.51	1.32	0.13	2.16	97.77	0.09	0.80	0.33	0.16	0.17	1.84	0.00	0.82	0.01	0.04	0.00	0.07	4.00
MD110-DR02-A50-15	Cpx	EPMA	MD110-DR02	A50	Sp-lherzolite	Porph.	Core	1.39	14.67	6.93	50.36	0.00	20.42	0.41	1.33	0.10	1.75	97.36	0.10	0.81	0.30	0.13	0.17	1.87	0.00	0.81	0.01	0.04	0.00	0.05	4.00
MD110-DR02-A50-16	Cpx	EPMA	MD110-DR02	A50	Sp-lherzolite	Porph.	Core	1.02	14.94	5.59	49.83	0.02	21.24	0.38	0.99	0.04	1.98	96.03	0.07	0.84	0.25	0.12	0.12	1.88	0.00	0.86	0.01	0.03	0.00	0.06	4.00
MD110-DR02-A50-1b	Cpx	EPMA	MD110-DR02	A50	Sp-lherzolite	Porph.	Core	1.29	14.29	7.14	50.22	0.00	21.44	0.34	1.20	0.06	1.78	97.76	0.09	0.79	0.31	0.14	0.17	1.86	0.00	0.85	0.01	0.04	0.00	0.06	4.00
MD110-DR02-A50-1c	Cpx	EPMA	MD110-DR02	A50	Sp-lherzolite	Porph.	Core	1.45	14.16	7.22	50.24	0.00	22.04	0.43	1.25	0.04	1.83	98.66	0.10	0.77	0.31	0.16	0.15	1.84	0.00	0.87	0.01	0.04	0.00	0.06	4.00
MD110-DR02-A50-4	Cpx	EPMA	MD110-DR02	A50	Sp-lherzolite	Porph.	Core	1.48	14.63	6.90	51.03	0.01	21.63	0.42	1.29	0.04	1.97	99.40	0.10	0.79	0.30	0.15	0.15	1.85	0.00	0.84	0.01	0.04	0.00	0.06	4.00
MD110-DR02-A50-5	Cpx	EPMA	MD110-DR02	A50	Sp-lherzolite	Porph.	Core	1.29	14.97	6.40	50.29	0.00	21.42	0.44	1.17	0.04	2.32	98.34	0.09	0.82	0.28	0.15	0.13	1.85	0.00	0.84	0.01	0.03	0.00	0.07	4.00
MD110-DR02-A50-6	Cpx	EPMA	MD110-DR02	A50	Sp-lherzolite	Porph.	Core	1.40	14.35	6.98	50.20	0.00	21.30	0.41	1.35	0.11	2.14	98.24	0.10	0.79	0.30	0.15	0.15	1.85	0.00	0.84	0.01	0.04	0.00	0.07	4.00
MD110-DR02-A58 00	Cpx	µXRF	MD110-DR02	A58	Sp-lherzolite	Porph.	Core	1.23	16.50	6.31	51.21	0.08	20.01	0.37	1.06	0.08	2.99	99.84	0.09	0.88	0.24	0.13	0.11	1.87	0.00	0.77	0.01	0.03	0.00	0.10	4.00
MD110-DR02-A58-5	Cpx	EPMA	MD110-DR02	A58	Sp-lherzolite	Porph.	Core	1.37	14.46	6.62	50.84	0.00	21.23	0.39	1.29	0.06	2.01	98.26	0.10	0.79	0.29	0.13	0.16	1.87	0.00	0.84	0.01	0.04	0.00	0.06	4.00
MD110-DR02-A58-6	Cpx	EPMA	MD110-DR02	A58	Sp-lherzolite	Porph.	Core	1.33	14.29	7.65	49.33	0.00	21.05	0.45	1.29	0.08	2.18	97.64	0.09	0.79	0.33	0.17	0.16	1.83	0.00	0.84	0.01	0.04	0.00	0.07	4.00
MD110-DR02-A64 00	Cpx	µXRF	MD110-DR02	A64	Sp-lherzolite	Porph.	Core	1.09	15.87	5.99	51.81	0.01	21.34	0.45	1.41	0.06	1.87	99.90	0.08	0.86	0.26	0.13	0.13	1.87	0.00	0.83	0.01	0.04	0.00	0.06	4.00
MD110-DR02-A64 00	Cpx	µXRF	MD110-DR02	A64	Sp-lherzolite	Porph.	Core	1.15	15.94	6.34	51.79	0.02	20.54	0.53	1.39	0.06	2.16	99.92	0.08	0.86	0.27	0.13	0.14	1.87	0.00	0.80	0.01	0.04	0.00	0.07	4.00
MD110-DR02-A64 00	Cpx	µXRF	MD110-DR02	A64	Sp-lherzolite	Porph.	Core	1.23	15.54	5.80	51.18	0.01	22.02	0.44	1.43	0.08	2.16	99.89	0.09	0.84	0.25	0.15	0.10	1.85	0.00	0.85	0.01	0.04	0.00	0.07	4.00
MD110-DR02-A64 00	Cpx	µXRF	MD110-DR02	A64	Sp-lherzolite	Porph.	Core	1.19	15.91	5.87	52.22	0.01	21.05	0.43	1.35	0.06	1.83	99.92	0.08	0.86	0.25	0.11	0.14	1.89	0.00	0.81	0.01	0.04	0.00	0.06	4.00
MD110-DR02-A64-10	Cpx	EPMA	MD110-DR02	A64	Sp-lherzolite	Porph.	Core	1.36	15.54	6.11	51.26	0.00	20.52	0.37	1.50	0.10	2.17	98.93	0.10	0.85	0.26	0.13	0.13	1.87	0.00	0.80	0.01	0.04	0.00	0.07	4.00
MD110-DR02-A64-11	Cpx	EPMA	MD110-DR02	A64	Sp-lherzolite	Porph.	Core	1.59	15.16	5.95	51.49	0.00	21.30	0.30	1.68	0.03	2.17	99.69	0.11	0.82	0.25	0.13	0.12	1.87	0.00	0.83	0.01	0.05	0.00	0.07	4.00

B.5. Table de données – compositions chimiques en éléments majeurs des clinopyroxènes

MD110-DR02-A64-2a	Cpx	EPMA	MD110-DR02	A64	Sp-lherzolite	Porph.	Core	1.53	15.25	6.19	49.03	0.00	21.34	0.45	1.59	0.14	1.88	97.40	0.11	0.84	0.27	0.19	0.08	1.81	0.00	0.85	0.01	0.05	0.00	0.06	4.00
MD110-DR02-A64-2b	Cpx	EPMA	MD110-DR02	A64	Sp-lherzolite	Porph.	Core	1.31	15.33	5.57	50.86	0.01	21.37	0.37	1.56	0.00	2.14	98.50	0.09	0.84	0.24	0.13	0.11	1.87	0.00	0.84	0.01	0.05	0.00	0.07	4.00
MD110-DR02-A64-2c	Cpx	EPMA	MD110-DR02	A64	Sp-lherzolite	Porph.	Core	1.37	14.99	5.73	51.36	0.00	21.70	0.45	1.55	0.08	1.76	98.97	0.10	0.82	0.25	0.12	0.12	1.88	0.00	0.85	0.01	0.04	0.00	0.05	4.00
MD110-DR02-A64-4	Cpx	EPMA	MD110-DR02	A64	Sp-lherzolite	Porph.	Core	1.38	15.40	5.94	51.25	0.00	21.52	0.41	1.61	0.06	1.76	99.32	0.10	0.83	0.25	0.14	0.12	1.86	0.00	0.84	0.01	0.05	0.00	0.05	4.00
MD110-DR02-A64-5	Cpx	EPMA	MD110-DR02	A64	Sp-lherzolite	Porph.	Core	1.58	15.21	6.30	51.59	0.00	21.42	0.42	1.76	0.07	1.95	100.30	0.11	0.82	0.27	0.14	0.12	1.86	0.00	0.83	0.01	0.05	0.00	0.06	4.00
MD110-DR02-A64-6	Cpx	EPMA	MD110-DR02	A64	Sp-lherzolite	Porph.	Core	1.39	15.26	5.56	51.73	0.00	21.83	0.51	1.65	0.14	2.01	100.09	######	0.823	0.237	0.129	0.108	1.871	0.000	0.846	0.014	0.047	0.004	0.061	######
MD110-DR02-A64-7	Cpx	EPMA	MD110-DR02	A64	Sp-lherzolite	Porph.	Core	1.61	15.41	5.56	52.12	0.00	21.59	0.43	1.48	0.00	1.74	99.94	######	0.829	0.236	0.119	0.117	1.881	0.000	0.835	0.012	0.042	0.000	0.053	######
MD110-DR02-A64-8	Cpx	EPMA	MD110-DR02	A64	Sp-lherzolite	Porph.	Core	1.52	15.26	5.66	51.76	0.02	22.07	0.50	1.58	0.03	1.75	100.16	######	0.820	0.241	0.133	0.107	1.867	0.001	0.853	0.014	0.045	0.001	0.053	######
MD110-DR02-A66 00	Cpx	µXRF	MD110-DR02	A66	Sp-lherzolite	Porph.	Core	1.30	15.93	5.86	51.99	0.01	21.01	0.46	1.24	0.06	1.93	99.79	######	0.858	0.250	0.121	0.129	1.879	0.000	0.813	0.013	0.035	0.002	0.058	######
MD110-DR06-158A 0	Cpx	µXRF	MD110-DR06	158A	Pl-lherzolite	Porph.	Core	0.43	17.38	5.86	50.18	0.02	20.45	0.33	1.25	0.24	3.24	99.38	######	0.943	0.251	0.174	0.077	1.826	0.001	0.797	0.009	0.036	0.007	0.099	######
MD110-DR06-158A 0	Cpx	µXRF	MD110-DR06	158A	Pl-lherzolite	Porph.	Rim	0.47	17.76	5.46	50.11	0.03	20.60	0.33	1.24	0.13	3.17	99.30	######	0.963	0.234	0.178	0.056	1.822	0.001	0.802	0.009	0.036	0.004	0.096	######
MD110-DR06-158A 0	Cpx	µXRF	MD110-DR06	158A	Pl-lherzolite	Porph.	Rim	0.75	17.49	5.23	50.90	0.00	21.01	0.33	1.22	0.08	2.88	99.89	######	0.941	0.223	0.162	0.060	1.838	0.000	0.813	0.009	0.035	0.002	0.087	######
MD110-DR06-158A 0	Cpx	µXRF	MD110-DR06	158A	Pl-lherzolite	Neoblast	Core	0.52	17.92	4.51	51.28	0.00	21.12	0.32	1.16	0.08	2.96	99.87	######	0.966	0.192	0.146	0.046	1.854	0.000	0.818	0.009	0.033	0.002	0.089	######
MD110-DR06-158A-1	Cpx	EPMA	MD110-DR06	158A	Pl-lherzolite	Porph.	Core	0.45	17.34	5.63	50.94	0.02	20.18	0.34	1.32	0.05	3.35	99.62	######	0.939	0.241	0.149	0.092	1.851	0.001	0.786	0.009	0.038	0.002	0.102	######
MD110-DR06-158A-1	Cpx	EPMA	MD110-DR06	158A	Pl-lherzolite	Inclusion	Core	0.45	16.78	5.23	51.07	0.00	21.79	0.37	1.37	0.08	2.91	100.05	######	0.907	0.223	0.148	0.075	1.852	0.000	0.846	0.010	0.039	0.002	0.088	######
MD110-DR06-158A-1	Cpx	EPMA	MD110-DR06	158A	Pl-lherzolite	Neoblast	Core	0.46	17.55	4.19	51.72	0.00	21.38	0.29	1.32	0.10	3.10	100.11	######	0.947	0.179	0.129	0.050	1.871	0.000	0.829	0.008	0.038	0.003	0.094	######
MD110-DR06-158A-1	Cpx	EPMA	MD110-DR06	158A	Pl-lherzolite	Porph.	Core	0.53	15.70	6.35	50.17	0.00	21.71	0.30	1.18	0.12	2.96	99.02	######	0.858	0.274	0.160	0.114	1.840	0.000	0.853	0.008	0.034	0.004	0.091	######
MD110-DR06-158A-4	Cpx	EPMA	MD110-DR06	158A	Pl-lherzolite	Neoblast	Core	0.50	16.48	4.66	50.64	0.00	21.98	0.41	1.37	0.23	2.86	99.13	######	0.900	0.201	0.145	0.056	1.855	0.000	0.863	0.011	0.040	0.007	0.088	######
MD110-DR06-158A-6	Cpx	EPMA	MD110-DR06	158A	Pl-lherzolite	Inclusion	Core	0.43	17.71	4.88	51.41	0.00	20.54	0.33	1.38	0.10	3.06	99.84	######	0.957	0.208	0.137	0.071	1.863	0.000	0.797	0.009	0.040	0.003	0.093	######
MD110-DR06-158A-7	Cpx	EPMA	MD110-DR06	158A	Pl-lherzolite	Porph.	Core	0.57	16.03	6.50	50.61	0.01	22.30	0.31	1.22	0.14	2.99	100.68	######	0.861	0.276	0.176	0.100	1.824	0.000	0.861	0.008	0.035	0.004	0.090	######
MD110-DR06-158B 0	Cpx	µXRF	MD110-DR06	158B	Pl-lherzolite	Neoblast	Core	0.46	17.73	5.76	50.61	0.00	20.96	0.35	1.17	0.07	2.78	99.89	######	0.955	0.245	0.172	0.073	1.828	0.000	0.811	0.010	0.033	0.002	0.084	######
MD110-DR06-158B-1	Cpx	EPMA	MD110-DR06	158B	Pl-lherzolite	Porph.	Core	0.49	16.78	6.25	50.39	0.00	20.48	0.30	1.15	0.01	3.03	98.88	######	0.915	0.269	0.157	0.113	1.843	0.000	0.803	0.008	0.033	0.000	0.093	######
MD110-DR06-158B-2	Cpx	EPMA	MD110-DR06	158B	Pl-lherzolite	Neoblast	Core	0.53	16.74	5.42	50.81	0.03	21.03	0.35	1.35	0.14	3.04	99.44	######	0.910	0.233	0.148	0.085	1.852	0.001	0.821	0.010	0.039	0.004	0.093	######
MD110-DR06-158B-6	Cpx	EPMA	MD110-DR06	158B	Pl-lherzolite	Porph.	Core	0.51	16.24	5.51	50.17	0.02	21.74	0.38	1.32	0.05	2.61	98.55	######	0.891	0.239	0.154	0.084	1.846	0.001	0.857	0.011	0.038	0.002	0.080	######
MD110-DR06-158B-8	Cpx	EPMA	MD110-DR06	158B	Pl-lherzolite	Neoblast	Core	0.50	16.73	4.76	51.55	0.02	21.29	0.32	1.19	0.07	2.81	99.24	######	0.911	0.205	0.117	0.088	1.883	0.001	0.833	0.009	0.034	0.002	0.086	######
MD110-DR06-161A 0	Cpx	µXRF	MD110-DR06	161A	Pl-lherzolite	Porph.	Core	0.56	17.08	6.71	49.54	0.46	21.01	0.39	0.96	0.09	3.10	99.90	######	0.919	0.285	0.212	0.074	1.788	0.021	0.812	0.011	0.027	0.003	0.094	######
MD110-DR06-161A 0	Cpx	µXRF	MD110-DR06	161A	Pl-lherzolite	Neoblast	Core	0.63	16.93	6.46	50.02	0.01	21.03	0.39	0.95	0.08	3.21	99.71	######	0.914	0.276	0.188	0.088	1.812	0.000	0.816	0.011	0.027	0.002	0.097	######
MD110-DR06-161A-1	Cpx	EPMA	MD110-DR06	161A	Pl-lherzolite	Neoblast	Core	0.43	15.70	5.47	49.75	0.03	22.25	0.56	1.10	0.03	2.91	98.23	######	0.866	0.239	0.158	0.080	1.842	0.001	0.882	0.016	0.032	0.001	0.090	######
MD110-DR06-161A-1	Cpx	EPMA	MD110-DR06	161A	Pl-lherzolite	Neoblast	Core	0.51	15.98	5.88	50.18	0.01	22.18	0.53	1.12	0.06	2.91	99.36	######	0.871	0.253	0.166	0.087	1.834	0.000	0.868	0.015	0.032	0.002	0.089	######
MD110-DR06-161A-7	Cpx	EPMA	MD110-DR06	161A	Pl-lherzolite	Neoblast	Core	0.53	15.69	5.90	50.41	0.01	22.81	0.47	1.08	0.12	2.75	99.77	######	0.852	0.253	0.164	0.089	1.836	0.000	0.890	0.013	0.031	0.004	0.084	######
MD110-DR06-161A-8	Cpx	EPMA	MD110-DR06	161A	Pl-lherzolite	Neoblast	Core	0.54	15.50	6.28	50.23	0.00	22.65	0.41	1.07	0.10	2.86	99.64	######	0.843	0.270	0.168	0.102	1.832	0.000	0.885	0.011	0.031	0.003	0.087	######
MD110-DR06-161C 0	Cpx	µXRF	MD110-DR06	161C	Pl-lherzolite	Inclusion	Core	0.56	16.48	6.95	49.65	0.01	21.38	0.48	1.02	0.08	3.27	99.88	######	0.890	0.297	0.201	0.096	1.799	0.000	0.830	0.013	0.029	0.002	0.099	######
MD110-DR06-161C 0	Cpx	µXRF	MD110-DR06	161C	Pl-lherzolite	Neoblast	Core	0.52	17.55	4.70	50.36	0.00	21.77	0.42	1.09	0.11	3.36	99.88	######	0.947	0.201	0.177	0.024	1.823	0.000	0.844	0.011	0.031	0.003	0.102	######
MD110-DR06-161C-1	Cpx	EPMA	MD110-DR06	161C	Pl-lherzolite	Porph.	Core	0.48	14.97	7.43	49.13	0.00	22.66	0.47	1.09	0.18	3.10	99.50	######	0.816	0.320	0.203	0.117	1.797	0.000	0.888	0.013	0.032	0.006	0.095	######
MD110-DR06-161C-3	Cpx	EPMA	MD110-DR06	161C	Pl-lherzolite	Inclusion	Core	0.54	15.28	6.62	50.46	0.00	22.66	0.46	1.32	0.13	2.92	100.40	######	0.826	0.283	0.170	0.113	1.830	0.000	0.880	0.013	0.038	0.004	0.089	######
MD110-DR06-161C-3	Cpx	EPMA	MD110-DR06	161C	Pl-lherzolite	Inclusion	Core	0.48	16.38	6.46	51.48	0.03	21.62	0.46	0.83	0.11	3.23	101.08	######	0.877	0.273	0.152	0.121	1.848	0.001	0.831	0.012	0.024	0.003	0.097	######
MD110-DR06-161C-3	Cpx	EPMA	MD110-DR06	161C	Pl-lherzolite	Inclusion	Core	0.45	16.09	5.70	51.38	0.00	21.82	0.41	1.34	0.07	3.06	100.33	######	0.870	0.244	0.137	0.107	1.863	0.000	0.848	0.011	0.038	0.002	0.093	######
MD110-DR06-161C-3	Cpx	EPMA	MD110-DR06	161C	Pl-lherzolite	Inclusion	Core	0.51	15.82	5.48	50.93	0.00	22.57	0.50	1.28	0.10	2.85	100.03	######	0.858	0.235	0.148	0.087	1.852	0.000	0.879	0.014	0.037	0.003	0.087	######
MD110-DR06-161C-4	Cpx	EPMA	MD110-DR06	161C	Pl-lherzolite	Inclusion	Core	0.51	16.11	6.81	50.43	0.00	21.18	0.50	1.06	0.14	3.36	100.09	######	0.871	0.291	0.171	0.120	1.829	0.000	0.823	0.014	0.030	0.004	0.102	######
MD110-DR06-161C-5	Cpx	EPMA	MD110-DR06	161C	Pl-lherzolite	Neoblast	Core	0.51	16.81	4.07	51.98	0.00	22.49	0.51	1.13	0.02	2.90	100.42	######	0.906	0.173	0.121	0.053	1.879	0.000	0.871	0.014	0.032	0.001	0.088	######
MD110-DR06-161C-5	Cpx	EPMA	MD110-DR06	161C	Pl-lherzolite	Porph.	Rim	0.51	16.48	6.73	50.07	0.01	21.99	0.39	1.09	0.05	3.28	100.58	######	0.885	0.286	0.197	0.089	1.803	0.000	0.848	0.011	0.031	0.002	0.099	######
MD110-DR06-161C-5	Cpx	EPMA	MD110-DR06	161C	Pl-lherzolite	Inclusion	Core	0.46	16.51	5.66	50.66	0.00	22.05	0.41	1.28	0.05	2.64	99.72	######	0.895	0.242	0.158	0.084	1.842	0.000	0.859	0.011	0.037	0.002	0.080	######
MD110-DR06-161C-5	Cpx	EPMA	MD110-DR06	161C	Pl-lherzolite	Inclusion	Core	0.53	16.74	5.19	51.47	0.00	21.73	0.43	1.17	0.14	3.13	100.53	######	0.901	0.221	0.142	0.078	1.858	0.000	0.840	0.012	0.033	0.004	0.094	######
MD110-DR06-161C-5	Cpx	EPMA	MD110-DR06	161C	Pl-lherzolite	Inclusion	Core	0.59	16.44	4.89	50.97	0.00	22.28	0.50	1.21	0.06	2.61	99.55	######	0.893	0.210	0.144	0.066	1.856	0.000	0.869	0.014	0.035	0.002	0.080	######
MD110-DR06-161C-5	Cpx	EPMA	MD110-DR06	161C	Pl-lherzolite	Inclusion	Core	0.55	16.08	7.15	49.37	0.00	21.66	0.56	1.13	0.16	3.42	100.09	######	0.869	0.305	0.210	0.095	1.790	0.000	0.841	0.015	0.032	0.005	0.104	######
MD110-DR06-161C-5	Cpx	EPMA	MD110-DR06	161C	Pl-lherzolite	Inclusion	Core	0.56	15.83	6.72	47.42	0.01	21.97	0.57	1.12	0.11	2.96	97.26	######	0.878	0.295	0.235	0.060	1.765	0.000	0.876	0.016	0.033	0.003	0.092	######
MD110-DR06-162B-1	Cpx	EPMA	MD110-DR06	162B	Pl-lherzolite	Porph.	Rim	0.54	16.16	4.89	50.40	0.01	21.90	0.49	1.25	0.14	2.76	98.54	######	0.888	0.212	0.143	0.069	1.857	0.000	0.864	0.014	0.036	0.004	0.085	######
MD110-DR06-162B-1	Cpx	EPMA	MD110-DR06	162B	Pl-lherzolite	Neoblast	Core	0.45	17.07	3.92	50.88	0.03	21.74	0.45	1.34	0.09	2.73	98.70	######	0.935	0.170	0.131	0.038	1.869	0.001	0.855	0.012	0.039	0.003	0.084	######
MD110-DR06-162b-2	Cpx	EPMA	MD110-DR06	162B	Pl-lherzolite	Porph.	Core	0.58	15.35	6.24	51.12	0.03	22.35	0.42	1.33	0.00	2.99	100.42	######	0.830	0.267	0.147	0.120	1.853	0.001	0.868	0.011	0.038	0.000	0.091	######
MD110-DR06-162B-2	Cpx	EPMA	MD110-DR06	162B	Pl-lherzolite	Porph.	Core	0.55	15.69	6.31	49.91	0.02	21.77	0.43	1.37	0.16	2.85	99.06	######	0.858	0.273	0.170	0.103	1.830	0.001	0.855	0.012	0.040	0.005	0.087	######
MD110-DR06-162b-2	Cpx	EPMA	MD110-DR06	162B	Pl-lherzolite	Neoblast	Core	0.53	16.48	5.46	51.59	0.00	22.43	0.74	1.27	0.17	2.75	101.42	######	0.880	0.231	0.152	0.079	1.848	0.000	0.861	0.020	0.036	0.005	0.082	######
MD110-DR06-162B-2	Cpx	EPMA	MD110-DR06	162B	Pl-lherzolite	Porph.	Core	0.57	15.64	5.67	50.03	0.00	21.79	0.62	1.24	0.07	2.75	98.38	######	0.861	0.247	0.152	0.095	1.848	0.000	0.862	0.017	0.036	0.002	0.085	######
MD110-DR06-162B-2	Cpx	EPMA	MD110-DR06	162B	Pl-lherzolite	Neoblast	Core	0.52	15.77	5.36	49.83	0.00	21.76	0.42	1.45	0.03	2.87	98.01	######	0.872	0.234	0.152	0.082	1.848	0.000	0.864	0.012	0.043	0.001	0.089	######

B.5. Table de données – compositions chimiques en éléments majeurs des clinopyroxènes

MD110-DR06-162B-2	Cpx	EPMA	MD110-DR06	162B	Pl-lherzolite	Neoblast	Core	0.51	15.97	5.06	50.16	0.01	22.10	0.42	1.36	0.04	2.44	98.07	######	0.881	0.221	0.144	0.077	1.856	0.000	0.876	0.012	0.040	0.001	0.076	######
MD110-DR06-167A 0	Cpx	µXRF	MD110-DR06	167A	Pl-lherzolite	Neoblast	Core	0.51	17.69	4.99	50.87	0.01	21.08	0.40	1.11	0.08	3.16	99.90	######	0.954	0.213	0.160	0.053	1.840	0.000	0.817	0.011	0.032	0.002	0.096	######
MD110-DR06-167A 0	Cpx	µXRF	MD110-DR06	167A	Pl-lherzolite	Neoblast	Core	0.37	17.76	6.45	50.34	0.00	20.11	0.33	1.10	0.08	3.35	99.89	######	0.957	0.275	0.180	0.094	1.820	0.000	0.779	0.009	0.031	0.002	0.101	######
MD110-DR06-167A-1	Cpx	EPMA	MD110-DR06	167A	Pl-lherzolite	Neoblast	Core	0.46	15.63	6.07	49.53	0.02	21.72	0.40	1.12	0.01	2.75	97.71	######	0.866	0.266	0.160	0.106	1.840	0.001	0.864	0.011	0.033	0.000	0.085	######
MD110-DR06-167A-1	Cpx	EPMA	MD110-DR06	167A	Pl-lherzolite	Porph.	Rim	0.41	16.54	4.86	50.60	0.00	21.88	0.41	1.07	0.11	2.76	98.64	######	0.907	0.211	0.139	0.071	1.861	0.000	0.862	0.011	0.031	0.003	0.085	######
MD110-DR06-167A-1	Cpx	EPMA	MD110-DR06	167A	Pl-lherzolite	Porph.	Core	0.48	15.53	6.48	49.58	0.01	22.10	0.35	1.06	0.09	2.85	98.53	######	0.853	0.281	0.173	0.108	1.827	0.000	0.872	0.010	0.031	0.003	0.088	######
MD110-DR06-167A-1	Cpx	EPMA	MD110-DR06	167A	Pl-lherzolite	Porph.	Core	0.48	15.53	6.48	49.58	0.01	22.10	0.35	1.06	0.09	2.85	98.53	######	0.853	0.281	0.173	0.108	1.827	0.000	0.872	0.010	0.031	0.003	0.088	######
MD110-DR06-167A-1	Cpx	EPMA	MD110-DR06	167A	Pl-lherzolite	Porph.	Core	0.48	15.41	7.30	49.35	0.00	21.32	0.41	1.16	0.01	2.93	98.37	######	0.848	0.318	0.179	0.139	1.821	0.000	0.843	0.011	0.034	0.000	0.090	######
MD110-DR06-167A-1	Cpx	EPMA	MD110-DR06	167A	Pl-lherzolite	Porph.	Core	0.50	15.21	6.76	49.15	0.01	21.77	0.38	1.09	0.02	2.92	97.81	######	0.842	0.296	0.175	0.121	1.825	0.000	0.866	0.011	0.032	0.001	0.091	######
MD110-DR06-167A-1	Cpx	EPMA	MD110-DR06	167A	Pl-lherzolite	Porph.	Core	0.46	15.56	6.61	49.38	0.01	21.60	0.37	1.09	0.11	2.75	97.94	######	0.860	0.289	0.170	0.118	1.830	0.000	0.857	0.010	0.032	0.003	0.085	######
MD110-DR06-167A-1	Cpx	EPMA	MD110-DR06	167A	Pl-lherzolite	Porph.	Core	0.52	16.02	6.48	50.25	0.01	21.95	0.33	1.09	0.19	3.18	100.02	######	0.867	0.277	0.177	0.100	1.823	0.000	0.853	0.009	0.031	0.006	0.096	######
MD110-DR06-167A-1	Cpx	EPMA	MD110-DR06	167A	Pl-lherzolite	Porph.	Core	0.52	15.43	6.84	49.56	0.02	21.82	0.37	1.08	0.00	2.82	98.46	######	0.848	0.297	0.173	0.124	1.827	0.001	0.862	0.010	0.031	0.000	0.087	######
MD110-DR06-167A-7	Cpx	EPMA	MD110-DR06	167A	Pl-lherzolite	Porph.	Core	0.44	16.51	6.75	49.67	0.00	19.75	0.38	1.15	0.19	3.31	98.15	######	0.908	0.294	0.167	0.127	1.833	0.000	0.781	0.011	0.034	0.006	0.102	######
MD110-DR06-168 00	Cpx	µXRF	MD110-DR06	168	Pl-lherzolite	Neoblast	Core	0.46	17.11	4.86	50.73	0.32	21.14	0.31	1.32	0.09	3.52	99.86	######	0.926	0.208	0.159	0.049	1.841	0.015	0.822	0.008	0.038	0.003	0.107	######
MD110-DR06-168 00	Cpx	µXRF	MD110-DR06	168	Pl-lherzolite	Neoblast	Core	0.50	17.17	4.09	51.41	0.00	21.99	0.36	1.35	0.08	2.94	99.89	######	0.929	0.175	0.134	0.041	1.866	0.000	0.855	0.010	0.039	0.002	0.089	######
MD110-DR06-168 01	Cpx	µXRF	MD110-DR06	168	Pl-lherzolite	Neoblast	Core	0.53	17.86	3.68	51.42	0.11	21.76	0.31	1.14	0.08	2.94	99.83	######	0.964	0.157	0.139	0.018	1.861	0.005	0.844	0.008	0.033	0.002	0.089	######
MD110-DR06-168 01	Cpx	µXRF	MD110-DR06	168	Pl-lherzolite	Neoblast	Core	0.38	17.43	4.19	51.08	0.00	21.69	0.67	1.27	0.12	3.08	99.91	######	0.944	0.179	0.145	0.034	1.855	0.000	0.844	0.018	0.036	0.004	0.094	######
MD110-DR06-168-1	Cpx	EPMA	MD110-DR06	168	Pl-lherzolite	Porph.	Core	0.55	15.53	5.85	49.99	0.02	22.21	0.26	1.29	0.05	2.74	98.49	######	0.854	0.254	0.157	0.098	1.843	0.001	0.877	0.007	0.038	0.002	0.085	######
MD110-DR06-168-15	Cpx	EPMA	MD110-DR06	168	Pl-lherzolite	Porph.	Rim	0.47	16.63	4.19	51.15	0.00	21.51	0.27	1.28	0.10	2.93	98.53	######	0.913	0.182	0.116	0.066	1.884	0.000	0.849	0.007	0.037	0.003	0.090	######
MD110-DR06-168-16	Cpx	EPMA	MD110-DR06	168	Pl-lherzolite	Neoblast	Core	0.51	16.85	3.83	51.11	0.00	22.07	0.35	1.28	0.00	2.64	98.64	######	0.923	0.166	0.122	0.044	1.878	0.000	0.869	0.010	0.037	0.000	0.081	######
MD110-DR06-168-17	Cpx	EPMA	MD110-DR06	168	Pl-lherzolite	Neoblast	Core	0.38	17.33	3.69	51.07	0.00	21.60	0.32	1.20	0.05	2.73	98.37	######	0.951	0.160	0.120	0.040	1.880	0.000	0.852	0.009	0.035	0.002	0.084	######
MD110-DR06-168-26	Cpx	EPMA	MD110-DR06	168	Pl-lherzolite	Neoblast	Core	0.43	17.77	3.28	51.67	0.00	21.59	0.40	1.05	0.04	2.68	98.91	######	0.969	0.141	0.111	0.031	1.889	0.000	0.846	0.011	0.030	0.001	0.082	######
MD110-DR06-168-7	Cpx	EPMA	MD110-DR06	168	Pl-lherzolite	Neoblast	Core	0.55	17.22	4.02	51.41	0.00	20.93	0.33	1.28	0.11	2.76	98.61	######	0.942	0.174	0.113	0.061	1.887	0.000	0.823	0.009	0.037	0.003	0.085	######
MD110-DR06-168-8	Cpx	EPMA	MD110-DR06	168	Pl-lherzolite	Neoblast	Core	0.47	16.10	4.33	50.53	0.00	22.13	0.39	1.43	0.26	2.49	98.13	######	0.889	0.189	0.128	0.061	1.872	0.000	0.878	0.011	0.042	0.008	0.077	######
MD110-DR06-168-9	Cpx	EPMA	MD110-DR06	168	Pl-lherzolite	Neoblast	Core	0.49	16.43	4.03	50.87	0.01	22.21	0.34	1.37	0.05	2.37	98.17	######	0.905	0.176	0.120	0.056	1.880	0.000	0.879	0.009	0.040	0.002	0.073	######
MD110-DR06-173-10	Cpx	EPMA	MD110-DR06	173	Pl-lherzolite	Neoblast	Core	0.57	16.19	5.67	50.86	0.00	21.74	0.31	1.26	0.10	2.51	99.21	######	0.882	0.244	0.142	0.102	1.858	0.000	0.851	0.009	0.036	0.003	0.077	######
MD110-DR06-173-7	Cpx	EPMA	MD110-DR06	173	Pl-lherzolite	Neoblast	Core	0.52	16.44	5.43	50.52	0.01	22.74	0.45	1.42	0.09	2.52	100.14	######	0.888	0.232	0.170	0.061	1.830	0.000	0.882	0.012	0.041	0.003	0.076	######
MD110-DR06-173-8	Cpx	EPMA	MD110-DR06	173	Pl-lherzolite	Neoblast	Core	0.60	15.87	5.30	50.48	0.04	22.39	0.33	1.37	0.10	2.41	98.89	######	0.868	0.229	0.148	0.081	1.852	0.002	0.880	0.009	0.040	0.003	0.074	######
MD110-DR06-173-9b	Cpx	EPMA	MD110-DR06	173	Pl-lherzolite	Neoblast	Core	0.55	16.11	5.93	50.49	0.02	21.30	0.26	1.44	0.10	2.49	98.69	######	0.882	0.257	0.146	0.111	1.854	0.001	0.838	0.007	0.042	0.003	0.076	######
MD110-DR06-B4-1	Cpx	EPMA	MD110-DR06	B4	Pl-lherzolite	Inclusion	Core	0.48	15.52	6.02	50.48	0.02	21.95	0.50	1.32	0.08	2.97	99.35	######	0.848	0.260	0.150	0.110	1.850	0.001	0.862	0.014	0.038	0.002	0.091	######
MD110-DR06-B4-10	Cpx	EPMA	MD110-DR06	B4	Pl-lherzolite	Porph.	Core	0.53	15.60	6.11	48.94	0.01	21.89	0.44	1.03	0.08	3.05	97.69	######	0.864	0.268	0.182	0.086	1.818	0.000	0.871	0.012	0.030	0.003	0.095	######
MD110-DR06-B4-14	Cpx	EPMA	MD110-DR06	B4	Pl-lherzolite	Porph.	Core	0.52	14.96	6.76	49.72	0.01	21.31	0.42	1.09	0.00	2.92	97.70	######	0.830	0.297	0.149	0.147	1.851	0.000	0.850	0.012	0.032	0.000	0.091	######
MD110-DR06-B4-21	Cpx	EPMA	MD110-DR06	B4	Pl-lherzolite	Porph.	Core	0.63	15.13	5.80	48.85	0.00	22.22	0.38	1.17	0.10	2.87	97.14	######	0.844	0.256	0.173	0.083	1.827	0.000	0.890	0.011	0.035	0.003	0.090	######
MD110-DR06-B4-32	Cpx	EPMA	MD110-DR06	B4	Pl-lherzolite	opx cliva	Core	0.53	15.60	5.70	49.01	0.00	21.96	0.61	1.35	0.14	2.59	97.48	######	0.867	0.250	0.174	0.077	1.826	0.000	0.877	0.017	0.040	0.004	0.081	######
MD110-DR06-B4-34-	Cpx	EPMA	MD110-DR06	B4	Pl-lherzolite	Porph.	Core	0.54	16.43	7.28	50.77	0.00	20.33	0.42	1.10	0.16	3.40	100.41	######	0.884	0.310	0.168	0.142	1.832	0.000	0.786	0.011	0.031	0.005	0.103	######
MD110-DR06-B4-37-	Cpx	EPMA	MD110-DR06	B4	Pl-lherzolite	Porph.	Core	0.44	16.10	8.86	47.45	0.00	19.96	0.38	1.05	0.17	3.24	97.66	######	0.888	0.386	0.244	0.142	1.756	0.000	0.791	0.011	0.031	0.005	0.100	######
MD110-DR06-B4-37-	Cpx	EPMA	MD110-DR06	B4	Pl-lherzolite	Porph.	Core	0.59	15.44	7.23	49.61	0.03	21.89	0.46	1.04	0.08	3.28	99.64	######	0.839	0.311	0.192	0.118	1.808	0.001	0.855	0.013	0.030	0.002	0.100	######
MD110-DR06-B4-4	Cpx	EPMA	MD110-DR06	B4	Pl-lherzolite	Porph.	Core	0.53	14.95	7.09	50.19	0.01	22.27	0.50	1.00	0.16	2.84	99.55	######	0.815	0.305	0.165	0.140	1.835	0.000	0.872	0.014	0.029	0.005	0.087	######
MD110-DR06-B5 011	Cpx	µXRF	MD110-DR06	B5	Pl-lherzolite	Neoblast	Core	1.01	16.43	6.20	50.56	0.23	20.79	0.44	1.22	0.08	2.94	99.90	######	0.885	0.264	0.173	0.091	1.827	0.011	0.805	0.012	0.035	0.002	0.089	######
MD110-DR06-B7-11	Cpx	EPMA	MD110-DR06	B7	Pl-lherzolite	Inclusion	Core	0.48	15.83	5.61	50.80	0.01	21.49	0.32	1.31	0.15	2.79	98.79	######	0.868	0.243	0.131	0.112	1.869	0.000	0.847	0.009	0.038	0.005	0.086	######
MD110-DR06-B7-13	Cpx	EPMA	MD110-DR06	B7	Pl-lherzolite	Neoblast	Core	0.47	16.06	5.10	51.26	0.01	21.95	0.32	1.25	0.01	2.66	99.09	######	0.878	0.220	0.121	0.099	1.879	0.000	0.862	0.009	0.036	0.000	0.082	######
MD110-DR06-B7-21	Cpx	EPMA	MD110-DR06	B7	Pl-lherzolite	Porph.	Rim	0.49	16.78	4.54	48.75	0.01	22.04	0.40	1.24	0.01	3.08	97.33	######	0.930	0.199	0.187	0.012	1.813	0.000	0.878	0.011	0.036	0.000	0.096	######
MD110-DR06-B7-23-	Cpx	EPMA	MD110-DR06	B7	Pl-lherzolite	Porph.	Core	0.57	16.27	6.37	50.18	0.01	21.57	0.28	1.16	0.12	2.89	99.43	######	0.884	0.273	0.172	0.101	1.828	0.000	0.842	0.008	0.033	0.004	0.088	######
MD110-DR06-B7-3	Cpx	EPMA	MD110-DR06	B7	Pl-lherzolite	Inclusion	Core	0.55	15.07	6.27	50.45	0.00	22.35	0.44	1.50	0.12	2.80	99.56	######	0.822	0.270	0.153	0.117	1.847	0.000	0.876	0.012	0.043	0.004	0.086	######
MD110-DR06-B8 004	Cpx	µXRF	MD110-DR06	B8	Pl-lherzolite	Inclusion	Core	0.58	16.91	6.42	50.03	0.01	21.25	0.35	1.09	0.07	3.13	99.84	######	0.912	0.274	0.189	0.085	1.811	0.000	0.824	0.010	0.031	0.002	0.095	######
MD110-DR06-B8 008	Cpx	µXRF	MD110-DR06	B8	Pl-lherzolite	Inclusion	Core	0.46	17.46	5.18	50.99	0.03	20.84	0.39	1.47	0.06	2.97	99.85	######	0.943	0.221	0.152	0.069	1.848	0.001	0.809	0.011	0.042	0.002	0.090	######
MD110-DR06-B8 014	Cpx	µXRF	MD110-DR06	B8	Pl-lherzolite	Inclusion	Core	0.47	17.27	5.64	50.36	0.00	21.09	0.36	1.39	0.11	3.15	99.84	######	0.933	0.241	0.175	0.066	1.825	0.000	0.819	0.010	0.040	0.003	0.095	######
MD110-DR09-273b 0	Cpx	µXRF	MD110-DR09	273b	Sp-lherzolite	Porph.	Core	1.13	16.08	5.77	51.34	0.01	21.67	0.24	1.29	0.07	2.30	99.90	######	0.866	0.246	0.145	0.101	1.855	0.000	0.839	0.007	0.037	0.002	0.069	######
MD110-DR09-273b 0	Cpx	µXRF	MD110-DR09	273b	Sp-lherzolite	Porph.	Core	1.17	16.41	5.41	50.98	0.37	21.40	0.23	1.29	0.07	2.55	99.88	######	0.883	0.230	0.161	0.069	1.839	0.017	0.827	0.006	0.037	0.002	0.077	######
MD110-DR09-273b 0	Cpx	µXRF	MD110-DR09	273b	Sp-lherzolite	Porph.	Core	1.14	16.22	5.75	51.01	0.01	22.11	0.23	1.28	0.06	2.10	99.91	######	0.872	0.244	0.160	0.085	1.840	0.000	0.855	0.006	0.037	0.002	0.063	######
MD110-DR09-273B-1	Cpx	EPMA	MD110-DR09	273B	Sp-lherzolite	Porph.	Core	1.40	14.69	6.70	49.93	0.01	20.96	0.20	1.48	0.04	1.87	97.29	######	0.812	0.293	0.148	0.145	1.852	0.000	0.833	0.006	0.043	0.001	0.058	######
MD110-DR09-273B-2	Cpx	EPMA	MD110-DR09	273B	Sp-lherzolite	Porph.	Core	1.33	14.91	6.85	50.14	0.01	21.21	0.22	1.45	0.00	2.11	98.22	######	0.817	0.297	0.157	0.140	1.843	0.000	0.835	0.006	0.042	0.000	0.065	######
MD110-DR09-273B-4	Cpx	EPMA	MD110-DR09	273B	Sp-lherzolite	Porph.	Core	1.61	14.88	6.65	50.29	0.02	21.52	0.20	1.49	0.04	1.92	98.61	######	0.810	0.286	0.163	0.124	1.837	0.001	0.842	0.005	0.043	0.001	0.059	######
MD110-DR09-273B-5	Cpx	EPMA	MD110-DR09	273B	Sp-lherzolite	Porph.	Core	1.26	16.09	5.73	50.40	0.00	21.39	0.22	1.37	0.06	2.07	98.60	######	0.876	0.247	0.159	0.087	1.841	0.000	0.837	0.006	0.040	0.002	0.063	######

B.5. Table de données – compositions chimiques en éléments majeurs des clinopyroxènes

MD110-DR09-273B-6	Cpx	EPMA	MD110-DR09	273B	Sp-lherzolite	Porph.	Core	1.24	15.59	5.29	51.35	0.06	21.15	0.21	1.15	0.09	1.94	98.08	######	0.855	0.229	0.111	0.118	1.889	0.003	0.834	0.006	0.033	0.003	0.060	######
MD110-DR09-277 00	Cpx	µXRF	MD110-DR09	277	Sp-lherzolite	Porph.	Core	1.00	15.98	6.19	51.51	0.00	21.84	0.12	1.07	0.06	2.13	99.90	######	0.861	0.264	0.139	0.124	1.861	0.000	0.845	0.003	0.031	0.002	0.064	######
MD110-DR09-277 00	Cpx	µXRF	MD110-DR09	277	Sp-lherzolite	Porph.	Core	0.91	16.01	6.41	51.35	0.01	21.67	0.12	1.06	0.07	2.25	99.86	######	0.863	0.273	0.143	0.130	1.857	0.000	0.839	0.003	0.030	0.002	0.068	######
MD110-DR09-277 00	Cpx	µXRF	MD110-DR09	277	Sp-lherzolite	Porph.	Core	0.87	16.60	6.15	51.06	0.00	21.85	0.11	1.11	0.06	2.10	99.91	######	0.892	0.261	0.159	0.103	1.841	0.000	0.844	0.003	0.032	0.002	0.063	######
MD110-DR09-277 00	Cpx	µXRF	MD110-DR09	277	Sp-lherzolite	Porph.	Core	0.78	16.09	5.91	51.33	0.01	22.45	0.14	1.05	0.07	2.05	99.88	######	0.868	0.252	0.143	0.109	1.857	0.000	0.870	0.004	0.030	0.002	0.062	######
MD110-DR09-277-2	Cpx	EPMA	MD110-DR09	277	Sp-lherzolite	Porph.	Core	1.04	15.57	6.01	52.49	0.00	22.46	0.14	1.03	0.02	2.08	100.84	######	0.832	0.254	0.118	0.136	1.882	0.000	0.863	0.004	0.029	0.001	0.062	######
MD110-DR09-277-3	Cpx	EPMA	MD110-DR09	277	Sp-lherzolite	Porph.	Core	1.01	15.62	6.34	52.02	0.01	22.27	0.13	1.23	0.16	2.10	100.90	######	0.835	0.268	0.135	0.133	1.865	0.000	0.855	0.004	0.035	0.005	0.063	######
MD110-DR09-277-4	Cpx	EPMA	MD110-DR09	277	Sp-lherzolite	Porph.	Core	1.00	15.36	6.41	52.54	0.00	22.67	0.14	1.15	0.15	1.89	101.31	######	0.818	0.270	0.123	0.147	1.877	0.000	0.868	0.004	0.032	0.005	0.056	######
MD110-DR09-277-5	Cpx	EPMA	MD110-DR09	277	Sp-lherzolite	Porph.	Core	1.05	15.44	5.78	52.53	0.00	22.66	0.11	1.06	0.00	2.06	100.68	######	0.827	0.245	0.112	0.132	1.888	0.000	0.872	0.003	0.030	0.000	0.062	######
MD110-DR09-277-7	Cpx	EPMA	MD110-DR09	277	Sp-lherzolite	Porph.	Core	0.92	15.46	5.68	53.33	0.00	22.93	0.13	1.17	0.03	2.00	101.65	######	0.822	0.239	0.098	0.141	1.902	0.000	0.876	0.003	0.033	0.001	0.060	######
MD110-DR09-279 00	Cpx	µXRF	MD110-DR09	279	Sp-lherzolite	Porph.	Core	1.12	15.95	6.11	51.77	0.01	21.33	0.25	1.26	0.07	2.04	99.91	######	0.859	0.260	0.130	0.130	1.870	0.000	0.825	0.007	0.036	0.002	0.062	######
MD110-DR09-279 00	Cpx	µXRF	MD110-DR09	279	Sp-lherzolite	Porph.	Core	1.07	16.13	6.02	51.88	0.00	21.18	0.41	1.13	0.07	2.03	99.92	######	0.869	0.256	0.126	0.130	1.874	0.000	0.820	0.011	0.032	0.002	0.061	######
MD110-DR09-279-2	Cpx	EPMA	MD110-DR09	279	Sp-lherzolite	Porph.	Core	1.13	14.97	5.76	51.26	0.00	21.89	0.17	1.40	0.00	1.97	98.55	######	0.820	0.249	0.117	0.132	1.883	0.000	0.861	0.005	0.041	0.000	0.061	######
MD110-DR09-279-3	Cpx	EPMA	MD110-DR09	279	Sp-lherzolite	Porph.	Core	1.23	15.16	6.34	50.72	0.02	21.32	0.21	1.25	0.00	1.64	97.89	######	0.833	0.275	0.131	0.144	1.869	0.001	0.842	0.006	0.036	0.000	0.051	######
MD110-DR09-279-4	Cpx	EPMA	MD110-DR09	279	Sp-lherzolite	Porph.	Core	1.36	15.03	6.08	51.13	0.03	21.05	0.16	1.52	0.00	1.75	98.11	######	0.824	0.264	0.119	0.145	1.881	0.001	0.830	0.004	0.044	0.000	0.054	######
MD110-DR09-280 00	Cpx	µXRF	MD110-DR09	280b	Sp-lherzolite	Porph.	Core	0.88	16.33	5.37	51.61	0.01	21.66	0.22	1.20	0.07	2.55	99.90	######	0.881	0.229	0.132	0.097	1.868	0.000	0.840	0.006	0.034	0.002	0.077	######
MD110-DR09-280 00	Cpx	µXRF	MD110-DR09	280b	Sp-lherzolite	Porph.	Core	0.88	16.33	5.37	51.61	0.01	21.66	0.22	1.20	0.07	2.55	99.90	######	0.881	0.229	0.132	0.097	1.868	0.000	0.840	0.006	0.034	0.002	0.077	######
MD110-DR09-280b 0	Cpx	µXRF	MD110-DR09	280b	Sp-lherzolite	Porph.	Core	0.98	16.64	5.49	50.99	0.00	21.42	0.24	1.32	0.09	2.63	99.80	######	0.897	0.234	0.156	0.078	1.844	0.000	0.830	0.007	0.038	0.003	0.080	######
MD110-DR09-280b 0	Cpx	µXRF	MD110-DR09	280b	Sp-lherzolite	Porph.	Core	1.08	16.14	5.30	51.19	0.01	22.14	0.24	1.26	0.09	2.26	99.71	######	0.871	0.226	0.146	0.080	1.854	0.000	0.859	0.007	0.036	0.003	0.068	######
MD110-DR09-280B-1	Cpx	EPMA	MD110-DR09	280B	Sp-lherzolite	Porph.	Core	1.28	15.29	6.61	51.29	0.01	21.29	0.19	1.31	0.00	1.89	99.15	######	0.829	0.283	0.134	0.150	1.866	0.000	0.830	0.005	0.038	0.000	0.058	######
MD110-DR09-280B-2	Cpx	EPMA	MD110-DR09	280B	Sp-lherzolite	Porph.	Core	1.16	15.20	5.72	51.77	0.00	22.20	0.23	1.32	0.00	1.84	99.45	######	0.824	0.245	0.117	0.128	1.883	0.000	0.865	0.006	0.038	0.000	0.056	######
MD110-DR09-280B-3	Cpx	EPMA	MD110-DR09	280B	Sp-lherzolite	Porph.	Core	1.33	15.32	5.86	51.94	0.02	22.16	0.19	1.48	0.11	1.88	100.31	######	0.823	0.249	0.128	0.120	1.872	0.001	0.855	0.005	0.042	0.003	0.057	######
MD110-DR09-280B-4	Cpx	EPMA	MD110-DR09	280B	Sp-lherzolite	Porph.	Core	1.10	16.33	5.19	51.73	0.01	21.18	0.20	1.19	0.13	2.04	99.10	######	0.886	0.223	0.118	0.105	1.882	0.000	0.826	0.005	0.034	0.004	0.062	######
MD110-DR09-281 00	Cpx	µXRF	MD110-DR09	281	Sp-lherzolite	Porph.	Core	1.01	16.90	5.81	50.87	0.03	20.78	0.37	1.31	0.08	2.66	99.82	######	0.910	0.247	0.163	0.084	1.837	0.001	0.804	0.010	0.037	0.002	0.080	######
MD110-DR09-281 00	Cpx	µXRF	MD110-DR09	281	Sp-lherzolite	Porph.	Core	1.01	16.90	5.81	50.87	0.03	20.78	0.37	1.31	0.08	2.66	99.82	######	0.910	0.247	0.163	0.084	1.837	0.001	0.804	0.010	0.037	0.002	0.080	######
MD110-DR09-281 00	Cpx	µXRF	MD110-DR09	281	Sp-lherzolite	Porph.	Core	1.01	16.90	5.81	50.87	0.03	20.78	0.37	1.31	0.08	2.66	99.82	######	0.910	0.247	0.163	0.084	1.837	0.001	0.804	0.010	0.037	0.002	0.080	######
MD110-DR09-281b 0	Cpx	µXRF	MD110-DR09	281b	Sp-lherzolite	Porph.	Core	1.18	15.93	5.68	51.25	0.00	21.72	0.23	1.36	0.08	2.46	99.89	######	0.859	0.242	0.147	0.095	1.853	0.000	0.841	0.006	0.039	0.002	0.074	######
MD110-DR09-281b 0	Cpx	µXRF	MD110-DR09	281b	Sp-lherzolite	Porph.	Core	1.05	16.84	4.99	51.05	0.01	21.40	0.25	1.28	0.08	2.94	99.89	######	0.907	0.212	0.156	0.056	1.844	0.000	0.828	0.007	0.037	0.002	0.089	######
MD110-DR09-281b 0	Cpx	µXRF	MD110-DR09	281b	Sp-lherzolite	Porph.	Core	1.08	16.08	5.66	51.34	0.00	21.51	0.23	1.28	0.07	2.56	99.81	######	0.868	0.241	0.142	0.100	1.858	0.000	0.834	0.006	0.037	0.002	0.077	######
MD110-DR09-281b 0	Cpx	µXRF	MD110-DR09	281b	Sp-lherzolite	Porph.	Core	1.18	16.48	5.63	50.74	0.01	21.14	0.27	1.34	0.08	2.99	99.86	######	0.888	0.240	0.167	0.073	1.833	0.000	0.818	0.007	0.038	0.002	0.090	######
MD110-DR09-281B-2	Cpx	EPMA	MD110-DR09	281B	Sp-lherzolite	Porph.	Core	1.29	15.73	6.02	51.31	0.01	21.46	0.30	1.47	0.21	2.02	99.82	######	0.848	0.257	0.145	0.112	1.855	0.000	0.831	0.008	0.042	0.006	0.061	######
MD110-DR09-281B-2	Cpx	EPMA	MD110-DR09	281B	Sp-lherzolite	Porph.	Core	1.32	15.89	5.82	51.61	0.01	21.50	0.24	1.44	0.00	2.03	99.87	######	0.855	0.248	0.136	0.111	1.864	0.000	0.832	0.007	0.041	0.000	0.061	######
MD110-DR09-281B-2	Cpx	EPMA	MD110-DR09	281B	Sp-lherzolite	Porph.	Core	1.44	15.45	6.04	51.55	0.00	21.65	0.30	1.33	0.13	2.10	99.99	######	0.831	0.257	0.140	0.117	1.860	0.000	0.837	0.008	0.038	0.004	0.063	######
MD110-DR09-281B-3	Cpx	EPMA	MD110-DR09	281B	Sp-lherzolite	Porph.	Core	1.23	16.31	4.66	51.62	0.03	21.89	0.22	1.35	0.11	2.19	99.62	######	0.881	0.199	0.131	0.068	1.869	0.001	0.849	0.006	0.039	0.003	0.066	######
MD110-DR09-281B-3	Cpx	EPMA	MD110-DR09	281B	Sp-lherzolite	Porph.	Core	1.20	15.46	5.06	52.50	0.02	22.50	0.24	1.24	0.10	1.45	99.75	######	0.835	0.216	0.098	0.118	1.902	0.001	0.873	0.007	0.036	0.003	0.044	######
MD110-DR09-281B-3	Cpx	EPMA	MD110-DR09	281B	Sp-lherzolite	Porph.	Core	1.18	15.47	5.68	51.72	0.00	22.42	0.23	1.31	0.15	1.66	99.84	######	0.835	0.242	0.128	0.114	1.872	0.000	0.869	0.006	0.037	0.005	0.050	######
MD110-DR09-281B-4	Cpx	EPMA	MD110-DR09	281B	Sp-lherzolite	Porph.	Core	1.33	15.91	5.26	51.50	0.01	21.48	0.18	1.22	0.03	2.04	98.96	######	0.864	0.226	0.125	0.101	1.875	0.000	0.838	0.005	0.035	0.001	0.062	######
MD110-DR09-281B-4	Cpx	EPMA	MD110-DR09	281B	Sp-lherzolite	Porph.	Core	1.23	16.38	5.31	51.34	0.01	21.63	0.27	1.34	0.01	2.15	99.67	######	0.883	0.226	0.144	0.082	1.856	0.000	0.838	0.007	0.038	0.000	0.065	######
MD110-DR09-281B-4	Cpx	EPMA	MD110-DR09	281B	Sp-lherzolite	Porph.	Core	1.18	15.87	5.80	51.61	0.02	21.91	0.27	1.27	0.13	2.07	100.14	######	0.853	0.246	0.139	0.107	1.861	0.001	0.846	0.007	0.036	0.004	0.062	######
MD110-DR09-281B-5	Cpx	EPMA	MD110-DR09	281B	Sp-lherzolite	Porph.	Core	1.22	15.51	5.50	52.02	0.03	21.76	0.24	1.21	0.07	2.09	99.66	######	0.839	0.235	0.113	0.122	1.887	0.001	0.846	0.007	0.035	0.002	0.063	######
MD110-DR09-281B-6	Cpx	EPMA	MD110-DR09	281B	Sp-lherzolite	Porph.	Core	1.27	15.99	4.83	52.71	0.00	22.01	0.20	1.09	0.00	2.12	100.21	######	0.859	0.205	0.102	0.103	1.898	0.000	0.849	0.005	0.031	0.000	0.064	######
MD110-DR09-281B-7	Cpx	EPMA	MD110-DR09	281B	Sp-lherzolite	Porph.	Core	1.22	15.71	5.96	51.81	0.00	21.75	0.26	1.43	0.00	1.89	100.02	######	0.845	0.254	0.130	0.123	1.870	0.000	0.841	0.007	0.041	0.000	0.057	######
MD110-DR09-281B-8	Cpx	EPMA	MD110-DR09	281B	Sp-lherzolite	Porph.	Core	1.12	16.00	5.21	51.53	0.00	21.91	0.16	1.36	0.04	1.92	99.25	######	0.867	0.223	0.126	0.097	1.874	0.000	0.854	0.004	0.039	0.001	0.058	######
MD80-DR3-D2 001	Cpx	µXRF	MD80-DR3	3D2	Sp-lherzolite	Porph.	Core	1.01	16.12	5.24	51.29	0.10	22.08	0.32	0.90	0.11	2.75	99.92	######	0.869	0.223	0.145	0.079	1.855	0.005	0.856	0.009	0.026	0.003	0.083	######
MD80-DR3-D2 003	Cpx	µXRF	MD80-DR3	3D2	Sp-lherzolite	Porph.	Core	0.89	16.20	5.71	51.24	0.00	21.87	0.10	0.97	0.08	2.78	99.84	######	0.874	0.244	0.145	0.098	1.855	0.000	0.848	0.003	0.028	0.002	0.084	######
MD80-DR3-D2 004	Cpx	µXRF	MD80-DR3	3D2	Sp-lherzolite	Porph.	Core	0.97	16.19	5.24	51.43	0.00	21.92	0.10	1.01	0.07	2.95	99.88	######	0.874	0.224	0.138	0.085	1.862	0.000	0.850	0.003	0.029	0.002	0.089	######
MD80-DR3-D2 005	Cpx	µXRF	MD80-DR3	3D2	Sp-lherzolite	Porph.	Core	0.95	16.50	5.56	51.17	0.00	21.90	0.14	0.91	0.08	2.66	99.87	######	0.888	0.237	0.152	0.085	1.848	0.000	0.847	0.004	0.026	0.002	0.080	######
MD80-DR3-D2 006	Cpx	µXRF	MD80-DR3	3D2	Sp-lherzolite	Porph.	Core	0.88	16.03	5.34	51.42	0.00	22.09	0.10	0.94	0.11	2.96	99.87	######	0.866	0.228	0.136	0.092	1.864	0.000	0.858	0.003	0.027	0.003	0.090	######
MD80-DR3-D2-10	Cpx	EPMA	MD80-DR3	3D2	Sp-lherzolite	Porph.	Core	1.15	15.50	5.62	51.82	0.00	22.13	0.09	0.94	0.09	2.30	99.64	######	0.838	0.240	0.121	0.119	1.879	0.000	0.860	0.002	0.027	0.003	0.070	######
MD80-DR3-D2-11	Cpx	EPMA	MD80-DR3	3D2	Sp-lherzolite	Porph.	Core	1.06	15.98	5.50	51.33	0.00	22.30	0.15	0.86	0.08	2.34	99.59	######	0.863	0.235	0.140	0.095	1.860	0.000	0.866	0.004	0.025	0.002	0.071	######
MD80-DR3-D2-12	Cpx	EPMA	MD80-DR3	3D2	Sp-lherzolite	Porph.	Core	1.13	15.53	5.67	52.27	0.00	22.09	0.08	0.86	0.06	2.32	100.02	######	0.837	0.241	0.111	0.130	1.889	0.000	0.855	0.002	0.025	0.002	0.070	######
MD80-DR3-D2-1a	Cpx	EPMA	MD80-DR3	3D2	Sp-lherzolite	Porph.	Core	1.03	16.22	4.80	52.43	0.00	21.94	0.12	0.89	0.14	2.23	99.81	######	0.875	0.205	0.103	0.102	1.897	0.000	0.850	0.003	0.025	0.004	0.067	######
MD80-DR3-D2-1b	Cpx	EPMA	MD80-DR3	3D2	Sp-lherzolite	Porph.	Core	1.00	16.06	4.55	52.21	0.00	21.92	0.09	0.85	0.00	2.34	99.02	######	0.874	0.196	0.095	0.101	1.905	0.000	0.857	0.002	0.025	0.000	0.071	######
MD80-DR3-D2-2a	Cpx	EPMA	MD80-DR3	3D2	Sp-lherzolite	Porph.	Core	1.15	15.62	5.89	50.91	0.01	21.64	0.12	1.03	0.05	2.19	98.60	######	0.852	0.254	0.138	0.116	1.862	0.000	0.848	0.003	0.030	0.002	0.067	######

B.5. Table de données – compositions chimiques en éléments majeurs des clinopyroxènes

MD80-DR3-D2-2b	Cpx	EPMA	MD80-DR3	3D2	Sp-lherzolite	Porph.	Core	1.09	15.28	5.86	50.93	0.00	21.69	0.09	0.98	0.14	2.38	98.43	######	0.837	0.254	0.130	0.124	1.870	0.000	0.853	0.002	0.028	0.004	0.073	######
MD80-DR3-D2-5	Cpx	EPMA	MD80-DR3	3D2	Sp-lherzolite	Porph.	Core	1.03	15.40	5.69	50.13	0.00	22.03	0.12	0.85	0.09	2.16	97.50	######	0.850	0.248	0.144	0.104	1.856	0.000	0.874	0.003	0.025	0.003	0.067	######
MD80-DR3-D4-1 001	Cpx	µXRF	MD80-DR3	3D4-1	Sp-lherzolite	Porph.	Core	1.06	16.11	6.08	51.75	0.01	21.73	0.10	0.91	0.07	2.07	99.89	######	0.867	0.259	0.133	0.126	1.867	0.000	0.840	0.003	0.026	0.002	0.062	######
MD80-DR3-D4-1 002	Cpx	µXRF	MD80-DR3	3D4-1	Sp-lherzolite	Porph.	Core	1.00	15.93	5.96	51.78	0.01	21.91	0.11	0.91	0.07	2.21	99.89	######	0.858	0.254	0.129	0.125	1.871	0.000	0.848	0.003	0.026	0.002	0.067	######
MD80-DR3-D4-1 005	Cpx	µXRF	MD80-DR3	3D4-1	Sp-lherzolite	Porph.	Core	0.98	16.19	5.83	51.91	0.01	21.57	0.10	1.15	0.05	2.12	99.91	######	0.872	0.248	0.125	0.123	1.875	0.000	0.835	0.003	0.033	0.002	0.064	######
MD80-DR3-D4-1 007	Cpx	µXRF	MD80-DR3	3D4-1	Sp-lherzolite	Porph.	Core	0.93	16.59	5.21	51.85	0.00	22.07	0.11	0.85	0.07	2.19	99.87	######	0.893	0.222	0.128	0.093	1.872	0.000	0.853	0.003	0.024	0.002	0.066	######
MD80-DR3-D4-1 008	Cpx	µXRF	MD80-DR3	3D4-1	Sp-lherzolite	Porph.	Core	0.96	16.84	5.60	52.17	0.00	21.38	0.10	0.75	0.07	2.05	99.92	######	0.904	0.238	0.121	0.116	1.879	0.000	0.825	0.003	0.021	0.002	0.062	######
MD80-DR3-D4-1 011	Cpx	µXRF	MD80-DR3	3D4-1	Sp-lherzolite	Porph.	Core	1.06	16.39	6.03	51.51	0.00	21.46	0.11	0.96	0.06	2.33	99.91	######	0.881	0.256	0.143	0.113	1.857	0.000	0.829	0.003	0.027	0.002	0.070	######
MD80-DR3-D4-1 012	Cpx	µXRF	MD80-DR3	3D4-1	Sp-lherzolite	Porph.	Core	1.01	16.06	6.30	51.28	0.01	21.68	0.11	0.98	0.07	2.43	99.93	######	0.864	0.268	0.149	0.119	1.851	0.000	0.839	0.003	0.028	0.002	0.073	######
MD80-DR3-D4-1-1	Cpx	EPMA	MD80-DR3	3D4-1	Sp-lherzolite	Porph.	Core	1.10	15.68	6.03	50.55	0.00	22.02	0.08	1.05	0.09	2.48	99.08	######	0.852	0.259	0.158	0.100	1.842	0.000	0.859	0.002	0.030	0.003	0.076	######
MD80-DR3-D4-1-10	Cpx	EPMA	MD80-DR3	3D4-1	Sp-lherzolite	Porph.	Core	1.18	15.85	5.62	50.23	0.00	22.08	0.14	0.93	0.06	2.21	98.31	######	0.866	0.243	0.159	0.083	1.841	0.000	0.867	0.004	0.027	0.002	0.068	######
MD80-DR3-D4-1-11	Cpx	EPMA	MD80-DR3	3D4-1	Sp-lherzolite	Porph.	Core	1.09	15.78	5.60	50.95	0.00	22.28	0.14	0.97	0.00	2.60	99.41	######	0.855	0.240	0.149	0.091	1.851	0.000	0.867	0.004	0.028	0.000	0.079	######
MD80-DR3-D4-1-12	Cpx	EPMA	MD80-DR3	3D4-1	Sp-lherzolite	Porph.	Core	1.23	15.37	5.98	51.08	0.01	22.27	0.14	1.03	0.00	2.16	99.27	######	0.833	0.256	0.143	0.113	1.857	0.000	0.867	0.004	0.030	0.000	0.066	######
MD80-DR3-D4-1-3	Cpx	EPMA	MD80-DR3	3D4-1	Sp-lherzolite	Porph.	Core	1.11	15.91	5.67	51.48	0.00	21.68	0.07	0.97	0.12	2.00	99.03	######	0.864	0.243	0.125	0.118	1.875	0.000	0.846	0.002	0.028	0.004	0.061	######
MD80-DR3-D4-1-5	Cpx	EPMA	MD80-DR3	3D4-1	Sp-lherzolite	Porph.	Core	1.20	16.06	5.86	50.30	0.04	21.28	0.08	1.01	0.09	2.47	98.38	######	0.876	0.253	0.160	0.093	1.840	0.002	0.834	0.002	0.029	0.003	0.076	######
MD80-DR3-D4-1-6	Cpx	EPMA	MD80-DR3	3D4-1	Sp-lherzolite	Porph.	Core	1.17	15.62	5.92	51.59	0.02	22.23	0.02	1.09	0.16	2.27	100.09	######	0.840	0.252	0.139	0.113	1.861	0.001	0.859	0.001	0.031	0.005	0.068	######
MD80-DR3-D4-1-7	Cpx	EPMA	MD80-DR3	3D4-1	Sp-lherzolite	Porph.	Core	1.19	16.03	5.11	51.25	0.00	21.97	0.03	0.88	0.00	2.46	98.91	######	0.871	0.219	0.133	0.087	1.867	0.000	0.858	0.001	0.025	0.000	0.075	######
MD80-DR3-D4-1-8	Cpx	EPMA	MD80-DR3	3D4-1	Sp-lherzolite	Porph.	Core	1.16	15.54	5.55	49.72	0.00	21.73	0.09	1.04	0.11	2.42	97.37	######	0.858	0.242	0.158	0.084	1.842	0.000	0.863	0.003	0.030	0.003	0.075	######
MD80-DR3-D4-1-9	Cpx	EPMA	MD80-DR3	3D4-1	Sp-lherzolite	Porph.	Core	1.11	16.20	5.79	50.85	0.00	21.03	0.06	1.08	0.15	2.29	98.56	######	0.883	0.249	0.142	0.108	1.858	0.000	0.823	0.002	0.031	0.005	0.070	######
MD80-DR3-D4-2 002	Cpx	µXRF	MD80-DR3	3D4-2	Sp-lherzolite	Porph.	Core	1.05	16.82	6.06	52.75	0.01	20.54	0.09	0.75	0.06	1.80	99.93	######	0.902	0.257	0.103	0.154	1.897	0.000	0.791	0.002	0.021	0.002	0.054	######
MD80-DR3-D4-2 003	Cpx	µXRF	MD80-DR3	3D4-2	Sp-lherzolite	Porph.	Core	0.89	16.34	5.34	52.36	0.01	21.79	0.10	0.74	0.08	2.21	99.86	######	0.880	0.227	0.108	0.120	1.892	0.000	0.844	0.003	0.021	0.002	0.067	######
MD80-DR3-D4-2 004	Cpx	µXRF	MD80-DR3	3D4-2	Sp-lherzolite	Porph.	Core	1.10	16.21	5.72	51.33	0.01	21.76	0.13	0.92	0.08	2.60	99.86	######	0.873	0.243	0.146	0.097	1.854	0.000	0.842	0.004	0.026	0.002	0.079	######
MD80-DR3-D4-2 006	Cpx	µXRF	MD80-DR3	3D4-2	Sp-lherzolite	Porph.	Core	0.97	16.24	5.97	51.65	0.01	21.54	0.10	0.92	0.07	2.43	99.90	######	0.874	0.254	0.135	0.119	1.865	0.000	0.833	0.003	0.026	0.002	0.073	######
MD80-DR3-D4-2 007	Cpx	µXRF	MD80-DR3	3D4-2	Sp-lherzolite	Porph.	Core	0.91	16.69	6.27	51.49	0.01	20.74	0.10	0.98	0.07	2.51	99.77	######	0.899	0.267	0.141	0.126	1.859	0.000	0.802	0.003	0.028	0.002	0.076	######
MD80-DR3-D4-2 008	Cpx	µXRF	MD80-DR3	3D4-2	Sp-lherzolite	Porph.	Core	1.05	16.33	5.63	51.46	0.01	21.83	0.10	0.84	0.09	2.33	99.67	######	0.880	0.240	0.140	0.100	1.860	0.000	0.846	0.003	0.024	0.003	0.070	######
MD80-DR3-D4-2-1	Cpx	EPMA	MD80-DR3	3D4-2	Sp-lherzolite	Porph.	Core	1.09	15.88	5.29	50.74	0.00	21.78	0.08	1.11	0.05	2.24	98.26	######	0.869	0.229	0.137	0.092	1.863	0.000	0.857	0.002	0.032	0.002	0.069	######
MD80-DR3-D4-2-14	Cpx	EPMA	MD80-DR3	3D4-2	Sp-lherzolite	Porph.	Core	1.24	15.24	6.32	51.63	0.00	22.14	0.07	1.05	0.19	2.38	100.28	######	0.819	0.269	0.139	0.130	1.861	0.000	0.855	0.002	0.030	0.006	0.072	######
MD80-DR3-D4-2-2	Cpx	EPMA	MD80-DR3	3D4-2	Sp-lherzolite	Porph.	Core	1.15	15.47	6.00	49.04	0.00	21.37	0.15	0.96	0.07	2.01	96.20	######	0.863	0.265	0.165	0.099	1.835	0.000	0.857	0.004	0.028	0.002	0.063	######
MD80-DR3-D4-2-3	Cpx	EPMA	MD80-DR3	3D4-2	Sp-lherzolite	Porph.	Core	1.16	15.85	5.10	50.81	0.00	21.82	0.00	0.87	0.25	1.97	97.83	######	0.870	0.221	0.129	0.092	1.871	0.000	0.861	0.000	0.025	0.008	0.061	######
MD80-DR3-D4-2-4	Cpx	EPMA	MD80-DR3	3D4-2	Sp-lherzolite	Porph.	Core	1.14	15.78	5.27	49.04	0.00	21.96	0.05	0.98	0.00	2.23	96.45	######	0.878	0.232	0.170	0.062	1.830	0.000	0.878	0.001	0.029	0.000	0.070	######
MD80-DR3-D4-2-8	Cpx	EPMA	MD80-DR3	3D4-2	Sp-lherzolite	Porph.	Core	1.35	15.13	5.94	51.43	0.02	21.67	0.09	0.85	0.09	2.13	98.69	######	0.824	0.256	0.120	0.136	1.880	0.001	0.849	0.002	0.025	0.003	0.065	######
MD80-DR3-D4-2-8bis	Cpx	EPMA	MD80-DR3	3D4-2	Sp-lherzolite	Porph.	Core	1.35	15.13	5.94	51.43	0.02	21.67	0.09	0.85	0.09	2.13	98.69	######	0.824	0.256	0.120	0.136	1.880	0.001	0.849	0.002	0.025	0.003	0.065	######
MD80-DR3-G2-2 002	Cpx	µXRF	MD80-DR3	*3G2-2*	Sp-lherzolite	Porph.	Core	1.49	15.86	7.22	51.07	0.02	20.22	0.31	1.16	0.07	2.34	99.76	######	0.852	0.307	0.159	0.148	1.841	0.001	0.781	0.008	0.033	0.002	0.071	######
MD80-DR3-G2-2 003	Cpx	µXRF	MD80-DR3	*3G2-2*	Sp-lherzolite	Porph.	Core	1.55	15.80	6.48	51.34	0.01	20.81	0.34	1.04	0.07	2.20	99.64	######	0.850	0.276	0.147	0.129	1.853	0.000	0.805	0.009	0.030	0.002	0.066	######
MD80-DR3-G2-2 004	Cpx	µXRF	MD80-DR3	*3G2-2*	Sp-lherzolite	Porph.	Core	1.51	15.54	6.66	51.81	0.00	20.78	0.35	1.06	0.07	2.10	99.88	######	0.835	0.283	0.132	0.151	1.868	0.000	0.803	0.009	0.030	0.002	0.063	######
MD80-DR3-G2-2 007	Cpx	µXRF	MD80-DR3	*3G2-2*	Sp-lherzolite	Porph.	Core	1.47	15.73	6.77	51.77	0.00	20.52	0.48	1.03	0.07	2.04	99.88	######	0.845	0.288	0.134	0.154	1.866	0.000	0.792	0.013	0.029	0.002	0.061	######
MD80-DR3-G2-2-3	Cpx	EPMA	MD80-DR3	3G2-2	Sp-lherzolite	Porph.	Core	1.76	14.24	7.29	52.62	0.00	21.65	0.34	1.30	0.00	2.26	101.48	######	0.757	0.306	0.124	0.182	1.876	0.000	0.827	0.009	0.037	0.000	0.067	######
MD80-DR3-G2-2-4	Cpx	EPMA	MD80-DR3	3G2-2	Sp-lherzolite	Porph.	Core	1.63	14.84	7.34	52.51	0.00	21.06	0.33	1.32	0.23	2.34	101.59	######	0.787	0.308	0.132	0.176	1.868	0.000	0.803	0.009	0.037	0.007	0.070	######
MD80-DR3-G2-2-5	Cpx	EPMA	MD80-DR3	3G2-2	Sp-lherzolite	Porph.	Core	1.73	14.28	6.72	52.95	0.00	21.40	0.33	1.15	0.08	2.15	100.79	######	0.764	0.284	0.100	0.184	1.900	0.000	0.823	0.009	0.033	0.002	0.065	######
MD80-DR3-G2-2-6	Cpx	EPMA	MD80-DR3	3G2-2	Sp-lherzolite	Porph.	Core	1.67	15.00	6.20	53.05	0.01	21.77	0.44	1.01	0.03	1.96	101.13	######	0.798	0.261	0.107	0.154	1.893	0.000	0.832	0.012	0.028	0.001	0.058	######
MD80-DR3-G2-2-7	Cpx	EPMA	MD80-DR3	3G2-2	Sp-lherzolite	Porph.	Core	1.52	15.88	5.55	52.75	0.00	21.39	0.36	1.02	0.07	1.81	100.36	######	0.849	0.235	0.107	0.127	1.893	0.000	0.822	0.010	0.029	0.002	0.054	######
MD80-DR3-I2-11	Cpx	EPMA	MD80-DR3	3I2	Sp-lherzolite	Porph.	Core	1.70	15.56	6.35	52.40	0.01	20.62	0.28	1.21	0.11	2.49	100.74	######	0.830	0.268	0.126	0.142	1.874	0.000	0.790	0.008	0.034	0.003	0.074	######
MD80-DR3-I2-12	Cpx	EPMA	MD80-DR3	3I2	Sp-lherzolite	Porph.	Core	1.62	15.03	6.44	50.54	0.00	21.14	0.30	1.24	0.00	2.27	98.58	######	0.819	0.277	0.153	0.125	1.847	0.000	0.828	0.008	0.036	0.000	0.069	######
MD80-DR3-I2-12	Cpx	EPMA	MD80-DR3	3I2	Sp-lherzolite	Porph.	Core	1.62	15.03	6.44	50.54	0.00	21.14	0.30	1.24	0.00	2.27	98.58	######	0.819	0.277	0.153	0.125	1.847	0.000	0.828	0.008	0.036	0.000	0.069	######
MD80-DR3-I2-15	Cpx	EPMA	MD80-DR3	3I2	Sp-lherzolite	Porph.	Core	1.56	15.34	5.92	52.60	0.00	20.85	0.31	1.01	0.02	2.40	100.02	######	0.825	0.252	0.102	0.150	1.898	0.000	0.806	0.008	0.029	0.001	0.072	######
MD80-DR3-I2-15b	Cpx	EPMA	MD80-DR3	3I2	Sp-lherzolite	Porph.	Core	1.56	15.34	5.92	52.60	0.00	20.85	0.31	1.01	0.02	2.40	100.02	######	0.825	0.252	0.102	0.150	1.898	0.000	0.806	0.008	0.029	0.001	0.072	######
MD80-DR3-I2-16	Cpx	EPMA	MD80-DR3	3I2	Sp-lherzolite	Porph.	Core	1.74	14.69	6.30	52.15	0.01	20.58	0.30	1.21	0.07	2.18	99.23	######	0.797	0.270	0.103	0.167	1.897	0.000	0.802	0.008	0.035	0.002	0.066	######
MD80-DR3-I2-3	Cpx	EPMA	MD80-DR3	3I2	Sp-lherzolite	Porph.	Core	1.60	14.94	6.08	53.60	0.02	21.37	0.32	1.07	0.17	2.33	101.50	######	0.794	0.255	0.090	0.166	1.910	0.001	0.816	0.009	0.030	0.005	0.069	######
MD80-DR3-I2-9	Cpx	EPMA	MD80-DR3	3I2	Sp-lherzolite	Porph.	Core	1.62	14.52	6.27	51.54	0.02	20.14	0.28	1.22	0.08	2.10	97.78	######	0.799	0.273	0.097	0.176	1.903	0.001	0.797	0.008	0.036	0.003	0.065	######
MD80-DR3-I2-9	Cpx	EPMA	MD80-DR3	3I2	Sp-lherzolite	Porph.	Core	1.62	14.52	6.27	51.54	0.02	20.14	0.28	1.22	0.08	2.10	97.78	######	0.799	0.273	0.097	0.176	1.903	0.001	0.797	0.008	0.036	0.003	0.065	######
MD80-DR3-I3 001	Cpx	µXRF	MD80-DR3	3I3	Sp-lherzolite	Porph.	Core	0.91	16.57	4.60	52.25	0.01	21.86	0.12	1.19	0.09	2.10	99.70	######	0.895	0.196	0.107	0.089	1.893	0.000	0.848	0.003	0.034	0.003	0.064	######
MD80-DR3-I3 002	Cpx	µXRF	MD80-DR3	3I3	Sp-lherzolite	Porph.	Core	0.99	16.47	4.65	52.26	0.04	22.00	0.13	1.09	0.06	1.99	99.68	######	0.889	0.198	0.108	0.090	1.892	0.002	0.853	0.004	0.031	0.002	0.060	######
MD80-DR3-I3 003	Cpx	µXRF	MD80-DR3	3I3	Sp-lherzolite	Porph.	Core	0.97	16.53	4.90	52.41	0.00	21.72	0.12	1.22	0.06	1.97	99.90	######	0.890	0.209	0.107	0.102	1.893	0.000	0.841	0.003	0.035	0.002	0.060	######
MD80-DR3-I3 004	Cpx	µXRF	MD80-DR3	3I3	Sp-lherzolite	Porph.	Core	1.07	17.07	4.91	51.60	0.01	21.58	0.12	1.24	0.06	2.22	99.88	######	0.917	0.208	0.141	0.068	1.859	0.000	0.833	0.003	0.035	0.002	0.067	######

B.5. Table de données – compositions chimiques en éléments traces des clinopyroxènes

Analysis	MD110-DR02-A13 007	MD110-DR02-A13 008	MD110-DR02-A13-11	MD110-DR02-A27 011	MD110-DR02-A27 012	MD110-DR02-A27-12	MD110-DR02-A27-2	MD110-DR02-A48 001	MD110-DR02-A48 002	MD110-DR02-A48 008	MD110-DR02-A48-11a	MD110-DR02-A48-11b	MD110-DR02-A48-1bis	MD110-DR02-A48-2	MD110-DR02-A48-23
Mineral	Cpx	Cpx	Cpx	Cpx	Cpx	Cpx	Cpx	Cpx	Cpx	Cpx	Cpx	Cpx	Cpx	Cpx	Cpx
Location	MD110-DR02	MD110-DR02	MD110-DR02	MD110-DR02	MD110-DR02	MD110-DR02	MD110-DR02	MD110-DR02	MD110-DR02	MD110-DR02	MD110-DR02	MD110-DR02	MD110-DR02	MD110-DR02	MD110-DR02
Sample	A13	A13	A13	A27	A27	A27	A27	A48	A48	A48	A48	A48	A48	A48	A48
Rock type	Sp-lherzolite	Sp-lherzolite	Sp-lherzolite	Sp-lherzolite	Sp-lherzolite	Sp-lherzolite	Sp-lherzolite	Sp-lherzolite	Sp-lherzolite	Sp-lherzolite	Sp-lherzolite	Sp-lherzolite	Sp-lherzolite	Sp-lherzolite	Sp-lherzolite
Texture	Porph.	Porph.	Porph.	Porph.	Porph.	Porph.	Porph.	Porph.	Porph.	Porph.	Porph.	Porph.	Porph.	Porph.	Porph.
Mineral location	Core	Core	Core	Core	Core	Core	Core	Core	Core	Core	Core	Core	Core	Core	Core
Li ppm	3.39	4.26	4.26	1.83	2.42	2.42	5.61	2.85	3.51	3.61	1.56	1.56	2.85	3.51	3.27
B ppm	<0.650	<0.565	<0.565	<2.47	4.25	4.25	9.58	2.84	2.94	4.02	<2.46	<2.46	2.84	2.94	6.69
Sc ppm	56.1	55.9	55.9	54.4	62.4	62.4	57.4	63.1	67.1	73.0	58.9	58.9	63.1	67.1	49.9
Ti ppm	1274	1930	1930	2239	2645	2645	2411	2557	2617	2726	2452	2452	2557	2617	2152
V ppm	254	269	269	245	272	272	261	268	273	279	260	260	268	273	234
Cr ppm	2674	2748	2748	7907	8313	8313	8207	10609	10565	10368	10575	10575	10609	10565	10909
Mn ppm															
Co ppm	20.7	21.2	21.2	21.8	18.8	18.8	19.5	18.9	18.7	16.7	20.5	20.5	18.9	18.7	21.8
Ni ppm	275	288	288	319	291	291	378	308	315	300	308	308	308	315	373
Rb ppm	0.0885	0.197	0.197	0.0234	0.0986	0.0986	0.205	<0.0426	<0.0491	<0.0492	<0.0530	<0.0530	<0.0426	<0.0491	0.505
Sr ppm	7.71	6.55	6.55	12.9	12.9	12.9	17.0	10.2	11.2	7.82	13.1	13.1	10.2	11.2	14.5
Y ppm	13.8	15.6	15.6	14.5	16.5	16.5	15.7	15.3	15.2	16.0	14.7	14.7	15.3	15.2	13.7
Zr ppm	5.25	13.2	13.2	14.1	17.3	17.3	20.4	21.5	22.2	22.3	20.4	20.4	21.5	22.2	18.9
Nb ppm	0.458	0.577	0.577	<0.00534	<0.00552	<0.00552	0.0775	<0.00432	<0.00433	<0.00525	<0.00499	<0.00499	<0.00432	<0.00433	0.0218
Cs ppm	<0.0239	<0.0192	<0.0192	<0.00516	<0.0381	<0.0381	<0.0447	<0.0270	<0.0270	<0.00511	0.0181	0.0181	<0.0270	<0.0270	<0.0343
Ba ppm	0.222	0.185	0.185	<0.0450	<0.0465	<0.0465	2.13	<0.0361	<0.0362	<0.0438	0.0417	0.0417	<0.0361	<0.0362	0.200
La ppm	0.518	0.748	0.748	0.0908	0.125	0.125	0.131	0.0605	0.0557	0.0902	0.0641	0.0641	0.0605	0.0557	0.187
Ce ppm	1.76	2.85	2.85	1.44	1.60	1.60	1.57	0.699	0.714	0.574	0.941	0.941	0.699	0.714	0.906
Pr ppm	0.319	0.554	0.554	0.321	0.372	0.372	0.411	0.296	0.270	0.192	0.311	0.311	0.296	0.270	0.372
Nd ppm	1.47	2.99	2.99	2.82	3.01	3.01	2.65	2.48	2.31	1.79	2.35	2.35	2.48	2.31	2.91
Sm ppm	0.656	1.23	1.23	1.06	1.33	1.33	1.33	1.37	1.13	1.16	1.66	1.66	1.37	1.13	1.44
Eu ppm	0.298	0.461	0.461	0.487	0.655	0.655	0.605	0.559	0.696	0.569	0.587	0.587	0.559	0.696	0.535
Gd ppm	1.25	1.88	1.88	1.84	2.67	2.67	2.25	1.93	2.05	2.15	2.10	2.10	1.93	2.05	2.05
Tb ppm	0.290	0.373	0.373	0.387	0.362	0.362	0.410	0.350	0.373	0.330	0.355	0.355	0.350	0.373	0.331
Dy ppm	1.94	2.46	2.46	2.83	2.67	2.67	3.00	2.75	2.79	2.47	2.87	2.87	2.75	2.79	2.46
Ho ppm	0.507	0.572	0.572	0.532	0.602	0.602	0.648	0.522	0.611	0.684	0.613	0.613	0.522	0.611	0.527
Er ppm	1.30	1.56	1.56	1.48	1.66	1.66	1.77	1.54	1.68	1.76	1.62	1.62	1.54	1.68	1.40
Tm ppm	0.225	0.214	0.214	0.218	0.194	0.194	0.217	0.223	0.221	0.219	0.184	0.184	0.223	0.221	0.159
Yb ppm	1.36	1.24	1.24	1.44	1.48	1.48	1.56	1.33	1.54	1.24	0.997	0.997	1.33	1.54	1.12
Lu ppm	0.190	0.209	0.209	0.214	0.193	0.193	0.159	0.165	0.179	0.194	0.175	0.175	0.165	0.179	0.200
Hf ppm	0.125	0.441	0.441	0.590	0.687	0.687	0.743	0.926	0.876	0.833	0.823	0.823	0.926	0.876	0.686
Ta ppm	0.0196	0.0333	0.0333	<0.00651	<0.00673	<0.00673	<0.0110	<0.00533	<0.00534	<0.00644	<0.00612	<0.00612	<0.00533	<0.00534	<0.00619
Pb ppm	0.0353	0.0250	0.0250	0.0409	<0.0859	<0.0859	0.0668	<0.0138	0.0188	0.0567	0.0532	0.0532	<0.0138	0.0188	0.104
Th ppm	0.0307	0.0378	0.0378	<0.00930	<0.00961	<0.00961	0.0270	<0.00769	<0.00769	<0.00926	<0.00879	<0.00879	<0.00769	<0.00769	<0.00882
U ppm	0.0124	0.0167	0.0167	<0.00966	<0.00999	<0.00999	<0.0163	<0.00792	<0.00792	<0.00955	<0.00906	<0.00906	<0.00792	<0.00792	0.0305
Eu/Eu*	1.00	0.92	0.92	1.06	1.06	1.06	1.06	1.04	1.39	1.09	0.96	0.96	1.04	1.39	0.95

B.5. Table de données – compositions chimiques en éléments traces des clinopyroxènes

Analysis	MD110-DR02-A48-23	MD110-DR02-A48-23	MD110-DR02-A48-8	MD110-DR02-A50-12	MD110-DR02-A50-13	MD110-DR02-A50-15	MD110-DR02-A50-1b	MD110-DR02-A50-1c	MD110-DR02-A50-4	MD110-DR02-A50-5	MD110-DR02-A50-6	MD110-DR02-A58 007	MD110-DR02-A58-5	MD110-DR02-A64 002	MD110-DR02-A64 006
Mineral	Cpx	Cpx	Cpx	Cpx	Cpx	Cpx	Cpx	Cpx	Cpx	Cpx	Cpx	Cpx	Cpx	Cpx	Cpx
Location	MD110-DR02	MD110-DR02	MD110-DR02	MD110-DR02	MD110-DR02	MD110-DR02	MD110-DR02	MD110-DR02	MD110-DR02	MD110-DR02	MD110-DR02	MD110-DR02	MD110-DR02	MD110-DR02	MD110-DR02
Sample	A48	A48	A48	A50	A50	A50	A50	A50	A50	A50	A50	A58	A58	A64	A64
Rock type	Sp-lherzolite	Sp-lherzolite	Sp-lherzolite	Sp-lherzolite	Sp-lherzolite	Sp-lherzolite	Sp-lherzolite	Sp-lherzolite	Sp-lherzolite	Sp-lherzolite	Sp-lherzolite	Sp-lherzolite	Sp-lherzolite	Sp-lherzolite	Sp-lherzolite
Texture	Porph.	Porph.	Porph.	Porph.	Porph.	Porph.	Porph.	Porph.	Porph.	Porph.	Porph.	Porph.	Porph.	Porph.	Porph.
Mineral location	Core	Core	Core	Core	Core	Core	Core	Core	Core	Core	Core	Core	Core	Core	Core
Li ppm	2.36	2.36	3.61	<1.10	<1.32	<1.15	2.79	4.69	1.43	<1.88	3.03	2.24	2.73	2.48	1.96
B ppm	<2.64	3.45	4.02	<3.37	<3.92	<3.11	<4.09	0.986	<3.69	<5.79	<5.67	<2.19	<2.63	4.03	<2.42
Sc ppm	49.6	49.2	73.0	17.2	20.5	20.5	51.9	49.0	18.2	51.1	48.6	57.1	52.8	56.8	63.7
Ti ppm	2090	2104	2726	555	644	711	2000	1779	583	2039	1981	2199	2173	2367	2471
V ppm	231	231	279	93.4	108	114	235	222	96.7	228	230	257	245	254	261
Cr ppm	11089	11309	10368	2625	4405	4876	8302	3337	3766	7269	7089	7138	8422	10336	10045
Mn ppm				861	824	845	620		822	590	611				
Co ppm	19.3	20.5	16.7	47.1	53.2	54.6	22.2	19.4	52.6	21.3	22.6	20.3	17.3	18.5	18.7
Ni ppm	288	319	300	568	734	697	338	284	694	321	312	313	299	308	289
Rb ppm	<0.0606	<0.0554	<0.0492	<0.102	<0.120	<0.130	<0.156	0.0786	<0.122	<0.202	<0.199	<0.0445	<0.0539	<0.0568	<0.0463
Sr ppm	14.8	15.1	7.82	0.140	0.244	0.347	11.8	13.3	0.385	11.9	11.7	14.9	15.3	15.2	15.8
Y ppm	14.0	14.2	16.0	0.877	1.41	1.74	13.7	14.5	1.21	13.9	14.1	14.9	16.6	14.5	14.4
Zr ppm	16.5	16.9	22.3	0.785	1.39	2.07	13.9	12.7	1.10	13.1	13.1	14.1	14.0	18.4	18.0
Nb ppm	<0.00547	<0.00562	<0.00525	<0.00641	<0.00783	<0.00785	<0.00864	0.00456	<0.0103	<0.0152	<0.0170	<0.00447	<0.00571	<0.00597	<0.00509
Cs ppm	<0.0329	<0.0395	<0.00511	<0.0666	<0.0805	<0.0991	<0.0933	<0.0307	<0.0956	<0.111	<0.137	<0.0297	<0.0391	<0.0368	<0.0348
Ba ppm	<0.0456	<0.0469	<0.0438	0.120	<0.0734	<0.0736	<0.0810	0.217	0.281	<0.142	<0.159	0.231	0.0649	0.0589	<0.0421
La ppm	0.0671	0.0705	0.0902	<0.00700	<0.00855	<0.00857	0.0821	0.111	<0.0113	0.0830	0.0877	0.113	0.108	0.0873	0.0939
Ce ppm	1.10	1.01	0.574	<0.00771	0.0145	0.0208	1.44	1.28	<0.0124	1.28	1.43	1.48	1.65	1.21	1.23
Pr ppm	0.352	0.429	0.192	<0.00678	<0.00828	<0.00830	0.399	0.356	<0.0109	0.342	0.360	0.381	0.370	0.419	0.389
Nd ppm	3.28	3.67	1.79	<0.0407	<0.0497	<0.0498	2.27	2.06	<0.0655	2.94	1.78	2.17	2.55	3.24	3.01
Sm ppm	1.71	1.54	1.16	<0.0470	<0.0575	<0.0576	1.01	0.972	<0.0757	0.918	0.895	1.25	1.23	1.73	1.83
Eu ppm	0.638	0.675	0.569	0.0298	<0.0165	<0.0165	0.524	0.410	<0.0217	0.396	0.442	0.425	0.501	0.723	0.731
Gd ppm	2.53	2.45	2.15	<0.0463	0.0618	0.0572	2.13	1.59	<0.0746	0.947	1.54	1.83	2.38	2.30	2.34
Tb ppm	0.394	0.413	0.330	<0.00729	0.0108	0.0161	0.429	0.320	0.0208	0.341	0.371	0.367	0.431	0.397	0.415
Dy ppm	2.86	2.57	2.47	0.0753	0.128	0.304	2.69	2.31	0.134	2.68	2.00	2.42	2.82	2.67	2.56
Ho ppm	0.483	0.547	0.684	0.0125	0.0421	0.0446	0.490	0.529	0.0280	0.631	0.515	0.541	0.632	0.579	0.619
Er ppm	1.40	1.54	1.76	0.134	0.190	0.275	1.41	1.36	0.219	1.75	1.55	1.44	1.82	1.80	1.39
Tm ppm	0.204	0.129	0.219	0.0379	0.0169	0.0240	0.216	0.220	0.0302	0.346	0.194	0.210	0.242	0.223	0.188
Yb ppm	1.12	0.993	1.24	0.158	0.257	0.221	1.47	1.17	0.168	1.32	1.27	1.29	1.60	1.13	1.23
Lu ppm	0.140	0.121	0.194	0.0381	0.0632	0.0427	0.186	0.179	0.0356	0.160	0.195	0.155	0.248	0.163	0.147
Hf ppm	0.710	0.734	0.833	<0.0302	0.0798	<0.0371	0.627	0.548	<0.0487	0.687	0.628	0.777	0.610	0.687	0.624
Ta ppm	<0.00672	<0.00691	<0.00644	<0.00916	<0.0112	<0.0112	<0.0123	<0.000952	<0.0147	0.0432	<0.0242	<0.00546	<0.00698	<0.00730	<0.00622
Pb ppm	<0.124	<0.0179	0.0567	0.114	<0.139	<0.190	<0.146	0.0346	<0.186	<0.254	<0.0656	0.0205	0.0277	0.0280	<0.0162
Th ppm	<0.00967	<0.00994	<0.00926	<0.0138	<0.0169	<0.0169	<0.0186	<0.00154	<0.0223	<0.0327	<0.0366	<0.00779	<0.00996	<0.0104	<0.00885
U ppm	<0.00997	<0.0102	<0.00955	<0.0151	<0.0184	<0.0185	<0.0203	0.00217	0.0404	0.0726	<0.0399	<0.00795	<0.0102	<0.0106	<0.00903
Eu/Eu*	0.93	1.06	1.09				1.09	1.00		1.29	1.14	0.85	0.89	1.10	1.07

B.5. Table de données – compositions chimiques en éléments traces des clinopyroxènes

Analysis	MD110-DR02-A64-2a	MD110-DR02-A64-2b	MD110-DR02-A64-2c	MD110-DR02-A64-6	MD110-DR06-158A 001	MD110-DR06-158A 007	MD110-DR06-158A-1	MD110-DR06-158A-14	MD110-DR06-158A-6	MD110-DR06-158A-7	MD110-DR06-161A-19a	MD110-DR06-161A-19b	MD110-DR06-161A-7	MD110-DR06-161C 006	MD110-DR06-161C 028
Mineral	Cpx	Cpx	Cpx	Cpx	Cpx	Cpx	Cpx	Cpx	Cpx	Cpx	Cpx	Cpx	Cpx	Cpx	Cpx
Location	MD110-DR02	MD110-DR02	MD110-DR02	MD110-DR02	MD110-DR06	MD110-DR06	MD110-DR06	MD110-DR06	MD110-DR06	MD110-DR06	MD110-DR06	MD110-DR06	MD110-DR06	MD110-DR06	MD110-DR06
Sample	A64	A64	A64	A64	158A	158A	158A	158A	158A	158A	161A	161A	161A	161C	161C
Rock type	Sp-lherzolite	Sp-lherzolite	Sp-lherzolite	Sp-lherzolite	Pl-lherzolite	Pl-lherzolite	Pl-lherzolite	Pl-lherzolite	Pl-lherzolite	Pl-lherzolite	Pl-lherzolite	Pl-lherzolite	Pl-lherzolite	Pl-lherzolite	Pl-lherzolite
Texture	Porph.	Porph.	Porph.	Porph.	Porph.	Porph.	Porph.	Inclusion	Inclusion	Porph.	Neoblast	Neoblast	Neoblast	Inclusion	Neoblast
Mineral location	Core	Core	Core	Core	Core	Rim	Core	Core	Core	Core	Core	Core	Core	Core	Core
Li ppm	2.48	2.48	2.48	1.96	5.94	2.78	5.94	199	<1.18	2.78	1.95	1.95	2.67	1.50	2.23
B ppm	4.03	4.03	4.03	<2.42	<3.85	6.25	<3.85	1244	<3.60	6.25	<0.628	<0.628	18.8	3.56	10.3
Sc ppm	56.8	56.8	56.8	63.7	53.1	26.5	53.1	19.1	29.0	26.5	53.2	53.2	46.9	59.2	45.7
Ti ppm	2367	2367	2367	2471	1784	649	1784	148	759	649	2279	2279	1646	2188	1761
V ppm	254	254	254	261	262	137	262	32.8	140	137	254	254	224	268	227
Cr ppm	10336	10336	10336	10045	7941	4700	7941	102	4873	4700	2658	2658	2531	2962	2827
Mn ppm					742	925	742	1150	970	925					
Co ppm	18.5	18.5	18.5	18.7	28.8	56.3	28.8	623	51.9	56.3	22.2	22.2	23.4	20.6	22.3
Ni ppm	308	308	308	289	441	762	441	9403	677	762	305	305	306	296	317
Rb ppm	<0.0568	<0.0568	<0.0568	<0.0463	0.397	<0.106	0.397	1.339	<0.115	<0.106	<0.0354	<0.0354	<0.0338	0.0432	0.0620
Sr ppm	15.2	15.2	15.2	15.8	1.24	0.391	1.24	94.5	0.0291	0.391	0.475	0.475	4.88	52.0	1.92
Y ppm	14.5	14.5	14.5	14.4	17.5	2.14	17.5	3.98	2.42	2.14	18.7	18.7	13.8	19.1	16.2
Zr ppm	18.4	18.4	18.4	18.0	6.64	0.914	6.64	<0.0645	0.842	0.914	9.52	9.52	4.79	10.0	7.31
Nb ppm	<0.00597	<0.00597	<0.00597	<0.00509	<0.00769	<0.00808	<0.00769	<0.0373	<0.0100	<0.00808	0.00349	0.00349	0.00381	0.103	0.0198
Cs ppm	<0.0368	<0.0368	<0.0368	<0.0348	<0.0652	<0.0820	<0.0652	<0.236	<0.0846	<0.0820	<0.0184	<0.0184	<0.0188	<0.0221	<0.0203
Ba ppm	0.0589	0.0589	0.0589	<0.0421	0.299	0.142	0.299	19.0	0.147	0.142	0.0236	0.0236	0.0776	0.0674	0.696
La ppm	0.0873	0.0873	0.0873	0.0939	0.0347	<0.00866	0.0347	<0.0400	<0.0108	<0.00866	0.0658	0.0658	0.0861	0.935	0.149
Ce ppm	1.21	1.21	1.21	1.23	0.555	0.0135	0.555	<0.0445	<0.0120	0.0135	1.02	1.02	0.841	2.95	1.10
Pr ppm	0.419	0.419	0.419	0.389	0.213	<0.00854	0.213	<0.0395	<0.0106	<0.00854	0.380	0.380	0.241	0.600	0.321
Nd ppm	3.24	3.24	3.24	3.01	1.72	<0.0514	1.72	<0.238	<0.0640	<0.0514	2.85	2.85	1.60	3.10	2.12
Sm ppm	1.73	1.73	1.73	1.83	1.12	<0.0600	1.12	0.421	<0.0747	<0.0600	1.56	1.56	0.803	1.20	1.15
Eu ppm	0.723	0.723	0.723	0.731	0.502	<0.0170	0.502	<0.0787	<0.0212	<0.0170	0.493	0.493	0.397	0.566	0.418
Gd ppm	2.30	2.30	2.30	2.34	2.46	0.229	2.46	0.337	0.139	0.229	2.67	2.67	1.50	2.07	1.95
Tb ppm	0.397	0.397	0.397	0.415	0.460	0.0374	0.460	0.140	0.0311	0.0374	0.517	0.517	0.313	0.444	0.412
Dy ppm	2.67	2.67	2.67	2.56	3.85	0.270	3.85	0.593	0.259	0.270	3.14	3.14	2.03	2.93	2.52
Ho ppm	0.579	0.579	0.579	0.619	0.702	0.0577	0.702	0.152	0.0981	0.0577	0.707	0.707	0.518	0.697	0.610
Er ppm	1.80	1.80	1.80	1.39	1.58	0.246	1.58	0.289	0.219	0.246	1.84	1.84	1.44	1.89	1.56
Tm ppm	0.223	0.223	0.223	0.188	0.262	0.0525	0.262	0.0770	0.0423	0.0525	0.251	0.251	0.211	0.252	0.220
Yb ppm	1.13	1.13	1.13	1.23	1.67	0.553	1.67	0.872	0.459	0.553	1.32	1.32	1.20	1.59	1.30
Lu ppm	0.163	0.163	0.163	0.147	0.209	0.0388	0.209	<0.0514	0.0394	0.0388	0.211	0.211	0.187	0.230	0.194
Hf ppm	0.687	0.687	0.687	0.624	0.369	<0.0398	0.369	<0.184	<0.0496	<0.0398	0.735	0.735	0.294	0.500	0.423
Ta ppm	<0.00730	<0.00730	<0.00730	<0.00622	<0.0113	<0.0119	<0.0113	<0.0550	<0.0148	<0.0119	<0.000411	<0.000411	<0.000408	0.0464	<0.000593
Pb ppm	0.0280	0.0280	0.0280	<0.0162	<0.145	<0.18087	<0.145	<0.455	<0.155	<0.18087	0.0114	0.0114	0.0141	0.0211	0.126
Th ppm	<0.0104	<0.0104	<0.0104	<0.00885	<0.0166	0.0263	<0.0166	<0.0806	<0.0217	0.0263	<0.000613	<0.000613	<0.000609	<0.00117	0.0162
U ppm	<0.0106	<0.0106	<0.0106	<0.00903	<0.0182	0.0602	<0.0182	0.314	<0.0238	0.0602	<0.000598	<0.000598	<0.000594	<0.00115	0.00852
Eu/Eu*	1.10	1.10	1.10	1.07	0.92		0.92				0.73	0.73	1.10	1.09	0.85

B.5. Table de données – compositions chimiques en éléments traces des clinopyroxènes

Analysis	MD110-DR06-161C-19	MD110-DR06-161C-57	MD110-DR06-161C-58	MD110-DR06-162B-10	MD110-DR06-162B-13	MD110-DR06-162b-20	MD110-DR06-162B-20	MD110-DR06-162B-28	MD110-DR06-162B-29	MD110-DR06-167A 003	MD110-DR06-167A 011	MD110-DR06-167A-12b	MD110-DR06-167A-13	MD110-DR06-167A-13	MD110-DR06-167A-14
Mineral	Cpx	Cpx	Cpx	Cpx	Cpx	Cpx	Cpx	Cpx	Cpx	Cpx	Cpx	Cpx	Cpx	Cpx	Cpx
Location	MD110-DR06	MD110-DR06	MD110-DR06	MD110-DR06	MD110-DR06	MD110-DR06	MD110-DR06	MD110-DR06	MD110-DR06	MD110-DR06	MD110-DR06	MD110-DR06	MD110-DR06	MD110-DR06	MD110-DR06
Sample	161C	161C	161C	162B	162B	162B	162B	162B	162B	167A	167A	167A	167A	167A	167A
Rock type	Pl-lherzolite	Pl-lherzolite	Pl-lherzolite	Pl-lherzolite	Pl-lherzolite	Pl-lherzolite	Pl-lherzolite	Pl-lherzolite	Pl-lherzolite	Pl-lherzolite	Pl-lherzolite	Pl-lherzolite	Pl-lherzolite	Pl-lherzolite	Pl-lherzolite
Texture	Porph.	Inclusion	Inclusion	Porph.	Neoblast	Porph.	Porph.	Neoblast	Neoblast	Neoblast	Neoblast	Porph.	Porph.	Porph.	Porph.
Mineral location	Core	Core	Core	Rim	Core	Core	Core	Core	Core	Core	Core	Rim	Core	Core	Core
Li ppm	1.59	1.50	1.50	2.03	1.53	1.53	1.53	1.53	1.53	4.47	3.37	3.36	2.67	2.85	2.91
B ppm	1.58	3.56	3.56	<0.479	1.24	1.24	1.24	1.24	1.24	0.889	<0.523	<0.548	0.572	<0.589	1.93
Sc ppm	46.2	59.2	59.2	48.6	63.9	63.9	63.9	63.9	63.9	61.1	52.3	54.6	45.4	43.7	40.4
Ti ppm	1753	2188	2188	1983	2403	2403	2403	2403	2403	1911	1573	1644	1354	1379	1346
V ppm	227	268	268	233	272	272	272	272	272	277	243	241	208	207	198
Cr ppm	2840	2962	2962	2987	2794	2794	2794	2794	2794	3373	3422	3311	3338	3409	3459
Mn ppm															
Co ppm	28.4	20.6	20.6	27.3	22.9	22.9	22.9	22.9	22.9	23.0	24.4	21.7	28.2	25.8	28.1
Ni ppm	374	296	296	362	317	317	317	317	317	319	341	303	387	363	385
Rb ppm	<0.0385	0.0432	0.0432	<0.0359	0.0420	0.0420	0.0420	0.0420	0.0420	<0.0579	0.0580	0.0608	<0.0585	<0.0606	0.0682
Sr ppm	1.06	52.0	52.0	2.06	1.82	1.82	1.82	1.82	1.82	1.79	2.04	3.85	3.46	4.34	4.32
Y ppm	16.0	19.1	19.1	18.6	21.2	21.2	21.2	21.2	21.2	19.2	17.0	17.4	13.1	13.0	12.5
Zr ppm	6.20	10.0	10.0	19.6	25.3	25.3	25.3	25.3	25.3	8.22	6.73	6.84	5.16	5.15	5.15
Nb ppm	0.00454	0.103	0.103	0.00500	0.00401	0.00401	0.00401	0.00401	0.00401	0.00166	0.00463	0.00196	0.00410	0.00404	0.00408
Cs ppm	<0.0197	<0.0221	<0.0221	<0.0181	0.0193	0.0193	0.0193	0.0193	0.0193	<0.0306	<0.0282	<0.0284	<0.0287	0.0373	<0.0294
Ba ppm	0.0137	0.0674	0.0674	<0.00378	0.0159	0.0159	0.0159	0.0159	0.0159	0.0234	<0.00631	<0.00656	0.0504	<0.00669	<0.00708
La ppm	0.0797	0.935	0.935	0.231	0.246	0.246	0.246	0.246	0.246	0.0512	0.0421	0.0506	0.0393	0.0375	0.0404
Ce ppm	1.00	2.95	2.95	2.08	2.36	2.36	2.36	2.36	2.36	0.700	0.649	0.638	0.495	0.521	0.506
Pr ppm	0.307	0.600	0.600	0.566	0.694	0.694	0.694	0.694	0.694	0.254	0.240	0.235	0.172	0.168	0.179
Nd ppm	2.09	3.10	3.10	3.39	4.36	4.36	4.36	4.36	4.36	2.07	1.66	1.78	1.38	1.38	1.30
Sm ppm	1.06	1.20	1.20	1.57	2.01	2.01	2.01	2.01	2.01	1.21	0.976	0.983	0.721	0.805	0.781
Eu ppm	0.419	0.566	0.566	0.560	0.606	0.606	0.606	0.606	0.606	0.477	0.421	0.427	0.320	0.355	0.348
Gd ppm	1.80	2.07	2.07	2.44	3.03	3.03	3.03	3.03	3.03	2.33	1.77	1.80	1.38	1.58	1.37
Tb ppm	0.366	0.444	0.444	0.495	0.615	0.615	0.615	0.615	0.615	0.469	0.367	0.367	0.289	0.301	0.274
Dy ppm	2.46	2.93	2.93	2.99	3.61	3.61	3.61	3.61	3.61	3.11	2.57	2.64	1.98	1.96	1.85
Ho ppm	0.590	0.697	0.697	0.707	0.804	0.804	0.804	0.804	0.804	0.721	0.609	0.624	0.468	0.496	0.464
Er ppm	1.62	1.89	1.89	1.87	2.09	2.09	2.09	2.09	2.09	1.89	1.73	1.75	1.37	1.33	1.19
Tm ppm	0.255	0.252	0.252	0.259	0.293	0.293	0.293	0.293	0.293	0.280	0.247	0.260	0.196	0.202	0.179
Yb ppm	1.43	1.59	1.59	1.49	1.52	1.52	1.52	1.52	1.52	1.57	1.46	1.58	1.21	1.18	1.24
Lu ppm	0.218	0.230	0.230	0.223	0.210	0.210	0.210	0.210	0.210	0.222	0.228	0.223	0.188	0.168	0.168
Hf ppm	0.304	0.500	0.500	0.584	0.973	0.973	0.973	0.973	0.973	0.435	0.301	0.379	0.310	0.279	0.308
Ta ppm	<0.000625	0.0464	0.0464	<0.000573	<0.000490	<0.000490	<0.000490	<0.000490	<0.000490	<0.000909	<0.000903	<0.000938	<0.000936	<0.000958	<0.00101
Pb ppm	<0.00184	0.0211	0.0211	0.0101	0.00835	0.00835	0.00835	0.00835	0.00835	0.0118	<0.00284	<0.00296	0.0204	<0.00302	<0.00320
Th ppm	<0.000987	<0.00117	<0.00117	<0.000901	<0.000771	<0.000771	<0.000771	<0.000771	<0.000771	<0.00145	<0.00144	<0.00150	<0.00150	<0.00153	<0.00162
U ppm	<0.000969	<0.00115	<0.00115	<0.000884	<0.000757	<0.000757	<0.000757	<0.000757	<0.000757	<0.00145	<0.00144	<0.00150	<0.00149	<0.00153	<0.00162
Eu/Eu*	0.92	1.09	1.09	0.87	0.75	0.75	0.75	0.75	0.75	0.86	0.97	0.98	0.98	0.96	1.02

B.5. Table de données – compositions chimiques en éléments traces des clinopyroxènes

Analysis	MD110-DR06-167A-15a	MD110-DR06-167A-15b	MD110-DR06-167A-16	MD110-DR06-168 008	MD110-DR06-168 009	MD110-DR06-168-1	MD110-DR06-168-15	MD110-DR06-168-8	MD110-DR06-168-9	MD110-DR06-173-10b	MD110-DR06-173-9b	MD110-DR06-B4-14	MD110-DR06-B4-4	MD110-DR09-273b 005	MD110-DR09-273b 006
Mineral	Cpx	Cpx	Cpx	Cpx	Cpx	Cpx	Cpx	Cpx	Cpx	Cpx	Cpx	Cpx	Cpx	Cpx	Cpx
Location	MD110-DR06	MD110-DR06	MD110-DR06	MD110-DR06	MD110-DR06	MD110-DR06	MD110-DR06	MD110-DR06	MD110-DR06	MD110-DR06	MD110-DR06	MD110-DR06	MD110-DR06	MD110-DR09	MD110-DR09
Sample	167A	167A	167A	168	168	168	168	168	168	173	173	B4	B4	273b	273b
Rock type	Pl-lherzolite	Pl-lherzolite	Pl-lherzolite	Pl-lherzolite	Pl-lherzolite	Pl-lherzolite	Pl-lherzolite	Pl-lherzolite	Pl-lherzolite	Pl-lherzolite	Pl-lherzolite	Pl-lherzolite	Pl-lherzolite	Sp-lherzolite	Sp-lherzolite
Texture	Porph.	Porph.	Porph.	Neoblast	Neoblast	Porph.	Porph.	Neoblast	Neoblast	Neoblast	Neoblast	Porph.	Porph.	Porph.	Porph.
Mineral location	Core	Core	Core	Core	Core	Core	Rim	Core	Core	Core	Core	Core	Core	Core	Core
Li ppm	3.31	2.58	2.28	3.90	2.92	7.41	3.79	3.90	2.92	3.37	5.02	2.07	1.87	3.45	4.50
B ppm	<0.551	0.902	0.640	3.82	<3.59	18.7	<3.30	3.82	<3.59	0.6	20.5	4.55	<0.477	2.90	3.45
Sc ppm	44.6	48.5	53.8	58.5	61.6	59.0	60.7	58.5	61.6	44.6	44.1	43.2	39.3	74.1	68.5
Ti ppm	1434	1463	1479	1916	2010	1833	1696.08	1916	2010	1434	1421	1540	1593	1459	1308
V ppm	208	220	239	283	293	288	280.28	283	293	212	210	216	204	271	255
Cr ppm	3386	3434	3442	8077	8060	8510	7589.61	8077	8060	2939	2918	2625	2644	8556	8720
Mn ppm				643	641	655	651.65	643	641						
Co ppm	25.9	26.3	24.7	23.0	22.8	22.8	24.84	23.0	22.8	24.6	21.9	27.0	27.0	17.8	19.1
Ni ppm	358	369	345	400	371	474	377.00	400	371	338	350	358	361	283	288
Rb ppm	0.0659	<0.0564	0.0691	<0.129	<0.127	0.154	0.38	<0.129	<0.127	<0.0364	0.0393	0.0446	<0.0348	<0.0305	<0.0481
Sr ppm	4.03	3.48	3.18	1.75	1.56	3.55	2.00	1.75	1.56	9.39	7.21	2.20	3.02	1.95	1.77
Y ppm	14.0	14.8	15.6	17.7	17.4	16.6	14.94	17.7	17.4	12.5	12.7	14.3	12.7	14.4	13.2
Zr ppm	5.71	5.70	6.05	6.83	6.90	5.66	4.95	6.83	6.90	9.50	10.1	3.87	4.02	2.46	1.97
Nb ppm	0.00331	0.00119	0.00337	<0.126	<0.00655	<0.00680	<0.00649226	<0.126	<0.00655	0.00758	0.00710	0.00390	0.00310	0.00526	<0.00465
Cs ppm	<0.0320	<0.0311	0.0310	<0.0897	<0.0802	<0.0786	<0.0707111	<0.0897	<0.0802	<0.0194	<0.0185	0.0184	<0.0190	<0.0195	0.0107
Ba ppm	0.0284	<0.00655	<0.00629	<0.188	0.144	0.657	<0.0608498	<0.188	0.144	0.0121	0.135	0.0415	<0.0343	0.247	<0.0395
La ppm	0.0511	0.0446	0.0399	0.241	0.234	0.251	0.20	0.241	0.234	0.259	0.223	0.0730	0.0821	0.0389	0.0286
Ce ppm	0.588	0.569	0.529	2.33	2.42	2.00	1.89	2.33	2.42	1.80	1.80	0.822	0.852	0.307	0.295
Pr ppm	0.202	0.193	0.191	0.575	0.685	0.499	0.47	0.575	0.685	0.434	0.439	0.252	0.253	0.0899	0.104
Nd ppm	1.52	1.48	1.56	3.65	3.30	3.69	2.83	3.65	3.30	2.34	2.50	1.65	1.57	0.839	0.648
Sm ppm	0.869	0.906	0.930	1.46	1.74	1.44	1.17	1.46	1.74	0.974	0.996	0.897	0.872	0.519	0.447
Eu ppm	0.367	0.376	0.334	0.409	0.482	0.383	0.41	0.409	0.482	0.389	0.399	0.383	0.364	0.236	0.201
Gd ppm	1.61	1.49	1.71	1.98	2.16	2.03	1.79	1.98	2.16	1.44	1.54	1.48	1.44	1.29	1.15
Tb ppm	0.313	0.324	0.337	0.400	0.419	0.379	0.32	0.400	0.419	0.300	0.313	0.326	0.305	0.319	0.235
Dy ppm	2.16	2.30	2.39	2.51	2.92	3.31	2.89	2.51	2.92	1.92	2.00	2.14	1.83	2.31	2.14
Ho ppm	0.523	0.540	0.565	0.607	0.676	0.651	0.59	0.607	0.676	0.455	0.488	0.522	0.464	0.566	0.492
Er ppm	1.48	1.55	1.55	1.83	1.78	1.68	1.92	1.83	1.78	1.21	1.25	1.42	1.29	1.71	1.36
Tm ppm	0.207	0.235	0.240	0.308	0.20	0.307	0.21	0.308	0.20	0.181	0.182	0.214	0.194	0.240	0.212
Yb ppm	1.28	1.42	1.41	1.39	1.50	1.15	1.28	1.39	1.50	1.02	1.03	1.31	1.14	1.50	1.29
Lu ppm	0.194	0.208	0.210	0.226	0.155	0.209	0.14	0.226	0.155	0.162	0.151	0.200	0.184	0.234	0.162
Hf ppm	0.275	0.346	0.308	0.296	0.352	0.301	0.34	0.296	0.352	0.344	0.396	0.248	0.264	0.178	0.138
Ta ppm	<0.00100	<0.000937	<0.000901	<0.0588	<0.00936	<0.00971	<0.00927717	<0.0588	<0.00936	<0.000521	<0.000519	<0.000491	<0.000530	<0.00399	<0.00589
Pb ppm	<0.00316	0.00577	0.00816	<0.149	<0.137	<0.130	<0.154587	<0.149	<0.137	0.0137	0.0118	0.00984	0.00482	0.0530	0.149
Th ppm	<0.00160	<0.00150	<0.00144	<0.169	<0.0141	<0.0147	<0.0140064	<0.169	<0.0141	<0.000800	<0.000798	<0.000754	<0.000814	<0.00582	<0.00857
U ppm	<0.00160	<0.00150	<0.00144	<0.250	<0.0154	0.117	0.03	<0.250	<0.0154	<0.000771	<0.000768	<0.000726	<0.000784	<0.00609	<0.00897
Eu/Eu*	0.94	0.99	0.81	0.73	0.76	0.68	0.85	0.73	0.76	1.00	0.98	1.01	0.99	0.88	0.85

B.5. Table de données – compositions chimiques en éléments traces des clinopyroxènes

Analysis	MD110-DR09-273B-1	MD110-DR09-273B-2	MD110-DR09-273B-4	MD110-DR09-273B-5	MD110-DR09-273B-6	MD110-DR09-277 003	MD110-DR09-277-3	MD110-DR09-277-4	MD110-DR09-279 001	MD110-DR09-279-2	MD110-DR09-279-3	MD110-DR09-279-4	MD110-DR09-280 005	MD110-DR09-280 005	MD110-DR09-280b 001
Mineral	Cpx	Cpx	Cpx	Cpx	Cpx	Cpx	Cpx	Cpx	Cpx	Cpx	Cpx	Cpx	Cpx	Cpx	Cpx
Location	MD110-DR09	MD110-DR09	MD110-DR09	MD110-DR09	MD110-DR09	MD110-DR09	MD110-DR09	MD110-DR09	MD110-DR09	MD110-DR09	MD110-DR09	MD110-DR09	MD110-DR09	MD110-DR09	MD110-DR09
Sample	273B	273B	273B	273B	273B	277	277	277	279	279	279	279	280b	280b	280b
Rock type	Sp-lherzolite	Sp-lherzolite	Sp-lherzolite	Sp-lherzolite	Sp-lherzolite	Sp-lherzolite	Sp-lherzolite	Sp-lherzolite	Sp-lherzolite	Sp-lherzolite	Sp-lherzolite	Sp-lherzolite	Sp-lherzolite	Sp-lherzolite	Sp-lherzolite
Texture	Porph.	Porph.	Porph.	Porph.	Porph.	Porph.	Porph.	Porph.	Porph.	Porph.	Porph.	Porph.	Porph.	Porph.	Porph.
Mineral location	Core	Core	Core	Core	Core	Core	Core	Core	Core	Core	Core	Core	Core	Core	Core
Li ppm	6.83	5.60	14.6	3.45	4.50	4.08	4.08	3.17	3.70	3.70	38.9	14.0	4.28	3.05	3.23
B ppm	32.2	28.2	46.7	2.90	3.45	<0.644	<0.644	1.32	<3.65	<3.65	249	126	<4.43	<4.41	<2.61
Sc ppm	52.6	54.0	51.9	74.1	68.5	58.8	58.8	46.6	66.1	66.1	28.6	12.6	78.2	76.0	78.0
Ti ppm	1035	1065	992	1459	1308	624	624	493	1130	1130	641	135	1160	1098	1353
V ppm	222	223	214	271	255	227	227	194	235	235	92.9	67.5	248	239	258
Cr ppm	8926	8785	8350	8556	8720	2637	2637	2548	6737	6737	6793	553	7732	7173	8211
Mn ppm									560	560	351	208	557	521	
Co ppm	19.3	18.4	25.8	17.8	19.1	18.0	18.0	14.6	19.7	19.7	48.4	36.7	21.1	18.5	18.1
Ni ppm	400	462	546	283	288	261	261	232	313	313	2771	3174	304	287	278
Rb ppm	0.0950	0.103	0.525	<0.0305	<0.0481	0.0438	0.0438	<0.0343	<0.112	<0.112	3.20	<0.763	<0.139	<0.142	<0.0487
Sr ppm	2.64	2.43	5.03	1.95	1.77	2.42	2.42	2.42	1.92	1.92	14.9	13.4	2.01	1.95	1.66
Y ppm	12.7	13.5	11.2	14.4	13.2	12.6	12.6	11.7	13.6	13.6	1.73	0.959	13.8	13.5	14.2
Zr ppm	2.18	2.05	1.76	2.46	1.97	2.58	2.58	2.12	2.17	2.17	2.58	0.158	2.06	2.18	2.45
Nb ppm	0.00771	<0.00357	<0.00483	0.00526	<0.00465	0.00394	0.00394	0.0141	<0.00652	<0.00652	<0.0864	<0.0794	<0.0121	<0.0105	<0.00485
Cs ppm	<0.0198	<0.0251	0.0323	<0.0195	0.0107	<0.0183	<0.0183	<0.0189	<0.0934	<0.0934	<0.656	<0.490	<0.0816	<0.108	<0.0248
Ba ppm	0.105	0.0919	0.630	0.247	<0.0395	0.0367	0.0367	0.107	<0.0611	<0.0611	3.95	<0.744	<0.113	<0.0987	<0.0409
La ppm	0.0323	0.0660	0.0604	0.0389	0.0286	0.0326	0.0326	0.0372	0.0349	0.0349	0.497	<0.0866	0.0269	0.0193	0.0382
Ce ppm	0.334	0.377	0.324	0.307	0.295	0.388	0.388	0.369	0.392	0.392	0.606	<0.0955	0.322	0.377	0.295
Pr ppm	0.103	0.104	0.0655	0.0899	0.104	0.127	0.127	0.132	0.105	0.105	0.109	<0.0839	0.0986	0.100	0.0719
Nd ppm	0.678	0.576	0.460	0.839	0.648	0.929	0.929	0.902	0.778	0.778	<0.549	<0.504	0.343	0.660	0.499
Sm ppm	0.467	0.684	0.421	0.519	0.447	0.451	0.451	0.413	0.552	0.552	<0.634	<0.582	0.351	0.445	0.473
Eu ppm	0.243	0.261	0.233	0.236	0.201	0.199	0.199	0.212	0.266	0.266	<0.182	<0.167	0.294	0.224	0.163
Gd ppm	1.24	1.31	1.06	1.29	1.15	0.908	0.908	0.806	1.32	1.32	<0.625	<0.573	1.39	0.930	1.09
Tb ppm	0.223	0.256	0.192	0.319	0.235	0.224	0.224	0.202	0.295	0.295	<0.0983	0.125	0.252	0.298	0.249
Dy ppm	2.16	2.31	1.78	2.31	2.14	1.68	1.68	1.51	2.22	2.22	<0.424	<0.389	1.93	2.41	2.21
Ho ppm	0.438	0.484	0.427	0.566	0.492	0.437	0.437	0.413	0.501	0.501	<0.111	<0.102	0.508	0.577	0.555
Er ppm	1.52	1.43	1.14	1.71	1.36	1.31	1.31	1.24	1.33	1.33	<0.340	0.676	1.76	1.46	1.70
Tm ppm	0.187	0.195	0.174	0.240	0.212	0.220	0.220	0.194	0.169	0.169	<0.109	<0.0996	0.216	0.240	0.240
Yb ppm	1.24	1.27	1.14	1.50	1.29	1.30	1.30	1.24	1.59	1.59	<0.514	<0.472	1.10	1.28	1.71
Lu ppm	0.181	0.177	0.173	0.234	0.162	0.210	0.210	0.203	0.201	0.201	<0.116	<0.106	0.280	0.197	0.241
Hf ppm	0.170	0.218	0.157	0.178	0.138	0.135	0.135	0.0967	0.130	0.130	<0.408	<0.374	0.274	0.0981	0.147
Ta ppm	<0.00433	<0.00455	<0.00614	<0.00399	<0.00589	<0.000409	<0.000409	<0.000396	<0.00932	<0.00932	<0.124	<0.113	<0.0178	<0.0155	<0.00605
Pb ppm	0.0451	0.0420	0.106	0.0530	0.149	0.00749	0.00749	0.00515	<0.146	<0.146	2.69	1.82	<0.209	<0.133	<0.0764
Th ppm	<0.00633	<0.00665	0.0180	<0.00582	<0.00857	<0.000610	<0.000610	<0.000591	<0.0141	<0.0141	<0.186	<0.171	<0.0261	0.0258	<0.00875
U ppm	0.113	0.177	0.290	<0.00609	<0.00897	<0.000594	<0.000594	0.0114	<0.0154	<0.0154	1.30	0.492	<0.0286	<0.0573	0.00986
Eu/Eu*	0.97	0.84	1.06	0.88	0.85	0.95	0.95	1.11	0.95	0.95			1.28	1.06	0.69

B.5. Table de données – compositions chimiques en éléments traces des clinopyroxènes

Analysis	MD110-DR09-280b 004	MD110-DR09-280B-1	MD110-DR09-280B-2	MD110-DR09-280B-3	MD110-DR09-280B-4b	MD110-DR09-281 003	MD110-DR09-281 003	MD110-DR09-281 003	MD110-DR09-281b 002	MD110-DR09-281b 003	MD110-DR09-281b 004	MD110-DR09-281b 005	MD110-DR09-281B-2a	MD110-DR09-281B-2b	MD110-DR09-281B-2c
Mineral	Cpx	Cpx	Cpx	Cpx	Cpx	Cpx	Cpx	Cpx	Cpx	Cpx	Cpx	Cpx	Cpx	Cpx	Cpx
Location	MD110-DR09	MD110-DR09	MD110-DR09	MD110-DR09	MD110-DR09	MD110-DR09	MD110-DR09	MD110-DR09	MD110-DR09	MD110-DR09	MD110-DR09	MD110-DR09	MD110-DR09	MD110-DR09	MD110-DR09
Sample	280b	280B	280B	280B	280B	281	281	281	281b	281b	281b	281b	281B	281B	281B
Rock type	Sp-lherzolite	Sp-lherzolite	Sp-lherzolite	Sp-lherzolite	Sp-lherzolite	Sp-lherzolite	Sp-lherzolite	Sp-lherzolite	Sp-lherzolite	Sp-lherzolite	Sp-lherzolite	Sp-lherzolite	Sp-lherzolite	Sp-lherzolite	Sp-lherzolite
Texture	Porph.	Porph.	Porph.	Porph.	Porph.	Porph.	Porph.	Porph.	Porph.	Porph.	Porph.	Porph.	Porph.	Porph.	Porph.
Mineral location	Core	Core	Core	Core	Core	Core	Core	Core	Core	Core	Core	Core	Core	Core	Core
Li ppm	1.92	3.23	2.92	2.48	1.92	4.74	13.0	4.18	3.57	3.69	3.66	3.51	3.57	3.57	3.57
B ppm	3.12	<2.61	3.97	<2.29	3.12	5.65	114	5.10	<2.16	2.45	2.30	3.01	<2.16	<2.16	<2.16
Sc ppm	80.4	78.0	62.0	62.5	80.4	77.5	13.3	108	70.0	79.0	76.8	83.3	70.0	70.0	70.0
Ti ppm	1334	1353	1130	1223	1334	1305	250	1358	1273	1318	1427	1476	1273	1273	1273
V ppm	264	258	234	229	264	279	46.5	280	252	264	267	277	252	252	252
Cr ppm	7872	8211	8850	8483	7872	7815	996	5669	9088	8117	8400	8221	9088	9088	9088
Mn ppm						577	246	451							
Co ppm	16.1	18.1	16.6	14.8	16.1	18.7	42.2	16.1	18.3	18.2	18.9	17.1	18.3	18.3	18.3
Ni ppm	254	278	296	244	254	375	2419	330	278	295	281	279	278	278	278
Rb ppm	<0.0404	<0.0487	<0.0474	<0.0431	<0.0404	<0.113	1.11	<0.0956	<0.0375	<0.0451	<0.0364	<0.0467	<0.0375	<0.0375	<0.0375
Sr ppm	1.45	1.66	1.67	1.65	1.45	2.06	11.9	1.90	1.65	1.92	1.82	1.70	1.65	1.65	1.65
Y ppm	14.3	14.2	14.3	14.3	14.3	14.9	1.92	16.1	14.8	14.7	15.4	15.6	14.8	14.8	14.8
Zr ppm	2.44	2.45	2.07	2.29	2.44	2.52	11.5	2.32	2.46	2.35	2.56	2.62	2.46	2.46	2.46
Nb ppm	<0.00431	<0.00485	<0.00475	0.00451	<0.00431	<0.00625	0.211	<0.00804	<0.00431	<0.00396	<0.00422	<0.00459	<0.00431	<0.00431	<0.00431
Cs ppm	<0.0351	<0.0248	<0.0323	<0.0258	<0.0351	<0.0717	<0.0843	<0.0679	<0.0225	<0.0240	0.0128	0.00519	<0.0225	<0.0225	<0.0225
Ba ppm	<0.0364	<0.0409	<0.0401	<0.0365	<0.0364	0.0933	10.5	<0.0755	<0.0365	<0.0334	<0.0357	<0.0387	<0.0365	<0.0365	<0.0365
La ppm	0.0258	0.0382	0.0723	0.0376	0.0258	0.0557	1.02	0.0491	0.0355	0.0399	0.0327	0.0268	0.0355	0.0355	0.0355
Ce ppm	0.335	0.295	0.275	0.341	0.335	0.316	1.56	0.281	0.387	0.323	0.303	0.369	0.387	0.387	0.387
Pr ppm	0.0623	0.0719	0.0737	0.0701	0.0623	0.0845	0.183	0.126	0.0849	0.0808	0.0737	0.0803	0.0849	0.0849	0.0849
Nd ppm	0.558	0.499	0.505	0.533	0.558	0.481	0.860	0.511	0.576	0.542	0.747	0.545	0.576	0.576	0.576
Sm ppm	0.429	0.473	0.495	0.475	0.429	0.478	0.252	0.625	0.519	0.428	0.387	0.401	0.519	0.519	0.519
Eu ppm	0.211	0.163	0.213	0.212	0.211	0.254	0.0816	0.152	0.206	0.265	0.305	0.244	0.206	0.206	0.206
Gd ppm	1.44	1.09	1.14	1.12	1.44	1.42	0.290	1.26	1.27	1.32	1.42	1.21	1.27	1.27	1.27
Tb ppm	0.275	0.249	0.250	0.264	0.275	0.332	0.0343	0.250	0.290	0.290	0.325	0.286	0.290	0.290	0.290
Dy ppm	2.32	2.21	2.12	2.41	2.32	2.40	0.367	1.92	2.19	2.30	2.59	2.33	2.19	2.19	2.19
Ho ppm	0.462	0.555	0.562	0.524	0.462	0.536	0.0484	0.718	0.590	0.562	0.557	0.694	0.590	0.590	0.590
Er ppm	1.66	1.70	1.67	1.61	1.66	1.88	0.288	2.06	1.86	1.76	1.61	1.65	1.86	1.86	1.86
Tm ppm	0.223	0.240	0.231	0.250	0.223	0.218	<0.0122	0.218	0.241	0.228	0.231	0.273	0.241	0.241	0.241
Yb ppm	1.62	1.71	1.40	1.87	1.62	1.70	0.181	2.03	1.66	1.46	1.67	1.58	1.66	1.66	1.66
Lu ppm	0.239	0.241	0.241	0.179	0.239	0.256	0.0399	0.190	0.231	0.228	0.258	0.221	0.231	0.231	0.231
Hf ppm	0.244	0.147	0.230	0.151	0.244	0.187	0.301	0.218	0.170	0.116	0.178	0.139	0.170	0.170	0.170
Ta ppm	<0.00538	<0.00605	<0.00592	<0.00539	<0.00538	<0.00920	0.0285	<0.0118418	<0.00545	<0.00500	<0.00532	<0.00579	<0.00545	<0.00545	<0.00545
Pb ppm	<0.0779	<0.0764	0.0540	0.0360	<0.0779	<0.134	0.578	0.059	<0.0143	0.0227	0.0207	<0.0152	<0.0143	<0.0143	<0.0143
Th ppm	<0.00779	<0.00875	<0.00858	<0.00781	<0.00779	<0.0135	0.293	<0.0173608	<0.00792	<0.00726	<0.00772	<0.00839	<0.00792	<0.00792	<0.00792
U ppm	<0.00795	0.00986	<0.00876	<0.00797	<0.00795	0.0229	1.10	<0.0190347	<0.00828	<0.00759	<0.00807	<0.00876	<0.00828	<0.00828	<0.00828
Eu/Eu*	0.82	0.69	0.86	0.88	0.82	0.94	0.92	0.52	0.77	1.07	1.25	1.06	0.77	0.77	0.77

B.5. Table de données – compositions chimiques en éléments traces des clinopyroxènes

Analysis	MD110-DR09-281B-3a	MD110-DR09-281B-3b	MD110-DR09-281B-3c	MD110-DR09-281B-4a	MD110-DR09-281B-4b	MD110-DR09-281B-4c	MD110-DR09-281B-5	MD110-DR09-281B-6	MD80-DR3-G2-2 002	MD80-DR3-G2-2 003	MD80-DR3-G2-2 004	MD80-DR3-G2-2 007	MD80-DR3-G2-2-3	MD80-DR3-G2-2-4	MD80-DR3-G2-2-5	MD80-DR3-G2-2-6
Mineral	Cpx	Cpx	Cpx	Cpx	Cpx	Cpx	Cpx	Cpx	Cpx	Cpx	Cpx	Cpx	Cpx	Cpx	Cpx	Cpx
Location	MD110-DR09	MD110-DR09	MD110-DR09	MD110-DR09	MD110-DR09	MD110-DR09	MD110-DR09	MD110-DR09	MD80-DR3	MD80-DR3	MD80-DR3	MD80-DR3	MD80-DR3	MD80-DR3	MD80-DR3	MD80-DR3
Sample	281B	281B	281B	281B	281B	281B	281B	281B	*3G2-2*	*3G2-2*	*3G2-2*	*3G2-2*	3G2-2	3G2-2	3G2-2	3G2-2
Rock type	Sp-lherzolite	Sp-lherzolite	Sp-lherzolite	Sp-lherzolite	Sp-lherzolite	Sp-lherzolite	Sp-lherzolite	Sp-lherzolite	Sp-	Sp-	Sp-	Sp-	Sp-	Sp-	Sp-	Sp-
Texture	Porph.	Porph.	Porph.	Porph.	Porph.	Porph.	Porph.	Porph.	Porph.	Porph.	Porph.	Porph.	Porph.	Porph.	Porph.	Porph.
Mineral location	Core	Core	Core	Core	Core	Core	Core	Core	Core	Core	Core	Core	Core	Core	Core	Core
Li ppm	3.69	3.69	3.69	3.66	3.66	3.66	3.51	3.45	2.46	2.38	1.42	1.65	2.46	2.46	2.38	1.42
B ppm	2.45	2.45	2.45	2.30	2.30	2.30	3.01	2.27	1.14	1.45	0.599	2.31	1.14	1.14	1.45	0.599
Sc ppm	79.0	79.0	79.0	76.8	76.8	76.8	83.3	79.9	43.3	53.7	53.5	60.7	43.3	43.3	53.7	53.5
Ti ppm	1318	1318	1318	1427	1427	1427	1476	1334	1506	1643	1716	1884	1506	1506	1643	1716
V ppm	264	264	264	267	267	267	277	268	202	221	218	237	202	202	221	218
Cr ppm	8117	8117	8117	8400	8400	8400	8221	8080	3599	3304	3392	3345	3599	3599	3304	3392
Mn ppm																
Co ppm	18.2	18.2	18.2	18.9	18.9	18.9	17.1	17.9	17.7	18.0	17.7	16.9	17.7	17.7	18.0	17.7
Ni ppm	295	295	295	281	281	281	279	284	274	273	266	270	274	274	273	266
Rb ppm	<0.0451	<0.0451	<0.0451	<0.0364	<0.0364	<0.0364	<0.0467	<0.0302	0.140	0.130	<0.0495	0.275	0.140	0.140	0.130	<0.0495
Sr ppm	1.92	1.92	1.92	1.82	1.82	1.82	1.70	2.09	41.6	41.6	39.2	38.1	41.6	41.6	41.6	39.2
Y ppm	14.7	14.7	14.7	15.4	15.4	15.4	15.6	14.4	13.9	14.3	14.5	14.6	13.9	13.9	14.3	14.5
Zr ppm	2.35	2.35	2.35	2.56	2.56	2.56	2.62	2.41	15.3	19.4	16.9	20.5	15.3	15.3	19.4	16.9
Nb ppm	<0.00396	<0.00396	<0.00396	<0.00422	<0.00422	<0.00422	<0.00459	<0.00385	0.119	0.141	0.0974	0.0631	0.119	0.119	0.141	0.0974
Cs ppm	<0.0240	<0.0240	<0.0240	0.0128	0.0128	0.0128	0.00519	<0.0253	<0.0281	<0.0269	<0.0257	<0.0284	<0.0281	<0.0281	<0.0269	<0.0257
Ba ppm	<0.0334	<0.0334	<0.0334	<0.0357	<0.0357	<0.0357	<0.0387	<0.0324	0.196	0.371	0.0267	0.297	0.196	0.196	0.371	0.0267
La ppm	0.0399	0.0399	0.0399	0.0327	0.0327	0.0327	0.0268	0.0634	0.547	0.563	0.513	0.529	0.547	0.547	0.563	0.513
Ce ppm	0.323	0.323	0.323	0.303	0.303	0.303	0.369	0.404	2.04	1.90	1.94	1.85	2.04	2.04	1.90	1.94
Pr ppm	0.0808	0.0808	0.0808	0.0737	0.0737	0.0737	0.0803	0.0844	0.416	0.387	0.370	0.336	0.416	0.416	0.387	0.370
Nd ppm	0.542	0.542	0.542	0.747	0.747	0.747	0.545	0.607	2.34	2.27	2.31	2.10	2.34	2.34	2.27	2.31
Sm ppm	0.428	0.428	0.428	0.387	0.387	0.387	0.401	0.510	0.982	0.930	1.03	1.05	0.982	0.982	0.930	1.03
Eu ppm	0.265	0.265	0.265	0.305	0.305	0.305	0.244	0.232	0.492	0.460	0.481	0.482	0.492	0.492	0.460	0.481
Gd ppm	1.32	1.32	1.32	1.42	1.42	1.42	1.21	1.18	1.63	1.70	1.70	1.64	1.63	1.63	1.70	1.70
Tb ppm	0.290	0.290	0.290	0.325	0.325	0.325	0.286	0.270	0.339	0.339	0.343	0.317	0.339	0.339	0.339	0.343
Dy ppm	2.30	2.30	2.30	2.59	2.59	2.59	2.33	2.26	2.23	2.19	2.26	2.11	2.23	2.23	2.19	2.26
Ho ppm	0.562	0.562	0.562	0.557	0.557	0.557	0.694	0.582	0.500	0.522	0.546	0.505	0.500	0.500	0.522	0.546
Er ppm	1.76	1.76	1.76	1.61	1.61	1.61	1.65	1.79	1.43	1.49	1.46	1.53	1.43	1.43	1.49	1.46
Tm ppm	0.228	0.228	0.228	0.231	0.231	0.231	0.273	0.241	0.197	0.223	0.192	0.197	0.197	0.197	0.223	0.192
Yb ppm	1.46	1.46	1.46	1.67	1.67	1.67	1.58	1.28	1.33	1.26	1.34	1.26	1.33	1.33	1.26	1.34
Lu ppm	0.228	0.228	0.228	0.258	0.258	0.258	0.221	0.216	0.177	0.191	0.201	0.208	0.177	0.177	0.191	0.201
Hf ppm	0.116	0.116	0.116	0.178	0.178	0.178	0.139	0.162	0.467	0.558	0.513	0.642	0.467	0.467	0.558	0.513
Ta ppm	<0.00500	<0.00500	<0.00500	<0.00532	<0.00532	<0.00532	<0.00579	<0.00484	0.00475	0.00712	0.0101	0.00437	0.00475	0.00475	0.00712	0.0101
Pb ppm	0.0227	0.0227	0.0227	0.0207	0.0207	0.0207	<0.0152	<0.0702	0.0222	0.0571	0.0309	0.0379	0.0222	0.0222	0.0571	0.0309
Th ppm	<0.00726	<0.00726	<0.00726	<0.00773	<0.00773	<0.00773	<0.00839	<0.00701	0.0134	0.0141	0.0104	0.0102	0.0134	0.0134	0.0141	0.0104
U ppm	<0.00759	<0.00759	<0.00759	<0.00807	<0.00807	<0.00807	<0.00876	<0.00732	<0.00203	0.00590	<0.00183	0.00681	<0.00203	<0.00203	0.00590	<0.00183
Eu/Eu*	1.07	1.07	1.07	1.25	1.25	1.25	1.06	0.91	1.18	1.11	1.11	1.12	1.18	1.18	1.11	1.11

B.5. Table de données – compositions chimiques en éléments traces des clinopyroxènes

Analysis	MD80-DR3-G2-2-7	MD80-DR3-I2-12	MD80-DR3-I2-12	MD80-DR3-I2-15	MD80-DR3-I2-15b	MD80-DR3-I2-3	MD80-DR3-I2-9	MD80-DR3-I2-9	MD80-DR3-I3 001	MD80-DR3-I3 002	MD80-DR3-I3 003	MD80-DR3-I3 004
Mineral	Cpx	Cpx	Cpx	Cpx	Cpx	Cpx	Cpx	Cpx	Cpx	Cpx	Cpx	Cpx
Location	MD80-DR3	MD80-DR3	MD80-DR3	MD80-DR3	MD80-DR3	MD80-DR3	MD80-DR3	MD80-DR3	MD80-DR3	MD80-DR3	MD80-DR3	MD80-DR3
Sample	3G2-2	3I2	3I2	3I2	3I2	3I2	3I2	3I2	3I3	3I3	3I3	3I3
Rock type	Sp-	Sp-	Sp-	Sp-	Sp-	Sp-	Sp-	Sp-	Sp-	Sp-	Sp-	Sp-
Texture	Porph.	Porph.	Porph.	Porph.	Porph.	Porph.	Porph.	Porph.	Porph.	Porph.	Porph.	Porph.
Mineral location	Core	Core	Core	Core	Core	Core	Core	Core	Core	Core	Core	Core
Li ppm	1.69	1.42	3.05	1.11	1.38	1.58	2.79	1.37	2.08	2.12	3.05	3.33
B ppm	1.79	1.44	2.08	<0.686	0.723	<0.674	2.40	0.855	<2.11	<1.91	2.04	2.37
Sc ppm	54.0	65.1	62.5	64.6	67.2	62.4	51.6	67.9	66.9	70.2	55.0	58.0
Ti ppm	1698	1661	1806	1716	1712	1639	1491	1545	667	735	653	663
V ppm	217	244	238	243	248	243	218	237	245	248	233	234
Cr ppm	3318	3388	3362	3278	3249	3421	3553	3151	8581	7602	8607	8631
Mn ppm												
Co ppm	16.8	17.1	20.2	17.5	18.3	18.7	18.2	15.7	19.7	17.0	18.6	18.3
Ni ppm	265	261	273	265	273	273	311	242	323	298	300	312
Rb ppm	0.285	0.0798	0.375	0.0575	<0.0630	0.0717	0.485	<0.0609	<0.0376	<0.0374	<0.0341	0.123
Sr ppm	39.9	39.7	43.6	39.4	41.0	43.2	71.0	37.5	20.0	18.8	23.9	24.8
Y ppm	14.1	13.1	12.3	13.2	13.7	13.7	12.5	12.2	5.86	6.21	5.68	5.85
Zr ppm	20.2	16.1	15.3	15.7	15.6	15.8	13.8	14.4	10.7	11.8	11.3	10.9
Nb ppm	0.0764	0.104	0.115	0.0759	0.107	0.140	0.744	0.0664	0.266	0.185	0.287	0.266
Cs ppm	0.0347	<0.0399	<0.0419	<0.0327	0.0489	<0.0363	0.0480	<0.0326	<0.0231	<0.0173	<0.0178	0.00873
Ba ppm	0.633	0.508	3.66	<0.0179	0.156	0.0673	1.90	0.390	<0.0334	<0.0307	0.143	0.452
La ppm	0.517	0.463	0.490	0.470	0.527	0.565	1.25	0.444	0.588	0.512	0.614	0.683
Ce ppm	1.87	1.75	1.73	1.76	1.82	1.89	3.18	1.66	1.70	1.67	1.92	2.14
Pr ppm	0.384	0.355	0.354	0.356	0.389	0.381	0.560	0.307	0.250	0.257	0.319	0.292
Nd ppm	2.15	2.03	1.88	2.03	2.00	2.32	2.93	2.14	1.31	1.45	1.59	1.69
Sm ppm	1.11	0.845	0.908	0.842	0.859	0.978	1.14	0.853	0.371	0.497	0.470	0.396
Eu ppm	0.482	0.433	0.344	0.383	0.383	0.429	0.444	0.372	0.150	0.208	0.245	0.227
Gd ppm	1.61	1.17	1.58	1.31	1.44	1.58	1.49	1.31	0.628	0.620	0.804	0.681
Tb ppm	0.320	0.277	0.263	0.316	0.323	0.303	0.261	0.264	0.151	0.150	0.152	0.158
Dy ppm	2.26	2.01	1.95	1.91	1.87	2.24	1.86	1.95	0.970	1.13	1.07	0.989
Ho ppm	0.518	0.468	0.427	0.465	0.502	0.525	0.446	0.433	0.203	0.272	0.187	0.229
Er ppm	1.44	1.34	1.21	1.49	1.35	1.39	1.25	1.29	0.616	0.757	0.590	0.623
Tm ppm	0.194	0.198	0.199	0.202	0.225	0.203	0.188	0.189	0.0813	0.113	0.0970	0.106
Yb ppm	1.25	1.27	1.30	1.41	1.24	1.31	1.08	1.11	0.500	0.604	0.486	0.535
Lu ppm	0.184	0.208	0.187	0.192	0.192	0.201	0.198	0.203	0.0958	0.0923	0.0843	0.0635
Hf ppm	0.562	0.546	0.422	0.513	0.526	0.439	0.282	0.473	0.356	0.353	0.291	0.256
Ta ppm	0.00667	0.00514	<0.00438	0.00427	0.0126	0.0122	0.0431	0.00502	0.0210	0.0194	0.0253	0.00969
Pb ppm	0.0665	0.424	0.771	0.0193	0.0588	0.124	0.209	0.129	0.0881	0.0668	0.0240	0.118
Th ppm	0.0127	0.0146	0.0147	0.00854	0.0104	0.0164	0.0776	<0.00432	<0.00688	<0.00632	<0.00598	0.00712
U ppm	0.00740	0.0256	0.0262	<0.00436	<0.00544	<0.00535	0.0116	<0.00431	<0.00717	<0.00659	<0.00623	<0.00622
Eu/Eu*	1.10	1.32	0.87	1.11	1.05	1.05	1.04	1.07	0.95	1.14	1.21	1.33

B.5. Table de données – compositions chimiques en éléments majeurs des orthopyroxènes

Analysis	Mineral	Analytical method	Location	Sample	Rock type	Texture	Mineral location	Na_2O	MgO	Al_2O_3	SiO_2	K_2O	CaO	TiO_2	Cr_2O_3	MnO	FeO	NiO	Total	Na	Mg	Al	AlIV	AlVI	Si	K	Ca	Ti	Cr	Mn	Fe_2	Ni	Total
MD110-DR02-A03 00	Opx	µXRF	MD110-DR02	A03	Sp-lhz	Porph.	Core	0.00	31.64	5.43	55.36	0.01	2.55	0.15	0.51	0.08	4.20		99.93	0.000	1.630	0.221	0.087	0.134	1.913	0.000	0.094	0.004	0.014	0.002	0.121	0.000	#####
MD110-DR02-A03 00	Opx	µXRF	MD110-DR02	A03	Sp-lhz	Porph.	Core	0.00	31.91	5.55	55.32	0.01	2.22	0.14	0.53	0.08	4.13		99.90	0.000	1.642	0.226	0.090	0.135	1.910	0.000	0.082	0.004	0.014	0.002	0.119	0.000	#####
MD110-DR02-A03 00	Opx	µXRF	MD110-DR02	A03	Sp-lhz	Porph.	Rim	0.00	33.63	4.49	54.92	0.00	1.12	0.10	0.44	0.09	5.10		99.89	0.000	1.724	0.182	0.111	0.071	1.889	0.000	0.041	0.003	0.012	0.003	0.147	0.000	#####
MD110-DR02-A03 01	Opx	µXRF	MD110-DR02	A03	Sp-lhz	Porph.	Core	0.00	32.12	5.60	54.24	0.00	2.30	0.17	0.61	0.09	4.79		99.91	0.000	1.653	0.228	0.128	0.100	1.872	0.000	0.085	0.004	0.017	0.003	0.138	0.000	#####
MD110-DR02-A05 00	Opx	µXRF	MD110-DR02	A5	Sp-lhz	Porph.	Core	0.00	30.25	5.26	55.84	0.00	3.02	0.07	0.55	0.07	4.85		99.92	0.000	1.569	0.216	0.058	0.158	1.942	0.000	0.113	0.002	0.015	0.002	0.141	0.000	#####
MD110-DR02-A05 00	Opx	µXRF	MD110-DR02	A5	Sp-lhz	Porph.	Core	0.00	30.44	5.26	55.88	0.00	2.81	0.05	0.55	0.08	4.84		99.90	0.000	1.578	0.215	0.057	0.158	1.943	0.000	0.105	0.001	0.015	0.002	0.141	0.000	#####
MD110-DR02-A13 00	Opx	µXRF	MD110-DR02	A13	Sp-lhz	Porph.	Core	0.00	32.88	3.17	55.86	0.01	1.70	0.13	0.60	0.11	5.46		99.92	0.000	1.695	0.129	0.068	0.061	1.932	0.000	0.063	0.003	0.016	0.003	0.158	0.000	#####
MD110-DR02-A13-10	Opx	EPMA	MD110-DR02	A13	Sp-lhz	Porph.	Core	0.05	32.70	3.51	55.39	0.01	1.37	0.12	0.67	0.18	6.33	0.15	#####	0.003	1.680	0.143	0.091	0.052	1.909	0.000	0.051	0.003	0.018	0.005	0.182	0.004	#####
MD110-DR02-A13-9	Opx	EPMA	MD110-DR02	A13	Sp-lhz	Porph.	Core	0.05	33.17	3.20	54.90	0.01	0.68	0.15	0.73	0.18	6.68	0.09	99.83	0.003	1.713	0.131	0.098	0.033	1.902	0.000	0.025	0.004	0.020	0.005	0.194	0.003	#####
MD110-DR02-A27 00	Opx	µXRF	MD110-DR02	A27	Sp-lhz	Porph.	Core	0.00	33.85	4.20	55.52	0.01	1.15	0.10	0.66	0.08	4.27		99.84	0.000	1.734	0.170	0.092	0.078	1.908	0.001	0.042	0.003	0.018	0.002	0.123	0.000	#####
MD110-DR02-A27 00	Opx	µXRF	MD110-DR02	A27	Sp-lhz	Porph.	Core	0.00	33.52	4.18	55.55	0.00	1.47	0.11	0.65	0.08	4.30		99.88	0.000	1.719	0.169	0.089	0.080	1.911	0.000	0.054	0.003	0.018	0.002	0.124	0.000	#####
MD110-DR02-A27 00	Opx	µXRF	MD110-DR02	A27	Sp-lhz	Porph.	Rim	0.00	32.12	4.83	54.97	0.01	2.19	0.13	0.68	0.09	4.87		99.89	0.000	1.656	0.197	0.099	0.097	1.901	0.001	0.081	0.003	0.019	0.003	0.141	0.000	#####
MD110-DR02-A27 00	Opx	µXRF	MD110-DR02	A27	Sp-lhz	Porph.	Core	0.00	32.59	4.99	54.53	0.00	2.06	0.13	0.71	0.09	4.79		99.90	0.000	1.676	0.203	0.119	0.084	1.881	0.000	0.076	0.003	0.019	0.003	0.138	0.000	#####
MD110-DR02-A27-6	Opx	EPMA	MD110-DR02	A27	Sp-lhz	Porph.	Rim	0.17	31.87	5.31	54.33	0.00	2.03	0.08	0.81	0.17	5.53		#####	0.011	1.637	0.216	0.128	0.088	1.872	0.000	0.075	0.002	0.022	0.005	0.159	0.000	#####
MD110-DR02-A40 00	Opx	µXRF	MD110-DR02	A40	Sp-lhz	Porph.	Core	0.00	33.11	3.64	55.85	0.03	2.61	0.14	0.59	0.08	3.88		99.93	0.000	1.699	0.148	0.078	0.070	1.922	0.001	0.096	0.004	0.016	0.002	0.112	0.000	#####
MD110-DR02-A40 00	Opx	µXRF	MD110-DR02	A40	Sp-lhz	Porph.	Core	0.00	33.09	3.79	55.70	0.01	2.39	0.14	0.65	0.08	4.08		99.93	0.000	1.699	0.154	0.082	0.071	1.918	0.001	0.088	0.004	0.018	0.002	0.117	0.000	#####
MD110-DR02-A40 00	Opx	µXRF	MD110-DR02	A40	Sp-lhz	Porph.	Core	0.00	33.36	3.85	55.50	0.00	1.95	0.14	0.70	0.09	4.33		99.92	0.000	1.712	0.156	0.090	0.066	1.910	0.000	0.072	0.004	0.019	0.003	0.125	0.000	#####
MD110-DR02-A40 00	Opx	µXRF	MD110-DR02	A40	Sp-lhz	Porph.	Rim	0.00	34.04	3.50	55.76	0.01	1.48	0.14	0.63	0.10	4.27		99.92	0.000	1.743	0.142	0.085	0.056	1.915	0.001	0.054	0.004	0.017	0.003	0.123	0.000	#####
MD110-DR02-A40-3	Opx	EPMA	MD110-DR02	A40	Sp-lhz	Porph.	Core	0.05	34.06	4.08	55.79	0.01	1.02	0.09	0.76	0.06	5.13		#####	0.003	1.727	0.164	0.102	0.061	1.898	0.000	0.037	0.002	0.020	0.002	0.146	0.000	#####
MD110-DR02-A40-4	Opx	EPMA	MD110-DR02	A40	Sp-lhz	Porph.	Core	0.11	32.12	4.54	54.65	0.00	2.26	0.17	0.78	0.19	5.16		99.99	0.007	1.655	0.185	0.111	0.074	1.889	0.000	0.084	0.004	0.021	0.006	0.149	0.000	#####
MD110-DR02-A40-5	Opx	EPMA	MD110-DR02	A40	Sp-lhz	Porph.	Core	0.07	33.87	4.20	55.13	0.00	0.66	0.09	0.83	0.16	5.68		#####	0.005	1.726	0.169	0.116	0.054	1.884	0.000	0.024	0.002	0.022	0.005	0.162	0.000	#####
MD110-DR02-A40-7	Opx	EPMA	MD110-DR02	A40	Sp-lhz	Porph.	Core	0.12	33.14	4.69	52.78	0.00	1.79	0.15	0.76	0.13	5.10		98.65	0.008	1.719	0.192	0.163	0.029	1.837	0.000	0.067	0.004	0.021	0.004	0.148	0.000	#####
MD110-DR02-A40-8	Opx	EPMA	MD110-DR02	A40	Sp-lhz	Porph.	Rim	0.14	32.88	3.53	52.82	0.00	1.97	0.10	0.72	0.08	5.13		97.36	0.010	1.729	0.147	0.137	0.010	1.863	0.000	0.074	0.003	0.020	0.002	0.151	0.000	#####
MD110-DR02-A48 00	Opx	µXRF	MD110-DR02	A48	Sp-lhz	Porph.	Rim	0.00	33.79	4.04	54.99	0.01	1.06	0.12	0.78	0.09	5.03		99.90	0.000	1.733	0.164	0.108	0.056	1.892	0.000	0.039	0.003	0.021	0.003	0.145	0.000	#####
MD110-DR02-A48 00	Opx	µXRF	MD110-DR02	A48	Sp-lhz	Porph.	Core	0.00	32.53	4.65	54.46	0.00	2.12	0.25	0.97	0.09	4.85		99.91	0.000	1.675	0.189	0.119	0.071	1.881	0.000	0.079	0.007	0.027	0.003	0.140	0.000	#####
MD110-DR02-A48 00	Opx	µXRF	MD110-DR02	A48	Sp-lhz	Porph.	Core	0.00	32.73	4.21	54.76	0.00	2.31	0.17	0.91	0.09	4.72		99.91	0.000	1.685	0.171	0.110	0.062	1.890	0.000	0.085	0.005	0.025	0.003	0.136	0.000	#####
MD110-DR02-A48 00	Opx	µXRF	MD110-DR02	A48	Sp-lhz	Porph.	Core	0.00	33.62	3.74	55.03	0.01	1.53	0.14	0.76	0.09	5.01		99.92	0.000	1.726	0.152	0.105	0.046	1.895	0.000	0.056	0.004	0.021	0.003	0.144	0.000	#####
MD110-DR02-A48 00	Opx	µXRF	MD110-DR02	A48	Sp-lhz	Porph.	Rim	0.00	34.10	3.41	56.19	0.00	1.17	0.12	0.58	0.09	4.25		99.93	0.000	1.746	0.138	0.071	0.067	1.929	0.000	0.043	0.003	0.016	0.003	0.122	0.000	#####
MD110-DR02-A48 01	Opx	µXRF	MD110-DR02	A48	Sp-lhz	Porph.	Core	0.00	33.54	3.81	55.90	0.00	1.53	0.13	0.66	0.09	4.25		99.93	0.000	1.720	0.155	0.077	0.077	1.923	0.000	0.056	0.003	0.018	0.003	0.122	0.000	#####
MD110-DR02-A48-10	Opx	EPMA	MD110-DR02	A48	Sp-lhz	Porph.	Core	0.08	33.02	3.99	54.31	0.01	1.44	0.17	0.90	0.00	5.74		99.66	0.005	1.704	0.163	0.121	0.042	1.879	0.000	0.053	0.004	0.025	0.000	0.166	0.000	#####
MD110-DR02-A48-20	Opx	EPMA	MD110-DR02	A48	Sp-lhz	Porph.	Core	0.13	33.56	4.24	54.60	0.02	0.60	0.10	0.81	0.07	5.45		99.57	0.009	1.727	0.172	0.115	0.057	1.885	0.001	0.022	0.003	0.022	0.002	0.157	0.000	#####
MD110-DR02-A48-4	Opx	EPMA	MD110-DR02	A48	Sp-lhz	Porph.	Core	0.18	31.36	4.79	53.02	0.00	1.81	0.18	0.95	0.17	5.07		97.54	0.012	1.655	0.200	0.123	0.077	1.877	0.000	0.069	0.005	0.027	0.005	0.150	0.000	#####
MD110-DR02-A48-5	Opx	EPMA	MD110-DR02	A48	Sp-lhz	Porph.	Core	0.05	33.10	4.76	53.46	0.01	0.62	0.11	0.87	0.07	5.52		98.57	0.003	1.722	0.196	0.135	0.061	1.865	0.000	0.023	0.003	0.024	0.002	0.161	0.000	#####
MD110-DR02-A48-6	Opx	EPMA	MD110-DR02	A48	Sp-lhz	Porph.	Core	0.13	32.68	4.02	54.00	0.00	0.71	0.07	0.78	0.20	5.22		97.80	0.009	1.714	0.167	0.100	0.067	1.900	0.000	0.027	0.002	0.022	0.006	0.154	0.000	#####
MD110-DR02-A48-9	Opx	EPMA	MD110-DR02	A48	Sp-lhz	Porph.	Rim	0.05	33.54	3.86	55.06	0.01	0.63	0.12	0.70	0.05	5.25		99.28	0.003	1.732	0.158	0.093	0.065	1.907	0.000	0.023	0.003	0.019	0.001	0.152	0.000	#####
MD110-DR02-A50 00	Opx	µXRF	MD110-DR02	A50	Sp-lhz	Porph.	Core	0.00	32.79	5.08	54.92	0.00	1.84	0.14	0.66	0.09	4.40		99.92	0.000	1.683	0.206	0.109	0.098	1.891	0.000	0.068	0.004	0.018	0.003	0.127	0.000	#####
MD110-DR02-A50-10	Opx	EPMA	MD110-DR02	A50	Sp-lhz	Porph.	Core	0.07	32.48	4.31	54.77	0.00	1.20	0.09	0.52	0.13	5.29		98.85	0.005	1.689	0.177	0.090	0.087	1.910	0.000	0.045	0.002	0.014	0.004	0.154	0.000	#####
MD110-DR02-A50-11	Opx	EPMA	MD110-DR02	A50	Sp-lhz	Porph.	Core	0.04	33.52	3.39	54.98	0.02	0.91	0.12	0.43	0.09	5.36		98.86	0.003	1.738	0.139	0.088	0.051	1.912	0.001	0.034	0.003	0.012	0.003	0.156	0.000	#####
MD110-DR02-A50-14	Opx	EPMA	MD110-DR02	A50	Sp-lhz	Porph.	Core	0.04	32.27	5.55	53.38	0.00	0.68	0.09	0.74	0.03	5.46		98.24	0.003	1.687	0.229	0.128	0.101	1.872	0.000	0.026	0.002	0.021	0.001	0.160	0.000	#####
MD110-DR02-A50-2b	Opx	EPMA	MD110-DR02	A50	Sp-lhz	Porph.	Core	0.02	31.72	4.79	53.83	0.02	1.95	0.15	0.63	0.21	5.21		98.53	0.001	1.658	0.198	0.112	0.086	1.888	0.001	0.073	0.004	0.017	0.006	0.153	0.000	#####
MD110-DR02-A50-2c	Opx	EPMA	MD110-DR02	A50	Sp-lhz	Porph.	Core	0.06	32.38	4.51	54.10	0.00	1.08	0.15	0.68	0.18	5.71		98.86	0.004	1.686	0.186	0.111	0.075	1.889	0.000	0.040	0.004	0.019	0.005	0.167	0.000	#####
MD110-DR02-A50-9	Opx	EPMA	MD110-DR02	A50	Sp-lhz	Porph.	Core	0.12	31.72	4.50	53.97	0.01	2.30	0.16	0.52	0.09	5.39		98.77	0.008	1.654	0.185	0.113	0.073	1.887	0.000	0.086	0.004	0.014	0.003	0.158	0.000	#####
MD110-DR02-A58 00	Opx	µXRF	MD110-DR02	A58	Sp-lhz	Porph.	Core	0.00	32.59	5.05	54.34	0.05	1.68	0.12	0.71	0.10	5.19		99.82	0.000	1.678	0.205	0.123	0.082	1.877	0.002	0.062	0.003	0.019	0.003	0.150	0.000	#####
MD110-DR02-A58 00	Opx	µXRF	MD110-DR02	A58	Sp-lhz	Porph.	Core	0.00	32.39	5.17	54.30	0.08	1.80	0.13	0.75	0.10	5.14		99.85	0.000	1.668	0.211	0.124	0.087	1.876	0.004	0.066	0.003	0.020	0.003	0.148	0.000	#####
MD110-DR02-A58-12	Opx	EPMA	MD110-DR02	A58	Sp-lhz	Porph.	Core	0.13	31.65	5.62	53.52	0.00	1.51	0.13	0.72	0.15	5.13		98.56	0.009	1.652	0.232	0.127	0.105	1.873	0.000	0.057	0.003	0.020	0.004	0.150	0.000	#####
MD110-DR02-A58-20	Opx	EPMA	MD110-DR02	A58	Sp-lhz	Porph.	Rim	0.17	31.79	5.64	53.00	0.00	1.39	0.12	0.77	0.16	5.65		98.69														
MD110-DR02-A58-9	Opx	EPMA	MD110-DR02	A58	Sp-lhz	Porph.	Rim	0.11	32.58	5.42	53.71	0.00	1.05	0.16	0.66	0.10	5.18		98.97														
MD110-DR02-A64 00	Opx	µXRF	MD110-DR02	A64	Sp-lhz	Porph.	Core	0.00	32.71	3.81	55.62	0.00	2.31	0.33	0.73	0.09	4.32		99.93	0.000	1.684	0.155	0.080	0.075	1.920	0.000	0.085	0.009	0.020	0.003	0.125	0.000	#####
MD110-DR02-A64 00	Opx	µXRF	MD110-DR02	A64	Sp-lhz	Porph.	Core	0.00	33.37	4.37	55.43	0.00	1.72	0.14	0.75	0.10	4.04		99.92	0.000	1.711	0.177	0.094	0.083	1.906	0.000	0.063	0.004	0.020	0.003	0.116	0.000	#####

B.5. Table de données – compositions chimiques en éléments majeurs des orthopyroxènes

Analysis	Mineral	Analytical method	Location	Sample	Rock type	Texture	Mineral location	Na_2O	MgO	Al_2O_3	SiO_2	K_2O	CaO	TiO_2	Cr_2O_3	MnO	FeO	NiO	Total	Na	Mg	Al	AlIV	AlVI	Si	K	Ca	Ti	Cr	Mn	Fe_2	Ni	Total
MD110-DR02-A64-9	Opx	EPMA	MD110-DR02	A64	Sp-lhz	Porph.	Core	0.09	33.45	4.24	55.54	0.00	1.24	0.11	0.99	0.12	5.11		######	0.006	1.703	0.171	0.104	0.067	1.896	0.000	0.045	0.003	0.027	0.003	0.146	0.000	######
MD110-DR02-A66 00	Opx	µXRF	MD110-DR02	A66	Sp-lhz	Porph.	Core	0.00	33.04	3.70	55.77	0.00	2.40	0.14	0.66	0.09	4.10		99.91	0.000	1.697	0.150	0.079	0.072	1.921	0.000	0.089	0.004	0.018	0.003	0.118	0.000	######
MD110-DR02-A66 00	Opx	µXRF	MD110-DR02	A66	Sp-lhz	Porph.	Rim	0.00	32.96	3.81	56.30	0.01	1.83	0.14	0.66	0.09	4.12		99.92	0.000	1.694	0.155	0.059	0.095	1.941	0.000	0.068	0.004	0.018	0.003	0.119	0.000	######
MD110-DR02-A66 00	Opx	µXRF	MD110-DR02	A66	Sp-lhz	Porph.	Core	0.00	31.71	4.17	56.37	0.06	2.50	0.16	0.75	0.08	4.08		99.87	0.000	1.637	0.170	0.048	0.122	1.952	0.003	0.093	0.004	0.021	0.002	0.118	0.000	######
MD110-DR02-A66 00	Opx	µXRF	MD110-DR02	A66	Sp-lhz	Porph.	Core	0.00	32.60	4.16	56.16	0.00	2.26	0.15	0.71	0.08	3.80		99.93	0.000	1.676	0.169	0.064	0.105	1.936	0.000	0.084	0.004	0.019	0.002	0.110	0.000	######
MD110-DR02-A66 00	Opx	µXRF	MD110-DR02	A66	Sp-lhz	Porph.	Core	0.00	33.07	3.84	55.95	0.01	1.84	0.15	0.69	0.09	4.28		99.91	0.000	1.699	0.156	0.072	0.084	1.928	0.000	0.068	0.004	0.019	0.003	0.123	0.000	######
MD110-DR02-A66 00	Opx	µXRF	MD110-DR02	A66	Sp-lhz	Porph.	Core	0.00	31.36	3.76	56.43	0.08	2.55	0.18	0.76	0.07	4.70		99.88	0.000	1.624	0.154	0.040	0.114	1.960	0.003	0.095	0.005	0.021	0.002	0.136	0.000	######
MD110-DR02-A66 00	Opx	µXRF	MD110-DR02	A66	Sp-lhz	Porph.	Rim	0.00	34.24	3.70	56.09	0.00	1.47	0.12	0.54	0.08	3.71		99.94	0.000	1.749	0.149	0.078	0.071	1.922	0.000	0.054	0.003	0.015	0.002	0.106	0.000	######
MD110-DR06-158A 00	Opx	µXRF	MD110-DR06	158A	Pl-lhz	Porph.	Core	0.00	33.34	3.65	54.69	0.00	1.72	0.12	0.84	0.09	5.45		99.90	0.000	1.715	0.148	0.113	0.035	1.887	0.000	0.064	0.003	0.023	0.003	0.157	0.000	######
MD110-DR06-158A 00	Opx	µXRF	MD110-DR06	158A	Pl-lhz	Porph.	Core	0.00	33.03	4.26	54.34	0.00	1.78	0.10	0.76	0.10	5.48		99.85	0.000	1.700	0.173	0.124	0.049	1.876	0.000	0.066	0.003	0.021	0.003	0.158	0.000	######
MD110-DR06-158A 00	Opx	µXRF	MD110-DR06	158A	Pl-lhz	Porph.	Core	0.00	32.98	4.33	54.31	0.06	1.83	0.12	0.79	0.10	5.40		99.91	0.000	1.696	0.176	0.126	0.050	1.874	0.003	0.068	0.003	0.022	0.003	0.156	0.000	######
MD110-DR06-158A 00	Opx	µXRF	MD110-DR06	158A	Pl-lhz	Porph.	Core	0.00	32.98	4.33	54.31	0.06	1.83	0.12	0.79	0.10	5.40		99.91	0.000	1.696	0.176	0.126	0.050	1.874	0.003	0.068	0.003	0.022	0.003	0.156	0.000	######
MD110-DR06-158A 01	Opx	µXRF	MD110-DR06	158A	Pl-lhz	Porph.	Core	0.00	33.36	3.28	55.16	0.00	1.96	0.14	0.77	0.10	5.13		99.91	0.000	1.716	0.133	0.097	0.036	1.903	0.000	0.073	0.004	0.021	0.003	0.148	0.000	######
MD110-DR06-158A 01	Opx	µXRF	MD110-DR06	158A	Pl-lhz	Porph.	Core	0.00	33.61	3.08	55.31	0.00	1.78	0.14	0.74	0.10	5.14		99.91	0.000	1.727	0.125	0.093	0.032	1.907	0.000	0.066	0.004	0.020	0.003	0.148	0.000	######
MD110-DR06-158A-1	Opx	EPMA	MD110-DR06	158A	Pl-lhz	Porph.	Core	0.02	33.31	3.36	55.06	0.00	1.10	0.12	0.82	0.28	5.86		99.92	0.001	1.716	0.137	0.098	0.039	1.902	0.000	0.041	0.003	0.022	0.008	0.169	0.000	######
MD110-DR06-158A-5	Opx	EPMA	MD110-DR06	158A	Pl-lhz	Porph.	Core	0.06	32.97	4.18	54.80	0.03	1.53	0.15	0.87	0.10	5.74		######	0.004	1.690	0.169	0.116	0.053	1.884	0.001	0.056	0.004	0.024	0.003	0.165	0.000	######
MD110-DR06-158B 00	Opx	µXRF	MD110-DR06	158B	Pl-lhz	Porph.	Core	0.00	34.01	2.97	55.10	0.00	1.72	0.12	0.72	0.16	5.11		99.91	0.000	1.745	0.120	0.103	0.017	1.897	0.000	0.063	0.003	0.019	0.005	0.147	0.000	######
MD110-DR06-158B 00	Opx	µXRF	MD110-DR06	158B	Pl-lhz	Porph.	Core	0.00	33.32	3.82	54.91	0.00	1.77	0.13	0.77	0.10	5.08		99.90	0.000	1.713	0.155	0.107	0.048	1.893	0.000	0.065	0.003	0.021	0.003	0.147	0.000	######
MD110-DR06-158B 00	Opx	µXRF	MD110-DR06	158B	Pl-lhz	Porph.	Core	0.00	33.68	2.77	55.38	0.00	1.71	0.12	0.76	0.10	5.37		99.89	0.000	1.732	0.113	0.089	0.023	1.911	0.000	0.063	0.003	0.021	0.003	0.155	0.000	######
MD110-DR06-158B 00	Opx	µXRF	MD110-DR06	158B	Pl-lhz	Porph.	Core	0.00	32.89	4.65	54.20	0.00	1.88	0.12	0.69	0.10	5.32		99.85	0.000	1.692	0.189	0.129	0.060	1.871	0.000	0.070	0.003	0.019	0.003	0.153	0.000	######
MD110-DR06-158B-1	Opx	EPMA	MD110-DR06	158B	Pl-lhz	Porph.	Core	0.05	32.75	3.28	55.13	0.04	1.68	0.10	0.82	0.24	5.67		99.75	0.003	1.692	0.134	0.090	0.044	1.910	0.002	0.062	0.003	0.022	0.007	0.164	0.000	######
MD110-DR06-158B-3	Opx	EPMA	MD110-DR06	158B	Pl-lhz	Porph.	Core	0.05	32.48	4.16	54.79	0.02	1.45	0.13	0.77	0.05	6.02		99.93	0.003	1.676	0.170	0.104	0.066	1.896	0.001	0.054	0.003	0.021	0.001	0.174	0.000	######
MD110-DR06-158B-4	Opx	EPMA	MD110-DR06	158B	Pl-lhz	Porph.	Core	0.07	32.96	3.63	54.95	0.00	1.05	0.10	0.91	0.17	6.40		######	0.005	1.696	0.148	0.104	0.044	1.896	0.000	0.039	0.003	0.025	0.005	0.185	0.000	######
MD110-DR06-158B-5	Opx	EPMA	MD110-DR06	158B	Pl-lhz	Porph.	Core	0.02	32.35	4.27	54.39	0.01	1.22	0.07	0.80	0.13	6.34		99.60	0.001	1.676	0.175	0.110	0.065	1.890	0.000	0.045	0.002	0.022	0.004	0.184	0.000	######
MD110-DR06-158B-7	Opx	EPMA	MD110-DR06	158B	Pl-lhz	Porph.	Core	0.06	31.35	5.35	53.41	0.02	2.27	0.08	0.82	0.12	5.85		99.34	0.004	1.629	0.220	0.138	0.082	1.862	0.001	0.085	0.002	0.023	0.004	0.171	0.000	######
MD110-DR06-158B-9	Opx	EPMA	MD110-DR06	158B	Pl-lhz	Porph.	Core	0.05	32.04	5.79	53.38	0.00	0.66	0.11	0.93	0.12	6.90		######	0.003	1.655	0.236	0.151	0.086	1.849	0.000	0.024	0.003	0.025	0.004	0.200	0.000	######
MD110-DR06-159B 01	Opx	µXRF	MD110-DR06	159B	Pl-lhz	Porph.	Core	0.00	34.05	2.40	56.04	0.00	1.52	0.03	0.74	0.10	5.01		99.90	0.000	1.748	0.097	0.070	0.027	1.930	0.000	0.056	0.001	0.020	0.003	0.144	0.000	######
MD110-DR06-159B 02	Opx	µXRF	MD110-DR06	159B	Pl-lhz	Porph.	Rim	0.00	34.29	2.52	55.65	0.00	1.77	0.04	0.78	0.09	4.77		99.90	0.000	1.757	0.102	0.087	0.016	1.913	0.000	0.065	0.001	0.021	0.003	0.137	0.000	######
MD110-DR06-159B 02	Opx	µXRF	MD110-DR06	159B	Pl-lhz	Porph.	Core	0.00	34.08	2.17	56.07	0.00	1.54	0.03	0.73	0.10	5.17		99.88	0.000	1.751	0.088	0.068	0.020	1.932	0.000	0.057	0.001	0.020	0.003	0.149	0.000	######
MD110-DR06-159B 02	Opx	µXRF	MD110-DR06	159B	Pl-lhz	Porph.	Core	0.00	33.91	2.43	55.82	0.00	1.55	0.03	0.99	0.09	5.06		99.87	0.000	1.743	0.099	0.075	0.024	1.925	0.000	0.057	0.001	0.027	0.003	0.146	0.000	######
MD110-DR06-159B-1	Opx	EPMA	MD110-DR06	159B	Pl-lhz	Porph.	Core	0.20	33.34	3.18	55.09	0.01	1.75	0.04	0.91	0.08	5.52		######	0.013	1.710	0.129	0.104	0.025	1.896	0.000	0.065	0.001	0.025	0.002	0.159	0.000	######
MD110-DR06-159B-2	Opx	EPMA	MD110-DR06	159B	Pl-lhz	Porph.	Rim	0.09	33.51	2.91	55.70	0.00	1.48	0.03	0.86	0.06	5.68		######	0.006	1.717	0.118	0.085	0.032	1.915	0.000	0.055	0.001	0.023	0.002	0.163	0.000	######
MD110-DR06-159B-2	Opx	EPMA	MD110-DR06	159B	Pl-lhz	Porph.	Rim	0.07	34.05	2.82	56.36	0.00	1.45	0.03	0.78	0.13	5.67		######	0.005	1.726	0.113	0.083	0.030	1.917	0.000	0.053	0.001	0.021	0.004	0.161	0.000	######
MD110-DR06-161A 00	Opx	µXRF	MD110-DR06	161A	Pl-lhz	Porph.	Core	0.00	32.69	4.39	54.73	0.00	1.77	0.15	0.67	0.12	5.38		99.90	0.000	1.684	0.179	0.109	0.070	1.891	0.000	0.065	0.004	0.018	0.004	0.155	0.000	######
MD110-DR06-161A 00	Opx	µXRF	MD110-DR06	161A	Pl-lhz	Porph.	Core	0.00	32.52	4.83	54.29	0.00	1.94	0.16	0.67	0.11	5.39		99.91	0.000	1.675	0.197	0.124	0.072	1.876	0.000	0.072	0.004	0.018	0.003	0.156	0.000	######
MD110-DR06-161A 00	Opx	µXRF	MD110-DR06	161A	Pl-lhz	Porph.	Core	0.00	32.29	5.06	54.07	0.00	1.95	0.15	0.70	0.11	5.56		99.88	0.000	1.665	0.206	0.130	0.076	1.870	0.000	0.072	0.004	0.019	0.003	0.161	0.000	######
MD110-DR06-161A 00	Opx	µXRF	MD110-DR06	161A	Pl-lhz	Porph.	Core	0.00	32.20	5.12	54.11	0.00	1.95	0.14	0.71	0.11	5.56		99.90	0.000	1.660	0.209	0.129	0.080	1.871	0.000	0.072	0.004	0.019	0.003	0.161	0.000	######
MD110-DR06-161A 00	Opx	µXRF	MD110-DR06	161A	Pl-lhz	Porph.	Rim	0.00	32.20	5.12	54.11	0.00	1.95	0.14	0.71	0.11	5.56		99.90	0.000	1.660	0.209	0.129	0.080	1.871	0.000	0.072	0.004	0.019	0.003	0.161	0.000	######
MD110-DR06-161A 00	Opx	µXRF	MD110-DR06	161A	Pl-lhz	Porph.	Core	0.00	32.00	5.23	53.60	0.30	2.00	0.14	0.67	0.11	5.84		99.89	0.000	1.651	0.213	0.145	0.068	1.855	0.013	0.074	0.004	0.018	0.003	0.169	0.000	######
MD110-DR06-161A-1	Opx	EPMA	MD110-DR06	161A	Pl-lhz	Porph.	Core	0.02	32.68	5.07	53.85	0.00	1.38	0.16	0.80	0.21	6.49		######	0.001	1.674	0.205	0.150	0.055	1.850	0.000	0.051	0.004	0.022	0.006	0.186	0.000	######
MD110-DR06-161A-2	Opx	EPMA	MD110-DR06	161A	Pl-lhz	Porph.	Core	0.00	33.24	2.67	55.25	0.00	1.08	0.23	0.69	0.19	6.14		99.50	0.000	1.722	0.109	0.080	0.029	1.920	0.000	0.040	0.006	0.019	0.006	0.178	0.000	######
MD110-DR06-161A-3	Opx	EPMA	MD110-DR06	161A	Pl-lhz	Porph.	Core	0.11	31.60	5.41	53.91	0.01	2.22	0.16	0.76	0.17	5.75		######	0.007	1.629	0.220	0.136	0.085	1.864	0.000	0.082	0.004	0.021	0.005	0.166	0.000	######
MD110-DR06-161A-4	Opx	EPMA	MD110-DR06	161A	Pl-lhz	Porph.	Rim	0.06	32.90	3.80	54.83	0.02	1.37	0.13	0.80	0.08	6.06		######	0.004	1.694	0.155	0.107	0.048	1.893	0.001	0.051	0.003	0.022	0.002	0.175	0.000	######
MD110-DR06-161A-9	Opx	EPMA	MD110-DR06	161A	Pl-lhz	Porph.	Core	0.11	31.76	4.16	54.03	0.04	2.26	0.10	0.73	0.20	5.61		99.01	0.007	1.654	0.171	0.112	0.059	1.888	0.002	0.085	0.003	0.020	0.006	0.164	0.000	######
MD110-DR06-161C 00	Opx	µXRF	MD110-DR06	161C	Pl-lhz	Porph.	Core	0.00	32.41	4.95	54.28	0.00	1.84	0.15	0.69	0.12	5.45		99.90	0.000	1.670	0.202	0.124	0.078	1.876	0.000	0.068	0.004	0.019	0.004	0.158	0.000	######
MD110-DR06-161C 00	Opx	µXRF	MD110-DR06	161C	Pl-lhz	Porph.	Rim	0.00	32.87	3.94	54.97	0.00	1.83	0.16	0.68	0.12	5.35		99.90	0.000	1.693	0.160	0.101	0.059	1.899	0.000	0.068	0.004	0.018	0.003	0.155	0.000	######
MD110-DR06-161C 00	Opx	µXRF	MD110-DR06	161C	Pl-lhz	Porph.	Core	0.00	32.80	4.39	54.51	0.00	1.69	0.15	0.73	0.11	5.52		99.90	0.000	1.689	0.179	0.117	0.062	1.883	0.000	0.063	0.004	0.020	0.003	0.160	0.000	######
MD110-DR06-161C 00	Opx	µXRF	MD110-DR06	161C	Pl-lhz	Porph.	Core	0.00	33.26	3.89	54.75	0.00	1.68	0.15	0.74	0.11	5.29		99.89	0.000	1.711	0.158	0.111	0.047	1.889	0.000	0.062	0.004	0.020	0.003	0.153	0.000	######
MD110-DR06-161C 00	Opx	µXRF	MD110-DR06	161C	Pl-lhz	Porph.	Core	0.00	32.16	5.34	54.01	0.00	2.06	0.14	0.65	0.11	5.39		99.87	0.000	1.658	0.218	0.132	0.085	1.868	0.000	0.076	0.004	0.018	0.003	0.156	0.000	######

B.5. Table de données – compositions chimiques en éléments majeurs des orthopyroxènes

Analysis	Mineral	Analytical method	Location	Sample	Rock type	Texture	Mineral location	Na_2O	MgO	Al_2O_3	SiO_2	K_2O	CaO	TiO_2	Cr_2O_3	MnO	FeO	NiO	Total	Na	Mg	Al	AlIV	AlVI	Si	K	Ca	Ti	Cr	Mn	Fe_2	Ni	Total
D110-DR06-161C 00	Opx	µXRF	MD110-DR06	161C	Pl-lhz	Porph.	Core	0.00	32.39	5.18	54.12	0.00	1.73	0.19	0.68	0.11	5.45		99.83	0.000	1.670	0.211	0.129	0.082	1.871	0.000	0.064	0.005	0.018	0.003	0.158	0.000	#####
D110-DR06-161C 02	Opx	µXRF	MD110-DR06	161C	Pl-lhz	Porph.	Rim	0.00	34.11	2.36	55.76	0.00	1.48	0.17	0.65	0.11	5.24		99.88	0.000	1.752	0.096	0.079	0.017	1.921	0.000	0.055	0.004	0.018	0.003	0.151	0.000	#####
D110-DR06-161C 02	Opx	µXRF	MD110-DR06	161C	Pl-lhz	Porph.	Rim	0.00	33.81	2.95	55.25	0.00	1.66	0.17	0.66	0.12	5.26		99.88	0.000	1.737	0.120	0.096	0.024	1.904	0.000	0.061	0.004	0.018	0.003	0.152	0.000	#####
D110-DR06-161C 02	Opx	µXRF	MD110-DR06	161C	Pl-lhz	Porph.	Core	0.00	33.15	3.38	55.18	0.00	1.76	0.17	0.76	0.11	5.37		99.87	0.000	1.708	0.138	0.094	0.044	1.906	0.000	0.065	0.004	0.021	0.003	0.155	0.000	#####
MD110-DR06-161C-1	Opx	EPMA	MD110-DR06	161C	Pl-lhz	Porph.	Core	0.05	32.10	5.17	55.48	0.00	1.65	0.13	0.78	0.10	6.45		#####	0.003	1.629	0.207	0.111	0.096	1.889	0.000	0.060	0.003	0.021	0.003	0.184	0.000	#####
MD110-DR06-161C-2	Opx	EPMA	MD110-DR06	161C	Pl-lhz	Porph.	Rim	0.06	33.02	2.97	56.31	0.01	1.12	0.15	0.65	0.13	6.56		#####	0.004	1.689	0.120	0.068	0.052	1.932	0.000	0.041	0.004	0.018	0.004	0.188	0.000	#####
0110-DR06-161C-56-	Opx	EPMA	MD110-DR06	161C	Sp-lhz	Porph.	Core	0.01	33.49	4.39	54.77	0.01	1.16	0.11	0.69	0.05	6.12		#####	0.001	1.708	0.177	0.126	0.050	1.874	0.000	0.043	0.003	0.019	0.001	0.175	0.000	#####
D110-DR06-162B 00	Opx	µXRF	MD110-DR06	162B	Pl-lhz	Porph.	Core	0.00	33.63	3.04	55.51	0.00	1.23	0.29	0.83	0.10	5.28		99.92	0.000	1.730	0.124	0.085	0.039	1.915	0.000	0.046	0.007	0.023	0.003	0.152	0.000	#####
D110-DR06-162B 00	Opx	µXRF	MD110-DR06	162B	Pl-lhz	Porph.	Core	0.00	34.30	2.50	55.33	0.00	1.29	0.23	0.68	0.15	5.42		99.90	0.000	1.761	0.101	0.095	0.007	1.905	0.000	0.048	0.006	0.019	0.004	0.156	0.000	#####
D110-DR06-162B 01	Opx	µXRF	MD110-DR06	162B	Pl-lhz	Porph.	Core	0.00	33.41	2.84	55.33	0.00	1.56	0.22	0.82	0.13	5.53		99.85	0.000	1.722	0.116	0.087	0.029	1.913	0.000	0.058	0.006	0.022	0.004	0.160	0.000	#####
D110-DR06-162b 01	Opx	µXRF	MD110-DR06	162B	Pl-lhz	Porph.	Rim	0.00	33.42	2.74	55.46	0.00	1.66	0.27	0.74	0.11	5.51		99.90	0.000	1.721	0.111	0.084	0.028	1.916	0.000	0.061	0.007	0.020	0.003	0.159	0.000	#####
D110-DR06-162B 02	Opx	µXRF	MD110-DR06	162B	Pl-lhz	Porph.	Core	0.00	33.11	3.52	55.05	0.15	1.52	0.32	0.22	0.20	5.64		99.73	0.000	1.707	0.143	0.096	0.047	1.904	0.006	0.056	0.008	0.006	0.006	0.163	0.000	#####
D110-DR06-162B 02	Opx	µXRF	MD110-DR06	162B	Pl-lhz	Porph.	Core	0.00	32.24	5.01	54.38	0.00	1.91	0.18	0.23	0.19	5.77		99.92	0.000	1.661	0.204	0.120	0.084	1.880	0.000	0.071	0.005	0.006	0.006	0.167	0.000	#####
D110-DR06-162b 02	Opx	µXRF	MD110-DR06	162B	Pl-lhz	Porph.	Core	0.00	32.80	3.25	55.07	0.00	1.98	0.22	0.82	0.11	5.65		99.90	0.000	1.693	0.133	0.094	0.039	1.906	0.000	0.073	0.006	0.022	0.003	0.163	0.000	#####
MD110-DR06-162B-1	Opx	EPMA	MD110-DR06	162B	Pl-lhz	Porph.	Core	0.07	31.27	3.97	53.85	0.00	2.33	0.26	0.92	0.14	5.23		98.03	0.005	1.647	0.165	0.097	0.068	1.903	0.000	0.088	0.007	0.026	0.004	0.155	0.000	#####
MD110-DR06-162B-17	Opx	EPMA	MD110-DR06	162B	Pl-lhz	Porph.	Rim	0.03	33.10	2.67	54.90	0.01	1.03	0.24	0.71	0.18	5.77		98.63	0.002	1.727	0.110	0.079	0.032	1.921	0.000	0.039	0.006	0.020	0.005	0.169	0.000	#####
D110-DR06-162B-17	Opx	EPMA	MD110-DR06	162B	Pl-lhz	Porph.	Rim	0.05	32.71	2.95	55.29	0.00	1.40	0.32	0.80	0.14	5.86		99.52	0.003	1.696	0.121	0.077	0.044	1.923	0.000	0.052	0.008	0.022	0.004	0.170	0.000	#####
MD110-DR06-162B-19	Opx	EPMA	MD110-DR06	162B	Pl-lhz	Porph.	Core	0.04	32.78	2.99	54.66	0.00	1.16	0.35	0.82	0.04	5.77		98.63	0.003	1.713	0.123	0.085	0.039	1.915	0.000	0.044	0.009	0.023	0.001	0.169	0.000	#####
MD110-DR06-162B-2	Opx	EPMA	MD110-DR06	162B	Pl-lhz	Porph.	Core	0.06	31.74	3.29	54.59	0.02	2.32	0.22	0.84	0.07	5.31		98.45	0.004	1.664	0.136	0.080	0.056	1.920	0.001	0.087	0.006	0.023	0.002	0.156	0.000	#####
MD110-DR06-162B-3	Opx	EPMA	MD110-DR06	162B	Pl-lhz	Porph.	Core	0.04	32.45	2.57	54.80	0.00	1.68	0.24	0.68	0.10	5.66		98.21	0.003	1.703	0.107	0.071	0.036	1.929	0.000	0.063	0.006	0.019	0.003	0.167	0.000	#####
MD110-DR06-162b-3	Opx	EPMA	MD110-DR06	162B	Pl-lhz	Porph.	Core	0.00	33.39	2.77	56.48	0.00	1.28	0.25	0.82	0.21	6.59		#####	0.000	1.696	0.111	0.076	0.035	1.924	0.000	0.047	0.006	0.022	0.006	0.188	0.000	#####
MD110-DR06-162B-6	Opx	EPMA	MD110-DR06	162B	Pl-lhz	Porph.	Core	0.07	32.06	3.23	54.68	0.00	2.32	0.25	0.89	0.23	5.68		99.42	0.005	1.666	0.133	0.094	0.039	1.906	0.000	0.087	0.007	0.025	0.007	0.166	0.000	#####
MD110-DR06-162b-7	Opx	EPMA	MD110-DR06	162B	Pl-lhz	Porph.	Rim	0.03	32.78	3.56	54.92	0.00	1.41	0.20	0.86	0.08	5.88		99.73	0.002	1.694	0.145	0.096	0.050	1.904	0.000	0.052	0.005	0.024	0.002	0.170	0.000	#####
D110-DR06-167A 00	Opx	µXRF	MD110-DR06	167A	Pl-lhz	Porph.	Core	0.00	32.48	4.47	54.39	0.00	1.89	0.26	0.68	0.11	5.63		99.91	0.000	1.675	0.182	0.119	0.063	1.881	0.000	0.070	0.007	0.019	0.003	0.163	0.000	#####
D110-DR06-167A 00	Opx	µXRF	MD110-DR06	167A	Pl-lhz	Porph.	Core	0.00	32.57	4.43	54.41	0.00	1.72	0.12	0.70	0.12	5.80		99.88	0.000	1.680	0.181	0.118	0.063	1.882	0.000	0.064	0.003	0.019	0.004	0.168	0.000	#####
D110-DR06-167A 00	Opx	µXRF	MD110-DR06	167A	Pl-lhz	Porph.	Core	0.00	32.80	4.07	54.76	0.00	1.72	0.14	0.70	0.11	5.59		99.89	0.000	1.690	0.166	0.107	0.059	1.893	0.000	0.064	0.004	0.019	0.003	0.162	0.000	#####
D110-DR06-167A 00	Opx	µXRF	MD110-DR06	167A	Pl-lhz	Porph.	Core	0.00	32.63	4.63	54.20	0.00	1.83	0.12	0.67	0.12	5.69		99.89	0.000	1.681	0.189	0.127	0.062	1.873	0.000	0.068	0.003	0.018	0.003	0.164	0.000	#####
D110-DR06-167A 00	Opx	µXRF	MD110-DR06	167A	Pl-lhz	Porph.	Core	0.00	32.49	4.47	54.61	0.14	1.81	0.13	0.64	0.18	5.42		99.91	0.000	1.674	0.182	0.113	0.070	1.887	0.006	0.067	0.003	0.018	0.005	0.157	0.000	#####
MD110-DR06-167A-1	Opx	EPMA	MD110-DR06	167A	Pl-lhz	Porph.	Core	0.06	31.89	5.11	53.40	0.00	2.00	0.09	0.78	0.09	5.90		99.31	0.004	1.655	0.210	0.141	0.068	1.859	0.000	0.075	0.002	0.021	0.003	0.172	0.000	#####
MD110-DR06-167A-1	Opx	EPMA	MD110-DR06	167A	Pl-lhz	Porph.	Core	0.07	30.97	5.13	53.39	0.04	2.01	0.19	0.73	0.20	5.83		98.56	0.005	1.624	0.213	0.122	0.091	1.878	0.002	0.076	0.005	0.020	0.006	0.172	0.000	#####
MD110-DR06-167A-5	Opx	EPMA	MD110-DR06	167A	Pl-lhz	Porph.	Core	0.06	31.89	4.97	53.53	0.00	1.69	0.11	0.71	0.07	5.98		99.01	0.004	1.660	0.205	0.131	0.074	1.869	0.000	0.063	0.003	0.020	0.002	0.175	0.000	#####
MD110-DR06-167A-6	Opx	EPMA	MD110-DR06	167A	Pl-lhz	Porph.	Core	0.03	32.23	4.60	54.33	0.00	1.01	0.18	0.60	0.10	5.83		98.90	0.002	1.678	0.189	0.102	0.087	1.898	0.000	0.038	0.005	0.017	0.003	0.170	0.000	#####
MD110-DR06-167A-9	Opx	EPMA	MD110-DR06	167A	Pl-lhz	Porph.	Core	0.09	32.10	4.41	53.66	0.02	1.08	0.08	0.75	0.12	5.73		98.03	0.006	1.685	0.183	0.111	0.072	1.889	0.001	0.041	0.002	0.021	0.004	0.169	0.000	#####
MD110-DR06-168 00	Opx	µXRF	MD110-DR06	168	Pl-lhz	Porph.	Core	0.00	32.90	3.58	54.51	0.03	1.63	0.20	0.95	0.11	5.83		99.74	0.000	1.700	0.146	0.111	0.035	1.889	0.001	0.061	0.005	0.026	0.003	0.169	0.000	#####
MD110-DR06-168 01	Opx	µXRF	MD110-DR06	168	Pl-lhz	Porph.	Core	0.00	32.52	4.67	53.59	0.00	1.74	0.12	0.94	0.09	6.14		99.81	0.000	1.679	0.191	0.144	0.047	1.856	0.000	0.065	0.003	0.026	0.003	0.178	0.000	#####
MD110-DR06-168-12	Opx	EPMA	MD110-DR06	168	Pl-lhz	Porph.	Core	0.01	31.94	4.95	53.07	0.01	1.02	0.07	0.89	0.14	5.44		97.54	0.001	1.685	0.206	0.123	0.084	1.877	0.000	0.039	0.002	0.025	0.004	0.161	0.000	#####
MD110-DR06-168-12	Opx	EPMA	MD110-DR06	168	Pl-lhz	Porph.	Core	0.05	32.11	4.97	53.39	0.00	1.12	0.11	0.79	0.02	5.77		98.33	0.003	1.680	0.206	0.126	0.080	1.874	0.000	0.042	0.003	0.022	0.001	0.169	0.000	#####
MD110-DR06-168-21	Opx	EPMA	MD110-DR06	168	Pl-lhz	Porph.	Core	0.03	32.75	3.66	54.88	0.02	1.66	0.13	0.92	0.10	6.28		#####	0.002	1.683	0.149	0.108	0.040	1.892	0.001	0.061	0.003	0.025	0.003	0.181	0.000	#####
MD110-DR06-168-27	Opx	EPMA	MD110-DR06	168	Pl-lhz	Porph.	Core	0.04	32.30	3.47	53.80	0.03	1.11	0.09	0.86	0.06	5.62		97.40	0.003	1.707	0.145	0.093	0.052	1.907	0.001	0.042	0.002	0.024	0.002	0.167	0.000	#####
MD110-DR06-173 00	Opx	µXRF	MD110-DR06	173	Pl-lhz	Porph.	Core	0.00	32.35	4.92	54.25	0.00	1.82	0.14	0.81	0.10	5.47		99.87	0.000	1.668	0.201	0.123	0.077	1.877	0.000	0.068	0.004	0.022	0.003	0.158	0.000	#####
MD110-DR06-173 00	Opx	µXRF	MD110-DR06	173	Pl-lhz	Porph.	Core	0.00	33.07	4.20	54.57	0.00	1.73	0.12	0.80	0.10	5.31		99.90	0.000	1.701	0.171	0.117	0.054	1.883	0.000	0.064	0.003	0.022	0.003	0.153	0.000	#####
MD110-DR06-173 00	Opx	µXRF	MD110-DR06	173	Pl-lhz	Interstitial	Core	0.00	31.53	1.47	58.26	0.36	0.81	0.10	0.34	0.09	6.85		99.82	0.000	1.643	0.061	#####	0.096	2.036	0.016	0.030	0.003	0.009	0.003	0.200	0.000	#####
MD110-DR06-173 00	Opx	µXRF	MD110-DR06	173	Pl-lhz	Porph.	Core	0.00	33.66	3.11	55.25	0.00	1.37	0.11	0.84	0.10	5.39		99.83	0.000	1.732	0.126	0.093	0.033	1.907	0.000	0.051	0.003	0.023	0.003	0.156	0.000	#####
MD110-DR06-173 01	Opx	µXRF	MD110-DR06	173	Pl-lhz	Porph.	Core	0.00	32.54	4.15	54.90	0.03	1.99	0.12	0.75	0.10	5.32		99.89	0.000	1.677	0.169	0.102	0.067	1.898	0.001	0.074	0.003	0.020	0.003	0.154	0.000	#####
MD110-DR06-173-2	Opx	EPMA	MD110-DR06	173	Pl-lhz	Porph.	Core	0.01	33.01	3.69	54.40	0.02	1.06	0.16	0.86	0.27	5.85		99.34	0.001	1.711	0.151	0.109	0.042	1.891	0.001	0.039	0.004	0.024	0.008	0.170	0.000	#####
MD110-DR06-173-2b	Opx	EPMA	MD110-DR06	173	Pl-lhz	Porph.	Core	0.01	32.52	4.48	54.05	0.01	1.14	0.10	0.81	0.17	5.51		98.80	0.001	1.693	0.184	0.112	0.072	1.888	0.000	0.043	0.003	0.022	0.005	0.161	0.000	#####
MD110-DR06-173-3a	Opx	EPMA	MD110-DR06	173	Pl-lhz	Porph.	Core	0.04	33.04	2.89	55.66	0.00	1.61	0.13	0.69	0.14	5.90		#####	0.003	1.701	0.118	0.078	0.040	1.922	0.000	0.060	0.003	0.019	0.004	0.170	0.000	#####
MD110-DR06-173-3b	Opx	EPMA	MD110-DR06	173	Pl-lhz	Porph.	Core	0.02	33.71	2.52	55.36	0.00	1.11	0.14	0.55	0.22	6.14		99.77	0.001	1.738	0.103	0.086	0.017	1.914	0.000	0.041	0.004	0.015	0.006	0.178	0.000	#####

B.5. Table de données – compositions chimiques en éléments majeurs des orthopyroxènes

Analysis	Mineral	Analytical method	Location	Sample	Rock type	Texture	Mineral location	Na_2O	MgO	Al_2O_3	SiO_2	K_2O	CaO	TiO_2	Cr_2O_3	MnO	FeO	NiO	Total	Na	Mg	Al	AlIV	AlVI	Si	K	Ca	Ti	Cr	Mn	Fe_2	Ni	Total
MD110-DR06-173-4	Opx	EPMA	MD110-DR06	173	Pl-lhz	Porph.	Core	0.06	32.90	3.10	55.30	0.00	1.95	0.12	0.65	0.17	5.20		99.43	0.004	1.702	0.127	0.082	0.045	1.918	0.000	0.072	0.003	0.018	0.005	0.151	0.000	######
MD110-DR06-B1 001	Opx	µXRF	MD110-DR06	B1	Pl-lhz	Porph.	Core	0.00	32.74	4.54	53.89	0.00	1.96	0.12	0.81	0.10	5.72		99.89	0.000	1.686	0.185	0.138	0.047	1.862	0.000	0.072	0.003	0.022	0.003	0.165	0.000	######
MD110-DR06-B1 002	Opx	µXRF	MD110-DR06	B1	Pl-lhz	Porph.	Core	0.00	32.77	4.52	54.04	0.00	1.76	0.12	0.81	0.11	5.77		99.89	0.000	1.688	0.184	0.132	0.051	1.868	0.000	0.065	0.003	0.022	0.003	0.167	0.000	######
MD110-DR06-B1 003	Opx	µXRF	MD110-DR06	B1	Pl-lhz	Porph.	Rim	0.00	33.33	3.55	54.49	0.00	1.63	0.14	0.82	0.11	5.83		99.89	0.000	1.716	0.145	0.118	0.027	1.882	0.000	0.060	0.004	0.022	0.003	0.168	0.000	######
MD110-DR06-B1 004	Opx	µXRF	MD110-DR06	B1	Pl-lhz	Porph.	Rim	0.00	33.05	4.25	54.03	0.00	1.79	0.13	0.86	0.11	5.68		99.89	0.000	1.701	0.173	0.135	0.038	1.865	0.000	0.066	0.003	0.023	0.003	0.164	0.000	######
MD110-DR06-B1 007	Opx	µXRF	MD110-DR06	B1	Pl-lhz	Porph.	Core	0.00	32.96	3.63	54.38	0.00	1.96	0.14	0.87	0.10	5.84		99.88	0.000	1.699	0.148	0.119	0.029	1.881	0.000	0.073	0.004	0.024	0.003	0.169	0.000	######
MD110-DR06-B1 008	Opx	µXRF	MD110-DR06	B1	Pl-lhz	Porph.	Rim	0.00	33.48	3.15	54.77	0.00	1.71	0.15	0.81	0.10	5.71		99.89	0.000	1.723	0.128	0.109	0.019	1.891	0.000	0.063	0.004	0.022	0.003	0.165	0.000	######
MD110-DR06-B4 001	Opx	µXRF	MD110-DR06	B4	Pl-lhz	Porph.	Core	0.00	32.60	4.27	54.70	0.00	1.89	0.15	0.76	0.11	5.42		99.90	0.000	1.680	0.174	0.109	0.065	1.891	0.000	0.070	0.004	0.021	0.003	0.157	0.000	######
MD110-DR06-B4 002	Opx	µXRF	MD110-DR06	B4	Pl-lhz	Porph.	Core	0.00	32.44	4.28	54.36	0.00	1.89	0.15	0.78	0.13	5.84		99.86	0.000	1.675	0.175	0.118	0.057	1.882	0.000	0.070	0.004	0.021	0.004	0.169	0.000	######
MD110-DR06-B4 012	Opx	µXRF	MD110-DR06	B4	Pl-lhz	Interstitial	Core	0.00	33.41	3.79	54.50	0.01	1.30	0.17	0.49	0.12	6.10		99.89	0.000	1.719	0.154	0.119	0.035	1.881	0.001	0.048	0.004	0.013	0.004	0.176	0.000	######
MD110-DR06-B4 013	Opx	µXRF	MD110-DR06	B4	Pl-lhz	Interstitial	Core	0.00	33.89	2.04	56.22	0.00	1.37	0.17	0.51	0.13	5.58		99.90	0.000	1.744	0.083	0.060	0.023	1.940	0.000	0.050	0.004	0.014	0.004	0.161	0.000	######
MD110-DR06-B4 016	Opx	µXRF	MD110-DR06	B4	Pl-lhz	Porph.	Core	0.00	32.96	3.58	55.16	0.00	1.86	0.16	0.75	0.12	5.29		99.88	0.000	1.698	0.146	0.094	0.052	1.906	0.000	0.069	0.004	0.021	0.003	0.153	0.000	######
MD110-DR06-B4-2	Opx	EPMA	MD110-DR06	B4	Pl-lhz	Porph.	Core	0.09	31.06	4.67	54.40	0.01	1.66	0.15	0.81	0.09	6.15		99.09	0.006	1.623	0.193	0.094	0.099	1.906	0.000	0.062	0.004	0.022	0.003	0.180	0.000	######
MD110-DR06-B4-29	Opx	EPMA	MD110-DR06	B4	Pl-lhz	Exsolution	Core	0.04	31.53	5.40	53.16	0.02	0.86	0.08	0.77	0.08	6.06		97.99	0.003	1.659	0.225	0.124	0.101	1.876	0.001	0.032	0.002	0.021	0.002	0.179	0.000	######
MD110-DR06-B4-31-1	Opx	EPMA	MD110-DR06	B4	Sp-lhz	Porph.	Core	0.05	33.76	2.71	54.01	0.01	1.10	0.17	0.49	0.35	6.11		98.76	0.003	1.755	0.111	0.111	0.000	1.883	0.000	0.041	0.004	0.014	0.010	0.178	0.000	######
MD110-DR06-B4-31-6	Opx	EPMA	MD110-DR06	B4	Sp-lhz	Porph.	Core	0.00	32.73	3.81	54.09	0.01	1.46	0.16	0.82	0.25	6.49		99.82	0.000	1.692	0.156	0.124	0.031	1.876	0.000	0.054	0.004	0.022	0.007	0.188	0.000	######
MD110-DR06-B5 001	Opx	µXRF	MD110-DR06	B5	Pl-lhz	Porph.	Core	0.00	32.80	4.28	54.25	0.00	1.71	0.15	0.91	0.09	5.67		99.87	0.000	1.691	0.175	0.124	0.050	1.876	0.000	0.063	0.004	0.025	0.003	0.164	0.000	######
MD110-DR06-B5 002	Opx	µXRF	MD110-DR06	B5	Pl-lhz	Porph.	Core	0.00	32.94	4.32	54.15	0.00	1.64	0.15	0.91	0.09	5.66		99.87	0.000	1.697	0.176	0.129	0.047	1.871	0.000	0.061	0.004	0.025	0.003	0.164	0.000	######
MD110-DR06-B5 003	Opx	µXRF	MD110-DR06	B5	Pl-lhz	Porph.	Core	0.00	34.18	4.17	53.12	0.00	1.71	0.14	0.71	0.09	5.72		99.85	0.000	1.752	0.169	0.169	0.000	1.826	0.000	0.063	0.004	0.019	0.003	0.164	0.000	######
MD110-DR06-B5 004	Opx	µXRF	MD110-DR06	B5	Pl-lhz	Porph.	Core	0.00	34.85	4.19	52.83	0.01	1.59	0.16	0.76	0.09	5.40		99.89	0.000	1.780	0.169	0.169	0.000	1.810	0.000	0.058	0.004	0.021	0.003	0.155	0.000	######
MD110-DR06-B5 005	Opx	µXRF	MD110-DR06	B5	Pl-lhz	Porph.	Core	0.00	33.73	4.11	54.13	0.00	1.67	0.15	0.67	0.10	5.34		99.90	0.000	1.730	0.167	0.137	0.029	1.863	0.000	0.062	0.004	0.018	0.003	0.154	0.000	######
MD110-DR06-B7 002	Opx	µXRF	MD110-DR06	B7	Pl-lhz	Porph.	Core	0.00	32.55	4.11	54.29	0.00	1.82	0.13	0.84	0.11	6.04		99.89	0.000	1.680	0.168	0.120	0.048	1.880	0.000	0.067	0.003	0.023	0.003	0.175	0.000	######
MD110-DR06-B7 004	Opx	µXRF	MD110-DR06	B7	Pl-lhz	Porph.	Core	0.00	32.46	4.30	54.30	0.00	1.87	0.13	0.86	0.10	5.87		99.89	0.000	1.675	0.176	0.120	0.055	1.880	0.000	0.069	0.003	0.024	0.003	0.170	0.000	######
MD110-DR06-B7-2	Opx	EPMA	MD110-DR06	B7	Pl-lhz	Porph.	Core	0.05	31.81	4.36	54.80	0.01	1.24	0.10	0.89	0.10	5.78		99.15	0.003	1.657	0.180	0.086	0.094	1.914	0.000	0.046	0.003	0.025	0.003	0.169	0.000	######
MD110-DR06-B7-22-9	Opx	EPMA	MD110-DR06	B7	Sp-lhz	Porph.	Core	0.03	31.91	3.75	54.04	0.03	1.25	0.11	0.83	0.06	6.20		98.20	0.002	1.677	0.156	0.095	0.061	1.905	0.001	0.047	0.003	0.023	0.002	0.183	0.000	######
MD110-DR06-B7-8	Opx	EPMA	MD110-DR06	B7	Pl-lhz	Porph.	Rim	0.05	31.76	4.47	54.78	0.00	0.96	0.11	0.74	0.26	6.21		99.34	0.003	1.653	0.184	0.088	0.096	1.912	0.000	0.036	0.003	0.020	0.008	0.181	0.000	######
MD110-DR06-B7-9	Opx	EPMA	MD110-DR06	B7	Pl-lhz	Porph.	Core	0.05	31.34	5.54	53.84	0.01	1.16	0.09	0.78	0.11	6.07		98.99	0.003	1.635	0.228	0.116	0.113	1.884	0.000	0.043	0.002	0.022	0.003	0.178	0.000	######
MD110-DR06-B8 001	Opx	µXRF	MD110-DR06	B8	Pl-lhz	Porph.	Core	0.00	32.38	4.98	53.79	0.00	2.10	0.12	0.81	0.11	5.57		99.85	0.000	1.670	0.203	0.140	0.063	1.860	0.000	0.078	0.003	0.022	0.003	0.161	0.000	######
MD110-DR06-B8 002	Opx	µXRF	MD110-DR06	B8	Pl-lhz	Porph.	Core	0.00	32.86	4.50	54.05	0.00	1.81	0.11	0.77	0.11	5.65		99.86	0.000	1.692	0.183	0.133	0.050	1.867	0.000	0.067	0.003	0.021	0.003	0.163	0.000	######
MD110-DR06-B8 005	Opx	µXRF	MD110-DR06	B8	Pl-lhz	Porph.	Core	0.00	32.83	4.42	54.35	0.00	1.70	0.12	0.72	0.10	5.64		99.88	0.000	1.691	0.180	0.123	0.058	1.877	0.000	0.063	0.003	0.020	0.003	0.163	0.000	######
MD110-DR06-B8 006	Opx	µXRF	MD110-DR06	B8	Pl-lhz	Porph.	Core	0.00	32.62	4.86	53.87	0.00	1.88	0.12	0.85	0.10	5.59		99.89	0.000	1.680	0.198	0.139	0.059	1.861	0.000	0.070	0.003	0.023	0.003	0.162	0.000	######
MD110-DR06-B8 007	Opx	µXRF	MD110-DR06	B8	Pl-lhz	Porph.	Core	0.00	33.39	3.25	54.93	0.15	1.81	0.15	0.80	0.10	5.30		99.89	0.000	1.718	0.132	0.105	0.027	1.895	0.007	0.067	0.004	0.022	0.003	0.153	0.000	######
MD110-DR09-273 001	Opx	µXRF	MD110-DR09	273	Sp-lhz	Porph.	Core	0.00	33.73	3.99	54.70	0.00	1.28	0.07	0.67	0.12	5.32		99.88	0.000	1.731	0.162	0.117	0.045	1.883	0.000	0.047	0.002	0.018	0.004	0.153	0.000	######
MD110-DR09-273 001	Opx	µXRF	MD110-DR09	273	Sp-lhz	Porph.	Core	0.00	33.80	3.90	54.95	0.00	1.17	0.07	0.64	0.12	5.23		99.89	0.000	1.734	0.158	0.109	0.050	1.891	0.000	0.043	0.002	0.017	0.004	0.151	0.000	######
MD110-DR09-273 003	Opx	µXRF	MD110-DR09	273	Sp-lhz	Porph.	Core	0.00	33.66	4.20	54.72	0.00	1.29	0.07	0.72	0.10	5.16		99.92	0.000	1.727	0.170	0.117	0.053	1.883	0.000	0.047	0.002	0.020	0.003	0.148	0.000	######
MD110-DR09-273 006	Opx	µXRF	MD110-DR09	273	Sp-lhz	Porph.	Core	0.00	33.89	4.02	55.55	0.00	1.33	0.06	0.53	0.12	4.34		99.85	0.000	1.736	0.163	0.092	0.071	1.908	0.000	0.049	0.002	0.014	0.004	0.125	0.000	######
MD110-DR09-273b 00	Opx	µXRF	MD110-DR09	273b	Sp-lhz	Porph.	Core	0.00	33.11	4.39	53.68	0.00	1.20	0.10	0.81	0.12	6.42		99.84	0.000	1.706	0.179	0.144	0.035	1.856	0.000	0.045	0.003	0.022	0.003	0.186	0.000	######
MD110-DR09-273b 00	Opx	µXRF	MD110-DR09	273b	Sp-lhz	Porph.	Core	0.00	33.44	4.28	54.05	0.00	1.04	0.19	0.79	0.11	5.97		99.86	0.000	1.720	0.174	0.135	0.039	1.865	0.000	0.038	0.005	0.022	0.003	0.172	0.000	######
MD110-DR09-273B-8	Opx	EPMA	MD110-DR09	273b	Sp-lhz	Porph.	Core	0.09	33.95	4.53	54.78	0.00	0.75	0.09	0.76	0.02	5.39		#######	0.006	1.732	0.183	0.126	0.057	1.874	0.000	0.027	0.002	0.021	0.001	0.154	0.000	######
MD110-DR09-273B-9	Opx	EPMA	MD110-DR09	273b	Sp-lhz	Porph.	Core	0.14	32.85	4.66	52.38	0.02	1.47	0.05	0.90	0.10	5.45		98.01	0.010	1.717	0.193	0.164	0.029	1.836	0.001	0.055	0.001	0.025	0.003	0.160	0.000	######
MD110-DR09-275 001	Opx	µXRF	MD110-DR09	275	Sp-lhz	Porph.	Core	0.00	33.01	4.84	54.42	0.02	1.54	0.09	0.77	0.10	5.09		99.88	0.000	1.697	0.197	0.124	0.073	1.876	0.001	0.057	0.002	0.021	0.003	0.147	0.000	######
MD110-DR09-275 002	Opx	µXRF	MD110-DR09	275	Sp-lhz	Porph.	Core	0.00	32.97	4.84	54.31	0.00	2.07	0.09	0.74	0.10	4.78		99.89	0.000	1.693	0.196	0.129	0.067	1.871	0.000	0.076	0.002	0.020	0.003	0.138	0.000	######
MD110-DR09-275b 00	Opx	µXRF	MD110-DR09	275b	Sp-lhz	Porph.	Core	0.00	32.84	4.34	54.40	0.08	1.49	0.08	0.84	0.09	5.69		99.84	0.000	1.692	0.177	0.120	0.057	1.880	0.004	0.055	0.002	0.023	0.003	0.164	0.000	######
MD110-DR09-275b 00	Opx	µXRF	MD110-DR09	275b	Sp-lhz	Porph.	Core	0.00	32.98	4.24	54.35	0.20	1.37	0.07	0.80	0.10	5.76		99.87	0.000	1.698	0.173	0.123	0.050	1.877	0.009	0.051	0.002	0.022	0.003	0.166	0.000	######
MD110-DR09-275b 00	Opx	µXRF	MD110-DR09	275b	Sp-lhz	Porph.	Core	0.00	33.12	4.25	54.43	0.04	1.35	0.07	0.80	0.10	5.70		99.86	0.000	1.705	0.173	0.121	0.052	1.879	0.002	0.050	0.002	0.022	0.003	0.165	0.000	######
MD110-DR09-275b 00	Opx	µXRF	MD110-DR09	275b	Sp-lhz	Porph.	Core	0.00	33.44	3.82	54.65	0.24	1.04	0.06	0.69	0.10	5.85		99.88	0.000	1.719	0.155	0.115	0.040	1.885	0.011	0.038	0.002	0.019	0.003	0.169	0.000	######
MD110-DR09-275b 00	Opx	µXRF	MD110-DR09	275b	Sp-lhz	Porph.	Core	0.00	32.66	4.34	54.21	0.38	1.50	0.08	0.81	0.10	5.80		99.87	0.000	1.683	0.177	0.126	0.050	1.874	0.017	0.055	0.002	0.022	0.003	0.168	0.000	######
MD110-DR09-275b 00	Opx	µXRF	MD110-DR09	275b	Sp-lhz	Porph.	Core	0.00	32.46	4.26	54.22	0.00	2.04	0.21	0.75	0.11	5.81		99.86	0.000	1.676	0.174	0.123	0.051	1.877	0.000	0.076	0.005	0.020	0.003	0.168	0.000	######
MD110-DR09-275b 00	Opx	µXRF	MD110-DR09	275b	Sp-lhz	Porph.	Rim	0.00	33.40	3.41	55.25	0.00	1.11	0.08	0.60	0.11	5.94		99.89	0.000	1.719	0.139	0.092	0.047	1.908	0.000	0.041	0.002	0.016	0.003	0.171	0.000	######

B.5. Table de données – compositions chimiques en éléments majeurs des orthopyroxènes

Analysis	Mineral	Analytical method	Location	Sample	Rock type	Texture	Mineral location	Na_2O	MgO	Al_2O_3	SiO_2	K_2O	CaO	TiO_2	Cr_2O_3	MnO	FeO	NiO	Total	Na	Mg	Al	AlIV	AlVI	Si	K	Ca	Ti	Cr	Mn	Fe_2	Ni	Total
D110-DR09-275b 00	Opx	µXRF	MD110-DR09	275b	Sp-lhz	Porph.	Rim	0.00	33.67	3.51	55.32	0.00	1.01	0.07	0.59	0.11	5.63		99.90	0.000	1.730	0.143	0.093	0.049	1.907	0.000	0.037	0.002	0.016	0.003	0.162	0.000	#####
D110-DR09-275b 00	Opx	µXRF	MD110-DR09	275b	Sp-lhz	Porph.	Rm	0.00	33.60	3.78	54.48	0.00	1.66	0.08	0.68	0.10	5.50		99.88	0.000	1.726	0.154	0.123	0.031	1.877	0.000	0.061	0.002	0.018	0.003	0.159	0.000	#####
D110-DR09-275b 01	Opx	µXRF	MD110-DR09	275b	Sp-lhz	Porph.	Core	0.00	33.14	3.83	55.20	0.00	1.36	0.07	0.66	0.10	5.53		99.89	0.000	1.706	0.156	0.094	0.061	1.906	0.000	0.050	0.002	0.018	0.003	0.160	0.000	#####
D110-DR09-275b 01	Opx	µXRF	MD110-DR09	275b	Sp-lhz	Porph.	Core	0.00	33.17	3.89	54.77	0.00	1.60	0.08	0.69	0.10	5.58		99.88	0.000	1.707	0.158	0.110	0.049	1.890	0.000	0.059	0.002	0.019	0.003	0.161	0.000	#####
MD110-DR09-275B-1	Opx	EPMA	MD110-DR09	275b	Sp-lhz	Porph.	Core	0.07	34.12	4.59	54.59	0.00	1.05	0.05	0.69	0.09	5.09		#####	0.005	1.738	0.185	0.134	0.051	1.866	0.000	0.038	0.001	0.019	0.003	0.145	0.000	#####
MD110-DR09-275B-1	Opx	EPMA	MD110-DR09	275b	Sp-lhz	Porph.	Core	0.09	32.87	4.39	55.29	0.02	1.48	0.08	0.65	0.24	5.43		#####	0.006	1.681	0.178	0.103	0.075	1.897	0.001	0.054	0.002	0.018	0.007	0.156	0.000	#####
MD110-DR09-275B-2	Opx	EPMA	MD110-DR09	275b	Sp-lhz	Porph.	Core	0.05	34.01	4.55	55.53	0.00	0.64	0.04	0.56	0.16	5.71		#####	0.003	1.722	0.182	0.114	0.068	1.886	0.000	0.023	0.001	0.015	0.005	0.162	0.000	#####
MD110-DR09-275B-6	Opx	EPMA	MD110-DR09	275b	Sp-lhz	Porph.	Core	0.08	35.00	4.34	53.40	0.00	0.49	0.06	0.75	0.15	5.98		#####	0.005	1.782	0.175	0.175	0.000	1.823	0.000	0.018	0.002	0.020	0.004	0.171	0.000	#####
MD110-DR09-275B-6	Opx	EPMA	MD110-DR09	275b	Sp-lhz	Porph.	Core	0.11	34.22	4.85	54.55	0.02	1.15	0.03	0.80	0.25	5.22		#####	0.007	1.730	0.194	0.151	0.043	1.849	0.001	0.042	0.001	0.021	0.007	0.148	0.000	#####
MD110-DR09-275B-6	Opx	EPMA	MD110-DR09	275b	Sp-lhz	Porph.	Core	0.05	34.91	4.21	54.19	0.00	0.53	0.02	0.66	0.05	5.31		99.93	0.003	1.781	0.170	0.145	0.024	1.855	0.000	0.019	0.001	0.018	0.001	0.152	0.000	#####
MD110-DR09-279 00	Opx	µXRF	MD110-DR09	279	Sp-lhz	Porph.	Core	0.00	32.90	4.27	55.92	0.00	1.93	0.18	0.65	0.08	3.99		99.92	0.000	1.690	0.173	0.074	0.100	1.926	0.000	0.071	0.005	0.018	0.002	0.115	0.000	#####
MD110-DR09-279 00	Opx	µXRF	MD110-DR09	279	Sp-lhz	Porph.	Core	0.00	32.86	4.22	55.76	0.00	2.37	0.12	0.65	0.07	3.86		99.92	0.000	1.687	0.171	0.080	0.092	1.920	0.000	0.087	0.003	0.018	0.002	0.111	0.000	#####
MD110-DR09-279-5	Opx	EPMA	MD110-DR09	279	Sp-lhz	Porph.	Core	0.07	33.11	4.52	55.08	0.00	0.70	0.05	0.69	0.08	5.37		99.67	0.005	1.705	0.184	0.097	0.087	1.903	0.000	0.026	0.001	0.019	0.002	0.155	0.000	#####
MD110-DR09-279-6	Opx	EPMA	MD110-DR09	279	Sp-lhz	Porph.	Core	0.15	32.37	3.73	54.98	0.00	2.16	0.07	0.57	0.04	4.90		98.98	0.010	1.680	0.153	0.086	0.068	1.914	0.000	0.081	0.002	0.016	0.001	0.143	0.000	#####
MD110-DR09-280 00	Opx	µXRF	MD110-DR09	280	Sp-lhz	Porph.	Core	0.00	32.44	4.78	54.72	0.00	2.32	0.08	0.79	0.09	4.69		99.91	0.000	1.669	0.194	0.111	0.083	1.889	0.000	0.086	0.002	0.021	0.003	0.135	0.000	#####
MD110-DR09-280 00	Opx	µXRF	MD110-DR09	280	Sp-lhz	Porph.	Core	0.00	32.67	4.79	54.67	0.00	2.19	0.08	0.80	0.09	4.64		99.92	0.000	1.679	0.195	0.115	0.080	1.885	0.000	0.081	0.002	0.022	0.003	0.134	0.000	#####
MD110-DR09-281 00	Opx	µXRF	MD110-DR09	280	Sp-lhz	Porph.	Core	0.00	32.95	4.24	54.32	0.03	2.56	0.09	0.78	0.11	4.85		99.90	0.000	1.694	0.172	0.127	0.045	1.873	0.001	0.094	0.002	0.021	0.003	0.140	0.000	#####
MD110-DR09-281 00	Opx	µXRF	MD110-DR09	281	Sp-lhz	Porph.	Core	0.00	33.35	4.14	55.40	0.00	2.47	0.10	0.57	0.08	3.79		99.93	0.000	1.708	0.168	0.097	0.071	1.903	0.000	0.091	0.003	0.016	0.002	0.109	0.000	#####
MD110-DR09-281 00	Opx	µXRF	MD110-DR09	281	Sp-lhz	Porph.	Core	0.00	32.84	4.24	54.87	0.00	2.26	0.12	0.69	0.09	4.80		99.92	0.000	1.688	0.172	0.107	0.065	1.893	0.000	0.084	0.003	0.019	0.003	0.139	0.000	#####
D110-DR09-281b 00	Opx	µXRF	MD110-DR09	281b	Sp-lhz	Porph.	Core	0.00	33.11	3.91	53.91	0.01	1.57	0.08	0.76	0.12	6.38		99.84	0.000	1.707	0.159	0.136	0.024	1.864	0.001	0.058	0.002	0.021	0.004	0.184	0.000	#####
MD110-DR09-281B-1	Opx	EPMA	MD110-DR09	281b	Sp-lhz	Porph.	Core	0.09	34.38	4.39	55.20	0.02	0.57	0.03	0.72	0.07	6.05		#####	0.006	1.735	0.175	0.131	0.044	1.869	0.001	0.021	0.001	0.019	0.002	0.171	0.000	#####
MD110-DR09-281B-1	Opx	EPMA	MD110-DR09	281b	Sp-lhz	Porph.	Core	0.15	33.43	4.35	55.30	0.02	0.67	0.01	0.64	0.16	5.34		#####	0.010	1.712	0.176	0.100	0.076	1.900	0.001	0.025	0.000	0.017	0.005	0.153	0.000	#####
MD110-DR09-281B-1	Opx	EPMA	MD110-DR09	281b	Sp-lhz	Porph.	Core	0.08	34.67	4.15	55.12	0.00	0.46	0.06	0.63	0.10	5.67		#####	0.005	1.756	0.166	0.127	0.039	1.873	0.000	0.017	0.002	0.017	0.003	0.161	0.000	#####
MD80-3G2-2 008	Opx	µXRF	MD80-DR3	3G2	Sp-lhz	Porph.	Core	0.00	30.41	5.29	56.57	0.23	1.63	0.11	0.57	0.08	4.98		99.88	0.000	1.578	0.217	0.032	0.185	1.968	0.010	0.061	0.003	0.016	0.002	0.145	0.000	#####

B.5. Table de données – compositions chimiques en éléments traces des orthopyroxènes

Analysis	MD110-DR02-A27 004	MD110-DR02-A27 005	MD110-DR02-A27 006	MD110-DR02-A27-6	MD110-DR02-A48 003	MD110-DR02-A48 004	MD110-DR02-A48 005	MD110-DR02-A48 006	MD110-DR02-A48 009	MD110-DR02-A48 010	MD110-DR02-A48-10	MD110-DR02-A48-20	MD110-DR02-A48-4	MD110-DR02-A48-5	MD110-DR02-A48-6	MD110-DR02-A48-9
Mineral	Opx	Opx	Opx	Opx	Opx	Opx	Opx	Opx	Opx	Opx	Opx	Opx	Opx	Opx	Opx	Opx
Location	MD110-DR02	MD110-DR02	MD110-DR02	MD110-DR02	MD110-DR02	MD110-DR02	MD110-DR02	MD110-DR02	MD110-DR02	MD110-DR02	MD110-DR02	MD110-DR02	MD110-DR02	MD110-DR02	MD110-DR02	MD110-DR02
Sample	A27	A27	A27	A27	A48	A48	A48	A48	A48	A48	A48	A48	A48	A48	A48	A48
Rock type	Sp-lhz	Sp-lhz	Sp-lhz	Sp-lhz	Sp-lhz	Sp-lhz	Sp-lhz	Sp-lhz	Sp-lhz	Sp-lhz	Sp-lhz	Sp-lhz	Sp-lhz	Sp-lhz	Sp-lhz	Sp-lhz
Texture	Porph.	Porph.	Porph.	Porph.	Porph.	Porph.	Porph.	Porph.	Porph.	Porph.	Porph.	Porph.	Porph.	Porph.	Porph.	Porph.
Mineral location	Core	Core	Rim	Rim	Rim	Core	Core	Core	Rim	Core	Core	Core	Core	Core	Core	Rim
Li ppm	0.882	0.824	1.82	1.82	1.29	2.88	2.74	1.01	0.903	0.991	0.991	1.42	2.88	2.74	1.01	0.903
B ppm	2.64	<2.26	<2.52	<2.52	2.25	3.28	<2.68	<2.18	<2.98	<3.14	<3.14	2.15	3.28	<2.68	<2.18	<2.98
Sc ppm	15.0	16.1	21.5	21.5	19.2	25.4	21.0	21.7	17.1	21.4	21.4	21.6	25.4	21.0	21.7	17.1
Ti ppm	625	634	797	797	706	995	773	794	681	794	794	825	995	773	794	681
V ppm	99.1	97.1	120	120	110	136	113	114	101	115	115	113	136	113	114	101
Cr ppm	4278	4192	5070	5070	5577	6911	5891	5340	4709	5310	5310	5867	6911	5891	5340	4709
Mn ppm																
Co ppm	52.1	52.1	56.3	56.3	53.4	53.6	54.3	51.7	49.5	53.2	53.2	51.3	53.6	54.3	51.7	49.5
Ni ppm	735	768	748	748	716	705	718	653	628	671	671	688	705	718	653	628
Rb ppm	<0.0456	<0.0353	<0.0402	<0.0402	<0.0372	<0.0426	<0.0495	<0.0410	<0.0505	<0.0628	<0.0628	<0.0381	<0.0426	<0.0495	<0.0410	<0.0505
Sr ppm	0.136	0.224	0.325	0.325	0.195	1.14	0.733	0.232	0.107	0.149	0.149	0.473	1.14	0.733	0.232	0.107
Y ppm	0.938	1.18	1.76	1.76	1.16	1.97	1.56	1.50	0.993	1.37	1.37	1.70	1.97	1.56	1.50	0.993
Zr ppm	1.19	1.22	2.21	2.21	1.36	3.25	1.95	1.73	1.11	1.57	1.57	2.13	3.25	1.95	1.73	1.11
Nb ppm	<0.00475	<0.00443	<0.00522	<0.00522	<0.00404	<0.00484	<0.00496	<0.00396	<0.00548	<0.00568	<0.00568	<0.00401	<0.00484	<0.00496	<0.00396	<0.00548
Cs ppm	0.00552	<0.0274	<0.00505	<0.00505	<0.0252	<0.0277	<0.0252	<0.0276	<0.0329	<0.0246	<0.0246	<0.0176	<0.0277	<0.0252	<0.0276	<0.0329
Ba ppm	<0.0399	<0.0373	<0.0440	<0.0440	<0.0337	0.177	<0.200	<0.0330	<0.0457	<0.0474	<0.0474	<0.0333	0.177	<0.200	<0.0330	<0.0457
La ppm	<0.00451	<0.00420	0.00887	0.00887	<0.00389	0.0185	<0.00477	<0.00380	<0.00526	<0.00544	<0.00544	<0.00382	0.0185	<0.00477	<0.00380	<0.00526
Ce ppm	0.0188	0.0135	0.0113	0.0113	<0.00399	0.0176	<0.0217	0.0144	<0.00542	0.0116	0.0116	0.00464	0.0176	<0.0217	0.0144	<0.00542
Pr ppm	<0.00409	<0.00382	0.0155	0.0155	<0.00350	<0.00419	<0.00430	<0.00343	<0.00475	<0.00492	<0.00492	<0.00346	<0.00419	<0.00430	<0.00343	<0.00475
Nd ppm	<0.0247	<0.0231	0.0628	0.0628	<0.0213	<0.0255	0.0299	0.0927	<0.0288	<0.0298	<0.0298	0.0411	<0.0255	0.0299	0.0927	<0.0288
Sm ppm	<0.0294	<0.0275	<0.0324	<0.0324	<0.0254	<0.0305	<0.0312	<0.0249	<0.0345	<0.0357	<0.0357	0.0622	<0.0305	<0.0312	<0.0249	<0.0345
Eu ppm	<0.00827	<0.00772	<0.00911	<0.00911	<0.00704	0.0379	<0.0382	<0.00689	<0.00952	<0.00986	<0.00986	0.0241	0.0379	<0.0382	<0.00689	<0.00952
Gd ppm	<0.0292	<0.0273	0.110	0.110	<0.0252	0.189	0.140	0.111	0.0451	0.204	0.204	0.169	0.189	0.140	0.111	0.0451
Tb ppm	0.0125	0.0106	0.00943	0.00943	0.0116	0.0282	0.00828	0.0165	0.00642	0.00840	0.00840	0.0242	0.0282	0.00828	0.0165	0.00642
Dy ppm	0.102	0.113	0.259	0.259	0.121	0.324	0.227	0.181	0.0503	0.174	0.174	0.205	0.324	0.227	0.181	0.0503
Ho ppm	0.0296	0.0353	0.0608	0.0608	0.0370	0.0639	0.0502	0.0568	0.0150	0.0401	0.0401	0.0625	0.0639	0.0502	0.0568	0.0150
Er ppm	0.0844	0.144	0.251	0.251	0.0903	0.245	0.180	0.208	0.121	0.190	0.190	0.209	0.245	0.180	0.208	0.121
Tm ppm	0.0295	0.0224	0.0503	0.0503	0.0266	0.0411	0.0177	0.0205	0.0364	0.0280	0.0280	0.0421	0.0411	0.0177	0.0205	0.0364
Yb ppm	0.131	0.235	0.379	0.379	0.354	0.190	0.187	0.222	0.196	0.175	0.175	0.243	0.190	0.187	0.222	0.196
Lu ppm	0.0272	0.0186	0.0552	0.0552	0.0395	0.0347	0.0446	0.0323	0.0338	0.0329	0.0329	0.0362	0.0347	0.0446	0.0323	0.0338
Hf ppm	0.100	0.0582	0.100	0.100	0.0860	0.146	<0.0547	0.118	0.0532	0.117	0.117	0.106	0.146	<0.0547	0.118	0.0532
Ta ppm	<0.00577	<0.00538	<0.00636	<0.00636	<0.00498	<0.00596	<0.00611	<0.00487	<0.00673	<0.00696	<0.00696	<0.00487	<0.00596	<0.00611	<0.00487	<0.00673
Pb ppm	<0.0152	0.0577	<0.0167	<0.0167	0.0135	<0.0154	<0.0763	<0.0126	<0.0174	0.0243	0.0243	0.0590	<0.0154	<0.0763	<0.0126	<0.0174
Th ppm	<0.00824	<0.00769	<0.00908	<0.00908	<0.00718	<0.00859	<0.00879	<0.00701	<0.00966	<0.0100	<0.0100	<0.00695	<0.00859	<0.00879	<0.00701	<0.00966
U ppm	<0.00857	<0.00800	<0.00944	<0.00944	<0.0329	<0.00884	<0.0245	<0.00722	<0.00997	<0.0103	<0.0103	<0.00720	<0.00884	<0.0245	<0.00722	<0.00997

B.5. Table de données – compositions chimiques en éléments traces des orthopyroxènes

MD110-DR02-A50 002	MD110-DR02-A50-10	MD110-DR02-A50-14	MD110-DR02-A50-2b	MD110-DR02-A50-2c	MD110-DR02-A50-9	MD110-DR02-A58-12	MD110-DR02-A58-20	MD110-DR02-A58-9	MD110-DR02-A64 001	MD110-DR02-A64 009	MD110-DR06-158A 005	MD110-DR06-158A 008	MD110-DR06-158A 008	MD110-DR06-158A 011	MD110-DR06-158A 012	MD110-DR06-158A-11
Opx	Opx	Opx	Opx	Opx	Opx	Opx	Opx	Opx	Opx	Opx	Opx	Opx	Opx	Opx	Opx	Opx
MD110-DR02	MD110-DR02	MD110-DR02	MD110-DR02	MD110-DR02	MD110-DR02	MD110-DR02	MD110-DR02	MD110-DR02	MD110-DR02	MD110-DR02	MD110-DR06	MD110-DR06	MD110-DR06	MD110-DR06	MD110-DR06	MD110-DR06
A50	A50	A50	A50	A50	A50	A58	A58	A58	A64	A64	158A	158A	158A	158A	158A	158A
Sp-lhz	Sp-lhz	Sp-lhz	Sp-lhz	Sp-lhz	Sp-lhz	Sp-lhz	Sp-lhz	Sp-lhz	Sp-lhz	Sp-lhz	Pl-lhz	Pl-lhz	Pl-lhz	Pl-lhz	Pl-lhz	Pl-lhz
Porph.	Porph.	Porph.	Porph.	Porph.	Porph.	Porph.	Porph.	Porph.	Porph.	Porph.	Porph.	Porph.	Porph.	Porph.	Porph.	Porph.
Core	Core	Core	Core	Core	Core	Core	Rim	Rim	Core	Core	Core	Core	Core	Core	Core	Core
1.36	<1.26	<1.58	29.4	1.36	1.91	1.40	1.26	1.42	0.914	1.17	2.12	<1.27	<1.36	<1.20	<1.12	<1.20
<0.588	<3.84	<4.32	118	<0.588	<3.97	3.41	<2.59	<2.364	4.33	<2.18	<4.16	<3.49	<4.12	<3.78	<3.66	<3.78
19.2	19.7	19.9	21.8	19.2	20.5	21.7	21.1	22.7	20.5	22.6	30.9	26.6	28.9	31.0	31.6	31.0
606	650	666	397	606	625	754	739	770	735	863	697	583	624	802	831	802
108	109	115	90.6	108	116	124	122	130	110	116	148	134	157	148	153	148
2476	3234	5207	1680	2476	3949	5140	4905	5099	5294	5873	5175	4684	5508	5044	5218	5044
	949	912	854		967						985	945	996	961	984	961
50.2	51.2	55.4	65.8	50.2	53.3	57.8	54.6	54.3	52.8	52.0	58.0	56.1	57.5	54.2	56.4	54.2
606	619	732	2303	606	679	728	719	728	687	677	772	750	742	744	737	744
0.0685	<0.120	<0.151	0.708	0.0685	<0.140	<0.0311	<0.0476	<0.0560	<0.0531	<0.0424	<0.127	<0.123	<0.135	<0.0952	<0.0988	<0.0952
0.444	0.0892	0.355	33.3	0.444	0.0926	0.291	0.308	0.410	0.121	0.447	0.216	0.0403	<0.00902	0.0144	0.0399	0.0144
1.75	0.997	1.53	0.752	1.75	1.07	1.75	1.75	1.75	1.05	1.54	2.86	2.25	2.42	2.91	2.98	2.91
1.71	1.01	2.07	8.90	1.71	0.965	1.83	1.95	1.88	1.08	2.10	1.36	0.741	0.963	1.17	1.19	1.17
0.00304	0.00752	0.327	<0.0300	0.00304	<0.00822	<0.00525	<0.00549	<0.00481	0.0640	<0.00458	<0.00983	<0.00757	<0.00801	<0.0101	<0.00932	<0.0101
<0.0314	<0.0885	<0.101	<0.148	<0.0314	<0.0997	<0.0275	<0.0316	<0.0256	<0.0361	0.00487	<0.0978	<0.0926	<0.0837	<0.0763	<0.0662	<0.0763
0.0331	<0.0617	<0.0855	8.03	0.0331	<0.0771	<0.0437	<0.0455	<0.0401	<0.0546	<0.0379	0.166	<0.0711	<0.0753	<0.0948	<0.0876	<0.0948
0.00305	<0.00718	0.0321	0.0486	0.00305	<0.00897	<0.00497	<0.00519	<0.00456	<0.00623	<0.00433	<0.0105	<0.00812	<0.00859	<0.0108	<0.00999	<0.0108
0.0384	0.00846	1.45	<0.0738	0.0384	<0.00989	0.0291	0.0217	0.0129	0.0125	0.0305	0.0330	<0.00902	<0.00955	<0.0120	<0.0111	<0.0120
0.00987	0.00978	0.0380	<0.0318	0.00987	<0.00870	<0.00451	0.00697	<0.00414	<0.00563	0.00969	<0.0104	<0.00801	<0.00847	<0.0107	<0.00986	<0.0107
0.0597	0.138	0.139	<0.191	0.0597	0.0821	<0.0269	<0.0281	<0.0247	<0.0336	0.0643	<0.0626	<0.0482	<0.0510	0.120	0.114	0.120
0.0320	<0.0483	<0.0670	<0.220	0.0320	<0.0603	0.100	<0.0339	<0.0299	<0.0406	0.0626	<0.0731	<0.0563	<0.0596	<0.0750	<0.0693	<0.0750
0.0224	0.0193	0.129	<0.0633	0.0224	<0.0173	0.0321	<0.00945	0.0123	<0.0114	0.0338	<0.0207	<0.0159	<0.0169	0.0397	0.0237	0.0397
0.0818	<0.0475	0.534	<0.217	0.0818	<0.0594	0.0726	0.131	0.0798	0.0588	0.0739	<0.0730	<0.0563	0.194	0.0943	0.129	0.0943
0.0199	0.0136	0.0241	<0.0342	0.0199	0.0132	0.0171	0.0180	0.0227	<0.00621	0.0247	0.0259	0.0395	0.0501	0.0393	0.0300	0.0393
0.190	0.198	0.214	0.178	0.190	<0.0403	0.279	0.253	0.307	0.0942	0.163	0.284	0.151	0.243	0.324	0.192	0.324
0.0658	0.0564	0.0523	<0.0385	0.0658	0.0224	0.0491	0.0713	0.0703	0.0340	0.0437	0.0904	0.0613	0.0812	0.102	0.0937	0.102
0.191	0.136	0.137	0.357	0.191	0.0911	0.178	0.185	0.233	0.118	0.197	0.341	0.323	0.210	0.278	0.390	0.278
0.0344	0.0422	0.0394	0.0543	0.0344	0.0210	0.0447	0.0274	0.0422	0.0102	0.0205	0.0786	0.0301	0.0516	0.0741	0.0699	0.0741
0.272	0.275	0.565	0.209	0.272	0.362	0.303	0.278	0.388	0.130	0.189	0.454	0.438	0.550	0.527	0.321	0.527
0.0461	0.0485	0.0764	<0.0402	0.0461	0.0341	0.0323	0.0345	0.0287	0.0114	0.0364	0.0701	0.0405	0.0775	0.0692	0.0892	0.0692
0.0705	<0.0310	0.445	<0.142	0.0705	<0.0388	0.0626	0.0313	0.124	0.0740	0.0925	<0.197	0.191	0.0714	0.106	<0.0460	0.106
<0.00118	<0.00940	0.0367	<0.0429	<0.00118	<0.0117	<0.00641	<0.00670	<0.00588	<0.00805	<0.00560	<0.0145	<0.0112	<0.0118	<0.0149	<0.0137	<0.0149
0.00654	0.244	<0.183	<0.337	0.00654	0.915	0.0335	0.0716	<0.0153	<0.131	0.0377	<0.146	<0.124	<0.207	<0.160	<0.146	<0.160
<0.00191	0.0396	<0.0702	<0.0648	<0.00191	<0.0177	<0.00920	<0.00957	<0.00845	<0.0115	<0.00797	<0.0212	<0.0163	<0.0173	<0.0218	<0.0201	<0.0218
<0.00188	0.0461	0.529	0.594	<0.00188	<0.0194	<0.00936	<0.00976	<0.00858	0.0283	<0.00814	<0.0233	<0.0179	<0.0190	<0.0501	<0.0221	<0.0501

B.5. Table de données – compositions chimiques en éléments traces des orthopyroxènes

MD110-DR06-158A-5	MD110-DR06-161A 002	MD110-DR06-161A 003	MD110-DR06-161A 004	MD110-DR06-161A 004b	MD110-DR06-161A 005	MD110-DR06-161A-3	MD110-DR06-161A-4b	MD110-DR06-161A-9	MD110-DR06-161C 001	MD110-DR06-161C 002	MD110-DR06-161C 003	MD110-DR06-161C 004	MD110-DR06-161C 005	MD110-DR06-161C 007	MD110-DR06-161C 024	MD110-DR06-161C-1
Opx	Opx	Opx	Opx	Opx	Opx	Opx	Opx	Opx	Opx	Opx	Opx	Opx	Opx	Opx	Opx	Opx
MD110-DR06	MD110-DR06	MD110-DR06	MD110-DR06	MD110-DR06	MD110-DR06	MD110-DR06	MD110-DR06	MD110-DR06	MD110-DR06	MD110-DR06	MD110-DR06	MD110-DR06	MD110-DR06	MD110-DR06	MD110-DR06	MD110-DR06
158A	161A	161A	161A	161A	161A	161A	161A	161A	161C	161C	161C	161C	161C	161C	161C	161C
Pl-lhz	Pl-lhz	Pl-lhz	Pl-lhz	Pl-lhz	Pl-lhz	Pl-lhz	Pl-lhz	Pl-lhz	Pl-lhz	Pl-lhz	Pl-lhz	Pl-lhz	Pl-lhz	Pl-lhz	Pl-lhz	Pl-lhz
Porph.	Porph.	Porph.	Porph.	Porph.	Porph.	Porph.	Porph.	Porph.	Porph.	Porph.	Porph.	Porph.	Porph.	Porph.	Porph.	Porph.
Core	Core	Core	Core	Rim	Core	Core	Rim	Core	Core	Rim	Core	Core	Core	Core	Core	Core
2.12	0.651	0.705	0.895	1.40	0.777	0.705	1.40		0.650	0.849			0.941	0.759	0.892	0.650
<4.16	<0.616	<0.658	<0.646	<0.609	<0.649	<0.658	<0.609		<0.439	<0.515			0.695	<0.561	<0.443	<0.439
30.9	27.5	26.9	26.2	25.2	26.1	26.9	25.2		28.6	29.0			26.3	25.6	24.9	28.6
697	735	667	641	784	664	667	784		712	742			669	649	757	712
148	150	145	134	138	130	145	138		150	159			135	137	140	150
5175	2312	2285	2192	2086	2211	2285	2086		2342	2510			2334	2380	2409	2342
985																
58.0	54.7	53.4	54.0	51.1	53.8	53.4	51.1		54.5	55.0			53.8	53.7	53.9	54.5
772	645	641	646	580	648	641	580		660	643			663	642	629	660
<0.127	<0.0361	<0.0360	<0.0342	<0.0336	<0.0365	<0.0360	<0.0336		0.0525	0.0363			<0.0399	<0.0402	<0.0364	0.0525
0.216	0.101	0.0963	0.121	0.0122	0.0950	0.0963	0.0122		0.251	0.0731			0.427	0.288	0.0549	0.251
2.86	2.69	2.46	2.29	2.05	2.08	2.46	2.05		2.68	2.73			2.37	2.11	2.32	2.68
1.36	1.33	1.25	1.02	0.897	0.917	1.25	0.897		1.29	1.27			1.21	1.20	0.990	1.29
<0.00983	0.00158	0.00100	0.00183	0.00161	0.00211	0.00100	0.00161		0.00403	0.00251			0.00375	0.00397	0.00208	0.00403
<0.0978	<0.0183	<0.0195	<0.0204	<0.0184	<0.0188	<0.0195	<0.0184		<0.0198	<0.0165			<0.0216	<0.0204	<0.0200	<0.0198
0.166	0.00349	<0.00277	<0.00270	0.0108	<0.00278	<0.00277	0.0108		<0.00379	<0.0409			0.00416	<0.00411	<0.00398	<0.00379
<0.0105	<0.000345	<0.000355	<0.000346	<0.000321	<0.000357	<0.000355	<0.000321		0.00471	<0.000507			0.00769	0.00301	<0.000491	0.00471
0.0330	0.0168	0.0153	0.0185	0.00644	0.0193	0.0153	0.00644		0.0289	0.0171			0.0337	0.0224	0.0160	0.0289
<0.0104	0.00608	0.00669	0.00518	0.00128	0.00427	0.00669	0.00128		0.00956	0.00614			0.0107	0.00713	0.00474	0.00956
<0.0626	0.0493	0.0497	0.0389	0.0195	0.0464	0.0497	0.0195		0.0698	0.0512			0.0777	0.0398	0.0321	0.0698
<0.0731	0.0573	0.0219	0.0360	0.0224	0.0267	0.0219	0.0224		0.0495	0.0378			0.0454	0.0369	0.0426	0.0495
<0.0207	0.0272	0.0217	0.0266	0.0137	0.0206	0.0217	0.0137		0.0239	0.0238			0.0209	0.0149	0.0194	0.0239
<0.0730	0.162	0.119	0.119	0.0944	0.102	0.119	0.0944		0.146	0.121			0.141	0.0900	0.107	0.146
0.0259	0.0396	0.0329	0.0305	0.0254	0.0258	0.0329	0.0254		0.0383	0.0354			0.0351	0.0276	0.0302	0.0383
0.284	0.320	0.272	0.231	0.218	0.218	0.272	0.218		0.282	0.310			0.283	0.207	0.287	0.282
0.0904	0.0926	0.0886	0.0734	0.0692	0.0674	0.0886	0.0692		0.0946	0.0963			0.0780	0.0745	0.0775	0.0946
0.341	0.309	0.294	0.254	0.274	0.252	0.294	0.274		0.334	0.334			0.276	0.250	0.292	0.334
0.0786	0.0556	0.0478	0.0457	0.0461	0.0461	0.0478	0.0461		0.0629	0.0578			0.0477	0.0478	0.0457	0.0629
0.454	0.367	0.369	0.358	0.336	0.319	0.369	0.336		0.414	0.448			0.346	0.334	0.355	0.414
0.0701	0.0639	0.0692	0.0672	0.0623	0.0577	0.0692	0.0623		0.0772	0.0761			0.0669	0.0667	0.0668	0.0772
<0.197	0.0700	0.0597	0.0439	0.0404	0.0642	0.0597	0.0404		0.0638	0.0660			0.0705	0.0602	0.0699	0.0638
<0.0145	<0.000402	<0.000413	<0.000403	<0.000373	<0.000415	<0.000413	<0.000373		<0.000570	<0.000620			<0.000605	<0.000621	<0.000601	<0.000570
<0.146	0.00363	0.0199	0.0117	<0.0112	<0.0133	0.0199	<0.0112		0.0244	0.0104			0.0108	<0.00183	<0.00177	0.0244
<0.0212	<0.000599	<0.000616	<0.000601	<0.000557	<0.000619	<0.000616	<0.000557		<0.000901	<0.000979			<0.000951	<0.000979	<0.000947	<0.000901
<0.0233	<0.000584	<0.000601	<0.000586	<0.000543	<0.000603	<0.000601	<0.000543		<0.000885	<0.000962			<0.000933	<0.000961	<0.000930	<0.000885

B.5. Table de données – compositions chimiques en éléments traces des orthopyroxènes

MD110-DR06-161C-2	MD110-DR06-162B 001	MD110-DR06-162B 007	MD110-DR06-162B-3	MD110-DR06-162b-3	MD110-DR06-162b-7b	MD110-DR06-167A 001	MD110-DR06-167A 005	MD110-DR06-167A 006	MD110-DR06-167A 007	MD110-DR06-167A 009	MD110-DR06-167A-11	MD110-DR06-167A-1b	MD110-DR06-167A-5	MD110-DR06-167A-6	MD110-DR06-167A-9	MD110-DR06-168 002
Opx	Opx	Opx	Opx	Opx	Opx	Opx	Opx	Opx	Opx	Opx	Opx	Opx	Opx	Opx	Opx	Opx
MD110-DR06	MD110-DR06	MD110-DR06	MD110-DR06	MD110-DR06	MD110-DR06	MD110-DR06	MD110-DR06	MD110-DR06	MD110-DR06	MD110-DR06	MD110-DR06	MD110-DR06	MD110-DR06	MD110-DR06	MD110-DR06	MD110-DR06
161C	162B	162B	162B	162B	162B	167A	167A	167A	167A	167A	167A	167A	167A	167A	167A	168
Pl-lhz	Pl-lhz	Pl-lhz	Pl-lhz	Pl-lhz	Pl-lhz	Pl-lhz	Pl-lhz	Pl-lhz	Pl-lhz	Pl-lhz	Pl-lhz	Pl-lhz	Pl-lhz	Pl-lhz	Pl-lhz	Pl-lhz
Porph.	Porph.	Porph.	Porph.	Porph.	Porph.	Porph.	Porph.	Porph.	Porph.	Porph.	Porph.	Porph.	Porph.	Porph.	Porph.	Porph.
Rim	Core	Core	Core	Core	Rim	Core	Core	Core	Core	Core	Core	Core	Core	Core	Core	Core
0.849	1.32	0.496	0.584	0.584	0.496	1.33	1.32	1.56	1.36	1.66	3.37	1.33	1.32	1.56	1.66	1.61
<0.515	1.38	<0.491	0.529	0.529	<0.491	<0.501	<0.525	<0.525	0.645	<0.532	<0.523	<0.501	<0.525	<0.525	<0.532	<3.71
29.0	26.9	26.1	25.5	25.5	26.1	29.9	28.7	31.3	31.1	30.1	52.3	29.9	28.7	31.3	30.1	27.9
742	1326	956	1118	1118	956	651	584	625	587	591	1573	651	584	625	591	723
159	143	139	127	127	139	158	145	160	145	153	243	158	145	160	153	156
2510	2456	2488	2096	2096	2488	2636	2615	2694	2635	2620	3422	2636	2615	2694	2620	5498
																960
55.0	54.1	54.6	48.3	48.3	54.6	52.4	52.7	52.1	51.6	51.2	24.4	52.4	52.7	52.1	51.2	57.6
643	569	630	554	554	630	623	642	634	630	622	341	623	642	634	622	773
0.0363	0.0731	<0.0362	<0.0302	<0.0302	<0.0362	<0.0498	<0.0529	<0.0536	<0.0534	<0.0524	0.0580	<0.0498	<0.0529	<0.0536	<0.0524	<0.116
0.0731	0.245	0.0368	0.0443	0.0443	0.0368	0.0709	0.0603	0.140	0.152	0.0616	2.04	0.0709	0.0603	0.140	0.0616	0.0163
2.73	2.76	2.98	3.02	3.02	2.98	2.57	2.30	2.62	2.54	2.50	17.0	2.57	2.30	2.62	2.50	1.94
1.27	6.10	5.54	7.40	7.40	5.54	1.15	1.09	1.23	1.14	1.09	6.73	1.15	1.09	1.23	1.09	0.689
0.00251	0.00338	0.00282	0.00280	0.00280	0.00282	0.00201	<0.000634	0.00162	<0.00262	0.000675	0.00463	0.00201	<0.000634	0.00162	0.000675	<0.00672
<0.0165	0.0201	<0.0200	0.0188	0.0188	<0.0200	0.0262	<0.0288	<0.0280	<0.0296	<0.0270	<0.0282	0.0262	<0.0288	<0.0280	<0.0270	<0.0758
<0.0409	0.0841	0.0134	0.00414	0.00414	0.0134	0.0200	<0.00638	<0.00580	<0.00579	<0.00628	<0.00631	0.0200	<0.00638	<0.00580	<0.00628	<0.308
<0.000507	<0.000418	0.00457	0.00361	0.00361	0.00457	<0.000700	<0.000749	<0.000681	<0.000679	<0.000737	0.0421	<0.000700	<0.000749	<0.000681	<0.000737	<0.00733
0.0171	0.0149	0.0574	0.0504	0.0504	0.0574	0.0121	0.00879	0.0137	0.0130	0.0113	0.649	0.0121	0.00879	0.0137	0.0113	<0.0324
0.00614	0.00640	0.0216	0.0160	0.0160	0.0216	0.00353	0.00317	0.00437	0.00477	0.00101	0.240	0.00353	0.00317	0.00437	0.00101	<0.00711
0.0512	0.0643	0.144	0.150	0.150	0.144	0.0527	0.0386	0.0310	0.0432	0.0412	1.66	0.0527	0.0386	0.0310	0.0412	<0.0427
0.0378	0.0645	0.0866	0.128	0.128	0.0866	0.0275	0.0325	0.0226	0.0234	0.0366	0.976	0.0275	0.0325	0.0226	0.0366	<0.0493
0.0238	0.0228	0.0321	0.0366	0.0366	0.0321	0.0228	0.0185	0.0240	0.0222	0.0196	0.421	0.0228	0.0185	0.0240	0.0196	<0.0489
0.121	0.159	0.217	0.228	0.228	0.217	0.111	0.128	0.121	0.144	0.107	1.77	0.111	0.128	0.121	0.107	<0.195
0.0354	0.0435	0.0589	0.0575	0.0575	0.0589	0.0304	0.0305	0.0321	0.0358	0.0301	0.367	0.0304	0.0305	0.0321	0.0301	0.0270
0.310	0.333	0.382	0.407	0.407	0.382	0.281	0.238	0.315	0.282	0.236	2.57	0.281	0.238	0.315	0.236	0.153
0.0963	0.0903	0.0980	0.113	0.113	0.0980	0.0867	0.0769	0.0920	0.0849	0.0739	0.609	0.0867	0.0769	0.0920	0.0739	0.0815
0.334	0.356	0.359	0.348	0.348	0.359	0.355	0.264	0.311	0.282	0.309	1.73	0.355	0.264	0.311	0.309	0.319
0.0578	0.0644	0.0564	0.0606	0.0606	0.0564	0.0612	0.0519	0.0571	0.0609	0.0536	0.247	0.0612	0.0519	0.0571	0.0536	0.0270
0.448	0.414	0.419	0.418	0.418	0.419	0.459	0.397	0.502	0.477	0.427	1.46	0.459	0.397	0.502	0.427	0.492
0.0761	0.0759	0.0701	0.0682	0.0682	0.0701	0.0733	0.0674	0.0921	0.0725	0.0846	0.228	0.0733	0.0674	0.0921	0.0846	0.0482
0.0660	0.335	0.184	0.340	0.340	0.184	0.0623	0.0462	0.0504	0.0422	0.0419	0.301	0.0623	0.0462	0.0504	0.0419	<0.0868
<0.000620	<0.000511	<0.000550	<0.000439	<0.000439	<0.000550	<0.000854	<0.000914	<0.000830	<0.000828	<0.000899	<0.000903	<0.000854	<0.000914	<0.000830	<0.000899	<0.00960
0.0104	0.00663	0.00780	0.00697	0.00697	0.00780	0.0109	0.00919	<0.00262	0.00934	0.0130	<0.00285	0.0109	0.00919	<0.00262	0.0130	<0.137
<0.000979	<0.000803	<0.000864	<0.000689	<0.000689	<0.000864	<0.00136	<0.00146	<0.00133	<0.00132	<0.00144	<0.00144	<0.00136	<0.00146	<0.00133	<0.00144	<0.0581
<0.000962	<0.000788	<0.000848	<0.000676	<0.000676	<0.000848	<0.00136	<0.00146	<0.00132	<0.00132	<0.00143	<0.00144	<0.00136	<0.00146	<0.00132	<0.00143	<0.310

B.5. Table de données – compositions chimiques en éléments traces des orthopyroxènes

MD110-DR06-168-12a	MD110-DR06-168-12b	MD110-DR06-168-27	MD110-DR06-173 001	MD110-DR06-173 002	MD110-DR06-173 003	MD110-DR06-173 004	MD110-DR06-173 011	MD110-DR06-173-2	MD110-DR06-173-2b	MD110-DR06-173-3a	MD110-DR06-173-3b	MD110-DR06-173-4	MD110-DR06-B4 001	MD110-DR06-B4 002	MD110-DR06-B4 013	MD110-DR06-B4 016
Opx	Opx	Opx	Opx	Opx	Opx	Opx	Opx	Opx	Opx	Opx	Opx	Opx	Opx	Opx	Opx	Opx
MD110-DR06	MD110-DR06	MD110-DR06	MD110-DR06	MD110-DR06	MD110-DR06	MD110-DR06	MD110-DR06	MD110-DR06	MD110-DR06	MD110-DR06	MD110-DR06	MD110-DR06	MD110-DR06	MD110-DR06	MD110-DR06	MD110-DR06
168	168	168	173	173	173	173	173	173	173	173	173	173	B4	B4	B4	B4
Pl-lhz	Pl-lhz	Pl-lhz	Pl-lhz	Pl-lhz	Pl-lhz	Pl-lhz	Pl-lhz	Pl-lhz	Pl-lhz	Pl-lhz	Pl-lhz	Pl-lhz	Pl-lhz	Pl-lhz	Pl-lhz	Pl-lhz
Porph.	Porph.	Porph.	Porph.	Porph.	Interstitial	Porph.	Porph.	Porph.	Porph.	Porph.	Porph.	Porph.	Porph.	Porph.	Interstitial	Porph.
Core	Core	Core	Core	Core	Core	Core	Core	Core	Core	Core	Core	Core	Core	Core	Core	Core
<1.38	1.21	1.28	1.17	1.15	1.11	0.910	1.09	1.15	1.15	1.11	1.11	0.910	0.707	0.593	19.1	0.860
<3.97	<3.70	<3.56	<0.481	<0.449	1.51	<0.488	0.650	<0.449	<0.449	1.51	1.51	<0.488	<0.493	<0.464	117	<0.437
29.5	26.6	27.0	20.1	23.2	24.0	21.8	22.4	23.2	23.2	24.0	24.0	21.8	25.4	25.0	2.68	22.8
703	784	723	544	558	695	589	501	558	558	695	695	589	745	714	35.5	714
164	143	151	111	131	129	121	116	131	131	129	129	121	148	149	3.11	129
5406	4402	5197	2463	2474	2268	2365	2292	2474	2474	2268	2268	2365	2356	2384	62.1	2120
944	982	951														
56.7	55.7	56.9	53.5	53.1	55.0	53.7	52.6	53.1	53.1	55.0	55.0	53.7	52.8	53.5	120	50.4
770	719	763	665	645	616	631	630	645	645	616	616	631	617	630	2763	577
<0.116	<0.117	<0.126	<0.0375	<0.0372	<0.0363	<0.0339	<0.0344	<0.0372	<0.0372	<0.0363	<0.0363	<0.0339	<0.0341	<0.0345	0.413	<0.0303
0.0535	<0.00775	0.0224	0.262	0.0992	0.141	0.100	0.190	0.0992	0.0992	0.141	0.141	0.100	0.0216	0.0770	18.1	0.0369
2.31	2.10	2.30	1.57	1.83	1.57	1.66	1.54	1.83	1.83	1.57	1.57	1.66	2.57	2.53	0.0343	2.30
0.974	0.813	1.04	1.50	1.64	1.03	1.50	1.20	1.64	1.64	1.03	1.03	1.50	1.01	0.973	<0.00720	0.835
0.0112	<0.00675	<0.00675	0.00246	0.00227	0.00142	0.00254	0.00260	0.00227	0.00227	0.00142	0.00142	0.00254	0.00238	0.00253	<0.000722	0.00241
<0.0978	<0.0809	<0.0904	<0.0181	<0.0189	<0.0190	<0.0177	<0.0197	<0.0189	<0.0189	<0.0190	<0.0190	<0.0177	<0.0186	<0.0202	0.0339	<0.0160
<0.0729	<0.0632	<0.0633	0.00774	0.0113	0.0309	0.0229	0.0115	0.0113	0.0113	0.0309	0.0309	0.0229	0.0198	0.0150	0.655	0.0163
<0.00849	<0.00736	<0.00737	0.00325	0.00225	0.000640	0.00261	0.00249	0.00225	0.00225	0.000640	0.000640	0.00261	0.00165	<0.000412	0.00392	<0.000379
0.0275	<0.00812	0.0103	0.0363	0.0254	0.00531	0.0188	0.0284	0.0254	0.0254	0.00531	0.00531	0.0188	0.0172	0.0183	0.0198	0.0157
0.0468	<0.00713	<0.00714	0.00811	0.00667	0.00281	0.00477	0.00495	0.00667	0.00667	0.00281	0.00281	0.00477	0.00622	0.00607	0.00319	0.00654
0.0833	<0.0428	<0.0428	0.0595	0.0577	0.0186	0.0423	0.0454	0.0577	0.0577	0.0186	0.0186	0.0423	0.0707	0.0575	0.00721	0.0611
0.157	<0.0495	<0.0495	0.0389	0.0420	0.0170	0.0328	0.0187	0.0420	0.0420	0.0170	0.0170	0.0328	0.0444	0.0447	<0.00466	0.0404
<0.0164	<0.0142	<0.0142	0.0240	0.0172	0.0116	0.0136	0.0197	0.0172	0.0172	0.0116	0.0116	0.0136	0.0281	0.0199	<0.0112	0.0181
0.0636	0.0784	0.124	0.0930	0.100	0.0633	0.0923	0.104	0.100	0.100	0.0633	0.0633	0.0923	0.146	0.159	0.00926	0.142
0.0506	0.0350	0.0321	0.0224	0.0241	0.0195	0.0248	0.0201	0.0241	0.0241	0.0195	0.0195	0.0248	0.0391	0.0344	<0.000837	0.0326
0.231	0.370	0.256	0.175	0.211	0.169	0.200	0.155	0.211	0.211	0.169	0.169	0.200	0.319	0.283	<0.00324	0.276
0.0534	0.0672	0.0596	0.0563	0.0705	0.0495	0.0592	0.0519	0.0705	0.0705	0.0495	0.0495	0.0592	0.0955	0.0883	<0.000929	0.0868
0.270	0.185	0.267	0.182	0.200	0.203	0.201	0.192	0.200	0.200	0.203	0.203	0.201	0.291	0.297	0.00847	0.267
<0.0325	0.0259	0.0669	0.0356	0.0389	0.0413	0.0355	0.0350	0.0389	0.0389	0.0413	0.0413	0.0355	0.0572	0.0554	0.00172	0.0532
0.301	0.475	0.202	0.256	0.276	0.294	0.265	0.264	0.276	0.276	0.294	0.294	0.265	0.407	0.377	0.0117	0.324
0.0779	0.0755	0.0402	0.0488	0.0495	0.0526	0.0515	0.0506	0.0495	0.0495	0.0526	0.0526	0.0515	0.0654	0.0763	0.00527	0.0571
0.0704	<0.0318	<0.0319	0.0470	0.0561	0.0508	0.0609	0.0563	0.0561	0.0561	0.0508	0.0508	0.0609	0.0454	0.0598	<0.00315	0.0631
<0.0111	<0.00964	<0.00965	<0.000535	<0.000523	<0.000513	<0.000497	<0.000509	<0.000523	<0.000523	<0.000513	<0.000513	<0.000497	<0.000491	<0.000499	<0.000969	<0.000457
<0.130	<0.168	<0.170	0.00480	0.00742	0.0106	0.0109	0.0101	0.00742	0.00742	0.0106	0.0106	0.0109	0.00799	0.0120	0.0582	0.0106
<0.0168	<0.0145	<0.0146	<0.000824	<0.000806	<0.000791	<0.000765	<0.000783	<0.000806	<0.000806	<0.000791	<0.000791	<0.000765	<0.000753	<0.000766	<0.00149	<0.000701
<0.0785	<0.0159	<0.0159	<0.000794	<0.000776	<0.000762	<0.000736	<0.000754	<0.000776	<0.000776	<0.000762	<0.000762	<0.000736	<0.000726	<0.000738	<0.00143	<0.000676

B.5. Table de données – compositions chimiques en éléments traces des orthopyroxènes

MD110-DR06-B4-2	MD110-DR06-B7 002	MD110-DR06-B7 004	MD110-DR06-B7-2	MD110-DR09-273b 007	MD110-DR09-275b 001	MD110-DR09-275b 002	MD110-DR09-275b 003	MD110-DR09-275b 004	MD110-DR09-275b 005	MD110-DR09-275b 006	MD110-DR09-275b 007	MD110-DR09-275b 008	MD110-DR09-275b 009	MD110-DR09-275b 010	MD110-DR09-275b 011	MD110-DR09-275B-1
Opx	Opx	Opx	Opx	Opx	Opx	Opx	Opx	Opx	Opx	Opx	Opx	Opx	Opx	Opx	Opx	Opx
MD110-DR06	MD110-DR06	MD110-DR06	MD110-DR06	MD110-DR09	MD110-DR09	MD110-DR09	MD110-DR09	MD110-DR09	MD110-DR09	MD110-DR09	MD110-DR09	MD110-DR09	MD110-DR09	MD110-DR09	MD110-DR09	MD110-DR09
B4	B7	B7	B7	273b	275b	275b	275b	275b	275b	275b	275b	275b	275b	275b	275b	275b
Pl-lhz	Pl-lhz	Pl-lhz	Pl-lhz	Sp-lhz	Sp-lhz	Sp-lhz	Sp-lhz	Sp-lhz	Sp-lhz	Sp-lhz	Sp-lhz	Sp-lhz	Sp-lhz	Sp-lhz	Sp-lhz	Sp-lhz
Porph.	Porph.	Porph.	Porph.	Porph.	Porph.	Porph.	Porph.	Porph.	Porph.	Porph.	Porph.	Porph.	Porph.	Porph.	Porph.	Porph.
Core	Core	Core	Core	Core	Core	Core	Core	Core	Core	Core	Rim	Rim	Rm	Core	Core	Core
0.593	1.07	0.865	1.07	2.34	2.13	2.28	1.88	2.10	2.44	2.21	1.55	1.97	2.41	1.57	1.56	2.13
<0.464	<0.417	<0.459	<0.417	<2.15	2.64	3.32	3.19	<1.97	<2.30	1.99	3.57	3.59	12.4	2.25	2.95	2.64
25.0	25.0	23.7	25.0	23.2	25.7	27.4	25.1	23.2	25.7	29.6	22.4	21.2	22.3	24.7	22.2	25.7
714	633	571	633	382	400	460	424	382	417	471	366	356	387	406	373	400
149	129	127	129	118	124	130	124	116	126	133	110	108	114	117	114	124
2384	2213	2294	2213	4728	4551	4615	4706	4051	4700	4734	3714	3794	4210	4205	4109	4551
53.5	53.5	52.8	53.5	49.2	51.0	48.3	51.3	50.0	50.0	48.9	50.5	50.2	49.7	50.6	48.6	51.0
630	611	625	611	638	641	620	654	629	617	618	609	634	662	639	621	641
<0.0345	<0.0310	<0.0331	<0.0310	<0.0400	<0.0412	<0.0396	<0.0410	<0.0394	<0.0608	<0.0316	<0.0243	0.0622	0.0920	<0.0219	<0.0306	<0.0412
0.0770	0.0872	0.154	0.0872	0.0359	0.0578	0.0755	0.0412	0.0175	0.0837	0.0913	0.0787	0.0437	0.390	0.0602	0.0871	0.0578
2.53	2.52	2.35	2.52	1.27	1.29	1.64	1.41	1.19	1.56	2.09	0.963	0.980	1.17	1.26	1.10	1.29
0.973	1.14	1.28	1.14	0.212	0.184	0.292	0.251	0.179	0.298	0.383	0.140	0.136	0.167	0.172	0.171	0.184
0.00253	0.00188	0.00271	0.00188	<0.00426	<0.00416	<0.00419	<0.00405	<0.00385	0.00685	<0.00344	<0.00308	<0.00288	<0.00298	<0.00318	<0.00292	<0.00416
<0.0202	0.0198	<0.0165	0.0198	0.0114	<0.00418	0.0219	<0.0301	<0.0286	<0.0298	<0.0272	<0.0189	<0.0171	<0.0225	<0.0221	0.00746	<0.00418
0.0150	0.00718	0.0165	0.00718	<0.0361	<0.0366	<0.0368	<0.0355	<0.0337	<0.0519	<0.0299	<0.0268	<0.0250	0.0732	<0.0275	<0.0253	<0.0366
<0.000412	0.00103	<0.000387	0.00103	<0.00412	<0.00413	<0.00415	<0.00401	<0.00381	<0.00587	<0.00339	<0.00304	<0.00284	0.0355	<0.00312	<0.00286	<0.00413
0.0183	0.00849	0.0131	0.00849	<0.00428	0.0159	<0.00429	<0.00414	<0.00393	0.0151	0.0151	0.0111	<0.00293	0.00914	0.00383	<0.00296	0.0159
0.00607	0.00323	0.00312	0.00323	<0.00375	<0.00371	<0.00373	<0.00361	<0.00343	<0.00529	<0.00305	<0.00274	<0.00256	<0.00264	<0.00282	<0.00259	<0.00371
0.0575	0.0346	0.0436	0.0346	<0.0225	<0.0223	<0.0225	<0.0217	<0.0206	<0.0318	<0.0184	<0.0165	<0.0154	0.0619	<0.0170	<0.0421	<0.0223
0.0447	0.0462	0.0430	0.0462	<0.0270	<0.0267	<0.0269	<0.0260	<0.0247	<0.0380	0.0771	<0.0197	<0.0184	<0.0190	<0.0203	<0.0186	<0.0267
0.0199	0.0250	0.0204	0.0250	0.0110	<0.00752	<0.00758	<0.00732	<0.00696	<0.0107	0.0171	<0.00556	<0.00519	0.0126	<0.00572	<0.00525	<0.00752
0.159	0.128	0.134	0.128	0.0498	<0.0271	0.0519	<0.0264	<0.0250	0.0989	0.0596	<0.0199	0.0589	0.0596	0.0250	<0.0188	<0.0271
0.0344	0.0331	0.0291	0.0331	<0.00413	0.0127	0.0133	0.00466	0.0121	0.0149	0.0351	0.00687	0.00762	0.0162	<0.00313	0.0185	0.0127
0.283	0.280	0.279	0.280	0.153	0.131	0.148	0.150	0.0455	0.221	0.244	0.126	0.0756	0.0836	0.131	0.0963	0.131
0.0883	0.0873	0.0815	0.0873	0.0564	0.0471	0.0413	0.0586	0.0380	0.0434	0.0901	0.0170	0.0293	0.0312	0.0526	0.0511	0.0471
0.297	0.303	0.259	0.303	0.157	0.211	0.249	0.182	0.0973	0.123	0.262	0.147	0.113	0.140	0.139	0.155	0.211
0.0554	0.0567	0.0529	0.0567	0.0350	0.0296	0.0273	0.0266	0.0219	0.0268	0.0422	0.0339	0.0157	0.0210	0.0214	0.0211	0.0296
0.377	0.390	0.342	0.390	0.344	0.343	0.266	0.332	0.243	0.317	0.375	0.215	0.175	0.295	0.244	0.218	0.343
0.0763	0.0737	0.0667	0.0737	0.0452	0.0471	0.0546	0.0384	0.0351	0.0523	0.0683	0.0476	0.0550	0.0672	0.0524	0.0437	0.0471
0.0598	0.0656	0.0693	0.0656	<0.0179	<0.0180	<0.0181	<0.0175	<0.0166	0.0479	<0.0148	<0.0132	<0.0124	<0.0127	<0.0136	0.0183	<0.0180
<0.000499	<0.000434	<0.000467	<0.000434	<0.00539	<0.00539	<0.00543	<0.00524	<0.00498	<0.00767	<0.00443	<0.00397	<0.00370	<0.00382	<0.00408	<0.00374	<0.00539
0.0120	0.00750	0.00867	0.00750	0.0683	<0.0143	<0.0961	0.0314	<0.0771	0.0388	0.0547	0.117	0.0392	0.153	0.0565	<0.0647	<0.0143
<0.000766	<0.000666	<0.000715	<0.000666	<0.00784	<0.00801	<0.00805	<0.00777	<0.00737	<0.0114	<0.00655	<0.00586	<0.00547	<0.00563	<0.00600	<0.00551	<0.00801
<0.000738	<0.000642	<0.000690	<0.000642	<0.00820	<0.00846	<0.00850	<0.00819	<0.00777	<0.0120	0.00853	<0.00617	0.00947	0.0334	<0.00631	<0.00579	<0.00846

B.5. Table de données – compositions chimiques en éléments traces des orthopyroxènes

MD110-DR09-275B-12	MD110-DR09-275B-2	MD110-DR09-275B-6a	MD110-DR09-275B-6b	MD110-DR09-275B-6c	MD110-DR09-279 005	MD110-DR09-279 006	MD110-DR09-279-5	MD110-DR09-279-6	MD110-DR09-280 001	MD110-DR09-281 004	MD110-DR09-281 008	MD110-DR09-281 009	MD110-DR09-281b 001	MD110-DR09-281B-1	MD110-DR09-281B-1b	MD110-DR09-281B-1c
Opx	Opx	Opx	Opx	Opx	Opx	Opx	Opx	Opx	Opx	Opx	Opx	Opx	Opx	Opx	Opx	Opx
MD110-DR09	MD110-DR09	MD110-DR09	MD110-DR09	MD110-DR09	MD110-DR09	MD110-DR09	MD110-DR09	MD110-DR09	MD110-DR09	MD110-DR09	MD110-DR09	MD110-DR09	MD110-DR09	MD110-DR09	MD110-DR09	MD110-DR09
275b	275b	275b	275b	275b	279	279	279	279	280	280	281	281	281b	281b	281b	281b
Sp-lhz	Sp-lhz	Sp-lhz	Sp-lhz	Sp-lhz	Sp-lhz	Sp-lhz	Sp-lhz	Sp-lhz	Sp-lhz	Sp-lhz	Sp-lhz	Sp-lhz	Sp-lhz	Sp-lhz	Sp-lhz	Sp-lhz
Porph.	Porph.	Porph.	Porph.	Porph.	Porph.	Porph.	Porph.	Porph.	Porph.	Porph.	Porph.	Porph.	Porph.	Porph.	Porph.	Porph.
Core	Core	Core	Core	Core	Core	Core	Core	Core	Core	Core	Core	Core	Core	Core	Core	Core
1.60	2.28	2.21	2.21	2.21	<1.53	62.0	<1.53	62.0	3.16	9.35	2.48	5.77	1.45	1.45	1.45	1.45
2.10	3.32	1.99	1.99	1.99	<4.97	329	<4.97	329	<5.16	248	<4.64	9.83	2.49	2.49	2.49	2.49
23.9	27.4	29.6	29.6	29.6	22.1	51.4	22.1	51.4	27.6	5.49	25.9	55.1	25.4	25.4	25.4	25.4
381	460	471	471	471	394	877	394	877	453	30.8	456	921	410	410	410	410
115	130	133	133	133	122	156	122	156	133	20.7	131	250	118	118	118	118
4278	4615	4734	4734	4734	4957	7363	4957	7363	5502	145	5326	9339	4421	4421	4421	4421
					1010	352	1010	352	903	80.2	1005	1770				
49.9	48.3	48.9	48.9	48.9	55.3	51.7	55.3	51.7	52.2	18.3	53.0	100	48.6	48.6	48.6	48.6
631	620	618	618	618	702	3568	702	3568	700	1166	693	1372	600	600	600	600
<0.0295	<0.0396	<0.0316	<0.0316	<0.0316	<0.153	3.81	<0.153	3.81	<0.172	<0.147	<0.147	0.720	<0.0452	<0.0452	<0.0452	<0.0452
0.0760	0.0755	0.0913	0.0913	0.0913	0.377	24.3	0.377	24.3	0.100	5.70	0.527	8.05	0.0316	0.0316	0.0316	0.0316
1.29	1.64	2.09	2.09	2.09	1.01	3.19	1.01	3.19	1.77	0.444	1.77	4.57	1.33	1.33	1.33	1.33
0.172	0.292	0.383	0.383	0.383	0.169	2.44	0.169	2.44	0.307	0.0644	0.248	11.7	0.231	0.231	0.231	0.231
<0.00303	<0.00419	<0.00344	<0.00344	<0.00344	<0.0139	<0.0883	<0.0139	<0.0883	<0.0106	<0.0128	<0.0122	0.169	<0.00472	<0.00472	<0.00472	<0.00472
0.0139	0.0219	<0.0272	<0.0272	<0.0272	<0.0917	<0.541	<0.0917	<0.541	<0.114	<0.0929	<0.0942	<0.216	<0.0301	<0.0301	<0.0301	<0.0301
<0.0261	<0.0368	<0.0299	<0.0299	<0.0299	<0.131	1.80	<0.131	1.80	<0.0995	0.838	<0.115	10.6	<0.0397	<0.0397	<0.0397	<0.0397
<0.00296	<0.00415	<0.00339	<0.00339	<0.00339	0.0374	0.233	0.0374	0.233	<0.0114	0.0262	0.118	0.856	<0.00454	<0.00454	<0.00454	<0.00454
<0.00307	<0.00429	0.0151	0.0151	0.0151	<0.0168	0.344	<0.0168	0.344	<0.0126	<0.0152	0.0407	1.57	0.0118	0.0118	0.0118	0.0118
<0.00268	<0.00373	<0.00305	<0.00305	<0.00305	<0.0148	<0.0933	<0.0148	<0.0933	<0.0112	<0.0135	0.0369	0.238	<0.00415	<0.00415	<0.00415	<0.00415
<0.0161	<0.0225	<0.0184	<0.0184	<0.0184	0.112	0.834	0.112	0.834	0.123	<0.0814	0.330	0.658	<0.0249	<0.0249	<0.0249	<0.0249
<0.0193	<0.0269	0.0771	0.0771	0.0771	<0.102	<0.648	<0.102	<0.648	<0.0787	<0.0951	<0.339	0.381	<0.0299	<0.0299	<0.0299	<0.0299
<0.00544	<0.00758	0.0171	0.0171	0.0171	<0.0294	<0.186	<0.0294	<0.186	<0.0223	<0.0269	<0.0257	<0.0359	<0.00842	<0.00842	<0.00842	<0.00842
0.0469	0.0519	0.0596	0.0596	0.0596	<0.101	<0.638	<0.101	<0.638	<0.0787	<0.325	<0.0907	0.585	<0.0297	<0.0297	<0.0297	<0.0297
0.00586	0.0133	0.0351	0.0351	0.0351	<0.0159	<0.100	<0.0159	<0.100	<0.0123	<0.0148	0.0217	0.0562	0.0242	0.0242	0.0242	0.0242
0.164	0.148	0.244	0.244	0.244	0.133	<0.433	0.133	<0.433	0.102	0.0859	0.262	0.425	0.187	0.187	0.187	0.187
0.0406	0.0413	0.0901	0.0901	0.0901	0.0351	0.130	0.0351	0.130	<0.0135	0.0207	0.0468	0.125	0.0379	0.0379	0.0379	0.0379
0.171	0.249	0.262	0.262	0.262	0.117	0.479	0.117	0.479	0.395	0.0844	0.199	0.684	0.173	0.173	0.173	0.173
0.0381	0.0273	0.0422	0.0422	0.0422	<0.0175	<0.111	<0.0175	<0.111	0.0374	<0.0162	0.0385	0.0459	0.0281	0.0281	0.0281	0.0281
0.270	0.266	0.375	0.375	0.375	0.257	<0.525	0.257	<0.525	0.474	<0.0782	0.283	0.870	0.246	0.246	0.246	0.246
0.0644	0.0546	0.0683	0.0683	0.0683	0.039	<0.118	0.039	<0.118	0.0687	<0.0176	0.0287	0.114	0.0780	0.0780	0.0780	0.0780
<0.0129	<0.0181	<0.0148	<0.0148	<0.0148	<0.0658	<0.416	<0.0658	<0.416	<0.0523	<0.0631	<0.0602	0.266	0.0374	0.0374	0.0374	0.0374
<0.00387	<0.00543	<0.00443	<0.00443	<0.00443	<0.0199	<0.126	<0.0199	<0.126	<0.0156	<0.0188	<0.0180	<0.0251	<0.00594	<0.00594	<0.00594	<0.00594
0.0796	<0.0961	0.0547	0.0547	0.0547	<0.188	<1.153	<0.188	<1.153	<0.0413	<0.206	<0.178	0.671	<0.0156	<0.0156	<0.0156	<0.0156
<0.00570	<0.00805	<0.00655	<0.00655	<0.00655	<0.0301	<0.190	<0.0301	<0.190	<0.0229	<0.0276	<0.0264	0.205	<0.00860	<0.00860	<0.00860	<0.00860
<0.00599	<0.00850	0.00853	0.00853	0.00853	<0.0328	2.12	<0.0328	2.12	<0.0251	1.18	0.0379	0.156	<0.00897	<0.00897	<0.00897	<0.00897

B.5. Table de données – compositions chimiques en éléments majeurs et traces des plagioclases

Analysis	MD110-DR06-1	MD110-DR06-1	MD110-DR06-1	MD110-DR06-1	MD110-DR06-1	MD110-DR06-1	MD110-DR06-1	MD110-DR06-1	MD110-DR06-1	MD110-DR06-1	MD110-DR06-1	MD110-DR06-1	MD110-DR06-1	MD110-DR06-1	MD110-DR06-168-6
Mineral	Plg	Plg	Plg	Plg	Plg	Plg	Plg	Plg	Plg	Plg	Plg	Plg	Plg	Plg	Plg
Analytical method	µXRF	µXRF	µXRF	µXRF	µXRF	µXRF	EPMA	EPMA	EPMA	EPMA	µXRF	µXRF	EPMA	EPMA	EPMA
Location	MD110-DR06	MD110-DR06	MD110-DR06	MD110-DR06	MD110-DR06	MD110-DR06	MD110-DR06	MD110-DR06	MD110-DR06	MD110-DR06	MD110-DR06	MD110-DR06	MD110-DR06	MD110-DR06	MD110-DR06
Sample	162B	162B	162B	162B	162B	162B	162B	162B	162B	162B	168	168	168	168	168
Type of rock	Pl-lherzolite	Pl-lherzolite	Pl-lherzolite	Pl-lherzolite	Pl-lherzolite	Pl-lherzolite	Pl-lherzolite	Pl-lherzolite	Pl-lherzolite	Pl-lherzolite	Pl-lherzolite	Pl-lherzolite	Pl-lherzolite	Pl-lherzolite	Pl-lherzolite
Texture	Neoblast	Neoblast	Neoblast	Neoblast	Neoblast	Neoblast	Neoblast	Neoblast	Neoblast	Neoblast	Neoblast	Neoblast	Neoblast	Neoblast	Neoblast
Na_2O	4.35	3.69	3.58	4.68	3.57	3.06	3.35	3.23	3.43	3.72	2.71	2.63	2.64	2.64	2.81
MgO	0.01	0.49	0.00	0.00	0.08	0.07	0.03	0.05	0.03	0.00	0.00	0.00	0.01	0.02	0.04
Al_2O_3	32.25	32.32	32.05	35.19	32.02	32.71	30.77	31.01	30.77	30.96	32.55	32.57	31.42	30.99	31.79
SiO_2	49.47	49.09	49.76	44.35	49.76	48.59	49.67	49.73	49.35	51.07	49.11	48.95	48.13	48.51	48.19
K_2O	0.14	0.06	0.03	0.02	0.01	0.22	0.00	0.00	0.02	0.02	0.04	0.19	0.03	0.21	0.01
CaO	13.54	14.10	14.28	15.47	14.31	15.12	14.51	14.31	14.44	14.18	15.37	15.39	15.15	14.87	15.11
TiO_2	0.03	0.04	0.04	0.02	0.05	0.03	0.04	0.01	0.03	0.00	0.02	0.03	0.00	0.00	0.00
Cr_2O_3	0.02	0.00	0.00	0.01	0.00	0.00	0.02	0.03	0.03	0.04	0.00	0.02	0.00	0.00	0.00
MnO	0.01	0.02	0.07	0.02	0.01	0.02	0.00	0.00	0.00	0.00	0.01	0.00	0.00	0.03	0.00
FeO	0.13	0.15	0.15	0.11	0.15	0.12	0.00	0.19	0.12	0.15	0.17	0.16	0.11	0.10	0.14
Total	99.97	99.97	99.95	99.86	99.97	99.95	98.37	98.56	98.22	100.14	99.98	99.94	97.48	97.37	98.09
Na	0.381	0.324	0.316	0.407	0.314	0.271	0.301	0.290	0.308	0.327	0.240	0.233	0.240	0.240	0.253
Mg	0.001	0.033	0.000	0.000	0.005	0.005	0.002	0.003	0.002	0.000	0.000	0.000	0.001	0.001	0.003
Al	1.715	1.725	1.717	1.858	1.714	1.755	1.678	1.690	1.680	1.656	1.753	1.755	1.736	1.715	1.743
Si	2.233	2.223	2.261	1.987	2.261	2.213	2.298	2.299	2.286	2.318	2.244	2.239	2.256	2.278	2.242
K	0.008	0.004	0.002	0.001	0.001	0.013	0.000	0.000	0.001	0.001	0.002	0.011	0.002	0.013	0.001
Ca	0.655	0.684	0.695	0.743	0.697	0.738	0.719	0.709	0.717	0.690	0.753	0.754	0.761	0.748	0.753
Ti	0.001	0.001	0.001	0.001	0.002	0.001	0.001	0.000	0.001	0.000	0.001	0.001	0.000	0.000	0.000
Cr	0.001	0.000	0.000	0.000	0.000	0.000	0.001	0.001	0.001	0.001	0.000	0.001	0.000	0.000	0.000
Mn	0.000	0.001	0.003	0.001	0.000	0.001	0.000	0.000	0.000	0.000	0.000	0.000	0.000	0.001	0.000
Fe_2	0.005	0.006	0.006	0.004	0.006	0.005	0.000	0.007	0.005	0.006	0.006	0.006	0.004	0.004	0.005
Ni	0.000	0.000	0.000	0.000	0.000	0.000	0.000	0.000	0.000	0.000	0.000	0.000	0.000	0.000	0.000
Total	5.000	5.000	5.000	5.000	5.000	5.000	5.000	5.000	5.000	5.000	5.000	5.000	5.000	5.000	5.000
An%	62.72	67.63	68.66	64.54	68.85	72.23	70.53	71.00	69.86	67.73	75.62	75.53	75.89	74.73	74.78
Al%	36.48	32.01	31.18	35.34	31.07	26.49	29.47	29.00	30.03	32.15	24.16	23.38	23.93	24.01	25.16
Or%	0.80	0.36	0.16	0.12	0.08	1.28	0.00	0.00	0.12	0.11	0.22	1.09	0.18	1.26	0.06
Total	100.00	100.00	100.00	100.00	100.00	100.00	100.00	100.00	100.00	100.00	100.00	100.00	100.00	100.00	100.00
Li ppm	1.95	17.6							17.6		<2.29		45.3	<2.29	62.7
B ppm	2.45	12.0							12.0		<7.48		26.5	<7.48	45.0
Sc ppm	0.143	0.117							0.117		0.6		0.598	0.6	0.706
Ti ppm	153	133							133		99.5		87.6	99.5	104
V ppm	0.909	0.615							0.615		1.0		1.17	1.0	1.17
Cr ppm	1.90	1.15							1.15		<1.18		1.21	<1.18	<1.12
Mn ppm											4.26		9.50	4.26	12.6
Co ppm	0.110	0.126							0.126		<0.105		0.101	<0.105	0.118
Ni ppm	<0.270	0.598							0.598		<1.68		21.6	<1.68	39.0
Rb ppm	0.962	0.358							0.358		<0.185		2.59	<0.185	5.85
Sr ppm	234	195							195		22.3		25.7	22.3	41.9
Y ppm	0.195	0.206							0.206		0.159		0.234	0.159	0.266
Zr ppm	0.0313	0.0290							0.0290		<0.0224		<0.0210	<0.0224	<0.0214
Nb ppm	<0.000852	<0.000892							<0.000892		<0.0127		<0.0119	<0.0127	<0.0122
Cs ppm	<0.0407	<0.0397							<0.0397		<0.195		<0.148	<0.195	<0.163
Ba ppm	11.7	9.16							9.16		<0.119		6.52	<0.119	11.7
La ppm	0.325	0.308							0.308		0.205		0.179	0.205	0.198
Ce ppm	1.17	1.07							1.07		0.786		0.856	0.786	0.795
Pr ppm	0.173	0.165							0.165		0.111		0.0778	0.111	0.0847
Nd ppm	0.625	0.670							0.670		0.475		0.405	0.475	0.284
Sm ppm	0.112	0.144							0.144		<0.0935		<0.0875	<0.0935	<0.0892
Eu ppm	0.338	0.292							0.292		0.251		0.228	0.251	0.145
Gd ppm	0.0953	0.118							0.118		0.172		<0.0861	0.172	<0.0878
Tb ppm	0.00534	0.0118							0.0118		<0.0145		<0.0136	<0.0145	0.0371
Dy ppm	0.0333	0.0281							0.0281		<0.0624		<0.0584	<0.0624	<0.0596
Ho ppm	0.00560	0.00608							0.00608		<0.0163		<0.0153	<0.0163	<0.0156
Er ppm	0.0144	0.0160							0.0160		<0.0500		<0.0468	<0.0500	<0.0478
Tm ppm	<0.00113	<0.00118							<0.00118		<0.0160		<0.0150	<0.0160	<0.0153
Yb ppm	<0.00485	<0.00507							<0.00507		<0.0758		<0.0709	<0.0758	<0.0723
Lu ppm	<0.00123	<0.00128							<0.00128		<0.0171		<0.0160	<0.0171	<0.0163
Hf ppm	<0.00387	<0.00405							<0.00405		<0.0601		<0.0563	<0.0601	<0.0574
Ta ppm	<0.00118	<0.00124							<0.00124		<0.0182		0.0196	<0.0182	<0.0174
Pb0 ppm	0.0508	0.0694							0.0694		0.0759		<0.262	0.0759	<0.230
Th ppm	<0.00186	<0.00194							<0.00194		<0.0275		<0.0257	<0.0275	<0.0262
U ppm	<0.00182	<0.00190							<0.00190		<0.0300		0.0313	<0.0300	0.0591

Analysis	Mineral	Analytical method	Location	Sample	Rock type	Texture	Na_2O	MgO	Al_2O_3	SiO_2	K_2O	CaO	TiO_2	Cr_2O_3	MnO	FeO	NiO	ZnO	Total		Na	Mg	Al	Si	K	Ca	Ti	Cr	Mn	Fe_2	Fe_3	Ni	Zn	Total	Mg#	Cr#
MD110-DR02-A03-spl 002	Spl	µXRF	MD110-DR02	A03	Sp-lherzolite		0.00	21.35	59.11	0.12	0.00	0.18	0.07	10.13	0.05	8.92	0.26	0.11	100.3		0.000	0.811	1.776	0.003	0.000	0.005	0.001	0.204	0.001	0.181	0.010	0.005	0.003	3.001	81.78	10.31
MD110-DR02-A03-spl 003	Spl	µXRF	MD110-DR02	A03	Sp-lherzolite		0.00	21.82	59.15	0.53	0.00	0.16	0.06	9.50	0.04	8.33	0.26	0.10	99.96		0.000	0.828	1.776	0.014	0.000	0.004	0.001	0.191	0.001	0.175	0.002	0.005	0.003	3.001	82.56	9.73
MD110-DR02-A03-spl 004	Spl	µXRF	MD110-DR02	A03	Sp-lherzolite		0.00	21.62	57.98	0.98	0.00	0.32	0.06	9.14	0.04	8.03	0.24	0.10	98.51		0.000	0.832	1.764	0.025	0.000	0.009	0.001	0.187	0.001	0.179	-0.006	0.005	0.002	3.001	82.24	9.57
MD110-DR02-A03-spl 006	Spl	µXRF	MD110-DR02	A03	Sp-lherzolite		0.00	21.62	59.20	0.73	0.00	0.21	0.05	8.78	0.09	8.97	0.27	0.15	100.1		0.000	0.821	1.776	0.019	0.000	0.006	0.001	0.177	0.002	0.185	0.006	0.006	0.004	3.001	81.61	9.05
MD110-DR02-A05-spl 001	Spl	µXRF	MD110-DR02	A5	Sp-lherzolite		0.00	20.43	55.79	0.91	0.00	0.21	0.03	11.18	0.06	9.73	0.26	0.14	98.74		0.000	0.797	1.720	0.024	0.000	0.006	0.001	0.231	0.001	0.214	-0.002	0.005	0.004	3.001	78.79	11.85
MD110-DR02-A05-spl 004	Spl	µXRF	MD110-DR02	A5	Sp-lherzolite		0.00	18.95	58.12	0.31	0.00	0.16	0.03	12.01	0.05	9.92	0.26	0.13	99.95		0.000	0.734	1.781	0.008	0.000	0.005	0.001	0.247	0.001	0.262	-0.046	0.005	0.003	3.001	73.69	12.17
MD110-DR02-A27-4	Spl	EPMA	MD110-DR02	A27	Sp-lherzolite		0.01	19.18	52.07	0.00	0.00	0.00	0.07	16.09	0.19	11.22			98.83		0.001	0.764	1.639	0.000	0.000	0.000	0.001	0.340	0.004	0.232	0.019	0.000	0.000	3.000	76.69	17.17
MD110-DR02-A27-5	Spl	EPMA	MD110-DR02	A27	Sp-lherzolite		0.02	18.72	52.36	0.00	0.00	0.04	0.08	16.23	0.06	10.95			98.47		0.001	0.749	1.656	0.000	0.000	0.000	0.001	0.344	0.001	0.248	-0.002	0.000	0.000	3.000	75.12	17.21
MD110-DR02-A27-spl3 001	Spl	µXRF	MD110-DR02	A27	Sp-lherzolite		0.00	21.19	56.21	0.00	0.00	0.15	0.52	12.90	0.03	8.55	0.25	0.10	99.91		0.000	0.817	1.713	0.000	0.000	0.004	0.010	0.264	0.001	0.183	0.002	0.005	0.003	3.001	81.71	13.35
MD110-DR02-A27-spl3 002	Spl	µXRF	MD110-DR02	A27	Sp-lherzolite		0.00	21.13	55.57	0.06	0.00	0.15	0.44	12.89	0.03	8.53	0.26	0.11	99.16		0.000	0.820	1.706	0.002	0.000	0.004	0.009	0.265	0.001	0.179	0.007	0.005	0.003	3.001	82.11	13.46
MD110-DR02-A27-spl3 004	Spl	µXRF	MD110-DR02	A27	Sp-lherzolite		0.00	20.77	54.68	0.05	0.00	0.20	0.42	13.64	0.03	8.74	0.29	0.10	98.92		0.000	0.812	1.690	0.001	0.000	0.006	0.008	0.283	0.001	0.185	0.007	0.006	0.002	3.001	81.48	14.34
MD110-DR02-A40-spl- 001	Spl	µXRF	MD110-DR02	A40	Sp-lherzolite		0.00	18.92	45.71	0.93	0.00	0.05	0.08	21.21	0.15	11.74	0.19	0.18	99.16		0.000	0.768	1.468	0.025	0.000	0.002	0.002	0.457	0.004	0.248	0.019	0.004	0.005	3.001	75.58	23.74
MD110-DR02-A40-spl- 002	Spl	µXRF	MD110-DR02	A40	Sp-lherzolite		0.00	19.38	46.36	0.64	0.00	0.18	0.12	21.27	0.08	11.56	0.19	0.17	99.93		0.000	0.779	1.473	0.017	0.000	0.005	0.002	0.453	0.002	0.228	0.032	0.004	0.004	3.001	77.33	23.53
MD110-DR02-A40-spl- 003	Spl	µXRF	MD110-DR02	A40	Sp-lherzolite		0.00	18.98	46.27	0.15	0.00	0.06	0.07	21.37	0.13	11.63	0.19	0.18	99.06		0.000	0.771	1.485	0.004	0.000	0.002	0.001	0.460	0.003	0.224	0.041	0.004	0.005	3.001	77.46	23.65
MD110-DR02-A40-spl- 004	Spl	µXRF	MD110-DR02	A40	Sp-lherzolite		0.00	18.52	44.48	0.31	0.00	0.08	0.10	23.07	0.11	12.48	0.18	0.19	99.52		0.000	0.756	1.435	0.008	0.000	0.002	0.002	0.500	0.003	0.244	0.041	0.004	0.005	3.001	75.58	25.82
MD110-DR02-A50-7	Spl	EPMA	MD110-DR02	A50	Sp-lherzolite		0.04	19.16	53.98	0.00	0.00	0.00	0.07	13.94	0.16	10.96			98.31		0.002	0.761	1.694	0.000	0.000	0.000	0.001	0.294	0.004	0.233	0.011	0.000	0.000	3.000	76.57	14.77
MD110-DR02-A50-8	Spl	EPMA	MD110-DR02	A50	Sp-lherzolite		0.00	18.87	53.67	0.00	0.00	0.00	0.06	14.59	0.07	11.69			98.96		0.000	0.748	1.682	0.000	0.000	0.000	0.001	0.307	0.002	0.251	0.009	0.000	0.000	3.000	74.85	15.42
MD110-DR02-A64-1	Spl	EPMA	MD110-DR02	A64	Sp-lherzolite		0.03	18.39	44.81	0.00	0.00	0.00	0.05	23.61	0.17	12.21			99.27		0.002	0.752	1.449	0.000	0.000	0.000	0.001	0.512	0.004	0.242	0.039	0.000	0.000	3.000	75.69	26.12
MD110-DR02-A64-1	Spl	EPMA	MD110-DR02	A64	Sp-lherzolite		0.03	18.39	44.81	0.00	0.00	0.00	0.05	23.61	0.17	12.21			99.28		0.002	0.752	1.449	0.000	0.000	0.000	0.001	0.512	0.004	0.242	0.039	0.000	0.000	3.000	75.69	26.12
MD110-DR02-A64-spl 001	Spl	µXRF	MD110-DR02	A64	Sp-lherzolite		0.00	18.95	45.99	0.01	0.00	0.10	0.14	21.44	0.07	11.20	0.18	0.15	98.24		0.000	0.776	1.487	0.000	0.000	0.003	0.003	0.465	0.002	0.218	0.039	0.004	0.004	3.001	78.05	23.82
MD110-DR02-A64-spl 002	Spl	µXRF	MD110-DR02	A64	Sp-lherzolite		0.00	18.64	44.84	0.00	0.00	0.11	0.09	23.54	0.08	12.27	0.20	0.17	99.93		0.000	0.757	1.441	0.000	0.000	0.003	0.002	0.507	0.002	0.234	0.046	0.004	0.005	3.001	76.42	26.05
MD110-DR02-A64-spl 003	Spl	µXRF	MD110-DR02	A64	Sp-lherzolite		0.00	19.40	47.19	0.00	0.00	0.15	0.07	21.22	0.07	11.48	0.19	0.16	99.93		0.000	0.778	1.497	0.000	0.000	0.004	0.001	0.451	0.001	0.212	0.046	0.004	0.004	3.001	78.59	23.17
MD110-DR02-A64-spl 004	Spl	µXRF	MD110-DR02	A64	Sp-lherzolite		0.00	18.91	46.11	0.00	0.00	0.05	0.09	21.85	0.10	12.09	0.19	0.19	99.57		0.000	0.766	1.476	0.000	0.000	0.002	0.002	0.469	0.002	0.227	0.048	0.004	0.004	3.001	77.18	24.12
MD110-DR02-A64-spl 005	Spl	µXRF	MD110-DR02	A64	Sp-lherzolite		0.00	19.33	45.02	0.80	0.00	0.15	0.07	22.47	0.07	11.61	0.23	0.17	99.93		0.000	0.781	1.437	0.022	0.000	0.004	0.001	0.481	0.002	0.230	0.033	0.005	0.004	3.001	77.21	25.09
MD110-DR02-A64-spl 006	Spl	µXRF	MD110-DR02	A64	Sp-lherzolite		0.00	19.59	47.93	0.05	0.00	0.12	0.10	20.62	0.07	11.05	0.24	0.16	99.93		0.000	0.783	1.515	0.001	0.000	0.003	0.002	0.437	0.002	0.209	0.039	0.005	0.004	3.001	78.96	22.40
MD110-DR02-A66-spl 001	Spl	µXRF	MD110-DR02	A66	Sp-lherzolite		0.00	19.02	45.60	0.00	0.00	0.03	0.13	23.49	0.10	12.63	0.20	0.19	101.4		0.000	0.761	1.443	0.000	0.000	0.001	0.003	0.499	0.002	0.233	0.051	0.004	0.005	3.001	76.58	25.68
MD110-DR02-A66-spl 002	Spl	µXRF	MD110-DR02	A66	Sp-lherzolite		0.00	19.36	46.90	0.05	0.00	0.12	0.12	21.53	0.06	11.47	0.18	0.16	99.93		0.000	0.778	1.490	0.001	0.000	0.003	0.002	0.459	0.001	0.216	0.042	0.004	0.004	3.001	78.23	23.54
MD110-DR02-A66-spl 003	Spl	µXRF	MD110-DR02	A66	Sp-lherzolite		0.00	19.08	45.79	0.23	0.00	0.15	0.09	22.36	0.06	11.76	0.21	0.21	100.3		0.000	0.769	1.458	0.006	0.000	0.004	0.002	0.473	0.002	0.227	0.050	0.005	0.004	3.001	77.22	24.49
MD110-DR02-A66-spl 004	Spl	µXRF	MD110-DR02	A66	Sp-lherzolite		0.00	19.11	44.75	0.63	0.00	0.06	0.08	22.30	0.09	12.71	0.24	0.19	100.2		0.000	0.772	1.430	0.017	0.000	0.002	0.002	0.478	0.002	0.236	0.052	0.005	0.005	3.001	76.61	25.05
MD110-DR06-158A-15	Spl	EPMA	MD110-DR06	158A	Pl-lherzolite		0.00	21.16	32.31	0.00	0.03	0.00	0.37	34.13	0.22	17.45			99.69		0.001	0.660	1.111	0.000	0.001	0.000	0.008	0.787	0.005	0.338	0.087	0.000	0.000	3.000	66.09	41.47
MD110-DR06-158A-16	Spl	EPMA	MD110-DR06	158A	Pl-lherzolite		0.01	14.59	32.28	0.01	0.00	0.00	0.38	34.67	0.24	17.74			99.93		0.001	0.636	1.113	0.000	0.000	0.000	0.008	0.802	0.006	0.365	0.069	0.000	0.000	3.000	63.53	41.88
MD110-DR06-160A-spl- 001	Spl	µXRF	MD110-DR02	160A	Pl-lherzolite	Inclusion	0.00	20.74	51.50	0.05	0.04	0.02	0.09	16.09	0.09	10.90	0.32	0.10	99.93		0.000	0.813	1.597	0.001	0.001	0.000	0.002	0.335	0.002	0.177	0.062	0.007	0.003	3.001	82.09	17.33
MD110-DR06-160A-spl- 002	Spl	µXRF	MD110-DR02	160A	Pl-lherzolite	Inclusion	0.00	20.69	51.48	0.03	0.04	0.02	0.09	16.23	0.09	10.84	0.32	0.10	99.93		0.000	0.812	1.597	0.001	0.001	0.000	0.002	0.337	0.002	0.178	0.061	0.007	0.003	3.001	82.01	17.45
MD110-DR06-160A-spl- 003	Spl	µXRF	MD110-DR02	160A	Pl-lherzolite		0.00	14.57	31.39	0.10	0.00	0.02	0.37	33.66	0.21	18.89	0.15	0.22	99.59		0.000	0.639	1.088	0.003	0.000	0.000	0.001	0.008	0.783	0.005	0.361	0.104	0.004	0.006	3.002	63.90	41.84
MD110-DR06-160A-spl- 004	Spl	µXRF	MD110-DR02	160A	Pl-lherzolite		0.00	14.63	31.29	0.82	0.00	0.03	0.32	33.07	0.19	18.52	0.20	0.24	99.30		0.000	0.642	1.086	0.024	0.000	0.001	0.001	0.007	0.770	0.005	0.377	0.079	0.005	0.007	3.002	62.99	41.49
MD110-DR06-161A-23	Spl	EPMA	MD110-DR06	161A	Pl-lherzolite		0.01	16.71	41.70	0.02	0.00	0.00	0.25	24.19	0.22	16.79			99.89		0.001	0.694	1.370	0.001	0.000	0.000	0.005	0.533	0.005	0.305	0.086	0.000	0.000	3.000	69.47	28.01
MD110-DR06-161A-24	Spl	EPMA	MD110-DR06	161A	Pl-lherzolite		0.00	16.87	43.00	0.02	0.00	0.00	0.24	23.60	0.16	15.60			99.48		0.000	0.699	1.409	0.001	0.000	0.000	0.005	0.519	0.004	0.302	0.061	0.000	0.000	3.000	69.82	26.91
MD110-DR06-161A-25	Spl	EPMA	MD110-DR06	161A	Pl-lherzolite		0.00	15.83	34.44	0.02	0.00	0.02	0.49	31.89	0.14	17.10			99.92		0.000	0.679	1.168	0.001	0.000	0.000	0.001	0.011	0.726	0.003	0.328	0.084	0.000	0.000	3.000	67.44	38.32
MD110-DR06-161A-Spl 001	Spl	µXRF	MD110-DR02	161A	Pl-lherzolite	Inclusion	0.00	22.42	55.28	0.58	0.00	0.07	0.08	12.07	0.09	9.80	0.36	0.11	100.9		0.000	0.854	1.664	0.015	0.000	0.002	0.002	0.244	0.002	0.151	0.058	0.007	0.003	3.001	84.97	12.78
MD110-DR06-161A-Spl 004	Spl	µXRF	MD110-DR02	161A	Pl-lherzolite		0.00	15.48	34.13	0.24	0.00	0.03	0.47	29.10	0.16	18.53	0.23	0.21	98.57		0.000	0.673	1.173	0.007	0.000	0.001	0.010	0.671	0.004	0.332	0.119	0.006	0.006	3.002	66.93	36.38
MD110-DR06-161C-35a	Spl	EPMA	MD110-DR06	161C	Pl-lherzolite	Inclusion	0.01	19.93	53.37	0.00	0.00	0.00	0.10	14.18	0.00	11.50			99.09		0.001	0.785	1.662	0.000	0.000	0.000	0.002	0.296	0.000	0.216	0.038	0.000	0.000	3.000	78.44	15.13
MD110-DR06-161C-35b	Spl	EPMA	MD110-DR06	161C	Pl-lherzolite	Inclusion	0.00	20.56	52.12	0.00	0.01	0.03	0.09	13.92	0.14	11.13			98.00		0.000	0.817	1.636	0.000	0.000	0.000	0.001	0.002	0.293	0.003	0.181	0.067	0.000	0.000	3.000	81.89	15.19
MD110-DR06-161C-37	Spl	EPMA	MD110-DR06	161C	Pl-lherzolite		0.00	14.90	32.76	0.29	0.00	0.00	0.51	32.76	0.20	18.32			99.73		0.000	0.648	1.126	0.008	0.000	0.000	0.000	0.011	0.755	0.005	0.367	0.080	0.000	0.000	3.000	63.83	40.15
MD110-DR06-161C-Spl 001	Spl	µXRF	MD110-DR06	161C	Pl-lherzolite		0.00	14.86	31.49	0.00	0.00	0.03	0.50	32.20	0.24	18.35	0.17	0.18	98.03		0.000	0.656	1.103	0.000	0.000	0.000	0.001	0.011	0.757	0.006	0.340	0.116	0.004	0.005	3.001	65.92	40.69
MD110-DR06-161C-Spl 002	Spl	µXRF	MD110-DR06	161C	Pl-lherzolite		0.00	14.91	30.54	0.24	0.00	0.04	0.49	33.81	0.25	19.21	0.16	0.19	99.86		0.000	0.653	1.057	0.007	0.000	0.001	0.011	0.785	0.006	0.352	0.120	0.004	0.006	3.001	64.95	42.62
MD110-DR06-161C-Spl 003	Spl	µXRF	MD110-DR06	161C	Pl-lherzolite		0.00	15.21	34.00	0.00	0.54	0.01	0.49	29.62	0.15	18.92	0.20	0.22	99.34		0.000	0.657	1.162	0.000	0.020	0.000	0.011	0.679	0.004	0.304	0.155	0.005	0.006	3.002	68.41	36.89
MD110-DR06-161C-Spl 005	Spl	µXRF	MD110-DR06	161C	Pl-lherzolite	Inclusion	0.00	21.67	55.07	0.00	0.00	0.07	0.10	12.48	0.03	9.99	0.36	0.15	99.92		0.000	0.835	1.678	0.000	0.000	0.002	0.002	0.255	0.001	0.156	0.061	0.007	0.004	3.001	84.30	13.20
MD110-DR06-162A-spl- 002	Spl	µXRF	MD110-DR06	162A	Pl-lherzolite	Inclusion	0.00	20.79	51.36	0.05	0.00	0.04	0.11	16.17	0.09	10.81	0.35	0.09	99.86		0.000	0.816	1.599	0.001	0.000	0.000	0.002	0.337	0.002	0.177	0.061	0.007	0.002	3.001	82.21	17.44
MD110-DR06-162B-26	Spl	EPMA	MD110-DR06	162B	Pl-lherzolite		0.00	14.57	30.07	0.05	0.00	0.02	0.79	36.29	0.21	16.51			98.52		0.000	0.648	1.058	0.001	0.000	0.000	0.001	0.018	0.856	0.005	0.365	0.047	0.000	0.000	3.000	63.99	44.74
MD110-DR06-162B-27	Spl	EPMA	MD110-DR06	162B	Pl-lherzolite		0.00	14.81	30.34	0.00	0.00	0.00	0.61	35.94	0.23	16.56			98.50		0.000	0.657	1.065	0.000	0.000	0.000	0.014	0.846	0.006	0.350	0.062	0.000	0.000	3.000	65.23	44.28
MD110-DR06-162b-spl1 002	Spl	µXRF	MD110-DR06	162B	Pl-lherzolite		0.00	15.93	32.21	0.00	0.00	0.04	0.55	34.05	0.14	16.46	0.16	0.22	99.76		0.000	0.690	1.103	0.000	0.000	0.000	0.001	0.012	0.782	0.003	0.312	0.088	0.004	0.006	3.002	68.85	41.50
MD110-DR06-162b-spl1 003	Spl	µXRF	MD110-DR06	162B	Pl-lherzolite		0.00	15.89	32.37	0.15	0.00	0.05	0.54	33.89	0.13	16.38	0.15	0.21	99.77		0.000	0.688	1.108	0.004	0.000	0.001	0.012	0.778	0.003	0.319	0.079	0.004	0.006	3.001	68.34	41.25
MD110-DR06-162b-spl1 004	Spl	µXRF	MD110-DR06	162B	Pl-lherzolite		0.00	16.99	33.24	0.97	0.00	0.07	0.52	31.88	0.12	15.63	0.15	0.21	99.78		0.000	0.727	1.124	0.028	0.000	0.002	0.011	0.723	0.003	0.303	0.072	0.003	0.006	3.001	70.59	39.15
MD110-DR06-162b-spl2 002	Spl	µXRF	MD110-DR06	162B	Pl-lherzolite		0.00	14.58	30.62	0.38	0.00	0.05	0.53	32.88	0.16	18.92	0.17	0.23	98.50		0.000	0.646	1.073	0.011	0.000	0.001	0.012	0.773	0.004	0.366	0.105	0.004	0.007	3.002	63.88	41.86
MD110-DR06-162b-spl2 003	Spl	µXRF	MD110-DR06	162B	Pl-lherzolite		0.00	14.74	29.97	0.88	0.00	0.06	0.52	32.21	0.16	20.78	0.15	0.23	99.69		0.000	0.647	1.040	0.026	0.000	0.002	0.011	0.750	0.004	0.379	0.133	0.004	0.007	3.002	63.05	41.89
MD110-DR06-162b-spl3 001	Spl	µXRF	MD110-DR06	162B	Pl-lherzolite		0.00	15.15	33.66	0.00	0.00	0.04	0.48	30.85	0.15	17.71	0.22	0.21	98.46		0.000	0.662	1.163	0.000	0.000	0.000	0.001	0.011	0.715	0.004	0.337	0.097	0.005	0.006	3.002	66.29	38.08
MD110-DR06-162b-spl3 002	Spl	µXRF	MD110-DR06	162B	Pl-lherzolite		0.00	15.86	35.10	0.05	0.00	0.05	0.47	30.00	0.16	17.69	0.19	0.20	99.77		0.000	0.679	1.189	0.001	0.000	0.001	0.010	0.681	0.004	0.321	0.104	0.004	0.006	3.001	67.90	36.44
MD110-DR06-162b-spl3 003	Spl	µXRF	MD110-DR06	162B	Pl-lherzolite		0.00	15.53	34.23	0.03	0.00	0.03	0.46	30.34	0.16	17.54	0.18	0.21	98.71		0.000	0.674	1.175	0.001	0.000	0.001	0.010	0.699	0.004	0.326	0.101	0.004	0.006	3.001	67.43	37.28
MD110-DR06-162C-spl- 001	Spl	µXRF	MD110-DR06	162C	Pl-lherzolite		0.00	19.71	49.19	0.00	0.00	0.05	0.21	18.94	0.09	12.21	0.30	0.16	100.9		0.000	0.779	1.537	0.000	0.000	0.001	0.004	0.397	0.002	0.214	0.056	0.006	0.004	3.001	78.42	20.53
MD110-DR06-162C-spl- 002	Spl	µXRF	MD110-DR06	162C	Pl-lherzolite		0.00	19.59	48.86	0.00	0.00	0.04	0.15	19.50	0.10	12.58	0.27	0.18	101.3		0.000	0.773	1.525	0.000	0.000	0.001	0.003	0.408	0.002	0.220	0.059	0.006	0.005	3.001	77.89	21.12
MD110-DR06-162C-spl- 003	Spl	µXRF	MD110-DR06	162C	Pl-lherzolite		0.00	19.67	49.29	0.00	0.00	0.04	0.15	19.16	0.10	12.56	0.31	0.17	101.4		0.000	0.774	1.533	0.000	0.000	0.001	0.003	0.400	0.002	0.218	0.059	0.007	0.004	3.001	78.00	20.69
MD110-DR06-162C-spl- 004	Spl	µXRF	MD110-DR06	162C	Pl-lherzolite		0.00	19.43	48.13	0.05	0.00	0.11	0.13	18.30	0.10	11.89	0.27	0.24	98.65		0.000	0.784	1.535	0.001	0.000	0.002	0.003	0.393	0.002	0.207	0.062	0.006	0.007	3.002	79.11	20.32
MD110-DR06-164A-spl- 001	Spl	µXRF	MD110-DR06	164A	Pl-lherzolite	Inclusion	0.00	20.49	52.10	0.00	0.00	0.04	0.09	15.53	0.07	11.16	0.29	0.15	99.93		0.000	0.803	1.615	0.000	0.000	0.001	0.002	0.323	0.002	0.189	0.057	0.006	0.004	3.001	80.98	16.67
MD110-DR06-164A-spl- 002	Spl	µXRF	MD110-DR06	164A	Pl-lherzolite	Inclusion	0.00	20.62	53.95	0.04	0.00	0.04	0.10	14.69	0.08	11.82	0.33	0.18	101.8		0.000	0.792	1.638	0.001	0.000	0.001	0.002	0.299	0.002	0.200	0.055	0.007	0.005	3.001	79.86	15.44
MD110-DR06-164A-spl- 003	Spl	µXRF	MD110-DR06	164A	Pl-lherzolite	Inclusion	0.00	20.85	51.98	0.08	0.00	0.04	0.22	15.37	0.07	10.84	0.30	0.19	99.94		0.000	0.816	1.608	0.002	0.000	0.001	0.004	0.319	0.002	0.180	0.058	0.006	0.005	3.001	81.95	16.55
MD110-DR06-167A-18	Spl	EPMA	MD110-DR06	167A	Pl-lherzolite		0.00	15.42	33.71	0.00	0.02	0.02	0.47	33.46	0.18	16.42			99.70		0.000	0.667	1.152	0.000	0.001	0.001	0.010	0.767	0.004	0.337	0.061	0.000	0.000	3.000	66.42	39.97
MD110-DR06-167A-Spl 001	Spl	µXRF	MD110-DR06	167A	Pl-lherzolite		0.00	16.61	40.24	0.00	0.00	0.03	0.26	24.72	0.12	16.11	0.24	0.20	98.52		0.000	0.702	1.344	0.000	0.000	0.000	0.001	0.006	0.554	0.003	0.293	0.088	0.005	0.006	3.001	70.53	29.18
MD110-DR06-167A-Spl 002	Spl	µXRF	MD110-DR06	167A	Pl-lherzolite		0.00	16.57	36.22	0.08	0.00	0.05	0.41	29.29	0.11	16.74	0.18	0.21	99.86		0.000	0.703	1.215	0.002	0.000	0.002	0.000	0.659	0.003	0.298	0.100	0.004	0.006	3.002	70.23	35.17
MD110-DR06-168-18	Spl	EPMA	MD110-DR06	168	Pl-lherzolite		0.00	11.00	23.22	0.01	0.01	0.02	0.42	43.13	0.38	20.28			98.48		0.000	0.515	0.860	0.000	0.000	0.000	0.010	1.071	0.010	0.484	0.049	0.000	0.000	3.000	51.58	55.48
MD110-DR06-168-19	Spl	EPMA	MD110-DR06	168	Pl-lherzolite		0.05	16.80	36.45	0.08	0.02	0.03	0.30	30.65

B.5. Table de données – compositions chimiques en éléments majeurs et mineurs des olivines

Analysis	Mineral	Analytical method	Location	Sample	Rock type	Na_2O	MgO	Al_2O_3	SiO_2	K_2O	CaO	TiO_2	Cr_2O_3	MnO	FeO	NiO	Total	Na	Mg	Al	Si	K	Ca	Ti	Cr	Mn	Fe_2	Fe_3	Ni	Total	Mg#	Li ppm	Sc ppm	Ti ppm	V ppm	Cr ppm	Co ppm	Ni ppm
MD110-DR06-159B 001	Ol	µXRF	MD110-DR06	159B	Pl-lherzolite	0.00	51.22	0.00	42.01	0.00	0.11	0.02	0.01	0.11	6.23	0.26	99.97	0.000	1.847	0.000	1.016	0.000	0.003	0.000	0.000	0.002	0.126	0.000	0.005	3.000	0.936							
MD110-DR06-159B 002	Ol	µXRF	MD110-DR06	159B	Pl-lherzolite	0.00	51.14	0.00	41.70	0.00	0.09	0.01	0.01	0.11	6.63	0.28	99.97	0.000	1.846	0.000	1.009	0.000	0.002	0.000	0.000	0.002	0.134	0.000	0.005	3.000	0.932							
MD110-DR06-159B 003	Ol	µXRF	MD110-DR06	159B	Pl-lherzolite	0.00	51.06	0.00	41.35	0.02	0.09	0.01	0.01	0.10	7.28	0.32	99.96	0.000	1.844	0.000	0.998	0.000	0.002	0.000	0.000	0.002	0.143	0.004	0.006	3.000	0.926							
MD110-DR06-159B 004	Ol	µXRF	MD110-DR06	159B	Pl-lherzolite	0.00	50.52	0.00	40.58	0.00	0.03	0.00	0.01	0.10	8.35	0.37	99.97	0.000	1.832	0.000	0.987	0.000	0.001	0.000	0.000	0.002	0.145	0.025	0.007	3.000	0.915							
MD110-DR06-159B 005	Ol	µXRF	MD110-DR06	159B	Pl-lherzolite	0.00	50.50	0.00	40.44	0.00	0.03	0.00	0.03	0.10	8.48	0.38	99.96	0.000	1.832	0.000	0.984	0.000	0.001	0.000	0.001	0.002	0.141	0.031	0.007	3.000	0.914							
MD110-DR06-159B 006	Ol	µXRF	MD110-DR06	159B	Pl-lherzolite	0.00	50.38	0.00	40.70	0.00	0.03	0.04	0.01	0.11	8.39	0.37	99.97	0.000	1.826	0.000	0.991	0.000	0.001	0.000	0.001	0.002	0.155	0.016	0.007	3.000	0.914							
MD110-DR06-159B 007	Ol	µXRF	MD110-DR06	159B	Pl-lherzolite	0.00	50.38	0.00	40.77	0.00	0.04	0.02	0.01	0.11	8.26	0.37	99.96	0.000	1.828	0.000	0.992	0.000	0.001	0.000	0.000	0.002	0.154	0.014	0.007	3.000	0.916							
MD110-DR06-159B 009	Ol	µXRF	MD110-DR06	159B	Pl-lherzolite	0.00	50.44	0.00	40.49	0.00	0.03	0.02	0.01	0.12	8.42	0.42	99.96	0.000	1.831	0.000	0.986	0.000	0.001	0.000	0.000	0.002	0.144	0.027	0.008	3.000	0.914							
MD110-DR06-159B 010	Ol	µXRF	MD110-DR06	159B	Pl-lherzolite	0.00	50.55	0.00	40.42	0.00	0.03	0.00	0.02	0.12	8.40	0.42	99.97	0.000	1.834	0.000	0.983	0.000	0.001	0.000	0.000	0.002	0.138	0.033	0.008	3.000	0.915							
MD110-DR06-159B 011	Ol	µXRF	MD110-DR06	159B	Pl-lherzolite	0.00	50.16	0.00	40.74	0.00	0.05	0.01	0.01	0.11	8.49	0.40	99.97	0.000	1.822	0.000	0.993	0.000	0.001	0.000	0.000	0.002	0.159	0.014	0.008	3.000	0.913							
MD110-DR06-159B 012	Ol	µXRF	MD110-DR06	159B	Pl-lherzolite	0.00	51.06	0.00	41.35	0.02	0.09	0.01	0.01	0.11	6.58	0.27	99.97	0.000	1.843	0.000	1.013	0.000	0.002	0.000	0.000	0.002	0.133	0.000	0.005	3.000	0.933							
MD110-DR06-159B 013	Ol	µXRF	MD110-DR06	159B	Pl-lherzolite	0.00	50.67	0.00	42.35	0.00	0.13	0.01	0.01	0.10	6.44	0.27	99.96	0.000	1.832	0.000	1.027	0.000	0.003	0.000	0.000	0.002	0.130	0.000	0.005	3.000	0.933							
MD110-DR06-159B 014	Ol	µXRF	MD110-DR06	159B	Pl-lherzolite	0.00	50.99	0.00	41.97	0.00	0.10	0.00	0.01	0.10	6.53	0.26	99.96	0.000	1.841	0.000	1.016	0.000	0.003	0.000	0.000	0.002	0.132	0.000	0.005	3.000	0.933							
MD110-DR06-159B 015	Ol	µXRF	MD110-DR06	159B	Pl-lherzolite	0.00	50.72	0.00	41.56	0.03	0.05	0.00	0.00	0.10	7.53	0.30	99.97	0.000	1.838	0.000	0.998	0.001	0.001	0.000	0.000	0.002	0.148	0.005	0.007	3.000	0.923							
MD110-DR06-159B 016	Ol	µXRF	MD110-DR06	159B	Pl-lherzolite	0.00	50.74	0.00	41.06	0.01	0.05	0.01	0.02	0.12	7.52	0.44	99.91	0.000	1.837	0.000	0.997	0.000	0.001	0.000	0.000	0.003	0.147	0.005	0.009	3.000	0.923							
MD110-DR06-159B 017	Ol	µXRF	MD110-DR06	159B	Pl-lherzolite	0.00	50.83	0.00	41.04	0.00	0.06	0.00	0.13	0.13	7.46	0.30	99.97	0.000	1.840	0.000	0.996	0.000	0.001	0.000	0.000	0.003	0.003	0.147	0.005	0.006	3.000	0.924							
MD110-DR06-159B 018	Ol	µXRF	MD110-DR06	159B	Pl-lherzolite	0.00	50.04	0.00	41.37	0.00	0.04	0.00	0.01	0.11	7.92	0.45	99.96	0.000	1.818	0.000	1.008	0.000	0.001	0.000	0.000	0.002	0.161	0.000	0.009	3.000	0.918							
MD110-DR06-159B-1	Ol	EPMA	MD110-DR06	159B	Pl-lherzolite	0.00	51.21	0.00	41.42	0.00	0.08	0.03	0.19	0.19	9.04		101.11	0.000	1.836	0.000	0.973	0.000	0.002	0.001	0.002	0.004	0.132	0.050	0.000	3.000	0.910							
MD110-DR06-159B-10	Ol	EPMA	MD110-DR06	159B	Pl-lherzolite	0.00	50.36	0.00	40.99	0.00	0.05	0.02	0.04	0.24	8.55		100.25	0.000	1.823	0.000	0.996	0.000	0.001	0.000	0.001	0.005	0.166	0.008	0.000	3.000	0.913							
MD110-DR06-159B-11	Ol	EPMA	MD110-DR06	159B	Pl-lherzolite	0.03	50.45	0.00	40.98	0.00	0.06	0.00	0.03	0.09	8.98		100.62	0.001	1.821	0.000	0.992	0.000	0.002	0.000	0.001	0.002	0.165	0.017	0.000	3.000	0.909							
MD110-DR06-159B-12	Ol	EPMA	MD110-DR06	159B	Pl-lherzolite	0.02	49.90	0.00	39.99	0.00	0.08	0.00	0.00	0.03	8.29		98.31	0.001	1.837	0.000	0.988	0.000	0.002	0.000	0.000	0.001	0.146	0.026	0.000	3.000	0.915							
MD110-DR06-159B-15	Ol	EPMA	MD110-DR06	159B	Pl-lherzolite	0.06	50.80	0.00	40.86	0.03	0.07	0.00	0.00	0.12	8.31		100.29	0.003	1.835	0.000	0.987	0.001	0.002	0.000	0.000	0.002	0.143	0.025	0.000	3.000	0.916							
MD110-DR06-159B-16	Ol	EPMA	MD110-DR06	159B	Pl-lherzolite	0.01	50.29	0.00	41.12	0.00	0.06	0.00	0.00	0.01	8.41		99.90	0.000	1.825	0.000	1.001	0.000	0.002	0.000	0.000	0.002	0.160	0.000	0.000	3.000	0.914							
MD110-DR06-159B-17	Ol	EPMA	MD110-DR06	159B	Pl-lherzolite	0.00	50.63	0.01	40.91	0.02	0.04	0.00	0.00	0.07	8.81		100.49	0.000	1.828	0.000	0.991	0.001	0.001	0.000	0.000	0.001	0.159	0.019	0.000	3.000	0.911							
MD110-DR06-159B-18	Ol	EPMA	MD110-DR06	159B	Pl-lherzolite	0.02	50.40	0.00	40.99	0.00	0.03	0.00	0.02	0.03	8.49		99.97	0.001	1.828	0.000	0.997	0.000	0.001	0.000	0.000	0.001	0.166	0.006	0.000	3.000	0.914							
MD110-DR06-159B-2	Ol	EPMA	MD110-DR06	159B	Pl-lherzolite	0.01	50.72	0.00	41.27	0.01	0.07	0.01	0.00	0.00	8.71		100.80	0.001	1.825	0.000	0.996	0.000	0.002	0.000	0.000	0.000	0.168	0.008	0.000	3.000	0.912							
MD110-DR06-159B-3	Ol	EPMA	MD110-DR06	159B	Pl-lherzolite	0.01	50.86	0.00	41.23	0.01	0.05	0.00	0.00	0.21	8.57		100.94	0.000	1.827	0.000	0.994	0.000	0.001	0.000	0.000	0.004	0.159	0.013	0.000	3.000	0.914							
MD110-DR06-159B-4	Ol	EPMA	MD110-DR06	159B	Pl-lherzolite	0.02	50.40	0.00	41.43	0.00	0.05	0.01	0.02	0.13	8.91		100.97	0.001	1.814	0.000	1.000	0.000	0.001	0.000	0.000	0.003	0.180	0.000	0.000	3.000	0.910							
MD110-DR06-159B-5	Ol	EPMA	MD110-DR06	159B	Pl-lherzolite	0.02	50.46	0.00	41.10	0.03	0.06	0.00	0.00	0.09	8.61		100.35	0.001	1.824	0.000	0.997	0.001	0.001	0.000	0.000	0.002	0.166	0.009	0.000	3.000	0.913							
MD110-DR06-159B-6	Ol	EPMA	MD110-DR06	159B	Pl-lherzolite	0.00	50.07	0.00	40.71	0.00	0.04	0.02	0.02	0.16	8.66		100.33	0.000	1.832	0.000	0.987	0.000	0.002	0.000	0.000	0.003	0.149	0.026	0.000	3.000	0.913							
MD110-DR06-159B-7	Ol	EPMA	MD110-DR06	159B	Pl-lherzolite	0.01	50.75	0.21	40.91	0.00	0.03	0.00	0.07	0.14	8.33		100.45	0.000	1.830	0.006	0.990	0.000	0.001	0.000	0.001	0.003	0.155	0.014	0.000	3.000	0.916							
MD110-DR06-159B-8	Ol	EPMA	MD110-DR06	159B	Pl-lherzolite	0.00	50.71	0.00	41.59	0.00	0.05	0.00	0.00	0.04	9.31		101.70	0.000	1.813	0.000	0.998	0.000	0.001	0.000	0.000	0.001	0.182	0.005	0.000	3.000	0.907							
MD110-DR06-159B-9	Ol	EPMA	MD110-DR06	159B	Pl-lherzolite	0.01	50.22	0.00	41.55	0.01	0.04	0.00	0.00	0.08	8.95		100.84	0.000	1.811	0.000	1.005	0.000	0.001	0.000	0.000	0.002	0.181	0.000	0.000	3.000	0.909							
MD110-DR06-161A 011	Ol	µXRF	MD110-DR06	161A	Pl-lherzolite	0.00	49.99	0.00	40.81	0.00	0.03	0.01	0.01	0.14	8.62	0.34	100.84	0.000	1.818	0.000	0.995	0.000	0.001	0.000	0.000	0.003	0.167	0.009	0.007	3.000	0.912	1.14	2.25	19.2	2.04	28.3	140	2291
MD110-DR06-161A 012	Ol	µXRF	MD110-DR06	161A	Pl-lherzolite	0.00	50.18	0.00	40.74	0.00	0.04	0.01	0.01	0.14	8.54	0.32	98.80	0.000	1.823	0.000	0.993	0.000	0.001	0.000	0.000	0.003	0.160	0.014	0.006	3.000	0.913	1.01	2.22	19.4	1.93	24.6	125	2113
MD110-DR06-161A 013	Ol	µXRF	MD110-DR06	161A	Pl-lherzolite	0.00	49.87	0.00	40.90	0.00	0.04	0.02	0.00	0.14	8.65	0.33	99.75	0.000	1.815	0.000	0.998	0.000	0.001	0.000	0.000	0.003	0.173	0.003	0.006	3.000	0.911							
MD110-DR06-161A 014	Ol	µXRF	MD110-DR06	161A	Pl-lherzolite	0.00	50.05	0.00	40.78	0.00	0.03	0.01	0.00	0.13	8.62	0.33	99.47	0.000	1.819	0.000	0.995	0.000	0.001	0.000	0.000	0.003	0.165	0.011	0.006	3.000	0.912	1.34	2.32	19.5	2.18	27.1	128	2161
MD110-DR06-161A 015	Ol	µXRF	MD110-DR06	161A	Pl-lherzolite	0.00	49.86	0.00	40.77	0.01	0.05	0.02	0.12	0.12	8.72	0.34	100.01	0.000	1.814	0.000	0.995	0.000	0.001	0.000	0.000	0.003	0.173	0.008	0.007	3.000	0.911	0.934	2.56	22.9	2.38	36.1	125	2108
MD110-DR06-161A-1	Ol	EPMA	MD110-DR06	161A	Pl-lherzolite	0.03	49.33	0.00	40.35	0.00	0.02	0.00	0.02	0.16	8.89		98.80	0.001	1.815	0.000	0.996	0.000	0.001	0.000	0.000	0.003	0.174	0.010	0.000	3.000	0.908							
MD110-DR06-161A-11	Ol	EPMA	MD110-DR06	161A	Pl-lherzolite	0.01	49.38	0.00	40.73	0.00	0.05	0.00	0.00	0.07	9.51		99.75	0.000	1.804	0.000	0.998	0.000	0.001	0.000	0.000	0.001	0.190	0.004	0.000	3.000	0.905	1.14	2.25	19.2	2.04	28.3	140	2291
MD110-DR06-161A-12	Ol	EPMA	MD110-DR06	161A	Pl-lherzolite	0.05	49.14	0.19	40.98	0.00	0.04	0.02	0.00	0.29	8.76		99.49	0.002	1.799	0.005	1.006	0.000	0.001	0.000	0.000	0.006	0.180	0.000	0.000	3.000	0.909	1.01	2.22	19.4	1.93	24.6	125	2113
MD110-DR06-161A-14	Ol	EPMA	MD110-DR06	161A	Pl-lherzolite	0.08	49.22	0.00	40.98	0.03	0.08	0.01	0.01	0.15	9.37		99.99	0.005	1.800	0.000	1.002	0.001	0.002	0.000	0.000	0.003	0.192	0.000	0.000	3.000	0.904	1.34	2.32	19.5	2.18	27.1	128	2161
MD110-DR06-161A-2	Ol	EPMA	MD110-DR06	161A	Pl-lherzolite	0.02	48.97	0.00	40.04	0.00	0.03	0.00	0.01	0.09	9.50		98.67	0.001	1.808	0.000	0.992	0.000	0.001	0.000	0.000	0.002	0.179	0.018	0.000	3.000	0.902							
MD110-DR06-161A-3	Ol	EPMA	MD110-DR06	161A	Pl-lherzolite	0.03	48.50	0.00	40.19	0.04	0.06	0.00	0.04	0.18	9.24		98.27	0.002	1.799	0.000	1.000	0.001	0.002	0.000	0.001	0.004	0.190	0.002	0.000	3.000	0.903	1.34	2.32	19.5	2.18	27.1	128	2161
MD110-DR06-161A-4	Ol	EPMA	MD110-DR06	161A	Pl-lherzolite	0.11	48.51	0.00	40.49	0.04	0.06	0.02	0.00	0.11	9.02		98.36	0.005	1.796	0.000	1.006	0.001	0.002	0.000	0.000	0.002	0.187	0.000	0.000	3.000	0.906							
MD110-DR06-161A-5	Ol	EPMA	MD110-DR06	161A	Pl-lherzolite	0.02	49.28	0.00	40.32	0.01	0.03	0.00	0.08	0.02	9.39		99.08	0.001	1.808	0.000	0.994	0.000	0.001	0.000	0.000	0.002	0.182	0.012	0.000	3.000	0.903	0.934	2.56	22.9	2.38	36.1	125	2108
MD110-DR06-161A-6	Ol	EPMA	MD110-DR06	161A	Pl-lherzolite	0.02	49.03	0.03	40.48	0.00	0.06	0.03	0.00	0.10	9.25		98.99	0.001	1.804	0.001	0.999	0.000	0.001	0.001	0.000	0.002	0.191	0.000	0.000	3.000	0.904							
MD110-DR06-161A-7	Ol	EPMA	MD110-DR06	161A	Pl-lherzolite	0.00	48.95	0.00	40.38	0.00	0.05	0.02	0.00	0.01	9.43		98.83	0.000	1.805	0.000	0.999	0.000	0.001	0.000	0.000	0.002	0.193	0.002	0.000	3.000	0.903							
MD110-DR06-161A-m 004	Ol	µXRF	MD110-DR06	161A	Pl-lherzolite	0.00	49.97	0.00	40.72	0.00	0.04	0.00	0.00	0.14	8.72	0.31	100.51	0.000	1.818	0.000	0.994	0.000	0.001	0.000	0.000	0.002	0.163	0.011	0.006	3.000	0.911							
MD110-DR06-161A-m 005	Ol	µXRF	MD110-DR06	161A	Pl-lherzolite	0.00	49.64	0.00	41.02	0.00	0.04	0.01	0.02	0.13	8.77	0.34	99.97	0.000	1.808	0.000	1.002	0.000	0.001	0.000	0.000	0.003	0.179	0.000	0.007	3.000	0.910	0.934	2.56	22.9	2.38	36.1	125	2108
MD110-DR06-161A-m 006	Ol	µXRF	MD110-DR06	161A	Pl-lherzolite	0.00	49.61	0.00	40.99	0.00	0.05	0.03	0.01	0.13	8.77	0.35	99.96	0.000	1.808	0.000	1.002	0.000	0.001	0.001	0.000	0.003	0.179	0.000	0.007	3.000	0.910							
MD110-DR06-161A-m 007	Ol	µXRF	MD110-DR06	161A	Pl-lherzolite	0.00	49.25	0.00	41.28	0.00	0.04	0.05	0.01	0.13	8.81	0.35	101.24	0.000	1.797	0.000	1.011	0.000	0.001	0.001	0.000	0.003	0.180	0.000	0.007	3.000	0.909							
MD110-DR06-161C 011	Ol	µXRF	MD110-DR06	161C	Pl-lherzolite	0.00	50.26	0.00	41.77	0.00	0.04	0.01	0.01	0.13	6.34	0.23	99.94	0.000	1.820	0.000	1.039	0.000	0.001	0.000	0.000	0.002	0.129	0.000	0.005	3.000	0.934							
MD110-DR06-161C 012	Ol	µXRF	MD110-DR06	161C	Pl-lherzolite	0.00	49.99	0.00	40.63	0.01	0.03	0.00	0.01	0.14	8.81	0.35	99.97	0.000	1.818	0.000	0.991	0.000	0.001	0.000	0.000	0.003	0.162	0.018	0.007	3.000	0.910	0.985	2.32	20.2	2.39	36.4	126	2133
MD110-DR06-161C 013	Ol	µXRF	MD110-DR06	161C	Pl-lherzolite	0.00	50.14	0.00	40.53	0.00	0.03	0.08	0.02	0.13	8.70	0.33	99.97	0.000	1.823	0.000	0.988	0.000	0.001	0.001	0.000	0.003	0.157	0.020	0.006	3.000	0.911	0.893	2.50	20.9	2.68	32.4	126	2125
MD110-DR06-161C 013	Ol	µXRF	MD110-DR06	161C	Pl-lherzolite	0.00	50.14	0.00	40.53	0.00	0.03	0.08	0.02	0.13	8.70	0.33	99.96	0.000	1.823	0.000	0.988	0.000	0.001	0.001	0.000	0.003	0.157	0.020	0.006	3.000	0.911	1.03	2.37	19.5	2.37	30.0	125	2154
MD110-DR06-161C 014	Ol	µXRF	MD110-DR06	161C	Pl-lherzolite	0.00	49.92	0.00	41.13	0.00	0.04	0.01	0.02	0.13	8.39	0.32	99.95	0.000	1.815	0.000	1.003	0.000	0.001	0.000	0.000	0.003	0.171	0.000	0.006	3.000	0.914	1.02	2.40	20.9	2.51	37.5	128	2181
MD110-DR06-161C 014	Ol	µXRF	MD110-DR06	161C	Pl-lherzolite	0.00	49.92	0.00	41.13	0.00	0.04	0.01	0.02	0.13	8.39	0.32	100.12	0.000	1.815	0.000	1.003	0.000	0.001	0.000	0.000	0.003	0.171	0.000	0.006	3.000	0.914	1.02	2.49	21.1	2.54	31.1	129	2210
MD110-DR06-161C 015	Ol	µXRF	MD110-DR06	161C	Pl-lherzolite	0.00	50.04	0.00	40.77	0.00	0.04	0.01	0.00	0.14	8.63	0.33	100.34	0.000	1.819	0.000	0.994	0.000	0.001	0.000	0.000	0.003	0.165	0.011	0.006	3.000	0.912							
MD110-DR06-161C 025	Ol	µXRF	MD110-DR06	161C	Pl-lherzolite	0.00	50.09	0.00	40.73	0.00	0.03	0.01	0.00	0.14	8.63	0.33	99.97	0.000	1.821	0.000	0.993	0.000	0.001	0.000	0.000	0.003	0.162	0.014	0.006	3.000	0.912	1.02	2.66	26.3	3.30	90.2	129	2197
MD110-DR06-161C 026	Ol	µXRF	MD110-DR06	161C	Pl-lherzolite	0.00	50.23	0.00	41.31	0.00	0.04	0.01	0.13	0.28	0.32	99.91	0.000	1.822	0.000	0.999	0.000	0.001	0.000	0.003	0.168	0.001	0.006	3.000	0.915	1.24	2.01	15.5	1.68	26.6	130	2219
MD110-DR06-161C 027	Ol	µXRF	MD110-DR06	161C	Pl-lherzolite	0.00	49.98	0.00	41.17	0.00	0.05	0.03	0.01	0.14	8.25	0.33	99.95	0.000	1.817	0.000	1.004	0.000	0.001	0.001	0.000	0.003	0.168	0.000	0.006	3.000	0.915							
MD110-DR06-161C-1a	Ol	EPMA	MD110-DR06	161C	Pl-lherzolite	0.01	49.04	0.01	40.69	0.00	0.04	0.00	0.02	0.12	9.57		99.50	0.000	1.798	0.000	1.001	0.000	0.001	0.000	0.000	0.002	0.197	0.000	0.000	3.000	0.901							
MD110-DR06-161C-25	Ol	EPMA	MD110-DR06	161C	Pl-lherzolite	0.00	49.34	0.00	42.30	0.00	0.06	0.00	0.05	0.05	9.40		101.20	0.000	1.782	0.000	1.025	0.000	0.002	0.000	0.001	0.001	0.190	0.000	0.000	3.000	0.903	1.02	2.66	26.3	3.30	90.2	129	2197
MD110-DR06-161C-40	Ol	EPMA	MD110-DR06	161C	Pl-lherzolite	0.00	49.37	0.05	41.49	0.01	0.06	0.00	0.02	0.06	9.41		100.47	0.000	1.793	0.001	1.011	0.000	0.002	0.000	0.000	0.001	0.192	0.000	0.000	3.000	0.903							
MD110-DR06-161C-42	Ol	EPMA	MD110-DR06	161C	Pl-lherzolite	0.00	48.82	0.02	42.13	0.00	0.05	0.01	0.00	0.12	8.87		100.02	0.000	1.782	0.001	1.032	0.000	0.001	0.000	0.000	0.002	0.182	0.000	0.000	3.000	0.908							
MD110-DR06-161C-59a	Ol	EPMA	MD110-DR06	161C	Pl-lherzolite	0.01	50.26	0.16	41.26	0.00	0.03	0.00	0.03	0.10	9.34		101.19	0.000	1.808	0.005	0.995	0.000	0.001	0.000	0.000	0.001	0.002	0.184	0.004	0.000	3.000	0.906							
MD110-DR06-161C-59b	Ol	EPMA	MD110-DR06	161C	Pl-lherzolite	0.00	50.60	0.00	40.76	0.04	0.06	0.00	0.06	0.19	8.80		100.51	0.000	1.827	0.000	0.987	0.001	0.002	0.000	0.000	0.001	0.004	0.152	0.026	0.000	3.000	0.911							
MD110-DR06-162 008	Ol	µXRF	MD110-DR06	162	Pl-lherzolite	0.00	50.23	0.00	41.11	0.00	0.05	0.07	0.02	0.14	8.05	0.29	100.43	0.000	1.823	0.000	1.001	0.000	0.001	0.002	0.000	0.003	0.164	0.006	0.006	3.000	0.917							
MD110-DR06-162 014	Ol	µXRF	MD110-DR06	162	Pl-lherzolite	0.00	49.87	0.00	40.95	0.01	0.15	0.01	0.01	0.13	8.52	0.32	100.75	0.000	1.814	0.000	0.999	0.000	0.004	0.000	0.000	0.003	0.172	0.002	0.006	3.000	0.913							
MD110-DR06-162b-8	Ol	EPMA	MD110-DR06	162B	Pl-lherzolite	0.03	50.08	0.01	41.52	0.03	0.04	0.03	0.00	0.26	9.24		101.24	0.001	1.802	0.000	1.002	0.001	0.001	0.001	0.000	0.005	0.187	0.000	0.000	3.000	0.906							
MD110-DR06-173 005	Ol	µXRF	MD110-DR06	173	Pl-lherzolite	0.00	50.10	0.00	40.79	0.01	0.04	0.01	0.02	0.11	8.54	0.34	100.71	0.000	1.821	0.000	0.994	0.000	0.001	0.000	0.000	0.002	0.163	0.011	0.007	3.000	0.913	1.32	1.67	11.6	1.31	27.0	130	2457
MD110-DR06-173 006

Annexes du chapitre n°3 - Classification des péridotites

Table 1 – Modal proportions of peridotites from the MD110-DR06 dredged point. The modal proportions were calculated with micro-XRF chemical mapping and phase isolation by determination of chemical properties. Modal proportion of olivine is calculated from olivine and serpentine representing the altered olivine (mesh structure), as well as orthopyroxene and bastite are counted for orthopyroxene, and chlorite and plagioclase are enumerated as plagioclase. Per cent alteration are calculated counting the modal proportion of serpentine (altered olivines), bastite (altered orthopyroxene) and altered chlorite (altered plagioclase).

	Olivine	Orthopyroxene	Clinopyroxene	Plagioclase	Spinel	Mg#	Alteration
159B	78.5 %	18.3 %	2.8 %		0.4%	0.9175	32 %
161A	70.1 %	24.1 %	2.8 %	2.5 %	0.5 %	0.9076	44 %
161C	60.5 %	28.7 %	5.1 %	5.5 %	0.3 %	0.9113	63 %
162B	74.5 %	19.4 %	2.5 %	3.3 %	0.2 %	0.9121	76 %
173	75.3 %	17.1 %	4.4 %	2.3 %	0.8 %	0.9111	73 %
B4	53.1 %	25.5 %	11.1 %	9.7 %	0.7 %	0.9068	45 %

Fig A – Mg# of olivine versus modal proportion olivine content in peridotites from the MD110-DR06 dredged point. Archean, Proterozoic and Phanerozoic fields are from Griffin *et al*, 1998b, modified after Boyd, 1996.

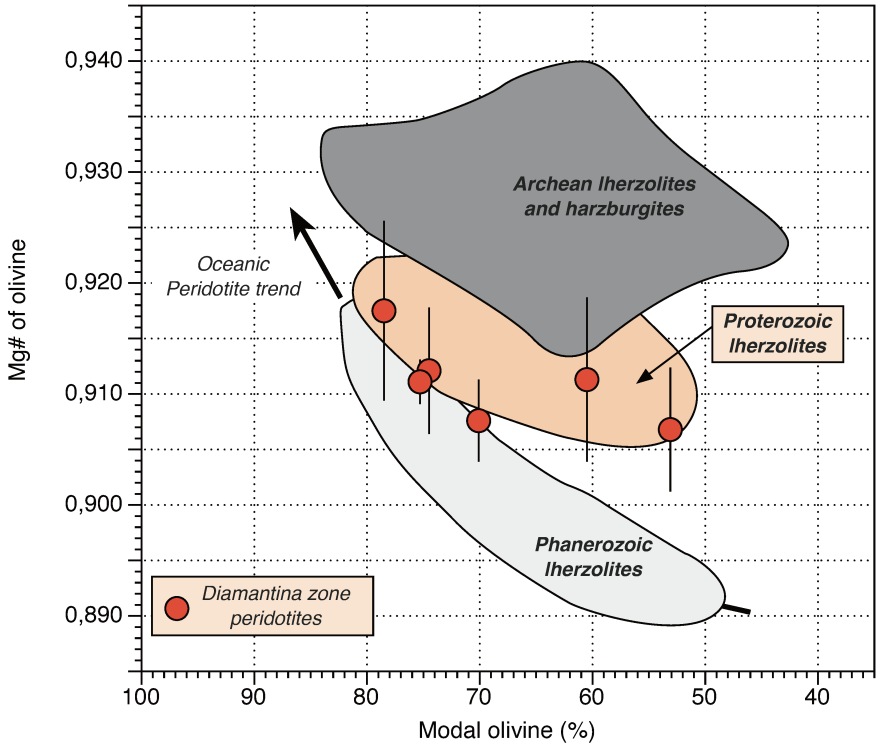


Table S1 - Major and trace elements compositions of clinopyroxene

Spectrum	MD110-DR01-	MD110-DR01-	MD110-DR10-	MD110-DR10-	MD110-DR01-	MD110-DR03t	MD110-DR01-	MD110-DR10-	MD110-DR10-
Campaign	MD110	MD110	MD110	MD110	MD110	MD110	MD110	MD110	MD110
Dredge point	DR01	DR01	DR10	DR10	DR01	DR03b	DR01	DR10	DR10
Thin section	067	067	312	312	067	101D	067	312	312
Na2O	1.16	1.16	0.09	0.09	0.51	0.35	0.72	0.20	0.20
MgO	10.94	10.94	18.55	18.55	12.79	16.74	12.34	18.55	18.55
Al2O3	8.20	8.20	3.00	3.00	6.32	4.25	5.63	3.43	3.43
SiO2	49.13	49.13	52.87	52.87	48.48	51.06	48.95	51.95	51.95
P2O5	0.09	0.09	0.01	0.01	0.03	0.03	0.02	0.00	0.00
K2O	0.37	0.37	0.00	0.00	0.03	0.00	0.03	0.19	0.19
CaO	19.66	19.66	20.28	20.28	20.64	21.02	20.51	19.72	19.72
TiO2	1.61	1.61	0.18	0.18	1.84	0.58	1.72	0.24	0.24
Cr2O3	0.22	0.22	0.50	0.50	0.46	0.72	0.10	0.53	0.53
MnO	0.18	0.18	0.17	0.17	0.16	0.12	0.24	0.19	0.19
FeO	8.30	8.30	4.26	4.26	8.58	5.04	9.58	4.91	4.91
NiO									
Total	99.86	99.86	99.91	99.91	99.84	99.91	99.84	99.91	99.91
Spot Size (µm)	40	40	40	40	40	40	40	40	40
Li	3.508	3.993	0.896	1.118	3.754	0.793	2.483	1.116	1.421
B									
P	181.871	225.133	155.456	100.858	84.011	<LOD	66.744	363.874	403.613
S									
K									
Sc	183.356	200.777	75.842	82.007	178.479	104.520	179.621	97.682	97.392
Ti	13205.482	12000.840	1060.437	1086.532	11968.472	2963.327	10433.914	1386.735	1504.357
V	799.173	806.063	245.591	261.919	763.312	321.083	808.938	306.127	330.797
Cr	1430.206	2015.049	3582.809	3557.817	1319.244	4647.035	927.092	4189.842	3472.735
Mn	1284.761	1355.114	905.654	948.344	1367.559	981.653	1523.781	1106.505	1055.223
Fe									
Co	37.861	39.130	36.194	39.441	41.058	36.726	44.814	41.854	42.449
Ni	63.809	72.766	191.299	194.441	62.517	115.608	57.551	195.822	185.975
Cu	0.995	1.234	1.401	1.237	1.103	1.262	0.987	1.332	1.425
Zn	34.664	35.922	19.713	19.503	38.124	22.953	44.194	23.228	23.030
Ga									
As									
Rb	<LOD	<LOD	<LOD	<LOD	0.025	<LOD	<LOD	<LOD	<LOD
Sr	17.431	16.890	7.152	7.287	17.254	17.733	18.065	6.605	6.425
Y	44.314	51.002	6.255	6.081	44.249	14.182	39.268	8.566	9.603
Zr	104.808	103.263	2.434	2.440	86.494	12.623	65.223	3.443	4.304
Nb	0.345	0.392	0.047	0.063	0.235	0.094	0.146	0.055	0.040
Mo	0.424	0.350	0.199	0.218	0.386	0.261	0.403	0.313	0.252
Ag									
Sn									
Sb	0.994	0.894	0.249	0.234	0.830	0.311	0.836	0.337	0.233
Cs	<LOD	<LOD	<LOD	<LOD	<LOD	<LOD	<LOD	<LOD	<LOD
Ba	<LOD	<LOD	<LOD	<LOD	0.062	0.092	<LOD	<LOD	<LOD
La	1.452	1.699	0.072	0.069	1.286	0.631	1.235	0.090	0.102
Ce	6.457	7.223	0.378	0.376	5.875	2.417	5.463	0.447	0.516
Pr	1.480	1.632	0.097	0.111	1.324	0.524	1.221	0.162	0.161
Nd	10.601	11.256	0.798	0.813	8.985	3.302	8.784	1.086	1.101
Sm	4.550	4.905	0.483	0.445	4.548	1.313	4.028	0.487	0.683
Eu	1.481	1.609	0.200	0.203	1.400	0.557	1.319	0.256	0.271
Gd	6.874	7.388	0.671	0.904	6.573	2.177	6.442	0.999	1.260
Tb	1.286	1.413	0.147	0.143	1.147	0.410	1.112	0.196	0.254
Dy	7.780	9.384	1.095	1.031	7.785	2.581	7.752	1.418	1.436
Ho	1.693	1.946	0.247	0.236	1.698	0.544	1.442	0.355	0.379
Er	4.922	5.411	0.678	0.795	4.719	1.482	4.075	0.901	1.095
Tm	0.645	0.747	0.094	0.113	0.687	0.222	0.646	0.140	0.166
Yb	4.698	5.217	0.741	0.701	4.370	1.366	4.033	0.812	1.103
Lu	0.597	0.675	0.107	0.116	0.597	0.190	0.562	0.130	0.146
Hf	4.631	4.522	0.156	0.165	4.136	0.531	2.876	0.221	0.238
Ta	0.075	0.071	<LOD	<LOD	0.045	<LOD	0.027	<LOD	<LOD
Au									
Tl									
Pb	<LOD	0.026	<LOD	<LOD	0.016	0.011	0.022	<LOD	<LOD
Bi	<LOD	<LOD	<LOD	0.004	<LOD	<LOD	<LOD	<LOD	<LOD
Th	0.034	0.038	<LOD	<LOD	0.016	0.005	0.011	<LOD	0.003
U	<LOD	<LOD	<LOD	<LOD	<LOD	<LOD	<LOD	<LOD	<LOD

Spectrum	MD110-DR10-312	MD110-DR10-312	MD110-DR10-312	MD110-DR01-067	MD110-DR10-312	MD110-DR01-067	MD110-DR10-312	MD110-DR10-312	MD110-DR10-312
Campaign	MD110	MD110	MD110	MD110	MD110	MD110	MD110	MD110	MD110
Dredge point	DR10	DR10	DR10	DR01	DR10	DR01	DR10	DR10	DR10
Thin section									
Na2O	0.15	0.15	0.20	0.27	0.28	0.27	0.09	0.30	0.30
MgO	18.75	18.75	18.55	13.37	18.30	13.37	18.55	18.20	18.20
Al2O3	3.27	3.27	3.43	4.72	2.98	4.72	3.00	2.42	2.42
SiO2	51.81	51.81	51.95	48.79	52.83	48.79	52.87	52.80	52.80
P2O5	0.00	0.00	0.00	0.03	0.01	0.03	0.01	0.01	0.01
K2O	0.10	0.10	0.19	0.09	0.00	0.09	0.00	0.00	0.00
CaO	20.03	20.03	19.72	21.40	19.78	21.40	20.28	18.16	18.16
TiO2	0.23	0.23	0.24	1.87	0.21	1.87	0.18	0.29	0.29
Cr2O3	0.66	0.66	0.53	0.18	0.54	0.18	0.50	0.13	0.13
MnO	0.12	0.12	0.19	0.18	0.12	0.18	0.17	0.20	0.20
FeO	4.74	4.74	4.91	8.94	4.84	8.94	4.26	7.40	7.40
NiO									
Total	99.86	99.86	99.91	99.85	99.90	99.85	99.91	99.92	99.92
Spot Size (µm)	40	40	40	40	40	40	40	40	40
Li	1.391	1.329	1.176	1.771	1.413	1.913	0.698	0.870	1.123
B									
P	253.769	306.049	254.094	149.862	309.017	182.693	168.809	236.112	204.613
S									
K									
Sc	97.043	91.165	92.145	193.286	86.983	191.352	80.690	100.998	102.292
Ti	1497.127	1360.813	1426.216	11303.765	1304.193	11951.295	1174.833	1896.171	1885.891
V	335.732	302.326	308.492	902.990	300.809	847.166	253.455	377.445	367.759
Cr	8768.185	8787.707	3855.751	1481.812	2982.421	1534.220	3169.754	712.231	719.766
Mn	1086.731	1020.266	1044.431	1380.703	1080.444	1447.205	898.278	1549.606	1608.987
Fe									
Co	43.660	40.604	42.921	41.330	41.784	36.403	36.323	51.985	53.959
Ni	260.880	241.665	190.562	56.317	168.841	48.859	197.459	123.143	130.233
Cu	1.815	1.476	1.534	1.009	1.536	1.093	1.297	1.179	1.366
Zn	23.573	21.264	22.755	40.940	22.846	36.631	19.323	36.641	36.518
Ga									
As									
Rb	<LOD	<LOD	<LOD	<LOD	<LOD	<LOD	<LOD	<LOD	<LOD
Sr	7.364	7.150	6.656	16.734	5.655	16.316	6.993	6.122	5.918
Y	7.702	7.700	8.657	42.065	7.650	40.691	5.988	11.610	12.351
Zr	3.768	3.508	3.780	86.350	2.834	89.352	2.233	4.057	4.474
Nb	0.120	0.128	0.064	0.317	0.037	0.320	0.037	0.020	0.013
Mo	0.332	0.256	0.420	0.392	0.272	0.434	0.220	0.361	0.388
Ag									
Sn									
Sb	0.265	0.350	0.399	0.900	0.308	0.826	0.377	0.304	0.344
Cs	<LOD	<LOD	<LOD	<LOD	<LOD	<LOD	<LOD	<LOD	<LOD
Ba	<LOD	<LOD	<LOD	0.102	0.051	0.091	<LOD	<LOD	0.078
La	0.110	0.091	0.094	1.360	0.077	1.280	0.063	0.131	0.125
Ce	0.469	0.450	0.504	6.104	0.362	6.415	0.378	0.586	0.613
Pr	0.105	0.120	0.128	1.319	0.116	1.402	0.097	0.173	0.190
Nd	1.093	1.019	1.091	9.889	0.954	9.944	0.723	1.266	1.333
Sm	0.578	0.577	0.616	4.739	0.565	4.306	0.384	0.723	0.770
Eu	0.252	0.222	0.244	1.460	0.249	1.384	0.182	0.293	0.314
Gd	0.946	0.891	1.026	6.982	0.952	6.755	0.837	1.305	1.334
Tb	0.183	0.195	0.192	1.210	0.205	1.193	0.142	0.268	0.260
Dy	1.387	1.247	1.357	7.688	1.477	8.108	1.064	2.053	2.013
Ho	0.289	0.287	0.313	1.649	0.302	1.744	0.240	0.462	0.472
Er	0.901	0.897	0.904	4.747	0.812	4.522	0.762	1.287	1.435
Tm	0.129	0.129	0.177	0.612	0.138	0.614	0.115	0.210	0.199
Yb	0.757	0.744	0.921	4.068	0.776	4.149	0.667	1.226	1.285
Lu	0.140	0.111	0.150	0.582	0.133	0.625	0.087	0.177	0.195
Hf	0.193	0.245	0.220	4.027	0.171	4.056	0.144	0.182	0.230
Ta	<LOD	<LOD	<LOD	0.073	<LOD	0.051	<LOD	<LOD	<LOD
Au									
Tl									
Pb	<LOD	<LOD	<LOD	<LOD	<LOD	0.025	0.015	<LOD	<LOD
Bi	<LOD	<LOD	<LOD	<LOD	<LOD	<LOD	<LOD	<LOD	<LOD
Th	<LOD	<LOD	<LOD	0.026	<LOD	0.021	<LOD	0.007	<LOD
U	<LOD	<LOD	<LOD	<LOD	<LOD	<LOD	<LOD	<LOD	<LOD

Spectrum	MD110-DR01-	MD110-DR03b	5A9 008	MD110-DR08-	MD110-DR08-	MD110-DR08-	MD110-DR08-	MD110-DR08-	MD110-DR08-
Campaign	MD110	MD110	MD80	MD110	MD110	MD110	MD110	MD110	MD110
Dredge point	DR01	DR03b	DR5	DR08	DR08	DR08	DR08	DR08	DR08
Thin section	067	101D	A9	296	296	296	296	296	296
Na2O	0.51	0.35	0.19	0.71	1.14	0.71	0.62	0.62	0.62
MgO	12.79	16.74	15.94	15.59	15.61	15.59	15.73	15.73	15.73
Al2O3	6.32	4.25	5.94	6.24	6.11	6.24	5.73	5.73	5.73
SiO2	48.48	51.06	49.22	50.24	50.18	50.24	50.51	50.51	50.51
P2O5	0.03	0.03	0.02	0.01	0.01	0.01	0.01	0.01	0.01
K2O	0.03	0.00	0.01	0.11	0.00	0.11	0.01	0.01	0.01
CaO	20.64	21.02	22.29	21.98	21.93	21.98	22.20	22.20	22.20
TiO2	1.84	0.58	1.07	0.85	0.77	0.85	0.86	0.86	0.86
Cr2O3	0.46	0.72	1.13	0.15	0.16	0.15	0.17	0.17	0.17
MnO	0.16	0.12	0.09	0.13	0.11	0.13	0.11	0.11	0.11
FeO	8.58	5.04	3.99	3.85	3.86	3.85	3.93	3.93	3.93
NiO									
Total	99.84	99.91	99.89	99.85	99.88	99.85	99.87	99.87	99.87
Spot Size (μm)	40	40	40	40	40	40	40	40	40
Li	3.849	0.901	1.35	0.988	1.133	0.898	1.149	1.105	0.951
B			15.12						
P	50.950	<LOD		<LOD	179.290	20.868	75.730	183.906	106.422
S			161.04						
K			5.03						
Sc	175.562	112.296	132.43	60.247	88.611	69.643	57.321	56.668	59.777
Ti	10343.634	3071.134	6370.13	4122.955	4811.034	5097.353	3853.497	3999.570	3967.253
V	735.280	328.890	380.31	362.780	528.022	460.460	366.727	370.752	414.055
Cr	1023.310	4854.166	7639.00	941.148	1330.164	1149.012	1037.766	971.949	1006.711
Mn	1465.466	994.419	571.76	892.583	990.745	881.268	933.865	937.430	966.010
Fe			30454.94						
Co	40.236	37.615	31.14	27.985	30.742	28.355	27.302	27.453	37.727
Ni	58.176	113.208	206.09	275.830	352.464	312.877	280.688	286.251	1679.368
Cu	0.942	1.125	0.76	0.602	1.175	0.719	0.633	0.589	1087.051
Zn	39.841	24.495	25.11	17.632	20.315	18.689	18.405	17.892	18.634
Ga			5.92						
As			1.25						
Rb	0.157	<LOD	0.02	<LOD	<LOD	<LOD	<LOD	<LOD	<LOD
Sr	17.301	18.313	49.34	34.698	36.352	39.629	32.835	31.539	32.159
Y	40.973	14.384	13.57	23.919	28.537	28.449	21.892	21.974	23.318
Zr	70.260	12.233	38.60	29.151	38.809	37.159	26.466	26.758	29.476
Nb	0.153	0.114	0.41	0.940	0.272	0.605	1.081	0.887	0.644
Mo	0.413	0.217	0.33	0.229	0.300	0.196	0.293	0.229	0.274
Ag			0.02						
Sn			0.30						
Sb	0.662	0.319	0.00	0.439	0.537	0.554	0.493	0.390	1.563
Cs	<LOD	<LOD	0.00	<LOD	<LOD	<LOD	<LOD	<LOD	<LOD
Ba	<LOD	0.029	0.04	<LOD	0.433	<LOD	<LOD	0.140	0.067
La	1.202	0.569	3.11	1.496	1.608	1.446	1.537	1.445	1.530
Ce	5.133	2.420	12.09	10.446	7.925	11.016	8.200	7.824	8.452
Pr	1.369	0.523	2.05	1.410	1.423	1.487	1.299	1.242	1.270
Nd	8.716	2.977	11.49	7.503	8.544	8.655	7.603	7.059	7.450
Sm	4.321	1.242	3.56	2.963	3.190	3.632	3.062	2.522	3.054
Eu	1.275	0.550	1.29	0.758	0.685	0.689	0.741	0.746	0.675
Gd	6.335	2.103	3.92	3.915	4.749	4.660	3.414	3.767	4.022
Tb	1.157	0.420	0.69	0.716	0.846	0.791	0.567	0.642	0.674
Dy	7.743	2.529	3.47	4.335	5.291	5.238	4.256	4.268	4.209
Ho	1.579	0.501	0.67	0.944	1.058	1.109	0.828	0.942	0.910
Er	4.902	1.495	1.94	2.587	3.050	2.703	2.418	2.284	2.400
Tm	0.617	0.215	0.22	0.370	0.424	0.428	0.361	0.342	0.377
Yb	4.236	1.300	1.57	2.113	2.360	2.557	2.200	2.254	2.283
Lu	0.591	0.182	0.22	0.300	0.293	0.339	0.279	0.287	0.317
Hf	3.348	0.523	2.67	0.865	1.515	1.306	0.882	0.935	1.137
Ta	0.024	0.010	0.09	0.119	0.057	0.128	0.081	0.084	0.076
Au			0.00						
Tl			0.00						
Pb	0.033	<LOD	0.12	0.021	0.092	0.042	0.031	0.034	3.128
Bi	<LOD	<LOD	0.00	<LOD	<LOD	<LOD	<LOD	<LOD	0.037
Th	0.010	0.014	0.17	0.179	0.068	0.131	0.147	0.168	0.158
U	<LOD	<LOD	0.06	0.051	0.046	0.045	0.045	0.045	0.043

Spectrum	MD110-DR08-	MD110-DR08-	MD110-DR08-	MD110-DR08-	MD110-DR08-	MD110-DR08-	MD110-DR08-	MD110-DR08-	MD110-DR08-
Campaign	MD110	MD110	MD110	MD110	MD110	MD110	MD110	MD110	MD110
Dredge point	DR08	DR08	DR08	DR08	DR08	DR08	DR08	DR08	DR08
Thin section	296	296	296	296	296	296	296	296	296
Na2O	0.56	0.62	0.62	0.76	0.62	0.56	0.71	0.56	0.62
MgO	15.47	15.22	15.22	15.37	15.22	15.47	15.59	15.47	15.73
Al2O3	6.70	6.56	6.56	6.20	6.56	6.70	6.24	6.70	5.73
SiO2	50.02	50.18	50.18	50.97	50.18	50.02	50.24	50.02	50.51
P2O5	0.01	0.00	0.00	0.00	0.00	0.01	0.01	0.01	0.01
K2O	0.06	0.03	0.03	0.00	0.03	0.06	0.11	0.06	0.01
CaO	21.74	21.78	21.78	21.50	21.78	21.74	21.98	21.74	22.20
TiO2	0.78	0.74	0.74	0.72	0.74	0.78	0.85	0.78	0.86
Cr2O3	0.19	0.17	0.17	0.15	0.17	0.19	0.15	0.19	0.17
MnO	0.12	0.12	0.12	0.13	0.12	0.12	0.13	0.12	0.11
FeO	4.24	4.27	4.27	4.08	4.27	4.24	3.85	4.24	3.93
NiO									
Total	99.88	99.69	99.69	99.88	99.69	99.88	99.85	99.88	99.87
Spot Size (µm)	40	40	40	40	40	40	40	40	40
Li	1.133	1.423	1.279	1.235	1.291	1.372	0.939	1.079	1.187
B									
P	111.785	181.242	139.222	100.057	111.544	31.158	45.844	<LOD	137.393
S									
K									
Sc	68.035	63.648	67.132	53.816	68.669	79.389	65.472	79.532	54.781
Ti	4731.674	4789.555	5187.757	4088.734	4926.017	5966.115	4621.747	5771.217	3822.117
V	438.697	459.109	477.034	383.201	439.382	507.664	431.394	510.166	389.512
Cr	1099.185	1192.768	1113.656	1061.831	1151.502	1253.552	1086.957	1222.787	978.267
Mn	981.532	1058.039	1066.881	957.694	1103.903	970.227	872.689	977.557	915.229
Fe									
Co	30.560	34.581	30.805	27.188	30.976	31.477	28.029	31.454	26.467
Ni	311.298	334.967	311.501	288.194	309.130	321.640	294.266	316.692	310.167
Cu	0.675	1.033	0.963	0.933	0.826	0.751	0.692	0.895	0.688
Zn	19.630	21.389	20.072	18.481	20.958	19.125	18.664	20.767	18.152
Ga									
As									
Rb	<LOD	0.102	<LOD	0.466	<LOD	<LOD	<LOD	<LOD	<LOD
Sr	46.907	43.729	42.138	21.371	42.360	45.038	43.172	43.318	33.905
Y	27.177	27.965	28.248	22.681	28.425	31.636	25.316	29.812	22.446
Zr	33.909	32.866	35.916	23.677	35.124	43.989	31.773	42.331	27.387
Nb	0.870	1.068	0.768	0.973	0.911	0.738	0.852	0.612	0.935
Mo	0.315	0.233	0.253	0.215	0.297	0.260	0.189	0.213	0.194
Ag									
Sn									
Sb	0.578	0.652	0.663	0.407	0.529	0.413	0.612	0.480	0.520
Cs	<LOD	<LOD	<LOD	<LOD	<LOD	<LOD	<LOD	<LOD	<LOD
Ba	0.088	0.153	0.159	0.427	<LOD	<LOD	0.094	<LOD	0.179
La	1.689	1.742	1.596	1.582	1.649	1.766	1.557	1.532	1.474
Ce	11.257	10.778	10.814	5.336	10.710	12.017	10.977	11.414	8.575
Pr	1.517	1.598	1.465	1.262	1.605	1.648	1.508	1.533	1.432
Nd	8.868	9.285	9.609	7.021	8.863	9.988	8.056	9.016	7.417
Sm	3.321	3.514	3.794	2.730	3.739	3.625	3.042	3.332	2.723
Eu	0.710	0.906	0.831	0.807	0.880	0.839	0.795	0.794	0.790
Gd	4.365	4.586	4.625	3.707	4.845	5.161	4.025	5.201	3.729
Tb	0.788	0.863	0.842	0.679	0.863	0.908	0.778	0.883	0.615
Dy	4.912	5.436	5.177	4.048	5.032	5.701	4.784	5.597	3.862
Ho	1.045	1.154	1.203	0.844	1.108	1.281	0.960	1.186	0.920
Er	2.705	2.936	2.809	2.569	3.091	3.548	2.696	3.310	2.250
Tm	0.394	0.427	0.472	0.344	0.436	0.486	0.386	0.498	0.336
Yb	2.511	2.448	2.580	2.055	2.543	2.717	2.492	2.785	2.038
Lu	0.365	0.373	0.372	0.298	0.365	0.319	0.316	0.362	0.259
Hf	1.034	1.062	1.059	0.713	1.100	1.376	1.045	1.349	0.945
Ta	0.095	0.138	0.130	0.067	0.116	0.131	0.092	0.131	0.078
Au									
Tl									
Pb	0.025	0.028	0.054	0.040	0.058	<LOD	0.074	0.036	0.039
Bi	<LOD	<LOD	<LOD	<LOD	<LOD	<LOD	<LOD	<LOD	<LOD
Th	0.176	0.162	0.148	0.137	0.136	0.155	0.144	0.102	0.142
U	0.043	0.042	0.041	0.041	0.040	0.038	0.037	0.034	0.031

Spectrum	MD110-DR08-296	MD110-DR08-296	MD110-DR08-296	MD110-DR08-296	MD110-DR08-296	5A15 001	5A33-1 007	MD110-DR10-312	5A9 009
Campaign	MD110	MD110	MD110	MD110	MD110	MD80	MD80	MD110	MD80
Dredge point	DR08	DR08	DR08	DR08	DR08	DR5	DR5	DR10	DR5
Thin section						A15	A33-1		A9
Na2O	0.62	0.76	1.14	0.76	0.62	0.27	0.39	0.30	0.33
MgO	15.73	15.37	15.61	15.37	15.73	15.44	15.35	18.20	16.94
Al2O3	5.73	6.20	6.11	6.20	5.73	6.00	6.39	2.42	3.79
SiO2	50.51	50.97	50.18	50.97	50.51	49.39	48.77	52.80	50.67
P2O5	0.01	0.00	0.01	0.00	0.01	0.07	0.03	0.01	0.01
K2O	0.01	0.00	0.00	0.00	0.01	0.07	0.09	0.00	0.02
CaO	22.20	21.50	21.93	21.50	22.20	22.17	21.65	18.16	22.31
TiO2	0.86	0.72	0.77	0.72	0.86	1.34	1.50	0.29	0.89
Cr2O3	0.17	0.15	0.16	0.15	0.17	0.40	0.31	0.13	0.86
MnO	0.11	0.13	0.11	0.13	0.11	0.12	0.11	0.20	0.11
FeO	3.93	4.08	3.86	4.08	3.93	4.63	5.28	7.40	4.00
NiO									
Total	99.87	99.88	99.88	99.88	99.87	99.90	99.88	99.92	99.94
Spot Size (µm)	40	40	40	40	40	40	40	40	40
Li	1.155	1.048	0.941	0.733	0.762	3.31	0.77	1.267	0.55
B						12.73	15.30		15.33
P	146.813	91.383	289.495	64.984	203.206			174.955	
S						196.60	137.86		160.65
K						791.48	3.75		4.17
Sc	58.076	60.748	74.722	60.493	58.759	142.67	118.21	105.330	101.84
Ti	3966.451	4664.476	4748.701	4574.530	3913.767	9528.25	5155.98	1932.220	4106.92
V	380.720	449.153	483.428	419.013	406.951	576.00	328.54	378.414	278.53
Cr	968.030	1164.676	1138.051	1087.243	1004.246	430.15	1370.16	833.402	4981.49
Mn	915.622	977.460	949.486	912.984	863.868	671.07	868.61	1632.301	590.31
Fe						32668.20	45042.28		29636.18
Co	27.380	30.423	28.119	30.320	44.598	41.21	40.65	56.741	31.29
Ni	288.145	298.936	307.831	303.814	4255.362	181.77	157.33	129.051	204.04
Cu	0.631	0.671	0.676	0.709	1486.525	10.81	0.76	1.727	0.74
Zn	16.646	17.911	17.512	18.435	15.922	38.30	34.61	35.190	24.75
Ga						13.70	5.00		4.01
As						1.04	1.44		1.04
Rb	<LOD	0.050	<LOD	<LOD	<LOD	1.64	0.02	<LOD	0.01
Sr	34.003	38.892	30.179	38.068	30.972	57.51	54.91	6.622	40.90
Y	22.986	25.149	25.565	24.046	22.281	11.01	15.94	11.985	9.44
Zr	27.321	29.843	32.101	30.611	29.774	31.16	37.96	5.167	20.84
Nb	1.105	0.767	0.540	0.805	0.310	0.94	0.26	<LOD	0.22
Mo	0.264	0.224	0.214	0.244	0.247	0.20	0.49	0.388	0.32
Ag						<LOD	0.00		0.01
Sn						0.30	0.27		0.23
Sb	0.544	0.542	0.434	0.553	1.178	<LOD	0.00	0.288	0.00
Cs	<LOD	<LOD	<LOD	<LOD	<LOD	0.05	0.00	<LOD	0.00
Ba	<LOD	0.316	0.029	0.050	<LOD	10.55	0.06	0.110	0.09
La	1.673	1.539	1.387	1.592	1.252	1.67	2.79	0.147	1.94
Ce	8.400	9.664	7.062	9.054	7.607	5.31	10.47	0.658	7.36
Pr	1.468	1.442	1.341	1.305	1.089	0.89	2.14	0.182	1.28
Nd	7.751	7.767	7.614	7.322	7.291	5.63	10.47	1.441	7.74
Sm	2.668	2.969	3.172	3.128	2.551	1.71	3.17	0.802	2.58
Eu	0.904	0.790	0.661	0.767	0.556	0.53	1.04	0.307	0.81
Gd	3.666	4.174	4.271	3.961	3.455	1.85	3.41	1.396	2.54
Tb	0.712	0.753	0.753	0.721	0.597	0.25	0.50	0.296	0.43
Dy	4.160	4.732	4.976	4.473	4.027	1.67	2.40	2.183	2.39
Ho	0.873	0.984	1.014	0.948	0.830	0.31	0.49	0.429	0.44
Er	2.340	2.669	2.612	2.379	2.354	0.86	1.56	1.501	1.35
Tm	0.335	0.404	0.425	0.368	0.355	0.10	0.14	0.182	0.16
Yb	2.188	2.438	2.500	2.466	1.911	0.80	1.01	1.390	1.01
Lu	0.328	0.262	0.336	0.286	0.234	0.11	0.13	0.207	0.14
Hf	0.978	0.867	1.154	0.924	1.069	1.48	1.44	0.265	1.39
Ta	0.083	0.075	0.087	0.092	0.060	0.06	0.03	<LOD	0.02
Au						<LOD	0.00		0.00
Tl						0.01	0.00		0.00
Pb	0.017	0.026	0.035	0.040	9.603	0.10	0.03	<LOD	0.03
Bi	<LOD	<LOD	<LOD	<LOD	0.061	<LOD	0.00	<LOD	0.00
Th	0.113	0.123	0.110	0.105	0.100	0.08	0.06	0.005	0.05
U	0.031	0.030	0.027	0.027	0.024	0.02	0.01	0.013	0.01

Spectrum	5A9 010	MD110-DR01-	5A29 003	5A33-1 003	5B9 003	MD110-DR01-	5A33-1 004	5A29 005	MD110-DR03b
Campaign	MD80	MD110	MD80	MD80	MD80	MD110	MD80	MD80	MD110
Dredge point	DR5	DR01	DR5	DR5	DR5	DR01	DR5	DR5	DR03b
Thin section	A9	067	A29	A33-1	B9	067	A33-1	A29	102C
Na2O	0.29	0.72	0.25	0.42	0.31	0.27	0.25	0.36	0.38
MgO	15.89	12.34	17.10	15.95	14.90	13.37	16.00	16.17	17.74
Al2O3	5.67	5.63	3.46	5.97	6.81	4.72	5.70	5.20	3.07
SiO2	48.81	48.95	51.51	48.71	47.40	48.79	49.12	49.77	52.12
P2O5	0.01	0.02	0.03	0.02	0.02	0.03	0.01	0.01	0.01
K2O	0.01	0.03	0.03	0.01	0.05	0.09	0.05	0.01	0.01
CaO	22.20	20.51	22.04	22.15	22.31	21.40	22.27	22.48	20.36
TiO2	1.64	1.72	0.76	1.40	2.09	1.87	1.30	1.01	0.42
Cr2O3	0.93	0.10	0.37	0.85	0.48	0.18	0.87	0.74	0.50
MnO	0.12	0.24	0.10	0.10	0.11	0.18	0.09	0.09	0.14
FeO	4.36	9.58	4.17	4.34	5.40	8.94	4.24	4.01	5.13
NiO									
Total	99.94	99.84	99.81	99.91	99.89	99.85	99.91	99.85	99.89
Spot Size (µm)	40	40	40	40	40	40	40	40	40
Li	0.75	2.033	0.28	0.46	<LOD	2.189	0.15	0.61	0.778
B	14.07		16.56	15.17	11.68		18.53	16.23	
P		141.168				208.090			369.450
S	152.79		151.17	114.27	126.27		147.21	141.50	
K	9.30		3.67	4.38	4.54		6.19	6.06	
Sc	120.41	161.278	104.91	140.94	156.90	222.068	130.71	111.89	94.063
Ti	5950.22	9294.912	4717.20	7632.07	9857.41	14143.329	6838.31	5593.85	2467.535
V	364.06	756.272	291.06	431.81	462.71	899.795	410.52	342.06	285.493
Cr	4840.04	529.060	3093.76	3669.42	2666.80	2613.822	5084.62	4637.84	3583.965
Mn	640.51	1695.801	551.22	655.04	649.62	1451.214	687.39	505.66	1109.323
Fe	28303.96		24988.94	39083.41	35751.34		39784.73	25275.60	
Co	30.00	41.579	28.65	34.10	24.76	41.499	37.99	28.33	39.348
Ni	166.90	52.045	156.33	160.51	106.46	63.657	223.47	169.05	127.472
Cu	1.36	1.256	0.58	0.77	0.51	1.494	0.77	0.69	1.820
Zn	22.95	47.638	24.60	27.50	19.07	41.464	29.18	23.14	27.838
Ga	6.30		3.37	6.53	4.64		7.17	4.64	
As	0.94		0.97	1.29	0.71		1.39	1.25	
Rb	0.02	<LOD	-1.87	0.02	0.02	<LOD	0.02	0.02	<LOD
Sr	43.64	17.481	37.55	57.73	30.57	17.155	67.26	43.29	12.876
Y	12.69	43.427	8.80	17.63	10.56	52.621	17.13	11.69	13.170
Zr	37.14	61.417	20.67	57.27	53.73	108.785	52.61	31.37	9.336
Nb	0.34	0.108	0.17	0.51	0.55	0.442	0.47	0.29	0.141
Mo	0.39	0.607	0.28	0.35	0.20	0.491	0.38	0.27	0.338
Ag	0.00		0.02	0.01	<LOD		0.00	0.01	
Sn	0.31		0.18	0.46	0.30		0.48	0.34	
Sb	0.01	0.667	0.01	0.00	<LOD	1.093	0.02	0.00	0.404
Cs	0.00	<LOD	0.00	0.00	0.00	<LOD	0.00	0.00	<LOD
Ba	4.52	2.261	0.04	0.03	0.04	<LOD	0.14	0.04	0.683
La	2.62	1.283	1.26	3.11	1.90	1.636	3.00	1.70	0.609
Ce	9.87	5.540	4.05	10.24	7.24	7.460	10.22	5.66	2.286
Pr	1.72	1.312	0.81	2.02	1.16	1.813	2.03	1.11	0.487
Nd	9.59	8.757	4.62	10.11	8.47	12.067	10.38	6.02	3.072
Sm	3.12	3.803	1.28	3.14	2.10	5.281	3.31	1.75	1.201
Eu	1.04	1.308	0.42	0.97	0.60	1.903	1.00	0.54	0.481
Gd	3.35	6.792	1.50	3.31	2.16	8.452	3.69	1.94	2.097
Tb	0.48	1.156	0.22	0.48	0.28	1.497	0.49	0.30	0.369
Dy	2.81	7.635	1.22	2.65	1.90	9.695	2.71	1.74	2.121
Ho	0.58	1.588	0.24	0.54	0.38	2.119	0.50	0.33	0.505
Er	1.61	4.458	0.60	1.47	0.95	5.697	1.52	0.89	1.496
Tm	0.19	0.658	0.08	0.15	0.13	0.806	0.15	0.10	0.180
Yb	1.19	4.204	0.45	1.00	0.94	5.383	0.96	0.68	1.231
Lu	0.16	0.577	0.07	0.15	0.12	0.707	0.14	0.10	0.167
Hf	2.05	2.560	0.69	1.95	2.00	5.288	1.76	1.02	0.455
Ta	0.05	0.015	0.01	0.06	0.12	0.083	0.05	0.03	0.010
Au	0.00		0.00	0.00	<LOD		0.00	0.00	
Tl	0.01		0.00	0.00	<LOD		0.00	0.00	
Pb	0.16	0.097	0.02	0.03	0.02	0.034	0.03	0.02	0.106
Bi	0.00	<LOD	0.00	0.00	<LOD	<LOD	0.00	0.00	0.004
Th	0.06	0.027	0.01	0.07	0.06	0.041	0.05	0.04	0.007
U	0.01	0.011	0.01	0.01	0.01	0.009	0.01	0.01	0.008

Spectrum	5B9 008	5B9 004	5B17 003	5A2 008	5A33-1 002	5B3 001	5B3 005	5B17 004	5A33-1 001
Campaign	MD80	MD80	MD80	MD80	MD80	MD80	MD80	MD80	MD80
Dredge point	DR5	DR5	DR5	DR5	DR5	DR5	DR5	DR5	DR5
Thin section	B9	B9	B17	A2	A33-1	B3	B3	B17	A33-1
Na2O	0.70	0.21	1.01	0.45	0.31	0.31	0.30	0.34	0.28
MgO	13.72	14.93	10.91	14.65	17.01	15.96	15.95	16.21	15.86
Al2O3	7.59	6.31	13.98	6.34	3.54	5.50	5.79	5.10	5.77
SiO2	48.57	47.82	48.19	49.71	51.01	49.61	49.31	49.26	48.93
P2O5	0.08	0.03	0.01	0.10	0.01	0.01	0.02	0.02	0.01
K2O	0.14	0.02	0.22	0.29	0.02	0.01	0.01	0.01	0.01
CaO	21.90	22.46	20.21	21.69	22.15	22.30	22.38	22.81	22.33
TiO2	1.62	1.93	1.24	1.48	0.99	1.17	1.01	1.12	1.20
Cr2O3	0.59	0.64	0.51	0.82	0.42	0.56	1.17	0.52	0.74
MnO	0.11	0.13	0.07	0.09	0.11	0.09	0.09	0.10	0.10
FeO	4.81	5.37	3.58	4.31	4.36	4.39	3.83	4.35	4.61
NiO									
Total	99.82	99.84	99.92	99.92	99.93	99.91	99.88	99.84	99.84
Spot Size (µm)	40	40	40	40	40	40	40	40	40
Li	<LOD	0.75	<LOD	0.28	0.04	<LOD	0.71	<LOD	0.27
B	11.46	12.51	13.76	15.06	18.15	15.25	15.06	15.88	16.11
P									
S	129.65	121.23	148.14	147.07	140.15	183.53	175.67	144.62	123.05
K	3.98	4.13	4.58	4.01	4.10	5.24	5.28	4.59	4.21
Sc	140.25	149.07	148.05	135.90	111.12	144.06	135.75	135.25	131.13
Ti	7303.76	9728.27	9067.83	6478.32	4811.10	8229.04	6795.81	6769.87	7142.96
V	392.36	457.21	495.91	367.29	325.50	471.90	406.17	417.25	425.06
Cr	3333.61	2218.98	4226.50	5430.97	3075.10	3286.85	7788.04	3500.16	4391.08
Mn	635.99	660.73	658.99	492.32	740.20	669.25	591.51	584.94	629.23
Fe	34958.72	36318.35	28059.16	24940.79	40538.57	32745.50	30005.37	25397.40	36237.23
Co	25.50	24.80	32.64	28.02	38.79	34.46	31.53	29.85	33.21
Ni	116.60	102.44	165.07	143.04	198.36	166.58	207.77	147.28	171.20
Cu	0.54	0.54	0.75	0.56	0.80	0.78	0.72	0.61	0.76
Zn	19.66	19.52	26.10	23.86	31.33	28.11	24.30	23.04	26.31
Ga	4.10	4.50	5.83	4.55	5.11	6.05	5.48	4.89	6.63
As	0.61	0.68	0.99	1.04	1.19	1.07	0.99	1.01	1.02
Rb	<LOD	<LOD	0.02	0.01	0.00	<LOD	0.02	0.01	0.01
Sr	29.58	29.20	48.32	41.61	56.06	54.68	47.15	46.27	58.45
Y	8.79	10.57	15.86	11.14	13.43	16.49	12.93	13.74	17.07
Zr	35.05	52.39	59.28	34.94	31.12	51.38	36.90	41.58	54.96
Nb	0.30	0.68	0.53	0.30	0.24	0.41	0.35	0.31	0.48
Mo	0.14	0.14	0.31	0.28	0.48	0.34	0.31	0.26	0.31
Ag	<LOD	<LOD	<LOD	0.00	0.00	<LOD	<LOD	<LOD	0.01
Sn	0.20	0.32	0.42	0.28	0.27	0.40	0.28	0.31	0.45
Sb	<LOD	<LOD	<LOD	0.01	0.01	<LOD	<LOD	<LOD	0.00
Cs	<LOD	<LOD	<LOD	0.00	0.00	<LOD	<LOD	<LOD	0.00
Ba	<LOD	<LOD	0.09	0.03	0.03	<LOD	<LOD	<LOD	0.04
La	1.53	2.25	2.97	1.60	2.18	3.14	2.48	2.70	2.87
Ce	5.61	8.42	10.42	5.03	7.42	10.85	8.18	9.41	9.61
Pr	0.95	1.35	1.88	1.00	1.48	1.96	1.44	1.69	1.89
Nd	7.00	9.79	10.24	5.24	7.69	11.24	8.41	9.47	9.75
Sm	1.82	2.49	3.14	1.51	2.45	3.42	2.52	2.87	2.97
Eu	0.50	0.70	0.98	0.45	0.73	1.20	0.79	0.93	0.93
Gd	1.90	2.62	3.38	1.63	2.62	3.65	2.63	3.32	3.46
Tb	0.25	0.35	0.48	0.24	0.37	0.56	0.38	0.49	0.45
Dy	1.67	2.21	3.05	1.36	2.06	3.60	2.60	3.06	2.57
Ho	0.33	0.42	0.56	0.25	0.40	0.62	0.50	0.59	0.52
Er	0.79	1.14	1.53	0.70	1.14	1.73	1.25	1.58	1.41
Tm	0.12	0.17	0.21	0.09	0.12	0.22	0.17	0.19	0.13
Yb	0.83	1.14	1.31	0.54	0.79	1.50	1.12	1.30	1.01
Lu	0.10	0.14	0.19	0.08	0.10	0.20	0.15	0.17	0.14
Hf	1.57	2.36	2.72	0.90	0.93	2.40	1.61	1.95	1.84
Ta	0.06	0.16	0.12	0.03	0.01	0.06	0.05	0.05	0.07
Au	<LOD	<LOD	<LOD	0.00	0.00	<LOD	<LOD	<LOD	0.00
Tl	<LOD	<LOD	<LOD	0.00	0.00	<LOD	<LOD	<LOD	0.00
Pb	0.02	0.02	0.02	0.02	0.02	0.03	0.02	0.03	0.03
Bi	<LOD	<LOD	<LOD	0.00	0.00	<LOD	<LOD	<LOD	0.00
Th	0.04	0.06	0.04	0.03	0.03	0.05	0.04	0.03	0.05
U	0.01	0.01	0.01	0.01	0.01	0.01	0.01	0.01	0.01

Spectrum	5B9 007	MD110-DR03b	5A29 007	5A2 001	5B17 002	MD110-DR01-	5B17 005	MD110-DR01-	5A2 009
Campaign	MD80	MD110	MD80	MD80	MD80	MD110	MD80	MD110	MD80
Dredge point	DR5	DR03b	DR5	DR5	DR5	DR01	DR5	DR01	DR5
Thin section	B9	102C	A29	A2	B17	067	B17	067	A2
Na2O	0.42	0.31	0.34	0.36	0.32	1.16	0.44	0.72	0.35
MgO	15.81	17.87	16.05	15.74	15.93	10.94	17.27	12.34	16.74
Al2O3	5.50	2.94	5.16	5.82	5.57	8.20	3.49	5.63	4.25
SiO2	49.37	52.34	49.43	48.94	50.04	49.13	51.61	48.95	51.36
P2O5	0.02	0.01	0.02	0.02	0.02	0.09	0.00	0.02	0.03
K2O	0.02	0.01	0.01	0.02	0.02	0.37	0.01	0.03	0.09
CaO	22.45	20.18	22.44	22.20	22.07	19.66	21.74	20.51	21.61
TiO2	1.21	0.42	1.10	1.34	1.13	1.61	0.73	1.72	0.84
Cr2O3	0.66	0.49	0.73	0.62	0.57	0.22	0.46	0.10	0.62
MnO	0.10	0.14	0.10	0.12	0.11	0.18	0.10	0.24	0.10
FeO	4.33	5.21	4.46	4.68	4.03	8.30	3.88	9.58	3.86
NiO									
Total	99.89	99.92	99.84	99.87	99.82	99.86	99.72	99.84	99.85
Spot Size (µm)	40	40	40	40	40	40	40	40	40
Li	<LOD	0.874	0.09	0.42	0.60	2.815	<LOD	2.133	0.41
B	11.77		15.65	16.28	13.91		14.73		13.39
P		316.739				175.444		167.749	
S	120.19		152.85	161.92	187.64		157.44		151.23
K	4.37		5.27	3.96	8.05		3.76		4.44
Sc	119.60	92.165	129.82	128.65	118.16	155.943	112.98	191.699	95.32
Ti	5861.87	2431.546	6073.30	7699.36	4976.00	10743.563	4806.33	9710.219	4313.65
V	342.49	278.453	367.53	426.82	317.05	705.618	314.03	804.763	281.63
Cr	3682.63	3273.933	4164.51	3882.94	2693.21	1130.149	2672.71	1235.582	3764.96
Mn	592.82	1157.023	551.54	562.32	739.64	1326.381	674.90	1714.093	510.10
Fe	31329.80		27924.33	27202.61	27311.86		27293.80		22657.68
Co	23.25	38.876	29.59	28.82	34.43	39.502	34.06	44.574	26.93
Ni	123.21	125.215	149.33	138.92	167.75	67.789	164.27	61.456	162.94
Cu	0.51	1.302	0.66	0.67	0.83	1.140	0.69	1.039	0.57
Zn	18.34	24.535	25.61	24.97	26.93	37.155	27.03	45.000	22.94
Ga	3.90		4.42	5.05	3.50		3.80		3.17
As	0.59		1.02	1.35	0.84		1.03		0.98
Rb	<LOD	<LOD	0.02	0.02	0.02	0.155	0.01	<LOD	0.01
Sr	29.21	12.140	39.90	38.73	36.81	17.648	43.68	17.170	33.87
Y	7.93	11.940	11.76	13.53	10.43	37.674	10.47	54.806	7.61
Zr	24.55	8.714	32.46	40.56	24.49	76.018	23.74	63.164	16.97
Nb	0.20	0.071	0.27	0.34	0.21	0.157	0.17	0.147	0.16
Mo	0.16	0.347	0.27	0.27	0.36	0.356	0.34	0.429	0.23
Ag	<LOD		0.01	0.01	<LOD		<LOD		0.00
Sn	0.21		0.28	0.31	0.19		0.21		0.12
Sb	0.01	0.424	0.00	0.00	<LOD	0.865	<LOD	0.720	0.01
Cs	<LOD	<LOD	0.00	0.00	<LOD	<LOD	<LOD	<LOD	0.00
Ba	0.04	0.079	0.08	0.02	0.13	<LOD	0.07	0.206	0.05
La	1.39	0.530	1.86	1.82	1.80	1.145	1.84	1.797	0.98
Ce	5.24	1.959	6.31	5.93	6.67	5.174	6.67	7.575	3.18
Pr	0.86	0.411	1.17	1.10	1.23	1.207	1.21	1.811	0.62
Nd	6.46	2.851	6.52	6.16	6.93	8.440	7.03	11.820	3.44
Sm	1.69	1.288	1.96	1.80	2.18	3.788	2.16	5.497	1.04
Eu	0.51	0.469	0.61	0.52	0.70	1.252	0.73	1.716	0.31
Gd	1.69	2.002	2.14	1.99	2.39	5.970	2.40	8.560	1.12
Tb	0.24	0.326	0.33	0.28	0.36	1.023	0.35	1.481	0.16
Dy	1.63	2.273	1.87	1.71	2.20	6.315	2.24	10.557	0.90
Ho	0.33	0.501	0.36	0.31	0.39	1.431	0.41	2.093	0.16
Er	0.78	1.301	1.04	0.86	1.14	4.266	1.06	5.934	0.46
Tm	0.13	0.184	0.12	0.11	0.15	0.592	0.14	0.811	0.06
Yb	0.82	1.223	0.77	0.70	0.97	3.645	0.89	5.277	0.35
Lu	0.10	0.165	0.11	0.09	0.13	0.562	0.12	0.793	0.05
Hf	1.24	0.407	1.21	1.04	1.23	3.612	0.99	2.922	0.41
Ta	0.04	0.012	0.03	0.04	0.03	0.037	0.02	0.021	0.01
Au	<LOD		0.00	0.00	<LOD		<LOD		0.00
Tl	0.00		0.00	0.00	<LOD		<LOD		0.00
Pb	0.02	0.023	0.02	0.01	0.03	0.027	0.02	<LOD	0.01
Bi	<LOD	<LOD	0.00	0.00	<LOD	<LOD	<LOD	<LOD	0.00
Th	0.04	0.004	0.03	0.03	0.02	0.033	0.02	0.021	0.01
U	0.01	0.006	0.01	0.01	0.00	0.004	0.00	0.004	0.00

Spectrum	5A15 006	5A2 002	MD110-DR1	MD110-DR0	MD110-DR0	5B3 009	5A9 006	5A9 004	5A15 007	5A15 008
Campaign	MD80	MD80	MD110	MD110	MD110	MD80	MD80	MD80	MD80	MD80
Dredge point	DR5	DR5	DR10	DR01	DR03b	DR5	DR5	DR5	DR5	DR5
Thin section	A15	A2	312	067	101D	B3	A9	A9	A15	A15
Na2O	0.33	0.34	0.15	0.51	0.35	0.33	0.15	0.26	1.19	0.36
MgO	13.78	15.66	18.75	12.79	16.74	17.10	17.00	15.09	15.17	16.24
Al2O3	5.14	6.42	3.27	6.32	4.25	3.87	3.30	5.91	3.00	4.13
SiO2	47.80	48.76	51.81	48.48	51.06	51.12	51.19	48.65	49.72	51.08
P2O5	0.07	0.03	0.00	0.03	0.03	0.02	0.01	0.04	0.04	0.07
K2O	0.05	0.02	0.10	0.03	0.00	0.01	0.06	0.09	0.00	0.05
CaO	21.62	22.02	20.03	20.64	21.02	22.30	22.03	22.21	21.11	22.24
TiO2	1.86	1.19	0.23	1.84	0.58	0.71	0.83	1.51	1.09	0.89
Cr2O3	0.12	1.10	0.66	0.46	0.72	0.80	0.24	0.59	0.11	0.35
MnO	0.19	0.11	0.12	0.16	0.12	0.09	0.12	0.10	0.20	0.12
FeO	8.91	4.20	4.74	8.58	5.04	3.51	4.99	5.40	8.27	4.36
NiO										
Total	99.87	99.83	99.86	99.84	99.91	99.86	99.91	99.84	99.89	99.90

Spot Size (μm)	40	40	40	40	40	40	40	40
Li	0.63	0.22	2.317	2.861	0.734	<LOD	0.17	0.44
B	9.67	15.60				14.34	14.79	17.35
P			279.043	114.309	24.942			
S	215.02	121.72				246.46	146.00	149.46
K	6.25	4.58				4.75	3.88	4.98
Sc	153.13	106.09	95.888	160.592	112.650	106.55	115.77	184.41
Ti	16126.59	5288.58	1405.149	8274.568	3159.130	4491.37	4736.39	10740.36
V	810.11	332.37	321.058	658.953	339.400	304.25	308.33	524.50
Cr	1002.59	3977.72	7094.144	795.263	5062.403	5713.38	2181.19	3766.17
Mn	1220.74	442.25	1060.792	1458.640	995.158	610.53	725.37	705.92
Fe	56536.50	21651.42				30428.05	36240.80	41633.32
Co	60.14	24.27	43.749	40.367	34.756	32.49	36.53	36.57
Ni	122.64	139.10	265.896	61.538	110.827	218.32	163.21	163.45
Cu	1.63	0.51	1.345	0.856	0.947	0.77	0.64	0.86
Zn	54.83	20.20	23.250	39.480	23.502	25.07	29.56	29.97
Ga	9.49	3.88				4.08	4.27	8.08
As	1.01	1.24				0.99	1.19	1.46
Rb	<LOD	0.00	<LOD	<LOD	<LOD	<LOD	0.01	0.03
Sr	38.13	36.00	7.248	16.761	17.061	43.46	48.88	60.38
Y	22.79	9.65	8.102	35.174	15.097	9.38	12.08	24.35
Zr	47.22	25.78	3.442	47.412	13.611	21.94	27.62	110.37
Nb	0.30	0.21	0.105	0.077	0.119	0.22	0.21	1.19
Mo	0.29	0.24	0.284	0.340	0.272	0.34	0.45	0.54
Ag	<LOD	0.00				<LOD	0.00	0.03
Sn	0.47	0.22				0.22	0.22	0.67
Sb	<LOD	0.00	0.294	0.490	0.284	<LOD	0.00	-0.01
Cs	<LOD	0.00	<LOD	<LOD	<LOD	<LOD	0.00	0.00
Ba	<LOD	0.03	0.081	<LOD	0.100	0.06	0.06	0.09
La	2.29	1.33	0.076	0.964	0.731	1.65	2.76	6.61
Ce	8.45	4.37	0.487	4.426	2.544	5.79	11.34	27.23
Pr	1.48	0.85	0.138	1.109	0.522	1.03	2.07	5.01
Nd	9.46	4.50	0.947	7.252	3.420	5.96	11.81	26.17
Sm	2.94	1.36	0.590	3.519	1.373	1.84	3.50	7.39
Eu	0.90	0.39	0.269	1.125	0.532	0.58	1.26	2.51
Gd	3.08	1.50	0.919	5.195	2.483	1.87	3.83	8.40
Tb	0.46	0.22	0.194	0.927	0.428	0.30	0.57	1.23
Dy	3.03	1.30	1.450	6.024	2.979	1.82	3.01	5.72
Ho	0.58	0.24	0.290	1.398	0.598	0.33	0.61	1.14
Er	1.57	0.66	0.979	3.928	1.694	0.92	2.07	3.89
Tm	0.19	0.07	0.130	0.538	0.213	0.11	0.20	0.33
Yb	1.53	0.49	0.807	3.710	1.426	0.73	1.37	2.38
Lu	0.20	0.07	0.129	0.520	0.185	0.12	0.18	0.30
Hf	1.63	0.66	0.253	2.410	0.691	0.89	1.94	6.82
Ta	0.05	0.02	<LOD	0.019	<LOD	0.02	0.03	0.31
Au	<LOD	0.00				<LOD	0.00	0.00
Tl	<LOD	0.00				<LOD	0.01	0.06
Pb	0.03	0.01	<LOD	0.014	0.019	0.02	0.28	14.29
Bi	<LOD	0.00	<LOD	<LOD	<LOD	0.00	0.01	0.02
Th	0.03	0.02	<LOD	0.017	0.019	0.01	0.56	-1.20
U	0.00	0.00	0.003	0.002	0.002	0.00	0.00	-0.04

Table S2 - Major and trace elements compositions of plagioclase

Spectrum	MD110-DR08-296-006	MD110-DR08-296-008	MD110-DR08-296-004	MD110-DR01-067-009	MD110-DR08-296-010	MD110-DR11-334 002	MD110-DR08-296-010	MD110-DR01-067-009	MD110-DR08-296-004	MD110-DR08-296-006	MD110-DR08-296-004
Campaign	MD110	MD110	MD110	MD110	MD110	MD110	MD110	MD110	MD110	MD110	MD110
Dredge point	DR08	DR08	DR08	DR01	DR08	DR11	DR08	DR01	DR08	DR08	DR08
Thin section	296	296	296	067	296	334	296	067	296	296	296
Mineral	Pl	Pl	Pl	Pl	Pl	Pl	Pl	Pl	Pl	Pl	Pl
Na2O	4.89	4.05	4.79	4.26	4.87	6.93	4.87	4.26	4.79	4.89	4.79
MgO	0.31	2.32	0.38	1.14	0.26	0.28	0.26	1.14	0.38	0.31	0.38
Al2O3	29.99	27.24	30.03	28.02	30.03	24.21	30.03	28.02	30.03	29.99	30.03
SiO2	52.31	51.78	52.05	51.11	52.29	60.85	52.29	51.11	52.05	52.31	52.05
P2O5	0.00	0.00	0.00	0.07	0.00	0.00	0.00	0.07	0.00	0.00	0.00
K2O	0.32	0.31	0.41	0.19	0.42	0.65	0.42	0.19	0.41	0.32	0.41
CaO	11.96	13.40	12.08	12.20	11.92	6.65	11.92	12.20	12.08	11.96	12.08
TiO2	0.04	0.12	0.05	0.60	0.04	0.04	0.04	0.60	0.05	0.04	0.05
Cr2O3	0.00	0.02	0.05	0.00	0.00	0.09	0.00	0.00	0.05	0.00	0.05
MnO	0.01	0.03	0.00	0.06	0.01	0.01	0.01	0.06	0.00	0.01	0.00
FeO	0.11	0.55	0.10	2.29	0.11	0.23	0.11	2.29	0.10	0.11	0.10
NiO											
Total	99.94	99.83	99.95	99.94	99.94	99.93	99.94	99.94	99.95	99.94	99.95
Spot Size (µm)	40	40	40	40	40	40	40	40	40	40	40
Li	<LOD	<LOD	<LOD	7.581	2.907	1.138	<LOD	9.432	5.265	<LOD	<LOD
B											
P	229.936	1545.851	694.372	<LOD	147.837	<LOD	<LOD	794.702	<LOD	438.857	713.908
S											
K											
Sc	1.899	7.611	2.337	2.796	2.139	1.702	1.574	2.708	<LOD	2.067	<LOD
Ti	751.664	3388.283	1011.199	2139.671	972.929	149.236	870.111	1796.189	934.009	786.091	780.809
V	3.241	7.880	3.464	18.799	2.423	<LOD	2.322	17.443	2.948	1.451	2.697
Cr	<LOD	<LOD	<LOD	<LOD	<LOD	115.282	<LOD	<LOD	<LOD	<LOD	22.796
Mn	272.248	1156.251	206.353	510.285	295.975	<15.7867	105.926	448.603	265.157	283.189	194.734
Fe											
Co	<LOD	<LOD	<LOD	4.382	<LOD	<LOD	<LOD	3.785	<LOD	<LOD	<LOD
Ni	<LOD	<LOD	<LOD	<LOD	<LOD	<LOD	2.673	5.806	<LOD	<LOD	<LOD
Cu	16.947	96.975	21.308	17.417	19.285	19.479	19.850	18.754	19.689	16.845	15.104
Zn	6.008	<LOD	<LOD	16.966	8.096	9.998	11.545	19.405	10.182	8.859	<LOD
Ga											
As											
Rb	0.605	3.732	1.075	1.147	1.688	2.632	1.106	2.090	3.971	0.721	0.802
Sr	4368.111	21341.357	5646.864	1428.589	2330.589	874.734	2034.111	1206.668	5049.683	4913.352	4205.898
Y	1.170	5.301	1.196	1.215	1.203	0.418	1.072	1.075	1.092	1.035	0.806
Zr	<LOD	<LOD	<LOD	0.173	<LOD	<LOD	<LOD	0.372	<LOD	<LOD	<LOD
Nb	<LOD	<LOD	<LOD	<LOD	<LOD	<LOD	<LOD	<LOD	0.024	<LOD	<LOD
Mo	<LOD	<LOD	<LOD	<LOD	<LOD	<LOD	<LOD	<LOD	<LOD	<LOD	<LOD
Ag											
Sn											
Sb	1.291	7.318	1.892	1.448	1.571	0.535	1.691	0.829	1.157	1.266	1.204
Cs	<LOD	<LOD	<LOD	<LOD	<LOD	<LOD	<LOD	<LOD	<LOD	<LOD	<LOD
Ba	760.680	3899.710	867.224	161.366	889.772	557.730	898.424	136.852	882.536	821.994	696.607
La	7.593	42.673	9.130	2.524	8.273	28.038	7.473	1.983	8.953	7.856	6.778
Ce	18.623	89.422	20.535	4.641	9.518	25.314	9.119	3.794	18.724	18.598	15.457
Pr	1.185	6.670	1.519	0.645	1.260	1.563	1.264	0.446	1.243	1.268	1.137
Nd	3.947	22.194	4.954	2.870	3.971	4.108	3.350	2.520	4.936	4.132	2.704
Sm	0.705	4.539	0.795	0.518	0.856	0.361	0.595	0.744	0.792	0.640	0.595
Eu	3.021	15.972	3.224	1.874	3.462	4.232	3.037	2.131	3.579	2.659	2.571
Gd	0.560	1.507	0.718	0.655	0.655	0.304	0.476	0.491	0.908	<LOD	0.569
Tb	0.073	<LOD	0.123	0.072	0.036	0.017	0.040	0.056	0.070	0.075	0.064
Dy	0.150	1.861	0.432	0.345	0.152	<LOD	0.391	0.426	<LOD	0.192	0.285
Ho	0.018	0.189	0.055	0.095	0.010	<LOD	0.008	0.077	0.048	<LOD	0.084
Er	0.070	0.471	<LOD	0.243	<LOD	<LOD	0.135	0.095	<LOD	<LOD	<LOD
Tm	<LOD	<LOD	<LOD	<LOD	<LOD	<LOD	<LOD	<LOD	<LOD	<LOD	<LOD
Yb	<LOD	<LOD	<LOD	0.067	<LOD	<LOD	<LOD	<LOD	0.130	0.096	<LOD
Lu	<LOD	<LOD	<LOD	<LOD	<LOD	<LOD	<LOD	<LOD	<LOD	<LOD	<LOD
Hf	<LOD	<LOD	<LOD	0.038	<LOD	<LOD	<LOD	<LOD	<LOD	<LOD	<LOD
Ta	<LOD	<LOD	<LOD	<LOD	<LOD	<LOD	<LOD	<LOD	<LOD	<LOD	<LOD
Pb	1.507	8.744	2.643	0.646	1.796	33.768	1.760	0.592	3.215	1.950	1.650
Bi	<LOD	<LOD	<LOD	<LOD	<LOD	<LOD	<LOD	<LOD	<LOD	<LOD	<LOD
Th	<LOD	<LOD	<LOD	<LOD	<LOD	<LOD	<LOD	<LOD	<LOD	<LOD	<LOD
U	<LOD	<LOD	<LOD	<LOD	<LOD	<LOD	<LOD	<LOD	<LOD	<LOD	<LOD

Spectrum	MD110-DR08-296-006	MD110-DR01-067-009	MD110-DR03b-102C-006	MD110-DR11-334 002	MD110-DR08-296-010	MD110-DR11-334 007	MD110-DR11-334 007	MD110-DR10-312-004	MD110-DR11-334 004	MD110-DR10-312-004	MD110-DR10-312-006
Campaign	MD110	MD110	MD110	MD110	MD110	MD110	MD110	MD110	MD110	MD110	MD110
Dredge point	DR08	DR01	DR03b	DR11	DR08	DR11	DR11	DR10	DR11	DR10	DR10
Thin section	296	067	102C	334	296	334	334	312	334	312	312
Mineral	Pl	Pl	Pl	Pl	Pl	Pl	Pl	Pl	Pl	Pl	Pl
Na2O	4.89	4.26	3.36	6.93	4.87	8.45	8.45	3.89	7.86	3.89	1.43
MgO	0.31	1.14	0.48	0.28	0.26	0.36	0.36	0.80	0.27	0.80	0.61
Al2O3	29.99	28.02	31.22	24.21	30.03	24.41	24.41	29.95	24.59	29.95	26.69
SiO2	52.31	51.11	49.51	60.85	52.29	60.31	60.31	50.22	60.19	50.22	54.75
P2O5	0.00	0.07	0.00	0.00	0.00	0.00	0.00	0.00	0.00	0.00	0.00
K2O	0.32	0.19	0.12	0.65	0.42	0.31	0.31	0.17	0.68	0.17	7.35
CaO	11.96	12.20	14.42	6.65	11.92	5.77	5.77	12.96	6.07	12.96	7.37
TiO2	0.04	0.60	0.07	0.04	0.04	0.07	0.07	0.05	0.03	0.05	0.17
Cr2O3	0.00	0.00	0.00	0.09	0.00	0.00	0.00	0.01	0.02	0.01	0.00
MnO	0.01	0.06	0.01	0.01	0.01	0.01	0.01	0.02	0.01	0.02	0.04
FeO	0.11	2.29	0.41	0.23	0.11	0.25	0.25	1.88	0.21	1.88	1.52
NiO											
Total	99.94	99.94	99.60	99.93	99.94	99.95	99.95	99.96	99.92	99.96	99.94
Spot Size (µm)	40	40	40	40	40	40	40	40	40	40	40
Li	<LOD	7.863	<LOD	<LOD	<LOD	<LOD	<LOD	<LOD	0.717	<LOD	<LOD
B											
P	<LOD	358.677	511.526	<LOD	<LOD	320.131	<LOD	975.499	361.022	1062.194	599.590
S											
K											
Sc	1.405	2.787	0.774	1.234	1.615	1.366	0.921	1.811	1.130	1.413	1.312
Ti	725.258	2074.230	285.608	183.154	836.913	126.137	137.725	720.127	160.797	824.028	435.555
V	1.972	18.605	2.964	<LOD	2.329	<LOD	0.870	13.584	<LOD	13.198	13.357
Cr	45.686	17.642	<LOD	47.651	<LOD	<LOD	<LOD	<LOD	<LOD	<LOD	<LOD
Mn	203.582	556.387	111.610	<17.6209	306.060	18.759	<14.5321	390.862	52.284	351.904	392.078
Fe											
Co	<LOD	2.995	0.962	<LOD	<LOD	<LOD	<LOD	3.263	<LOD	3.934	2.744
Ni	<LOD	<LOD	<LOD	<LOD	<LOD	<LOD	<LOD	<LOD	<LOD	<LOD	<LOD
Cu	16.871	19.456	2.751	22.270	16.295	17.881	16.481	8.921	15.873	8.885	6.949
Zn	<LOD	13.745	2.991	10.555	4.850	8.999	8.351	14.654	7.249	14.117	9.428
Ga											
As											
Rb	1.054	0.948	0.281	0.443	0.684	0.556	0.534	0.263	0.622	0.360	0.216
Sr	4569.220	1433.832	279.550	1035.372	2096.646	921.186	828.647	464.705	803.286	461.909	489.855
Y	1.202	1.428	0.218	0.462	1.087	0.348	0.445	0.530	0.455	0.478	0.670
Zr	0.348	<LOD	0.088	<LOD	0.257	<LOD	<LOD	<LOD	<LOD	<LOD	<LOD
Nb	<LOD	<LOD	<LOD	<LOD	<LOD	<LOD	<LOD	<LOD	0.035	<LOD	<LOD
Mo	<LOD	<LOD	<LOD	<LOD	<LOD	<LOD	<LOD	<LOD	<LOD	<LOD	<LOD
Ag											
Sn											
Sb	0.944	1.775	0.233	1.093	1.152	<LOD	<LOD	0.664	0.638	0.635	0.802
Cs	<LOD	<LOD	<LOD	<LOD	<LOD	<LOD	<LOD	<LOD	<LOD	<LOD	<LOD
Ba	792.687	120.093	37.503	527.892	780.200	584.428	489.364	45.128	550.063	62.472	50.272
La	7.152	2.427	0.513	31.711	7.135	27.633	23.021	0.525	26.684	0.765	0.766
Ce	18.330	3.812	0.778	28.606	8.940	25.270	20.891	1.084	24.748	1.194	1.181
Pr	1.395	0.432	0.099	1.539	1.268	1.436	1.279	0.168	1.514	0.162	0.174
Nd	3.438	2.559	0.378	3.871	2.973	3.578	3.815	0.970	3.952	1.034	0.682
Sm	0.330	0.906	0.079	0.383	0.858	0.489	0.495	0.372	0.427	0.122	0.360
Eu	3.158	2.292	0.302	4.865	2.820	4.771	3.894	0.932	3.746	1.020	0.903
Gd	0.535	0.722	<LOD	0.383	0.314	<LOD	<LOD	<LOD	0.380	<LOD	0.206
Tb	0.052	0.099	0.010	0.009	0.044	0.018	0.018	0.040	0.031	0.030	<LOD
Dy	0.281	0.347	0.108	<LOD	0.353	<LOD	0.077	0.133	0.086	0.205	0.186
Ho	<LOD	0.085	0.005	0.034	0.017	0.032	<LOD	0.024	<LOD	0.067	0.038
Er	<LOD	<LOD	<LOD	<LOD	0.059	<LOD	<LOD	<LOD	<LOD	0.051	<LOD
Tm	0.027	<LOD	0.008	<LOD	0.017	<LOD	<LOD	<LOD	<LOD	<LOD	<LOD
Yb	<LOD	<LOD	0.013	<LOD	<LOD	<LOD	<LOD	<LOD	<LOD	<LOD	<LOD
Lu	<LOD	<LOD	<LOD	<LOD	<LOD	<LOD	<LOD	<LOD	<LOD	<LOD	<LOD
Hf	<LOD	<LOD	<LOD	0.047	<LOD	<LOD	0.033	<LOD	0.057	<LOD	<LOD
Ta	<LOD	<LOD	<LOD	<LOD	<LOD	<LOD	<LOD	<LOD	<LOD	<LOD	<LOD
Pb	1.581	0.663	0.100	36.098	1.359	35.579	30.792	0.175	30.831	0.257	0.348
Bi	<LOD	0.053	<LOD	<LOD	<LOD	<LOD	<LOD	<LOD	<LOD	<LOD	<LOD
Th	<LOD	<LOD	<LOD	<LOD	<LOD	<LOD	<LOD	<LOD	0.009	<LOD	<LOD
U	<LOD	<LOD	<LOD	<LOD	<LOD	<LOD	<LOD	<LOD	<LOD	<LOD	<LOD

Spectrum	MD110-DR01-067-008	MD110-DR10-312-004	MD110-DR10-312-006	MD110-DR11-334 007	MD110-DR10-312-003	MD110-DR11-334 004	MD110-DR10-312-004	MD110-DR10-312-006	MD110-DR11-334 003	MD110-DR11-332-005	MD110-DR11-332-004	MD110-DR11-334 009-003
Campaign	MD110	MD110	MD110	MD110	MD110	MD110	MD110	MD110	MD110	MD110	MD110	MD110
Dredge point	DR01	DR10	DR10	DR11	DR10	DR11	DR10	DR10	DR11	DR11	DR11	DR11
Thin section	067	312	312	334	312	334	312	312	334	332	332	334
Mineral	Pl	Pl	Pl	Pl	Pl	Pl	Pl	Pl	Pl	Pl	Pl	Pl
Na2O	3.94	3.89	1.43	8.45	4.45	7.86	3.89	1.43	7.88	3.92	3.40	7.47
MgO	0.72	0.80	0.61	0.36	1.25	0.27	0.80	0.61	0.31	1.13	0.81	0.28
Al2O3	30.02	29.95	26.69	24.41	28.65	24.59	29.95	26.69	24.46	29.68	30.42	24.17
SiO2	50.61	50.22	54.75	60.31	51.92	60.19	50.22	54.75	60.40	51.48	50.31	60.78
P2O5	0.00	0.00	0.00	0.00	0.00	0.00	0.00	0.00	0.00	0.00	0.00	0.02
K2O	0.21	0.17	7.35	0.31	0.55	0.68	0.17	7.35	0.63	0.30	0.15	1.16
CaO	13.44	12.96	7.37	5.77	11.17	6.07	12.96	7.37	6.06	12.01	13.36	5.70
TiO2	0.15	0.05	0.17	0.07	0.21	0.03	0.05	0.17	0.03	0.07	0.03	0.07
Cr2O3	0.05	0.01	0.00	0.00	0.00	0.02	0.01	0.00	0.00	0.01	0.00	0.03
MnO	0.01	0.02	0.04	0.01	0.03	0.01	0.02	0.04	0.01	0.02	0.02	0.01
FeO	0.82	1.88	1.52	0.25	1.72	0.21	1.88	1.52	0.17	1.35	1.41	0.28
NiO												
Total	99.97	99.96	99.94	99.95	99.94	99.92	99.96	99.94	99.95	99.96	99.93	99.96
Spot Size (µm)	40	40	40	40	40	40	40	40	40	40	40	40
Li	5.493	<LOD	1.653	0.473	<LOD	<LOD	<LOD	1.631	<LOD	2.416	1.390	<LOD
B												
P	343.303	845.480	493.911	<LOD	1097.936	<LOD	987.059	402.780	438.268	654.504	686.124	857.118
S												
K												
Sc	0.602	2.037	1.594	0.244	1.204	0.692	1.261	1.560	1.000	1.214	1.438	0.904
Ti	858.703	753.150	397.262	45.126	881.848	135.245	974.455	370.555	106.302	301.417	330.108	182.589
V	1.938	12.889	13.457	1.938	5.085	<LOD	12.054	12.051	<LOD	8.257	9.701	<LOD
Cr	<LOD	<LOD	<LOD	<LOD	<LOD	<LOD	<LOD	<LOD	<LOD	<LOD	<LOD	14.108
Mn	214.757	421.065	314.200	33.402	354.068	<12.4889	345.775	335.803	15.856	296.254	329.995	106.752
Fe												
Co	<LOD	3.362	2.159	1.221	2.667	<LOD	3.538	2.675	<LOD	3.245	6.358	<LOD
Ni	<LOD	<LOD	<LOD	1.861	<LOD	<LOD	<LOD	<LOD	<LOD	<LOD	<LOD	<LOD
Cu	12.506	8.046	5.602	6.260	11.770	13.841	8.731	6.418	12.948	5.632	5.601	22.335
Zn	11.568	15.192	7.546	5.886	25.991	6.036	16.186	11.177	6.391	9.932	11.884	11.958
Ga												
As												
Rb	1.220	1.654	0.694	1.733	0.901	0.497	0.411	0.275	0.403	0.346	2.910	0.811
Sr	735.233	446.763	475.886	322.406	631.750	689.148	458.404	435.272	632.049	330.524	361.755	1065.465
Y	0.353	0.586	0.569	0.234	0.657	0.456	0.588	0.479	0.417	0.281	0.312	0.519
Zr	0.163	<LOD	0.150	<LOD	<LOD	<LOD	<LOD	0.135	<LOD	<LOD	0.161	<LOD
Nb	0.012	<LOD	<LOD	0.010	0.030	<LOD	<LOD	<LOD	<LOD	<LOD	<LOD	<LOD
Mo	<LOD	<LOD	<LOD	<LOD	<LOD	<LOD	<LOD	<LOD	<LOD	<LOD	<LOD	<LOD
Ag												
Sn												
Sb	0.490	1.059	1.141	0.199	0.579	0.517	0.946	0.817	0.650	0.495	0.378	0.821
Cs	<LOD	<LOD	<LOD	<LOD	<LOD	<LOD	<LOD	0.428	<LOD	<LOD	<LOD	<LOD
Ba	397.651	56.201	51.178	231.729	217.874	510.066	76.495	46.082	458.786	47.460	72.515	782.903
La	2.180	0.692	0.665	8.922	1.324	21.922	0.716	0.547	19.252	0.406	0.422	31.774
Ce	3.280	0.988	1.323	8.055	2.348	21.166	1.311	1.063	18.303	0.698	0.748	31.340
Pr	0.356	0.198	0.168	0.530	0.366	1.237	0.128	0.195	1.218	0.126	0.124	1.922
Nd	1.503	1.047	0.886	1.286	1.411	3.244	0.677	0.677	2.607	0.403	0.380	4.412
Sm	0.285	0.255	0.157	0.188	0.508	0.345	0.353	0.164	0.450	0.049	0.046	0.553
Eu	4.728	0.928	0.865	1.566	3.302	3.432	1.097	0.669	3.255	0.343	0.383	5.830
Gd	0.230	0.260	0.254	0.054	0.311	0.300	<LOD	0.133	0.233	0.130	0.114	0.207
Tb	<LOD	0.024	0.046	0.007	0.047	0.011	0.043	0.037	<LOD	<LOD	<LOD	0.014
Dy	0.161	0.126	0.192	0.060	0.279	0.059	0.133	0.115	0.107	0.070	<LOD	0.145
Ho	0.008	0.026	0.032	<LOD	0.015	0.009	0.012	0.016	0.011	0.021	0.017	<LOD
Er	<LOD	0.114	<LOD	<LOD	<LOD	<LOD	<LOD	0.022	0.089	<LOD	<LOD	0.141
Tm	<LOD	<LOD	<LOD	<LOD	0.011	<LOD	<LOD	0.008	<LOD	<LOD	<LOD	0.014
Yb	<LOD	<LOD	0.044	<LOD	<LOD	<LOD	<LOD	<LOD	<LOD	<LOD	<LOD	0.061
Lu	<LOD	<LOD	<LOD	<LOD	<LOD	<LOD	<LOD	<LOD	<LOD	<LOD	<LOD	<LOD
Hf	<LOD	<LOD	<LOD	<LOD	<LOD	0.041	<LOD	<LOD	<LOD	<LOD	0.073	0.060
Ta	0.012	0.024	<LOD	<LOD	<LOD	<LOD	<LOD	0.039	<LOD	<LOD	0.021	<LOD
Pb	0.486	0.236	0.340	10.660	0.360	25.487	0.392	0.279	23.116	0.190	0.343	40.800
Bi	<LOD	<LOD	<LOD	<LOD	<LOD	<LOD	<LOD	<LOD	<LOD	<LOD	<LOD	<LOD
Th	<LOD	<LOD	<LOD	<LOD	<LOD	<LOD	<LOD	<LOD	<LOD	<LOD	<LOD	<LOD
U	<LOD	<LOD	<LOD	<LOD	<LOD	<LOD	<LOD	<LOD	<LOD	<LOD	<LOD	<LOD

Spectrum	MD110-DR11-334 003	MD110-DR01-067-007	MD110-DR11-334 003	MD110-DR03b-101D 001	MD110-DR11-332-005	MD110-DR11-332-007	MD110-DR01-067-005	MD110-DR01-067-005	MD110-DR11-332-004	MD110-DR11-334 004	MD110-DR11-332-004	MD110-DR11-332-007
Campaign	MD110	MD110	MD110	MD110	MD110	MD110	MD110	MD110	MD110	MD110	MD110	MD110
Dredge point	DR11	DR01	DR11	DR03b	DR11	DR11	DR01	DR01	DR11	DR11	DR11	DR11
Thin section	334	067	334	101D	332	332	067	067	332	334	332	332
Mineral	Pl	Pl	Pl	Pl	Pl	Pl	Pl	Pl	Pl	Pl	Pl	Pl
Na2O	7.88	4.16	7.88	3.59	3.92	3.55	3.65	3.65	3.40	7.86	3.40	3.55
MgO	0.31	0.66	0.31	0.56	1.13	1.08	0.54	0.54	0.81	0.27	0.81	1.08
Al2O3	24.46	29.92	24.46	31.26	29.68	30.08	29.88	29.88	30.42	24.59	30.42	30.08
SiO2	60.40	50.85	60.40	49.64	51.48	50.36	50.67	50.67	50.31	60.19	50.31	50.36
P2O5	0.00	0.00	0.00	0.00	0.00	0.00	0.00	0.00	0.00	0.00	0.00	0.00
K2O	0.63	0.19	0.63	0.20	0.30	0.14	0.07	0.07	0.15	0.68	0.15	0.14
CaO	6.06	13.04	6.06	14.19	12.01	13.32	14.38	14.38	13.36	6.07	13.36	13.32
TiO2	0.03	0.10	0.03	0.09	0.07	0.04	0.08	0.08	0.03	0.03	0.03	0.04
Cr2O3	0.00	0.29	0.00	0.00	0.01	0.00	0.14	0.14	0.00	0.02	0.00	0.00
MnO	0.01	0.02	0.01	0.01	0.02	0.02	0.01	0.01	0.02	0.01	0.02	0.02
FeO	0.17	0.64	0.17	0.39	1.35	1.38	0.53	0.53	1.41	0.21	1.41	1.38
NiO												
Total	99.95	99.88	99.95	99.94	99.96	99.96	99.93	99.93	99.93	99.92	99.93	99.96
Spot Size (µm)	40	40	40	40	40	40	40	40	40	40	40	40
Li	<LOD	2.104	<LOD	<LOD	1.452	2.862	1.577	1.493	2.492	<LOD	4.011	3.248
B												
P	176.145	114.417	194.352	<LOD	653.330	676.294	79.620	66.152	690.071	<LOD	239.083	1002.158
S												
K												
Sc	0.811	0.947	0.805	0.580	1.034	1.348	0.544	0.764	0.911	0.571	0.801	1.509
Ti	104.482	553.904	95.284	256.164	249.696	358.922	482.005	475.767	385.323	111.784	443.622	361.820
V	<LOD	5.002	<LOD	2.915	9.452	8.154	4.551	4.685	7.799	0.807	6.936	9.013
Cr	<LOD	35.362	<LOD	<LOD	<LOD	<LOD	68.088	67.757	<LOD	<LOD	<LOD	<LOD
Mn	<9.75039	152.584	25.144	88.394	219.604	261.963	111.881	116.131	215.173	<7.36929	187.905	258.528
Fe												
Co	<LOD	1.432	<LOD	0.819	4.913	3.025	1.116	1.097	3.322	0.407	2.433	3.173
Ni	<LOD	1.582	<LOD	0.406	<LOD	<LOD	<LOD	<LOD	<LOD	<LOD	<LOD	<LOD
Cu	11.461	4.826	10.982	3.123	10.716	5.338	4.024	4.218	7.406	11.241	5.038	6.317
Zn	4.975	4.452	5.141	2.255	9.556	11.127	4.153	3.396	12.593	8.051	12.684	10.160
Ga												
As												
Rb	0.533	0.150	0.699	0.286	2.939	0.212	0.164	0.154	0.624	0.467	0.386	0.425
Sr	578.021	409.671	564.551	301.643	259.602	363.620	359.009	352.392	312.968	551.540	311.644	344.540
Y	0.313	0.353	0.383	0.209	0.224	0.335	0.381	0.273	0.309	0.522	0.257	0.226
Zr	<LOD	<LOD	<LOD	0.061	0.233	<LOD	<LOD	<LOD	0.145	0.121	<LOD	0.110
Nb	<LOD	<LOD	<LOD	<LOD	<LOD	<LOD	0.012	0.011	<LOD	0.104	<LOD	<LOD
Mo	<LOD	<LOD	<LOD	<LOD	<LOD	<LOD	<LOD	<LOD	<LOD	<LOD	<LOD	<LOD
Ag												
Sn												
Sb	0.607	<LOD	<LOD	0.246	<LOD	0.671	0.247	0.315	0.353	0.489	0.455	0.337
Cs	<LOD	<LOD	<LOD	<LOD	<LOD	<LOD	<LOD	<LOD	<LOD	<LOD	<LOD	<LOD
Ba	367.157	26.793	443.359	35.740	74.017	58.961	35.241	32.124	68.450	378.463	84.023	51.487
La	16.856	0.537	16.099	0.414	0.299	0.508	0.493	0.484	0.480	17.434	0.547	0.446
Ce	16.270	1.012	16.601	0.769	0.511	0.857	1.034	1.027	0.824	15.787	0.816	0.821
Pr	1.035	0.155	1.032	0.093	0.058	0.104	0.115	0.120	0.121	1.032	0.083	0.094
Nd	2.628	0.672	2.611	0.351	0.402	0.592	0.577	0.530	0.419	2.500	0.424	0.387
Sm	0.215	0.192	0.282	0.069	0.093	0.053	0.055	0.230	0.074	0.377	0.080	0.071
Eu	3.109	0.633	3.027	0.299	0.325	0.431	0.538	0.486	0.493	2.558	0.531	0.491
Gd	<LOD	<LOD	0.104	0.111	<LOD	<LOD	0.108	0.134	<LOD	0.158	0.099	0.108
Tb	0.018	0.018	0.018	<LOD	<LOD	0.007	0.021	<LOD	0.032	0.025	0.020	0.003
Dy	0.071	0.094	<LOD	0.029	0.095	<LOD	0.094	0.106	0.055	0.045	0.051	0.139
Ho	<LOD	0.037	0.006	0.012	0.008	0.009	0.013	0.020	0.019	0.031	<LOD	0.019
Er	0.061	0.029	<LOD	0.011	0.023	0.023	<LOD	0.040	0.041	0.095	0.017	0.061
Tm	<LOD	<LOD	<LOD	0.004	<LOD	<LOD	<LOD	0.011	<LOD	0.006	<LOD	<LOD
Yb	<LOD	<LOD	<LOD	0.018	<LOD	<LOD	<LOD	<LOD	0.037	<LOD	<LOD	<LOD
Lu	<LOD	<LOD	<LOD	<LOD	<LOD	<LOD	<LOD	<LOD	<LOD	<LOD	<LOD	<LOD
Hf	<LOD	<LOD	<LOD	<LOD	<LOD	<LOD	<LOD	<LOD	0.017	<LOD	<LOD	<LOD
Ta	<LOD	<LOD	<LOD	<LOD	<LOD	<LOD	<LOD	<LOD	<LOD	<LOD	<LOD	<LOD
Pb	20.863	0.149	19.921	0.100	0.551	0.282	0.094	0.066	0.354	20.719	0.384	0.260
Bi	<LOD	<LOD	<LOD	<LOD	<LOD	<LOD	<LOD	<LOD	<LOD	<LOD	<LOD	0.009
Th	<LOD	<LOD	<LOD	<LOD	<LOD	<LOD	<LOD	<LOD	<LOD	<LOD	<LOD	<LOD
U	<LOD	<LOD	<LOD	<LOD	<LOD	<LOD	<LOD	<LOD	<LOD	<LOD	<LOD	<LOD

Spectrum	MD110-DR01-067-005	MD110-DR11-334 010	MD110-DR11-332-005	MD110-DR10-312-009	MD110-DR04-129A-006	MD110-DR11-334 010	MD110-DR04-129A-006	5B3 003	5B17 001	MD110-DR03b-116-002	MD110-DR01-067-002	MD110-DR01-067-002
Campaign	MD110	MD110	MD110	MD110	MD110	MD110	MD110	MD80	MD80	MD110	MD110	MD110
Dredge point	DR01	DR11	DR11	DR10	DR04	DR11	DR04	DR5	DR5	DR03b	DR01	DR01
Thin section	067	334	332	312	129A	334	129A	R3	R17	116	067	067
Mineral	Pl	Pl	Pl	Pl	Pl	Pl	Pl	Pl	Pl	Pl	Pl	Pl
Na2O	3.65	8.26	3.92	3.81	3.53	8.26	3.53	2.67	2.57	2.06	4.10	4.10
MgO	0.54	0.27	1.13	0.94	0.74	0.27	0.74	0.48	0.40	0.65	0.57	0.57
Al2O3	29.88	24.37	29.68	29.62	30.65	24.37	30.65	32.77	32.66	33.53	31.00	31.00
SiO2	50.67	60.39	51.48	51.04	50.37	60.39	50.37	47.45	48.03	46.78	50.01	50.01
P2O5	0.00	0.00	0.00	0.00	0.00	0.00	0.00	0.00	0.01	0.00	0.00	0.00
K2O	0.07	0.58	0.30	0.35	0.08	0.58	0.08	0.24	0.37	0.02	0.08	0.08
CaO	14.38	5.81	12.01	13.08	13.84	5.81	13.84	15.89	15.43	16.47	13.64	13.64
TiO2	0.08	0.03	0.07	0.06	0.10	0.03	0.10	0.07	0.08	0.03	0.13	0.13
Cr2O3	0.14	0.00	0.01	0.00	0.00	0.00	0.00	0.00	0.00	0.00	0.00	0.00
MnO	0.01	0.02	0.02	0.01	0.02	0.02	0.02	0.04	0.01	0.01	0.01	0.01
FeO	0.53	0.21	1.35	0.93	0.59	0.21	0.59	0.29	0.30	0.37	0.41	0.41
NiO												
Total	99.93	99.96	99.96	99.84	99.92	99.96	99.92	99.89	99.86	99.92	99.95	99.95
Spot Size (µm)	40	40	40	40	40	40	40	40	40	40	40	40
Li	0.959	<LOD	2.120	<LOD	7.046	<LOD	8.542	<LOD	<LOD	0.876	1.124	1.287
B								16.43	16.95			
P	44.532	306.156	470.574	173.000	<LOD	<LOD	<LOD			41.745	95.841	<LOD
S								136.63	423.61			
K								2033.04	2151.45			
Sc	0.647	0.764	0.663	0.671	0.632	0.888	0.756	0.61	0.76	0.704	0.565	0.609
Ti	428.172	100.944	212.543	404.844	357.553	112.335	410.995	395.69	396.71	158.256	474.134	433.321
V	3.980	0.435	10.163	6.082	3.794	0.330	4.212	2.84	2.83	3.150	4.330	4.056
Cr	43.919	<LOD	<LOD	<LOD	<LOD	6.375	4.284	<LOD	<LOD	3.111	<LOD	<LOD
Mn	122.086	<6.84485	258.142	165.434	123.756	46.470	125.381	15.51	18.26	130.507	99.447	107.389
Fe								2537.67	2126.85			
Co	0.765	<LOD	8.521	1.696	1.124	<LOD	1.391	0.89	0.49	0.814	0.634	0.699
Ni	<LOD	<LOD	4.604	<LOD	2.134	<LOD	1.584	1.40	1.24	1.672	<LOD	<LOD
Cu	3.693	16.188	18.136	4.492	3.431	16.589	4.935	2.75	3.41	2.517	3.408	3.439
Zn	3.668	8.197	12.870	8.089	3.828	8.971	4.159	3.60	3.77	1.443	3.223	2.603
Ga								56.90	61.75			
As								0.90	1.29			
Rb	0.140	2.073	1.258	0.232	0.395	1.022	0.336	0.59	0.66	<LOD	0.128	0.122
Sr	302.634	811.182	224.603	315.907	293.123	824.218	304.210	952.92	1010.95	341.739	263.619	256.100
Y	0.215	0.600	0.216	0.265	0.217	0.384	0.238	0.17	0.18	0.248	0.234	0.220
Zr	<LOD	<LOD	0.265	<LOD	0.840	<LOD	0.480	<LOD	<LOD	<LOD	0.061	<LOD
Nb	<LOD	0.021	<LOD	<LOD	0.039	0.014	0.020	0.01	0.01	<LOD	0.012	0.005
Mo	<LOD	<LOD	0.113	<LOD	<LOD	<LOD	<LOD	<LOD	<LOD	<LOD	<LOD	<LOD
Ag								<LOD	0.03			
Sn								<LOD	0.09			
Sb	0.364	0.831	0.230	0.363	0.336	0.632	0.380	<LOD	<LOD	0.219	0.195	0.288
Cs	<LOD	<LOD	<LOD	<LOD	<LOD	<LOD	<LOD	<LOD	<LOD	<LOD	<LOD	<LOD
Ba	27.856	499.769	40.708	30.128	40.899	518.376	45.840	147.24	167.83	6.114	19.615	18.624
La	0.431	26.879	0.309	0.333	0.502	24.228	0.599	1.67	1.65	0.230	0.399	0.347
Ce	0.844	25.367	0.495	0.692	0.965	22.533	1.055	2.51	2.53	0.503	0.719	0.692
Pr	0.118	1.603	0.075	0.081	0.125	1.342	0.118	0.21	0.25	0.091	0.099	0.089
Nd	0.498	3.891	0.285	0.410	0.478	3.301	0.569	0.87	0.86	0.340	0.519	0.433
Sm	0.075	0.392	0.032	0.091	<LOD	0.434	0.107	0.17	0.13	0.127	0.145	0.084
Eu	0.384	5.398	0.286	0.517	0.352	4.712	0.345	0.48	0.50	0.273	0.414	0.391
Gd	0.159	0.334	0.134	0.154	0.162	0.491	0.086	<LOD	<LOD	0.065	0.102	<LOD
Tb	<LOD	0.039	0.022	<LOD	0.018	0.026	0.026	<LOD	<LOD	<LOD	0.008	0.019
Dy	0.039	0.105	0.053	0.128	0.064	0.046	0.122	<LOD	0.05	0.034	0.055	0.056
Ho	0.007	0.029	0.014	<LOD	0.013	0.028	0.007	0.01	0.01	0.011	0.008	0.011
Er	<LOD	0.107	<LOD	0.039	0.031	0.043	<LOD	0.02	<LOD	<LOD	<LOD	0.011
Tm	<LOD	<LOD	<LOD	<LOD	<LOD	<LOD	<LOD	<LOD	<LOD	<LOD	<LOD	<LOD
Yb	<LOD	0.102	0.053	<LOD	0.039	<LOD	<LOD	<LOD	<LOD	0.037	<LOD	<LOD
Lu	<LOD	<LOD	<LOD	<LOD	<LOD	<LOD	<LOD	0.00	<LOD	<LOD	<LOD	0.004
Hf	<LOD	<LOD	<LOD	<LOD	0.027	0.030	<LOD	<LOD	<LOD	<LOD	<LOD	<LOD
Ta	<LOD	<LOD	<LOD	<LOD	<LOD	<LOD	<LOD	0.00	0.01	<LOD	<LOD	<LOD
Pb	0.056	29.937	0.477	0.155	0.088	28.492	0.158	0.34	0.25	0.062	0.084	0.096
Bi	<LOD	<LOD	<LOD	<LOD	<LOD	<LOD	<LOD	<LOD	<LOD	<LOD	0.011	<LOD
Th	<LOD	<LOD	<LOD	<LOD	<LOD	<LOD	<LOD	<LOD	<LOD	<LOD	<LOD	<LOD
U	<LOD	<LOD	<LOD	<LOD	<LOD	<LOD	<LOD	<LOD	<LOD	<LOD	<LOD	<LOD

Spectrum	MD110-DR03b-116-002	MD110-DR11-334009	MD110-DR03b-102C-008	MD110-DR03b-116-012	MD110-DR03b-102C-007	MD110-DR03b-116-012	MD110-DR03b-102C-008	MD110-DR03b-116-012	MD110-DR11-332-007	MD110-DR03b-116-001	MD110-DR03b-101D006	MD110-DR03b-101D005
Campaign	MD110	MD110	MD110	MD110	MD110	MD110	MD110	MD110	MD110	MD110	MD110	MD110
Dredge point	DR03b	DR11	DR03b	DR03b	DR03b	DR03b	DR03b	DR03b	DR11	DR03b	DR03b	DR03b
Thin section	116	334	102C	116	102C	116	102C	116	332	116	101D	101D
Mineral	Pl	Pl	Pl	Pl	Pl	Pl	Pl	Pl	Pl	Pl	Pl	Pl
Na2O	2.06	7.96	3.37	1.76	3.65	1.76	3.37	1.76	3.55	2.09	3.23	3.58
MgO	0.65	0.31	0.50	0.55	0.53	0.55	0.50	0.55	1.08	0.52	0.56	0.51
Al2O3	33.53	24.51	31.23	34.11	30.25	34.11	31.23	34.11	30.08	33.73	31.73	31.20
SiO2	46.78	60.18	49.46	46.34	50.81	46.34	49.46	46.34	50.36	46.77	49.36	49.85
P2O5	0.00	0.00	0.00	0.00	0.00	0.00	0.00	0.00	0.00	0.00	0.01	0.00
K2O	0.02	0.98	0.10	0.02	0.95	0.02	0.10	0.02	0.14	0.02	0.69	0.16
CaO	16.47	5.78	14.49	16.86	12.90	16.86	14.49	16.86	13.32	16.53	13.92	14.10
TiO2	0.03	0.05	0.07	0.05	0.07	0.05	0.07	0.05	0.04	0.03	0.06	0.11
Cr2O3	0.00	0.00	0.00	0.00	0.00	0.00	0.00	0.00	0.00	0.00	0.01	0.02
MnO	0.01	0.01	0.01	0.01	0.01	0.01	0.01	0.01	0.02	0.01	0.01	0.01
FeO	0.37	0.19	0.41	0.26	0.42	0.26	0.41	0.26	1.38	0.26	0.39	0.43
NiO												
Total	99.92	99.97	99.64	99.96	99.60	99.96	99.64	99.96	99.96	99.96	99.97	99.97
Spot Size (µm)	40	40	40	40	40	40	40	40	40	40	40	40
Li	1.247	<LOD	0.850	1.203	<LOD	0.796	<LOD	1.164	2.085	0.846	<LOD	<LOD
B												
P	<LOD	<LOD	537.632	87.474	330.124	42.409	395.803	31.178	489.852	<LOD	<LOD	58.097
S												
K												
Sc	0.559	0.301	0.561	0.493	0.736	0.668	0.545	0.416	0.738	0.382	0.405	0.558
Ti	163.210	74.960	260.082	114.579	263.879	148.021	289.010	144.058	255.414	130.164	233.310	272.898
V	3.063	0.242	2.901	2.469	2.946	2.569	3.134	2.586	10.851	2.285	2.637	3.077
Cr	<LOD	<LOD	<LOD	3.694	2.953	2.975	<LOD	<LOD	<LOD	2.967	2.576	3.308
Mn	121.694	<4.74197	125.216	102.672	105.955	127.954	111.588	79.034	201.354	95.621	103.626	118.580
Fe												
Co	0.930	<LOD	0.857	0.357	0.589	0.550	0.834	0.362	3.771	0.364	0.697	0.775
Ni	2.011	<LOD	<LOD	1.070	<LOD	1.178	<LOD	1.397	2.711	1.287	<LOD	<LOD
Cu	3.008	10.146	2.633	2.334	2.696	1.916	3.166	1.936	11.293	1.864	2.884	3.187
Zn	1.948	7.333	3.314	1.648	2.851	<LOD	2.291	1.509	10.923	1.856	1.923	2.996
Ga												
As												
Rb	<LOD	0.413	1.374	<LOD	0.233	<LOD	0.206	<LOD	0.881	<LOD	0.198	0.266
Sr	331.278	513.845	257.525	236.161	269.272	255.195	268.694	244.228	224.648	260.021	296.245	320.655
Y	0.242	0.288	0.165	0.194	0.151	0.233	0.154	0.204	0.197	0.193	0.164	0.171
Zr	<LOD	<LOD	<LOD	<LOD	0.069	<LOD	<LOD	<LOD	0.143	<LOD	<LOD	<LOD
Nb	<LOD	<LOD	<LOD	<LOD	<LOD	<LOD	0.009	0.005	<LOD	<LOD	<LOD	<LOD
Mo	0.101	<LOD	<LOD	<LOD	<LOD	<LOD	<LOD	<LOD	<LOD	0.086	<LOD	<LOD
Ag												
Sn												
Sb	0.256	0.336	0.363	0.190	0.205	0.190	0.189	0.304	0.240	0.248	0.196	0.182
Cs	<LOD	<LOD	<LOD	<LOD	<LOD	<LOD	<LOD	<LOD	<LOD	<LOD	<LOD	<LOD
Ba	6.083	302.277	54.595	5.992	39.671	5.343	38.053	3.968	43.909	4.639	33.417	39.828
La	0.169	15.475	0.435	0.176	0.433	0.187	0.439	0.186	0.356	0.145	0.423	0.439
Ce	0.452	14.208	0.550	0.389	0.697	0.485	0.779	0.525	0.662	0.414	0.725	0.764
Pr	0.082	0.886	0.091	0.067	0.086	0.084	0.100	0.070	0.083	0.079	0.085	0.103
Nd	0.421	2.145	0.423	0.315	0.326	0.319	0.253	0.461	0.291	0.299	0.333	0.501
Sm	0.099	0.172	0.100	0.064	0.059	0.053	0.085	0.071	0.022	0.080	0.011	0.085
Eu	0.350	2.894	0.249	0.227	0.314	0.282	0.351	0.296	0.256	0.233	0.258	0.307
Gd	<LOD	0.219	0.058	0.088	0.159	<LOD	0.070	0.135	0.092	0.055	0.114	<LOD
Tb	0.008	<LOD	0.004	0.014	0.012	0.017	0.013	0.011	0.010	0.016	0.011	0.015
Dy	0.075	0.032	0.055	0.045	<LOD	0.069	0.052	0.048	0.060	0.025	0.060	0.064
Ho	0.011	0.010	<LOD	0.007	0.012	0.007	0.005	0.003	0.014	0.009	0.010	0.013
Er	0.032	<LOD	<LOD	<LOD	<LOD	<LOD	<LOD	0.017	0.026	<LOD	0.036	<LOD
Tm	0.004	<LOD	<LOD	<LOD	0.005	<LOD	<LOD	<LOD	<LOD	0.015	<LOD	<LOD
Yb	<LOD	<LOD	<LOD	<LOD	0.037	<LOD	0.047	0.036	0.017	<LOD	<LOD	<LOD
Lu	<LOD	0.006	<LOD	<LOD	<LOD	<LOD	<LOD	<LOD	<LOD	<LOD	<LOD	<LOD
Hf	<LOD	<LOD	<LOD	0.021	0.021	<LOD	<LOD	<LOD	<LOD	<LOD	<LOD	<LOD
Ta	<LOD	<LOD	<LOD	<LOD	0.004	0.007	<LOD	<LOD	<LOD	<LOD	<LOD	<LOD
Pb	0.111	19.267	0.105	0.085	0.095	0.053	0.078	0.062	0.266	0.068	0.093	0.081
Bi	<LOD	<LOD	<LOD	<LOD	<LOD	<LOD	<LOD	<LOD	<LOD	0.009	<LOD	<LOD
Th	<LOD	0.005	<LOD	<LOD	<LOD	<LOD	<LOD	<LOD	<LOD	<LOD	<LOD	<LOD
U	<LOD	<LOD	<LOD	<LOD	<LOD	<LOD	<LOD	<LOD	<LOD	<LOD	<LOD	<LOD

Spectrum	MD110-DR03b-101D 006	5B9 009	MD110-DR03b-101D 005	MD110-DR03b-102C-003	MD110-DR03b-116-006	MD110-DR03b-101D 006	MD110-DR03b-101D 005	MD110-DR03b-116-013	MD110-DR03b-116-013	MD110-DR03b-102C-003	MD110-DR03b-116-013	MD110-DR03b-116-001
Campaign	MD110	MD80	MD110	MD110	MD110	MD110	MD110	MD110	MD110	MD110	MD110	MD110
Dredge point	DR03b	DR5	DR03b	DR03b	DR03b	DR03b	DR03b	DR03b	DR03b	DR03b	DR03b	DR03b
Thin section	101D	B9	101D	102C	116	101D	101D	116	116	102C	116	116
Mineral	Pl	Pl	Pl	Pl	Pl	Pl	Pl	Pl	Pl	Pl	Pl	Pl
Na2O	3.23	2.66	3.58	3.31	2.07	3.23	3.58	2.54	2.54	3.31	2.54	2.09
MgO	0.56	0.48	0.51	0.57	0.60	0.56	0.51	0.55	0.55	0.57	0.55	0.52
Al2O3	31.73	32.90	31.20	31.13	33.64	31.73	31.20	33.12	33.12	31.13	33.12	33.73
SiO2	49.36	47.52	49.85	49.71	46.47	49.36	49.85	47.40	47.40	49.71	47.40	46.77
P2O5	0.01	0.00	0.00	0.00	0.00	0.01	0.00	0.00	0.00	0.00	0.00	0.00
K2O	0.69	0.22	0.16	0.09	0.22	0.69	0.16	0.01	0.01	0.09	0.01	0.02
CaO	13.92	15.71	14.10	14.64	16.57	13.92	14.10	16.01	16.01	14.64	16.01	16.53
TiO2	0.06	0.05	0.11	0.05	0.02	0.06	0.11	0.03	0.03	0.05	0.03	0.03
Cr2O3	0.01	0.00	0.02	0.00	0.06	0.01	0.02	0.01	0.01	0.00	0.01	0.00
MnO	0.01	0.03	0.01	0.01	0.01	0.01	0.01	0.01	0.01	0.01	0.01	0.01
FeO	0.39	0.35	0.43	0.44	0.30	0.39	0.43	0.28	0.28	0.44	0.28	0.26
NiO												
Total	99.97	99.93	99.97	99.95	99.96	99.97	99.97	99.96	99.96	99.95	99.96	99.96
Spot Size (µm)	40	40	40	40	40	40	40	40	40	40	40	40
Li	<LOD	<LOD	<LOD	<LOD	0.654	<LOD	<LOD	1.160	0.784	<LOD	1.137	0.624
B		15.91										
P	<LOD		18.740	408.924	53.870	<LOD	37.961	<LOD	<LOD	355.357	49.342	<LOD
S		146.01										
K		1904.23										
Sc	0.453	0.48	0.643	0.728	0.526	0.390	0.438	0.420	0.450	0.594	0.461	0.465
Ti	244.334	285.84	261.287	285.138	94.467	232.196	265.745	119.963	117.179	283.776	118.050	116.996
V	2.850	2.31	3.077	3.462	1.999	2.790	2.936	2.423	2.490	3.370	2.452	2.106
Cr	<LOD	<LOD	3.018	<LOD	<LOD	<LOD	3.523	3.825	3.774	<LOD	4.101	2.471
Mn	86.596	16.05	123.880	125.209	138.687	105.226	100.977	85.385	84.260	125.644	97.327	100.656
Fe		2790.99										
Co	0.702	0.55	0.990	0.734	0.778	0.901	0.723	0.374	0.356	0.744	0.351	0.455
Ni	<LOD	0.69	<LOD	<LOD	0.950	<LOD	0.771	1.684	0.742	0.817	1.128	1.259
Cu	2.876	2.03	3.202	2.901	2.083	2.980	3.100	2.292	1.960	3.048	2.067	1.825
Zn	2.933	2.61	3.287	3.601	1.341	2.728	2.890	1.801	1.821	3.332	1.753	1.559
Ga		41.81										
As		0.64										
Rb	0.272	0.34	0.236	0.214	<LOD	0.206	0.272	0.038	<LOD	0.229	0.042	<LOD
Sr	292.570	578.85	321.988	306.160	253.082	297.136	318.584	224.042	232.520	300.497	227.214	240.048
Y	0.201	0.09	0.187	0.214	0.127	0.148	0.177	0.192	0.176	0.218	0.190	0.172
Zr	<LOD	0.02	<LOD	<LOD	0.048	<LOD	<LOD	<LOD	<LOD	<LOD	<LOD	<LOD
Nb	<LOD	0.01	0.004	0.005	<LOD	0.018	<LOD	<LOD	<LOD	0.014	<LOD	<LOD
Mo	0.053	<LOD	0.101	<LOD	<LOD	<LOD	<LOD	<LOD	<LOD	<LOD	<LOD	<LOD
Ag		<LOD										
Sn		0.06										
Sb	0.122	<LOD	0.200	0.225	0.176	0.145	0.290	0.188	0.219	0.314	0.210	0.241
Cs	<LOD	<LOD	<LOD	<LOD	<LOD	<LOD	<LOD	<LOD	<LOD	<LOD	<LOD	<LOD
Ba	36.102	66.67	38.296	40.357	5.687	34.146	37.214	5.186	5.325	39.025	5.092	4.080
La	0.455	0.71	0.469	0.538	0.149	0.405	0.462	0.194	0.206	0.558	0.155	0.153
Ce	0.753	1.16	0.809	0.870	0.347	0.716	0.746	0.353	0.375	0.778	0.358	0.332
Pr	0.099	0.10	0.111	0.112	0.049	0.091	0.086	0.062	0.070	0.121	0.072	0.045
Nd	0.423	0.45	0.542	0.536	0.266	0.385	0.366	0.204	0.257	0.401	0.292	0.250
Sm	0.041	0.06	0.078	0.120	0.115	0.062	0.056	0.053	0.046	0.134	0.108	0.062
Eu	0.259	0.23	0.277	0.319	0.279	0.260	0.295	0.242	0.227	0.321	0.237	0.236
Gd	0.039	<LOD	<LOD	<LOD	0.069	0.088	<LOD	0.130	<LOD	<LOD	0.035	<LOD
Tb	0.005	<LOD	0.006	<LOD	0.006	0.011	0.016	0.019	0.008	<LOD	0.010	<LOD
Dy	0.031	<LOD	<LOD	0.094	0.050	0.050	0.016	0.102	0.042	0.012	0.029	0.065
Ho	0.010	<LOD	0.014	0.013	0.003	<LOD	0.014	0.005	0.007	0.007	0.005	0.017
Er	0.050	<LOD	<LOD	<LOD	0.014	0.035	<LOD	0.018	<LOD	0.043	0.014	0.040
Tm	<LOD	<LOD	<LOD	0.009	0.008	<LOD	<LOD	<LOD	0.002	<LOD	<LOD	<LOD
Yb	0.015	<LOD	<LOD	0.021	<LOD	<LOD	0.016	0.039	0.039	<LOD	<LOD	0.024
Lu	<LOD	<LOD	<LOD	<LOD	<LOD	<LOD	<LOD	<LOD	<LOD	<LOD	<LOD	<LOD
Hf	<LOD	<LOD	<LOD	<LOD	<LOD	<LOD	<LOD	<LOD	<LOD	<LOD	<LOD	<LOD
Ta	<LOD	<LOD	<LOD	<LOD	<LOD	<LOD	<LOD	<LOD	<LOD	<LOD	<LOD	<LOD
Pb	0.092	0.18	0.107	0.113	0.066	0.088	0.089	0.068	0.042	0.093	0.096	0.062
Bi	<LOD	<LOD	<LOD	<LOD	<LOD	<LOD	<LOD	<LOD	0.020	<LOD	<LOD	<LOD
Th	<LOD	<LOD	<LOD	<LOD	<LOD	<LOD	<LOD	<LOD	<LOD	<LOD	<LOD	<LOD
U	<LOD	<LOD	<LOD	<LOD	<LOD	<LOD	<LOD	<LOD	<LOD	<LOD	<LOD	<LOD

Spectrum	MD110-DR03b-116-006	MD110-DR03b-116-004	MD110-DR03b-102C-004	MD110-DR11-334009-002	5B9010	MD110-DR03b-116-003	5B9005	MD110-DR03b-116-004	5B17010	MD110-DR03b-116-005	5B9001	MD110-DR04-129A-006
Campaign	MD110	MD110	MD110	MD110	MD80	MD110	MD80	MD110	MD80	MD110	MD80	MD110
Dredge point	DR03b	DR03b	DR03b	DR11	DR5	DR03b	DR5	DR03b	DR5	DR03b	DR5	DR04
Thin section	116	116	102C	334	R9	116	R9	116	R17	116	R9	129A
Mineral	Pl	Pl	Pl	Pl	Pl	Pl	Pl	Pl	Pl	Pl	Pl	Pl
Na2O	2.07	2.14	3.24	7.79	2.61	2.06	2.67	2.14	2.57	2.19	3.96	3.53
MgO	0.60	0.57	0.60	0.34	0.47	0.58	0.48	0.57	0.61	0.59	0.36	0.74
Al2O3	33.64	33.63	31.36	24.35	32.99	33.71	32.64	33.63	31.62	33.27	30.96	30.65
SiO2	46.47	46.57	49.40	60.45	47.44	46.60	47.55	46.57	48.68	47.00	50.45	50.37
P2O5	0.00	0.00	0.00	0.00	0.01	0.00	0.01	0.00	0.01	0.00	0.00	0.00
K2O	0.22	0.18	0.08	0.65	0.19	0.18	0.26	0.18	1.17	0.21	0.28	0.08
CaO	16.57	16.53	14.78	6.15	15.85	16.49	15.78	16.53	14.36	16.35	13.36	13.84
TiO2	0.02	0.03	0.05	0.03	0.07	0.03	0.12	0.03	0.13	0.03	0.10	0.10
Cr2O3	0.06	0.05	0.01	0.02	0.00	0.05	0.00	0.05	0.01	0.05	0.01	0.00
MnO	0.01	0.01	0.01	0.01	0.04	0.01	0.01	0.01	0.34	0.01	0.01	0.02
FeO	0.30	0.25	0.44	0.16	0.28	0.25	0.44	0.25	0.45	0.26	0.42	0.59
NiO												
Total	99.96	99.96	99.97	99.96	99.96	99.96	99.95	99.96	99.95	99.96	99.92	99.92
Spot Size (µm)	40	40	40	40	40	40	40	40	40	40	40	40
Li	0.700	0.849	<LOD	0.270	<LOD	0.537	1.36	0.795	16.82	<LOD	1.42	4.770
B					14.95		12.98		26.01		11.61	
P	<LOD	<LOD	411.695	195.835		<LOD		79.961		<LOD		63.771
S					42.93		139.10		122.53		101.49	
K					2312.13		1765.29		3549.09		2163.03	
Sc	0.472	0.465	0.699	0.587	0.49	0.383	0.41	0.395	0.65	0.363	0.28	0.486
Ti	85.886	116.052	259.898	72.608	318.12	127.098	259.23	127.880	378.23	83.351	481.12	269.386
V	1.664	1.981	2.966	0.778	2.29	2.330	1.91	2.116	2.79	1.616	1.93	2.872
Cr	3.786	2.761	<LOD	16.340	<LOD	<LOD	<LOD	<LOD	<LOD	3.451	<LOD	2.638
Mn	139.520	98.303	101.947	13.376	22.31	77.711	15.32	75.710	34.45	78.584	22.96	82.747
Fe					2675.88		2195.32		2390.02		3977.07	
Co	0.593	0.640	0.912	0.430	0.64	0.477	0.61	0.633	7.59	0.767	0.41	0.751
Ni	0.927	1.753	<LOD	1.403	1.13	1.364	0.69	1.136	2.08	1.416	0.62	2.300
Cu	2.249	2.417	2.752	9.770	2.36	2.280	1.93	2.529	4.27	2.163	3.04	2.487
Zn	1.600	1.223	2.762	4.844	2.84	1.223	1.89	1.193	3.82	1.120	3.99	3.702
Ga					42.18		36.04		65.77		53.06	
As					0.82		0.74		1.79		0.84	
Rb	0.040	0.037	0.239	0.620	0.54	<LOD	0.39	<LOD	1.85	0.045	0.41	0.450
Sr	245.047	212.577	284.063	471.235	619.61	199.752	503.12	214.808	936.12	214.745	562.17	181.960
Y	0.086	0.124	0.183	0.260	0.10	0.170	0.09	0.129	0.17	0.100	0.12	0.146
Zr	<LOD	<LOD	<LOD	<LOD	0.05	<LOD	0.02	<LOD	0.16	<LOD	0.03	1.044
Nb	<LOD	<LOD	0.007	<LOD	0.01	<LOD	0.00	<LOD	0.01	<LOD	0.01	0.051
Mo	<LOD	<LOD	<LOD	<LOD	<LOD	<LOD	<LOD	<LOD	<LOD	<LOD	<LOD	<LOD
Ag					<LOD		<LOD		<LOD		<LOD	
Sn					<LOD		0.06		0.10		0.05	
Sb	0.265	0.255	0.293	0.513	<LOD	0.168	<LOD	0.192	<LOD	0.258	<LOD	0.190
Cs	<LOD	<LOD	<LOD	<LOD	<LOD	<LOD	<LOD	<LOD	0.00	<LOD	<LOD	<LOD
Ba	5.592	5.106	38.699	327.341	75.04	5.565	63.55	5.011	190.17	6.369	99.56	29.197
La	0.160	0.164	0.522	14.258	0.79	0.146	0.66	0.166	1.65	0.141	1.29	0.338
Ce	0.328	0.280	0.736	13.339	1.37	0.347	1.03	0.316	2.49	0.257	2.00	0.614
Pr	0.063	0.047	0.095	0.855	0.12	0.048	0.10	0.049	0.24	0.053	0.17	0.078
Nd	0.272	0.297	0.470	1.936	0.61	0.231	0.46	0.233	0.79	0.130	0.73	0.304
Sm	0.064	0.022	0.094	0.092	0.06	0.017	0.07	0.059	0.07	0.042	0.11	0.074
Eu	0.228	0.209	0.371	2.707	0.23	0.189	0.18	0.256	0.45	0.164	0.36	0.228
Gd	0.111	0.053	0.055	0.176	<LOD	0.083	0.07	0.063	<LOD	0.072	<LOD	0.050
Tb	<LOD	0.003	0.010	0.022	<LOD	0.007	<LOD	0.009	<LOD	0.010	<LOD	0.003
Dy	0.032	0.034	0.044	0.011	<LOD	0.043	0.03	0.016	<LOD	<LOD	<LOD	0.033
Ho	<LOD	0.007	0.006	0.004	0.00	0.014	<LOD	0.002	<LOD	0.006	0.01	0.005
Er	0.010	0.023	<LOD	<LOD	0.01	<LOD	<LOD	<LOD	<LOD	<LOD	<LOD	<LOD
Tm	<LOD	<LOD	<LOD	<LOD	<LOD	<LOD	<LOD	<LOD	<LOD	<LOD	<LOD	<LOD
Yb	<LOD	<LOD	<LOD	<LOD	0.01	0.009	0.01	<LOD	<LOD	0.017	<LOD	0.031
Lu	<LOD	<LOD	<LOD	<LOD	<LOD	<LOD	<LOD	0.003	<LOD	<LOD	<LOD	0.003
Hf	<LOD	<LOD	<LOD	<LOD	<LOD	<LOD	<LOD	<LOD	<LOD	<LOD	<LOD	0.037
Ta	<LOD	<LOD	<LOD	<LOD	<LOD	<LOD	<LOD	<LOD	0.01	<LOD	<LOD	<LOD
Pb	0.058	0.059	0.097	18.708	0.18	0.033	0.13	0.048	0.31	0.075	0.22	0.106
Bi	<LOD	<LOD	<LOD	<LOD	<LOD	<LOD	<LOD	<LOD	<LOD	<LOD	<LOD	<LOD
Th	<LOD	<LOD	<LOD	<LOD	<LOD	<LOD	<LOD	<LOD	<LOD	<LOD	<LOD	<LOD
U	<LOD	<LOD	<LOD	<LOD	<LOD	<LOD	<LOD	<LOD	<LOD	<LOD	<LOD	<LOD

Spectrum	MD110-DR03b-116-003	MD110-DR03b-102C-003	MD110-DR03b-116-005	5B9 002	MD110-DR03b-102C-003	5B17 009	MD110-DR03b-101D 004-	5B17 006	MD110-DR03b-101D 004-	MD110-DR03b-101D 004-	MD110-DR03b-116-007	MD110-DR03b-101D 001
Campaign	MD110	MD110	MD110	MD80	MD110	MD80	MD110	MD80	MD110	MD110	MD110	MD110
Dredge point	DR03b	DR03b	DR03b	DR5	DR03b	DR5	DR03b	DR5	DR03b	DR03b	DR03b	DR03b
Thin section	116	102C	116	B9	102C	B17	101D	B17	101D	101D	116	101D
Mineral	Pl	Pl	Pl	Pl	Pl	Pl	Pl	Pl	Pl	Pl	Pl	Pl
Na2O	2.06	3.31	2.19	2.59	3.31	2.60	4.78	2.89	4.78	4.19	1.97	3.59
MgO	0.58	0.57	0.59	0.45	0.57	0.43	0.52	0.51	0.52	0.51	0.59	0.56
Al2O3	33.71	31.13	33.27	32.76	31.13	33.11	29.67	32.62	29.67	29.25	33.64	31.26
SiO2	46.60	49.71	47.00	47.74	49.71	47.62	52.33	48.40	52.33	52.70	46.38	49.64
P2O5	0.00	0.00	0.00	0.00	0.00	0.01	0.00	0.00	0.00	0.00	0.00	0.00
K2O	0.18	0.09	0.21	0.31	0.09	0.42	0.25	0.27	0.25	1.04	0.22	0.20
CaO	16.49	14.64	16.35	15.72	14.64	15.34	11.97	14.87	11.97	11.82	16.79	14.19
TiO2	0.03	0.05	0.03	0.07	0.05	0.08	0.06	0.07	0.06	0.06	0.02	0.09
Cr2O3	0.05	0.00	0.05	0.00	0.00	0.03	0.01	0.01	0.01	0.01	0.05	0.00
MnO	0.01	0.01	0.01	0.02	0.01	0.04	0.03	0.01	0.03	0.02	0.01	0.01
FeO	0.25	0.44	0.26	0.29	0.44	0.26	0.36	0.30	0.36	0.36	0.28	0.39
NiO												
Total	99.96	99.95	99.96	99.94	99.95	99.96	99.97	99.95	99.97	99.97	99.96	99.94
Spot Size (µm)	40	40	40	40	40	40	40	40	40	40	40	40
Li	0.784	<LOD	0.850	<LOD	<LOD	<LOD	<LOD	<LOD	<LOD	<LOD	2.303	0.901
B				13.88		17.66		20.44				
P	<LOD	469.019	<LOD		496.273		<LOD		<LOD	<LOD	<LOD	<LOD
S				148.88		122.03		156.41				
K				2056.25		2050.81		2000.08				
Sc	0.392	0.622	0.486	0.40	0.776	0.73	0.429	0.67	0.440	0.341	0.311	0.415
Ti	123.785	295.766	124.251	307.05	270.409	361.89	219.987	373.63	217.321	212.252	124.393	240.541
V	2.350	3.102	1.825	2.20	3.050	2.55	2.520	2.81	2.344	2.484	2.511	2.811
Cr	4.611	<LOD	3.984	<LOD	<LOD	<LOD	<LOD	<LOD	<LOD	<LOD	<LOD	2.015
Mn	87.633	143.233	76.663	17.23	104.872	19.88	104.205	20.50	110.183	76.719	87.431	84.391
Fe				2395.95		2030.45		2289.70				
Co	0.480	0.759	0.520	0.39	0.679	0.49	0.539	0.56	0.490	0.540	0.301	0.978
Ni	1.153	<LOD	1.181	0.83	<LOD	1.14	<LOD	1.24	0.389	<LOD	0.560	3.179
Cu	2.198	2.884	2.553	2.13	2.857	2.99	3.454	2.96	2.618	2.647	1.712	4.108
Zn	1.444	2.513	1.171	2.43	2.713	2.69	2.714	3.03	2.186	2.886	1.813	2.707
Ga				39.55		55.60		60.53				
As				0.66		1.14		1.19				
Rb	<LOD	0.264	<LOD	0.51	0.249	0.66	0.289	0.55	0.235	0.218	0.068	0.517
Sr	199.046	302.942	196.721	588.87	295.526	905.66	336.812	981.66	263.546	265.309	237.388	405.158
Y	0.149	0.209	0.109	0.10	0.156	0.17	0.167	0.19	0.154	0.136	0.177	0.178
Zr	<LOD	<LOD	<LOD	0.05	<LOD	0.05	0.120	0.04	<LOD	0.047	<LOD	0.117
Nb	0.010	<LOD	<LOD	0.01	<LOD	0.00	<LOD	0.01	<LOD	0.010	0.005	0.010
Mo	<LOD	<LOD	<LOD	<LOD	<LOD	<LOD	<LOD	<LOD	<LOD	<LOD	<LOD	<LOD
Ag				<LOD		<LOD		<LOD				
Sn				0.05		0.06		0.08				
Sb	0.219	0.307	0.199	<LOD	0.181	<LOD	0.140	<LOD	0.146	0.170	0.250	0.191
Cs	<LOD	<LOD	<LOD	<LOD	<LOD	<LOD	<LOD	<LOD	<LOD	<LOD	<LOD	0.150
Ba	5.916	42.309	4.944	67.85	40.353	144.39	40.311	161.16	32.632	33.359	6.014	57.227
La	0.168	0.502	0.117	0.75	0.482	1.50	0.343	1.66	0.412	0.374	0.163	0.450
Ce	0.290	0.823	0.277	1.22	0.742	2.24	0.679	2.48	0.695	0.694	0.420	0.632
Pr	0.040	0.103	0.042	0.11	0.094	0.22	0.082	0.25	0.094	0.080	0.066	0.093
Nd	0.206	0.523	0.199	0.53	0.507	0.80	0.402	0.86	0.347	0.356	0.324	0.275
Sm	0.092	0.096	0.044	0.07	0.105	0.13	0.047	0.10	0.087	0.080	0.099	0.083
Eu	0.207	0.321	0.193	0.21	0.336	0.43	0.264	0.47	0.243	0.244	0.245	0.231
Gd	0.094	0.105	0.081	<LOD	0.096	<LOD	0.055	<LOD	0.028	0.057	0.089	0.121
Tb	0.003	0.013	0.005	<LOD	0.010	<LOD	0.014	<LOD	0.009	0.012	0.012	0.010
Dy	0.037	0.030	0.035	<LOD	0.039	<LOD	0.036	0.07	0.040	0.041	0.035	0.020
Ho	<LOD	<LOD	0.008	0.01	<LOD	<LOD	0.013	0.00	0.004	<LOD	0.010	0.013
Er	<LOD	0.024	<LOD	<LOD	<LOD	0.01	<LOD	0.01	0.056	<LOD	0.015	<LOD
Tm	<LOD	<LOD	<LOD	<LOD	<LOD	<LOD	<LOD	<LOD	0.004	<LOD	0.003	<LOD
Yb	<LOD	0.013	<LOD	<LOD	<LOD	<LOD	<LOD	<LOD	<LOD	0.019	<LOD	0.018
Lu	<LOD	<LOD	<LOD	0.00	<LOD	<LOD	<LOD	<LOD	<LOD	<LOD	0.004	<LOD
Hf	<LOD	<LOD	<LOD	<LOD	<LOD	<LOD	<LOD	<LOD	0.022	<LOD	<LOD	<LOD
Ta	<LOD	<LOD	<LOD	<LOD	<LOD	<LOD	<LOD	<LOD	<LOD	<LOD	<LOD	0.002
Pb	0.055	0.261	0.071	0.12	0.066	0.25	0.142	0.28	0.057	0.090	0.058	0.091
Bi	<LOD	<LOD	<LOD	<LOD	<LOD	<LOD	<LOD	<LOD	<LOD	<LOD	<LOD	<LOD
Th	<LOD	<LOD	<LOD	<LOD	<LOD	<LOD	<LOD	<LOD	<LOD	<LOD	<LOD	<LOD
U	<LOD	<LOD	<LOD	<LOD	<LOD	<LOD	<LOD	<LOD	<LOD	<LOD	<LOD	<LOD

Spectrum	5B3 004	5B3 008	MD110-DR03b-101D 004-	MD110-DR03b-101D 003	5A15 005	MD110-DR03b-101D 004-	MD110-DR03b-101D 003	5A15 002	5B3 002	5B3 006	5B3 007	MD110-DR03b-101D 003
Campaign	MD80	MD80	MD110	MD110	MD80	MD110	MD110	MD80	MD80	MD80	MD80	MD110
Dredge point	DR5	DR5	DR03b	DR03b	DR5	DR03b	DR03b	DR5	DR5	DR5	DR5	DR03b
Thin section	B3	B3	101D	101D	A15	101D	101D	A15	B3	B3	B3	101D
Mineral	Pl	Pl	Pl	Pl	Pl	Pl	Pl	Pl	Pl	Pl	Pl	Pl
Na2O	2.54	2.61	4.19	3.54	4.09	4.78	3.54	2.83	2.72	2.70	2.78	3.54
MgO	1.02	0.47	0.51	0.48	0.61	0.52	0.48	0.46	0.61	0.47	0.58	0.48
Al2O3	32.44	33.09	29.25	31.40	29.59	29.67	31.40	31.90	32.75	32.66	32.39	31.40
SiO2	47.75	47.77	52.70	49.51	51.19	52.33	49.51	48.31	47.80	48.11	48.33	49.51
P2O5	0.01	0.00	0.00	0.00	0.03	0.00	0.00	0.04	0.01	0.00	0.01	0.00
K2O	0.34	0.32	1.04	0.10	0.45	0.25	0.10	0.29	0.29	0.27	0.48	0.10
CaO	15.11	15.29	11.82	14.41	13.18	11.97	14.41	15.62	15.38	15.36	14.94	14.41
TiO2	0.07	0.12	0.06	0.11	0.16	0.06	0.11	0.08	0.06	0.07	0.08	0.11
Cr2O3	0.00	0.00	0.01	0.02	0.00	0.01	0.02	0.03	0.00	0.00	0.00	0.02
MnO	0.01	0.01	0.02	0.02	0.02	0.03	0.02	0.01	0.02	0.02	0.02	0.02
FeO	0.62	0.28	0.36	0.36	0.61	0.36	0.36	0.34	0.32	0.28	0.34	0.36
NiO												
Total	99.91	99.96	99.97	99.96	99.93	99.97	99.96	99.90	99.96	99.94	99.94	99.96
Spot Size (µm)	40	40	40	40	40	40	40	40	40	40	40	40
Li	3.47	3.66	<LOD	<LOD	<LOD	<LOD	<LOD	<LOD	1.31	<LOD	<LOD	<LOD
B	16.45	14.89			11.72			12.88	17.45	16.94	17.58	
P			<LOD	<LOD		<LOD	36.279					33.031
S	163.12	188.79			203.03			178.49	141.22	148.34	163.88	
K	1884.25	2013.94			3304.75			2622.50	2125.89	2133.00	2203.48	
Sc	0.47	0.54	0.289	0.443	0.56	0.366	0.422	0.58	0.66	0.63	0.60	0.533
Ti	360.62	354.33	215.302	236.622	903.13	227.606	228.722	551.17	396.07	362.99	418.39	245.578
V	2.61	2.76	2.500	2.579	3.81	2.472	2.552	3.55	2.75	2.59	2.79	2.701
Cr	3.09	<LOD	1.887	3.007	<LOD	<LOD	<LOD	<LOD	<LOD	<LOD	<LOD	2.462
Mn	19.07	16.89	114.064	91.434	20.98	81.155	75.954	18.90	15.27	19.60	21.11	79.828
Fe	2305.17	2707.62			3788.09			2499.94	2236.23	2658.91	2465.57	
Co	0.59	0.52	0.590	0.929	0.96	0.701	0.417	0.74	0.64	1.04	0.58	0.985
Ni	1.15	1.25	<LOD	0.630	1.52	<LOD	0.723	1.44	1.18	2.95	1.19	0.691
Cu	2.63	2.65	2.861	3.095	6.07	2.895	2.753	4.33	2.90	3.36	3.17	3.080
Zn	2.91	3.18	2.655	2.247	6.89	2.674	2.397	4.39	3.08	3.52	3.69	2.167
Ga	57.26	58.42			143.87			79.74	56.39	60.75	59.38	
As	1.21	2855.29			1.39			0.98	1.32	1.35	1.09	
Rb	0.63	0.62	0.180	0.243	0.62	0.226	0.206	0.50	0.62	0.77	0.66	0.271
Sr	936.27	972.53	256.091	284.446	1147.47	250.876	276.111	968.03	923.22	994.54	939.63	301.784
Y	0.15	0.18	0.150	0.162	0.20	0.149	0.180	0.15	0.18	0.17	0.21	0.140
Zr	0.04	0.06	<LOD	0.028	0.04	<LOD	<LOD	0.04	0.04	0.04	0.06	<LOD
Nb	0.01	0.01	<LOD	<LOD	0.01	<LOD	0.008	0.01	0.01	0.01	0.02	0.008
Mo	<LOD	<LOD	<LOD	0.048	<LOD	<LOD	<LOD	<LOD	<LOD	<LOD	<LOD	<LOD
Ag	<LOD	<LOD			<LOD			<LOD	0.03	<LOD	<LOD	
Sn	0.10	0.08			0.10			0.09	0.13	<LOD	0.09	
Sb	<LOD	<LOD	0.294	0.132	<LOD	0.145	0.225	<LOD	<LOD	<LOD	<LOD	0.173
Cs	<LOD	<LOD	<LOD	<LOD	<LOD	<LOD	<LOD	<LOD	<LOD	0.00	<LOD	<LOD
Ba	156.85	150.21	34.438	37.010	177.49	34.713	34.679	96.77	139.45	158.89	158.25	36.829
La	1.61	1.64	0.375	0.436	1.61	0.371	0.432	0.98	1.50	1.65	1.63	0.458
Ce	2.37	2.46	0.591	0.726	2.25	0.665	0.675	1.45	2.22	2.46	2.54	0.772
Pr	0.22	0.23	0.074	0.096	0.20	0.090	0.089	0.14	0.23	0.20	0.26	0.087
Nd	0.86	0.84	0.387	0.270	0.82	0.341	0.366	0.52	0.87	0.78	0.90	0.399
Sm	0.11	0.14	0.112	0.057	0.12	0.081	0.104	0.08	0.12	0.13	0.08	0.070
Eu	0.39	0.43	0.284	0.282	0.43	0.226	0.277	0.28	0.37	0.48	0.41	0.230
Gd	<LOD	<LOD	<LOD	<LOD	<LOD	<LOD	0.053	<LOD	<LOD	0.11	<LOD	0.095
Tb	<LOD	<LOD	0.010	0.013	<LOD	0.003	0.009	<LOD	<LOD	<LOD	<LOD	0.010
Dy	0.04	0.06	0.051	0.034	0.05	0.026	0.051	<LOD	<LOD	0.05	<LOD	0.037
Ho	<LOD	0.00	0.011	0.004	0.01	0.005	0.010	<LOD	0.01	0.01	0.01	0.003
Er	0.02	0.01	0.015	0.008	<LOD	0.012	<LOD	<LOD	<LOD	0.01	<LOD	0.033
Tm	<LOD	0.00	<LOD	<LOD	<LOD	<LOD	0.004	<LOD	<LOD	0.00	<LOD	0.007
Yb	<LOD	<LOD	<LOD	<LOD	<LOD	<LOD	<LOD	<LOD	<LOD	<LOD	<LOD	0.009
Lu	<LOD	<LOD	0.003	<LOD	0.00	<LOD	<LOD	<LOD	0.01	<LOD	<LOD	<LOD
Hf	0.03	<LOD	<LOD	0.042	<LOD	<LOD	0.012	<LOD	<LOD	<LOD	<LOD	0.010
Ta	0.00	<LOD	<LOD	<LOD	<LOD	<LOD	<LOD	<LOD	0.00	0.00	<LOD	<LOD
Pb	0.24	0.25	0.070	0.090	0.28	0.092	0.097	0.18	0.25	0.27	0.27	0.090
Bi	<LOD	<LOD	<LOD	<LOD	<LOD	<LOD	<LOD	<LOD	<LOD	<LOD	<LOD	<LOD
Th	<LOD	<LOD	<LOD	<LOD	<LOD	<LOD	<LOD	<LOD	<LOD	0.00	<LOD	<LOD
U	<LOD	<LOD	<LOD	<LOD	<LOD	<LOD	<LOD	<LOD	<LOD	<LOD	<LOD	<LOD

Spectrum	MD110-DR03b-116-007	5A15 004	5B17 008	5B17 007	MD110-DR03b-102C 011	MD110-DR10-312-004	5A9 007	5A33-1 010	MD110-DR11-332-004	5A33-1 006	MD110-DR11-334 010	MD110-DR03b-102C-008
Campaign	MD110	MD80	MD80	MD80	MD110	MD110	MD80	MD80	MD110	MD80	MD110	MD110
Dredge point	DR03b	DR5	DR5	DR5	DR03b	DR10	DR5	DR5	DR11	DR5	DR11	DR03b
Thin section	116	A15	B17	B17	102C	312	A9	A33-1	332	A33-1	334	102C
Mineral	Pl	Pl	Pl	Pl	Pl	Pl	Pl	Pl	Pl	Pl	Pl	Pl
Na2O	1.97	3.53	2.70	2.81	4.73	3.89	2.59	2.56	3.40	2.45	8.26	3.37
MgO	0.59	0.44	0.63	0.65	2.02	0.80	0.43	0.49	0.81	0.99	0.27	0.50
Al2O3	33.64	31.09	32.45	32.05	27.11	29.95	32.35	32.89	30.42	32.35	24.37	31.23
SiO2	46.38	49.52	48.24	48.36	52.52	50.22	47.99	47.55	50.31	47.56	60.39	49.46
P2O5	0.00	0.03	0.00	0.00	0.19	0.00	0.01	0.01	0.00	0.01	0.00	0.00
K2O	0.22	0.30	0.26	0.33	0.20	0.17	0.37	0.23	0.15	0.68	0.58	0.10
CaO	16.79	14.41	15.18	14.90	10.64	12.96	15.71	15.67	13.36	15.21	5.81	14.49
TiO2	0.02	0.10	0.07	0.08	0.12	0.05	0.07	0.07	0.03	0.07	0.03	0.07
Cr2O3	0.05	0.08	0.00	0.00	0.00	0.01	0.00	0.02	0.00	0.03	0.00	0.00
MnO	0.01	0.01	0.03	0.02	0.04	0.02	0.01	0.05	0.02	0.01	0.02	0.01
FeO	0.28	0.44	0.38	0.71	2.37	1.88	0.40	0.42	1.41	0.60	0.21	0.41
NiO												
Total	99.96	99.94	99.94	99.91	99.92	99.96	99.93	99.95	99.93	99.95	99.96	99.64
Spot Size (µm)	40	40	40	40	40	40	40	40	40	40	40	40
Li	2.608	<LOD	1.66	<LOD	<LOD	2.558	4.39	3.62	0.214	11.76	<LOD	2.040
B		13.04	17.85	15.92			18.53	19.37		36.09		
P	38.386				344.874	967.960			21.786		1490.623	88.048
S		209.59	124.85	125.22			141.82	141.47		151.33		
K		2543.24	2205.40	2075.73			2519.10	2120.74		2833.25		
Sc	0.412	0.58	0.69	0.62	0.458	2.250	0.64	0.84	3.785	0.84	0.779	0.309
Ti	137.504	659.28	377.67	424.14	272.803	850.569	411.58	382.74	83.656	372.91	138.283	84.089
V	2.258	3.28	2.69	2.61	2.596	13.887	2.77	2.85	16.849	3.12	0.330	1.079
Cr	2.544	<LOD	<LOD	<LOD	<LOD	<LOD	0.85	3.06	0.128	2.41	<LOD	<LOD
Mn	73.166	20.89	17.57	16.64	76.273	400.000	22.85	22.26	126.335	35.31	79.918	26.562
Fe		3331.88	2252.16	2237.50			2978.77	3212.31		5813.62		
Co	0.628	0.98	0.47	0.66	0.804	3.522	0.79	0.68	2.993	1.55	<LOD	0.226
Ni	1.118	1.64	1.14	1.30	0.928	2.671	1.13	1.41	3.275	11.84	<LOD	0.433
Cu	2.138	4.99	2.80	3.13	2.722	13.887	2.94	3.11	3.975	8.19	17.196	1.290
Zn	1.339	6.44	2.94	3.27	2.824	23.234	4.60	5.31	5.784	8.44	8.145	1.534
Ga		90.70	59.15	61.99			72.18	81.87		81.04		
As		1.02	0.93	1.03			1.26	1.66		1.95		
Rb	0.118	0.43	0.63	0.67	0.295	1.004	0.87	0.84	0.374	1.70	1.645	3.360
Sr	199.139	1017.77	909.01	939.39	203.702	428.287	1023.30	1310.36	0.816	1430.54	816.065	86.762
Y	0.140	0.16	0.14	0.17	0.152	2.158	0.19	0.22	0.938	0.22	0.512	0.058
Zr	0.113	0.03	0.06	0.06	0.053	24.017	0.33	0.07	0.434	0.59	<LOD	0.037
Nb	0.008	<LOD	0.01	0.01	0.007	0.297	0.04	0.02	0.009	0.05	<LOD	0.005
Mo	<LOD	<LOD	<LOD	<LOD	<LOD	<LOD	-0.01	<LOD	0.047	-0.03	<LOD	<LOD
Ag		<LOD	<LOD	<LOD			-0.01	0.04		-0.02		
Sn		0.06	0.12	0.19			0.16	0.17		0.18		
Sb	0.177	<LOD	<LOD	<LOD	0.204	9.918	0.00	0.03	0.017	0.03	0.460	0.085
Cs	<LOD	<LOD	<LOD	<LOD	0.153	<LOD	0.00	0.00	0.077	0.02	<LOD	<LOD
Ba	6.951	101.72	155.42	162.85	70.581	71.819	193.87	177.45	0.406	162.57	520.794	19.110
La	0.200	1.09	1.57	1.57	0.501	2.172	2.25	2.52	0.062	2.27	25.626	0.131
Ce	0.368	1.61	2.39	2.48	0.679	2.903	3.87	4.26	0.206	3.41	24.579	0.224
Pr	0.063	0.15	0.24	0.26	0.098	0.467	0.38	0.45	0.030	0.38	1.453	0.022
Nd	0.279	0.60	0.75	0.88	0.370	1.892	1.30	1.21	0.183	1.18	3.289	0.095
Sm	0.119	0.11	0.11	0.11	0.026	0.421	0.21	0.17	0.064	0.23	0.280	<LOD
Eu	0.256	0.31	0.40	0.45	0.271	0.956	0.72	0.69	0.021	0.59	4.372	0.097
Gd	0.058	<LOD	<LOD	0.10	0.048	0.464	0.15	0.08	0.103	0.06	0.282	<LOD
Tb	0.011	<LOD	<LOD	0.01	0.006	0.045	0.02	0.03	0.022	0.02	0.021	0.002
Dy	0.051	0.04	<LOD	0.06	0.037	0.272	0.04	0.07	0.151	0.04	0.110	0.039
Ho	0.010	<LOD	<LOD	0.01	0.004	0.093	0.01	0.00	0.037	0.01	0.016	0.002
Er	0.025	0.01	<LOD	0.02	<LOD	0.171	0.01	0.07	0.117	0.01	<LOD	<LOD
Tm	<LOD	<LOD	0.00	<LOD	0.002	0.054	0.00	0.01	0.018	0.00	<LOD	<LOD
Yb	<LOD	0.01	<LOD	0.02	<LOD	0.225	0.01	0.02	0.116	0.00	<LOD	<LOD
Lu	0.002	<LOD	<LOD	0.00	<LOD	0.027	0.00	0.00	0.021	0.00	<LOD	<LOD
Hf	<LOD	<LOD	<LOD	<LOD	<LOD	0.551	0.01	0.03	0.019	0.02	<LOD	<LOD
Ta	<LOD	<LOD	<LOD	<LOD	<LOD	0.041	0.00	0.00	0.000	0.01	<LOD	<LOD
Pb	0.071	0.22	0.29	0.26	0.065	2.887	1.59	2.28	0.018	0.64	28.612	0.023
Bi	<LOD	<LOD	<LOD	<LOD	<LOD	<LOD	0.00	-0.01	0.000	-0.01	<LOD	<LOD
Th	<LOD	<LOD	<LOD	0.00	0.001	0.264	0.01	0.00	0.004	0.00	<LOD	<LOD
U	<LOD	<LOD	<LOD	<LOD	<LOD	0.210	0.09	0.01	0.009	0.01	0.008	0.003

Spectrum	5A15 003	MD110-DR03b-101D 001	5A29 002	5A33-1 008	5A33-1 009	5A33-1 005	5A29 006	5A29 008	5A2 004	5A29 004	5A29 001	5A2 005
Campaign	MD80	MD110	MD80	MD80	MD80	MD80	MD80	MD80	MD80	MD80	MD80	MD80
Dredge point	DR5	DR03b	DR5	DR5	DR5	DR5	DR5	DR5	DR5	DR5	DR5	DR5
Thin section	A15	101D	A29	A33-1	A33-1	A33-1	A29	A29	A2	A29	A29	A2
Mineral	Pl	Pl	Pl	Pl	Pl	Pl	Pl	Pl	Pl	Pl	Pl	Pl
Na2O	2.90	3.59	2.59	2.54	2.55	2.63	2.79	3.09	2.52	3.07	2.68	2.48
MgO	0.43	0.56	0.48	0.55	0.47	0.46	0.46	0.49	0.55	0.51	0.50	0.45
Al2O3	32.07	31.26	32.57	32.83	32.96	32.70	32.61	32.35	32.77	32.02	32.75	32.98
SiO2	48.18	49.64	48.10	47.53	47.50	47.93	48.26	48.08	47.75	49.18	47.80	47.30
P2O5	0.02	0.00	0.01	0.00	0.01	0.00	0.00	0.00	0.01	0.00	0.01	0.01
K2O	0.35	0.20	0.41	0.31	0.21	0.30	0.26	0.44	0.28	0.23	0.39	0.29
CaO	15.48	14.19	15.27	15.75	15.81	15.50	15.10	14.96	15.56	14.50	15.35	15.93
TiO2	0.09	0.09	0.09	0.06	0.06	0.08	0.07	0.12	0.07	0.09	0.07	0.07
Cr2O3	0.00	0.00	0.00	0.01	0.02	0.00	0.00	0.00	0.08	0.00	0.00	0.06
MnO	0.05	0.01	0.01	0.04	0.05	0.01	0.05	0.01	0.01	0.02	0.01	0.01
FeO	0.36	0.39	0.40	0.33	0.33	0.33	0.30	0.30	0.34	0.33	0.36	0.35
NiO												
Total	99.94	99.94	99.93	99.95	99.95	99.95	99.91	99.84	99.93	99.95	99.93	99.94
Spot Size (µm)	40	40	40	40	40	40	40	40	40	40	40	40
Li	4.12	3.499	0.75	0.36	0.30	0.83	<LOD	<LOD	0.48	1.09	<LOD	0.30
B	17.13		18.11	20.57	19.92	21.09	26.52	15.76	18.60	18.28	19.05	18.20
P		<LOD										
S	210.60		150.93	167.78	141.46	121.65	170.50	145.99	150.20	135.16	149.69	188.92
K	3219.98		1790.86	2142.76	2185.70	2514.28	2521.31	1943.41	1797.60	2168.08	1853.42	1610.32
Sc	0.93	0.582	0.60	0.69	0.65	0.75	0.91	0.64	0.61	0.69	0.64	0.68
Ti	636.90	262.878	327.31	338.47	360.64	392.65	512.25	409.06	341.71	384.61	359.62	290.22
V	6.10	3.961	2.37	2.65	2.57	2.68	3.09	2.40	2.40	2.41	2.58	1.97
Cr	3.96	<LOD	2.66	-2.48	1.78	1.07	2.98	0.32	2.67	2.91	2.16	3.54
Mn	29.33	86.477	17.82	24.83	25.12	21.27	17.30	19.16	20.12	19.79	19.59	19.84
Fe	5428.16		1887.56	2883.96	3044.64	3233.25	2792.67	2357.58	1952.52	2124.93	2026.85	1707.12
Co	1.77	0.603	0.60	0.84	0.63	0.91	0.84	0.40	0.61	0.55	0.55	0.40
Ni	17.03	0.752	1.09	1.23	1.34	1.41	1.44	1.03	1.05	1.07	1.08	1.07
Cu	21.50	3.650	2.32	3.57	3.30	3.47	3.51	2.57	2.42	3.04	2.84	2.39
Zn	14.63	2.634	3.36	3.88	4.79	2.75	3.92	4.07	3.87	3.15	3.41	2.21
Ga	86.80		47.42	73.40	75.89	86.03	71.85	62.68	49.47	58.80	49.44	41.09
As	1.63		1.20	1.53	1.79	1.50	1.60	1.38	0.63	1.12	1.39	1.22
Rb	1.29	2.581	0.50	0.87	0.90	0.94	0.76	0.64	0.57	0.65	0.52	0.46
Sr	1038.84	345.617	747.08	1247.33	1248.83	1288.72	1072.34	937.49	754.37	797.38	796.75	700.17
Y	0.17	0.206	0.13	0.23	0.21	0.23	0.21	0.17	0.12	0.14	0.16	0.13
Zr	0.33	0.140	0.04	0.06	0.05	0.06	0.07	0.08	0.04	0.06	0.04	0.04
Nb	0.04	0.021	0.01	0.01	0.01	0.00	0.01	0.00	0.00	0.01	0.01	0.01
Mo	<LOD	<LOD	-0.01	0.16	0.01	0.02	0.06	-0.02	0.00	0.06	-0.04	-0.03
Ag	<LOD		0.00	0.00	0.01	-0.01	0.01	0.00	-0.02	0.00	0.01	0.01
Sn	0.08		0.07	0.18	0.19	0.12	0.07	0.08	0.11	0.06	0.05	0.14
Sb	<LOD	0.249	-0.01	-0.02	-0.01	0.01	-0.01	0.04	0.00	0.00	0.00	0.00
Cs	0.03	<LOD	0.00	0.00	0.00	0.00	0.00	0.00	0.00	0.00	0.00	0.00
Ba	97.83	56.789	91.74	152.16	161.55	180.37	162.20	153.83	84.66	117.21	91.93	72.26
La	0.98	0.437	0.94	2.17	2.24	2.08	1.67	1.48	0.89	1.04	1.01	0.78
Ce	1.48	0.759	1.35	3.23	3.49	3.13	2.26	2.25	1.15	1.40	1.37	1.06
Pr	0.13	0.091	0.13	0.33	0.36	0.35	0.25	0.22	0.12	0.15	0.14	0.11
Nd	0.58	0.375	0.47	0.96	1.18	0.99	0.83	0.76	0.43	0.46	0.50	0.38
Sm	0.12	0.040	0.06	0.17	0.21	0.15	0.11	0.05	0.07	0.10	0.09	0.04
Eu	0.29	0.266	0.22	0.51	0.64	0.55	0.43	0.38	0.19	0.25	0.20	0.18
Gd	<LOD	0.084	0.04	0.16	0.18	0.05	0.05	0.04	0.05	0.03	0.03	0.05
Tb	<LOD	0.008	0.01	0.01	0.01	0.02	0.01	0.02	0.00	0.00	0.00	0.00
Dy	0.04	0.074	0.04	0.07	0.04	0.03	0.03	0.04	0.03	0.02	0.04	0.01
Ho	<LOD	0.009	0.00	0.01	0.01	0.00	0.00	0.00	0.00	0.00	0.00	0.00
Er	0.01	0.015	0.01	0.01	0.00	0.00	0.00	0.01	0.00	0.00	0.02	0.00
Tm	0.00	0.006	0.00	0.00	0.00	0.00	0.00	0.00	0.00	0.00	0.00	0.00
Yb	<LOD	0.028	0.00	0.00	0.00	0.01	0.00	0.00	0.01	0.01	0.00	0.01
Lu	<LOD	<LOD	0.00	0.00	0.00	0.00	0.00	0.00	0.00	0.00	0.00	0.00
Hf	<LOD	<LOD	0.00	0.03	0.02	0.02	0.01	0.00	0.01	-0.01	0.00	0.00
Ta	<LOD	<LOD	0.00	0.00	0.00	0.00	0.00	0.00	0.00	0.00	0.00	0.00
Pb	0.77	0.091	0.18	0.84	1.17	0.51	0.35	0.27	0.14	0.21	0.22	0.13
Bi	<LOD	<LOD	0.00	0.00	-0.01	0.00	0.01	0.00	0.00	0.00	0.00	0.00
Th	<LOD	0.002	0.00	0.01	0.01	0.00	0.00	0.00	0.00	0.00	0.00	0.00
U	0.00	0.002	0.00	0.00	0.00	0.00	0.00	0.00	0.00	0.00	0.00	0.00

Spectrum	5A2007	5A9002	5A9005	5A9001	5A2003	5A2006	5A9003	MD110-DR03b-116-008	MD110-DR03b-116-010	MD110-DR11-332-003
Campaign	MD80	MD80	MD80	MD80	MD80	MD80	MD80	MD110	MD110	MD110
Dredge point	DR5	DR5	DR5	DR5	DR5	DR5	DR5	DR03b	DR03b	DR11
Thin section	A2	A9	A9	A9	A2	A2	A9	116	116	332
Mineral	Pl	Pl	Pl	Pl	Pl	Pl	Pl	Pl	Pl	Pl
Na2O	2.72	2.66	2.73	2.80	2.62	2.55	2.25	1.98	0.53	2.94
MgO	0.44	0.53	0.48	0.46	0.46	0.47	0.87	1.00	15.92	0.81
Al2O3	32.64	31.38	32.67	32.62	32.93	33.13	28.94	33.15	36.51	30.92
SiO2	48.56	48.08	47.76	47.92	47.57	47.17	51.16	46.88	12.14	49.59
P2O5	0.01	0.01	0.00	0.01	0.00	0.01	0.04	0.00	0.00	0.00
K2O	0.14	0.71	0.27	0.24	0.27	0.22	2.50	0.04	0.03	0.03
CaO	15.05	16.13	15.54	15.52	15.63	15.93	13.38	16.30	3.19	14.83
TiO2	0.07	0.08	0.06	0.07	0.07	0.06	0.16	0.05	0.36	0.04
Cr2O3	0.02	0.00	0.01	0.00	0.00	0.08	0.00	0.03	19.13	0.02
MnO	0.01	0.02	0.04	0.01	0.02	0.01	0.01	0.01	0.07	0.02
FeO	0.30	0.35	0.34	0.30	0.32	0.31	0.63	0.52	11.85	0.77
NiO										
Total	99.95	99.95	99.91	99.95	99.89	99.93	99.95	99.96	99.73	99.97
Spot Size (µm)	40	40	40	40	40	40	40			
Li	0.42	1.18	0.40	0.46	0.33	1.51	7.02			
B	17.34	22.10	22.90	26.74	18.33	22.47	53.93			
P										
S	153.49	146.85	227.06	196.15	129.82	193.75	182.72			
K	2020.80	2271.20	2414.61	2821.82	1984.55	1900.79	48110.38			
Sc	0.60	0.74	0.75	1.01	0.58	0.74	3.26			
Ti	369.26	378.97	406.18	446.63	346.79	362.70	368.82			
V	2.33	2.80	2.85	3.06	2.31	2.78	2.86			
Cr	0.84	3.60	2.12	3.16	2.08	3.87	2.30			
Mn	16.77	22.04	25.87	27.78	14.42	20.49	23.19			
Fe	2046.36	3050.79	3129.00	3582.55	1697.08	2260.76	4432.17			
Co	0.55	0.86	1.10	0.88	0.48	0.81	1.90			
Ni	0.87	1.31	1.90	1.80	0.98	1.30	13.88			
Cu	3.00	3.43	3.58	3.85	2.44	2.63	9.31			
Zn	3.02	3.97	3.67	4.86	2.73	3.27	9.45			
Ga	51.61	79.08	74.00	96.57	45.76	52.04	73.86			
As	1.31	1.83	1.62	1.66	1.15	1.49	1.52			
Rb	0.59	0.90	0.92	1.01	0.54	0.51	46.21			
Sr	737.20	1261.29	1248.52	1546.38	694.64	822.31	767.95			
Y	0.13	0.21	0.23	0.25	0.14	0.11	0.17			
Zr	0.05	0.07	0.07	0.08	0.04	0.05	6.12			
Nb	0.01	0.01	0.02	0.01	0.01	0.01	0.10			
Mo	0.01	0.09	0.03	-0.01	-0.03	0.08	-0.01			
Ag	-0.01	-0.02	0.00	-0.02	0.01	0.01	0.01			
Sn	0.12	0.19	0.10	0.14	0.04	0.11	0.17			
Sb	0.00	-0.01	-0.03	0.04	-0.01	-0.01	0.03			
Cs	0.00	0.00	0.00	0.00	0.00	0.00	0.24			
Ba	85.38	191.51	190.39	215.32	77.26	82.57	192.00			
La	0.85	2.63	2.68	2.78	0.82	0.89	1.75			
Ce	1.18	4.52	4.67	4.72	1.09	1.19	3.30			
Pr	0.14	0.46	0.48	0.45	0.12	0.12	0.28			
Nd	0.45	1.51	1.75	1.48	0.41	0.47	1.02			
Sm	0.07	0.21	0.20	0.25	0.06	0.06	0.15			
Eu	0.18	0.81	0.84	0.92	0.18	0.18	0.58			
Gd	-0.01	0.03	0.11	0.19	0.01	0.06	0.13			
Tb	0.01	0.03	0.01	0.02	0.00	0.00	0.02			
Dy	0.04	0.03	0.09	0.02	0.02	0.03	0.07			
Ho	0.00	0.01	0.01	0.01	0.00	0.00	0.00			
Er	0.01	0.07	-0.03	0.04	0.00	0.00	0.01			
Tm	0.00	0.00	0.00	0.00	0.00	0.00	0.00			
Yb	0.01	0.01	0.00	-0.01	0.00	0.01	0.02			
Lu	0.00	0.00	0.00	0.01	0.00	0.00	0.00			
Hf	0.00	0.05	0.01	-0.02	0.00	0.01	0.38			
Ta	0.00	0.00	0.00	0.00	0.00	0.00	0.02			
Pb	0.14	20.82	8.37	5.02	0.14	0.16	-57.62			
Bi	0.00	-0.04	0.00	0.00	0.00	0.00	-0.03			
Th	0.00	-0.01	-0.05	-0.08	0.00	0.00	-0.01			
U	0.00	0.00	0.00	0.00	0.00	0.00	-0.10			

Table S3 - Major and trace elements compositions of olivine

Spectrum	DR04-129A-6	DR04-129A-4	129A 001-m	129A 001-m	129A 001-m	129A 001-m	DR04-129A-2	DR04-129A-2	129A 005-m	DR04-129A-2	129A 005-m	DR04-129A-2	129A 005-m	DR04-129A-7
Campaign	MD110	MD110	MD110	MD110	MD110	MD110	MD110	MD110	MD110	MD110	MD110	MD110	MD110	MD110
Dredge point	DR04	DR04	DR04	DR04	DR04	DR04	DR04	DR04	DR04	DR04	DR04	DR04	DR04	DR04
Thin section	129A	129A	129A	129A	129A	129A	129A	129A	129A	129A	129A	129A	129A	129A
Mineral	Ol	Ol	Ol	Ol	Ol	Ol	Ol	Ol	Ol	Ol	Ol	Ol	Ol	Ol
Na2O	0.02	0.02	0.00	0.00	0.00	0.00	0.07	0.07	0.00	0.07	0.00	0.07	0.00	0.04
MgO	45.93	45.51	46.06	46.06	46.06	46.06	42.52	42.52	46.57	42.52	46.57	42.52	46.57	45.41
Al2O3	0.15	0	0.00	0.00	0.00	0.00	0.91	0.91	0.00	0.91	0.00	0.91	0.00	0.1
SiO2	39.7	38.85	40.42	40.42	40.42	40.42	39.02	39.02	40.90	39.02	40.90	39.02	40.90	37.14
P2O5			0.00	0.00	0.00	0.00			0.00		0.00		0.00	
K2O	0.03	0	0.00	0.00	0.00	0.00	0	0	0.00	0	0.00	0	0.00	0
CaO	0.29	0.29	0.12	0.12	0.12	0.12	1.55	1.55	0.13	1.55	0.13	1.55	0.13	0.29
TiO2	0	0	0.01	0.01	0.01	0.01	0.09	0.09	0.02	0.09	0.02	0.09	0.02	0
Cr2O3	0.04	0	0.14	0.14	0.14	0.14	0.04	0.04	0.04	0.04	0.04	0.04	0.04	0.03
MnO	0.15	0.25	0.21	0.21	0.21	0.21	0.2	0.2	0.19	0.2	0.19	0.2	0.19	0.16
FeO	13.34	13.3	12.79	12.79	12.79	12.79	12.55	12.55	11.89	12.55	11.89	12.55	11.89	13.14
NiO	0.19	0.21	0.20	0.20	0.20	0.20	0.22	0.22	0.21	0.22	0.21	0.22	0.21	0.2
Total	99.84	98.43	99.96	99.96	99.96	99.96	97.17	97.17	99.95	97.17	99.95	97.17	99.95	96.51
Spot Size (µm)	40	40	40	40	40	40	40	40	40	40	40	40	40	40
Li	2.108	1.996	1.883	1.956	1.899	1.863	1.753	1.979	1.633	2.062	1.632	2.060	1.855	1.829
P	52.106	61.857	41.592	<LOD	51.408	37.077	58.426	184.269	24.484	87.332	52.931	105.518	65.574	79.474
Sc	7.676	6.983	7.061	6.148	5.832	5.822	6.876	7.298	6.638	7.570	6.342	7.417	5.630	7.555
Ti	49.472	52.407	53.338	31.395	36.079	50.612	50.322	55.284	38.700	56.307	39.955	54.242	19.705	51.836
V	10.555	9.283	9.661	8.713	7.939	7.512	9.225	9.548	8.625	9.330	8.642	9.096	6.744	10.459
Cr	439.739	348.523	372.378	320.819	300.250	299.905	336.675	359.447	336.467	353.114	310.178	334.742	261.050	418.577
Mn	1464.787	1546.995	1500.619	1515.182	1472.552	1427.260	1404.397	1410.179	1406.089	1474.240	1356.939	1442.398	1426.462	1490.300
Co	154.928	161.003	159.202	149.841	145.842	140.632	146.529	142.125	142.485	151.213	138.374	145.361	141.229	162.742
Ni	1952.841	1770.629	1661.991	1677.215	1554.067	1435.933	1658.125	1590.446	1597.908	1669.892	1547.885	1586.601	1541.187	1939.420
Cu	1.823	1.848	1.680	1.701	1.655	1.670	1.759	1.832	1.420	1.815	1.485	1.731	1.702	1.873
Zn	95.485	98.742	94.216	92.724	86.359	85.641	89.785	91.565	88.599	91.753	81.032	89.848	84.242	103.153
Rb	<LOD	<LOD	<LOD	<LOD	<LOD	<LOD	<LOD	<LOD	<LOD	<LOD	<LOD	<LOD	<LOD	<LOD
Sr	<0.021673	0.050	<0.0394093	0.046	0.057	<0.0326428	0.038	<0.0347942	0.038	0.034	<0.0315026	<0.0302253	<0.0319209	0.032
Y	0.230	0.224	0.202	0.144	0.147	0.159	0.194	0.191	0.200	0.212	0.190	0.236	0.144	0.193
Zr	0.049	0.043	0.047	<LOD	<LOD	<LOD	0.038	0.053	0.039	0.055	<LOD	0.046	0.033	0.070
Nb	0.015	<LOD	<LOD	0.012	<LOD	<LOD	<LOD	0.008	0.010	<LOD	<LOD	<LOD	0.010	0.010
Mo	0.423	0.498	0.412	0.508	0.409	0.525	0.473	0.427	0.409	0.555	0.450	0.481	0.490	0.412
Sb	0.241	0.218	0.156	0.190	0.259	0.205	0.241	0.182	0.248	0.213	0.159	0.258	0.284	0.297
Ba	<LOD	<LOD	<LOD	<LOD	<LOD	<LOD	<LOD	<LOD	<LOD	<LOD	<LOD	<LOD	<LOD	<LOD
La	<LOD	0.006	<LOD	<LOD	0.007	<LOD	0.004	<LOD	<LOD	<LOD	<LOD	<LOD	<LOD	<LOD
Ce	<LOD	<LOD	<LOD	<LOD	<LOD	<LOD	<LOD	<LOD	<LOD	<LOD	<LOD	<LOD	<LOD	<LOD
Pr	<LOD	<LOD	<LOD	<LOD	<LOD	<LOD	<LOD	<LOD	<LOD	0.002	<LOD	<LOD	<LOD	<LOD
Nd	<LOD	<LOD	<LOD	<LOD	<LOD	<LOD	<LOD	<LOD	0.015	<LOD	<LOD	<LOD	<LOD	<LOD
Sm	<LOD	<LOD	<LOD	<LOD	<LOD	<LOD	<LOD	<LOD	<LOD	<LOD	<LOD	<LOD	0.008	<LOD
Eu	<LOD	<LOD	<LOD	<LOD	<LOD	0.008	<LOD	<LOD	<LOD	<LOD	<LOD	<LOD	<LOD	0.010
Gd	<LOD	<LOD	<LOD	<LOD	<LOD	<LOD	<LOD	0.016	<LOD	<LOD	<LOD	0.009	<LOD	<LOD
Tb	0.003	<LOD	0.003	0.005	<LOD	<LOD	0.003	<LOD	0.003	0.006	<LOD	0.003	<LOD	<LOD
Dy	0.042	0.035	0.027	0.024	<LOD	0.019	<LOD	0.033	0.019	<LOD	0.034	<LOD	0.022	0.038
Ho	0.005	<LOD	0.004	0.006	0.009	0.006	0.010	0.012	0.010	0.006	0.003	0.008	0.005	0.013
Er	0.034	0.044	0.044	0.018	0.044	0.042	<LOD	0.030	<LOD	0.031	<LOD	0.054	<LOD	0.036
Tm	0.010	0.011	0.006	<LOD	0.012	0.011	0.003	0.010	0.008	0.010	0.013	0.013	0.008	0.002
Yb	0.068	0.063	0.073	0.099	0.071	0.089	0.067	0.094	0.071	0.068	0.089	0.127	0.045	0.083
Lu	0.014	0.013	0.011	0.012	0.011	0.007	0.016	0.019	0.016	0.019	0.013	0.014	0.015	0.026
Hf	<LOD	0.015	<LOD	<LOD	<LOD	<LOD	<LOD	<LOD	<LOD	<LOD	<LOD	<LOD	<LOD	<LOD
Ta	<LOD	<LOD	<LOD	<LOD	<LOD	<LOD	0.007	<LOD	<LOD	<LOD	<LOD	<LOD	<LOD	<LOD
Pb	<LOD	0.012	<LOD	<LOD	0.015	<LOD	<LOD	<LOD	<LOD	<LOD	<LOD	<LOD	0.009	<LOD
Th	0.002	<LOD	<LOD	<LOD	<LOD	<LOD	<LOD	<LOD	<LOD	<LOD	<LOD	<LOD	<LOD	<LOD
U	<LOD	<LOD	<LOD	<LOD	<LOD	<LOD	<LOD	<LOD	<LOD	<LOD	<LOD	<LOD	<LOD	<LOD

Spectrum	DR04-129A-7	DR04-129A-6	DR04-129A-7	DR04-129A-4	DR04-129A-6	DR04-129A-4	129A 003-m	129A 003-m	129A 003-m	129A 004-m	129A 004-m	129A 002-m	129A 006-m	129A 007-m	DR04-129A-1	DR04-129A-5
Campaign	MD110	MD110	MD110	MD110	MD110	MD110	MD110	MD110	MD110	MD110	MD110	MD110	MD110	MD110	MD110	MD110
Dredge point	DR04	DR04	DR04	DR04	DR04	DR04	DR04	DR04	DR04	DR04	DR04	DR04	DR04	DR04	DR04	DR04
Thin section	129A	129A	129A	129A	129A	129A	129A	129A	129A	129A	129A	129A	129A	129A	129A	129A
Mineral	Ol	Ol	Ol	Ol	Ol	Ol	Ol	Ol	Ol	Ol	Ol	Ol	Ol	Ol	Ol	Ol
Na2O	0.04	0.02	0.04	0.02	0.02	0.02	0.00	0.00	0.00	0.00	0.00	0.00	0.00	0.00	0	0
MgO	45.41	45.93	45.41	45.51	45.93	45.51	44.02	44.02	44.02	46.78	46.78	45.54	46.64	46.39	45.05	45.7
Al2O3	0.1	0.15	0.1	0	0.15	0	0.00	0.00	0.00	0.00	0.00	0.00	0.00	0.00	0.03	0.32
SiO2	37.14	39.7	37.14	38.85	39.7	38.85	43.93	43.93	43.93	41.32	41.32	42.90	40.74	40.90	39.72	40.56
P2O5							0.02	0.02	0.02	0.00	0.00	0.00	0.00	0.01		
K2O	0	0.03	0	0	0.03	0	0.02	0.02	0.02	0.01	0.01	0.02	0.00	0.00	0.01	0
CaO	0.29	0.29	0.29	0.29	0.29	0.29	0.35	0.35	0.35	0.16	0.16	0.23	0.12	0.13	0.31	0.28
TiO2	0	0	0	0	0	0	0.09	0.09	0.09	0.01	0.01	0.02	0.01	0.02	0.01	0
Cr2O3	0.03	0.04	0.03	0	0.04	0	0.05	0.05	0.05	0.04	0.04	0.05	0.06	0.05	0.06	0.06
MnO	0.16	0.15	0.16	0.25	0.15	0.25	0.18	0.18	0.18	0.23	0.23	0.19	0.19	0.19	0.28	0.26
FeO	13.14	13.34	13.14	13.3	13.34	13.3	11.08	11.08	11.08	11.17	11.17	10.82	11.92	12.07	12.95	13.16
NiO	0.2	0.19	0.2	0.21	0.19	0.21	0.22	0.22	0.22	0.24	0.24	0.17	0.24	0.21	0.22	0.25
Total	96.51	99.84	96.51	98.43	99.84	98.43	99.94	99.94	99.94	99.96	99.96	99.95	99.93	99.96	98.64	100.59

Spot Size (µm)	40	40	40	40	40	40	40	40	40	40	40
Li	1.820	2.060	1.859	2.157	1.986	1.864	2.061	1.760	1.618	1.670	1.992
P	74.641	58.153	41.543	107.834	48.202	52.352	291.263	114.227	81.186	81.345	58.184
Sc	6.919	7.827	7.004	7.770	7.848	7.571	7.732	6.634	6.355	6.173	6.522
Ti	45.480	51.836	47.568	62.464	50.304	48.428	52.677	46.942	45.198	42.996	121.199
V	9.372	10.137	8.926	10.151	10.270	8.932	8.640	8.090	7.583	7.699	9.512
Cr	361.694	417.980	348.197	383.516	402.148	328.388	295.847	271.937	262.107	283.344	282.177
Mn	1428.388	1542.472	1514.450	1562.624	1461.591	1460.489	1283.045	1286.368	1222.561	1313.989	1260.030
Co	154.468	167.819	154.323	156.679	155.645	153.537	128.357	130.619	127.780	131.465	137.437
Ni	1760.485	1924.392	1775.921	1740.352	1830.105	1615.106	1316.787	1293.027	1312.640	1383.188	1355.639
Cu	1.624	1.516	1.757	1.974	1.700	1.548	1.612	1.453	1.425	1.464	1.986
Zn	92.026	99.636	97.251	95.802	96.381	93.472	78.781	77.612	76.269	82.835	86.762
Rb	<LOD	<LOD	<LOD	<LOD	<LOD	<LOD	<LOD	<LOD	<LOD	<LOD	0.050
Sr	0.023	<0.0240119	<0.022822	0.041	0.029	<0.0187583	0.022	0.024	0.026	0.028	0.530
Y	0.188	0.234	0.191	0.223	0.238	0.198	0.198	0.189	0.192	0.172	0.503
Zr	0.048	0.046	0.036	0.071	0.083	0.057	0.069	0.056	0.028	0.038	0.865
Nb	0.010	0.011	0.010	0.018	0.019	0.010	0.006	0.016	0.004	0.008	0.090
Mo	0.470	0.483	0.448	0.508	0.446	0.456	0.428	0.400	0.360	0.347	0.432
Sb	0.217	0.224	0.231	0.205	0.242	0.164	0.199	0.242	0.218	0.186	0.178
Ba	<LOD	<LOD	<LOD	<LOD	<LOD	<LOD	<LOD	<LOD	0.033	<LOD	0.137
La	<LOD	0.005	<LOD	0.005	<LOD	0.007	<LOD	<LOD	<LOD	<LOD	0.124
Ce	<LOD	<LOD	0.005	0.003	<LOD	<LOD	<LOD	<LOD	0.005	<LOD	0.256
Pr	<LOD	<LOD	<LOD	<LOD	<LOD	<LOD	<LOD	<LOD	<LOD	<LOD	0.031
Nd	<LOD	<LOD	<LOD	<LOD	<LOD	<LOD	<LOD	<LOD	<LOD	<LOD	0.155
Sm	<LOD	<LOD	<LOD	<LOD	<LOD	<LOD	<LOD	<LOD	<LOD	<LOD	0.035
Eu	<LOD	0.002	<LOD	<LOD	<LOD	<LOD	<LOD	<LOD	<LOD	<LOD	0.014
Gd	0.048	<LOD	<LOD	<LOD	<LOD	<LOD	<LOD	<LOD	<LOD	0.018	0.054
Tb	<LOD	<LOD	0.001	<LOD	<LOD	<LOD	0.001	0.005	0.003	<LOD	0.015
Dy	0.042	0.028	0.008	0.019	0.029	0.009	0.011	0.022	0.026	0.026	0.070
Ho	0.011	0.008	0.017	0.009	0.010	0.008	0.008	0.007	0.008	0.007	0.012
Er	0.048	0.028	0.005	0.043	0.056	0.021	0.017	0.053	0.023	0.034	0.070
Tm	0.005	<LOD	0.018	0.015	0.009	0.012	0.011	0.008	0.002	0.006	0.016
Yb	0.061	0.075	0.088	0.075	0.062	0.042	0.104	0.057	0.047	0.083	0.068
Lu	0.022	0.018	0.016	0.020	0.026	0.014	0.017	0.016	0.018	0.016	0.019
Hf	<LOD	<LOD	<LOD	<LOD	<LOD	<LOD	<LOD	<LOD	<LOD	<LOD	0.036
Ta	0.008	<LOD	<LOD	<LOD	<LOD	<LOD	<LOD	<LOD	<LOD	<LOD	<LOD
Pb	<LOD	<LOD	<LOD	<LOD	<LOD	0.011	<LOD	0.013	<LOD	<LOD	0.059
Th	<LOD	<LOD	<LOD	<LOD	<LOD	<LOD	<LOD	<LOD	<LOD	<LOD	0.010
U	<LOD	<LOD	<LOD	<LOD	<LOD	<LOD	<LOD	<LOD	<LOD	<LOD	0.005

Table S4 - Major and trace elements (µXRF) compositions of bulk rocks

Sample	E1-4	C4	C3	B8	B6	B5	B3	B17	B16	B14	A9	A5	A33-1	A29	A27	A24	A23	A2	A15	7E1	7C1	7A7	3F
Campaign	MD80	MD80	MD80	MD80	MD80	MD80	MD80	MD80	MD80	MD80	MD80	MD80	MD80	MD80	MD80	MD80	MD80	MD80	MD80	MD80	MD80	MD80	MD80
Dredged point	DR5	DR5	DR5	DR5	DR5	DR5	DR5	DR5	DR5	DR5	DR5	DR5	DR5	DR5	DR5	DR5	DR5	DR5	DR5	DR7	DR7	DR7	DR3
Rock type	Basalt	Basalt	Basalt	Basalt	Basalt	Basalt	Basalt	Basalt	Basalt	Basalt	Basalt	Basalt	Basalt	Basalt	Basalt	Basalt	Basalt	Basalt	Basalt	Basalt	Basalt	Basalt	Basalt
ppm																							
S	0	607	0	0	0	0	0	0	0	0	0	0	0	0	0	0	0	0	0	0	0	0	0
V	213	203	213	203	211	190	210	182	211	209	185	225	210	184	217	151	201	203	213	197	209	182	267
Cr	260	240	453	333	443	233	221	218	224	204	214	248	278	205	230	155	492	241	240	605	858	568	236
Ni	120	107	121	118	130	65.4	114	76.7	65.9	110	64	110	119	75.7	103	71.3	171	86.1	101	192	139	115	84.9
Cu	113	84.3	66	57.8	67.8	51.6	47.4	54.3	41.2	57.4	44.5	50.7	50.9	67.7	53.4	64.3	46.9	53.6	56.2	60.7	62.6	62.7	71.6
Zn	206	92.1	130	106	136	68.1	72.6	86.7	69.2	89.4	67.7	67.7	79.1	70.6	90.4	76.9	127	77.1	76.9	130	110	116	62
Ga	12	16.1	15	13.7	14.9	15.7	14.3	15.3	16.1	13.6	14.3	13.9	14.7	16.4	15.6	17.2	14.3	14.9	13.8	13.3	14.4	15.9	10.7
As	1.72	2.15	2.35	1.89	2.86	1.72	1.46	2.33	1.76	1.36	1.77	1.07	0.885	2.21	1.56	2.83	1.44	1.96	2.46	0.836	6.13	6.29	0.669
Rb	5.02	71.1	49.5	47.6	49	62.1	48.5	63.9	63	45.8	61.9	45.8	50.8	66.4	55.2	69.9	46.5	59.8	52.4	43.7	17	69.6	6.51
Sr	35	540	400	404	401	505	447	513	484	412	449	450	421	506	464	528	413	480	421	383	251	557	74.4
Y	15	24.6	26.1	25.1	27.7	24	22.9	24.2	23.7	23	23	23.1	22.1	24	23.9	25.2	21.1	24.1	21.9	22	24.8	24.8	31.8
Zr	22.8	180	156	154	152	171	161	175	165	161	156	161	160	169	165	182	146	169	160	153	202	165	66.6
Nb	10.9	58.6	35.9	35	35	44.9	40.4	46.4	42	41.1	40.4	40.3	41.1	43.1	43	46.9	36.4	42.1	42	35.9	49.3	42.9	3.5
wt%																							
Na2O	0.98	3.52	2.82	2.84	2.94	2.82	2.79	2.88	2.95	2.55	2.53	2.33	2.71	3.45	2.83	3.24	2.19	2.86	2.96	2.43	0.63	2.78	3.14
MgO	11.27	4.53	4.6	5.46	4.82	3.1	5.66	3.94	3.71	5.43	3.02	5.81	6.3	3.12	5.01	2.48	6.99	4.4	5.28	8.49	6.8	3.26	7.67
Al2O3	13.94	15.64	16	15.89	15.93	17.31	16.3	16.32	16.51	15.13	15.35	16.37	15.75	17.15	16.03	17.59	15.47	16.2	15.54	14.83	16.76	16.83	11.14
SiO2	46.87	47.4	48.38	47.79	48.19	50.47	49.05	49.01	49.84	46.07	46.28	48.95	48.37	50.01	48.7	50.33	47.84	48.62	47.56	47.09	39.26	48.45	51.55
P2O5	0	0.42	0.48	0.41	0.43	0.44	0.4	0.4	0.42	0.4	0.45	0.41	0.37	0.41	0.41	0.42	0.36	0.38	0.39	0.36	0.1	0.39	0.01
K2O	0.32	2.81	2.11	2	1.98	3.09	2.21	2.71	2.95	2.28	2.87	2.14	2.14	3	2.31	3.18	1.86	2.54	2.29	1.77	0.71	2.95	0.32
CaO	8.79	9.85	9.85	9.83	10.03	9.18	10.34	8.3	9.92	9.11	8.69	10.53	9.66	8.88	10.15	6.75	10.11	8.97	9.07	9.49	9.56	6.8	7.19
TiO2	0.63	2.24	2.01	1.96	1.97	2.19	2.06	2.18	2.12	2.03	2.01	2.06	2.02	2.16	2.07	2.28	1.82	2.1	1.99	1.81	2.18	2.17	1.26
MnO	0.27	0.13	0.11	0.15	0.17	0.11	0.11	0.14	0.13	0.13	0.1	0.11	0.12	0.13	0.14	0.11	0.13	0.14	0.13	0.12	0.13	0.09	0.15
Fe2O3	11.25	8.65	9.58	8.78	9.39	7.99	7.79	9.61	8.26	7.85	7.49	7.84	8.52	7.71	8.83	8.22	8.93	9.03	9.69	8.76	11.78	10.4	13.44
Sub-Total	94.33	95.19	95.94	95.1	95.85	96.69	96.69	95.5	96.8	90.98	88.78	96.55	95.96	96.02	96.48	94.61	95.7	95.24	94.9	95.14	87.91	94.11	95.87
LOI	5.55	4.57	3.88	4.73	3.97	3.55	3.15	4.34	3.04	8.87	11.07	3.29	3.88	3.82	3.36	5.24	4.11	4.6	4.94	4.66	11.87	5.68	4.01
Total	99.88	99.76	99.82	99.83	99.82	99.84	99.84	99.84	99.84	99.85	99.85	99.84	99.84	99.84	99.84	99.85	99.81	99.84	99.84	99.8	99.78	99.79	99.88

Sample	101-D	102-C	103-E	104-D	116	126	129A	130	140	241	262	296	306	310	321	332	333	334	341	37	67	78
Campaign	MD110	MD110	MD110	MD110	MD110	MD110	MD110	MD110	MD110	MD110	MD110	MD110	MD110	MD110	MD110	MD110	MD110	MD110	MD110	MD110	MD110	MD110
Dredged point	DR03B	DR03B	DR03B	DR03B	DR04	DR04	DR04	DR04	DR04	DR08	DR08	DR09	DR10	DR10	DR11	DR11	DR11	DR11	DR11	DR02	DR01	DR01
Rock type	Basalt	Basalt	Gabbro	Gabbro	Basalt	Basalt	Basalt	Basalt	Basalt	Basalt	Basalt	Dolérite	Basalt	Basalt	Gabbro	Gabbro	Gabbro	Gabbro	Gabbro	Basalt	Basalt	Basalt
ppm																						
S	0	0	29.6	0	4.93	0	40.2	0	0	0	0	0	0	0	0	0	0	0	0	9.95	0	0
V	253	242	200	311	188	197	233	134	197	105	48.4	91.6	289	266	54.9	233	441	249	251	194	239	149
Cr	206	231	229	163	378	402	834	351	413	169	152	464	138	183	33.8	181	125	92.4	88.3	543	397	746
Ni	58.5	59.2	75.1	64.4	71.5	77.4	222	65.9	80.5	63.7	57.1	346	62.3	64.7	45.7	68.8	50	59.8	50	292	92.4	171
Cu	3.43	4.95	11.2	18.6	50.2	49.9	45.5	41.1	63.1	40.3	59	35.1	63.6	166	12.4	106	116	139	74.9	78.4	59.7	104
Zn	25.8	25.5	47.9	36.4	79.4	113	72.1	50.3	79.1	57.7	48.8	30.3	107	107	73.1	78.3	131	89.5	108	218	125	255
Ga	19.8	18.6	15.7	19.5	17.1	17.2	13.8	15.7	15.8	15	15.1	12.4	17.7	15.2	26.2	12.4	18.7	14.2	16.9	18.8	17	14.4
As	0.883	0.891	3.05	4.41	0.337	2	0.09	0.553	1.04	0.55	1.15	0.284	1.23	5.73	3.97	0.745	4.07	0.868	5.32	10.5	3	0.947
Rb	4.76	5.73	6.41	3.91	8.93	9.22	5.54	6.33	7.45	8.07	27.7	12.4	27.9	13.5	15.2	17.7	64.6	17.5	12.4	10.3	35.5	20.3
Sr	206	197	185	231	168	168	145	157	142	219	214	409	119	122	429	103	164	110	272	240	141	146
Y	30.8	29.7	13.2	32.9	24.6	27.7	33.9	15.4	27.1	10.3	9.25	1.04	34.5	31.5	24.8	17.4	35.6	21.9	26.1	25.3	36.8	20
Zr	107	103	12.5	87.7	77.1	81.8	97.2	41.6	70	37.5	37.2	0	107	84.8	166	36.6	125	50.7	98.4	82	114	63.4
Nb	14.9	14.2	11.6	13.5	13.6	4.03	5.97	12.3	13.5	4.22	12.9	11.9	10.5	6.87	12	12.2	4.67	3.59	6.05	10.5	6.87	11.9
wt%																						
Na2O	2.36	2.83	2.25	3.22	2.42	2.74	2.3	2.52	2.42	1.98	2.45	3.28	2.66	2.28	5.17	1.9	2.23	2.48	3.31	2.48	3.12	2.77
MgO	7.89	7.65	8.59	6.05	5.24	4.24	9.24	4.8	6.22	3.83	0.83	6	5.36	7.3	3.65	6.53	4.54	6.49	6.41	6.95	5.27	5.35
Al2O3	14.04	14.42	14.52	15.69	17.98	18.12	14.11	20.69	16.48	22.06	23.35	20.64	14.56	13.93	19.77	14.26	13.59	13.66	14.19	14.73	15.82	17.04
SiO2	49.96	49.91	49.46	49.94	48.58	48.47	47.9	48.34	48.12	49.16	50.13	52.27	49.28	48.34	56.83	50.55	49.15	49.53	49.93	45.77	49.66	48.21
P2O5	0.07	0.06	0	0.38	0.01	0.02	0.03	0	0.01	0	0.04	0	0.05	0.05	0.37	0	0.08	0	0.03	0.1	0.05	0
K2O	0.26	0.29	0.27	0.32	0.34	0.47	0.26	0.28	0.36	0.42	1.56	0.63	0.99	0.57	0.68	0.42	0.77	0.56	0.6	0.49	0.8	0.77
CaO	11.42	10.99	11.86	11.09	12.83	11.98	10.86	14.36	12.73	14.75	11.48	11.88	10.36	8.09	6.92	11.49	8.44	10.37	7.51	7.88	9.88	8
TiO2	1.67	1.6	0.86	1.87	1.31	1.4	1.55	0.82	1.24	0.68	0.67	0.24	1.69	1.46	0.25	0.83	2.61	0.98	1.38	1.47	1.84	1.07
MnO	0.12	0.13	0.14	0.12	0.1	0.13	0.18	0.09	0.12	0.07	0.08	0.07	0.23	0.19	0.07	0.18	0.23	0.21	0.21	0.16	0.15	0.14
Fe2O3	10.38	10.27	9.78	9.89	8.63	9.25	11.25	6.14	8.96	4.82	4.76	3.79	11.82	13.39	5.32	11.97	16.27	13.37	13.38	13.29	10.13	11.05
Sub-Total	98.18	98.14	97.73	98.58	97.43	96.83	97.67	98.04	96.66	97.77	95.35	98.8	96.98	95.6	99.05	98.14	97.9	97.64	96.94	93.32	96.72	94.4
LOI	1.71	1.75	2.17	1.31	2.45	3.04	2.14	1.86	3.22	2.15	4.36	1.98	2.9	4.27	1.83	1.75	1.95	2.25	2.94	6.49	3.14	5.41
Total	99.89	99.89	99.9	99.89	99.88	99.87	99.81	99.9	99.88	99.92	99.71	100.78	99.88	99.87	100.88	99.89	99.85	99.89	99.88	99.81	99.86	99.81

Table S5 - Trace elements compositions of bulk rocks

Spectrum	E1-4	C4	C3	B8	B6	B5	B3	B17	B16	B14	A9	A5	A33-1	A29	A27	A24	A23
Campaign	MD80	MD80	MD80	MD80	MD80	MD80	MD80	MD80	MD80	MD80	MD80	MD80	MD80	MD80	MD80	MD80	MD80
Dredged point	DR5	DR5	DR5	DR5	DR5	DR5	DR5	DR5	DR5	DR5	DR5	DR5	DR5	DR5	DR5	DR5	DR5
Rock type	Basalt	Basalt	Basalt	Basalt	Basalt	Basalt	Basalt	Basalt	Basalt	Basalt	Basalt	Basalt	Basalt	Basalt	Basalt	Basalt	Basalt
ppm																	
Li	58.38	23.00	43.18	51.80	51.82	12.00	48.05	27.28	13.55	54.52	11.83	57.12	60.78	13.59	35.74	21.17	55.75
P	NaN	NaN	NaN	NaN	NaN	NaN	NaN	NaN	NaN	NaN	NaN	NaN	NaN	NaN	NaN	NaN	NaN
Sc	49.72	38.31	45.83	38.24	33.49	39.01	44.17	36.28	39.11	37.94	33.24	44.26	36.64	39.96	36.01	41.71	39.17
Ti	3706.50	13024.60	13650.84	11857.63	11553.34	13086.51	13078.80	12372.32	12422.48	12546.84	10968.24	13563.54	12650.60	13620.97	11657.82	14197.28	13049.58
V	277.53	204.19	276.17	227.59	213.12	198.62	263.95	133.85	220.65	247.02	97.21	251.47	237.86	203.56	166.48	152.21	260.88
Cr	213.63	230.97	194.79	244.29	348.22	198.99	376.29	184.72	281.08	187.45	191.12	253.42	176.88	157.22	212.46	154.67	1051.21
Mn	2153.91	1202.68	1271.10	1246.66	1631.58	1249.67	1239.51	1159.48	1360.15	1390.12	715.16	1107.76	1408.29	1430.57	988.49	1265.28	1677.45
Co	56.55	60.45	46.93	43.87	44.67	35.32	51.22	37.51	35.15	44.74	34.22	55.13	50.41	49.18	43.81	36.15	48.53
Ni	136.84	98.92	146.07	117.44	154.52	64.21	150.78	74.14	70.49	123.91	61.03	133.56	144.56	90.02	101.85	77.11	164.98
Cu	141.48	79.79	93.58	78.44	99.10	68.47	82.54	67.02	60.50	77.79	57.27	80.02	78.03	99.85	64.64	86.36	105.20
Zn	215.98	94.39	149.20	86.18	159.18	82.56	88.10	96.26	80.43	101.65	68.14	86.85	95.91	88.58	100.00	91.93	165.47
As	1.14	1.72	4.46	1.29	3.83	2.56	1.60	2.28	2.14	1.59	1.82	1.30	1.35	1.91	1.82	2.46	3.65
Se	0.38	0.20	0.24	0.29	0.32	0.14	0.24	0.18	0.11	0.15	0.03	0.24	0.25	0.22	0.28	0.07	0.26
Rb	5.87	68.94	57.03	50.70	56.16	63.29	57.94	66.66	67.05	49.95	61.94	57.02	61.08	72.86	57.15	73.67	59.13
Sr	37.81	631.09	520.16	504.28	472.50	621.08	533.98	594.02	580.39	469.16	518.70	545.93	544.40	645.52	500.51	618.28	497.45
Y	15.30	26.90	33.09	24.51	29.23	26.39	28.34	25.33	25.73	26.27	24.88	29.29	26.42	28.09	26.62	27.18	32.00
Zr	26.84	194.63	202.37	174.37	174.87	191.23	201.29	188.73	182.72	192.91	161.94	208.28	196.34	206.51	180.05	207.77	191.56
Nb	1.36	51.00	40.64	43.55	39.12	50.51	50.20	50.02	48.18	48.60	42.04	51.15	53.15	53.64	45.59	54.99	43.41
Mo	<LOD	1.93	2.25	1.50	3.34	1.49	2.47	2.03	1.45	1.72	0.91	2.54	2.42	2.37	2.15	2.08	3.62
Ag	0.00	0.05	0.03	0.04	0.04	0.06	0.05	0.04	0.04	0.05	0.05	0.04	0.04	0.09	0.05	0.04	0.09
Sn	0.02	1.77	1.83	1.81	1.64	1.77	1.91	1.81	1.72	1.95	1.51	1.87	1.98	1.91	1.77	2.06	1.79
Sb	0.38	0.70	0.92	0.24	0.84	0.65	0.25	0.65	0.58	0.36	0.64	0.25	0.30	0.65	0.35	0.91	0.84
Ba	35.91	802.06	633.47	631.74	607.78	787.61	695.67	773.12	719.74	639.17	699.14	722.25	709.53	788.83	696.11	789.76	651.22
La	1.51	34.55	31.88	28.32	29.02	33.38	34.48	31.84	31.96	31.58	29.60	35.35	34.62	35.12	31.39	34.56	32.81
Ce	3.01	68.20	61.23	56.95	52.89	64.89	68.53	61.63	62.57	62.35	55.91	69.52	67.17	68.92	60.61	67.35	59.65
Pr	0.55	8.12	7.97	7.02	6.92	8.02	8.26	7.52	7.74	7.68	6.82	8.29	8.06	8.37	7.50	8.25	7.82
Nd	3.09	31.50	32.38	28.19	28.35	31.50	32.56	29.79	30.25	30.42	26.85	32.81	31.17	32.75	29.27	32.57	31.43
Sm	1.16	6.27	6.84	5.78	5.96	6.40	6.65	6.02	6.18	6.25	5.35	6.54	6.18	6.68	5.88	6.64	6.65
Eu	0.43	2.10	2.19	1.88	1.95	2.14	2.12	1.99	2.01	1.95	1.78	2.10	1.99	2.19	1.90	2.14	2.17
Gd	1.77	5.75	6.66	5.43	5.87	5.95	6.07	5.63	5.79	5.77	5.08	6.09	5.70	6.14	5.56	6.11	6.40
Tb	0.35	0.87	1.01	0.82	0.89	0.88	0.92	0.84	0.86	0.87	0.75	0.92	0.85	0.93	0.82	0.92	0.97
Dy	2.45	5.07	5.99	4.74	5.09	5.08	5.34	4.82	4.99	4.99	4.43	5.36	4.90	5.31	4.88	5.23	5.66
Ho	0.56	1.00	1.18	0.95	1.06	1.02	1.06	0.98	1.01	1.00	0.89	1.06	0.98	1.05	0.95	1.05	1.15
Er	1.66	2.68	3.22	2.45	2.74	2.61	2.85	2.59	2.54	2.56	2.40	2.87	2.57	2.74	2.63	2.63	3.02
Tm	0.26	0.39	0.47	0.36	0.40	0.38	0.42	0.38	0.38	0.37	0.35	0.42	0.38	0.40	0.38	0.40	0.44
Yb	1.76	2.48	2.91	2.27	2.56	2.46	2.64	2.39	2.41	2.42	2.22	2.63	2.45	2.59	2.38	2.51	2.82
Lu	0.27	0.37	0.44	0.34	0.38	0.35	0.39	0.35	0.35	0.35	0.33	0.39	0.35	0.38	0.36	0.37	0.42
Hf	0.78	4.28	4.60	4.12	3.94	4.41	4.49	4.32	4.25	4.35	3.72	4.58	4.24	4.59	4.10	4.70	4.23
Ta	0.09	2.98	2.42	2.54	2.26	2.92	2.94	2.82	2.75	2.78	2.36	2.98	3.04	3.05	2.55	3.13	2.51
Au	0.00	0.00	0.00	0.00	0.01	0.00	0.00	0.00	0.00	0.00	0.00	0.00	0.00	0.00	0.00	0.00	0.00
Tl	0.28	0.19	0.37	0.22	0.43	0.19	0.21	0.41	0.15	0.26	0.17	0.16	0.23	0.25	0.24	0.47	0.46
Pb	0.59	3.03	2.94	2.28	3.10	2.73	2.89	2.70	2.79	2.73	2.47	2.64	2.84	2.94	2.45	2.93	3.39
Bi	0.01	0.01	0.01	0.01	0.01	0.01	0.01	0.01	0.01	0.01	0.01	0.01	0.01	0.01	0.01	0.01	0.01
Th	0.24	3.59	2.92	3.14	2.97	3.49	3.59	3.56	3.40	3.36	3.01	3.60	3.69	3.62	3.34	3.71	3.03
U	0.06	1.14	0.73	0.82	0.76	0.97	1.00	1.14	0.92	0.95	0.89	0.97	1.02	1.21	0.94	1.32	0.77

Spectrum	A2	A15	7E1	7C1	7A7	3F	101-D	102-C	103-E	104-D	116	126	129A	130	140	241	262
Campaign	MD80	MD80	MD80	MD80	MD80	MD80	MD110	MD110	MD110	MD110	MD110	MD110	MD110	MD110	MD110	MD110	MD110
Dredged point	DR5	DR5	DR7	DR7	DR7	DR3	DR03B	DR03B	DR03B	DR03B	DR04	DR04	DR04	DR04	DR04	DR08	DR08
Rock type	Basalt	Basalt	Basalt	Basalt	Basalt	Basalt	Basalt	Basalt	Gabbro	Gabbro	Basalt	Basalt	Basalt	Basalt	Basalt	Basalt	Basalt
ppm																	
Li	30.29	47.03	80.22	119.00	48.32	20.62	5.01	4.66	5.33	3.07	37.18	26.14	20.28	24.88	39.23	17.37	20.33
P	NaN	NaN	NaN	NaN	NaN	NaN	1050.79	946.39	303.95	1830.60	591.00	621.48	687.35	246.84	495.18	546.81	826.94
Sc	33.95	37.65	36.36	36.51	38.69	51.33	47.09	47.10	57.53	56.48	21.25	26.92	36.37	<LOD	17.87	<LOD	<LOD
Ti	11353.09	12355.25	11759.31	12027.84	12546.65	9685.26	12413.41	9017.70	5376.19	9626.27	7851.23	8686.88	9765.23	4741.78	6942.23	4485.20	4538.12
V	95.12	249.32	208.68	177.23	193.03	374.92	327.91	323.50	236.16	334.72	208.65	218.42	260.73	141.01	209.19	107.27	47.85
Cr	158.91	222.01	296.27	432.98	230.43	194.91	240.46	232.00	161.59	121.17	260.39	477.48	1695.82	234.06	314.36	115.24	108.22
Mn	961.53	1464.46	1223.50	1109.07	1220.59	1481.56	573.45	513.29	1109.56	1029.89	904.05	1029.47	1339.15	719.07	941.24	626.61	728.03
Co	38.98	39.44	55.20	41.96	39.50	54.59	49.21	47.19	48.06	42.29	27.12	32.51	53.57	23.11	33.81	21.57	21.67
Ni	83.22	112.73	225.73	137.07	128.14	94.37	63.16	63.06	71.37	58.99	58.95	69.36	258.05	52.57	71.36	46.03	39.88
Cu	65.78	80.68	80.24	69.28	82.48	93.86	9.85	11.68	14.02	26.37	58.51	65.86	63.65	51.42	77.55	50.15	70.38
Zn	79.24	87.95	153.00	116.35	126.53	66.49	<LOD	<LOD	37.74	29.04	64.03	105.68	78.06	50.25	72.20	53.70	43.31
As	1.74	3.20	1.52	10.98	7.76	1.45	1.47	1.42	2.80	4.61	0.77	2.66	0.27	0.44	1.27	0.58	1.16
Se	0.29	0.21	0.55	0.57	0.19	0.00	0.15	0.12	0.15	0.11	0.13	0.20	0.20	0.60	0.60	0.18	0.36
Rb	59.87	57.87	47.89	17.06	73.58	6.49	4.49	4.97	5.87	3.21	6.77	7.83	5.06	4.62	6.50	5.89	24.21
Sr	542.11	525.19	443.28	245.54	679.45	75.11	242.05	240.05	185.38	234.53	164.41	164.63	154.91	146.08	138.45	200.67	196.33
Y	24.71	25.45	25.73	21.99	26.62	34.75	34.84	33.57	15.96	33.18	24.65	26.84	32.71	15.71	24.43	12.90	12.10
Zr	175.52	187.31	187.30	185.57	181.25	55.93	138.17	85.85	18.98	40.97	76.16	82.60	102.17	40.67	66.97	39.27	38.94
Nb	45.34	48.27	42.92	46.20	45.87	3.09	19.61	15.31	1.00	11.25	3.87	4.33	8.10	1.95	3.52	4.04	3.99
Mo	2.10	3.28	<LOD	<LOD	0.39	<LOD	<LOD	<LOD	0.14	<LOD	<LOD	0.12	0.73	<LOD	<LOD	<LOD	0.84
Ag	0.05	0.04	0.03	0.04	0.05	0.00	0.04	0.04	0.02	0.03	0.03	0.03	0.05	0.02	0.03	0.02	0.02
Sn	1.67	1.81	1.64	1.84	1.81	1.63	0.91	1.00	0.29	0.78	0.94	0.74	1.10	0.62	0.73	0.30	0.42
Sb	0.46	0.60	0.24	1.83	1.59	0.22	0.18	0.14	0.54	0.66	0.18	0.69	0.13	0.06	0.15	0.19	0.47
Ba	660.56	689.72	611.56	77.24	736.43	17.24	99.70	115.19	63.07	78.50	23.09	46.28	85.38	11.93	18.27	38.57	51.55
La	29.81	31.67	27.53	29.29	29.59	3.25	8.42	9.75	2.64	14.09	4.68	5.34	7.60	2.14	4.32	3.86	3.54
Ce	57.84	62.26	54.25	49.50	58.69	10.09	20.86	21.81	5.18	25.29	12.05	12.40	18.03	6.24	10.16	8.60	8.47
Pr	7.06	7.51	6.72	6.60	7.32	1.83	3.01	3.07	0.82	3.33	1.83	1.88	2.56	0.89	1.56	1.11	1.08
Nd	27.60	29.48	27.33	26.50	29.42	9.98	14.70	14.94	4.37	15.55	9.22	9.71	12.52	4.80	8.20	5.30	5.06
Sm	5.58	5.96	5.64	5.46	6.27	3.52	4.34	4.32	1.65	4.51	2.97	3.08	3.89	1.51	2.51	1.45	1.39
Eu	1.79	1.94	1.83	1.69	2.05	1.41	1.56	1.52	0.89	1.41	1.09	1.18	1.33	0.69	1.01	0.66	0.65
Gd	5.13	5.47	5.43	5.04	5.89	5.00	5.66	5.43	2.26	5.68	3.83	4.09	4.90	1.90	3.32	1.62	1.62
Tb	0.77	0.82	0.82	0.76	0.88	0.92	0.97	0.92	0.45	0.98	0.70	0.74	0.89	0.39	0.63	0.33	0.33
Dy	4.54	4.78	4.67	4.40	5.07	6.09	6.14	5.80	3.02	6.11	4.49	4.78	5.70	2.73	4.10	2.35	2.29
Ho	0.89	0.96	0.95	0.88	1.02	1.35	1.28	1.22	0.61	1.21	0.91	0.98	1.20	0.60	0.90	0.51	0.48
Er	2.47	2.43	2.49	2.30	2.57	3.70	3.69	3.48	1.64	3.39	2.59	2.78	3.46	1.68	2.51	1.32	1.24
Tm	0.35	0.37	0.36	0.34	0.38	0.56	0.56	0.51	0.24	0.48	0.38	0.41	0.51	0.24	0.37	0.19	0.18
Yb	2.25	2.36	2.33	2.15	2.40	3.69	3.44	3.20	1.53	3.03	2.54	2.61	3.33	1.34	2.15	1.06	1.01
Lu	0.34	0.34	0.33	0.31	0.35	0.55	0.52	0.47	0.22	0.43	0.36	0.38	0.49	0.20	0.34	0.15	0.14
Hf	3.97	4.16	4.21	4.16	4.17	2.08	3.49	2.49	0.73	1.63	2.11	2.28	2.83	1.11	1.80	1.04	1.03
Ta	2.52	2.75	2.44	2.52	2.64	0.22	1.10	0.84	0.06	0.59	0.21	0.25	0.46	0.11	0.20	0.25	0.24
Au	0.00	0.00	0.00	0.00	0.00	0.00	0.00	0.00	0.00	0.00	0.00	0.00	0.00	0.00	0.00	0.00	0.00
Tl	0.37	0.38	0.11	0.08	0.13	0.30	0.03	0.03	0.05	0.07	0.02	0.05	0.40	0.01	0.04	0.04	0.21
Pb	2.49	2.80	2.01	2.30	2.45	<LOD	<LOD	<LOD	-0.44	<LOD	0.24	<LOD	0.27	<LOD	<LOD	<LOD	0.24
Bi	0.01	0.01	0.01	0.01	0.01	0.01	0.00	0.00	0.00	0.00	0.00	0.00	0.00	0.00	0.00	0.00	0.00
Th	3.28	3.30	2.97	3.08	3.21	0.40	1.47	1.30	0.09	0.71	0.35	0.38	0.79	0.14	0.26	0.31	0.29
U	0.98	0.98	0.72	0.61	1.11	0.12	0.36	0.22	0.11	0.17	0.09	0.16	0.17	0.04	0.08	0.17	0.13

Spectrum	296	306	310	321	332	333	334	341	37	67	78
Campaign	MD110	MD110	MD110	MD110	MD110	MD110	MD110	MD110	MD110	MD110	MD110
Dredged point	DR09	DR10	DR10	DR11	DR11	DR11	DR11	DR11	DR02	DR01	DR01
Rock type	Dolérite	Basalt	Basalt	Gabbro	Gabbro	Gabbro	Gabbro	Gabbro	Basalt	Basalt	Basalt
ppm											
Li	6.17	29.42	18.59	11.32	11.25	7.12	16.48	14.63	68.08	45.09	78.75
P	-42.44	818.40	648.86	1498.33	324.16	787.11	368.71	934.60	1527.25	996.17	618.20
Sc	2.23	58.00	45.10	<LOD	85.23	104.58	152.37	51.98	29.03	52.85	36.46
Ti	2999.76	10212.08	7015.08	2271.05	4831.21	9064.46	5366.80	10177.37	9647.04	10151.57	6276.06
V	114.72	334.46	266.81	37.58	288.38	389.44	340.10	301.76	255.13	313.50	195.19
Cr	388.60	109.41	107.85	16.37	101.74	76.43	55.67	114.09	335.00	273.61	370.36
Mn	677.86	1672.96	1319.28	657.79	1475.20	1542.43	1752.00	1576.40	1097.49	1088.72	641.83
Co	23.88	52.19	41.65	12.84	52.37	44.46	58.07	45.21	66.83	41.01	55.88
Ni	325.49	60.65	59.29	30.33	67.27	48.98	62.05	45.25	373.27	106.71	202.88
Cu	38.87	85.06	176.25	21.62	131.37	131.37	156.37	72.79	105.78	87.07	137.93
Zn	19.14	111.75	92.92	71.63	88.88	123.05	108.20	92.75	351.86	129.18	353.14
As	0.87	1.21	5.36	0.53	0.78	4.42	0.70	4.98	20.25	3.80	9.08
Se	0.11	0.11	0.80	1.17	1.00	1.13	0.24	<LOD	0.16	0.28	0.18
Rb	10.97	26.91	13.79	13.64	14.71	51.37	14.95	10.64	12.11	41.34	24.18
Sr	392.21	121.01	113.25	428.82	108.12	172.01	105.46	234.84	271.68	181.38	188.71
Y	6.05	35.52	25.68	20.57	19.89	31.65	25.71	32.21	28.40	45.68	21.69
Zr	9.69	106.59	66.68	47.26	40.77	115.19	55.50	108.48	96.94	162.71	72.22
Nb	0.22	10.36	4.82	1.43	2.67	3.06	3.51	12.87	13.91	6.20	1.53
Mo	<LOD	1.19	<LOD	<LOD	0.07	1.19	0.55	0.45	1.31	<LOD	1.66
Ag	0.11	0.04	0.03	0.02	0.03	0.05	0.02	0.04	0.01	0.02	0.01
Sn	0.21	1.18	0.72	1.21	0.19	0.87	0.29	1.10	1.77	1.46	1.00
Sb	0.14	0.60	0.50	0.02	0.12	0.51	0.12	0.49	2.45	0.93	1.89
Ba	122.15	180.02	142.89	308.57	96.02	163.09	107.29	223.42	55.93	75.14	24.76
La	1.37	9.22	5.47	28.46	3.43	7.57	5.41	9.57	10.60	7.33	3.63
Ce	3.17	20.19	13.70	62.15	8.65	21.21	13.11	24.90	20.48	18.79	8.56
Pr	0.36	2.80	1.95	6.73	1.11	2.99	1.74	3.37	2.96	3.07	1.43
Nd	1.79	13.24	9.84	26.48	5.64	14.45	8.41	15.88	13.38	15.53	7.32
Sm	0.64	3.95	2.80	4.77	1.64	3.86	2.34	4.26	3.93	5.26	2.39
Eu	0.52	1.29	0.95	1.34	0.70	1.41	0.87	1.50	1.49	1.79	1.07
Gd	0.85	5.22	3.52	4.11	2.13	4.68	3.13	4.99	4.86	6.75	3.29
Tb	0.19	0.96	0.67	0.63	0.44	0.84	0.61	0.90	0.80	1.20	0.61
Dy	1.42	6.13	4.48	3.67	3.14	5.50	4.15	5.81	4.88	7.57	3.90
Ho	0.26	1.30	0.98	0.76	0.75	1.19	0.96	1.21	0.99	1.61	0.84
Er	0.59	3.71	2.78	2.01	2.18	3.37	2.79	3.33	2.75	4.82	2.40
Tm	0.10	0.56	0.40	0.26	0.32	0.49	0.42	0.50	0.40	0.72	0.36
Yb	0.60	3.62	2.37	1.27	1.89	3.00	2.55	3.02	2.39	4.58	2.25
Lu	0.08	0.51	0.36	0.18	0.32	0.48	0.42	0.43	0.36	0.67	0.31
Hf	0.39	3.02	1.87	1.31	1.16	2.92	1.55	3.01	2.31	4.03	1.80
Ta	0.02	0.59	0.27	0.08	0.15	0.19	0.19	0.73	0.75	0.38	0.10
Au	0.00	0.00	0.00	0.00	0.00	0.00	0.00	0.00	0.00	0.00	<LOD
Tl	0.15	0.32	0.33	0.11	0.03	0.47	0.07	0.10	0.50	0.67	0.35
Pb	0.17	0.86	<LOD	13.83	0.19	1.92	0.75	2.99	0.83	2.41	<LOD
Bi	0.00	0.01	0.01	0.01	0.00	0.01	0.01	0.01	0.01	0.02	0.01
Th	0.02	1.10	0.50	0.92	0.38	0.90	0.61	1.65	1.08	0.94	0.16
U	0.04	0.49	0.55	0.34	0.24	0.52	0.18	0.40	0.74	0.78	0.36

Université de Strasbourg

Mélanie Ballay

École doctorale Sciences de la terre et de l'environnement | ED 413 Université de Strasbourg

Étude pétrologique et géochimique d'une marge passive pauvre en magma : le cas de la transition océan-continent Australie-Antarctique

Résumé

Les marges passives représentent la transition intraplaque entre un domaine lithosphérique continental et un domaine lithosphérique océanique. Elles enregistrent l'arrivée des premiers produits magmatiques lors de l'océanisation et constituent ainsi de véritables archives spatio-temporelles de la rupture continentale et l'initiation de l'accrétion océanique. Pourtant, les études des marges riftées peu magmatiques sont limitées à quelques rares endroits géographiques dont les marges actuelles conjuguées d'Ibérie-Terre-Neuve et les paléo-marges téthysiennes présentes dans les Alpes. Cette thèse explore les processus complexes de la transition entre la lithosphère continentale et la lithosphère océanique au niveau de la zone Diamantine, marge passive pauvre en magma située au sud-ouest de l'Australie. Les résultats s'appuient sur des données pétrologiques et géochimiques issues de l'analyse d'échantillons dragués par les campagnes MD80 et MD110. Ils permettent de souligner l'importance de l'héritage mantellique dans la formation de ces zones, tant sur le budget magmatique des marges pauvres en magma que sur la nature des produits magmatiques émis, ainsi que des processus d'interactions liquides magmatiques et roche (i.e. refertilisation).

Mots clés : marge passive pauvre en magma, manteau sous-continental hérité, refertilisation, basaltes, zone Diamantine.

Abstract

Rifted margins represent the intraplate transition between a continental lithospheric domain and an oceanic lithospheric domain. They record the first occurrence of magmatic products during oceanization and are therefore exceptional space-time archives recording continental breakup and onset of seafloor spreading. However, studies of magma-poor rifted margins are limited to a few geographical locations, including the present-day conjugate Iberia and Newfoundland rifted margins and the Tethyan paleomargins exposed the Alps in Western Europe. This thesis explores the complex processes involved in the transition from continental to oceanic lithosphere in the Diamantina Zone, a magma-poor rifted margin in south-western Australia. The results are based on petrological and geochemical data derived from the analysis of samples dredged during the MD80 and MD110 campaigns and highlight the importance of the mantle inheritance during crustal breakup and formation of new oceanic crust, both in terms of the effect on the magma budget of magma-poor rifted margins and the nature of the magma products released, as well as the processes of magma-liquid-rock interactions (i.e. refertilisation).

Key words: magma-poor rifted margin, inherited sub-continental mantle, refertilisation, basalts, Diamantina zone.